

Tsuguo Fukuda  
Valery I. Chani  
*Editors*

ADVANCES IN MATERIALS RESEARCH 8

# Shaped Crystals

Growth by Micro-Pulling-Down Technique

 Springer



# advances in materials research

---

*Series Editor-in-Chief:* Y. Kawazoe

*Series Editors:* M. Hasegawa A. Inoue N. Kobayashi T. Sakurai L. Wille

The series *Advances in Materials Research* reports in a systematic and comprehensive way on the latest progress in basic materials sciences. It contains both theoretically and experimentally oriented texts written by leading experts in the field. *Advances in Materials Research* is a continuation of the series *Research Institute of Tohoku University (RITU)*.

- 1 **Mesoscopic Dynamics of Fracture**  
Computational Materials Design  
Editors: H. Kitagawa, T. Aihara, Jr., and Y. Kawazoe
  - 2 **Advances in Scanning Probe Microscopy**  
Editors: T. Sakurai and Y. Watanabe
  - 3 **Amorphous and Nanocrystalline Materials**  
Preparation, Properties, and Applications  
Editors: A. Inoue and K. Hashimoto
  - 4 **Materials Science in Static High Magnetic Fields**  
Editors: K. Watanabe and M. Motokawa
  - 5 **Structure and Properties of Aperiodic Materials**  
Editors: Y. Kawazoe and Y. Waseda
  - 6 **Fiber Crystal Growth from the Melt**  
Editors: T. Fukuda, P. Rudolph, and S. Uda
  - 7 **Advanced Materials Characterization for Corrosion Products  
Formed on the Steel Surface**  
Editors: Y. Waseda and S. Suzuki
  - 8 **Shaped Crystals**  
Growth by Micro-Pulling-Down Technique  
Editors: T. Fukuda and V.I. Chani
-

T. Fukuda V.I. Chani (Eds.)

---

# Shaped Crystals

Growth by Micro-Pulling-Down Technique

With 254 Figures and 20 Tables

Prof. Tsuguo Fukuda  
Prof. Valery I. Chani  
Tohoku University  
2-1-1 Katahira, Aoba-ku  
Sendai 980-8577, Japan  
e-mail: t-fukuda@tagen.tohoku.ac.jp  
chani@tagen.tohoku.ac.jp

*Series Editor-in-Chief:*

Professor Yoshiyuki Kawazoe  
Institute for Materials Research, Tohoku University  
2-1-1 Katahira, Aoba-ku, Sendai 980-8577, Japan

*Series Editors:*

Professor Masayuki Hasegawa  
Professor Akihisa Inoue  
Professor Norio Kobayashi  
Professor Toshio Sakurai  
Institute for Materials Research, Tohoku University  
2-1-1 Katahira, Aoba-ku, Sendai 980-8577, Japan

Professor Luc Wille  
Department of Physics, Florida Atlantic University  
777 Glades Road, Boca Raton, FL 33431, USA

Library of Congress Control Number: 2007922726

ISSN 1435-1889

ISBN 978-3-540-71294-7 Springer Berlin Heidelberg New York

This work is subject to copyright. All rights are reserved, whether the whole or part of the material is concerned, specifically the rights of translation, reprinting, reuse of illustrations, recitation, broadcasting, reproduction on microfilm or in any other way, and storage in data banks. Duplication of this publication or parts thereof is permitted only under the provisions of the German Copyright Law of September 9, 1965, in its current version, and permission for use must always be obtained from Springer. Violations are liable for prosecution under the German Copyright Law.

Springer is a part of Springer Science+Business Media

springer.com

© Springer-Verlag Berlin Heidelberg 2007

The use of general descriptive names, registered names, trademarks, etc. in this publication does not imply, even in the absence of a specific statement, that such names are exempt from the relevant protective laws and regulations and therefore free for general use.

Typesetting and Production: LE-TeX Jelonek, Schmidt & Vöckler GbR, Leipzig

Cover: eStudio Calmar Steinen

Printed on acid-free paper SPIN 1188870 57/3180/YL - 5 4 3 2 1 0

# Preface

Crystal growth is one of the basic disciplines of materials science, which determines progress, industrial development, and the transfer of various fundamental ideas from sophisticated mathematical equations and original hypotheses to our daily life. A number of crystal growth techniques were developed during the last century. Most of these are well known not only to materials scientists, but also to chemists, physicists and engineers. Crystal growth methods such as Czochralski, Bridgman, and floating zone are widely practiced in research and industry and are considered to be classic technologies from both fundamental and practical points of view. These techniques are well described in the literature and are the subject of many scientific publications distributed around the world.

On the other hand, some systems that permit the crystallization process and the growth of single crystalline materials to be controlled are relatively innovative and exotic compared to the conventional crystal growth procedures listed above. This is the case for the pulling-down technique and/or the micro-pulling-down technique ( $\mu$ -PD), which has undergone intensive development since 1994. The growth and characterization of numerous crystals, including very popular ones as Si, LiNbO<sub>3</sub>, Y<sub>3</sub>Al<sub>5</sub>O<sub>12</sub>, and Al<sub>2</sub>O<sub>3</sub> (sapphire), have been demonstrated during this period. The technique itself has also been greatly modified in terms of, for example, the development of apparatus, the accurate control of parameters, and the methodology employed. This has been achieved through a great deal of coeducation and collaboration between academic research groups and their industrial partners. Most of these partnerships have been international in nature. As a result, crystal growth by the  $\mu$ -PD method has become established technique in a number of universities, national research institutions and industrial companies in Japan, France, Germany, Italy, Korea, Brazil, and Poland. Most of these research communities are represented by contributors to this book.

An anthology of review articles on fiber crystal growth and the  $\mu$ -PD technique was recently published [Fukuda T, Rudolph P, Uda S (eds) (2004) Fiber crystal growth from the melt (Advances in Materials Research). Springer, Berlin]. That book provides a preliminary overview of the fundamentals and practice of  $\mu$ -PD fiber crystal growth based on the results obtained and reported in the scientific literature before the year 2000. However, the method has developed considerably since 2000, both technically and methodologically.

A number of new materials that could not be grown at that time are now routinely produced using this technique in universities and industrial laboratories. It is believed that the current stage of development of this technology is associated with its commercialization.

The idea behind the book you are currently reading was to systematically describe all of the advantages and abilities of this method. Special attention was paid to the controlled growth of a whole range of shaped crystals (from ultrathin 50- $\mu\text{m}$ -diameter fibers to bulk macro crystals with well controlled shape and cross-sections of up to 20 mm). It is hoped that this book will further increase the popularity, reputation, and spread of this crystal growth process and support its development still further.

The authors of this volume tried to avoid extremely complicated fundamental speculations that require specialized knowledge and in-depth consideration. The book was intended to be a practical introduction to  $\mu$ -PD for material scientists (who are often not crystal growers). Thus, comparatively complex theoretical discussions were not included in this volume to make it easier to read and understand (although such discussions can be found in the book noted above if required). A considerable number of illustrations have also been included to aid understanding. Where possible, the reader is also referred to papers published in scientific journals, proceedings of conferences and meetings, and other scientific resources for more detailed discussions of the subjects of interest.

The book is mainly targeted at individuals who want to understand the basics of this crystal growth method and its ability to control specific physical properties of crystals, including shape. Therefore, a variety of practical examples of crystals grown by  $\mu$ -PD and the properties of these materials are presented in detail. The crystals produced with  $\mu$ -PD technology are often compared with those produced with other conventional melt growth processes in order to highlight the pros and cons of applying the  $\mu$ -PD method of crystal growth.

The first part of the book (Chaps. 1–4) provides a general review of the  $\mu$ -PD method: its history, the basic principles involved, the design of the equipment employed, and a general comparison of  $\mu$ -PD with related melt growth techniques. A basic analysis of segregation phenomena and the dimensional limits of the crystals available is also given. Since this is obviously the introductory part of the book, it is particularly relevant to those readers who are not familiar with  $\mu$ -PD as well as those who wish to gain a basic understanding of the fundamentals of the method.

Chapters 5–8 concentrate on the methodological development of  $\mu$ -PD. In particular, the ability of the  $\mu$ -PD system to produce crystals from flux is discussed. The compositions of the liquid (melt) and the solid (crystal) in flux systems are unavoidably different. As a result, the behavior of the meniscus at the vicinity of the solid/liquid interface is also different to that observed in simple melt systems where the compositions of the liquid and the solid are the same. This behavior is generally not well known, even in

the case of highly developed edge-defined film-fed growth (EFG) and/or the Stepanov technique. The growth of single-phase mixed crystals (i.e., homogeneous solid solutions) and the solidification and structural appearance of dual-phase solids are also outlined.

Chapters 9–23 focus on the practical application of the  $\mu$ -PD system to the growth of actual crystals of technical importance, which are normally produced by other melt or flux growth methods. The properties of these  $\mu$ -PD crystals are analyzed and compared with prototype materials grown by alternative crystal growth methods when possible. These chapters are particularly important because they provide direct instructions for readers who wish to reproduce the procedures and the materials studied in their laboratories. It is certainly much easier to establish a technology when a model process is available. Some readers will certainly try to improve on or modify the procedures tested and described by the authors of these chapters. They can find some useful tips in Chaps. 1–8, where the authors overview some general experiences about using  $\mu$ -PD and related processes.

Hundreds of expert-level professionals and university students representing various nations and countries were involved, to some degree, in developing the method and growth procedures and characterizing the  $\mu$ -PD crystals. A number of them collaborated with the authors and contributed considerably to the chapters of this book, both directly and by sharing their knowledge and skills. All of the authors express their sincerest thanks to each and every person who contributed to this book. Some of their names appear in the Afterword. The list of experts included in the Afterword should make it easier for readers to find the members of the “ $\mu$ -PD community” that were involved in the development of this technology to some degree. This should enable readers to get in contact with the person associated with the method of interest as quickly as possible.

The authors would like to thank the Japan Society for the Promotion of Science (JSPS), and especially its 161st Committee of the “Science and Technology of Crystal Growth,” for supporting this book. Moreover, many of the authors of this volume were involved, to some degree, in scientific activities initiated by the JSPS due to its support of their research projects and grants. A considerable number of the research findings overviewed in this volume are the direct result of this assistance.

The editors also wish to thank Prof. Y. Kawazoe of the Institute for Materials Research, Tohoku University as well as Dr. C. Ascheron from Springer for their support and help in forming the general concept of the book from the earliest stages of manuscript preparation.

January 2007

*T. Fukuda*  
*V.I. Chani*

# Contents

---

## Part I Introduction to Micro-Pulling-Down Method

---

<b>1 Micro-Pulling-Down (<math>\mu</math>-PD) and Related Growth Methods</b> <i>Valery I. Chani</i> .....	3
<b>2 Basics of the <math>\mu</math>-PD Method</b> <i>Tsuguo Fukuda</i> .....	27
<b>3 Equipment Configuration</b> <i>Tsuguo Fukuda</i> .....	47
<b>4 Growth Phenomena and Crystal Chemistry</b> <i>Valery I. Chani</i> .....	69

---

## Part II Modification and Evolution of $\mu$ -PD Method

---

<b>5 Flux Growth of Miniature Bulk Crystals by the <math>\mu</math>-PD Method</b> <i>Boris M. Epelbaum</i> .....	93
<b>6 Mixed Crystals: <math>\mu</math>-PD vs. Czochralski Method</b> <i>Andrey Novoselov</i> .....	101
<b>7 Isothermal Flux Evaporation Diameter Control</b> <i>Valery I. Chani, Kheirreddine Lebbou</i> .....	115
<b>8 Eutectic Fibers with Self-Organized Structures</b> <i>Dorota A. Pawlak</i> .....	129

---

## Part III Growth and Characterization of Oxide $\mu$ -PD Crystals I: Scintillation and Laser Materials

---

<b>9 Scintillating Bulk Oxide Crystals</b> <i>Akira Yoshikawa, Martin Nikl</i> .....	143
---	-----

**10 Scintillating Crystals:  $Ce^{3+}:YAlO_3$  and  $Yb^{3+}:Lu_3Al_5O_{12}$**   
*Mohamed Alshourbagy, Alessandra Toncelli, Mauro Tonelli* ..... 159

**11 YAG:Nd<sup>3+</sup>:  
 $\mu$ -PD and Czochralski Growth and Properties**  
*Kherreddine Lebbou, Didier Perrodin* ..... 173

**12 High-Melting Rare-Earth Sesquioxides:  
 $Y_2O_3$ ,  $Lu_2O_3$ , and  $Sc_2O_3$**   
*Akira Yoshikawa, Andrey Novoselov* ..... 187

**13  $MgAl_2O_4$  Spinel Laser Crystals:  
 Pure and Ti-, Mn-, or Ni-Doped**  
*Anis Jouini* ..... 203

**Part IV Growth and Characterization of Oxide  $\mu$ -PD Crystals II:  
 Assorted Materials**

**14  $K_3Li_2Nb_5O_{15}$  Fiber and Plate Crystals**  
*Minoru Imaeda, Katsuhiko Imai* ..... 219

**15 Piezoelectric Langanite-Type Crystals**  
*Tsuguo Fukuda, Hiroshi Machida* ..... 229

**16 Shaped Sapphire: Rods, Tubes, and Plates**  
*Hiroki Sato* ..... 239

**17 Doped  $LiNbO_3$  Crystals**  
*Dae-Ho Yoon* ..... 251

**18 Growth of Olivine and Wüstite Crystals**  
*Steffen Ganschow, Detlef Klimm* ..... 265

**Part V Growth and Characterization of Non-Oxide  $\mu$ -PD Crystals**

**19 Silicon Fiber Crystals**  
*Mohamed Alshourbagy, Alessandra Toncelli, Mauro Tonelli* ..... 277

**20  $LiF$ ,  $LiYF_4$ , and Nd- and Er-Doped  $LiYF_4$  Fluoride Fibers**  
*Ana Maria do Espirito Santo, Sonia Licia Baldochi* ..... 287

**21 Binary Fluorides:  $(Gd,Y)F_3$  and  $K(Y,Lu)_3F_{10}$**   
*Akira Yoshikawa, Tomohiko Satonaga* ..... 301

**22 Shaped Fluorides**  
*Tomohiko Satonaga* ..... 323

**23 Metal Alloy Fibers**

*Akira Yosikawa, Yuji Sutou* ..... 331

**Afterword** ..... 335

**Index** ..... 337

# List of Contributors

Mohamed Alshourbagy  
National Institute  
for Nuclear Physics  
(INFN, Pisa section)  
and  
Physics Department  
Pisa University  
Largo Pontecorvo 3  
Pisa 56127, Italy  
shourba@df.unipi.it  
malshourbagy@yahoo.com

Sonia Licia Baldochi  
Institute for Energy  
and Nuclear Research  
IPEN – CNEN/SP  
Center for Lasers and Applications  
Av. Prof. Lineu Prestes, 2242 –  
Cidade Universitária  
05508-000, São Paulo, SP, Brazil  
baldochi@ipen.br

Valery I. Chani  
Institute of Multidisciplinary  
Research for Advanced Materials  
Tohoku University  
Katahira 2-1-1, Aoba-ku  
Sendai 980-8577, Japan  
chani@tagen.tohoku.ac.jp  
vchani@gmail.com

Boris M. Epelbaum  
Department of Material Science 6  
University of Erlangen-Nuremberg  
Martensstr. 7, D-91058 Erlangen

Germany  
boris.epelbaum  
@ww.uni-erlangen.de

Tsuguo Fukuda  
Institute of Multidisciplinary  
Research for Advanced Materials  
Tohoku University  
Katahira 2-1-1, Aoba-ku  
Sendai 980-8577, Japan  
fukuda@fxtal.co.jp

Steffen Ganschow  
Institute for Crystal Growth  
Max-Born-Straße 2  
12489 Berlin, Germany  
ganschow@ikz-berlin.de

Minoru Imaeda  
NGK Insulators, Ltd.  
2-56 Suda-cho, Mizuho  
Nagoya 467-8530 Japan  
imaeda@ngk.co.jp

Katsyhiro Imai  
NGK Insulators, Ltd.  
2-56 Suda-cho, Mizuho  
Nagoya 467-8530 Japan  
k-imai@ngk.co.jp

Anis Jouini  
CEA, GRENOBLE  
Laboratoire  
des Matériaux Semiconducteurs  
DRT/DOPT/STM/LMS  
17 rue des Martyrs  
38054 Grenoble Cedex, France  
anis.jouini@cea.fr

XIV List of Contributors

Detlef Klimm  
Institute for Crystal Growth  
Max-Born-Straße 2  
12489 Berlin, Germany  
klimm@ikz-berlin.de

Kherreddine Lebbou  
Claude Bernard Lyon 1 University  
Physical-Chemistry of Luminescent  
Materials Laboratory  
UMR 5620 CNRS  
bât A. Kastler  
10, rue André Marie Ampère  
Domaine scientifique de la Doua  
69622 Villeurbanne Cedex, France  
lebbou@pcml.univ-lyon1.fr

Hiroshi Machida  
Research & Development Unit  
NEC TOKIN Corporation  
7-1, Koriyama 6-Chome, Taihaku-ku  
Sendai, Miyagi 982-8510, Japan  
machidah@nec-tokin.com

Martin Nikl  
Institute of Physics AS CR,  
Cukrovarnicka 10, 16253 Prague,  
Czech Republic  
nikl@fzu.cz

Andrey Novoselov  
Institute of Multidisciplinary  
Research for Advanced Materials  
Tohoku University  
2-1-1, Katahira, Aoba-ku  
Sendai 980-8577, Japan  
anvn@tagen.tohoku.ac.jp

Dorota A. Pawlak  
Institute of Electronic  
Materials Technology  
ul. Wólczyńska 133  
01-919 Warsaw, Poland  
Dorota.Pawlak@itme.edu.pl

Didier Perrodin  
FiberCryst SAS  
23, rue Royale  
F-69001 Lyon, France  
d.perrodin@fibercryst.com

Ana Maria do Espirito Santo  
Institute for Research  
and Development, IP&D  
Vale do Paraiba University, UNIVAP  
Av. Shishima Hifumi, 2911  
São José dos Campos 12244-000 SP  
Brazil  
amesanto@univap.br

Hiroki Sato  
Fukuda X'tal Laboratory  
c/o ICR 6-6-3, Minami-Yoshinari,  
Aoba-ku, Sendai, Miyagi, 989-3204  
Japan  
h\_sato@fxtal.co.jp

Tomohiko Satonaga  
Stella Chemifa Corporation  
1-41, Rinkai-cho, Izumiootsu  
Osaka, 595-0075 Japan.  
satonaga@stella-chemifa.co.jp

Yuji Sutou  
Biomedical Engineering  
Research Organization  
Tohoku University  
Seiryomachi-2-1, Aoba-ku  
Sendai 980-8575, Japan  
ysutou@tubero.tohoku.ac.jp

Alessandra Toncelli  
Physics Department  
Pisa University  
Largo Pontecorvo 3  
Pisa 56127, Italy  
toncelli@df.unipi.it

Mauro Tonelli  
Physics Department  
Pisa University  
Largo Pontecorvo 3  
Pisa 56127, Italy  
`tonelli@df.unipi.it`

Dae Ho Yoon  
Department of Advanced  
Materials Engineering  
Sungkyunkwan University

300 Cheoncheon-dong, Jangan-gu  
Suwon, Gyeonggi-do 440-746, Korea  
`dhyoon@skku.edu`

Akira Yoshikawa  
Institute of Multidisciplinary  
Research for Advanced Materials  
Tohoku University  
Katahira 2-1-1, Aoba-ku  
Sendai 980-8577, Japan  
`yosikawa@tagen.tohoku.ac.jp`

Part I

**Introduction  
to Micro-Pulling-Down Method**

# 1 Micro-Pulling-Down ( $\mu$ -PD) and Related Growth Methods

Valery I. Chani

**Abstract.** A comparison of the  $\mu$ -PD technique with other (sometimes very similar) melt growth configurations is made. Both well known and relatively rare procedures are reviewed. An attempt is made to classify melt growth methods where crystal growth is achieved through displacement of the solidified material in the downward direction. This classification scheme was based on the appearance and spatial positioning of the basic components of the growth system: the melt, the solids, the crucible, etc. The advantages and shortcomings of  $\mu$ -PD are summarized from the point of view of the process, the degree of control over the shape of the crystal, and the ability of the technique to be industrialized. Some historical comments demonstrate the evolution of the method from methodological and technical points of view.

There are a number of melt growth techniques that permit the production of relatively uniform quasi-one-dimensional single-crystalline materials. Most of them were well classified and described in [1–3] in terms of the arrangement of the growth system: the relative positions of the feed material, the crucible, the melt, and the crystalline solid produced. Micro floating zone methods and techniques that involve pulling from the die have been concluded to be the two main principles suitable for the growth of small-diameter fiber crystals from the melt. Laser-heated pedestal growth (LHPG), the micro-pulling-down ( $\mu$ -PD) technique, edge-defined film-fed growth (EFG, also known as the Stepanov method), as well as the inverted Stepanov method have been considered to be the systems most suited to the production of fiber-shaped materials (crystals with diameters of about 1 mm and aspect ratios of  $10^2$  or greater).

The term “micro-pulling-down” that appears on the cover of this book does not provide an exceptionally clear explanation of the actual performance of this system. However, it does describe the organization and general behavior of the growth unit well. “Pulling-down” represents the direction of solidification. On the other hand, “micro” reflects the presence of microchannel(s) or micro-outlets (sometimes called nozzles) about 1 mm in diameter at the bottom of the melt reservoir (the crucible). These channels allow mass (melt) transport between the liquid mass in the crucible, the meniscus zone below the crucible bottom, and the growth interface.

The performance of such a crucible depends on the presence of an additional dense (liquid or solid) substance just below the bottom (Fig. 1.1).

In general, the crucible behaves like conventional crucible (i.e., one without holes) when there is no such a substance: the melt remains stationary inside the crucible due to surface tension (Fig. 1.1, left). This behavior also depends on the wetting properties of the melt. However, the crucible becomes “bottomless” when the dense substance (seed or crystal) contacts the crucible (initiating crystal growth); from this moment onwards the melt can flow through the opening(s) due to the action of surface forces and gravity.

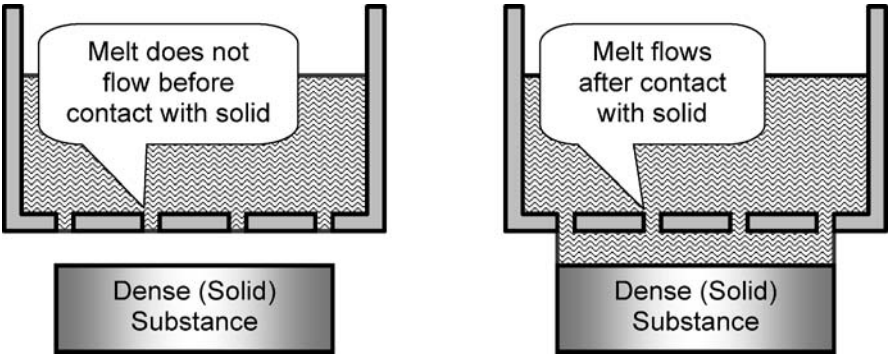


Fig. 1.1. Behavior of the melt in the crucible container with micro-channels (outlets) on the bottom

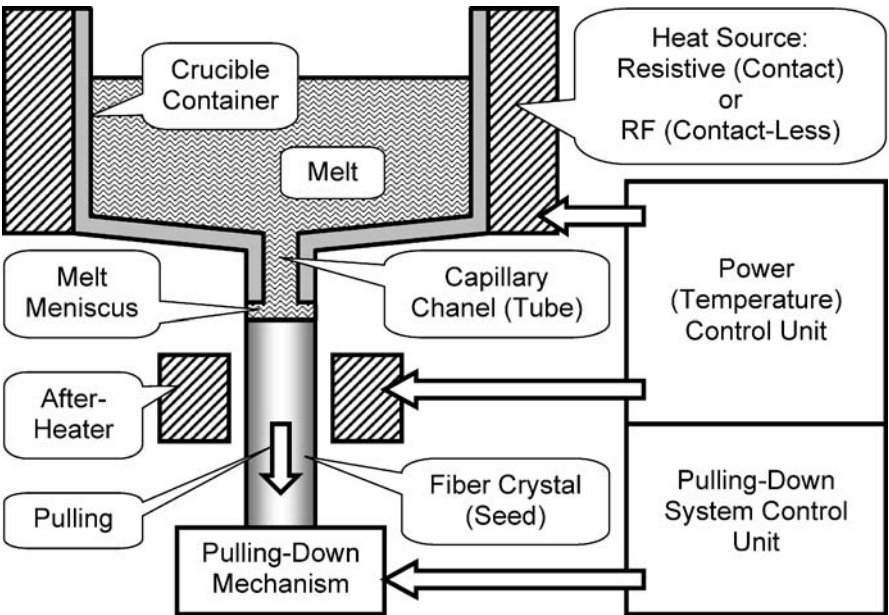
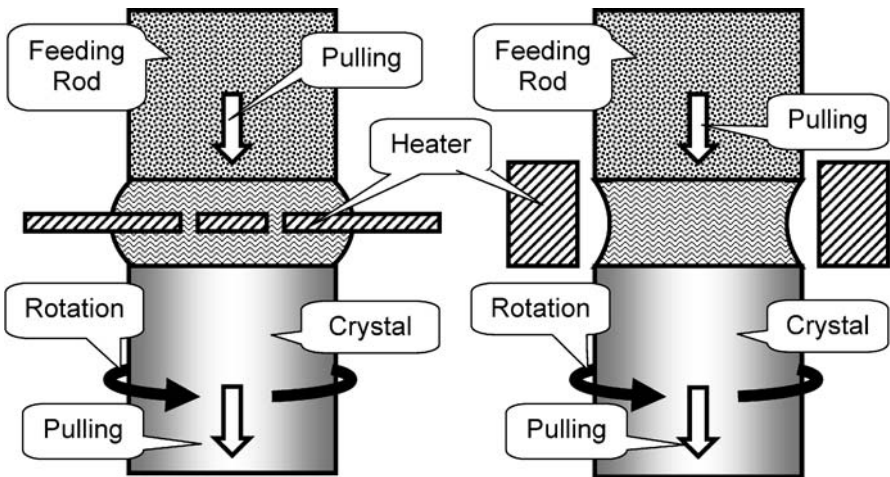


Fig. 1.2. General schematic diagram of  $\mu$ -PD system

The abbreviation “ $\mu$ -PD” has been widely used since 1992–93, when the first modern design of resistively heated  $\mu$ -PD apparatus was created in Tohoku University, Japan, for the growth of  $\text{LiNbO}_3$  [4–6] and  $\text{K}_3\text{Li}_2\text{Nb}_5\text{O}_{15}$  [7, 8] thin-fiber crystals. Soon after, a prototype  $\mu$ -PD apparatus with a radiofrequency (RF) inductive heater was built to produce  $\text{Si}_{1-x}\text{Ge}_x$  mixed (solid solution) crystals. Bulk crystal growth was achieved using graphite crucibles with multiple capillary channels [9]. However, the crucibles used to grow thin fibers had only one opening in the geometrical center of the conical bottom of the crucible container [10, 11]. Tens of other  $\mu$ -PD machines have been developed and built since then. However, the general layout and the principles of the process have not changed very much. Most of  $\mu$ -PD equipment reproduces the general structure of the  $\mu$ -PD system illustrated in Fig. 1.2.

### 1.1 Internal and External Melt Heating

One of the earliest growth methods to apply pulling-down to produce  $\text{CaWO}_4$  crystals similar to those shown in Fig. 1.3 (left) was reported over four decades ago [12] (see Sect. 1.3 for details). Not surprisingly, it was called the “modified floating zone recrystallization technique” by the author. Upon comparing them, the similarity of this set-up to the conventional floating zone (FZ) method quickly becomes apparent. However, one of the techniques uses a strip heater (Fig. 1.3, left), that, after appropriate development (Sect. 1.3), could play the role of the crucible, while the other technique is evidently crucible-less (Fig. 1.3, right). In spite of this fundamental difference, the schemes are



**Fig. 1.3.** Comparison of “modified floating zone re-crystallization technique” [12] with strip-like heater/crucible (*left*) and conventional floating zone method (*right*) corresponding to internal and external heating of the melt, respectively

almost identical except for the positioning of the heating source (internal or external with respect to the melt). The main difference between them is that the melt is not in direct contact with the heating element in one case, while it is in the other. Of course, this difference is important because it affects many significant and critical parameters that determine the final quality of the crystal, including the temperature distribution on the growth interface, the shape of the melt/crystal interface, wetting of the melt to the strip heater, and the shape of the meniscus.

In the case of internal heating, the shape of the crystal depends considerably on the shape and properties of the heater. The appearance of the heater can easily be customized, depending on the requirements, to the crystal shape and properties. Thus, the use of an internal heater provides an additional way to control the shape of the molten zone compared to the crucible-less FZ method. Needless to say, the insertion of the heater into the melt will also increase the probability of crystal contamination, which is certainly a disadvantage of an internal heater when compared to a typical crucible-less FZ (Fig. 1.3, right).

On the other hand, the direct coupling of the metal strip heater with the melt substantially decreases heat losses [13], which is another benefit of the scheme shown on the left. The quantity of molten material is also considerably smaller; the thickness of the molten zone is only 2–3 mm. Therefore, the power that needs to be supplied to the growth system can be reduced significantly, making the strip-heated system more cost-effective. In spite of the presence of a foreign substance in the melt, this method still represents a zone melting process based on two phase transitions (solid–liquid–solid or feed–melt–crystal). This makes it an attractive method for the preparation of chemically uniform crystals compared to the Czochralski (CZ) system, for example, where only one phase transition (liquid–solid) is established.

One additional advantage of internal heating is its ability to provide more accurate temperature control compared to external heating systems (optical for instance). This was particularly noted in [14], where the growth of  $(\beta_{II})\text{-Li}_3\text{VO}_4$  was achieved using a “heater-in-zone” strip heater.  $(\beta_{II})\text{-Li}_3\text{VO}_4$  phase formation is observed over a very narrow temperature range. Therefore, exceptionally precise temperature control was required to achieve the solidification of the single-phase material and to avoid undesired phase transformations.

## 1.2 Pulling Up and Pulling Down

### 1.2.1 Effect of Gravity

In most growth techniques, the crystals are produced through the continuous transport of the seed and the as-grown part of the crystal in the upward

direction (Fig. 1.4, left). Industrial production of high-quality crystals is generally based on such methods (CZ, typical EFG, etc.). The action of gravity in such schemes together with the directions of the temperature gradients help to separate the crystallized solid from as-yet unsolidified fluid. This simplifies the control of the growth process by separating the ordered substance (the crystal) from the predominantly chaotic one (melt). In this way, most uncontrolled events (for example vibrations or temperature fluctuations) are not accompanied by the movement of disordered melt onto the surface of the as-grown crystal followed by the fast (and uncontrolled) solidification of the liquid into polycrystalline solid. Thus, the pulling-up process is more stable than pulling-down (Fig. 1.4, right).

On the other hand, one significant advantage of pulling-down schemes is that there is a reduced probability of incorporating bubbles into the crystals, a factor that often determines the overall quality of the as grown material, especially that produced by the EFG method. The action of gravity results in the redistribution of the bubbles inside the melt such that they move to the top of the melt (Fig. 1.4, left). In the case of pulling-down growth, this movement means that most of the bubbles will be located far from the growth interface, making it unlikely that they will be “frozen” inside the crystal. This is not the case for pulling-up growth, where the crystal is positioned at the upper interface of the melt.

It is evident that the pulling direction (upward or downward) also affects the redistribution of the heavy solid particles often formed in melts due to the recrystallization of crucible material that is partially dissolved in the melt at high temperatures. The densities of Pt and Ir (the materials most often used for crucible fabrication) are 21.45 and 22.45 g/cm<sup>3</sup>, respectively. This is much greater than the densities of oxide crystals (and corresponding melts) such as LiNbO<sub>3</sub> (4.64 g/cm<sup>3</sup>), Y<sub>3</sub>Al<sub>5</sub>O<sub>12</sub> (4.57 g/cm<sup>3</sup>), Bi<sub>4</sub>Ge<sub>3</sub>O<sub>12</sub> (7.13 g/cm<sup>3</sup>).

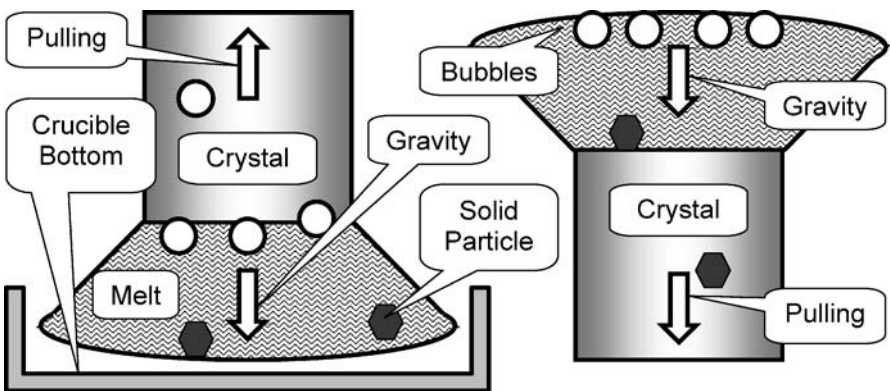


**Fig. 1.4.** Effect of crystal pulling direction up (*left*) and down (*right*), respectively and gravity on separation of solid from liquid and defect location (light bubbles and non-dissociated heavy solid particles)

Therefore, these particles will most likely be found in the bottom of the melt. The probability that they will be incorporated into the crystal is therefore greater when the crystals are produced using a pulling-down scheme.

### 1.2.2 Melt Feeding

One of the advantages of pulling-down growth is that it is relatively simple to continuously feed the melt with additional raw materials. In the case of pulling-up growth, the bottom and side interfaces of the melt are surrounded by the crucible (Fig. 1.4, left). Therefore, the only way to add extra raw material (continuous charging [15]) to the liquid in the single crucible scheme is between the crystal and the crucible wall at the top of the melt. However, this is not appropriate because the melt surface is in direct contact with the growth interface. The probability of depositing these (still solid) feed particles onto the interface and therefore the crystal is too high, potentially changing the growth of a single crystal into the solidification of a polycrystalline ingot. A higher degree of dissociation of the feed particles and a better melt homogeneity can be achieved in a double-crucible Czochralski process [16]. However, this technique requires more complicated crucible design and process control equipment and so it is often not cost-effective.

In contrast, in a pulling-down system, the top surface of the melt is generally free (Figs. 1.1–1.4) and available for feeding. The atmosphere/melt interface that absorbs the feed particles or the grains of the polycrystalline feeding rod is well isolated from the growth interface by the molten zone. This prevents immediate contact between solid particles and the crystal. Moreover, the particles have a higher porosity (and therefore a lower density) than the melt, which keeps them on the surface of the liquid for enough time for them to dissolve completely. Figure 1.4 also illustrates the general behavior of these particles if we assume that the particles behave in a similar way to bubbles due to their relatively low density.

Furthermore, the strip heater or the crucible inside the molten zone acts as an additional solid barrier, as suggested by Fig. 1.3, left. This makes the trajectory of an average particle from the atmosphere/melt interface (inlet) to the melt/crystal interface (outlet) more complicated and therefore more time-consuming. As a result, the probability that the particles completely decompose in the melt increases considerably.

### 1.2.3 Shaped Crystal Growth with Internal Heating

In most cases, pulling-down growth with internal heating (Fig. 1.3, left) yields shaped crystal growth because the crystallization interface is not sited on the free surface of the melt as in Czochralski or top-seeded solution growth (TSSG). The position and shape of the growth interface is determined by the position and shape of the solid heater/crucible inside the fluid. This affects the shape of the meniscus and in this way influences the shape of the

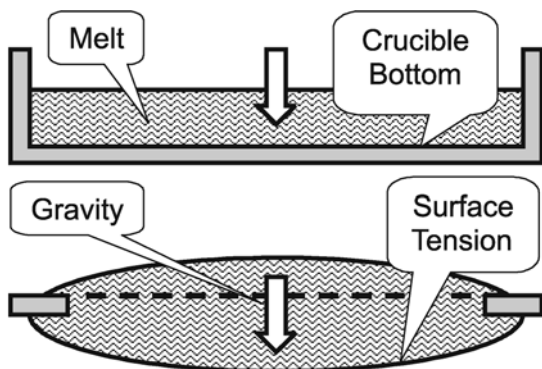


**Fig. 1.5.** Effect of gravity on stability of the melt for pulling-up (*above*) and pulling-down (*below*) growth

solid produced. It is generally impossible to create a free melt surface when the crystal is positioned below the melt because the melt pours out of the container in a downward direction because of gravity (Fig. 1.5).

Moreover, from practical experience of  $\mu$ -PD, the inner capillary channel diameter that allows the melt to sit stationary inside the crucible reservoir (before contacting with the seed) is about 2.0 mm. This was observed in the  $\mu$ -PD growth of  $\text{KNbO}_3$  from a Pt crucible [17]. Similar conclusions follow from the practical application of other melt/crucible combinations. Moreover, it was demonstrated (Chap. 7, [18]) that the crystal/capillary diameter ratio can be as low as 1:6 for  $\text{Bi}_4\text{Ge}_3\text{O}_{12}$   $\mu$ -PD flux growth. Taking into account both of these facts, it is expected that a  $\mu$ -PD system is appropriate for pulling-down fiber growth with a negligible influence of capillary shape on crystal shape.

For pulling-up growth from the crucible, the free surface of the melt is certainly very stable due to gravity and surface tension. As a result, crystals grown via pulling-up technology from a free surface are cylindrical in shape if the anisotropy in the growth rate and subsequent faceting are not considered. Moreover, it is generally simple to create an “endless” melt surface when the crystal is positioned above the melt (Fig. 1.5, above). However, this is impossible when the crystal is growing under the melt (Fig. 1.5, below) and gravity acts as normal.

### 1.3 Pulling-Down Shaped Growth with Continuous Feeding

The principles of the pulling-down (PD) technique have been used for a long time, particularly for bulk crystal growth. The growth of  $\text{CaWO}_4\text{:Nd}$  calcium tungstate bulk crystals is one example of its use. It was first reported by

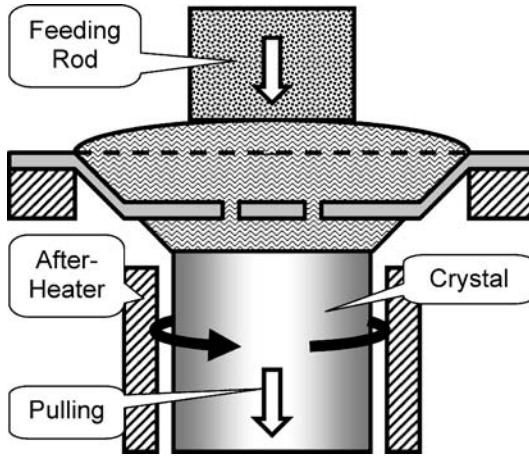


**Fig. 1.6.**  $\text{CaWO}_4$  bulk crystal growth by “modified floating zone recrystallization technique” [12] with crystal rotation at 60 rpm

Gasson [12] in 1965 and thereafter reproduced by Takei et al. [19] in 1969 (Fig. 1.6) with an increased crystal diameter and a larger growth system. This technique did not become very popular, but it is still applied for the growth of some oxide materials [20–23]. In most cases, continuous feeding (charging) of the crucible with raw material powder is performed since it enables larger crystalline ingots to be grown, making the process industrially attractive. In this way, relatively large crystals can be produced without the need for comparatively large crucibles. Therefore, it is also considered to be a cost-effective technique.

The aspect ratios of the bulk PD crystals grown in this way are low (generally less than 10). As a result, occasional vibrations at the position of the crystallization interface have a negligible effect. This is one reason why crystal rotation is often applied during growth to improve the transport of the melt and its exchange between the neighborhood of the melt/crystal interface and volume of the melt. Note that rotation is generally not practiced when the ratio is greater than  $10^2$  because vibrations and the bendability of elongated crystals result in reduced shape quality (see Fig. 4.14).

### 1.3.1 Feeding with Polycrystalline Solid

In the  $\text{CaWO}_4$  growth process reported in [12] (Fig. 1.6), a horizontal iridium strip heater ( $50 \times 10 \times 1$  mm) was applied to produce the molten zone (the melting point of  $\text{CaWO}_4$  is  $1620^\circ\text{C}$  [12]). The crystals were rotated at 60 rpm. Two openings 1 mm in diameter were positioned symmetrically along the long axis of the strip at a distance of 6 mm. This allows the melt to pass through the heater, making transport of the feed material in the downward direction (to the growth interface) possible. When one opening in the center of the

strip positioned along the rotation axis was used, the crystals grown were found to be inhomogeneous along this axis. Cylindrically shaped crystals with dimensions of about  $\varnothing 6 \times 50$  mm were produced using this technique at pulling-down rates of 6–12 mm/h.

A similar process was applied to the growth of  $YVO_4$  [24] at a pulling-down rate of 5 mm/h and a rotation rate of 40 rpm. The dimensions of the iridium heating strip were  $80 \times 10 \times 1$  mm (there were several holes in the middle). A charging rod of size  $\varnothing 7 \times 100$  mm was sintered at 1400 °C for three hours. Different growth atmospheres were tested. The best molten zone stability and the largest crystal (5 mm in diameter and 18 mm long) was obtained when an argon gas flow (21/min) containing 0.3% oxygen was used to protect the strip heater from oxidation and to maintain the most favorable configuration of the molten zone.

Another procedure (called the “metal strip-heated zone melting technique” by the authors of [13]) was utilized recently for the growth of near-stoichiometric  $LiNbO_3$ . The process used was similar to that shown in Fig. 1.3, left, with coaxial rotation of both the feeding rod and the crystal. The strip heater was made of platinum and was as large as  $160 \times 50 \times 1$  mm. The growth parameters used included rotation at 30 rpm and a pulling-down rate of 2 mm/h. The molten zone was 2–3 mm thick. The melt/crystal interface was comparatively flat due to the flatness of the strip heater.

It is clear that above pulling-down process is also applicable to the fabrication of polycrystalline materials, if desired. Sometimes it is impossible to grow single crystals because the chemical properties of the target material do not permit it (incongruent melting). In this case, the solidification of polycrystalline material (sometimes with portion of the second phase) with a well-developed texture can suffice. As an illustration, a process similar to that shown in Fig. 1.6 was applied to solidify highly textured  $Bi_{2.1}Y_{0.1}Sr_{1.9}CaCu_{2-x}Li_xO_8$  polycrystalline ingots [25, 26] that have superconducting properties.

### 1.3.2 Feeding with Powder

Powder feeding is generally more appropriate from the point of view of process industrialization. The feeding rods do not need to be prepared in such a configuration, which simplifies the process. Moreover, it is not necessary to set up an upper pulling mechanism, which simplifies the apparatus; a powder supply system is used instead. An additional benefit of powder feeding is the practically unlimited ability of the growth system to produce large crystals. The length of the lower pulling mechanism is the only limitation on the amount of solidified material. It is not difficult to increase the volume of powder supplied, which means that a larger volume of crystalline material can be produced in a single growth run. Therefore, this type of apparatus is more appropriate for the mass production of crystals. A number of oxide materials, such as rutile,  $TiO_2$  (Fig. 1.7) [20],  $Bi_{12}SiO_{20}$  [21],

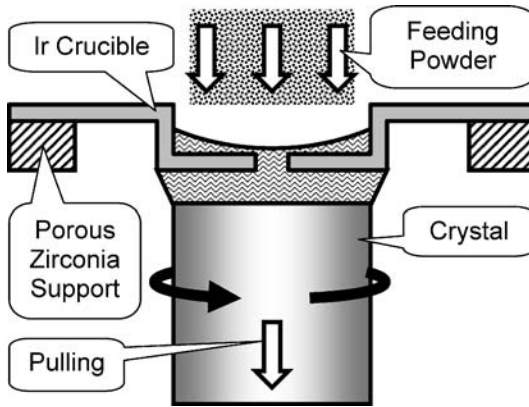


**Fig. 1.7.** Rutile bulk crystal growth by pulling-down technique with RF heating according to [20]

$\text{Li}_2\text{B}_4\text{O}_7$  [22], and  $\text{LiNbO}_3$  [23], have been produced using powder-feeding equipment. Examples of procedures that apply this type of process are reviewed below.

Rutile ( $\text{TiO}_2$ ) crystals (melting point:  $\sim 1850^\circ\text{C}$ ) were grown from a cylindrical iridium crucible 30 mm in diameter and 20 mm in height heated with RF generator. A crucible with one opening 2 mm in diameter made in the geometric center of the crucible bottom was reported [20] to be suitable for growing crystals 25 mm in diameter and up to 60 mm long. The crucible was continuously charged with  $\text{TiO}_2$  grains in a similar fashion to that shown in Fig. 1.7. The powder contained grains of weight 0.02–0.05 g, and the powder was supplied to the crucible once every minute. The crystals were grown at a pulling-down rate of 5 mm/h with the molten zone adjusted to be 2–3 mm thick. A rotation rate of 10 rpm was applied to increase the uniformity of the melt and the overall quality of the crystal.

Attempts were also made to use sintered polycrystalline  $\text{TiO}_2$  rods (up to  $\varnothing 10 \times 140$  mm in size) to feed the crucible (see the previous subsection). In this case, the diameter of the crystal was controlled by optimizing the mass balance. This was achieved by choosing a suitable relationship between the pulling-down rates applied to the feeding rod and the crystal. However, the amount of recrystallized material obtained in this process (i.e., the size of the crystal grown) was limited: it was difficult to fabricate long and well-shaped cylindrical feeding rods with high aspect ratios. Attempts to increase the total amount of charged material by increasing the diameter of the feed rod resulted in the formation of very big droplets when melting. These accidents generated a step change in the total amount of the melt in the crucible and resulted in fluctuations in the crystal diameter. It is evident that the variations in the melt temperature resulting from the addition of relatively large droplets affected the stability of the process.

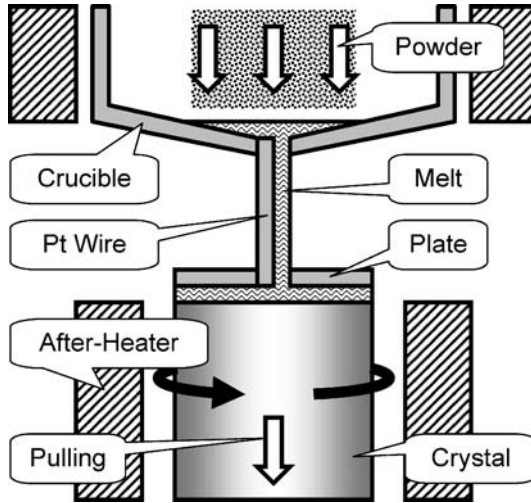


**Fig. 1.8.** Growth of  $\text{Bi}_{12}\text{SiO}_{20}$  bulk crystals according to [21]. The heat to the crucible is supplied from external SiC resistive heater

$\text{Bi}_{12}\text{SiO}_{20}$  crystals were produced using a similar technique and rotation at 20 rpm [21]. Another innovation applied in this process was related to the (more complicated) design of the crucible. This is illustrated in Fig. 1.8. The raw material powder supplied to the crucible is first melted in the container section. It then passes through the opening in the bottom of the crucible and flows out of the crucible, guided by a Pt wire attached close to the opening at the crucible bottom. Thereafter, the melt moves into the plate shaper (the lower part of the crucible), passing through an additional opening made in the center of the plate, and finally forms a molten film between the plate and the seed during the initial stage of growth. Later on, the cross-section of the crystal is adjusted to be identical to the cross-section of the plate. The growth of bulk  $\text{Bi}_{12}\text{SiO}_{20}$  crystals about 40 mm in both diameter and length has been demonstrated using this technique. The crystals were produced from the melts containing an excess of  $\text{Bi}_2\text{O}_3$ . This was necessary to compensate for  $\text{Bi}_2\text{O}_3$  evaporation from the surface of the melt, as described in [18, 27]. The shape of the solid/liquid interface was flat, as expected from the flatness of the plate shaper (Fig. 1.8).

### 1.3.3 Double Strip Heater Growth

The use of the double strip heater arrangement illustrated in Fig. 1.9 was described in [28, 29]. In particular, it has been used to grow  $\text{Gd}_3\text{Sc}_2\text{Al}_3\text{O}_{12}$  (melting point: 2090 °C) and other rare-earth scandium–aluminum garnet crystals [29]. However, no details (including the dimensions of the whole set-up and the quality of the crystals produced with this technique) were

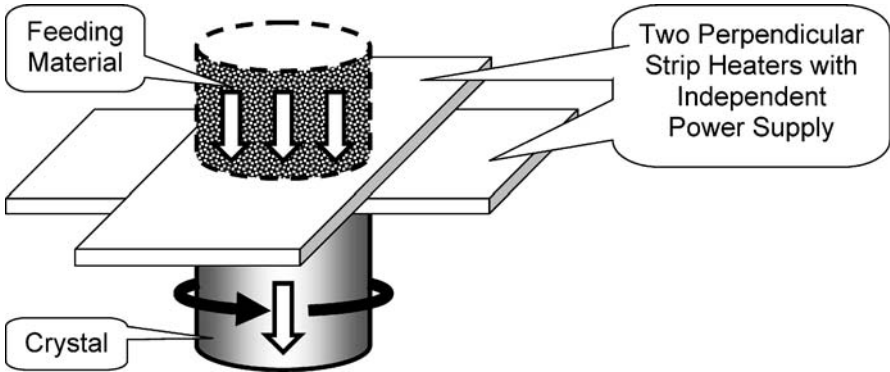


**Fig. 1.9.** Growth of  $\text{Gd}_3\text{Sc}_2\text{Al}_3\text{O}_{12}$  garnet crystals with two perpendicular stripe heaters according to [28, 29]

reported, although the ability of the system to heat the strips independently was mentioned. This allowed independent control of position of the melting (i.e., of the feeding material) and the solidification (i.e., the as-grown crystal) interfaces. The heaters were made of molybdenum 0.3 mm in thickness, and were 12–16 mm wide. Iridium heaters were also applied and these were  $80 \times 16 \times 0.3$  mm in size.

A number of additional shapers allowing the growth of bulk cylindrical crystals as well as plates, tubes, and other shaped ingots were also designed and introduced in [28, 29]. The top sections of these schemes were generally similar to those shown in Figs. 1.6 and 1.7, with either polycrystalline rod or powder feeding. However, the lower sections of the crucibles (the heaters) had more complicated profiles corresponding to the desired shape of the solidified material. Unfortunately, practical applications of these schemes to the growth of actual crystals were not mentioned.

### 1.3.4 Flux Growth with Traveling Solvent

It is evident (especially from Fig. 1.3, left) that  $\mu$ -PD growth with traveling solvent, similar to that practiced by means of a more conventional FZ set-up (Fig. 1.3, right), is also possible when feeding material is constantly supplied to the melt in the solid state (as a polycrystalline rod or a powder of constant chemical composition). This is a significant advantage of continuously feeding system because it allows a constant melt composition to be maintained throughout the entire growth process except for the initial and final stages. This is especially important for crystals that melt incongruently and for growth conditions that require that the compositions of the original liquid (the melt) and the resulting solid (the crystal) are somewhat different. A similar environment is desirable for the growth of doped crystals when the segregation coefficient of the dopant dif-

fers greatly from unity. Application of a traveling solvent allows the production of crystals with fundamentally uniform distributions of all constituents along the growth axis when the composition of the feed solid is constant.

An example of such a process was reported in [14] for the growth of ( $\beta_{\text{II}}$ )- $\text{Li}_3\text{VO}_4$  single crystals (a nonlinear optical material used for second harmonic generation) with  $\text{LiVO}_3$  flux. The platinum strip heater used contained many openings, each of which were 0.8 mm in diameter, and the temperature of the heater was controlled via a thermocouple. The growth rates applied in this flux growth process were 0.25–1.00 mm/h, which were somewhat lower than those applied for melt growth [12, 13, 24] when the compositions of the melt and the crystal were equal. Low growth rates are required for any flux growth independent of the design of the system used because redistributing and reordering the particles transported from liquid mass to the growth interface takes time (see Chap. 4). The rotation rate of the crystal varied from 10 to 30 rpm. However, no rotation was applied to the feeding rod. The crystals were 20–30 mm long with diameters of about 3 mm. The crystals grown with a low pulling-down rate of 0.25 mm/h and a fast rotation rate of 30 rpm were bubble-free. The effects of both the pulling rate and the rotation rate on bubble formation in the solid can be gauged from Fig. 1.4, right. Moreover, a positive influence of melt stirring on the elimination of gas-containing defects was also noticed in [30].

The scheme used for ( $\beta_{\text{II}}$ )- $\text{Li}_3\text{VO}_4$  flux growth was generally identical to that shown in Fig. 1.3, left. The molten zone contained a flux surplus, making it possible to form the target phase. The compositions of the incoming and outgoing solids were generally equal, as normally anticipated for the conventional traveling solvent (flux) technique; both were automatically balanced due to the presence of the extrastochiometric flux in the intermediate fluid between the two solids.

Growth with a traveling solvent cannot be realized in a feedless process like conventional Czochralski or EFG. However, all of the above schemes (Figs. 1.3, left, 1.6–1.9) that involve feeding can be used for this technique. Both of the schemes in Fig. 1.3 become practically identical when the principles of traveling solvent use (intentional mismatch of the compositions of the feed rod and the melt) are applied to growth from flux.

## 1.4 Pulling-Down Shaped Growth without Feeding

### 1.4.1 Solid/Liquid Interfaces and Melt Homogeneity

One of the most important disadvantages of the schemes with feeding presented in previous section (Figs. 1.6–1.9) follows from the existence of the additional solid/liquid interface in the growth system [31], as shown in Fig. 1.10.

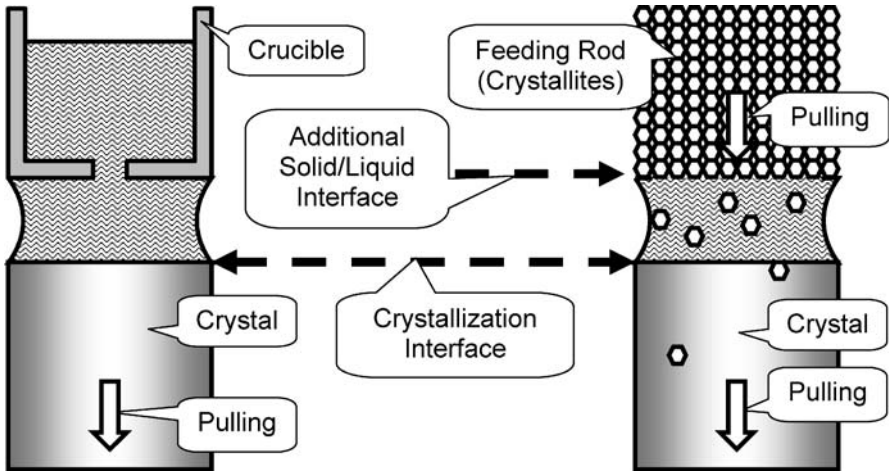


**Fig. 1.10.** Illustration of effect of additional solid/liquid interface on crystal quality according to [31]

Solid particles (crystallites or grains) of feed substance in those systems are continuously introduced into the melt. A significant period of time is generally needed for these particles to completely dissociate. The time required depends on the intensity of mass exchange that occurs inside the fluid (due to free and forced convection, thermocapillary flows and diffusion), the height of the molten zone, and the temperature. It is also a function of the strength of the chemical bonds in the starting solid, which determines the rate of dissolution of the crystallites in the melt. Thus, the probability that the crystallites in the melt have not dissolved completely in the melt before coming to contact with the growth interface is generally greater than zero. This means that these particles can also bond to the crystal during pulling-down. This transforms single-crystal growth into the solidification of polycrystalline material. Note that this phenomenon has little to do with density effects (Fig. 1.4, right) because the densities of a liquid and a solid of same composition are practically equal.

As a result, the structural quality of crystals grown in systems with two solid/liquid interfaces (Fig. 1.10, right) is generally lower than those produced from a single-phase homogeneous melt situated in the crucible (Fig. 1.10, left). If we consider fiber crystal growth, the schemes shown in Fig. 1.10 correspond well to the  $\mu$ -PD and LHPG (or FZ) techniques, respectively (left and right). The growth of single-crystalline materials from homogeneous melts (with one liquid/solid interface and without feeding) is discussed in detail below. In general, the chemical homogeneity and the structural uniformity of such a fluid (Fig. 1.10, left) are ensured by considerable overheating and/or by maintaining the melt at a constant temperature well above the melting point.

### 1.4.2 Micro-Pulling-Down Growth

The typical micro-pulling-down system shown in Fig. 1.2 yields the growth of thin fiber crystals (with high aspect ratios) without feeding and with one solid/liquid interface. A number of other examples (crucible designs, procedures, etc.) of crystal growth based on this scheme are considered in detail in Chaps. 5–23. Crucibles with conical bottoms are normally used to grow fiber type crystals about 1 mm in diameter. However, those applied for the growth of bulk and/or shaped crystals generally have more complicated profiles at the bottom (i.e., a die).

For some highly wettable melts, bulk crystals can also be produced with dimensions that are close to the external diameter of the crucible. This was demonstrated in particular for the growth of  $\text{Tb}_3\text{Ga}_5\text{O}_{12}$  garnet crystals [32], as shown in Fig. 1.11. Crystals with diameters of up to 10 mm were grown from an ordinary  $\mu$ -PD crucible initially designed for the growth of fiber materials (note the conical shape of the bottom of the crucible).

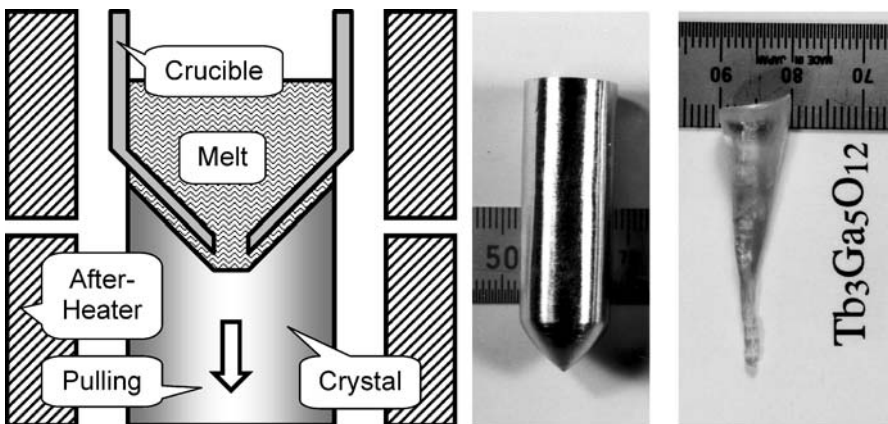


**Fig. 1.11.** Growth of bulk  $\text{Tb}_3\text{Ga}_5\text{O}_{12}$  garnet crystal according to [32]: diagram (left), crucible (center), and as grown crystal (right)

## 1.5 Pulling-Up Shaped Growth without Feeding

Pulling-up is the most popular direction of growth. It is applied in numerous growth techniques, including the Czochralski method (see Sect. 1.2 for details). However, all solidification processes that are performed from the free surface of the melt are not discussed here; specifically we overlook the cases where the shape of the crystal is controlled exclusively by surface action (tension) and the anisotropy in the growth rate (crystallographic structure of the solid). However, we do discuss processes where the shape of the crystal is

determined by surface action between two solid materials (a crucible/shaper that does not interact with the melt, and the crystal that is produced from the melt). Thus, we can classify most of the pulling-up melt growth techniques known into the following three types:

- (1) Those with the melt between the crystal and a chemically inert crucible die (EFG)
- (2) Those with the melt between the crystal and the solid feeding material (FZ and LHPG)
- (3) Those with just an “endless” melt and the crystal (Czochralski; see Fig. 1.4, left).

In this section, usually only those of type (1) using the upward pulling direction are discussed since they have the most features in common with the pulling-down process illustrated in Figs. 1.2, 1.6–1.8, and 1.11. The effect of changing the system such that gravity acts opposite to the direction of crystal growth, a situation encountered when the melt is placed between the die material and the crystal, is now overviewed.

### 1.5.1 Edge-Defined Film-Fed Growth (EFG/Stepanov)

In terms of the geometry of the experimental set-up, the growth of a shaped crystal by the edge-defined film-fed (EFG) or Stepanov technique [30, 33–35] is the method most similar to the  $\mu$ -PD process. In most cases it is performed such that displacement of the as-produced solid occurs continuously in the upward direction. The process itself is based on the continuous conversion of shaped fluid into solid. The formation of a shaped fluid (or a liquid column) is achieved through the application of a solid shaper element that provides

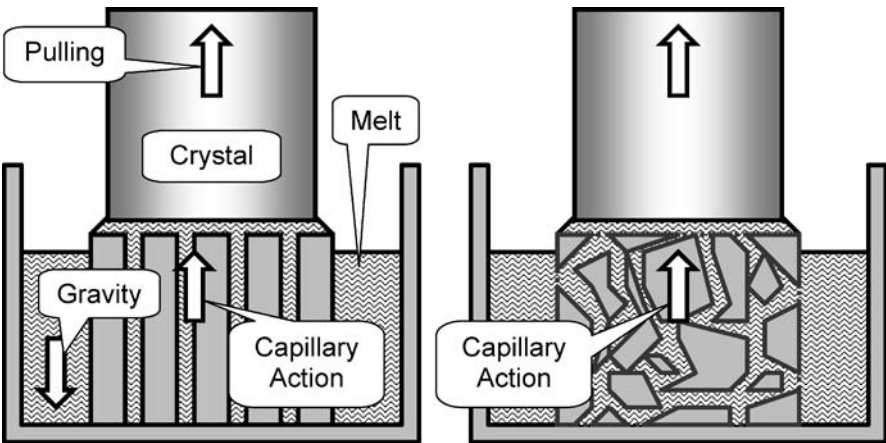


**Fig. 1.12.** Schematic diagram of EFG technique (*left*) and variation of that with porous iridium ingot according to [36]

the liquid/solid interface with the melt through the column (Fig. 1.12). The shape of the column is determined by the configuration of the shaper or die.

In the case of the conventional pulling-up EFG process, a fluid film is formed on the top of the shaper element containing one or a number of capillary channels, as shown in Fig. 1.12, left. These channels makes it possible for the melt to rise to the top of the die through the action of capillary forces. It should be noted here that in this arrangement gravity acts in the direction opposite to crystal growth, unlike the situation in the  $\mu$ -PD process (Fig. 1.2). Nevertheless, movement of the melt in the upward direction is generally achievable, depending on the wetting properties of the fluid.

The shapes of the channels can also be more complicated than this, as shown in Fig. 1.12, right. Therefore, the application of porous shapers that contain a natural capillary network is also possible [36]. Consider the porous die shown in Fig. 1.13. Relatively few studies of the application of porous materials to shaped crystal growth have been published so far, but the idea appears to be very promising, especially considering its potential to suppress the segregation that is easily detectable in number of  $\mu$ -PD processes [18, 31, 37–39].

EFG growth is often considered to be an attractive industrial technique because a shape different to a cylinder (as obtained with CZ-grown crystals) is necessary for most applications related to actual devices. It is assumed



**Fig. 1.13.** Porous Ir die ( $\varnothing$  27 mm) used in pulling-up EFG process. *Left view* represents actual position of the die in the growth (Fig. 1.12, *right*). The die was used for the growth of rare-earth vanadate crystals with details available in [36] (Courtesy of V.V. Kochurikhin, 2005)

that the production of shaped crystals (mostly slices or plates) eliminates the large losses of single crystalline material enduring when a cylindrical bulk crystal is cut. However, EFG crystals often have low levels of crystallographic perfection (compared with those produced by CZ method), and this is often seen as an unavoidable disadvantage of EFG technology [40].

### 1.5.2 Effect of Die Properties on Melt Behavior

One important requirement for successful EFG growth procedure is to keep the melt level in the crucible high enough to maintain complete contact between the melt and the crystal (indeed, this is a vital requirement for any crystal growth technique). Therefore a measurement of the capillary action is commonly needed before the shape of the die and its capillaries can be designed, and before the process can be configured. This can be achieved using a capillary-forming guide made from a couple of plates of the material that is intended for use as the shaper material. An example of this type of guide, produced from iridium plates welded together [41], is illustrated in Fig. 1.14. A guide with a maximum slot thickness of 5 mm was applied to study the behavior of melts of  $\text{TiO}_2$  [41] and the rare-earth vanadates  $\text{YVO}_4$  and  $\text{GdVO}_4$  [31].

The dependence of the capillary height ( $h$ ) on the slot width ( $t$ ) is reported [41, 42] to be well described by following equation:

$$h = \frac{2\gamma \cos \theta}{\rho t g}, \quad (1.1)$$

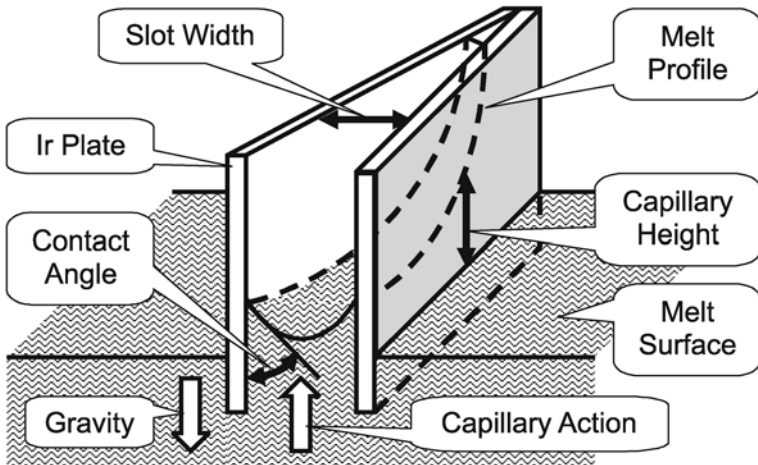


**Fig. 1.14.** Schematic diagram of measurement of capillary action with capillary-forming guide according to [41]

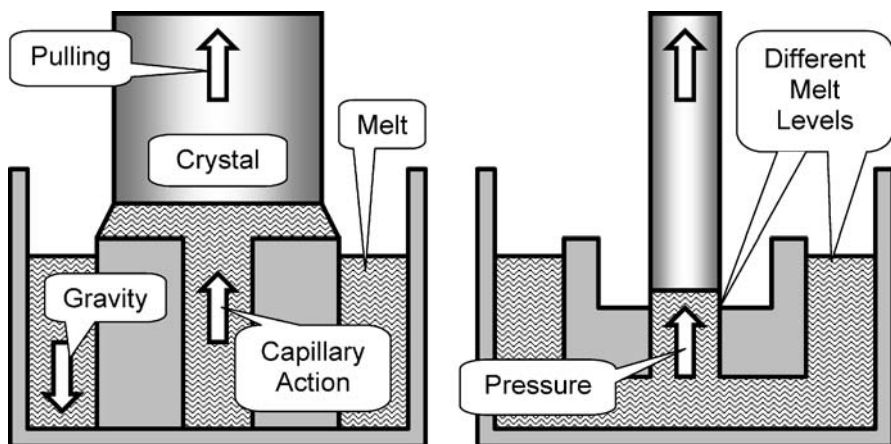


**Fig. 1.15.** Effect of wetting properties of performance of the melt column in shaped crystal growth

where  $\gamma$  is the surface tension,  $\theta$  is the contact angle,  $\rho$  is the density of the melt, and  $g$  is the gravitational acceleration.

EFG growth according to the schemes shown in Fig. 1.12 generally requires good wetting between the die and the melt (Fig. 1.15, left). In the opposite case, additional pressure should be applied outside of the die to promote upward melt flow from the body of the melt to the liquid film that is in contact with the edges of the shaper. This can also be done by displacing the shaping element in the downward direction. As a result, the hydrostatic pressure that is originated from the difference in the melt levels inside and outside of the shaper allows melt to be supplied to the growth interface. This case is demonstrated in Fig. 1.15, right.

As for the pulling-down EFG configuration, the effect of wetting properties on the ability of the system to support contact between liquid and solid is not as critical as in the case of the pulling-up system shown in Fig. 1.2. In the pulling-down set-up, the action of gravity aids the flow of the melt in the downward direction, even when the hydrostatic pressure is relatively low (for melt levels of just a few millimeters). Therefore, a number of melts that are nonwetttable with respect to the crucible material have been successfully used for actual  $\mu$ -PD crystal growth.  $Y_3Al_5O_{12}$  garnet fiber crystal growth [31] is one such process.

### 1.5.3 Inverted EFG/Stepanov Growth

If we think about the geometry of the growth system used, the  $\mu$ -PD technique can be considered to be a particular variant of the so-called inverted EFG/Stepanov technique [30]. Almost all of the characteristics and properties that are representative of the EFG/Stepanov set-up can also be found

in the  $\mu$ -PD system. In both schemes, the shape of the crucible determines the shape of the crystal grown. Moreover, the crystal is produced from the liquid film that is situated between the die and the solidified material, and the solid is pulled in the downward direction.

However, the melt performance (melt exchange, segregation, etc.) of a conventional  $\mu$ -PD system (see Fig. 1.2) is often different from that of the EFG technique. In some cases it is comparable to the Czochralski scheme due to miniaturization and strong Marangoni convection [39]. A detailed comparison of these techniques is presented in Chaps. 5 and 6.

## 1.6 History and Popularity of $\mu$ -PD

While it is not the purpose of this chapter to provide a complete history of the development of  $\mu$ -PD crystal growth techniques, in terms of both the development of the equipment used and the materials produced with this method, it is interesting to list some important facts, events and innovations that have resulted in the present status of this technology. Table 1.1 lists

**Table 1.1.** Selected events and/or innovations resulting in the development of  $\mu$ -PD apparatus and methodology from 1993 to the present

Year	Event/Innovation	Heating	Crystal	Reference
1993	Fiber growth	RES	LiNbO <sub>3</sub>	[5–8]
1995	Graphite crucible, multichannel	RF	Si–Ge bulk	[9]
1996	Graphite crucible	RF	Si–Ge fiber	[10]
1996	Melt optimization by $\mu$ -PD	RES	Ca <sub>3</sub> (Li,Nb,Ga) <sub>5</sub> O <sub>12</sub>	[43]
1997	Concentric die-in-die crucible	RES	Mn:LiNbO <sub>3</sub>	[44]
1998	Ir crucible and afterheater	RF	eutectic	[45]
1998	Oxide crystal, Ir crucible	RF	Y <sub>3</sub> Al <sub>5</sub> O <sub>12</sub>	[31]
1998	Flux crystal growth	RES	KNbO <sub>3</sub>	[17, 37]
1998	In situ orientation correction	RES	KNbO <sub>3</sub>	[17, 37]
1999	∅ 10 mm bulk crystal growth	RF	Tb <sub>3</sub> Ga <sub>5</sub> O <sub>12</sub>	[32]
2000	Textured polycrystalline fiber	RES	Bi <sub>2</sub> Sr <sub>2</sub> CaCuO <sub>y</sub>	[46]
2003	Fluoride fiber growth	RF/RES	PrF <sub>3</sub> , LiF	[47, 48]
2003	Application of growth chamber	RF/RES	PrF <sub>3</sub> , LiF	[47, 48]
2005	Application of Re crucible	RF	Y <sub>2</sub> O <sub>3</sub>	[49]
2005	Crystal weight measurement	RF	Y <sub>3</sub> Al <sub>5</sub> O <sub>12</sub>	[50]
2005	1-m-long fiber crystal	RF	Y <sub>3</sub> Al <sub>5</sub> O <sub>12</sub>	[50]
2006	Diameter control by evaporation	RES	Bi <sub>4</sub> Ge <sub>3</sub> O <sub>12</sub>	[18]
2006	∅ 50 $\mu$ m, stationary growth	RES	Bi <sub>4</sub> Ge <sub>3</sub> O <sub>12</sub>	[18]
2006	Shaped (non-cylinder) growth	RF	Sapphire	Chap. 16
2006	Multicrystal growth	RF	Pr:Lu <sub>3</sub> Al <sub>5</sub> O <sub>12</sub>	Chap. 3
2006	Continuous feeding	RF	Pr:Lu <sub>3</sub> Al <sub>5</sub> O <sub>12</sub>	Chap. 3

some of the events that are relevant to the development of this method and which are discussed in current and following chapters.

It would not be accurate to consider every type of  $\mu$ -PD system to be a particular variant of the inverted EFG technique [39]. Therefore the term “micro-pulling-down” has become very popular over the past decades. Even a quick search through Internet databases that accumulate information on the number of citations of particular phrases clearly demonstrates that the term “ $\mu$ -PD” is widely used in both scientific literature (journals) as well as in other sources of information (webpages, reports, in advertising). This is illustrated by Table 1.2, where this information is listed along with other

**Table 1.2.** Number of references to various phrases retrieved by various Internet search engines and scientific databases (the terms “crystal” and “growth” were also included in each search) as of December 12, 2006 [51–54] (data obtained from Science Direct using the “full text” option are from 1994 onwards)

“Phrase” + crystal + growth	Google	Yahoo	Scirus Total	Scirus Journal	Science Direct
“Liquid phase epitaxy”	89 000	2300	7018	2994	757
“Czochralski method”	80 900	1740	5634	2622	1370
“Floating zone method”	28 300	487	1755	968	462
“Edge defined film”	14 400	597	936	335	107
“Laser-heated pedestal”	12 000	330	658	343	160
“TSSG”	10 400	233	638	411	342
“Micro-pulling-down”	707	171	4590	440	127
“Kyropoulos method”	677	200	161	127	30
“Verneuil method”	435	82	240	140	27
“Stepanov method”	298	95	121	82	27

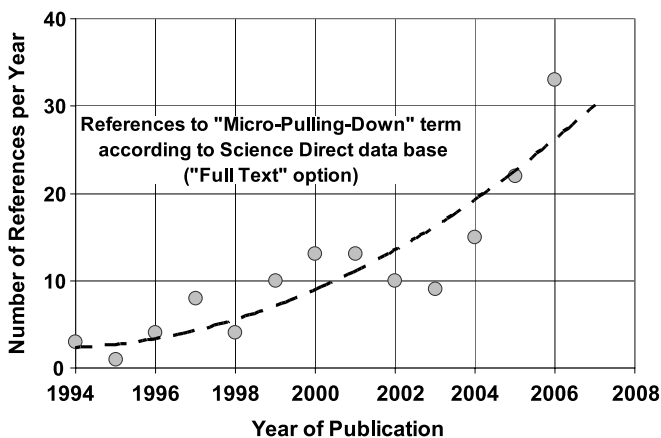


**Fig. 1.16.** Number of references on “Micro-pulling-down” phrase per year according to Science Direct data base [54]

terms and phrases that represent related crystal growth methods commonly used within the crystal growth community. Surprisingly, the total number of references to  $\mu$ -PD in these sources was sometimes more frequent than references to classical growth techniques such as Kyropulos, Verneuil, and Stepanov. This is another reason why the term “micro-pulling-down” was used in the title of this book.

The trend line presented in Fig. 1.16 provides a visual illustration of the popularity of the  $\mu$ -PD crystal growth method in terms of the number of times the method is referred to in publications from a particular year. Note that the term “micro-pulling-down” dates back to 1993–1994, when the general principles of this system were published for the first time, and so the plot only reaches back that far. Also, the Fig. 1.16 represents the reports found in just one particular data base [54], which does not cover all of the institutions involved in publishing research reports on crystal growth, and so the plot is included here for illustrative purposes only. However, a general increase in the popularity of  $\mu$ -PD is evident from the plot.

## 1.7 Summary

Practically all of the schemes described in this chapter will seem to be relatively simple to those who are familiar with crystal growth. Using appropriate heating elements and temperature gradients and accurately controlling the power supplied to the heater, and therefore the shape and length of the molten zone, permits controllable solidification of the fluid and therefore a level of control over crystal quality. These are the principles behind any crystal growth process. However, any attempt to reproduce any of these crystal growth set-ups practically will require exceptional skills and experience from the experimentalist; it is generally not an easy task.

It is also difficult to monitor the process visually during operation. High temperatures and chemical interactions of the constituents of the melt with the ceramic insulators, supports and especially window materials make it difficult for the operator to observe the actual behavior of the system. The situation is even worse when a chemically aggressive environment (as in case of fluoride crystal growth) is necessary. Weight measurement through the application of loading cells, a practice widely used with the Czochralski method, provides a way to automate process control, but the physical ability of the weighing system to measure the weight of the crystal accurately enough is often not sufficient.

The  $\mu$ -PD technique is relatively young compared to other related methods overviewed in this chapter. However, it is growing rapidly in popularity, as illustrated by Table 1.2 and Fig. 1.16.

## References

1. T. Fukuda, P. Rudolph, S. Uda, (eds.), *Fiber Crystal Growth from the Melt* (Springer, Berlin, 2004)
2. P. Rudolph, T. Fukuda, *Cryst. Res. Technol.*, **34**, 3 (1999)
3. D.H. Yoon, *Opto-Electron. Rev.*, **12**(2), 199 (2004)
4. D.H. Yoon, I. Yonenaga, T. Fukuda, N. Ohnishi, *J. Cryst. Growth*, **142**, 339 (1994)
5. D.H. Yoon, T. Fukuda, *J. Cryst. Growth*, **144**, 201 (1994)
6. D.H. Yoon, I. Yonenaga, T. Fukuda, *Crys. Res. Technol.*, **29**(8), 1119 (1994)
7. D.H. Yoon, M. Hashimoto T. Fukuda, *Jpn. J. Appl. Phys.*, **33**, 3510 (1994)
8. D.H. Yoon, P. Rudolph, T. Fukuda, *J. Cryst. Growth*, **144**, 207 (1994)
9. H.J. Koh, T. Fukuda, *Crys. Res. Technol.*, **31**(2), 151 (1996)
10. N. Schäfer, T. Yamada, K. Shimamura, H.J. Koh, T. Fukuda, *J. Cryst. Growth*, **166**, 675 (1996)
11. H.J. Koh, N. Schäfer, K. Shimamura, T. Fukuda, *J. Cryst. Growth*, **167**, 38 (1996)
12. D.B. Gasson, *J. Sci. Instrum.*, **42**, 114 (1965)
13. D.Q. Ni, W.Y. Wang, D.F. Zhang, X. Wu, X.L. Chen, K.Q. Lu, *J. Cryst. Growth*, **263**(1-4), 421 (2004)
14. M. Higuchi, Y. Chuman, T. Kitagawa, K. Kodaira, *J. Cryst. Growth*, **216**, 322 (2000)
15. S.J. Kan, M. Sakamoto, Y. Okano, K. Hoshikawa, T. Fukuda, *J. Cryst. Growth*, **119**, 215 (1992)
16. S.J. Kan, M. Sakamoto, Y. Okano, K. Hoshikawa, T. Fukuda, *J. Cryst. Growth*, **128**, 915 (1993)
17. V.I. Chani, K. Nagata, T. Fukuda, *Ferroelectrics*, **218**, 9 (1998)
18. V.I. Chani, K. Lebbou, B. Hautefeuille, O. Tillement, J.-M. Fourmigue, *Cryst. Res. Technol.*, **41**(10), 972 (2006)
19. F. Takei, S. Takasu, J. Ushizawa, M. Sakurai, *Optoelectric Mater.*, **24**(12), 1507 (1969) (in Japanese)
20. M. Higuchi, T. Togi, K. Kodaira, *J. Cryst. Growth*, **203**(3), 450 (1999)
21. S. Maida, M. Higuchi, K. Kodaira, *J. Cryst. Growth*, **205**(3), 317 (1999)
22. K. Suzuki, M. Higuchi, K. Kodaira, in *The 1st Asian Conference on Crystal Growth and Crystal Technology*, Tohoku University, Sendai, Japan, 29 August – 1 September, 2000, W-P-57
23. K. Kodaira, T. Kitagawa, Y. Miyamoto, M. Higuchi, in *The 1st Asian Conference on Crystal Growth and Crystal Technology*, Tohoku University, Sendai, Japan, 29 August – 1 September, 2000, W-P-105
24. K. Muto, K. Avazu, *Jpn. J. Appl. Phys.*, **8**, 1360 (1969)
25. P. Prabhakaran, A. Thamizhavel, R. Jayavel, C. Subramanian, *J. Cryst. Growth*, **183**, 573 (1998)
26. P. Prabhakaran, C. Subramanian, *Supercond. Sci. Technol.*, **11**, 788 (1998)
27. J.B. Shim, J.H. Lee, A. Yoshikawa, M. Nikl, D.H. Yoon, T. Fukuda, *J. Cryst. Growth*, **243**, 157 (2002)
28. A.A. Mayer, *Protsessi Rosta Kristallov* (Processes of Crystal Growth). (RHTU im. D.I. Mendeleeva, Moscow, 1999) (in Russian)
29. I.A. Scherbakov (ed.), *Trudi Instituta Obschej Fiziki* (Proceedings of General Physics Institute), Vol. 26 (Nauka, Moscow, 1990), p. 95 (in Russian)

30. P.I. Antonov, V.N. Kurlov, *Prog. Cryst. Growth Ch.*, **44**, 63 (2002)
31. V.I. Chani, A. Yoshikawa, Y. Kuwano, K. Hasegawa, T. Fukuda, *J. Cryst. Growth*, **204**, 155 (1999)
32. V.I. Chani, A. Yoshikawa, H. Machida, T. Satoh, T. Fukuda, *J. Cryst. Growth*, **210**(4), 663 (2000)
33. A.V. Stepanov, *The Future of Metalworking* (Lenizdat, Leningrad, 1963) (in Russian)
34. H.E. LaBelle Jr., A.I. Mlavsky, *Nature*, **216**, 574 (1967)
35. V.N. Kurlov, in *Encyclopedia of Materials: Science and Technology*, ed. by K. H. J. Buschow et al. (Elsevier, Amsterdam, 2001), p. 8259
36. V.V. Kochurikhin, A.V. Klassen, E.V. Kvyat, M.A. Ivanov, *J. Cryst. Growth*, **296**, 248 (2006)
37. V.I. Chani, K. Shimamura, T. Fukuda, *Cryst. Res. Technol.* **34**, 519 (1999)
38. S. Ganschow, D. Klimm, B.M. Epelbaum, A. Yoshikawa, J. Doerschel, T. Fukuda, *J. Cryst. Growth*, **225**, 454 (2001)
39. B.M. Epelbaum, G. Schierning, A. Winnacker, *J. Cryst. Growth*, **275**, e867 (2005)
40. J.C. Brice, *Rep. Prog. Phys.*, **40**, 567 (1977)
41. H. Machida, K. Hoshikawa, T. Fukuda, *Jpn. J. Appl. Phys.*, **31**(7B), L974 (1992)
42. B.M. Epelbaum, K. Shimamura, K. Inaba, S. Uda, V.V. Kochurikhin, H. Machida, Y. Terada, T. Fukuda, *Cryst. Res. Technol.*, **34**(3), 301 (1999)
43. Y.M. Yu, V.I. Chani, K. Shimamura, T. Fukuda, *J. Cryst. Growth*, **171**, 463 (1997)
44. B.M. Epelbaum, K. Inaba, S. Uda, K. Shimamura, M. Imaeda, V.V. Kochurikhin, T. Fukuda, *J. Cryst. Growth*, **179**, 559 (1997)
45. A. Yoshikawa, B.M. Epelbaum, T. Fukuda, K. Suzuki, Y. Waku, *Jpn. J. Appl. Phys.*, **38**(1A/B), L55 (1999)
46. K. Lebbou, A. Yoshikawa, M. Kikuchi, T. Fukuda, M.Th. Cohen-Adad, G. Boulon, *Physica C*, **336**, 254 (2000)
47. A. Yoshikawa, T. Satonaga, K. Kamada, H. Sato, M. Nikl, N. Solovieva, T. Fukuda, *J. Cryst. Growth*, **270**(3/4), 427 (2004)
48. M.E. Santo, B.M. Epelbaum, S.P. Morato, N.D. Vieira, Jr., S.L. Baldochi, *J. Cryst. Growth*, **270**(1/2), 121 (2004)
49. J.H. Mun, A. Novoselov, A. Yoshikawa, G. Bpulon, T. Fukuda, *Mater. Res. Bull.*, **40**, 1235 (2005)
50. K. Lebbou, D. Perrodin, V.I. Chani, O. Aloui, A. Brenier, J.M. Fourmigue, O. Tillement, J. Didierjean, F. Balembois, P. Gorges, *J. Am. Ceram. Soc.*, **89**(1), 75 (2006)
51. Google Inc., *Google Search Engine*, Accessed February 12, 2007, <http://www.google.com/>
52. Yahoo! Inc., *Yahoo Search Engine*, Accessed February 12, 2007, <http://www.yahoo.com/>
53. Elsevier B.V., *Scirus Search Engine*, Accessed February 12, 2007, <http://www.scirus.com/srsapp/>
54. Elsevier B.V., *ScienceDirect Website*, Accessed February 12, 2007, <http://www.sciencedirect.com/>

# 2 Basics of the $\mu$ -PD Method

Tsuguo Fukuda

**Abstract.** The basic principles and details of the configurations employed for crystal growth in micro-pulling-down systems, as well as their classification, are presented. The technique is based on continuous transport of the melt through an opening in the bottom of the crucible and its controllable solidification in an environment just below the melt container with a temperature gradient. The designs and properties of all of the elements comprising the system (the crucible, the heat supply, the atmosphere, etc.) affect the growth performance and properties of the crystals grown. Therefore, these elements are discussed and examples of the materials grown are described.

The main modules of a micro-pulling-down ( $\mu$ -PD) growth system include the crucible (with a suitable heating source) and the thermal insulation, which determines the temperature distributions around the crucible and the solid/liquid interface. The quality of the crystal produced by the system depends on the configurations and/or properties of these parts as well as the pulling-down mechanism that ensures the proper removal of the solidified single- or polycrystalline material away from the growth zone. The growth system is often operated in a gaseous environment; the specific gas used depends upon the temperature and the chemical/physical properties of the three fundamental condensed substances that comprise the system (the crucible material, the source melt, and the target crystal). Thus, the system contains an additional substance, namely the growth atmosphere. This affects not only the chemical interactions between the condensed materials, but also the physical appearance and behavior of the growth system as a whole. Considering the characteristics of all of the above elements forming the  $\mu$ -PD system is crucial to understanding how the quality of the crystals can be controlled and improved whenever possible [1–3]. This chapter discusses these considerations.

## 2.1 Heating Systems

According to the schematic diagram of the typical  $\mu$ -PD system shown in Fig. 1.2, heat is supplied to two basic elements of the system: the crucible itself and the afterheater. The crucible heating is essential in any crystal growth process based on a liquid/solid phase transformation to produce a melt and thus permit its subsequent solidification. An afterheater is generally not required if an appropriate temperature gradient can be established by other

ways, for example through the use of appropriately configured thermal insulation. In this case, however, it is impossible to manage the thermal environment close to the growth interface, because the heat supply is fixed from the start of growth. The heat transfer from the system is not constant during growth because the shape of the crystal and the amount of the melt in the crucible are not constant also. Adjusting these parameters is a difficult task. It is therefore evident that controlling the temperature of both (the crucible and the afterheater) independently is definitely preferable because it permits relatively simple modification of the growth conditions based on observations of the solid already produced.

### 2.1.1 Internal Resistive Heating

If we look back at the recent history of  $\mu$ -PD growth of fiber-shaped crystals, which began in 1994 (see Fig. 1.15), a system with resistive heating was the first one to be established. Its design was similar to that shown in Fig. 1.2. Resistive heating is widely applied in a number of growth techniques, including Czochralski (CZ), top-seeded solution growth (TSSG), liquid-phase epitaxy (LPE), floating zone (FZ), etc. However, in most of these systems the temperature of the melt situated in the crucible can be modified by transferring heat from an external heat source. Alternatively, a number of  $\mu$ -PD systems make use of internal heating of the melt (Fig. 1.3). Thus, the crucible combines two important functions; it acts as both the melt container and the heater [4–7], as illustrated in Fig. 2.1.

In most cases this type  $\mu$ -PD apparatus is supplied with an additional outer heater (Fig. 2.1) that controls the thermal environment of the sur-

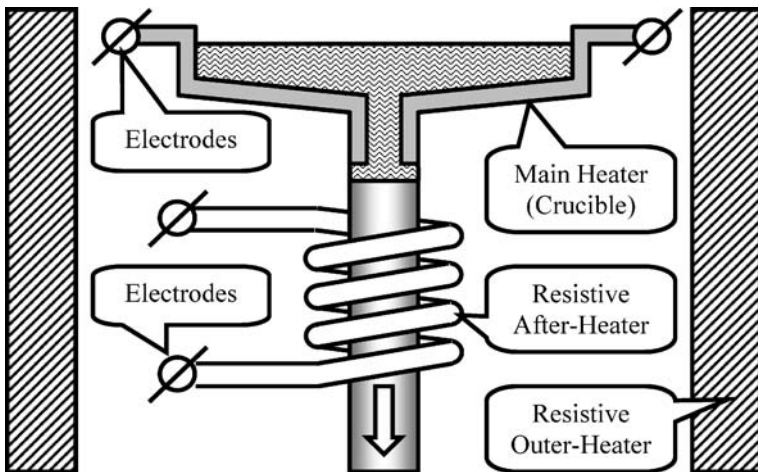


**Fig. 2.1.** Schematic diagram of  $\mu$ -PD system with internal resistive heating of the crucible

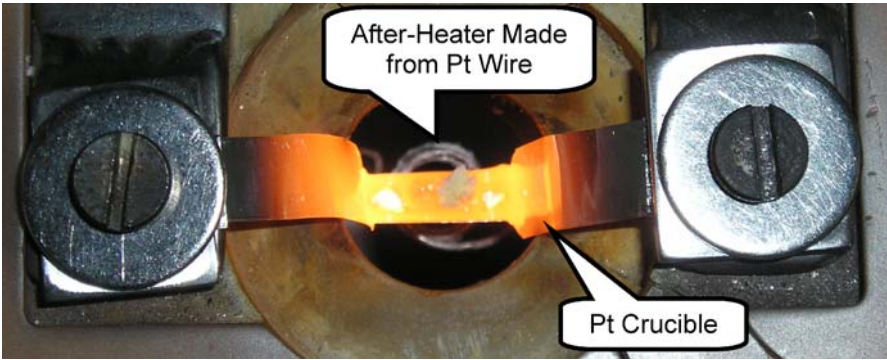


**Fig. 2.2.** View of  $\mu$ -PD set up with resistive heating at the stage of pre-melting of raw materials. The length of the crucible reservoir is 12 mm and the width of the electrode legs is 8 mm (Fig. 2.3)

roundings of the actual hot zone. This outer (external) heater is also typically resistive. As an example, the outer heater is used to establish a uniform temperature of 800 °C within its confines. This approach allows the voltage and corresponding currents applied to both the crucible and the afterheater to be reduced considerably when crystals are grown from material with a relatively high melting point (i.e., m.p. = 1000 °C). This, in turn, permits the power supplies to the crucible and the afterheater to be simplified and their lifetimes to be extended due to the reduction in the heat released through the surfaces of heated parts. An image showing an actual  $\mu$ -PD system with resistive heating during crucible charging is given in Fig. 2.2. Note the (solid; i.e., not yet melted) starting material positioned at the top (not far from the geometrical center) of the surface of the melt.

Normally the crucible is charged with starting powder 3–5 times in order to fill its reservoir completely with melt. It is clear that the effectiveness of the charge depends on the shape of the crucible (the reservoir height/width ratio) and the nature of the starting material. The charging process can be



**Fig. 2.3.** View of  $\mu$ -PD resistive crucible manufactured at laboratory conditions. The reservoir length is 12 mm

accelerated when a starting mixture containing several constituents is presintered. Presintering is especially important when some substances (oxides) are extracted as a result of the thermal decomposition of some of the constituents (i.e., carbonates:  $\text{Li}_2\text{CO}_3$ ,  $\text{K}_2\text{CO}_3$ , etc.). The charging process can be simplified into a single step when fragments of single crystalline material, pre-melted solid, or pieces of dense polycrystalline substance are used as starting material.

### 2.1.2 External Resistive Heating

A schematic diagram of a  $\mu$ -PD system with external resistive heating is shown in Fig. 2.4. In this case, the crucible behaves as a passive component in the system, and its temperature is controlled through heat transfer from an outer heater. Currently no data are available regarding the application of this type of heating to the growth of fiber-shaped materials. However, external resistive heating was successfully used to grow bulk  $\text{Bi}_{12}\text{SiO}_{20}$  crystals [56], with the crucible heated by an external SiC resistive heater.

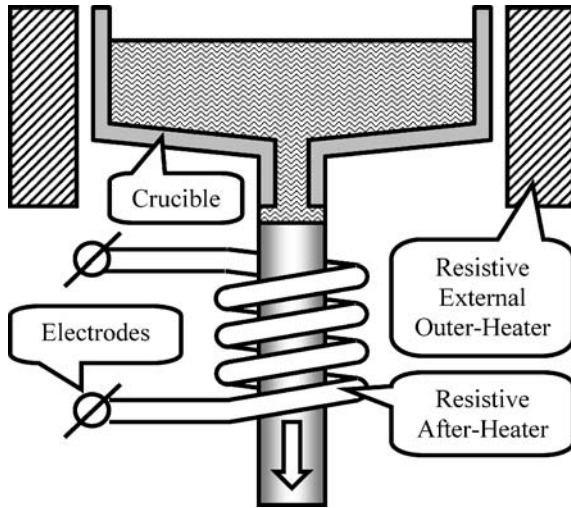
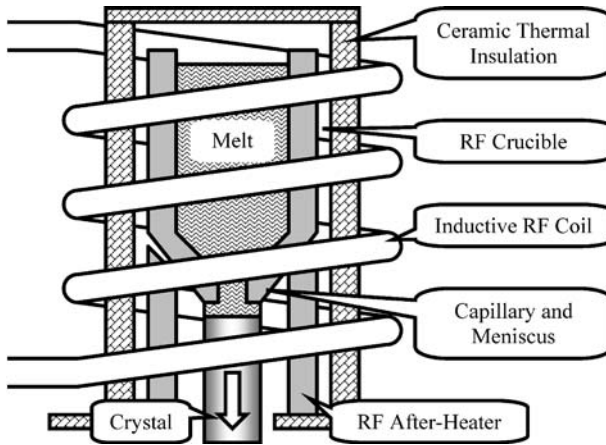


Fig. 2.4. Schematic diagram of  $\mu$ -PD system with external resistive heating

### 2.1.3 Internal Inductive RF Heating

Inductive radiofrequency (RF) heating is also widely used in a number of crystal growth technologies. CZ and edge-defined film-fed growth (EFG) are two examples of processes often performed with heating systems similar to those introduced here for  $\mu$ -PD growth. A typical basic schematic of this process is illustrated in Fig. 2.5. A cylindrical crucible with (normally) a conical bottom is situated on a tubular afterheater which is usually (but not every



**Fig. 2.5.** Schematic diagram of  $\mu$ -PD system with internal inductive RF heating

case) made from the same material as the crucible. Both are heated inductively by supplying alternating current (AC) to the surrounding induction coil. The power supply generator sends alternating current through the coil, generating a magnetic field that induces eddy currents (or Foucault currents) in the crucible and the afterheater. These currents produce heat, which is localized on conducting components (the crucible and the afterheater) and subsequently transferred to the starting material and/or the melt (in the crucible) and modifies the thermal conditions not far from the growth interface (this is the function of the afterheater).

Ceramic thermal insulation is incorporated between the coil and the inductively heated active elements to save heat (and RF power) and to establish an appropriate temperature distribution inside the coil. The temperature profile just below the bottom of the crucible is especially important because it influences a number of parameters that affect the growth process and the crystal. These include the shape and height of the meniscus, the mass exchange inside the meniscus (see Chap. 5 for details), the segregation, the shape of the crystal, the spatial distributions of its constituents, its structural quality, etc. In situ observation of the meniscus, the crystal, and all of the events that occur during growth is extremely desirable. Therefore a window opening is typically cut in the afterheater and the areas of ceramic insulation surrounding the afterheater (Fig. 2.6). In this way, it is possible to continuously inspect the growth interface. Observations are usually made with CCD cameras coupled to a monitor and/or personal computer. Sometimes the process is continuously recorded in order to associate fluctuations in crystal properties with the events that occur at every stage of growth. It is generally possible to achieve process control through continuous inspection of the weight of the crystal with the loading cell. Completely symmetric construction of the hot zone can be applied in such cases. However, this procedure is not yet well developed.



**Fig. 2.6.** View of the hot zone arrangement made from Ir crucible and the after-heater (*left*), typical components of the thermal insulation made of high purity  $\text{Al}_2\text{O}_3$  ceramic (*middle*), and as assembled construction (*right*) used in inductively heated  $\mu$ -PD (Scales in mm)

An additional function of the afterheater of a typical  $\mu$ -PD system with inductive heating is to support the crucible and the whole geometry of the hot zone (Figs. 2.5 and 2.6). The afterheater can generally be substituted for a similar tube-like element (also with a window) made from a passive material that is not affected by the alternating magnetic field sent from the coil. This approach allows high temperature gradient conditions to be established.

#### 2.1.4 External Inductive RF Heating

Fundamentally, the  $\mu$ -PD arrangement with external RF heating (Fig. 2.7) corresponds well to the arrangement with resistive heating, seen in Fig. 2.4 above. However, structurally it is very similar to that shown in Fig. 2.5. The only exception is that the cylindrical element surrounding the crucible and positioned inside the inductive coil is made from electrically conducting material [47, 50, 54] that allows secondary eddy currents to be induced in the surrounding cylinder when an alternating electromagnetic field is generated by the coil. Therefore, the same apparatus can be used for both processes (with internal and external RH heating) after a very simple modification of the configuration of the hot zone.

The  $\mu$ -PD system with external RF heating is somewhat less efficient than that with internal RF heating because the heat is not induced directly in the crucible. Therefore, the system is less rapid and sensitive due to limitations arising from relatively slow heat diffusion. This is a common disadvantage of any arrangement based on external heating. However, these limitations are not very important in the  $\mu$ -PD technique due to the small dimensions and partial self-stabilization of the system arising from the release and/or absorption of latent heat of solidification.

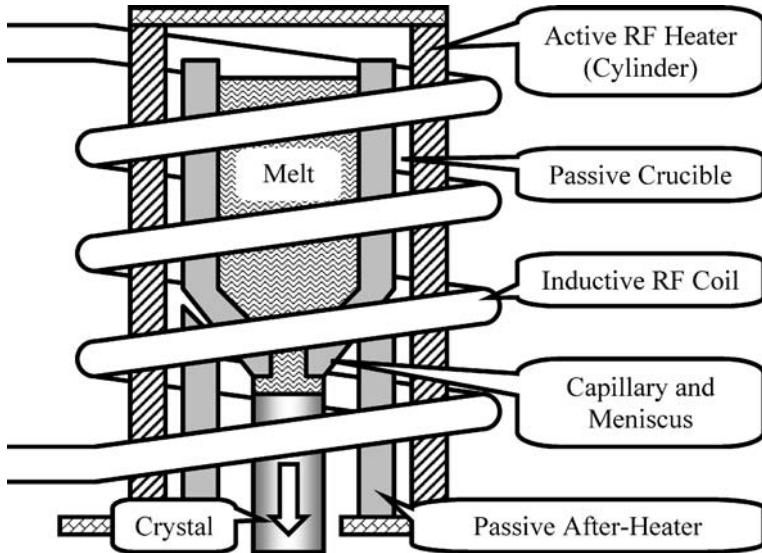


Fig. 2.7. Schematic diagram of  $\mu$ -PD system with external inductive RF heating

## 2.2 Crucibles

### 2.2.1 Materials

The selection of a crucible material suitable for growing a particular crystal is generally based on several requirements common to any crystal growth methods. The most important criteria for the crucible material are listed below:

- (1) The melting point of the material must be considerably greater than the growth temperature
- (2) The material must be chemically resistant to the melt and the surrounding atmosphere
- (3) The mechanical performance of the material at elevated growth temperatures (and during heating/cooling cycles) must be good enough to retain the shape of the container over a long working life (see Fig. 2.8)
- (4) The mechanical properties of the material at room temperature must permit easy machining and fabrication of crucibles of the desired shape (see for example Fig. 2.3)
- (5) The material must demonstrate appropriate wetting properties with respect to the desired melt (this requirement is not universal and depends upon the final goal of the growth process)
- (6) The material must be reasonably priced with good availability of components in desired shapes (plates, capillary tubes, etc.)
- (7) The material must demonstrate sufficient chemical resistance to the actions of the solvents (acids, etc.) used during crucible cleaning.



**Fig. 2.8.** Illustration of unsatisfactory mechanical properties of thin Pt plate used for manufacturing of the crucibles for resistively heated  $\mu$ -PD. The crucible of original shape shown in Fig. 2.3 was deformed when pulling of the crystal

Table 2.1 lists the crucible materials most commonly used in  $\mu$ -PD systems applying both types of heating. For simplicity, most of the crucibles used in  $\mu$ -PD systems are often made from pure metals. However, the physical properties of those are very limited because of the limited number of metals that satisfy all (or most) of the conditions listed above. Therefore, mixed alloys that demonstrate appropriate combination of required properties are also used. Some pure metals such as Rh and Au are rarely used as crucible materials, but alloys of them with more popular materials such as Pt and

**Table 2.1.**  $\mu$ -PD crucible materials, their melting points (m.p.), and appropriate growth atmospheres

Material	m.p., °C	Growth atmosphere	Notes
C (dense graphite)	3500	Ar, Ar + CF,	[50]
C (vitreous)	–	Ar	Chap. 19
Re	3180	Ar+H <sub>2</sub> (3–4%)	[51]
Mo	2617	Ar, Ar+H <sub>2</sub> (2%)	[58, 59, 61]
Ir	2410	Ar, N <sub>2</sub> , N <sub>2</sub> +O <sub>2</sub> (1%)	[52]
Al <sub>2</sub> O <sub>3</sub>	2054	Air	–
Rh	1966	–	–
Pt	1772	Air, Ar + CF	–
SiO <sub>2</sub>	1600	–	–
Au	1064	–	–
Al	660	–	[14]
Ir+2%Re	–	Ar	[53]

**Table 2.2.** List of  $\mu$ -PD crucible materials and the crystals grown from these crucibles

Material	Heating	Heater	Crystals Grown	References
Pt	RES	Internal	LiNbO <sub>3</sub>	[4–6, 8]
Pt	RES	Internal	K <sub>3</sub> Li <sub>2</sub> Nb <sub>5</sub> O <sub>15</sub>	[7, 9]
Pt	RES	Internal	KNbO <sub>3</sub>	[10, 11]
Pt	RES	Internal	La <sub>2</sub> (WO <sub>4</sub> ) <sub>3</sub>	[29]
Pt	RES	Internal	Ba <sub>2</sub> NaNb <sub>5</sub> O <sub>15</sub>	[35]
Pt	RES	Internal	(Bi,Sr) <sub>2</sub> CaCu <sub>2</sub> O <sub>y</sub> , polycrystalline	[37]
Pt	RES	Internal	Bi <sub>4</sub> Ge <sub>3</sub> O <sub>12</sub>	[43, 44]
Pt	RES	Internal	La <sub>2</sub> (WO <sub>4</sub> ) <sub>3</sub>	[46]
Pt	RF	External	PrF <sub>3</sub> :Ce	[47]
Pt	RES	Internal	La <sub>2</sub> (WO <sub>4</sub> ) <sub>3</sub>	
Pt–Rh(10%)	RES	Internal	Sr <sub>3</sub> Nb <sub>1–x</sub> Ga <sub>3+(5/3)x</sub> Si <sub>2</sub> O <sub>14</sub>	[39]
Pt–Rh(30%)	RES	Internal	Ca <sub>3</sub> (Nb,Ga) <sub>5</sub> O <sub>12</sub>	[22, 27]
Pt–Rh	RES	Internal	Ca <sub>3</sub> (Li,Nb,Ga) <sub>5</sub> O <sub>12</sub>	[12]
Pt–Rh	RES	Internal	NaCa <sub>2</sub> Mg <sub>2</sub> V <sub>3</sub> O <sub>12</sub>	[13]
Pt–Rh	RES	Internal	La <sub>3</sub> M <sub>0.5</sub> Ga <sub>5.5</sub> O <sub>14</sub> (M=Nb,Ta)	[21]
Pt–Rh	RES	Internal	La <sub>3</sub> MGa <sub>5</sub> O <sub>14</sub> (M=Ti,Zr,Hf)	[23]
Pt–Rh	RES	Internal	La <sub>3</sub> M <sub>0.33</sub> Ga <sub>5.67</sub> O <sub>14</sub> (M=Mo,W)	[28]
Ir	RF	Internal	Al <sub>2</sub> O <sub>3</sub> /Y <sub>3</sub> Al <sub>5</sub> O <sub>12</sub> , eutectic	[19, 20]
Ir	RF	Internal	Y <sub>3</sub> Al <sub>5</sub> O <sub>12</sub> (:Nd/Yb)	[24–26]
Ir	RF	Internal	Tb <sub>3</sub> Ga <sub>5</sub> O <sub>12</sub>	[30]
Ir	RF	Internal	(Tb,Lu) <sub>3</sub> Al <sub>5</sub> O <sub>12</sub>	[31]
Ir	RF	Internal	(Tb,Yb) <sub>3</sub> Al <sub>5</sub> O <sub>12</sub>	[32]
Ir	RF	Internal	(Tb,Lu) <sub>3</sub> Al <sub>5</sub> O <sub>12</sub>	[33]
Ir	RF	Internal	GdVO <sub>4</sub>	[34]
Ir	RF	Internal	Tb <sub>3</sub> Al <sub>5</sub> O <sub>12</sub>	[28]
Ir	RF	Internal	Tb <sub>3</sub> Sc <sub>2</sub> Al <sub>3</sub> O <sub>12</sub>	[40]
Ir	RF	Internal	Ca <sub>8</sub> La <sub>2</sub> (PO <sub>4</sub> ) <sub>6</sub> O <sub>2</sub> :Yb	[41]
Ir	RF	Internal	(Y,Yb) <sub>3</sub> Ga <sub>5</sub> O <sub>12</sub> , (Lu,Yb) <sub>3</sub> Al <sub>5</sub> O <sub>12</sub>	[42, 57]
Ir	RF	Internal	Lu <sub>3</sub> Ga <sub>5</sub> O <sub>12</sub> :Yb	[45]
Ir	RF	Internal	Gd <sub>3</sub> Ga <sub>5</sub> O <sub>12</sub> :Bi	[48, 49]
Ir	RF	Internal	Y <sub>3</sub> Ga <sub>5</sub> O <sub>12</sub> :Bi	[49]
Ir–Re(2%)	RF	Internal	MgAl <sub>2</sub> O <sub>4</sub> :Ti, Mn	[53]
Re	RF	Internal	Y <sub>2</sub> O <sub>3</sub> :Yb	[51]
Re	RF	Internal	Y <sub>2</sub> SiO <sub>5</sub> :Pr, Lu <sub>2</sub> SiO <sub>5</sub> :Pr	[52]
C	RF	Internal	Si <sub>1–x</sub> Ge <sub>x</sub>	[15–18]
C	RF	External	PrF <sub>3</sub> :Ce	[47]
C	RF	External	KY <sub>3</sub> F <sub>10</sub> :Pr	[50]
C	RF	External	(Gd,Yb)F <sub>3</sub> :Pr	[54]
Al	–	External	K(Li,Na)NO <sub>3</sub>	[14]

Ir are often used since these exhibit improved behavior in particular crystal growth processes. For instance, alloys of Pt with Rh are widely used to increase the melting points of Pt-based materials and to improve their mechanical properties. The Pt–Rh binary system is characterized by unlimited solubility in solid and liquid phases [36], which makes it simple to optimize alloy composition. Alloying Ir with Au allows wetting properties to be modified (see Chap. 15 for details). Examples of common crucible materials and the crystals produced using them in the  $\mu$ -PD process are listed in Table 2.2.

### 2.2.2 Crucible Shape

$\mu$ -PD shaped crystal growth is only in the initial stages of its development. Therefore, the range of crystal shapes examined so far is not as great as has been reported for alternative EFG processes [60]. However, crystals with basic shapes, including cylinders, rectangular rods with square cross-sections and with high aspect ratios (plates), and tubes have been successfully grown. A number of shaped materials grown using  $\mu$ -PD architecture are listed in Table 2.3. In the future, it is generally assumed that  $\mu$ -PD will be used to grow crystals with more complicated shapes, similar to those produced with pulling-up EFG processes. The development of procedures that allow this partially depends on the requirements of industry.

**Table 2.3.** List of selected shaped crystals produced by the  $\mu$ -PD technique in Tohoku University, Japan

Shape	Cross-section, mm	Length, mm	Crystals
Fiber	$\varnothing 0.1 \sim 1.0$	–	LiNbO <sub>3</sub> , Al <sub>2</sub> O <sub>3</sub> , Si, SiGe, Ba <sub>2</sub> NaNb <sub>5</sub> O <sub>15</sub> , Tb <sub>3</sub> Sc <sub>2</sub> Al <sub>5</sub> O <sub>12</sub> , Y <sub>2</sub> SiO <sub>5</sub> , Lu <sub>2</sub> SiO <sub>5</sub> , Gd <sub>2</sub> SiO <sub>5</sub> , Y <sub>3</sub> Al <sub>5</sub> O <sub>12</sub> , YAlO <sub>3</sub> , La <sub>3</sub> Ga <sub>5</sub> SiO <sub>14</sub>
Rod	$\varnothing 1 \sim 10$	–	Y <sub>3</sub> Al <sub>5</sub> O <sub>12</sub> , Lu <sub>3</sub> Al <sub>5</sub> O <sub>12</sub>
Rod	$\varnothing 1 \sim 5$	–	Al <sub>2</sub> O <sub>3</sub> , Y <sub>2</sub> SiO <sub>5</sub> , Lu <sub>2</sub> SiO <sub>5</sub> , Gd <sub>2</sub> SiO <sub>5</sub> , Y <sub>3</sub> Al <sub>5</sub> O <sub>12</sub> , Lu <sub>3</sub> Al <sub>5</sub> O <sub>12</sub> , Tb <sub>3</sub> Sc <sub>2</sub> Al <sub>3</sub> O <sub>12</sub> , YAlO <sub>3</sub> , CaF <sub>2</sub> , BaF <sub>2</sub> , PrF <sub>3</sub> , KYF <sub>4</sub> , eutectic melt-grown composites (MGC) materials, Fig. 2.9
Tube	$\varnothing$ (outer) $6 \times \varnothing$ (inner) 4	200	Al <sub>2</sub> O <sub>3</sub> , MGC
Plate	$5 \sim 10 \times 2$	100	K <sub>3</sub> Li <sub>2</sub> Nb <sub>5</sub> O <sub>15</sub> , KNbO <sub>3</sub> , PrF <sub>3</sub> , Al <sub>2</sub> O <sub>3</sub> (Fig. 2.10), La <sub>3</sub> Ga <sub>5</sub> SiO <sub>14</sub> , La <sub>3</sub> Ta <sub>0.5</sub> Ga <sub>5.5-x</sub> Al <sub>x</sub> O <sub>14</sub> , La <sub>3</sub> Nb <sub>0.5</sub> Ga <sub>5.5-x</sub> Al <sub>x</sub> O <sub>14</sub> , MGC, Fig. 2.10

Similar to the EFG method, the shape of the solids produced by pulling-down processes depends on the shape of the die part of the crucible positioned at the bottom of the melt reservoir. Several different crucible bottom configurations have been tested over the past decade in order to find those applicable to pulling-down growth of shaped crystals. Examples of some iridium crucibles examined for the actual growth of shaped materials are illustrated in Fig. 2.11.

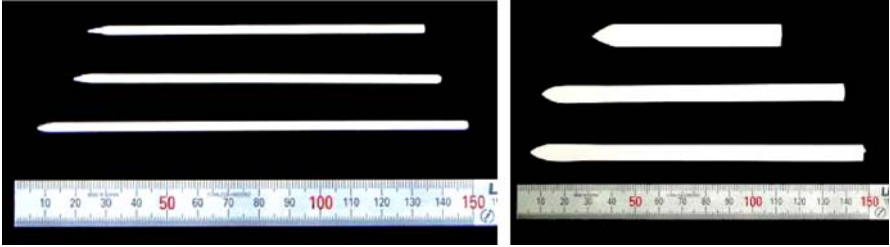


**Fig. 2.9.** Rod-like (*left*) and plate-like (*right*) shaped eutectic composites produced by  $\mu$ -PD (Scales in mm)

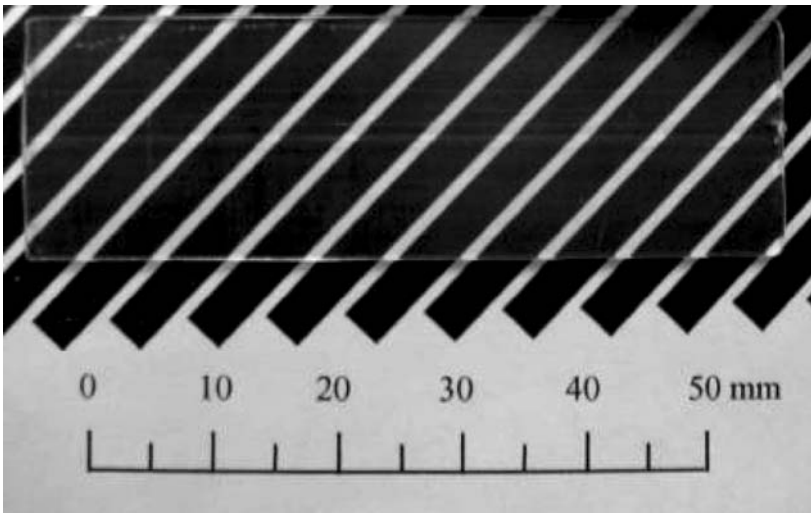


**Fig. 2.10.** View of sapphire plate grown by  $\mu$ -PD technique with width of 20 mm



**Fig. 2.11.** Side (*left*) and bottom (*right*) views of Pt crucibles with various shapes of the dies

### 2.2.3 Crystal Shape vs. Crucible Shape

In shaped crystal growth, ideally the outer perimeter of the die determines the cross-section of the shaped crystal. Thus, the perimeters of both the die and the crystal are identical. However, in real  $\mu$ -PD processes the perimeters are generally different because surface tension minimizes the surface area of the meniscus in the melt column. Thus, most  $\mu$ -PD crystals are “more cylindrical” than the shape of the original die. This phenomenon becomes more evident for both  $\mu$ -PD and EFG systems when height of the melt column is relatively large.

Decreasing the thickness of the meniscus improves the correlation between the shape of the die and that of the crystal due to simple geometrical considerations. However, the use of an exceptionally thin meniscus is occasionally accompanied by the freezing [61] of the crystal to the die when the bottom of the die is flat (Fig. 2.12). This often results from curvature of the growth interface. The probability of freezing is decreased in a pulling-up EFG configuration by changing the shape of the top of the die from flat to concave [61]. The influence of gravity on the shape of the meniscus is negligible when the meniscus is thin. Therefore, an equivalent modification is often performed to the shape of the bottom of the  $\mu$ -PD crucible die. The positive effects of such a modification have been confirmed experimentally by applying crucibles with concave die bottoms (Fig. 2.13).

The general idea behind modifying the shape of the surface of the die is to keep the thickness of the meniscus uniform along the whole growth interface. This keeps the probability of freezing (due to uncontrollable fluctuations that occasionally occur during solidification) low, because the meniscus loses its “weak link”; the fragment of the meniscus with shortest distance between the die and solidification (crystallization) interface. Thus, the concave shape of the die fits better with the convex shape of the growth interface. In the best cases, the fit is perfect.

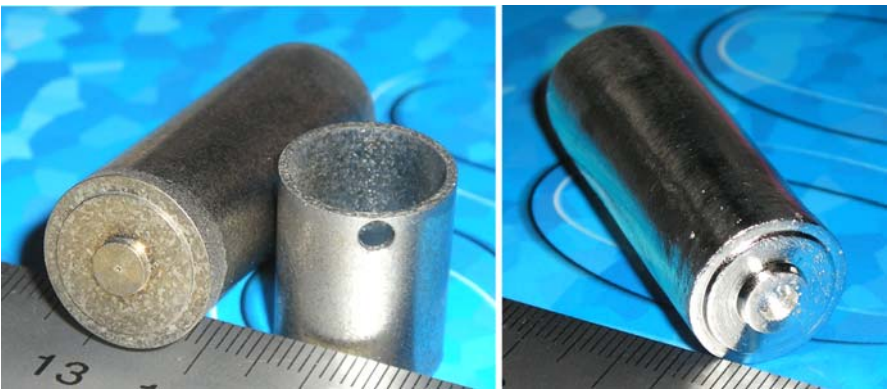


**Fig. 2.12.** View of bottom of Mo crucible (and the after-heater) with rod type die (*left*) and Pt crucible with tube type die (*right*). The lower extremities of the dies are flat. (Scales in mm)



**Fig. 2.13.** View of bottom of Mo crucible with plate type die. The lower extremity of the die has concave shape

Another potential source of irregularity in crystal shape (and/or quality) is an asymmetrical temperature distribution just below the crucible. If we consider internal RF heating (Fig. 2.5), an appropriate temperature gradient is maintained in this area by the active afterheater. However, the afterheater contains a window opening (Fig. 2.12, left) that is required to enable visual control of the process, especially at the stages of seeding and growth (Figs. 2.6 and 2.14). The presence of this window, together with that of a coincident window cut into some areas of the thermal insulation (Fig. 2.6), make the area of the meniscus and that of the growing crystal located closest to these windows considerably colder. There are two reasons for this: (i) insufficient heating due to a local deficiency in electromagnetically active material in the afterheater, and (ii) additional heat loss due to a local deficiency in thermal insulation. Partial improvement of the temperature distribution and its symmetry is often achieved by creating additional (nonfunctional) windows in the system, as illustrated in Fig. 2.15.

For  $\mu$ -PD systems with resistive heating and a spiral-type afterheater (Figs. 2.1, 2.2, and 2.4), the shape of the afterheater is practically symmetric. Therefore, the temperature distribution is not as irregular as in RF-heated designs, and in fact such irregularities have never been observed experimentally. Observation of the meniscus zone in a resistively heated  $\mu$ -PD is performed via appropriate adjustment of the position of the afterheater in the vertical direction. Thus, the meniscus is observed between the windings of the afterheater when monitored from the side.

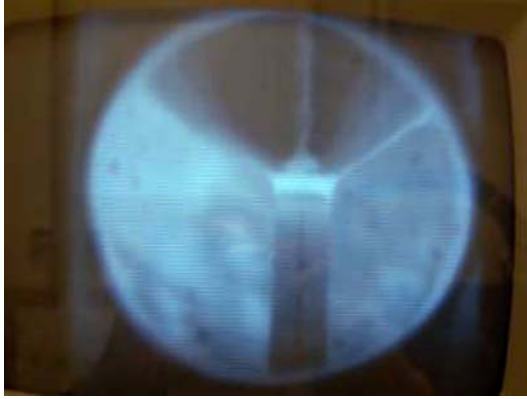


**Fig. 2.14.** Observation of the meniscus through the window opening made in the after-heater (case of  $\mu$ -PD system with inductive RF heating)



**Fig. 2.15.** Multi-window Ir after-heater used to improve symmetry of temperature distribution just below the crucible

### 2.3 Wetting Properties of the Melts

The wetting properties of the melt have a great influence over shaped crystal growth. In the case of the classical EFG technique (Figs. 1.12–1.14, and 2.16, left), good wetting is essential because the method is based upon the principles of capillarity. Good wetting and capillarity allow the melt to reach the top of the die and spread over its top surface. Such melts have relatively low surface tensions: they are easily bonded to the surface of the crucible die, with corresponding minimization of the interfacial energy. The melt/crucible

material combination is optimized by optimizing the contact angle (the angle between the flat surface of the crucible material and the surface of the melt droplet; see Chap. 15 for details).

In contrast to EFG, the  $\mu$ -PD system allows controllable solidification from both wettable and nonwettable melts (Fig. 2.16) because the supply of the melt to the growth interface is supported by an additional driving force that is independent of the wetting properties: gravity (and the hydrostatic pressure caused by it, which can be easily calculated using Fig. 2.17). In

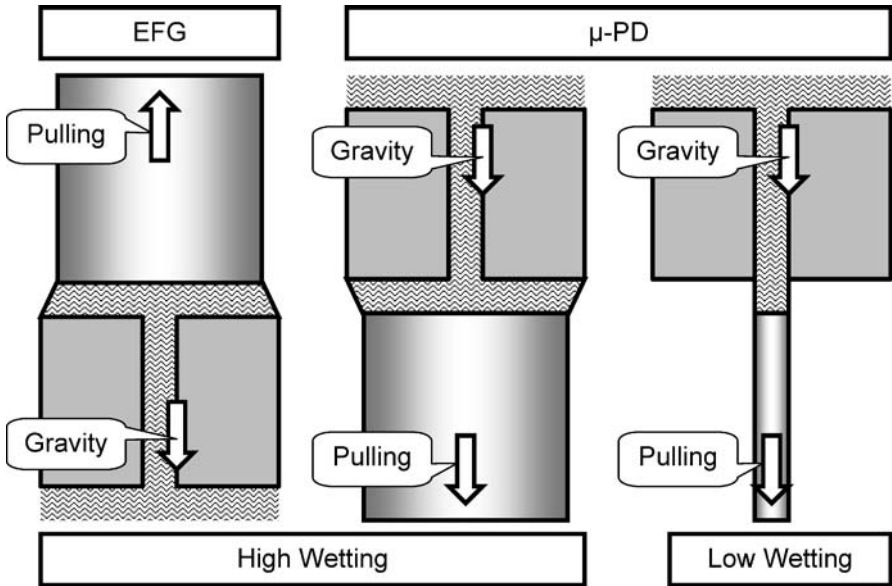


**Fig. 2.16.** Illustration of influence of wetting properties of the melt on its behavior in EFG (pulling-up) and  $\mu$ -PD systems.

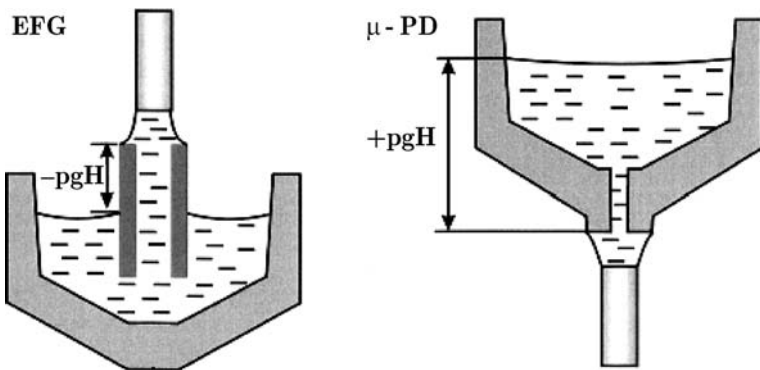


**Fig. 2.17.** Hydrostatic pressure in EFG and  $\mu$ -PD.  $H$  is height (*level*) of the melt,  $\rho$  is the melt density, and  $g$  is gravitational constant

the case of  $\mu$ -PD, the melt pressure is positive. Therefore, the  $\mu$ -PD method is also suitable for growing crystals from poor-wetting melts, because the direction of growth is coincident with the direction of gravity.

### 2.4 Orientation Adjustment

Precise orientation control systems that allow highly accurate angle adjustment were recently developed in order to permit the crystallographic orientation of the seed to be set precisely. The seed orientation often affects not only the orientation of the resulting crystal (obviously), but also the performance

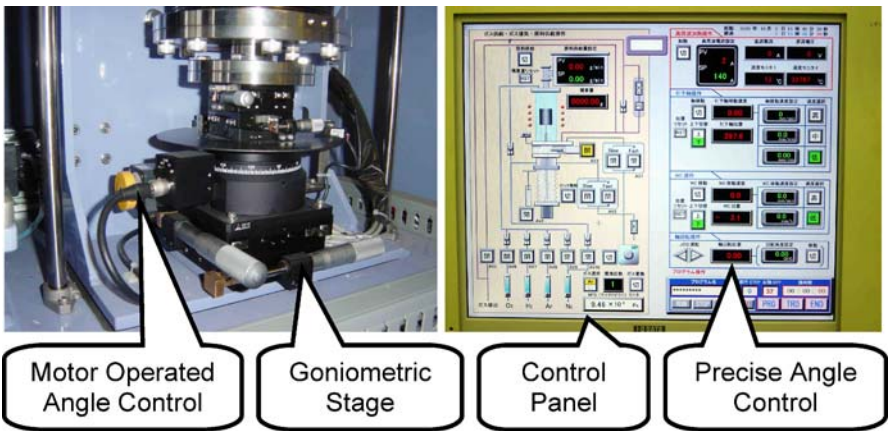


Fig. 2.18. Precise angle control in  $\mu$ -PD system

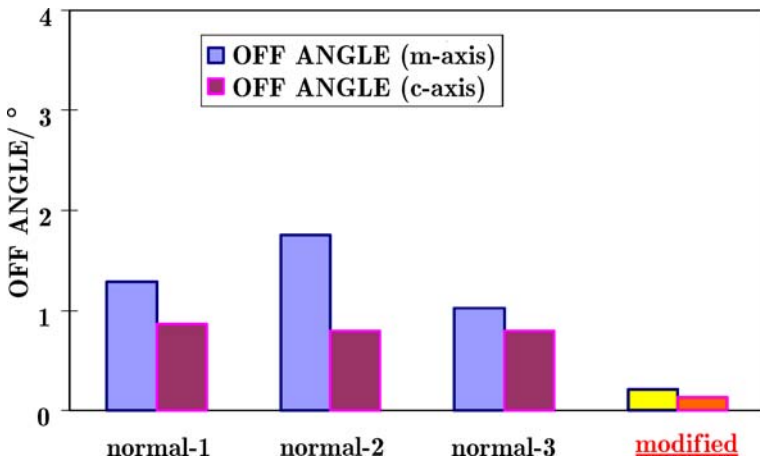


Fig. 2.19. Off-angle misorientation of sapphire plate crystals produced by  $\mu$ -PD process with and without application of precise angle control system

of the meniscus, the solidification process itself, and the crystal quality. Currently, equipment employing such systems can control the angle electronically to an accuracy of as high as  $0.01^\circ$ . An example of such a system is shown in Fig. 2.18.

In particular, this type of system has been used to reduce the misorientation between the surface of a plate sapphire crystal (see Chap. 16) and its crystallographic axes. The orientations of the plate die of the crucible and the plate seed crystal were precisely set at room temperature using light reflection before the growth zone (the crucible) was heated. At this stage, the angle was controlled using the system shown in Fig. 2.18. The misorientations (off-angle) of sapphire plate crystals produced by the  $\mu$ -PD technique before and after the installation of the orientation adjustment system and the modified angle control instrumentation are shown in Fig. 2.19. As can be seen from the plot, a considerable improvement in crystal orientation was achieved using the modified system, with the off-angle decreasing to below  $0.5^\circ$ .

Accurate orientation control is also important when the composition of the melt does not match that of the crystal (whether intentionally or not), causes flux-like behavior in the system and subsequent faceting of the crystal. In such cases, the performance of the system is particularly sensitive to misorientation, especially when the aspect ratio of the crystal is high.

## References

1. P. Rudolph, T. Fukuda, *Crys. Res. Technol.*, **34**, 3 (1999)
2. D.H. Yoon, *Opto-Electron. Rev.*, **12**(2), 199 (2004)
3. T. Fukuda, P. Rudolph, S. Uda, (eds.), *Fiber Crystal Growth from the Melt*, (Springer, Berlin, 2004)
4. D.H. Yoon, I. Yonenaga, T. Fukuda, N. Ohnishi, *J. Cryst. Growth*, **142**, 339 (1994)
5. D.H. Yoon, T. Fukuda, *J. Cryst. Growth*, **144**, 201 (1994)
6. D.H. Yoon, I. Yonenaga, T. Fukuda, *Crys. Res. Technol.*, **29**(8), 1119 (1994)
7. D.H. Yoon, M. Hashimoto T. Fukuda, *Jpn. J. Appl. Phys.*, **33**, 3510 (1994)
8. D.H. Yoon, P. Rudolph, T. Fukuda, *J. Cryst. Growth*, **144**, 207 (1994)
9. V.I. Chani, K. Nagata, T. Kawaguchi, M. Imaeda, T. Fukuda, *J. Cryst. Growth*, **194**, 374 (1998)
10. V.I. Chani, K. Shimamura, T. Fukuda, *Crys. Res. Technol.*, **34**, 519 (1999)
11. V.I. Chani, K. Nagata, T. Fukuda, *Ferroelectrics*, **218**, 9 (1998)
12. Y.M. Yu, V.I. Chani, K. Shimamura, T. Fukuda, *J. Cryst. Growth*, **171**, 463 (1997)
13. Y.M. Yu, V.I. Chani, K. Shimamura, K. Inaba, T. Fukuda, *J. Cryst. Growth*, **177**, 74 (1997)
14. H.J. Koh, Y. Furukawa, P. Rudolph, T. Fukuda, *J. Cryst. Growth*, **149**(3-4), 236 (1995)
15. H.J. Koh, T. Fukuda, *Crys. Res. Technol.* **31**, 151 (1996)
16. N Schäfer, T. Yamada, K. Shimamura, H.J. Koh, T. Fukuda, *J. Cryst. Growth*, **166**, 675 (1996)

17. B.M. Epelbaum, P.A. Gurjiyants, K. Inaba, K. Shimamura, S. Uda, H.J. Koh, T. Fukuda, *Jpn. J. Appl. Phys.*, **36**, 2788 (1997)
18. N Schäfer, T. Yamada, K. Shimamura, H.J. Koh, T. Fukuda, *J. Cryst. Growth*, **166**, 675 (1996)
19. A. Yoshikawa, B.M. Epelbaum, T. Fukuda, K. Suzuki, Y. Wako, *Jpn. J. Appl. Phys.*, **38**, L55 (1999)
20. B.M. Epelbaum, A. Yoshikawa, K. Shimamura, T. Fukuda, K. Suzuki, Y. Wako, *J. Cryst. Growth*, **198/199**, 471 (1999)
21. H. Takeda, T. Kato, V.I. Chani, H. Morikoshi, K. Shimamura, T. Fukuda, *J. Alloys Compd.*, **290**, 79 (1999)
22. T. Tsuboi, K. Shimamura, T. Fukuda, *Phys. Stat. Sol. B* **214**, 479 (1999)
23. H. Takeda, T. Kato, V.I. Chani, K. Shimamura, T. Fukuda, *J. Alloys Compd.* **290**, 244 (1999)
24. V.I. Chani, A. Yoshikawa, Y. Kuwano, K. Hasegawa, T. Fukuda, *J. Cryst. Growth*, **204**, 155 (1999)
25. V.I. Chani, A. Yoshikawa, Y. Kuwano, K. Inaba, K. Omote, T. Fukuda, *Mater. Res. Bull.*, **35**(10), 1615 (2000)
26. K. Lebbou, D. Perrodin, V.I. Chani, O. Aloui, A. Brenier, J.M. Fourmigue, O. Tillement, J. Didierjean, F. Balembois, P. Gorges, *J. Am. Ceram. Soc.*, **89**(1), 75 (2006)
27. A. Brenier, G. Boulon, K. Shimamura, T. Fukuda, *J. Cryst. Growth*, **204**, 145 (1999)
28. H. Takeda, J. Sato, H. Morikoshi, T. Kato, K. Shimamura, T. Fukuda, *Mater. Lett.*, **41**, 104 (1999)
29. Y. Urata, S. Wada, H. Tashiro, T. Fukuda, *Appl. Phys. Lett.*, **75**(5), 636 (1999)
30. V.I. Chani, A. Yoshikawa, H. Machida, T. Satoh, T. Fukuda, *J. Cryst. Growth*, **210**(4), 663 (2000)
31. V.I. Chani, A. Yoshikawa, H. Machida, T. Fukuda, *J. Cryst. Growth*, **212**(3-4), 469 (2000)
32. V.I. Chani, A. Yoshikawa, H. Machida, T. Fukuda, *Mater. Sci. Eng. B* **75**(1), 53 (2000)
33. H. Sato, V.I. Chani, A. Yoshikawa, Y. Kagamitani, H. Machida, T. Fukuda, *J. Cryst. Growth*, **264**(1-3), 253 (2004)
34. V.I. Chani, A. Yoshikawa, H. Machida, T. Fukuda, in: *Extended Abstracts* (The 60th Autumn Meeting, 1999), *Jap. Soc. Appl. Phys.*, September 1-4, Kobe, Japan, 3a-S-2
35. K. Lebbou, H. Itagaki, A. Yoshikawa, T. Fukuda, F. Carillo-Romo, G. Boulon, A. Brenier, M.Th. Cohen-Adad, *J. Cryst. Growth*, **210**, 655 (2000)
36. K.T. Jacob, S. Priya, Y. Waseda, *Bull. Mater. Sci.*, **21**(1), 99 (1998)
37. K. Lebbou, A. Yoshikawa, M. Kikuchi, T. Fukuda, M.Th. Cohen-Adad, G. Boulon, *Physica C*, **336**, 254 (2000)
38. S. Ganschow, D. Klimm, B.M. Epelbaum, A. Yoshikawa, J. Doerschel, T. Fukuda, *J. Cryst. Growth*, **225**, 451 (2001)
39. I.H. Jung, A. Yoshikawa, K. Lebbou, T. Fukuda, K.H. Auh, *J. Cryst. Growth*, **226**, 101 (2001)
40. D.A. Pawlak, Y. Kagamitani, A. Yoshikawa, K. Wozniak, H. Sato, H. Machida, T. Fukuda, *J. Cryst. Growth*, **226**, 341 (2001)
41. G. Boulon, A. Collombert, A. Brenier, M.Th. Cohen-Adad, A. Yoshikawa, K. Lebbou, J.-H Lee, T. Fukuda, *Adv. Funct. Mater.*, **11**(4), 263 (2001)

42. A. Yoshikawa, T. Akagi, M. Nikl, N. Solovieva, K. Lebbou, C. Dujardin, C. Pedrini, T. Fukuda, Nucl. Instr. Meth. A, **486**, 79 (2002)
43. J.B. Shim, J.H. Lee, A. Yoshikawa, M. Nikl, D.H. Yoon, T. Fukuda, J. Cryst. Growth, **243**, 157 (2002)
44. V.I. Chani, K. Lebbou, B. Hautefeuille, O. Tillement, J.-M. Fourmigue, Cryst. Res. Technol., **41**(10), 972 (2006)
45. J.B. Shim, J.H. Lee, A. Yoshikawa, M. Nikl, D.H. Yoon, T. Fukuda, J. Cryst. Growth, **243**, 157 (2002)
46. Y. Urata, T. Fukuda, H. Ito, S. Wada, Jpn. J. Appl. Phys., **40**, 6453 (2001)
47. A. Yoshikawa, T. Satonaga, K. Kamada, H. Sato, M. Nikl, N. Solovieva, T. Fukuda, J. Cryst. Growth, **270**, 427 (2004)
48. A. Novoselov, A. Yoshikawa, M. Nikl, N. Solovieva, T. Fukuda, Nucl. Instr. Meth. A, **537**, 247 (2005)
49. A. Novoselov, A. Yoshikawa, M. Nikl, N. Solovieva, T. Fukuda, Cryst. Res. Technol., **40**(4/5), 419 (2005)
50. A. Yoshikawa, K. Kamada, M. Nikl, K. Aoki, H. Sato, J. Pejchal, T. Fukuda, J. Cryst. Growth, **285**, 445 (2005)
51. J.H. Mun, A. Novoselov, A. Yoshikawa, G. Boulon, T. Fukuda, Mater. Res. Bull., **40**, 1235 (2005)
52. A. Novoselov, H. Ogino, A. Yoshikawa, M. Nikl, J. Pejchal, J.A. Mares, A. Beitlerova, C. D'Ambrosio, T. Fukuda, J. Cryst. Growth, **287**, 309 (2006)
53. A. Jouini, H. Sato, A. Yoshikawa, T. Fukuda, G. Boulon, K. Kato, E. Hanamura, J. Cryst. Growth, **287**, 313 (2006)
54. R. Simura, A. Jouini, K. Kamada, A. Yoshikawa, K. Aoki, Y. Guyot, G. Boulon, T. Fukuda, J. Cryst. Growth, **291**, 309 (2006)
55. A. Karek, K. Lebbou, M. Diaf, A. Brenier, G. Boulon, Mat. Res. Bull, in press (2006)
56. S. Maida, M. Higuchi, K. Kodaira, J. Cryst. Growth, **205**(3), 317 (1999)
57. H. Ogino, A. Yoshikawa, M. Nikl, A. Krasnikov, K. Kamada, T. Fukuda, J. Cryst. Growth, **287**, 335 (2006)
58. J. Kvapil, J. Kvapil, K. Blazek, J. Zikmund, R. Autrata, P. Schauer, Czech. J. Phys. B, **30**, 185 (1980)
59. V.N. Kurlov, N.V. Klassen, A.M. Dodonov, S.Z. Shmurak, G.K. Strukova, I.M. Shmut'ko, S.E. Derezno, M.J. Weber, Nucl. Instr. Meth. A, **537**, 197 (2005)
60. P.I. Antonov, V.N. Kurlov, Prog. Cryst. Growth Ch., **44**, 63 (2002)
61. V.N. Kurlov, B.M. Epelbaum, Cryst. Growth, **187**, 107 (1998)

# 3 Equipment Configuration

Tsuguo Fukuda

**Abstract.** Micro-pulling-down equipment design is overviewed with special attention paid to its adaptation to industrial crystal growth. Therefore, strategies for improving the commercial efficiency of this technology, some cost-effective technological innovations, and crystal yield and quality are discussed. Real growth process performance is illustrated using examples of crystals grown with a view to their industrialization.

The application of a micro-pulling-down ( $\mu$ -PD) apparatus [1] to the growth of bulk or relatively large shaped macrocrystals does not transform the nature of the basic processes that occur in the  $\mu$ -PD system. In both micro- and macrocrystal growth, the melt is transported through *microchannel(s)* in the crucible, as illustrated in Fig. 3.1 (see Fig. 1.2 for comparison). Therefore, the same phenomena are observed in the capillary channel(s), and the same apparatus is used in both cases. The only specific limitation in terms of the dimensions of the crystals is related to the space available inside the thermal insulation of a resistively heated system or inside the inductor coil in the case of a RF-heated  $\mu$ -PD. However, this problem can be resolved relatively easily because large-scale resistive furnaces and RF-heated systems are produced for and widely used in other crystal growth techniques. Thus, these functional

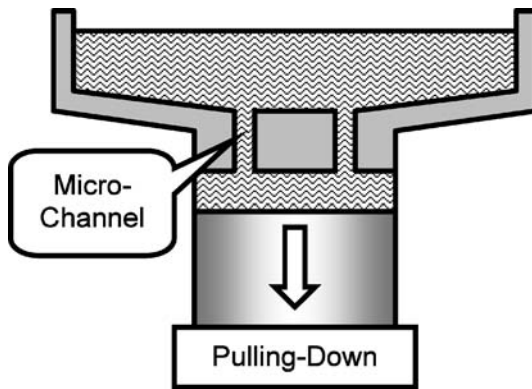


**Fig. 3.1.** Schematic diagram of “Macro”-crystal growth by “Micro”-pulling-down method

parts can be imported from any large-scale apparatus available. Even existing  $\mu$ -PD equipment is largely universal because it can be applied to the growth of materials with a wide range of cross-sections (from 0.1 to 10 mm or even larger).

### 3.1 History of Development

According to the best knowledge of the author, the total number of  $\mu$ -PD machines constructed around the world during the period 1994–2006 was approximately 30. This is considered as an initial demonstration of the general success of this technology. The trend shown in Fig. 3.2 illustrates a continuous growth in the number of  $\mu$ -PD systems operating in various research and industrial institutions. And extensive but not complete list of the  $\mu$ -PD equipment available is given in Table 3.1.

Recall that Fig. 1.15 demonstrated that research into the growth and properties of  $\mu$ -PD crystals has been steadily accelerating and intensifying for over a decade. Figure 3.2 illustrates a similar trend in the number of  $\mu$ -PD machines designed and assembled over this period of time. The plot seen in Fig. 3.2 can obviously be interpreted as reflecting a general increase in the interest in developing  $\mu$ -PD technology. In most cases, it corresponds closely to the increase in the number of research personnel involved in this technology, and therefore the increase in the levels of funding provided by

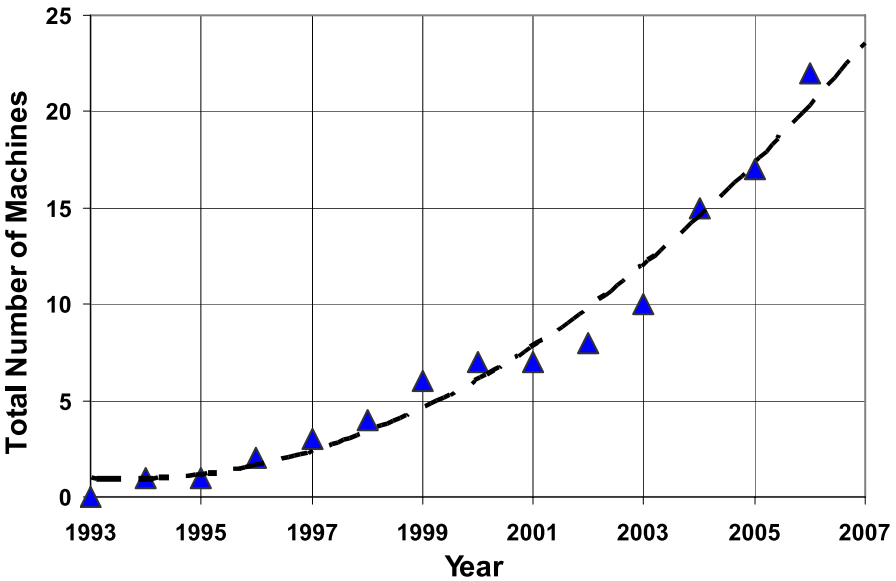


Fig. 3.2. Trend of increasing of total number of operating  $\mu$ -PD machines based on Table 3.1

**Table 3.1.** List of  $\mu$ -PD systems around the world in order of year of construction. For each system, the type of heating used (RES: resistive; RF: inductive), the owner ( $\rightarrow$  indicates a change of user/owner), and the name of the manufacturer (available from the contributors to this book, users of the systems, and references) is provided

Type	Year	User/Owner	Manufacturer	Notes
RES	1994	IMR $\rightarrow$ IMRAM, Tohoku Univ., Japan	Tohoku Kikai Mfg. Co. Ltd., Japan	First version, [2–9]
RES	1996	NGK Co. Ltd., Japan	NGK Co. Ltd., Japan	KLN plate growth
RES	1997	Sungkyunkwan Univ., Korea	Silver Star System, Korea	LN fiber
RF	1998	IMR $\rightarrow$ IMRAM, Tohoku Univ., Japan	TDK Co. Ltd., Japan	Oxide crystals
RF	1999	JST $\rightarrow$ IMR, Tohoku Univ., Japan	Daiichi Kiden Co. Ltd., Japan	Oxide growth, chamber
RF	1999	Institute for Crystal Growth, Germany	Nürmont GmbH, Freiberg/Sa., Germany	Water-cooled stainless steel chamber, vacuum down to $< 10^{-5}$ mbar
RF	2000	IMRAM, Tohoku Univ., Japan	TDK Co. Ltd., Japan	Oxide crystals
RES	2002	Nuclear and Energy Research Inst., IPEN – CNEN/SP, Brazil	Linn High Therm, Germany	Modified for vacuum operation, see Chap. 20
RF	2003	Fukuda X'tal Lab., Japan	Not available	Fluoride (oxide growth with modified chamber) See Chap. 19
RF	2003	NMLA, Physics Dept., Pisa Univ., Italy	The National Institute for the Physics of Matter (INFM), Pisa Univ., Italy	See Chap. 10
RF	2004	NMLA, Physics Dept., Pisa Univ, Italy.	The National Institute of Nuclear Physics (INFN), Pisa Univ., Italy	See Chap. 10
RF	2004	IMRAM, Tohoku Univ., Japan	TDK Co. Ltd., Japan	Fluorides, chamber
RES	2004	IMR, Tohoku Univ., Japan	NGK, Japan	Oxide crystals
RF	2004	NEC TOKIN Co., Japan	Not available	See Chap. 15
RF	2004	Institute of Electronic Materials Technology, Poland	Cyberstar, France	Redesigned CZ apparatus

**Table 3.1.** (continued)

Type	Year	User/Owner	Manufacturer	Notes
RF	2005	Fukuda X'tal Lab., Japan	Nissin Giken Corp., Japan	Continuous charging and multocrystal growth
RF	2005	NEOMAX Co. Ltd., Japan	Nissin Giken Corp., Japan	Oxide crystals
RF	2006	Fukuda X'tal Lab., Japan	Nissin Giken Corp., Japan	Oxide, multocrystal growth
RF	2006	Sungkyunkwan Univ., Korea	Qualiflow Naratech, Korea	Vacuum chamber
RF	2006	Nuclear and Energy Research Inst., IPEN – CNEN/SP, Brazil	Crystal Growth Lab., Center for Lasers and Applications, IPEN – CNEN/SP, Brazil	Vacuum chamber
RF	2006	Graduate school of Engineering, Tohoku Univ., Japan	TDK Co. Ltd., Japan	Alloy growth, chamber
RES	2006	LMOPS, Metz University, France	LMOPS/Fibercryst	
RES	–	LPCML Claude Bernard Lyon 1 Univ., France	Japan	[10]
RES	–	LPCML Claude Bernard Lyon 1 Univ., France	Not available	
RF	–	LPCML Claude Bernard Lyon 1 Univ., France	Not available	
RF	–	Fibercryst SAS, France	Not available	[24]
RES	–	Univ. of Erlangen–Nuremberg, Germany	Not available	[23]

governmental and industrial partners to aid the technical development of  $\mu$ -PD equipment in both academia and industry.

In addition to those described in this table, several Japanese manufacturers (such as Nissin Giken Corp.) have supplied  $\mu$ -PD equipment

## 3.2 Hardware Design of Growth Systems

The schematic diagram of a  $\mu$ -PD system shown in Fig. 1.2 shows only the fundamentals of the method. In fact, the growth apparatus used contains many more hardware elements that are responsible for the proper functioning of each part of the system and the system as a whole. A relatively detailed scheme of the  $\mu$ -PD system from the point of view of hardware configuration is shown in Fig. 3.3. In reality, a system that contains all of the functionality listed in Fig. 3.3 is probably yet to be constructed. However, most of the parts illustrated in Fig. 3.3 have been actually manufactured and tested separately in different  $\mu$ -PD systems.

So far, the information available from the image of the meniscus has been considered to be the most important for controlling crystal quality and possibly for stabilizing the growth conditions and the crystal properties along the growth axis. In most cases, the technical personnel (operators) that use the machine have a good understanding of this information. However, these images have yet to be translated in such a way that they can be interpreted by computing systems capable of managing the whole growth process. A few attempts have been made to use pyrometric measurements to determine the temperature distributions in the crucible, the meniscus zone, and the crystal. However, the application of this strategy to actual process control has also not been reported so far.

The sections below will describe the general design, construction, and operational principles of the components of the system that are responsible for some of the functions listed in Fig. 3.3. In most cases these components have been installed in actual  $\mu$ -PD systems.

## 3.3 $\mu$ -PD with Resistive Heating

A general view of a typical  $\mu$ -PD system with resistive heating is shown in Fig. 3.4. The apparatus has two main functional units. One of them (the unit on the left) is responsible for the physical performance of the growth system, including the heating of all functional parts and the precise displacement of the seed/crystal in any potential direction: horizontally to adjust the seed position (with angle/orientation correction) and vertically for pulling-down growth.

The control unit (the unit on the right in Fig. 3.4) generates electric signals that are supplied to all heated elements, including the crucible, the after-heater, and the outer heater. This unit also precisely controls the translation

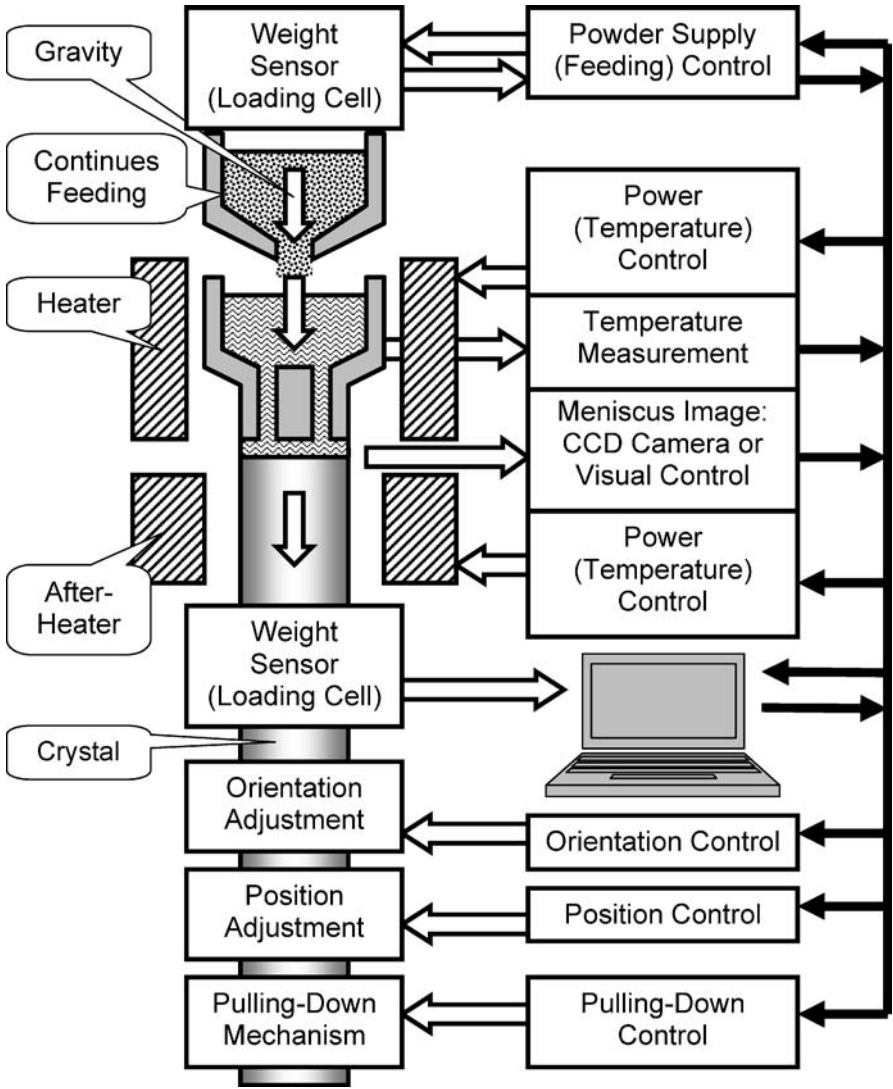


Fig. 3.3. General hardware configuration of  $\mu$ -PD system

of the crystal in the vertical direction (upward when seeding and downward when pulling-down growth is being performed) and sometimes performs precise measurements of the position of the crystal. Data on pulling rates and the relative position of the crystal registered by sensors situated in the pulled-down unit are displayed on its control panel.

The temperature inside the outer heater (see Fig. 3.5), as measured by a thermocouple, is also monitored and sometimes adjusted to stabilize the thermal environment around the crucible and the growth interface. However

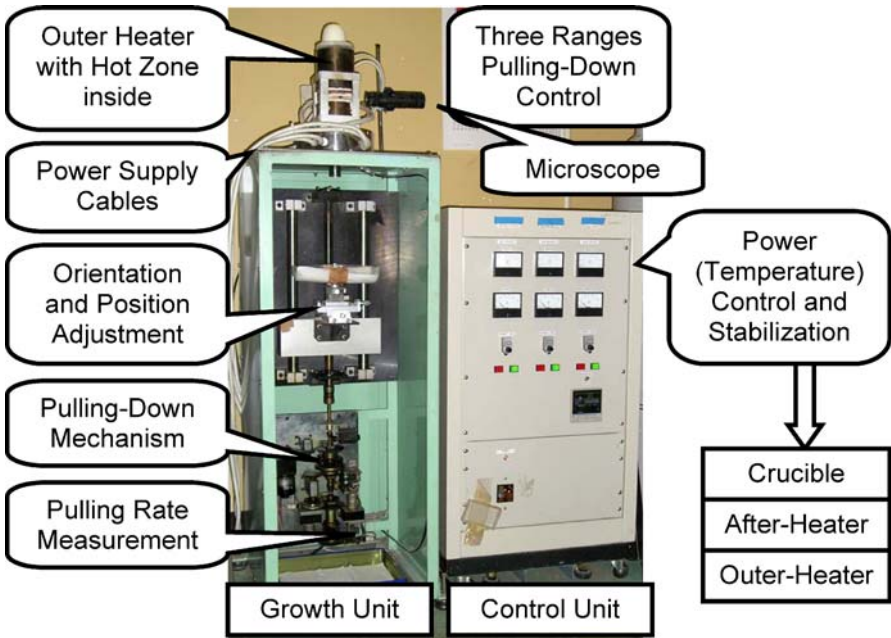


Fig. 3.4. Design of typical  $\mu$ -PD system with resistive heating

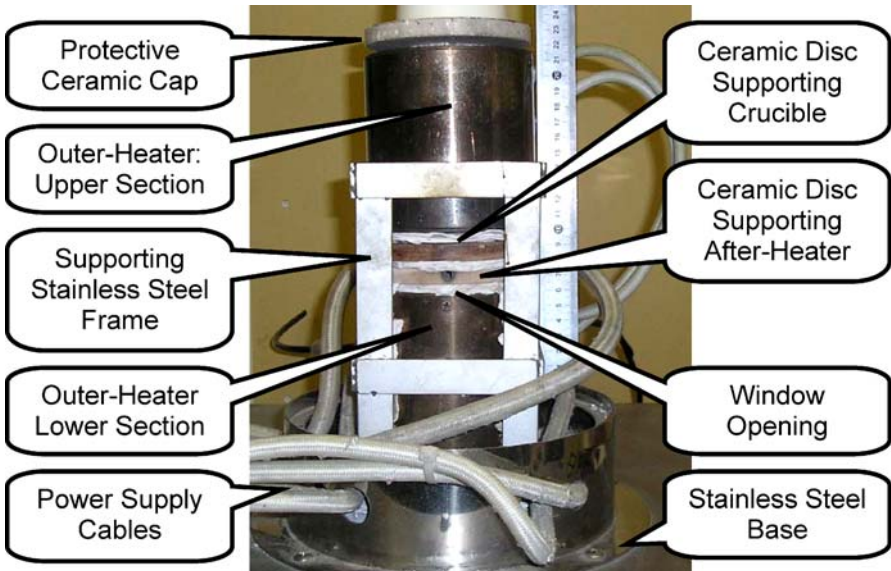
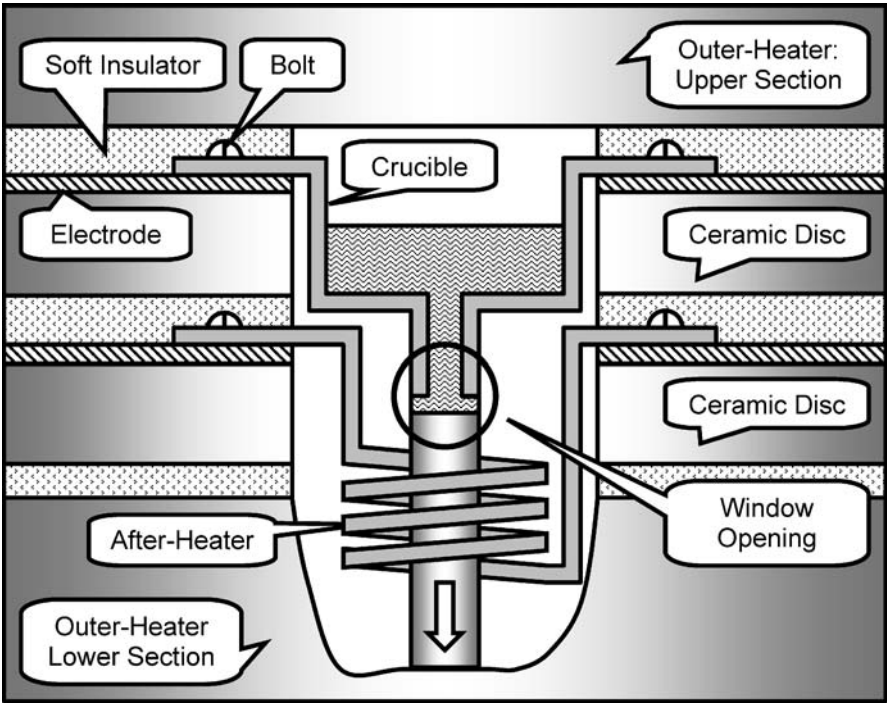


Fig. 3.5. Typical configuration of hot zone in  $\mu$ -PD system with resistive heating (see Fig. 3.6 for details)



**Fig. 3.6.** Detailed schematic diagram of hot zone in  $\mu$ -PD system with resistive heating (see Fig. 3.5 for reference)

precise control of the melt temperature at any location (the crucible, the capillary, or the meniscus) is generally not attempted because of the exceptionally high temperature gradients (up to  $300^\circ/\text{mm}$  according to [2, 10] and Fig. 4.12). Thus, accurate temperature data cannot be obtained from thermocouple measurements because the dimensions of the thermocouple itself are similar to those of the crucible, the meniscus, and the crystal (mm-scale). The use of a pyrometer to monitor the spatial temperature distributions in these miniature objects probably shows the most potential of any of these methods, because it is possible to perform color analysis on objects with dimensions of several micrometers.

### 3.4 $\mu$ -PD with Inductive RF Heating

#### 3.4.1 Systems with Fused Quartz Isolation

Systems with inductive RF heating normally contain two functional units, similar to those shown in Fig. 3.4, along with an RF power generator that is sometimes supplied separately (from a functional point of view the generator belongs in the control unit). In most cases, this equipment is designed

to provide growth atmosphere control, similar to that used in conventional Czochralski (CZ) growth systems employed to grow materials with high melting points of 1500–2500 °C. Two ways of isolating the atmospheric environment of the growth zone from that of the rest of the laboratory are generally practiced. One is based on controlling the gas flow through the hot zone and isolating the zone from its surroundings through the use of a quartz tube placed between the coil and the hot zone. Another type of apparatus makes use of a metal chamber (see Table 3.1) that provides the ability to increase or decrease the pressure to much lower or higher than normal. Both types of isolation are also common in CZ equipment.

Figures 3.7 [1] and 3.8 illustrate a typical chamberless system used to grow a number of oxide fiber crystals and eutectic composites with melting points of up to 2000 °C [11–18]. Details of the hot zone configuration used for this system were described in the previous chapter (see Figs. 2.5 and 2.6). In most RF-heated systems, the meniscus is observed with a CCD camera coupled to a monitor. It is viewed between the windings of the coil. Therefore,

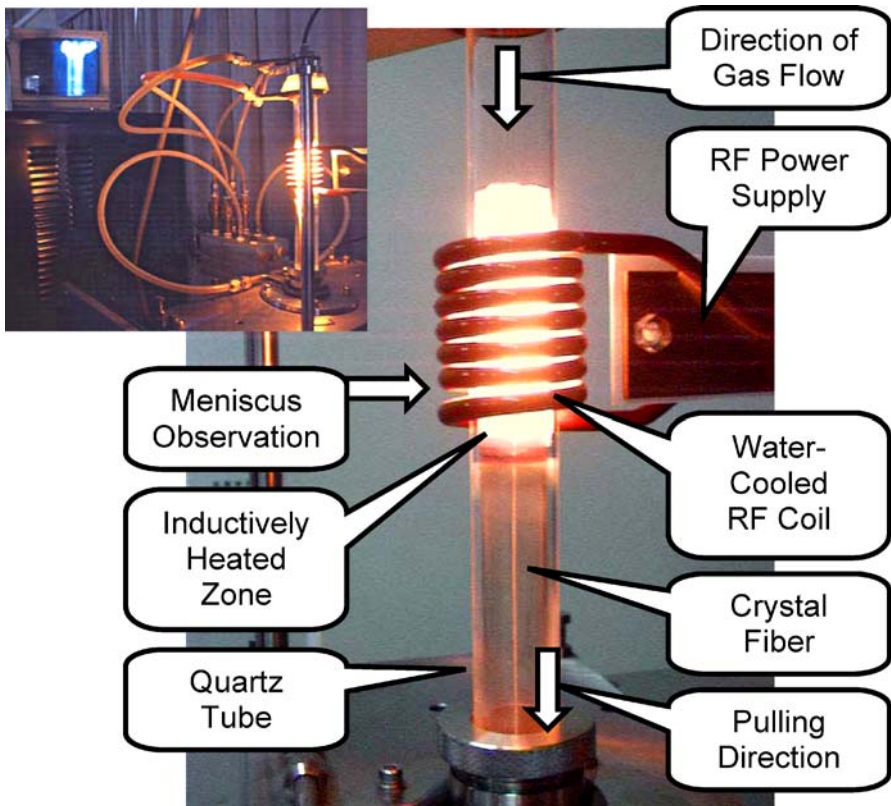


**Fig. 3.7.** Typical configuration of hot zone in chamber-less  $\mu$ -PD system with inductive RF heating [1]

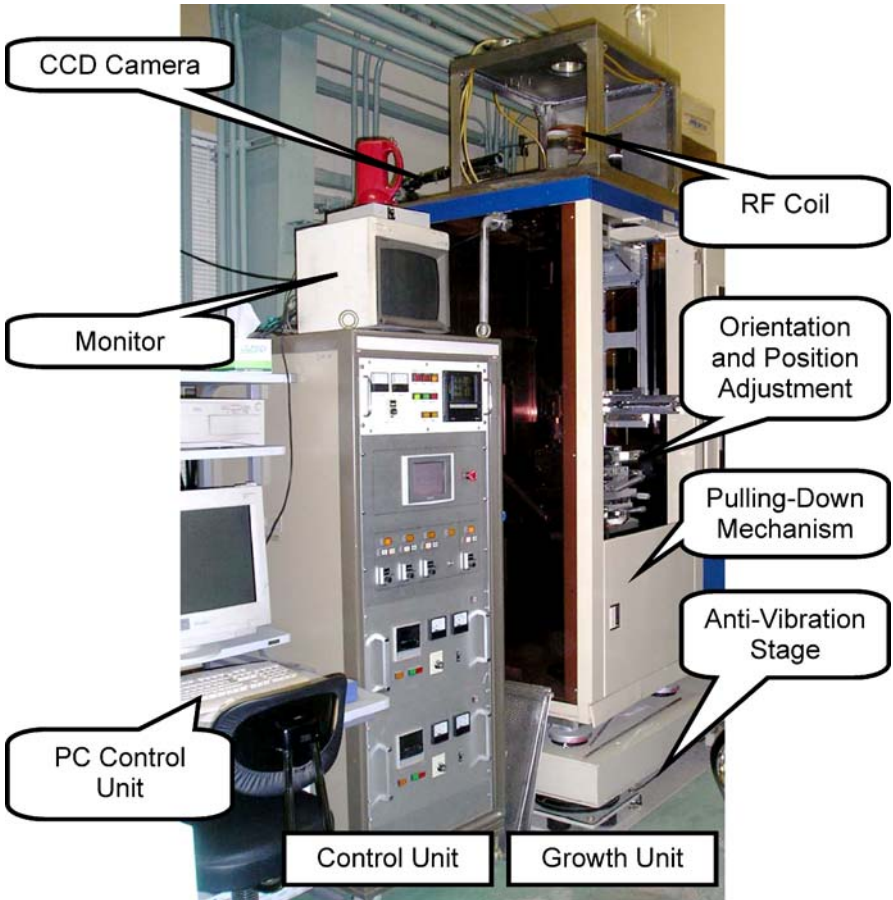


**Fig. 3.8.** Design of typical  $\mu$ -PD system with inductive RF heating and chamber-less configuration

it is absolutely essential that the components in the hot zone (see Figs. 2.5 and 2.6), including the windows in the afterheater and in the surrounding thermal insulation, are arranged appropriately.

It is important to note that the direction of gas flow also affects the growth parameters. The gas flow rate used in most cases is about 2 l/min, and it flows in the downward direction (Fig. 3.7). The gas is supplied to the system from reservoirs maintained at room temperature. As a result, the temperature of the gas is much lower than the temperature of the melt, which undoubtedly influences the temperature distribution around the crucible and in the vicinity of the growth interface. Changing the flow direction modifies the thermal conditions. The best flow direction to use should therefore be considered for any particular process.

One more important phenomenon related to the direction of gas flow is the transport of vaporized material if the melt contains one or more constituents

that evaporate at melting temperature during the growth. It is evident that presence of the quartz tube (even if it is transparent and has high-quality surfaces) between the object (the growth interface) and CCD camera will decrease the quality of the image. However, if evaporated material is deposited on the relatively cold inner surface of the tube (and this is often observed), the quality of the image will degrade even further.

From general considerations, it is possible to improve the visualization of the process by configuring the gas to flow in the upward direction. Considering the structure of the  $\mu$ -PD system (Fig. 3.1), two surfaces of the melt are in direct contact with the gas environment: the surface of the melt inside the crucible and the surface of the meniscus. Melt is evaporated from both of these surfaces. However, the meniscus has a smaller surface area and its temperature is less than that of the melt in the crucible because it is situated close to the solidification interface. Also, most deposition will occur at the region of the quartz tube closest to the window. Thus, if the gas moves upward past this region, it contains less vaporized material (i.e., that evaporated from the meniscus) than if the gas moves downward past this region of the quartz tube (in which case the gas would contain the material evaporated from the top of the melt in the crucible); see Fig. 3.7.

### 3.4.2 Systems with a Growth Chamber

There is no fundamental difference between the  $\mu$ -PD systems employing inductive RF heating that are described in previous and current subsections. However, from a practical point of view, the application of a hermetic chamber (Figs. 3.9 and 3.10) to separate the growth atmosphere from the rest of the

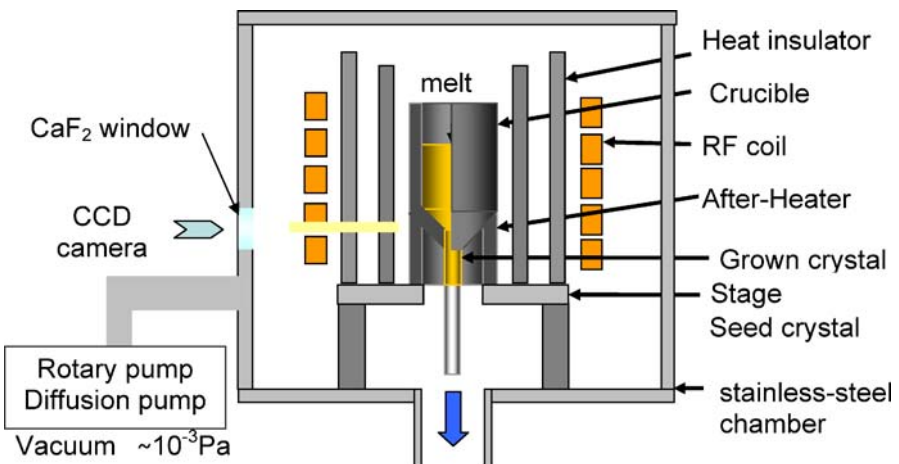


**Fig. 3.9.** Design of typical  $\mu$ -PD system with inductive RF heating and the hot zone positioned inside chamber

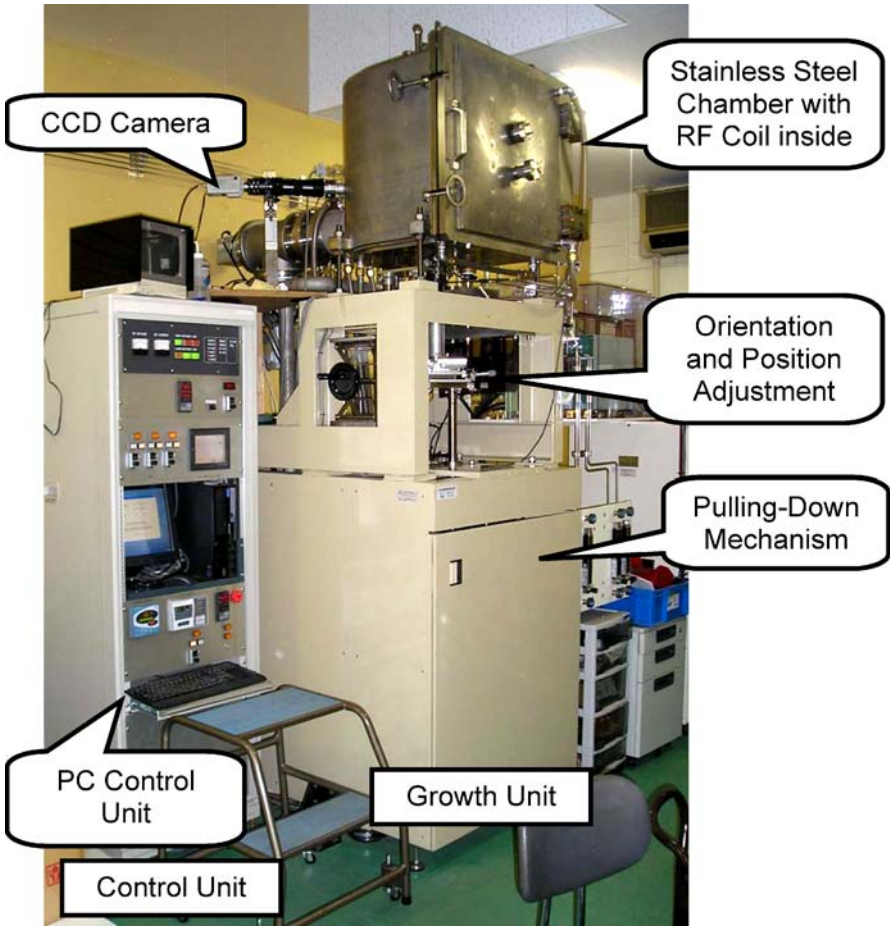


**Fig. 3.10.** Design of typical  $\mu$ -PD system with inductive RF heating inside stainless steel chamber designed for the growth of fluoride crystals

laboratory environment is generally more appropriate. Although additional financial resources are required to manufacture the chamber in the first place, this design does not require expensive fused quartz tubes (see Fig. 3.7); the optical quality of such a tube can degrade very quickly, depending on the melt used.

When a quartz (silica) tube is used, the diameter of the tube is typically not much larger than the diameter of the crucible and the hot zone (Figs. 2.6 and 3.7). Therefore, the tube also becomes involved in the heating/cooling cycles of the hot zone. While the temperature of the tube is not as high as that of the crucible, it is generally high enough to decrease the transparency of the tube due to the partial crystallization of fused silica, which is a noncrystalline form of silicon dioxide ( $\text{SiO}_2$ ). This also

hinders the ability of the operator to monitor the meniscus, the growth interface, and the crystal and therefore to control them optimally. Visual control is almost always used to manage the growth parameters of current  $\mu$ -PD systems. Therefore, the lifetime of a quartz tube is very short not because of mechanical damage, but because its transparency degrades rapidly. This degradation in transparency can also be accelerated by chemical interactions between the quartz and the materials evaporated from the melt. As noted above, such reactions can be partially suppressed by changing the direction of gas flow from downward to upward. Systems that employ chambers (see Fig. 3.9) do not have these disadvantages.

Figure 3.9 illustrates a particular  $\mu$ -PD system with a stainless steel chamber that was used to grow fluoride crystals. The gas environment used for fluoride melts must meet exceptionally strict requirements, independent of the growth technique applied. Some details of those are discussed in Chap. 20 later. The growth atmosphere used is very aggressive. Therefore, careful selection of the chamber material and consideration of its chemical resistance to the environment inside is necessary. An image of the actual equipment that comprises this type of  $\mu$ -PD system is given in Fig. 3.10. It is arranged in a very similar way to the apparatus illustrated in Fig. 3.8.

### 3.5 Industrialization of the $\mu$ -PD Process

Broadly speaking, the main reason for researching and developing any particular technology is to commercialize it, and  $\mu$ -PD is no exception. Therefore, the problems associated with increasing both the quality and the quantity of the crystalline materials produced by  $\mu$ -PD have attracted much attention from the very earliest stages of the development of the processes and equipment used in  $\mu$ -PD.

From its earliest developmental stages, the potential to achieve very high growth rates ( $> 5$  mm/min) when fabricating fiber-shaped crystals [13] of reasonable quality using the  $\mu$ -PD process suggested that it was a very promising technique from the point of view of possible industrialization. These high growth rates are not typically achievable in most other melt growth technologies. The ability of the  $\mu$ -PD system to produce exceptionally long crystals (fiber crystals up to 1 m in length; see Chap. 11) is another advantage of this technology. The crystal length is generally limited only by the length of the pulling-down system, and it can be elongated without considerable technical effort. Thus, the growth of elongated bulk crystals is another important advantage of  $\mu$ -PD technology lending it to actual mass production (Fig. 3.11)

The availability of a vertically elongated space in the factory room and the suppression of vibrations are the two main problems to address when a vertically extended system is designed. In order to protect the meniscus

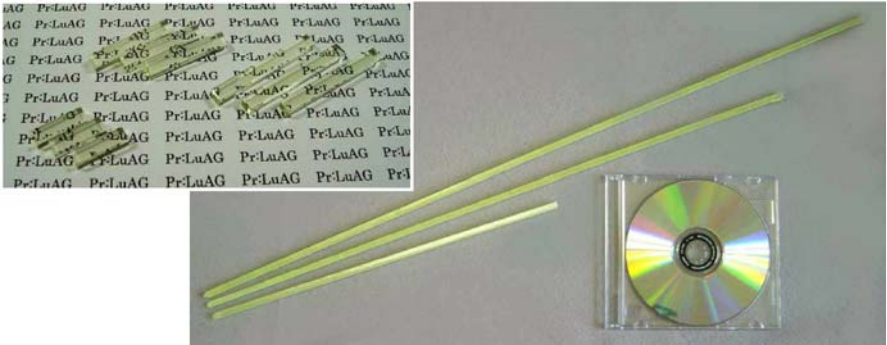


Fig. 3.11. View of  $\text{Lu}_3\text{Al}_5\text{O}_{12}:\text{Pr}$   $\mu$ -PD scintillator crystals produced with dimensions  $5 \times 5 \times 600$  mm. As polished specimens are shown in *upper left corner*



Fig. 3.12.  $\mu$ -PD system with anti-vibration stages (Nov. 1998)

zone against vibrations, most recent versions of such equipment are supplied with antivibration stages (Fig. 3.12) that allow mechanical stabilization. Constructing the equipment on the ground floor is also certainly desirable.

On the other hand, it is possible to increase the amount of crystal product produced by modernizing existing apparatus. Two examples of such modifications, namely (i) continuous feeding growth and (ii) multicrystal growth, are discussed below from the viewpoint of increasing the efficiency and productivity of  $\mu$ -PD technology.

### 3.5.1 Continuous Feeding Growth

The history of continuous feeding in pulling-down crystal growth was overviewed in some depth in Chap. 1. Nonstop charging of the crucible is also widely practiced in other growth methods. Continuous feeding (Figs. 1.6–1.9) probably originated as an idea from the floating zone (FZ) method (Fig. 1.3), because feeding is an essential attribute of any FZ system. It is also practiced in Czochralski (CZ) and flux/solution growths. In the latter case, appropriately designed crucibles are used to avoid the direct contact of solid feeding materials (mostly powders) with the growth interface. The classic Verneuil method is another crystal growth technique that employs continuous feeding [19]. It can also be considered to be a prototype of the  $\mu$ -PD systems discussed here because the same pulling direction is used and the positions of the feeding source, the melt, and the crystal with respect to the direction of action of gravity are also the same as used in  $\mu$ -PD. Continuous feeding is also applicable to  $\mu$ -PD growth (Fig. 3.13).

Pulling-down growth systems have an obvious advantage over other techniques due to the spatial configuration used: the melt surface is free and has

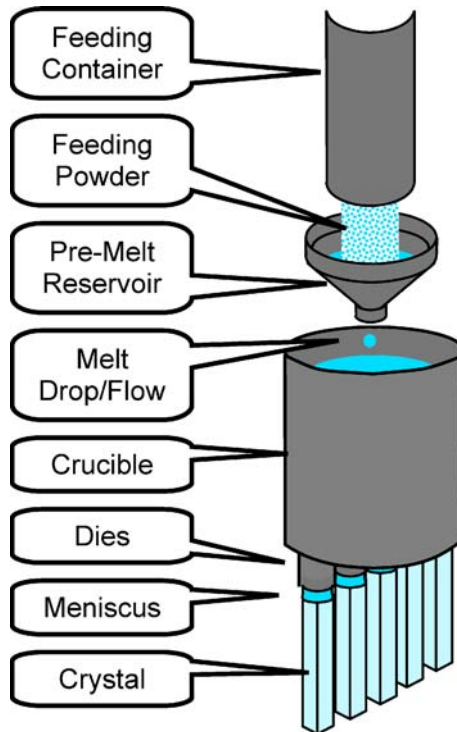


**Fig. 3.13.** Schematic diagram of continuous feeding  $\mu$ -PD system with multi-crystal growth

no direct contact with other elements of the system (i.e., the crystal; Figs. 3.1, 3.3, 3.6 and 3.13). Therefore, the feed material can be supplied using gravity as a driving force (Fig. 3.13). In this type of arrangement, the particles first enter the melt, whereupon they pass through it and probably fully dissolve, and only after this does the feeding material (dissolved or not) approach the growth interface. If the starting particles are completely dissociated then the solid is produced continuously in single-crystalline form. On the other hand, undissolved solid particles can form new crystal nuclei at the growth interface, transforming the process into the solidification of a polycrystalline substance. This can be avoided when the feed material is pre-melted in an additional (heated) reservoir, as shown schematically in Fig. 3.13. In this case, the starting material passes through a solid/liquid phase transformation before arriving at the crucible. Therefore, no additional heat is required to perform these transformations in the crucible and the probability of cofreezing undissolved particles with the body of the main crystal becomes negligible.

The general configuration of a continuous feeding system used with  $\mu$ -PD is illustrated in Fig. 3.14. In this design, the powder particles initially travel horizontally and then they drop vertically into the crucible of the  $\mu$ -PD system.

A schematic diagram of the feeding system is shown in Fig. 3.15. The melt is maintained at a constant level in the crucible by measuring the quantity of powder supplied to the crucible container. The powder is pulled out of the feeding chamber as the screw rotates, providing a uniform powder “flow”. The amount of powder supplied is controlled by adjusting the rotation speed of the screw in the feeder.

It is also evident that the chemical uniformity of the crystals produced with continuous feeding  $\mu$ -PD is exceptionally high so long as the composition

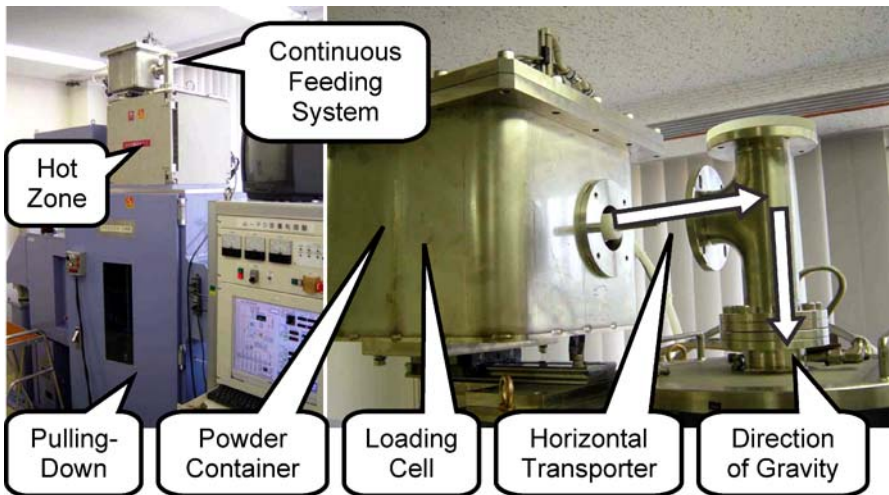


Fig. 3.14. View of continuous feeding system installed in  $\mu$ -PD equipment

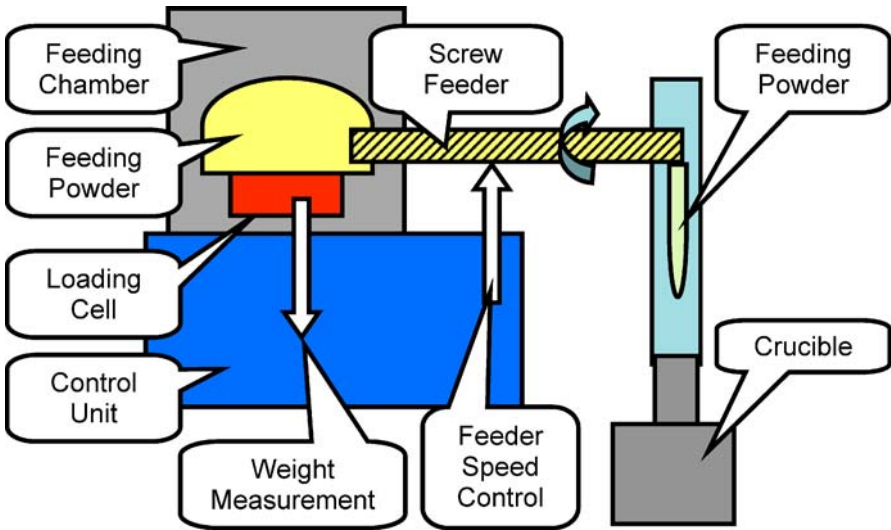


Fig. 3.15. Schematic diagram of continuous feeding system of  $\mu$ -PD equipment

of the starting powder is uniform, as noted for the FZ method. Even when there is a mismatch between the compositions of the melt and the crystal, a process similar to that obtained with a traveling solvent zone is established in the crucible automatically.

The main requirement for a typical  $\mu$ -PD system (Fig. 3.1), is that the constituents of the solid starting material should be distributed relatively uniformly across the volume of the powder. However, in  $\mu$ -PD systems with continuous feeding (Figs. 3.13–3.15), there is an additional condition: that the particles/grain size distribution is uniform throughout the whole volume of the powder. This is necessary to ensure that the material is supplied to the crucible or to the pre-melt reservoir at a uniform rate. Such powders can be prepared based on methods imported from well-developed ceramic technologies or powder metallurgy.

### 3.5.2 Multicrystal Growth

The system configuration shown in Fig. 3.13 represents a particular case where multi-crystal growth is performed in single process. This approach is widely practiced in systems that employ the pulling-up edge-defined film-fed growth (EFG) technique [20–22]. Here, bottom of the crucible contains a collection of melt columns, each ending in a die, and so the system can be used to grow a collection of crystals at the same time. A similar crucible design can also be used in the pulling-down arrangement. A schematic of this growth configuration together with an image of the crucible and the afterheater is provided in Fig. 3.16. Note the multiwindow design of the

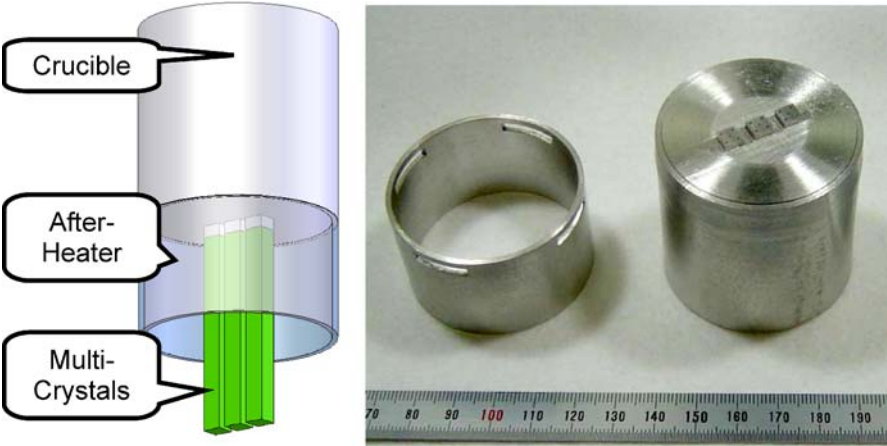


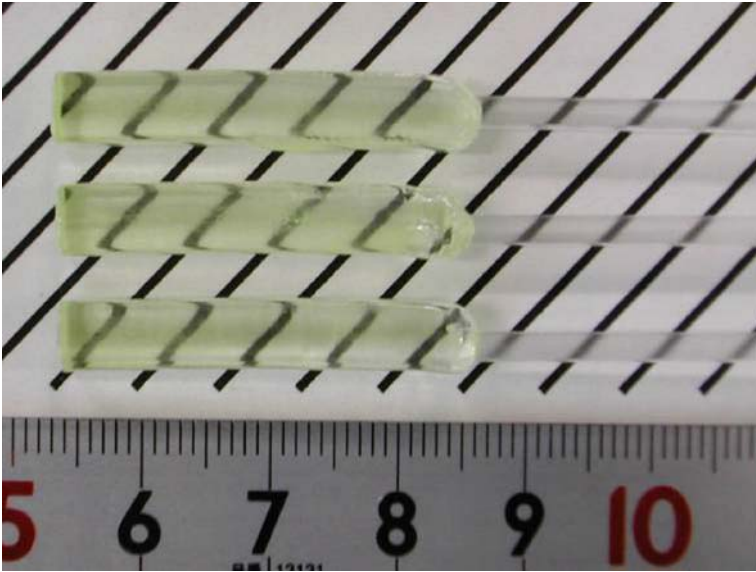
Fig. 3.16. Schematic diagram, the crucible and the after-heater applied for the  $\mu$ -PD growth of three square shaped rods



Fig. 3.17.  $\mu$ -PD system designed for the multi-crystal growth

afterheater, which improves the homogeneity of the temperature distribution below the crucible.

Thus, the application of multidie crucibles is an additional methodological tool that allows the total productivity of the  $\mu$ -PD technique to be increased. An image of a continuous feeding  $\mu$ -PD system that yields multicrystal growth is shown in Fig. 3.17. As an example, Fig. 3.18 shows an image of a set of three rod-shaped crystals grown on three separate seeds in the systems sketched in Figs. 3.13 and 3.16.



**Fig. 3.18.** View of  $\text{Lu}_3\text{Al}_5\text{O}_{12}:\text{Pr}$  crystals produced from multi-die crucible on set of three seeds

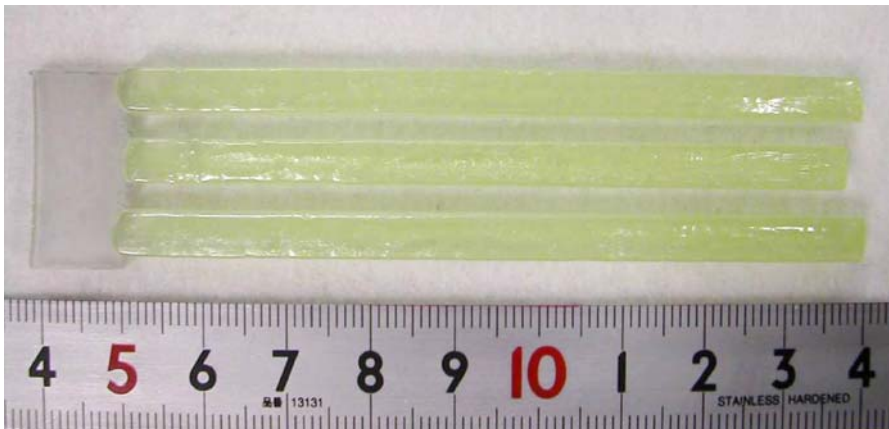


**Fig. 3.19.** View of  $\text{Lu}_3\text{Al}_5\text{O}_{12}:\text{Pr}$  crystals produced from multi-die crucible on single plate shaped seed

Multicrystal growth can also be achieved with a single seed crystal (see Fig. 3.19), provided that the shape of the seed allows it to contact all of the dies during the seeding stage. Several crystals that have the same crystallographic orientations in both the axial and the radial directions can then be grown at the same time. This is important when precise control over the orientation in the radial direction (for example with respect to the orientation of a noncylindrical die) is necessary. In the set-up illustrated in Fig. 3.19, the precise in situ orienting of just one crystal from the group is evidently accompanied by the analogous orienting of all of the other crystals from the group.

## References

1. T. Fukuda, P. Rudolph, S. Uda, (eds.), *Fiber Crystal Growth from the Melt*, (Springer, Berlin, 2004)
2. D.H. Yoon, *Opto-Electron. Rev.*, **12**(2), 199 (2004)
3. D.H. Yoon, M. Hashimoto T. Fukuda, *Jpn. J. Appl. Phys.*, **33**, 3510 (1994)
4. V.I. Chani, K. Nagata, T. Kawaguchi, M. Imaeda, T. Fukuda, *J. Cryst. Growth*, **194**, 374 (1998)
5. V.I. Chani, K. Shimamura, T. Fukuda, *Cryst. Res. Technol.* **34**, 519 (1999)
6. V.I. Chani, K. Nagata, T. Fukuda, *Ferroelectrics*, **218**, 9 (1998)
7. Y.M. Yu, V.I. Chani, K. Shimamura, T. Fukuda, *J. Cryst. Growth*, **171**, 463 (1997)
8. Y.M. Yu, V.I. Chani, K. Shimamura, K. Inaba, T. Fukuda, *J. Cryst. Growth*, **177**, 74 (1997)
9. D.H. Yoon, T. Fukuda, *J. Cryst. Growth*, **144**, 201 (1994)
10. V.I. Chani, K. Lebbou, B. Hautefeuille, O. Tillement, J.-M. Fourmigue, *Cryst. Res. Technol.*, **41**(10), 972 (2006)
11. A. Yoshikawa, B.M. Epelbaum, T. Fukuda, K. Suzuki, Y. Wako, *Jpn. J. Appl. Phys.*, **38**, L55 (1999)
12. B.M. Epelbaum, A. Yoshikawa, K. Shimamura, T. Fukuda, K. Suzuki, Y. Wako, *J. Cryst. Growth*, **198/199**, 471 (1999)
13. V.I. Chani, A. Yoshikawa, Y. Kuwano, K. Hasegawa, T. Fukuda, *J. Cryst. Growth*, **204**, 155 (1999)
14. V.I. Chani, A. Yoshikawa, Y. Kuwano, K. Inaba, K. Omote, T. Fukuda, *Mater. Res. Bull.* **35**(10), 1615 (2000)
15. V.I. Chani, A. Yoshikawa, H. Machida, T. Satoh, T. Fukuda, *J. Cryst. Growth*, **210**(4), 663 (2000)
16. V.I. Chani, A. Yoshikawa, H. Machida, T. Fukuda, *J. Cryst. Growth*, **212**(3-4), 469 (2000)
17. V.I. Chani, A. Yoshikawa, H. Machida, T. Fukuda, *Mater. Sci. Eng. B* **75**(1), 53 (2000)
18. V.I. Chani, A. Yoshikawa, H. Machida T. Fukuda, in *Extended Abstracts* (The 60th Autumn Meeting, 1999), *Jap. Soc. Appl. Phys.*, September 1-4, Kobe, Japan, 3a-S-2
19. H.J. Sheel, *J. Cryst. Growth*, **211**, 1 (2000)

20. V.V. Kochurikhin, A.E. Borisova, M.A. Ivanov, V.E. Shukshin, S.N. Ushakov, S.J. Suh, D.H. Yoon, *J. Ceram. Proc. Res*, **4**(3), 109 (2003)
21. V.V. Kochurikhin, A.V. Klassen, E.V. Kvyat, M.A. Ivanov, *J. Cryst. Growth*, **292**, 248 (2006)
22. J.W. Shur, V.V. Kochurikhin, A.E. Borisova, M.A. Ivanov, D.H. Yoon, *Opt. Mater*, **26**, 347 (2004)
23. B.M. Epelbaum, G. Schierning, A. Winnacker, *J. Cryst. Growth*, **275**, e867 (2005)
24. K. Lebbou, D. Perrodin, V.I. Chani, O. Aloui, A. Brenier, J.M. Fourmigue, O. Tillement, J. Didierjean, F. Balembois, P. Gorges, *J. Am. Ceram. Soc.*, **89**(1), 75 (2006)

# 4 Growth Phenomena and Crystal Chemistry

Valery I. Chani

**Abstract.** The general behavior of the  $\mu$ -PD system is reviewed from the viewpoint of the effect of the design of the system and the growth parameters on the distribution of crystal constituents between the liquid and solid phases. Shape and surface defects are discussed in relation to the flux growth procedure that represents the most common case, including solidification from a stoichiometric (congruent) melt. The influence of the chemistry of the crystal on  $\mu$ -PD growth and the ability of the technique to produce crystals with a wide range of dimensions are explored in some depth.

## 4.1 Phase Interfaces and Melt Composition

The composition of the liquid phase is one of the basic parameters of any crystal growth system based on liquid/solid phase transformation. It determines phase formation, the shape and performance of the meniscus, and the behavior of the solid/liquid interface. It is obvious that the composition of the crystal grown will also depend on the composition of the feeding melt. Therefore, for any growth technique, it is very important to keep the melt composition as constant as possible during the entire growth process. The ability of the growth method to do this determines both its ability to produce uniform material under steady conditions and the reproducibility of such growth. Considering that the melt that was once overheated and homogenized, all of the solid particles of starting material will be dissolved if the temperature of the melt is kept well above the liquidus temperature. Thereafter, any changes in the properties of the melt throughout the volume of the liquid phase are generally impossible (except in the case of boiling, with its corresponding bubble formation). Therefore all subsequent melt modifications generally occur at the boundaries of the melt. The three types of phase interface (namely melt/crucible, melt/atmosphere, and melt/crystal) that coexist in a typical  $\mu$ -PD system [1–6] are illustrated in Fig. 4.1.

The effect of the melt/crucible interface on the melt composition is often assumed to be negligible in  $\mu$ -PD growth from the point of view universal growth parameters (phase formation, melting and/or solidification temperatures, meniscus behavior, wettability, etc). Of course, the influence of the partial dissolution of crucible material on the formation of microdefects cannot be ignored, because the existence of such imperfections in the crystal lattice is generally unavoidable. Platinum, iridium, and recently rhenium [7],

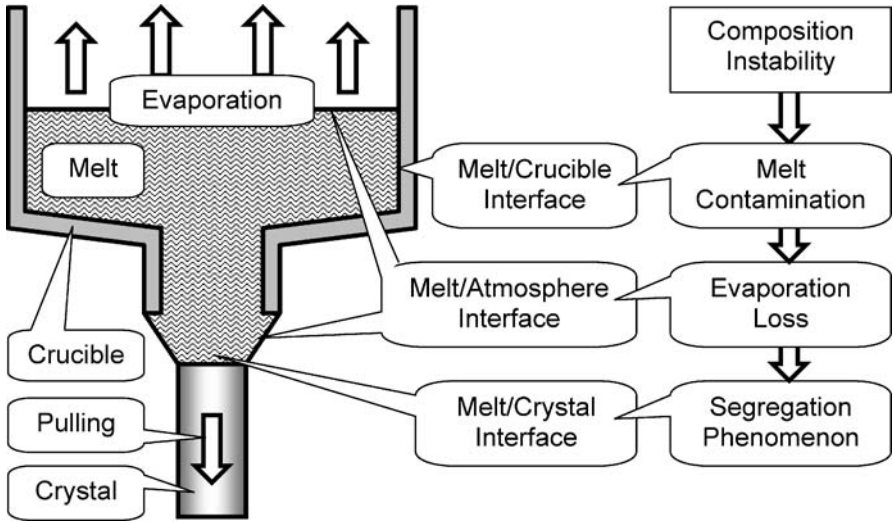


**Fig. 4.1.** Instability of the melt composition associated with liquid phase boundaries in  $\mu$ -PD system

as well as their corresponding alloys are the most popular crucible materials used when growing oxide crystals. All of these are highly resistant to high-temperature oxide melts, which makes chemical interaction between the liquid and the container difficult. In some cases, the growth atmosphere is modified in order to decrease the dissolution of the crucible and therefore the melt (and the crystal) contamination still further.

It is more difficult to reduce melt transformations associated with partial evaporation of the melt-forming constituents [8, 9]. It is often not possible to completely seal the growth system due to the design of the apparatus. Partial suppression of evaporation can be achieved by covering the top part of the crucible with a lid. However, this is also often not possible, especially in resistively heated  $\mu$ -PD systems: the height of the crucible is commonly just a few millimeters, as shown in Chap. 7. In such an arrangement, the melt can easily come into contact with the lid due to wetting or evaporation and subsequent condensation. As a result, it is difficult to separate the lid from the crucible as it is co-bonded with the melt at the post-growth stage. This means that these parts of the set-up (the crucible and the lid) are not reusable. Evaporation from the free melt surface positioned between the crucible and the crystal (Fig. 4.2) also results in melt loss. This surface sits independently on the edge of the growth interface. It is evident that protecting this surface from evaporation is a more complicated task than for the top surface of the melt.

Instability of the melt composition due to evaporation is especially great when the melting temperature of a complex crystal is much greater than the melting temperature of one of its constituents.  $\text{Bi}_2\text{O}_3$  is one example of such a low-melting constituent. Significant amounts of it evaporate when

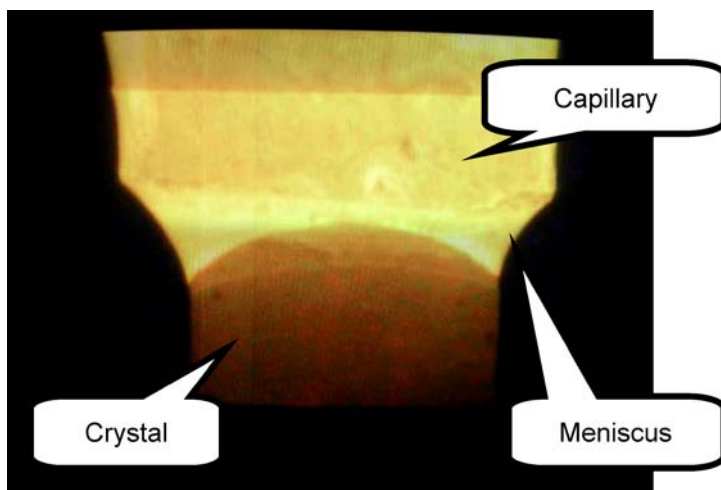


**Fig. 4.2.** View of liquid/solid and liquid/atmosphere interfaces in  $\text{KNbO}_3$  growth from  $\text{K}_2\text{O}$  flux. Outer diameter of the capillary is 1.4 mm

Bi-based or Bi-doped oxide crystals of  $\text{Bi}_4\text{Ge}_3\text{O}_{12}$  (BGO) [8, 9],  $\text{Gd}_3\text{Ga}_5\text{O}_{12}$  (GGG) [10],  $\text{Lu}_3\text{Ga}_5\text{O}_{12}$  (LuGG) [11], etc., are grown from the melt (particularly when  $\mu$ -PD is employed to do so).

Finally, the most complicated and generally unavoidable phenomenon is related the change in the melt composition arising from the segregation of constituents between the liquid and solid phases [1, 5, 9, 12–17]. This phenomenon occurs at the growth interface. Its performance depends on a number of growth parameters, including the melt composition, the nature of the crystalline material and the natures of the dopants (the crystal chemistry), the solidification rate, etc. Complete suppression of segregation is usually impossible. This phenomenon is discussed in more detail below as well as in Chaps. 5 and 7.

## 4.2 Segregation and Crystal Chemistry

Crystal chemistry involves the study of the processes by which crystalline solid materials are formed, which depend on the chemical properties of their constituents and geometrical factors (the sizes of the atoms in the crystal). Crystals (and solid minerals) are three-dimensional arrays of particles that are arranged in exceptionally symmetric order. The particles interact with one another, and this ultimately determines the physical and structural properties of the crystal. Each single crystal can be considered to be gigantic molecule in which each atom interacts with all of the others in the crystal. The sizes of the particles are important because they adopt a close packing arrangement in the crystal. In oxide structures, the symmetry of the close packing depends

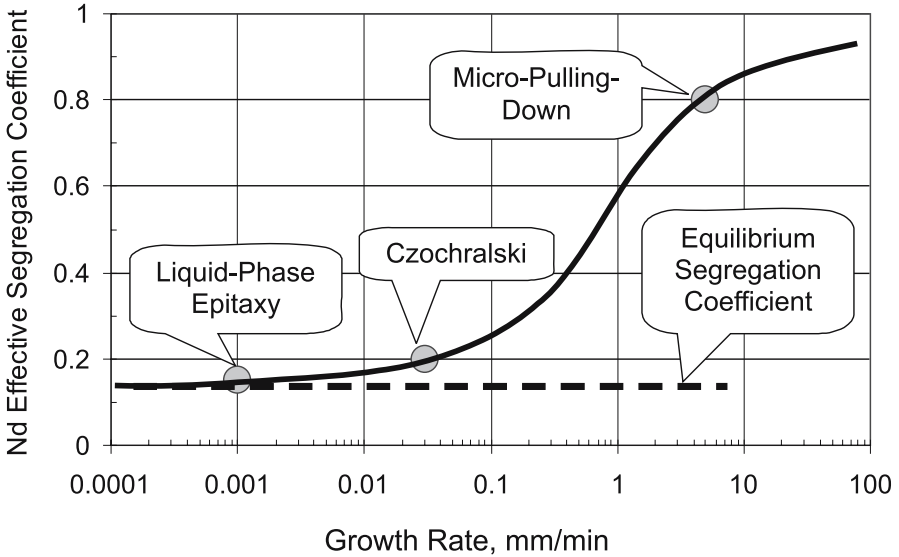


**Fig. 4.3.** Effect of growth rate on segregation coefficient of  $\text{Nd}^{3+}$  in  $\text{Y}_3\text{Al}_5\text{O}_{12}$  (YAG) garnet produced by various growth techniques

upon the sizes of (i) the oxygen anions, (ii) the cationic sites filled with smaller cations, and (iii) those cations [18].

The kinetics of crystal formation from the melt is determined by the segregation coefficients of every constituent transported from the starting liquid phase to the crystal. The levels of incorporation of the different particles into the solid can be compared by growing solid solution (mixed) crystals or doped crystals (which are actually also mixed crystals). When such cosolidification occurs, all of the conditions of growth are identical for both member compounds in the solid solution. The degree of attraction of each particle to the specified structure does not depend on the growth conditions very much. Therefore, in most cases, the most attractive (or preferable) atom or cation remains the most attractive one for the selected structure independent of the growth conditions. Figure 4.3 illustrates the result of a competition between two cations ( $\text{Y}^{3+}$  and  $\text{Nd}^{3+}$ ) participating in the formation of the garnet structure. The segregation coefficient of  $\text{Nd}^{3+}$  is less than that of  $\text{Y}^{3+}$  independently on the growth method applied. However, their relative magnitudes depend on the growth rate applied.

#### 4.2.1 Growth from Stoichiometric Melt

$\mu$ -PD growth [1,2] of wide range of congruently melting complex oxide crystals including  $\text{LiNbO}_3$  (LN) [2, 3],  $\text{Ca}_3(\text{Li,Nb,Ga})_5\text{O}_{12}$  (CLNGG) [4],  $\text{Y}_3\text{Al}_5\text{O}_{12}$  (YAG) [5, 6],  $\text{Bi}_4\text{Ge}_3\text{O}_{12}$  (BGO) [8],  $\text{Tb}_3\text{Ga}_5\text{O}_{12}$  (TGG) [19], etc., was es-

tablished within past decade. In most of these growths, compositions of the liquid and solid were equal (melt growth) that simplified solidification process considerably. In the melt growth, long distance (at least several inter-atomic distances) re-distribution of crystal forming particles (atoms or ions) sited on the boundary melt layer not far from solidification interface is generally not necessary. Single phase and single crystalline fiber material is generally formed via short distance displacement of the particles in the liquid phase and their reordering into solid. As a result, completely disordered fluid transforms into highly ordered periodical crystalline structure. Direct contact between the atoms and interaction of their outer electron shells produces chemical bonding specified by composition of original liquid, temperature of the system, and pressure. All these conditions determine phase formation. This process is illustrated in Fig. 4.4, left.

During melt growth, the proportions of particles of different types are the same in solid and liquid phase. Taking into consideration the random spatial distribution of these particles in the melt (structural disordering), and assuming that the particles are distributed uniformly, crystal solidification (ordering) can occur relatively quickly. Crystal growth can therefore be carried out at comparatively high pulling-down rates without any risk of polycrystallization. In general, this process is similar to any other melt growth method when the compositions of the solid and the liquid are the same.

Continuous control of the melt meniscus and crystal shape (diameter) is also achieved relatively easily when the compositions of the melt and the crystal are the same and the process is in the steady state. The application of constant growth conditions (temperature of the melt and pulling-down

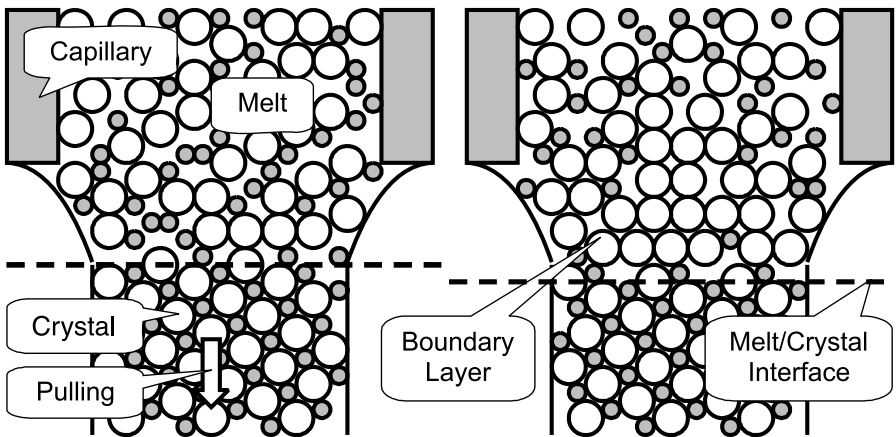


**Fig. 4.4.** Illustration of segregation phenomenon in  $\mu$ -PD system. Compositions of liquid and solid are equal on *left scheme* (melt growth), but those are not on *right one* (Note excess of “white” particles just above the melt/crystal interface on the *right scheme*)

rate) makes the system stationary. A pre-grown crystal (bulk or fiber) of sufficient length is also necessary to achieve stable conditions. This length determines the intensity of the heat transfer from the solid/liquid interface through the crystal. In most existing  $\mu$ -PD designs and configurations, the minimum length of the pre-grown crystal that allows stationary growth (stationary heat transfer) is estimated to be approximately 50 mm. Under such conditions, the equilibrium between solid and liquid phases of the same composition determines the growth process. Any disadvantages related to segregation between the solid and liquid phases (nonuniform distributions of the crystal constituents, changes in the melt composition, decreases in the melting temperature of the liquid with increasing solidification fraction, and downward displacements of the position of the liquid/solid interface, the shape of the meniscus, and the shape and diameter of the crystal, etc.) are ideally not observed. Nevertheless, in practice, most of these disadvantages are observed, even in binary systems that melt congruently, because the ideal congruent melting composition is generally not achievable (due to a misfit between the actual melt composition and the congruent one, evaporation, etc.). As a result, the growth process is accompanied by the continuous dilution of the (originally stoichiometric) melt (see Fig. 7.1). For this reason, at least the final part of any feeding-less growth process (Figs. 1.1, right, 1.2, and 4.1) will represent flux growth (Fig. 4.4, right). This is also common to any melt growth process.

#### 4.2.2 Flux Growth

The potential for  $\mu$ -PD flux growth from melts that contain an excess of one of the constituents has also been demonstrated.  $\text{KNbO}_3$  (KN) [12],  $\text{Tb}_3\text{Al}_5\text{O}_{12}$  (TAG) [13], and  $\text{Li}(\text{Tb},\text{Eu})\text{PO}_{12}$  [14] are three examples of crystals that have been grown via self-flux (an excess of  $\text{K}_2\text{O}$ ,  $\text{Al}_2\text{O}_3$ , and  $\text{LiPO}_3$ , respectively) in a  $\mu$ -PD system. These materials melt incongruently. Therefore, the addition of extrastochiometric constituents was required to support the formation of the target phases and thus to achieve the solidification of a single-phase ingot. It is evident that  $\mu$ -PD flux growth of congruently melting materials is also possible when necessary.  $\text{Bi}_4\text{Ge}_3\text{O}_{12}$  is example of a congruently melted compound produced as a fiber via  $\text{Bi}_2\text{O}_3$  self-flux [9] in a  $\mu$ -PD system (See Chap. 7 for details). Figure 4.4 (right) represents a flux growth system in which one of the constituents is added to the crucible in excess on purpose.

In all of the above flux growths, the diameter of the fiber crystal was similar to or less than the diameter of the capillary channel positioned at the bottom of the crucible (Figs. 1.2, 4.1–4.5, left). Therefore, the velocity of the melt flow inside the capillary was similar to or less than the pulling-down rate. In these circumstances, segregation between the crystal and the main volume of the melt was observed [5, 9, 12–14].

Any attempt to grow crystals of incongruently melting compounds (flux growth) makes the process more complicated from the start than melt growth [12–14]. The intentional and unavoidable presence of the flux (in most

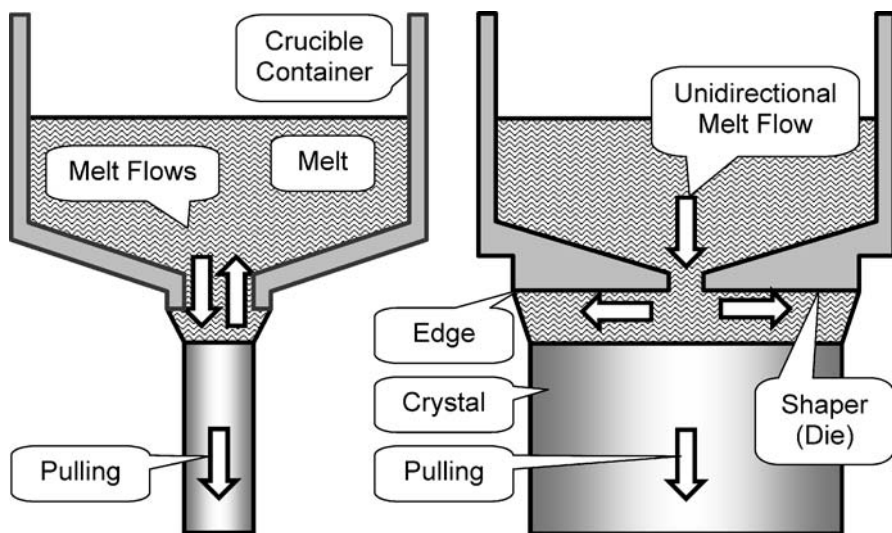


**Fig. 4.5.**  $\mu$ -PD system for fiber (*left*) and bulk (*right*) crystal growth. Note ratio of crystal to capillary diameters

favorable cases this is an excess of one of the constituents of the crystal) means that the melt composition changes continually, which is natural for any flux growth. A subsequent drop in the melting temperature is the only outcome that can follow from this if we consider phase diagrams (see Fig. 7.1). The decrease in the melting (solidification) temperature is accompanied by a displacement of the solid/liquid interface in the downward direction (Fig. 4.3, from left to right) and a corresponding change in the shape of the liquid meniscus situated between the growing crystal and the crucible. Finally, the system behaves as if it has been overheated, resulting in a decrease in the crystal diameter and in the worst-case scenario the complete separation of the as-grown solid from the melt. This is typical of how a nonfeeding flux growth system evolves when constant power is applied to the crucible.

Similar events are often observed in the growth of congruently melting compounds that contain volatile ingredients [9]. Evaporation of one of the constituents results in a change in the composition of the originally congruently melting system. Eventually this transforms the process from melt growth to flux growth spontaneously. Thereafter, all of the disadvantages of flux growth are encountered in the process, which began with a congruent melt.

### 4.2.3 Growth of Doped and Solid Solution Crystals

The growth of any doped crystal can be thought of as the formation of a mixed single-phase material (or solid solution). In rare cases, the segregation coefficients of the different cations that occupy the same crystallographic sites in

the structure are equal [15, 16, 20]. The growth of this type of mixed crystal is similar to the melt growth of congruently melting compounds. However, in most cases the segregation coefficients of the doping (or co-solidified) constituents are different from unity. The behavior of such systems is very similar to the typical flux growth of a host crystal that is intentionally “contaminated” with dopants that generally play the role of the flux. This case also corresponds to the growth conditions illustrated in Fig. 4.4 (right).

#### 4.2.4 Bulk Crystal Growth

If we consider the standard  $\mu$ -PD growth of a fiber with a diameter similar to the diameter of the capillary channel, melt exchange between the meniscus and the main volume of the crucible is possible due to a variety of mechanisms, including convection [14]. This can be represented as two oppositely directed flows (upward and downward), as demonstrated in Fig. 4.5, left. This melt exchange was proven experimentally by observing the segregation of Nd in  $Y_3Al_5O_{12}$  fiber crystals [5] produced at a very high pulling-down rate (about 5 mm/min) and also by noting the ability of the  $\mu$ -PD system to perform flux growth of incongruently melting compounds [12–14].

However, in the case of  $\mu$ -PD bulk crystal growth (Fig. 4.5, right), the probability that the melt flow is directed upward decreases considerably. In most cases, the shaped crystals produced by  $\mu$ -PD according to Fig. 4.5 (right) are bulk materials with low aspect ratios ( $< 10$ ). The diameters (or cross-sections) of these crystals are generally 3–10 mm (see for example Chap. 13). However, the diameter of the capillary channel in the crucible bottom is much smaller than this ( $< 1.0$  mm). Therefore, the velocity of the melt flow through this small-diameter capillary must be extremely high in order to supply the meniscus zone with the melt originally situated inside the crucible (as follows from the principles of mass conservation). The velocity of the melt flow through a capillary of 0.6 mm was calculated in [19] and was found to be about 300 mm/min for the growth of  $Tb_3Ga_5O_{12}$  bulk garnet crystals, and it can be even greater than this (see Chap. 18). If we consider a capillary length of about 1 mm, the melt in the channel is replaced 5–15 times every second. This value is too high to assume any opposite flow, as shown in the left part of Fig. 4.4.

When the ratio between the cross-section of the crystal and the capillary (crystal/capillary diameter ratio) becomes very high, the  $\mu$ -PD system again starts to act like a system based on the FZ technique (see Chap. 1 and Fig. 4.6). The main advantage of FZ is ability of the system to maintain a constant melt composition over the entire growth run (the compositions of the feed solid input and the crystalline solid output are equal, but the composition of the melt is different). These conditions are applied in the traveling zone method (Sect. 1.3.4). In the case of FZ, the melt cannot be transported back to the feed solid because the solid only travels downward into the melt. As for bulk  $\mu$ -PD growth (Fig. 4.6, left), the feed material

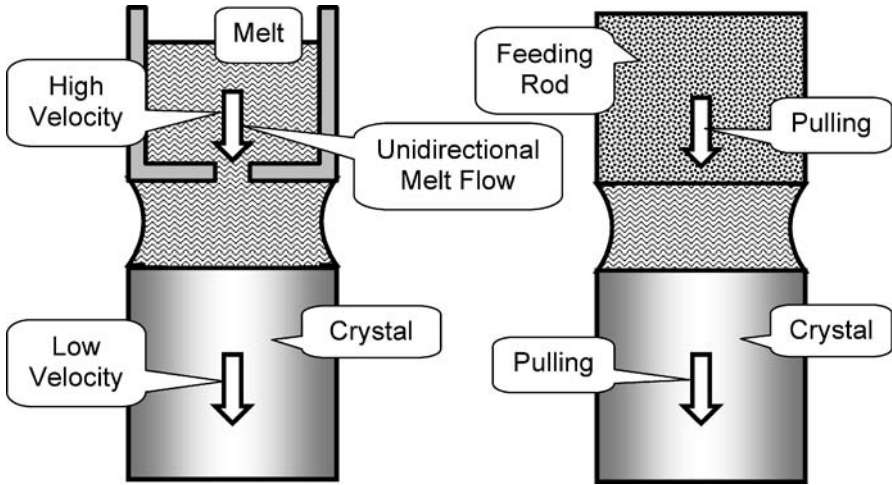


**Fig. 4.6.** Comparison of mass transport in  $\mu$ -PD bulk crystal growth (*left*) and FZ method (*right*) without crystal rotation

(the fluid inside the crucible) only travels in the downward direction. The reasons for this one-way transport of feed material (the fluid in Fig. 4.6, left, or the solid in Fig. 4.6, right) are different in each case; for  $\mu$ -PD bulk crystal growth it is due to the very high velocity of the melt flow through the narrow opening in the bottom of the crucible, and in the case of the FZ method it is due to the unidirectional phase transformation of the feed solid (the rod) into the melt, respectively. However, the resulting behavior of the bottom parts of both schemes shown in Fig. 4.6 is identical.

The segregation that occurs at the boundary layer of the melt/crystal interface is similar to that which occurs in a conventional pulling-up Czochralski system for both cases. It typically depends on the growth rate (Fig. 4.3). However, the maximal pulling rate that results in the solidification of single-phase and single-crystalline material of high structural quality is limited by the convective and Marangoni flows in the meniscus, which determine melt mixing and the replacement of the melt at the interface boundary layer [14]. Again, this is the same in both systems.

Because of the similarity of the two schemes presented in Fig. 4.6, the chemical uniformity of the  $\mu$ -PD bulk crystals produced with a high crystal/capillary diameter ratio along the growth axis is also very high (except for the starting and ending segments). This is further demonstrated in Chap. 13, and in general they should be at least as uniform as analogous materials produced by the corresponding FZ process. If there is only one liquid/solid interface in the  $\mu$ -PD system (see Fig. 1.10), the quality of bulk crystals produced by  $\mu$ -PD should be even better than those produced by FZ, which obviously makes  $\mu$ -PD growth very attractive.

Unfortunately, the bulk crystals produced via the  $\mu$ -PD system illustrated in Fig. 4.6 (right) are chemically homogeneous only in the axial direction.

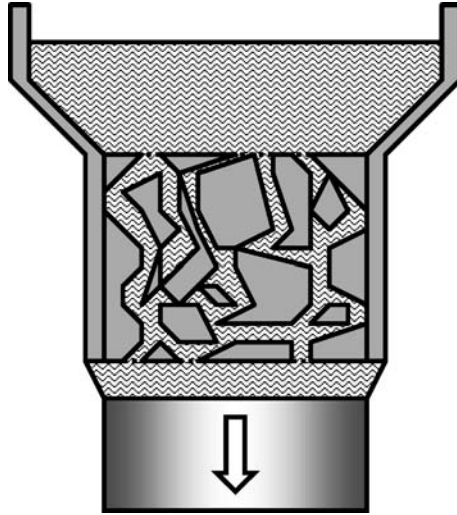


**Fig. 4.7.** Hypothetical  $\mu$ -PD system with porous die (see Figs. 1.12 and 4.5 for comparison)

Therefore the conditions of FZ are preferable if a high degree of radial uniformity is required. The feed (in the form of a polycrystalline solid) is delivered to the melt uniformly along the entire cross-section of the melt column and the melt/crystal interface (including central and peripheral parts). In bulk  $\mu$ -PD growth, on the other hand, the central part of the interface positioned just under the orifice obtains a “fresher” (i.e., not modified due to segregation) melt supply.

It is worth noting that the uniformity in the radial direction can be improved by using multicapillary crucibles. However, the minimal capillary channel diameter achievable at the moment is measured in hundreds of microns. Thus, the diameter and the meniscus thickness are very similar. In such a design, the distribution of the dopants in the radial direction will, to some degree, reflect the perforations at the bottom of the crucible. Hypothetically, this disadvantage can be avoided by using a porous die (see Fig. 4.7) similar to that tested experimentally for pulling-up EFG growth [21] (see also Figs. 1.12 and 1.13). The dimensions of the pores in such materials are typically measured in microns. Thus, the homogeneity of the melt supplied to the meniscus in schemes similar to that in Fig. 4.7 can be exceptionally high.

### 4.3 Shape and Surface Defects

In general, all shaped crystal growth techniques (including pulling-up and pulling-down) allow the shape of the meniscus to be controlled. In the ideal case of the solidification of anisotropic material, the crystal shape replicates the shape of the meniscus if the thickness of the melt film between the cru-

cible/shaper and the crystal is low enough. This is illustrated in Figs. 4.5–4.7. Therefore, the main strategy used to control the shape is to keep the thickness of the melt as low as possible. In this case, surface tension aids die-shape replication.

When the thickness of the molten zone increases, the tendency of the fluid to minimize the surface area of the melt/atmosphere interface modifies the shape of the melt (and therefore the solidified material), such that its shape approaches that of an ideal cylinder. Increasing the height of the molten zone liberates the fluid from the influence of the shaper: in this situation, the growth conditions approach those corresponding to the solidification of isotropic solid from the free surface of the melt, similar to those found in the Czochralski method.

### 4.3.1 Diameter Control in $\mu$ -PD

Accurate shape (diameter) control of the crystals produced using  $\mu$ -PD systems (Figs. 4.5–4.7) has not yet been achieved for all types of materials (with congruent and incongruent melting) because the hard- and software required are not yet available. The two most obvious ways of controlling the diameter are generally considered. One of them is based on visual examination (i.e., an operator observes the image of the meniscus and the crystal; see Fig. 4.2) via an optical microscope or CCD camera coupled with a monitor. Visual control of  $\mu$ -PD growth is commonly applied in practice. The growth parameters (pulling rate, power applied to the crucible, etc.) are adjusted manually based on observations and the shape of crystal desired. This process can be automated at a basic level by developing image analysis software that can be coupled to the power generator.

Another method that is well developed, particularly for the Czochralski technique, is based on weight control. However, for low rates of solidification (amount of crystallized material per unit of time, g/min), the process cannot be controlled accurately enough using this approach. Thus, its inapplicability to small crystal diameters (normally 0.5–1.0 mm) and a lack of exceptionally precise loading cells are the two main problems to solve for this method. Furthermore, noise signals originating from mechanical vibrations and related phenomena can produce signals in the weight sensor that are comparable to those arising from true crystal weight increase, which provides another difficulty to overcome. Some attempts to use weight sensors to measure the quantity of solidified material have been reported [6, 22]. However, such systems are yet to demonstrate the ability to manage the growth of uniformly shaped (diameter) crystals.

### 4.3.2 Anisotropy of Growth Rate in Flux Growth

Single crystals are highly anisotropic materials. The arrangement of the particles inside the structure of a single crystal is anisotropic, and its growth

rate (which is determined by the ordering of the particles in the structure and their bonding strengths) is also anisotropic. This is the case for any crystal growth method and so it is also observed for crystals grown using  $\mu$ -PD. This growth rate anisotropy ultimately results in crystal faceting. Facet formation is especially noticeable when the growth is performed from flux (and  $\mu$ -PD growth is no exception). This phenomenon is shown schematically in Fig. 4.8, where seeding on a metallic rod (polycrystalline foreign material) is illustrated. This type of seeding is often applied when seed material is not available.

In the case of  $\mu$ -PD flux growth, the boundary layer is formed just above the melt/crystal interface. It contains extrastochiometric substances from the outset of the process (Fig. 4.4, right). As a result of solidification, this boundary layer is continuously enriched with flux-forming compounds, which makes subsequent phase formation of the target material difficult because of the corresponding local dilution of the flux. The composition of the main part of the melt (that above the boundary layer) still facilitates the phase formation of target material if other types of loss (Fig. 4.1) are negligible.

In the worst case, the composition of the boundary layer corresponds to another phase formation field. When the melt is supercooled sufficiently, conditions conducive to second phase nucleation are established. If we consider a fiber crystal grown by a  $\mu$ -PD process, a nucleus can form in either the target or the foreign phase (in which case the single crystal growth would be transformed into the solidification of a polycrystalline, and possibly not single-phase, solid). To avoid this situation, the stirring rate (when applicable) must be increased and the pulling-down rate decreased to allow proper

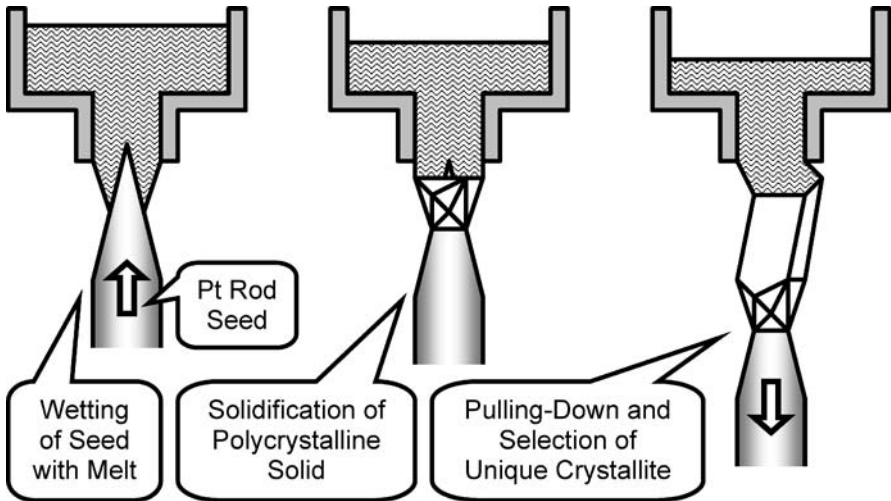


**Fig. 4.8.** Schematic of seeding of  $\text{KNbO}_3$  on sharpened Pt rod ( $\varnothing 0.5$  mm) according to [12, 23]

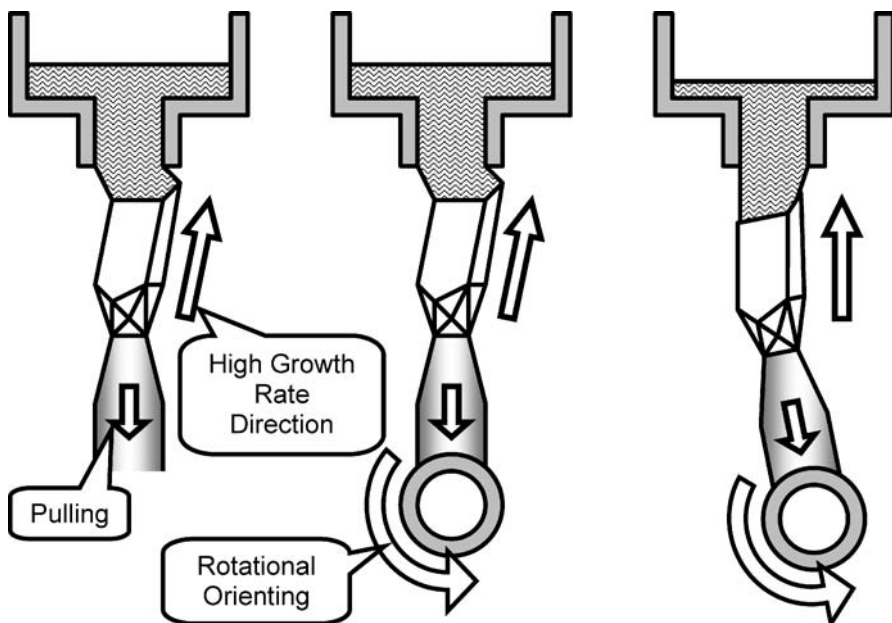


Fig. 4.9. Schematic diagram of *in situ* re-orienting of spontaneous single crystal by rotational re-positioning

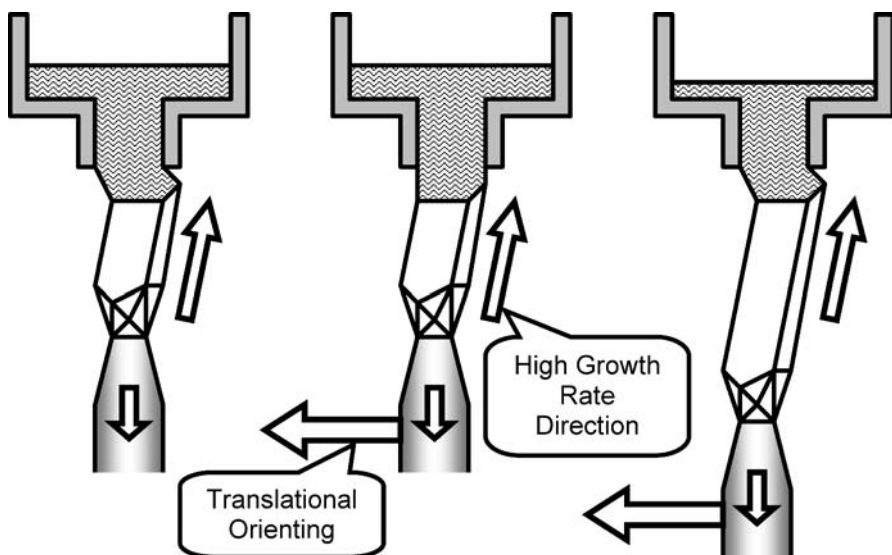
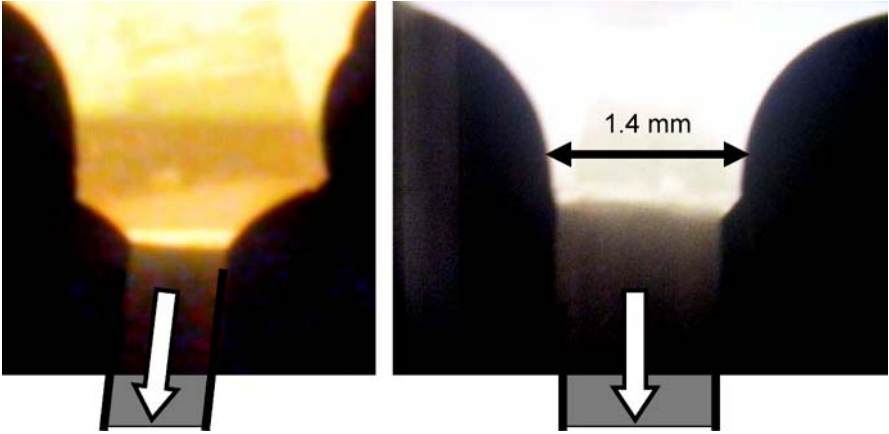


Fig. 4.10. Schematic diagram of *in situ* re-orienting of spontaneous single crystal by translational re-positioning



**Fig. 4.11.** Growth anisotropy of  $\text{KNbO}_3$  produced from  $\text{K}_2\text{O}$  flux at 0.3 mm/min pulling rate using misoriented (*left*) and oriented (*right*) seeds. *Left image* represents orienting of the seed crystal according to Figs. 4.9 and 4.10

delivery of feeding material of the correct (the original) composition from the melt situated in the crucible container to the growth interface.

Visual observation of faceting (especially in the case of flux growth) can be used to facilitate in situ orienting of the fiber, as demonstrated in [12, 23]. This procedure is illustrated schematically in Figs. 4.9 and 4.10. The as-produced polycrystalline solid with the selected single-crystalline grain oriented along the crystallographic direction of highest growth rate can be set parallel to the pulling-down direction. This can be done by manipulating the as-crystallized solid via rotational or translational displacements. Both types of repositioning can be applied at the same time in the same pulling process when the apparatus is equipped with an appropriate stage mechanism and goniometer.

An image showing the actual procedure of seed orientation is provided in Fig. 4.11, left. This process is normally performed with a fiber diameter that is considerably (2–3 times) less than the diameter of the capillary. This allows the risk of “growth out” displacement of the crystal (Figs. 4.9 and 4.10), with the subsequent loss of shape perfection, to be minimized. Some more details on crystal orientation adjustment are also provided in Chap. 3.

### 4.3.3 Faceting and Steps in Flux Growth

Growth steps are also often observed when the growth process is performed from flux. Figure 4.12 illustrates the typical surface of a  $\text{KNbO}_3$  fiber crystal produced from  $\text{K}_2\text{O}$  flux. Faceting and growth steps are easy to spot during  $\mu$ -PD flux growth, and are similar to those observed in growth processes performed from nonstoichiometric melts. In an ideal procedure, step formation

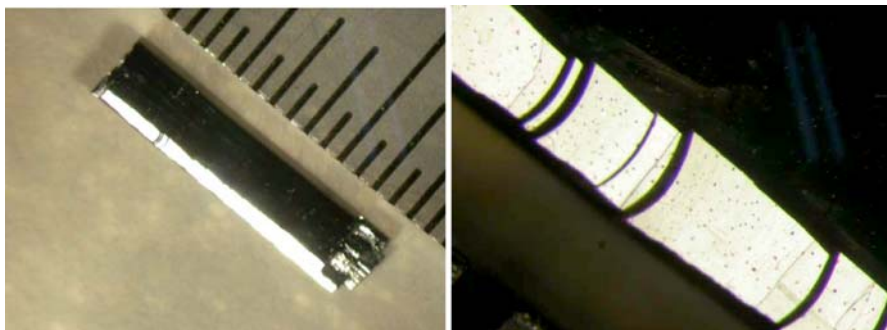


**Fig. 4.12.**  $\text{KNbO}_3$  crystal produced from  $\text{K}_2\text{O}$  flux with rectangular cross-section or pseudo-plate (minimal division of the scale is 0.5 mm) and magnified view of one of the facets with growth steps (*right*)

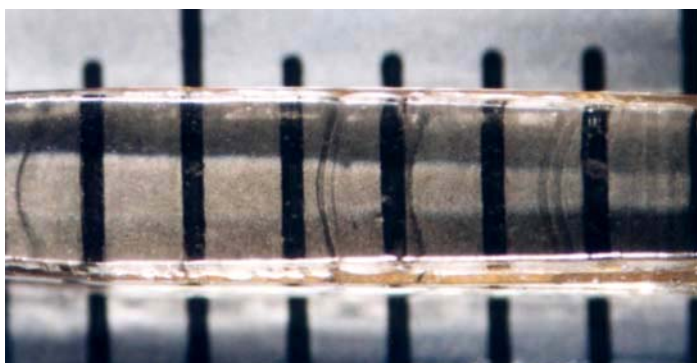


**Fig. 4.13.** Appearance of growth steps on  $\text{K}_3\text{Li}_2\text{Nb}_5\text{O}_{12}$  (KLN) crystal surface (scale in mm). The crystal was grown from capillary of 2 mm in diameter

can be avoided by increasing the accuracy of seed orientation, particularly through the processes illustrated in Figs. 4.9 and 4.10. Figure 4.13 shows the presence of similar steps on a  $\text{K}_3\text{Li}_2\text{Nb}_5\text{O}_{12}$  (KLN) fiber crystal.

#### 4.3.4 Deposition of the Flux on the Surface

One more surface defect associated with flux growth is related to the deposition of residual flux that is not properly transported back to the melt situated in the crucible container and/or capillary. Depending on the wetting properties involved, it is either deposited in a drop-like shape onto the surface of the as-grown crystal or it coats the surface uniformly. The depositions of such drops have been observed in particular on the surfaces of  $\text{KNbO}_3$  fiber crystals grown from  $\text{K}_2\text{O}$  flux (Figs. 4.2, 4.11, and 4.12). In the case of  $\text{KNbO}_3$ , the final removal of this substance was easily achieved because the melt contained large amounts of  $\text{K}_2\text{O}$ , which is water soluble.

$\text{Bi}_4\text{Ge}_3\text{O}_{12}$  (BGO) fiber crystal [8, 9] is another material that has been produced from melts containing an excess of one of the oxides that form the crystal (see Chap. 7 for details). In the case of BGO growth from  $\text{Bi}_2\text{O}_3$  flux [9], the presence of a thin layer of  $\text{Bi}_2\text{O}_3$ -enriched liquid is often observed on the surfaces of the fibers. This is not surprising, because the melt in the crucible container, the capillary, and the meniscus (Fig. 1.2) contains an excess of  $\text{Bi}_2\text{O}_3$  (Table 7.1 and Fig. 7.1). The crystals do not accumulate this excess into their structures due to the stoichiometry of BGO. Moreover, the formation of  $\text{Bi}_2\text{O}_3$  or corresponding  $\text{Bi}_{12}\text{GeO}_{20}$ /BGO eutectic inclusions inside the crystals was also not observed. Therefore, the excess was deposited on the surfaces of the fibers.

Figure 4.14 shows two easily distinguishable parts of the crystal that reflect light differently. The upper part of the transparent BGO crystal is coated with a transparent  $\text{Bi}_2\text{O}_3$ -enriched melt. As the crystal is pulled in the downward direction, the composition of this liquid film gradually moves towards the  $\text{Bi}_{12}\text{GeO}_{20}$ /BGO eutectic according to the phase diagram of the  $\text{Bi}_2\text{O}_3$ - $\text{GeO}_2$  binary system (Fig. 7.1) [20]. Finally, the film solidifies at the eutectic temperature (880–882 °C). Two solid/liquid interfaces corresponding to melt/BGO or melt/eutectic phase transitions are visible in Fig. 4.14. Therefore, the melting points of BGO and the  $\text{Bi}_{12}\text{GeO}_{20}$ /BGO eutectic ob-

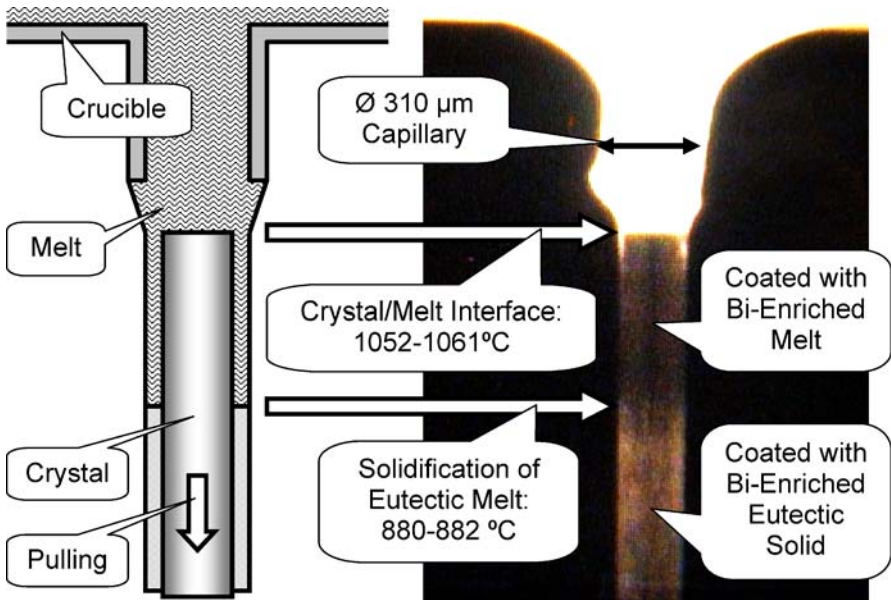


**Fig. 4.14.** Two parts of just grown BGO fiber crystal coated with fluid (upper fragment of the fiber) and solid (lower fragment) Bi-rich films. Two solid/liquid interfaces with corresponding melting temperatures ([9, 24], Fig. 7.1) are shown to illustrate estimation of temperature gradient under the crucible

tained from the phase diagram [24] were used to estimate the temperature gradient just below the capillary [9].

The formation of this type of film is also unavoidable during BGO fiber growth from a stoichiometric melt (Sect. 7.4). According to the phase diagram (Fig. 7.1), evaporation of the  $\text{Bi}_2\text{O}_3$  from the surface of the originally stoichiometric melt displaces the system towards the  $\text{GeO}_2$ -rich region. This allows the formation of  $\text{GeO}_2$ -enriched melt on the fiber surface. In this case, the composition and solidification performance of this liquid film depend on the properties of another  $\text{GeO}_2$ /BGO eutectic [20] positioned on the  $\text{GeO}_2$ -rich (right) side of the phase diagram (Fig. 7.1).

#### 4.4 Dimensional (Diameter) Limits of $\mu$ -PD

The diameters of the capillary channels applied in  $\mu$ -PD usually range from 0.3 mm to 2.0 mm. Thinner capillaries are difficult to use because it is not always possible to establish melt flow through the orifice. In some cases solid particles formed in the melt block the channel, stopping melt flow. This is a particularly common phenomenon during the growth of Si-Ge mixed crystals. The formation of small bubbles with diameters equal to or bigger than the diameter of the capillary is another phenomenon that can result in melt supply irregularity. On the other hand, the application of channels with larger diameters is also complicated, because of the possibility of spontaneous melt flow out of the crucible due to gravity (Fig. 1.5).

The growth of ultrathin (less than 100  $\mu\text{m}$  in diameter) crystals by  $\mu$ -PD has attracted much attention right from the initial development of this technology. However, most of the research has concentrated on congruently melting compounds, with growth performed from stoichiometric melts similar to those of  $\text{LiNbO}_3$  (LN) [2, 3] or  $\text{Y}_3\text{Al}_5\text{O}_{12}$  (YAG) [5, 6]. In these cases, the minimal diameter possible for stationary growth conditions was reported to be about half the diameter of the capillary [1]. Based on a theoretical examination of the pulling-up EFG process (see Chap. 1), it was concluded that the stable growth of crystals with smaller diameters is impossible because the system loses capillary stability.

The behavior of flux systems was not considered. However, the ability to control the crystal diameter in some systems (such as  $\text{Bi}_4\text{Ge}_3\text{O}_{12} + \text{Bi}_2\text{O}_3$ ) by controlling the rate of evaporation of a volatile constituent was recently demonstrated (see Chap. 7 for details). Maintaining constant evaporation is generally a simple task achieved through appropriate crucible design (melt/air surface area). This allows the solidification rate to be predetermined exclusively by the rate of evaporation of the volatile constituent. The process was confirmed to be applicable to the stationary growth of ultrathin fibers with crystal:capillary diameter ratios of considerably less than 1:2, as illustrated in Fig. 4.15.

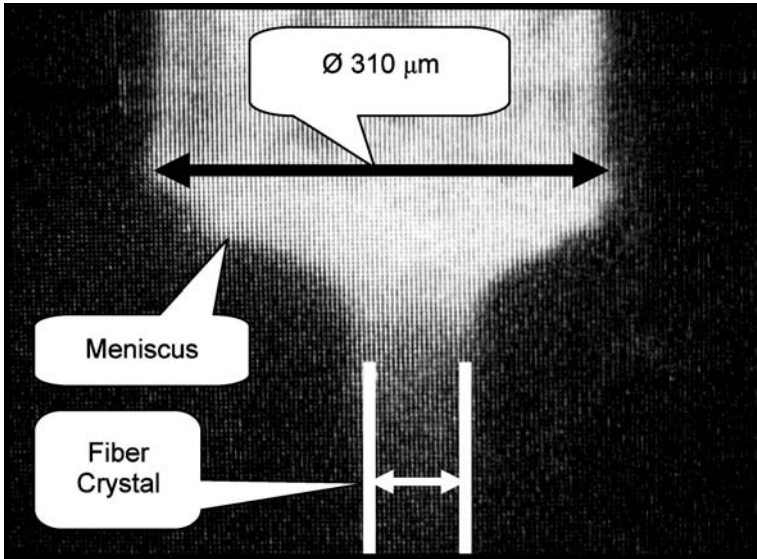


**Fig. 4.15.** Stationary growth of  $\text{Bi}_4\text{Ge}_3\text{O}_{12}$  (BGO) fiber crystal with diameter less than  $100\ \mu\text{m}$ ). The process was stationary for up to 72 hours

The lowest crystal/capillary diameter ratio was found to be approximately 1:6 for crystals  $50\ \mu\text{m}$  in diameter. The BGO fiber demonstrated in Fig. 1.16 is currently one of the thinnest grown reproducibly by the  $\mu$ -PD technique. Previous attempts to produce ultrathin fibers by  $\mu$ -PD were usually unsuccessful because big capillaries and congruently melting materials were used. Short sections of thin fibers were sometimes successfully grown under nonstationary conditions, but the results were not reproducible and the processes were only stable for a relatively short time.

A growth system controlled through the evaporation of  $\text{Bi}_2\text{O}_3$  was found to be suitable for fabricating fibers up to 400 mm long, as described in [9]. The aspect ratios of the fibers were not far from  $10^4$ , which is also the highest value ever reported for  $\mu$ -PD growth. The flexibility and bendability of the  $\varnothing 50\ \mu\text{m}$  fibers were extremely high (Figs. 4.16 and 4.17). The fibers could be bent around a solid cylinder 100 mm in diameter without incurring fracture. The geometrical and mechanical properties of these fibers are comparable to those of optical glass fibers.

The growth of ultrathin fibers of other industrially important materials that do not have volatile constituents is also anticipated. Introducing a foreign volatile flux constituent can also convert the system from melt to flux. This permits isothermal flux evaporation growth [25–29] of target material to be achieved through the stabilization of flux loss and after stabilizing the supercooling, supersaturation, and growth (solidification) rates. The evaporation rate can be controlled using a suitable crucible design and a melt/atmosphere

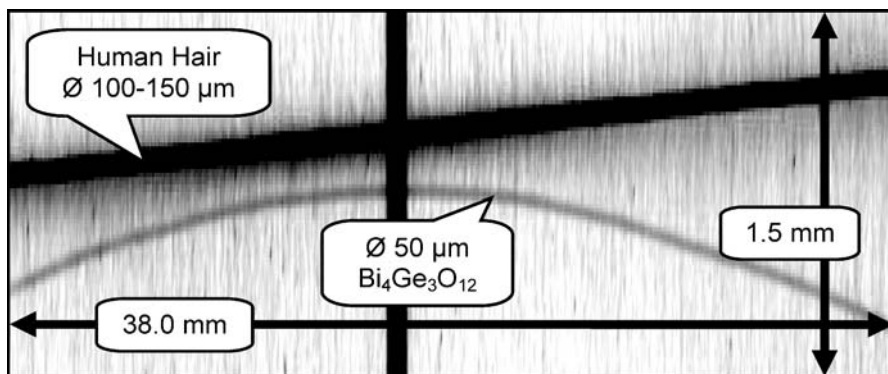


**Fig. 4.16.** Vertically expanded scanograph image of  $\varnothing 50 \mu\text{m}$   $\text{Bi}_4\text{Ge}_3\text{O}_{12}$  fiber crystal grown from the melt  $\text{Bi}_2\text{O}_3:\text{GeO}_2 = 46:54$  (mol)

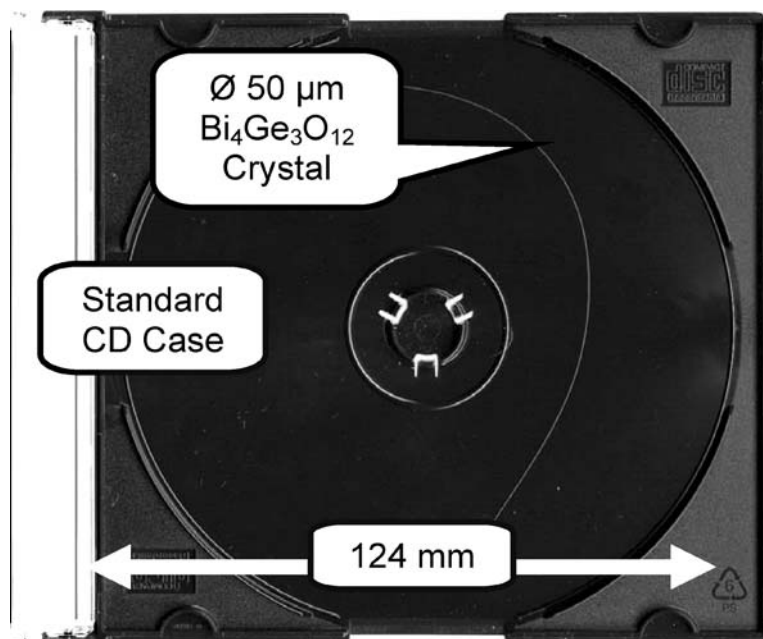


**Fig. 4.17.** Demonstration of bendability of  $\varnothing 50 \mu\text{m}$   $\text{Bi}_4\text{Ge}_3\text{O}_{12}$  crystal placed in CD case

interface with an appropriate surface area (Chap. 7), or through enforced vapor removal from the surface of the melt, with corresponding gas flow. The segregation coefficient of the flux-forming constituent must be as low as possible to minimize the effects of flux contaminations on the physical properties of the target material. Complete prevention of the incorporation of flux into the crystal structure is generally impossible. Therefore the flux must be cho-

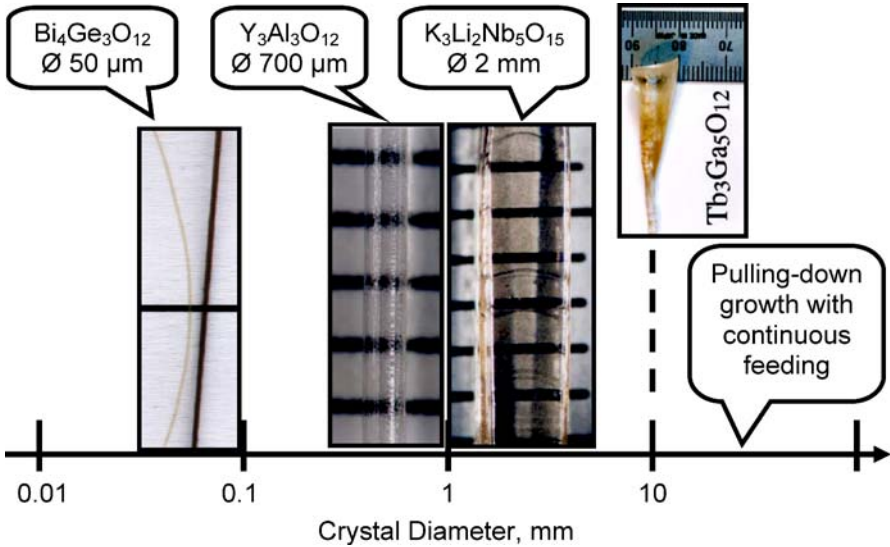


Fig. 4.18. Diameter range of the oxide single crystals produced by  $\mu$ -PD

sen considering that effect of contaminations originated from the flux on the crystal properties must be negligible.

Examples of the growth of bulk crystals up to several centimeters in diameter can be found in Chap. 1. Moreover, some of the crystals discussed in the following chapters have radial dimensions of greater than 10 mm. These are actually bulk materials with low aspect ratios. The range of crystal diameters produced by  $\mu$ -PD is illustrated in Fig. 4.18.

## References

1. T. Fukuda, P. Rudolph, S. Uda, (eds.), *Fiber Crystal Growth from the Melt* (Springer, Berlin, 2004)
2. D.H. Yoon, *Opto-Electron. Rev.*, **12**(2), 199 (2004)
3. D.H. Yoon, T. Fukuda, *J. Cryst. Growth*, **144**, 201 (1994)
4. Y.M. Yu, V.I. Chani, K. Shimamura, T. Fukuda, *J. Cryst. Growth*, **171**, 463 (1997)
5. V.I. Chani, A. Yoshikawa, Y. Kuwano, K. Hasegawa, T. Fukuda, *J. Cryst. Growth*, **204**, 155 (1999)
6. K. Lebbou, D. Perrodin, V.I. Chani, O. Aloui, A. Brenier, J.M. Fourmigue, O. Tillement, J. Didierjean, F. Balembois, P. Gorges, *J. Am. Ceram. Soc.*, **89**(1), 75 (2006)
7. J.H. Mun, A. Novoselov, A. Yoshikawa, G. Bpulon, T. Fukuda, *Mater. Res. Bull.*, **40**, 1235 (2005)
8. J.B. Shim, J.H. Lee, A. Yoshikawa, M. Nikl, D.H. Yoon, T. Fukuda, *J. Cryst. Growth*, **243**, 157 (2002)

9. V.I. Chani, K. Lebbou, B. Hautefeuille, O. Tillement, J.-M. Fourmigue, *Cryst. Res. Technol.*, **41**(10), 972 (2006)
10. A. Novoselov, A. Yoshikawa, M. Nikl, N. Solovieva, T. Fukuda, *Nucl. Instrum. Meth. A*, **537**, 247 (2005)
11. A. Novoselov, A. Yoshikawa, M. Nikl, J. Pejchal, T. Fukuda, *J. Cryst. Growth*, **292**, 236 (2006)
12. V.I. Chani, K. Shimamura, T. Fukuda, *Cryst. Res. Technol.*, **34**, 519 (1999)
13. S. Ganschow, D. Klimm, B.M. Epelbaum, A. Yoshikawa, J. Doerschel, T. Fukuda, *J. Cryst. Growth*, **225**, 454 (2001)
14. B.M. Epelbaum, G. Schierning, A. Winnacker, *J. Cryst. Growth*, **275**, e867 (2005)
15. V.I. Chani, A. Yoshikawa, H. Machida, T. Fukuda, *Mater. Sci. Eng.* **B75**(1), 53 (2000)
16. V.I. Chani, A. Yoshikawa, H. Machida, T. Fukuda, *J. Cryst. Growth*, **212**(3-4), 469 (2000)
17. J.C. Brice, *Rep. Prog. Phys.*, **40**, 567 (1977)
18. V.I. Chani, Y.M. Yu, K. Shimamura, T. Fukuda, *Mat. Sci. Eng. R*, **20**(6), 281 (1997)
19. V.I. Chani, A. Yoshikawa, H. Machida, T. Satoh, T. Fukuda, *J. Cryst. Growth*, **210**(4), 663 (2000)
20. H. Sato, V.I. Chani, A. Yoshikawa, Y. Kagamitani, H. Machida, T. Fukuda, *J. Cryst. Growth*, **264**, 253 (2004)
21. V.V. Kochurikhin, A.V. Klassen, E.V. Kvyat, M.A. Ivanov, *J. Cryst. Growth*, **296**, 248 (2006)
22. B. Hautefeuille, K. Lebbou, C. Dujardin, J.M. Fourmigue, L. Grosvalet, O. Tillement, C. Pédrini, *J. Cryst. Growth*, **289**, 172, (2006)
23. V.I. Chani, K. Nagata, T. Fukuda, *Ferroelectrics*, **218**, 9 (1998)
24. A.B. Kaplun, A.B. Meshalkin, *J. Cryst. Growth*, **167**, 171 (1996)
25. C.M. Jones II, *J. Am. Ceram. Soc.*, **54**(7), 347 (1971)
26. E.A. Goodilin, E.A. Pomerantseva, V.V. Krivetsky, D.M. Itkis, J. Hester, Yu.D. Tretyakov, *J. Mater. Chem.*, **15**, 1614 (2005)
27. W.H. Grodkiewicz, D.J. Nitti, *J. Am. Ceram. Soc.*, **49**(10), 576 (1966)
28. M. Kajivara, *J. Mater. Sci.*, **23**, 3600 (1988)
29. S. Armaki, R. Roy, *J. Mater. Sci.*, **3**, 643 (1968)

Part II

**Modification and Evolution  
of  $\mu$ -PD Method**

# 5 Flux Growth of Miniature Bulk Crystals by the $\mu$ -PD Method

Boris M. Epelbaum

**Abstract.** Effective use of the micro-pulling-down ( $\mu$ -PD) growth method for flux growth is shown to be feasible due to very strong Marangoni convection in the  $\mu$ -PD meniscus. Modifications to the crucible geometry and to the growth procedure permit the growth of fiber samples in which excessive flux is captured periodically or even miniature bulk single crystals completely free of flux inclusions. This is demonstrated by the successful growth of  $\text{LiTb}_{0.9}\text{Eu}_{0.1}\text{P}_4\text{O}_{12}$  from  $\text{LiPO}_4$  flux.

## 5.1 Introduction

The micro-pulling-down ( $\mu$ -PD) method is usually considered in the crystal growth community as being only suitable for the melt growth of congruently melting compounds. This viewpoint is actually reinforced by the categorization of  $\mu$ -PD as shaped growth from the melt using capillary feeding. Thus  $\mu$ -PD is considered to be a miniaturized variant of edge-defined film-fed (EFG) growth (for more on EFG, see [1]) where the direction of crystal growth is downwards instead of upwards. In the EFG method, the melt is delivered to the growth interface through narrow capillary channels, and melt flow inside the channels is laminar, so only diffusion-controlled partitioning need be considered [2]. In practice, this means that in EFG the effective distribution coefficient is always equal to unity: the melt and crystal compositions during steady-state growth are always equal. The absence of partitioning stops any flux growth using EFG arrangement.

However, the intuitive categorization of  $\mu$ -PD as a variant of EFG does not take into account the fact that in  $\mu$ -PD the cross-sections of the capillary and the fiber crystal itself are practically the same (we consider only the original  $\mu$ -PD configuration here; other versions of  $\mu$ -PD described in later chapters where the cross-section of the crystal is much greater than the cross-section of the capillary channel are not taken into account). This, together with the intense natural melt mixing that occurs in the meniscus due to thermocapillary convection, opens up the possibility of using  $\mu$ -PD processing for incongruent melts and for flux growth, as discussed later in this chapter. The beneficial effect of melt stirring (it encourages stable growth at the high growth rates typical of the  $\mu$ -PD method) derives from the resulting decrease in interface boundary layer thickness. As shown by Elwell

and Scheel [4], an increase in the rate of solution flow along the interface surface always leads to stabilization, since the local temperature gradient at the interface is steepened by stirring to a greater extent than the solute gradient (see for details Chap. 6 in [4]). This is why controllable convection is highly desirable in solution growth. In the  $\mu$ -PD system, it is difficult to apply forced convection (such as crystal rotation for example). Therefore, it is of great practical importance to understand the characteristics of natural convection and how it influences the growth process and the results obtained. It is appropriate to recall at this point that the first successful attempt to use  $\mu$ -PD for the flux growth of  $\text{KNbO}_3$  was made by Chani et al. at a very early stage of  $\mu$ -PD development in 1998 [3] (also note that the self-flux growth of incongruently melting  $\text{Tb}_3\text{Al}_3\text{O}_{12}$  is described in [7].).

## 5.2 Fluid Flow and the Marangoni Effect in the $\mu$ -PD Method

Buoyancy convection is very weak in the  $\mu$ -PD due to the small physical dimensions of the system. However, thermocapillary (Marangoni) convection plays a very important role [5]. The Marangoni effect arises at any free liquid surface if a temperature gradient exists along the surface (which is always the case for any crystal growth arrangement with a free liquid surface). The surface tension of the hotter region of the melt is normally lower than that of the colder one. Therefore, the melt surface tends to minimize its energy by extending the area of the “hot surface”, see Fig. 5.1. The surface tension is balanced by viscous forces which transfer momentum into the underlying liquid. This causes the development of a bulk Marangoni flow in the whole melt volume.

Let us now consider a standard resistively heated  $\mu$ -PD crucible. In Fig. 5.2, the most functional part of such a crucible is schematically illustrated together with bulk flow patterns. The system involves: (1) a main crucible reservoir containing a melt stirred effectively by thermocapillary con-

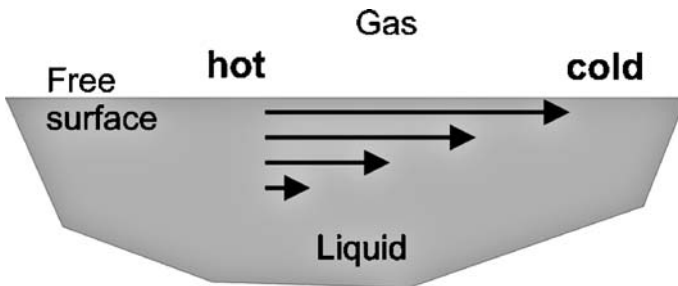


**Fig. 5.1.** Marangoni convection produced by temperature gradient along free liquid surface

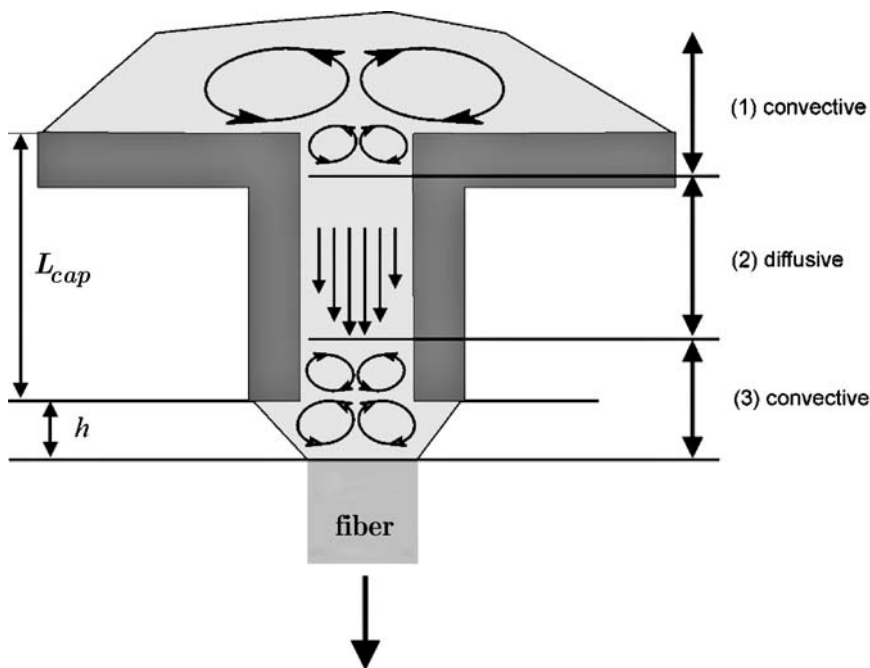


**Fig. 5.2.** Flow patterns induced by thermocapillary convection in a standard  $\mu$ -PD crucible

vection (the crucible center close to the capillary nozzle is always sufficiently hotter than the crucible legs, sometimes called electrodes, attached to the cooled electrical feedthroughs); a nozzle (2) with steady Poiseuille flow; and the meniscus (3) where the melt is again subjected to strong Marangoni convection. Marangoni flow in the meniscus area (3) depends strongly on the height of the meniscus. From observations of a number of fiber growth routines, it has been noted that relatively thick fibers with diameters close to the diameter of the nozzle can generally only be pulled from a low meniscus. However, thinner fibers with a thickness of about 50% of the nozzle diameter can be produced by keeping the meniscus height close to the maximum stable value (see [1] for details). Evidently a high meniscus has a larger free surface and is subjected to pronounced thermocapillary convection. The height of the meniscus can change considerably within a single growth run. Usually very little attention is given to such changes until the diameter of the fiber changes significantly. However, one very important point to remember is that deviations in the meniscus height cause strong changes in meniscus flows.

The flow velocity in the meniscus can be estimated using a simple parametric approach suggested in [6]. When calculating for typical oxide melts according to [6], flow velocities varied in the range of 2–300 mm/s (!) were

obtained for meniscus heights of 0.01–0.3 mm. These are indeed very high values, not even comparable to the values achievable by forced convection. If it was possible to eliminate Marangoni convection in the meniscus, one would have to rotate a 0.5 mm fiber crystal at about 1000 rpm (!) in order to achieve the same stirring effect (see the calculations in [7] for more details).

### 5.3 Growth in Standard $\mu$ -PD Geometry

When a standard  $\mu$ -PD geometry with a relatively long capillary nozzle and a length:diameter ratio of 3–10:1, the growth procedure should include three consecutive steps that are repeated, see Fig. 5.3. In step 1, the pulling process starts from an extended (high) meniscus. A fiber crystal is grown from the flux contained in the meniscus, which steadily gets diluted during growth, as the solute is removed away. The composition of the melt in the main volume of the crucible remains constant because of the long channel separating

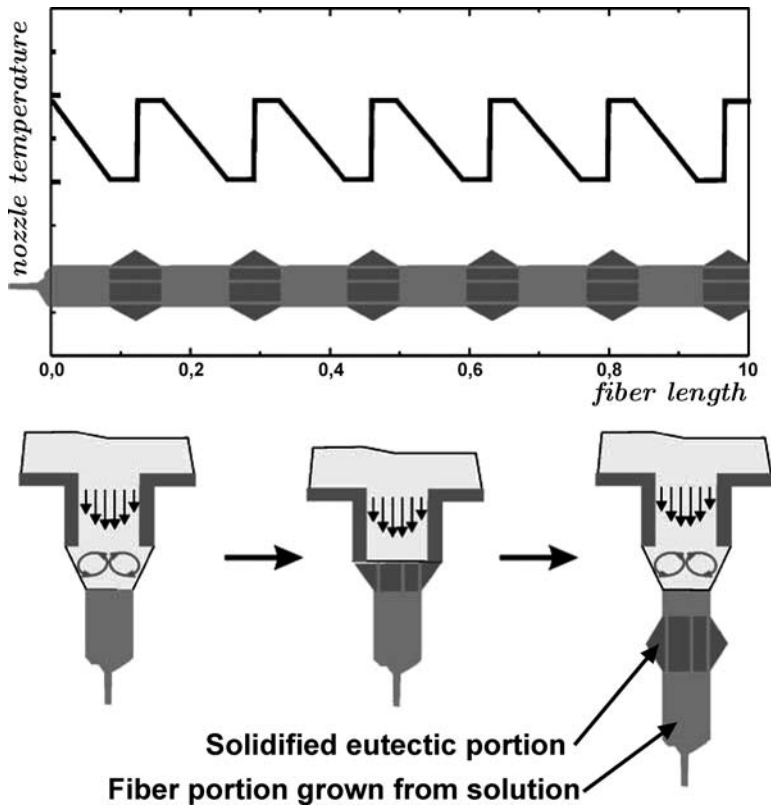


**Fig. 5.3.** Progression of growth steps leading to irregular portions in grown fiber in the case of standard crucible geometry

it from the meniscus. Thus, these two volumes (the crucible reservoir and the meniscus) do not affect each other. The change in the melt composition in the meniscus is accompanied by a decrease in the crystallization (solidification) temperature. As a result, the melt appears to be overheated, and the height of the meniscus increases. In order to keep the meniscus height constant, the heat supplied (i.e., the meniscus temperature) must be steadily decreased.

In step 2, at an even lower temperature usually very close to the nearest eutectic temperature in the corresponding material system, constitutional supercooling of the eutectic melt (or solvent itself, if no eutectic is present) is achieved. The melt in the meniscus then solidifies very quickly. Therefore, the nozzle temperature must be sharply increased to prevent the fiber from freezing onto the nozzle. This requires appropriate action from a skilled operator. In step 3, after the excess solvent has been removed from the meniscus, the temperature is decreased slowly and flux growth starts again. Since the rapidly solidified eutectic portion actually consists of two interpenetrated single crystals ([8]; Chap. 8 of this book), the crystallographic orientation of the solution-grown portion is very often (but not always) preserved along the whole fiber length.

#### 5.4 Growth in a “Capillaryless” $\mu$ -PD Geometry

In the modified geometry shown in Fig. 5.4, the nozzle length is made as small as possible. This practically eliminates the laminar flow in the capillary channel and the meniscus flow is directly coupled to the melt flow inside the crucible reservoir. Both volumes are effectively stirred by Marangoni convection and are mixed together. This makes it possible to perform the solution growth of a single crystal until the composition of the melt in the crucible approaches the corresponding eutectic point. A reasonable diame-

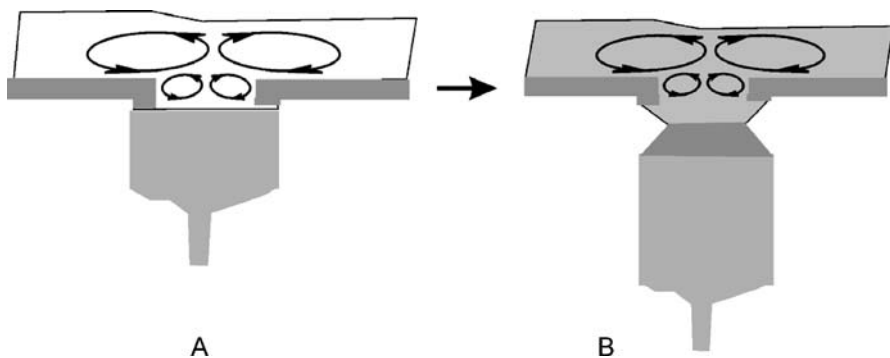


**Fig. 5.4.** Solution growth in modified  $\mu$ -PD crucible: **A** is beginning and **B** is the end of growth process

ter for a crystal grown using this geometry is 2–3 mm (slightly bigger than the typical diameter of a fiber crystal). This process is convenient for growing small but three-dimensional crystals that are often required for routine characterization purposes. It should be mentioned that in the flux version of  $\mu$ -PD the crystal diameter will not obey the rules of capillary shaping [1], as the condition of growth angle on triple line crystal–melt–gas becomes invalid. This topic is beyond the scope of the present chapter, but the reader should note that in flux growth the crystal diameter can be much smaller or bigger than the nozzle diameter.

## 5.5 Growth of $\text{LiTb}_{1-x}\text{Eu}_x\text{P}_4\text{O}_{12}$ Phosphor Crystals

The effectiveness of the crucible modification introduced above has been demonstrated by the successful growth of  $\text{LiTb}_{1-x}\text{Eu}_x\text{P}_4\text{O}_{12}$  crystals from  $\text{LiPO}_4$  flux. A phase diagram for the  $\text{LiPO}_3$ – $\text{TbP}_3\text{O}_9$  system is not available, but it is presumably analogous to  $\text{LiPO}_3$ – $\text{NdP}_3\text{O}_9$ , which has been published by Nakano et al. [9]; see Fig. 5.5 (top). For the growth experiment discussed here, the starting components were present in the ratio  $\text{Li}_2\text{CO}_3:\text{RE}_2\text{O}_3:\text{NH}_4\text{H}_2\text{PO}_4 = 2.1:1.0:8.3$  (mol:mol:mol). The excess of about 50 mol% of  $\text{LiPO}_3$  (in relation to  $\text{LiREP}_4\text{O}_{12}$ ) acted as the flux. Crystals were grown in air at pulling-down rates of 0.25–1.0 mm/h. A representative crystal of composition  $\text{LiTb}_{0.9}\text{Eu}_{0.1}\text{P}_4\text{O}_{12}$  is shown in Fig. 5.5 (bottom).

A comparison of photoluminescence spectra from a single-crystalline specimen produced by  $\mu$ -PD with those from powder specimens of the same composition prepared by solid state sintering has shown that the  $\text{Tb}^{3+}$  host lattice emission (main peak at 545 nm) is present only in the powder material. It is completely quenched in the single-crystalline sample due to highly efficient energy transfer from the  $\text{Tb}^{3+}$  to the  $\text{Eu}^{3+}$ . More on this phenomenon can be found in [10].

## 5.6 Discussion and Conclusions

It is often questioned whether the  $\mu$ -PD method should be considered to be a particular crystal growth method in its own right or just a miniaturized variant of the EFG method. In the opinion of the author, the case of  $\mu$ -PD is an excellent example of how quantity turns into quality. Here the miniaturization brings radically new properties. In any case,  $\mu$ -PD cannot be considered to be a version of EFG because they use totally different mechanisms of segregation. It may sound odd, but from the segregation perspective it is much more reasonable to link  $\mu$ -PD to the vertical Bridgman technique, since the crystal size and the size of the liquid pool from which the crystal is grown are comparable, and partitioning effects, particularly those allowing

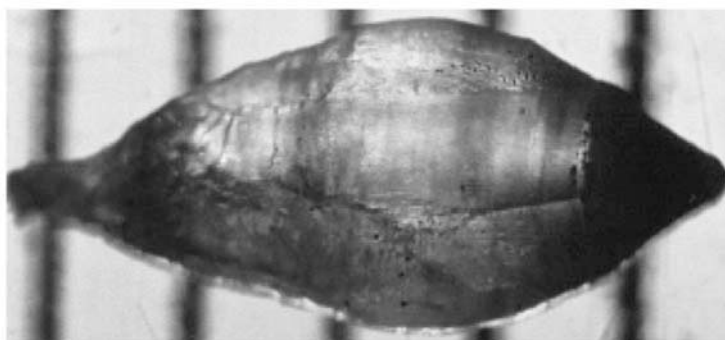
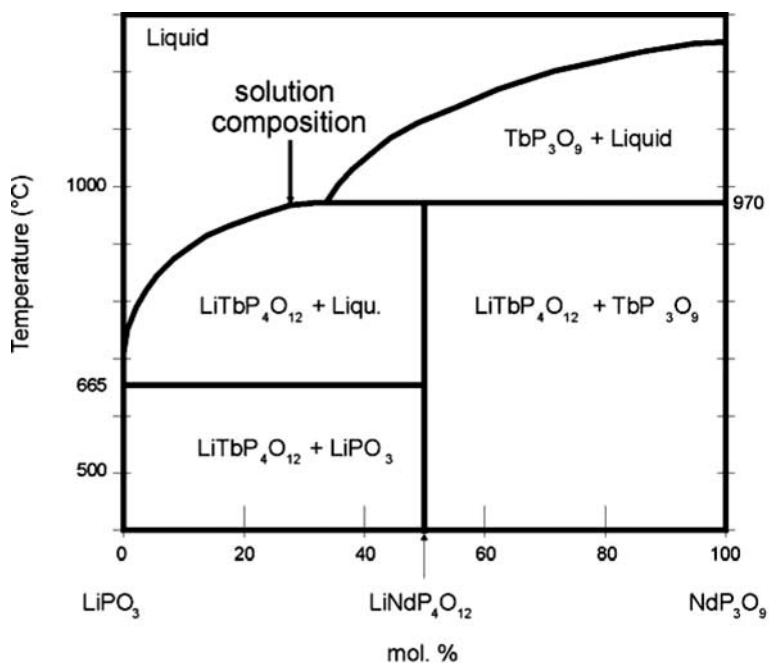


**Fig. 5.5.** Estimated phase diagram of  $\text{LiPO}_3\text{-TbP}_3\text{O}_9$  system with indication of melt composition used (*above*), and  $\text{LiTb}_{0.9}\text{Eu}_{0.1}\text{P}_4\text{O}_{12}$  “bulk” crystal grown from flux

solution growth, are common. Additionally, exceptionally strong Marangoni convection in the  $\mu$ -PD meniscus brings about perfect melt mixing and even stronger partitioning. Changing the meniscus height can control the degree of mixing. An extended meniscus corresponds to more effective melt mixing, as discussed in detail elsewhere [7].

In summary, effective use of the micro-pulling-down ( $\mu$ -PD) growth method for high-temperature solution growth is possible due to very strong

Marangoni convection in the  $\mu$ -PD meniscus. Appropriate modifications to the crucible geometry and the growth procedure permit the growth of fiber-shaped crystals in which excess flux is captured periodically or even miniature bulk single crystals completely free of flux inclusions. This has been demonstrated by the successful growth of  $\text{LiTb}_{0.9}\text{Eu}_{0.1}\text{P}_4\text{O}_{12}$  from  $\text{LiPO}_4$  flux.

*Acknowledgement.* The author cordially acknowledges Prof. T. Fukuda of IMRAM of Tohoku University for stimulating discussions on the topic of  $\mu$ -PD growth, Prof. A. Winnacker of WW6 of Erlangen University for continuous support of this research topic, and Dr. G. Schierning for performing growth experiments with  $\text{LiTb}_{0.9}\text{Eu}_{0.1}\text{P}_4\text{O}_{12}$ .

## References

1. V.A. Tatarchenko, *Shaped Crystal Growth* (Kluwer Academic, Dordrecht, 1993)
2. P. Rudolph, T. Fukuda, *Cryst. Res. Technol.*, **34**, 3 (1999)
3. V.I. Chani, K. Shimamura, T. Fukuda, *Cryst. Res. Technol.*, **34**, 519 (1999)
4. D. Elwell and H.J. Scheel, *Crystal Growth from High-Temperature Solutions* (Academic, London, 1975)
5. C.W. Lan, *J. Cryst. Growth*, **169**, 269 (1996)
6. Y. Okano, M. Ito, A. Hirata, *J. Chem. Eng. Japan*, **22**, 275 (1989)
7. T. Fukuda, P. Rudolph, S. Uda, (eds.), *Fiber Crystal Growth from the Melt* (Springer, Berlin, 2004)
8. V. S. Stubican, R. C. Bradt, *Ann. Rev. Mater. Sci.*, **11**, 267 (1981)
9. J. Nakano, T. Yamada, S. Miyazawa, *J. Cryst. Growth*, **47**, 693 (1979)
10. G. Schierning, M. Batenchuk, A. Osvet, A. Winnaker, *Radiat. Meas.*, **38**, 529 (2004)

# 6 Mixed Crystals: $\mu$ -PD vs. Czochralski Method

Andrey Novoselov

**Abstract.** The purpose of this chapter is to demonstrate, through a case study approach, how beneficial the  $\mu$ -PD method can be for growing mixed crystals.

## 6.1 Garnets in Nature and Technology

The garnet family is an excellent example of a “mixed” crystal family. Natural garnets have long been used as semi-precious jewellery stones, but their technological importance has been limited to their use as mild abrasives. They are classified as silicates, and belong to the subclass of nesosilicates, which includes all silicates where the  $(\text{SiO}_4)$  tetrahedrons are unbounded to other tetrahedrons. They are also sometimes referred to as orthosilicates. The general formula of most natural garnets is  $\text{C}_3\text{A}_2(\text{SiO}_4)_3$ , where C represents divalent metals such as Ca, Fe, Mg and Mn, and A represents trivalent metals such as Al, Cr, Fe, V, Ti and Zr. The most important natural garnets are almandine  $\text{Fe}_3\text{Al}_2(\text{SiO}_4)_3$ , grossular  $\text{Ca}_3\text{Al}_2(\text{SiO}_4)_3$  and pyrope  $\text{Mg}_3\text{Al}_2(\text{SiO}_4)_3$ . The garnet crystal structure was solved by Menzer [1] to be  $\{\text{C}_3\}[\text{A}_2](\text{D}_3)\text{O}_{12}$ , where {C} denotes a big dodecahedral (distorted cube) site surrounded by eight oxygen atoms, [A] the middle-size octahedral site (coordinated to six oxygens), and (D) the small tetrahedral site (coordinated to four oxygens), see Fig. 6.1. One interesting example of a rather “mixed” natural garnet, a particular sample of grossular  $\{\text{Ca}_{2.84}\text{Mg}_{0.18}\}[\text{Al}_{1.63}\text{Fe}_{0.25}\text{Mg}_{0.11}\text{Ti}_{0.02}](\text{Si}_{2.96}\text{Al}_{0.06})\text{O}_{12}$ , was provided in a detailed review on crystal chemistry of garnets by Geller [2].

A new chapter in the long history of garnets started with the successful synthesis of the first silicon-free synthetic garnet  $\{\text{Y}_3\}[\text{Al}_2](\text{Al}_3)\text{O}_{12}$ , better known as  $\text{Y}_3\text{Al}_5\text{O}_{12}$  or YAG, by Yoder and Keith in 1951 [3], which was followed by the discovery of the synthetic ferromagnetic yttrium and other rare-earth garnets  $\text{Y}_3\text{Fe}_2(\text{FeO}_4)_3$ ,  $\text{Sm}_3\text{Fe}_2(\text{FeO}_4)_3$  and  $\text{Gd}_3\text{Fe}_2(\text{FeO}_4)_3$  [4]. Laser action in single crystals of Nd-doped YAG,  $\text{Y}_3\text{Ga}_5\text{O}_{12}$  and  $\text{Gd}_3\text{Ga}_5\text{O}_{12}$  (GGG) grown by the Verneuil method and the flux process was demonstrated by Geusic and coworkers [5], but further optimization of the crystal quality was requested. Advances in single crystal growth using the Czochralski (CZ) method and subsequent application of the technique to oxides in order to

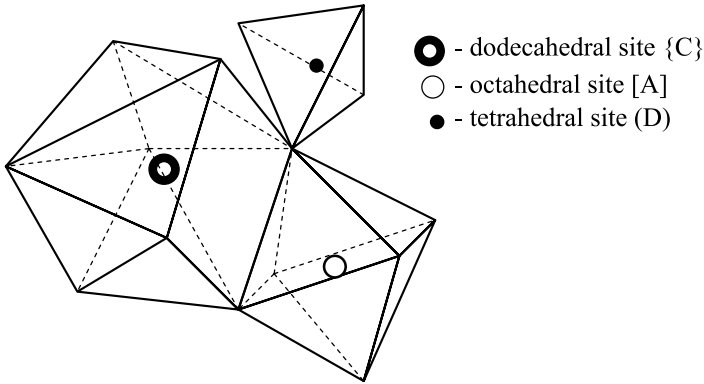


**Fig. 6.1.** Coordination about an oxygen ion in garnets

obtain reliable laser hosts resulted in the growth of Nd-doped GGG and YAG single crystals with practical dimensions by Linares [6].

GGG did not repeat the huge industrial success of YAG as a solid-state laser host. However, because its crystal lattice parameter was noted to increase continuously from 12.383 (GGG) to 12.504 Å ( $\text{Nd}_3\text{Ga}_5\text{O}_{12}$ ), in the early 1970s, Nd-doped GGG received interest as a substrate for the epitaxy of magnetic rare-earth iron gallium, and Bi-doped iron garnets as Faraday effect optical isolators [7]. When the range of lattice constants of iron gallium garnets is considered, it is apparent that the lattice parameters of rare-earth gallium garnets cover the same range and allow the lattice mismatch which strongly affects the properties of deposited iron gallium garnet films to be completely eliminated. As an extra advantage, a number of rare-earth gallium garnets are congruent melting compounds and thus can be readily grown using the Czochralski method. Comprehensive work on the single-crystal growth of numerous mixed garnet crystals was conducted by Brandle and coworkers [8–10]. The other excellent example is the work done by Mateika and coworkers [11,12], which has yielded about 300 garnet compositions.

## 6.2 Czochralski Growth of Gallium Garnets

With the progression of bubble memory and magneto-optical technologies from research to industrial stage, the need for large-diameter substrates has increased, while the liquid-phase epitaxy technology used for the deposition of garnet films requires substrates of high crystalline perfection. The main problems encountered during CZ growth of synthetic rare-earth garnets, and particularly of GGG, were the nonstoichiometry of the melt and crystal imperfections.

In the very first growth experiments, it was assumed that the growing crystals were stoichiometric 3:5 mixtures of rare-earth oxide and gallium ox-

ide. As a consequence, it was commonly assumed that the initial crucible charge and the melt compositions obtained are stoichiometric, which is not always correct. Because GGG was considered as a substrate material, its lattice parameter received special attention. It was found that the lattice parameter values obtained by different authors on GGG ceramics (12.376 Å) [13] or GGG crystals grown by flux (12.3771 Å) [14], hydrothermally (12.3753–12.3768 Å) [14], or via CZ (12.376 Å [6] and 12.384 Å [9]) were considerably different.

An explanation of this phenomenon was provided by Brandle [8–10]. First of all, it was noticed that after 3–4 h of growth the melt had lost some gallium oxide, resulting in a drop in the melting point. It was suggested that this was due to the gallium suboxide ( $\text{Ga}_2\text{O}$ ) vaporization. To suppress this process, an excess of  $\text{Ga}_2\text{O}_3$ , 1 wt% or more, was added. At this point, the influence of the growth atmosphere in the Czochralski chamber was highlighted for the first time. As a rule, crystals of high-melting oxides ( $T_m > 1500^\circ\text{C}$ ) are pulled from an iridium crucible ( $T_m = 2443^\circ\text{C}$ ) which is sensitive to oxygen at elevated temperatures. Hence, growth runs are usually conducted in a neutral atmosphere ( $\text{N}_2$ , Ar, etc.) to protect the crucible from oxidation. Ignoring the resulting shortening of the (expensive) iridium crucible, iridium oxidation products detrimentally contaminate growing crystals. It is much easier to pull a GGG crystal from a melt containing an excess of  $\text{Ga}_2\text{O}_3$  than from a stoichiometric melt: growth in a neutral atmosphere can be performed for extended periods of time and iridium contamination is low. For a melt containing a 2 wt% excess of  $\text{Ga}_2\text{O}_3$ , weight losses of around 2–3% were observed over a 12-h period, while under the same conditions the stoichiometric melt lost 5–6 wt%. Under an oxidizing atmosphere containing 2 vol% of oxygen, the congruent melting composition becomes stoichiometric, yielding good-quality single crystals without dislocations. It was finally concluded that the congruent melting composition was not necessarily stoichiometric; it could be expressed as, for example,  $\{\text{Gd}_3\}[\text{Gd}_{0.04}\text{Ga}_{1.96}](\text{Ga}_3)\text{O}_{12}$  [10].

The differences between the lattice parameters of the GGG samples obtained by different methods were attributed to some of the Gd cations occupying the octahedral sites, which was due to a shift in the congruent melting composition toward the Gd-rich region on the  $\text{Gd}_2\text{O}_3$ – $\text{Ga}_2\text{O}_3$  phase diagram [10]. Although the material obtained still had a garnet structure, it was evident that the probability of multiple substitutions on various sites increased as the complexity of the cation substitution increased. This effect is known as *antisite defect*, and its harmful influence on the scintillating properties of Pr-doped Lu-containing gallium and aluminum garnets is discussed elsewhere [15].

A theoretical approach to modeling the thermal dissociation of the GGG melt in an iridium crucible under a neutral-to-oxidizing atmosphere was developed by Piekarczyk and Pajackowska [16], and calculated values of the optimal oxygen content coincided well with those observed practically. Because most of the foreign inclusions found in the grown crystals were small

(6  $\mu\text{m}$ ) triangular or pseudo-hexagonal platelets of iridium, it was suggested that these defects could be eliminated by using a precisely controlled atmosphere in the growth chamber and by careful crucible cleaning [8].

The appearance of facets (as well as the strains associated with these facets) in CZ-grown GGG crystals depends on the shape of the growth interface. Since facet strain and growth striations were also produced during the epitaxy of iron garnet films, their reduction was required to enable the industrial-scale production of these magnetic films [16]. Initially, most crystals were grown with a conical growth interface and so  $\{211\}$  facets and large areas associated with high strain were formed. Supposedly, a conical growth interface maintains stable growth conditions while a flat or convex interface shape is attributed to unstable growth and thus should be avoided. Elimination of the facets on the growth interface (and therefore the associated strain) was accomplished by increasing the rotation rate from 20 to 45 rpm, which actually leads to a flat growth interface. Thus facets were moved from the central part of the crystal to the outside surface, yielding a strain-free central section that could be processed into substrate or optical parts [8].

Rare-earth gallium garnets form a continuous series of solid solutions, such as  $\text{Gd}_3\text{Ga}_5\text{O}_{12}$ – $\text{Nd}_3\text{Ga}_5\text{O}_{12}$ ,  $\text{Gd}_3\text{Ga}_5\text{O}_{12}$ – $\text{Sm}_3\text{Ga}_5\text{O}_{12}$ ,  $\text{Sm}_3\text{Ga}_5\text{O}_{12}$ – $\text{Nd}_3\text{Ga}_5\text{O}_{12}$ ,  $\text{Gd}_3\text{Ga}_5\text{O}_{12}$ – $\text{Dy}_3\text{Ga}_5\text{O}_{12}$ ,  $\text{Gd}_3\text{Ga}_5\text{O}_{12}$ – $\text{Y}_3\text{Ga}_5\text{O}_{12}$ ,  $\text{Dy}_3\text{Ga}_5\text{O}_{12}$ – $\text{Y}_3\text{Ga}_5\text{O}_{12}$ , and other combinations [8, 17], with the liquidus and solidus lines of the phase diagram being very close together. The only difficulty encountered here was constitutional supercooling, but this was minimized by decreasing the growth rate. The pulling rate permitted depends on the difference in the melting points of the individual garnets: the larger the difference, the slower the pulling rate. For example, in the  $\text{Gd}_3\text{Ga}_5\text{O}_{12}$ – $\text{Nd}_3\text{Ga}_5\text{O}_{12}$  system, the melting points differ by about 180  $^\circ\text{C}$ , and the pulling rate is  $\leq 0.76$  mm/h. However, in the  $\text{Ho}_3\text{Ga}_5\text{O}_{12}$ – $\text{Er}_3\text{Ga}_5\text{O}_{12}$  system, this difference is only about 13  $^\circ\text{C}$ , so a much higher pulling rate of 4.5 mm/h is selected [8].

Multicomponent melt compositions were developed in order to eliminate lattice mismatch between substrates and iron garnet films [11]. During growth, it was found that the distribution coefficients of the melt constituents were different from unity, even for compositions far from being “highly” multicomponent in nature, such as  $\{\text{Gd}_3\}\{\text{Sc}_x\text{Ga}_{2-x}\}(\text{Ga}_3)\text{O}_{12}$  [18]. Again, the pulling rate needs to be kept low to achieve uniformity within the crystal boule. On the other hand, only a small fraction of the melt should be solidified to an acceptably homogeneous crystal; for example, about 20–30% of the initial crucible charge should be used to get laser-quality Nd:GGG. The optical quality of faceted crystals grown with a convex growth interface, enabled by a low rotation rate, was better than that of unfaceted crystals grown with a flat growth interface produced by fast rotation [19].

It should be pointed out that the crystal rotation rate used to establish a proper growth interface shape as well as the crystal pulling rate required to obtain compositional uniformity of the crystal should be tailored to the particular end use of the crystal.

## 6.3 The $\mu$ -PD Method Approach to Mixed Crystals

### 6.3.1 Motivation and Basic Features

Application of the  $\mu$ -PD method allows us to overcome some of the problems mentioned above. The case study described in this chapter is based on our experience of the  $\mu$ -PD growth of mixed rare-earth gallium and aluminum garnet single crystals. This work was motivated by two research projects carried out by the Fukuda Laboratory: one on scintillating and another on the laser properties of Yb-doped materials.

Materials based on the garnet structure are promising candidates for scintillator applications because the technology developed for laser hosts is highly matured, and because such materials have high optical transparency and are relatively easy to dope with rare-earth elements. The luminescence of Yb<sup>3+</sup>-containing crystals has become of great interest due to its charge transfer origins, involving allowed transitions between the  $p$  levels of ligands (oxygen, halides), which comprise the top of the valence band of the crystal, and the previously mentioned  $4f$  states of Yb<sup>3+</sup>. This can provide, in oxide compounds, a luminescence spectrum covering the near ultraviolet to visible range, a fast radiative lifetime of the order of 100 ns, and reduced concentration quenching with respect to other widely used emission centers such as Ce<sup>3+</sup> [20, 21]. On the other hand, with recent advances in high-performance InGaAs laser diodes with wavelengths of between 900 and 1100 nm, interest in Yb<sup>3+</sup>-doping has been increasing due to its applications in high-efficiency and high-power diode-pumped laser systems. The ytterbium ion has intense and broad absorption lines that are ideally suited to diode pumping since it has the simplest energy level scheme of any rare-earth active ion, consisting of only two levels: the <sup>2</sup>F<sub>7/2</sub> ground state and the <sup>5</sup>F<sub>5/2</sub> excited state [22, 23].

A comprehensive study on single-crystal growth and the optical properties of Yb-doped (Yb<sub>*x*</sub>Y<sub>1-*x*</sub>)<sub>3</sub>Ga<sub>5</sub>O<sub>12</sub> ( $x = 0.05, 0.165$  and  $0.33$ ), (Yb<sub>*x*</sub>Lu<sub>1-*x*</sub>)<sub>3</sub>Ga<sub>5</sub>O<sub>12</sub> ( $x = 0.02, 0.05$  and  $0.10$ ), and a continuous series of solid solutions [(Yb<sub>*x*</sub>Gd<sub>1-*x*</sub>)<sub>3</sub>Ga<sub>5</sub>O<sub>12</sub> ( $0.0 \leq x \leq 1.0$ ), (Lu<sub>*x*</sub>Gd<sub>1-*x*</sub>)<sub>3</sub>Ga<sub>5</sub>O<sub>12</sub> ( $0.0 \leq x \leq 1.0$ ), (Yb<sub>0.05</sub>Lu<sub>*x*</sub>Gd<sub>0.95-*x*</sub>)<sub>3</sub>Ga<sub>5</sub>O<sub>12</sub> ( $0.0 \leq x \leq 0.9$ ), Yb<sub>0.15</sub>Gd<sub>0.15</sub>Lu<sub>2.7</sub>(Al<sub>*x*</sub>Ga<sub>1-*x*</sub>)<sub>5</sub>O<sub>12</sub> ( $0.0 \leq x \leq 1.0$ ) and (Yb<sub>*x*</sub>Lu<sub>1-*x*</sub>)<sub>3</sub>Al<sub>5</sub>O<sub>12</sub> ( $0.0 \leq x \leq 1.0$ )] was performed [24–34]. Experimental details for  $\mu$ -PD growth runs are easy to find, especially in the papers cited. Examples of the crystals grown are shown in Fig. 6.2. As can be seen, the crystals are transparent and free of cracks and visible inclusions. The roughness of the crystal surface depends on many factors. Although the shape of the die plays a specific role in the  $\mu$ -PD method, the final crystal shape, in accordance with the symmetry principle of Curie, is determined by the symmetry of the melt column or the meniscus, the thermal field at the crystallization interface, the growth rate, and natural faceting.

For some shape classes, for example rectangular, triangular or square, the effect of shape is maximal when the symmetry of the melt column, defined by the die geometry, and that of the naturally faceted crystal match each

other. Early on in the history of crystal shaping, it was established that weak faceting of crystals and good control of shaping can be attained in round-shaped dies by some overheating of the melt. In the cases of square or plate-shaped dies it is more difficult to control the geometry of the growing crystal [35].

We used  $\langle 111 \rangle$  YAG fiber crystals to seed all of the growths presented below. Of course, mismatch of lattice parameters was significant in some cases, but good mechanical properties of YAG and the relative simplicity of YAG fiber crystal growth made it the seed crystal of choice. Sometimes the fibers grown were slightly faceted, with an evident hexagonal cross-section, typical of garnets grown in the  $\langle 111 \rangle$  direction [36], but the crystals grown using round-shaped dies had a regular round shape, as seen in Fig. 6.2. The surfaces of the round-shaped crystals were generally smooth, although sometimes rough regions were formed due to partial faceting. The surfaces of square-shaped crystals were not smooth. However, this was because of the higher pulling rate applied, 0.3 mm/min (0.05 mm/min was applied to the round-shaped crystals). Scanning electron microscopy (SEM) images of an edge of a square-shaped crystal (see Fig. 6.3) show the structure of the defective crystal skin. It consisted of numerous inclusions of eutectic mixtures of  $\text{GdGaO}_3$  and GGG or  $\text{Ga}_2\text{O}_3$  and GGG, depending upon whether the melt was  $\text{Gd}_2\text{O}_3$ - or  $\text{Ga}_2\text{O}_3$ -rich. These inclusions were often associated with small hollow channels.

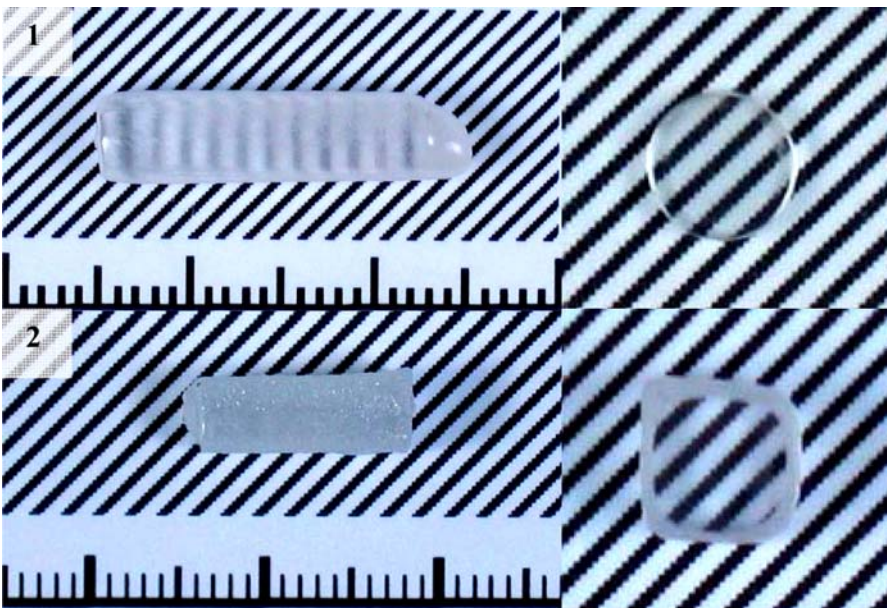


**Fig. 6.2.** Examples of as-grown  $(\text{Yb}_{0.05}\text{Gd}_{0.95})_3\text{Ga}_5\text{O}_{12}$  (1) and  $(\text{Yb}_{0.05}\text{Lu}_{0.95})_3\text{Ga}_5\text{O}_{12}$  (2) crystals and their cross-sections. Scale is given in cm

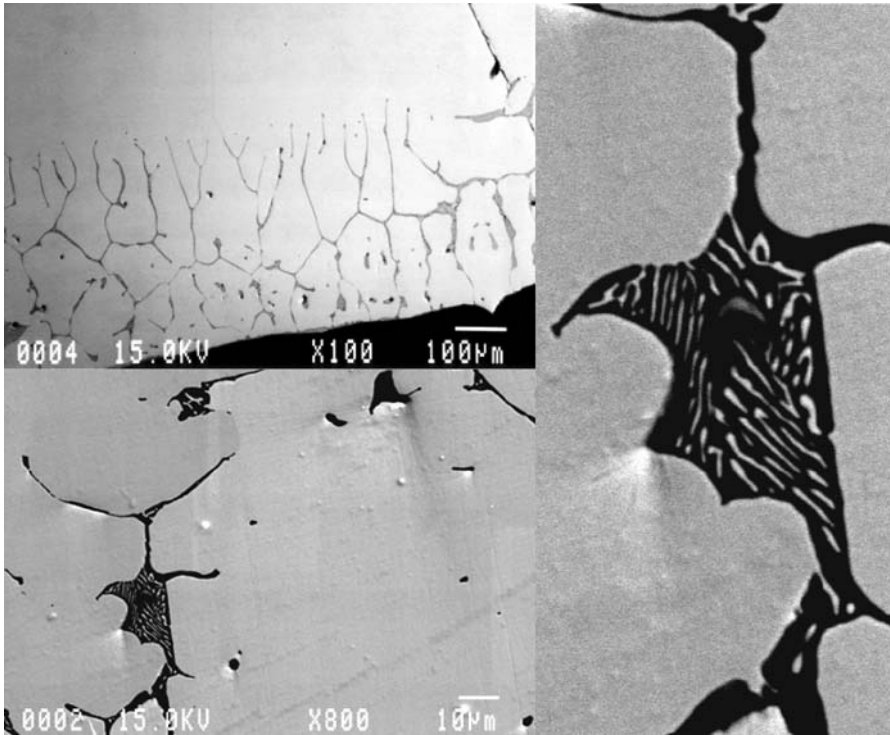


**Fig. 6.3.** SEM images of a square-shaped  $\text{Gd}_3\text{Ga}_5\text{O}_{12}$  crystal. Crystal edge with defective skin (*top*) and magnification of the hollow channel (*bottom*) with eutectic structure apparent (*right*)

All of the crystals grown were examined using the XRD technique and typically consisted of a single garnet phase with no impurity phase present. Examples of the compositional dependencies of the lattice constants are given in Fig. 6.4. All of the dependencies of the lattice parameter  $a$  were linear across the whole compositional interval  $x$ , following Vegard's law. It can be concluded that a continuous series of solid solutions are formed in all of the cases presented here.

### 6.3.2 Growth Interface in the $\mu$ -PD System

Because the  $\mu$ -PD technique is very similar to other shaped crystal growth techniques, such as the Stepanov and/or EFG methods, it is easy to get any desired curvature of the growth interface. Sketches of different shapes of the crucible dies, including flat, concave (yielding a convex crystal growth interface) and convex (leading to a concave crystal growth interface), are presented in Fig. 6.5. Crucibles with a flat die are commonly used in  $\mu$ -PD growth experiments, since they eliminate any strain-induced facets leading to core formation.

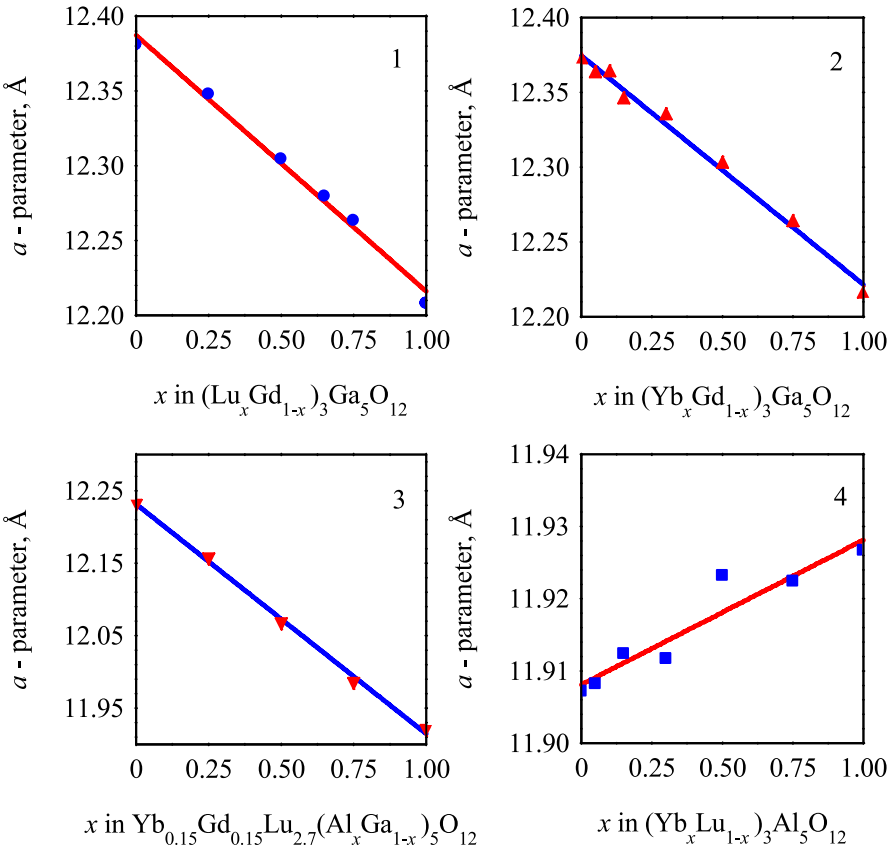


**Fig. 6.4.** Concentration dependence of the lattice parameter  $a$  on  $\mu$ -PD crystal composition: 1,  $(\text{Lu}_x\text{Gd}_{1-x})_3\text{Ga}_5\text{O}_{12}$ ; 2,  $(\text{Yb}_x\text{Gd}_{1-x})_3\text{Ga}_5\text{O}_{12}$ ; 3,  $\text{Yb}_{0.15}\text{Gd}_{0.15}\text{Lu}_{2.7}(\text{Al}_x\text{Ga}_{1-x})_5\text{O}_{12}$ ; 4,  $(\text{Yb}_x\text{Lu}_{1-x})_3\text{Al}_5\text{O}_{12}$

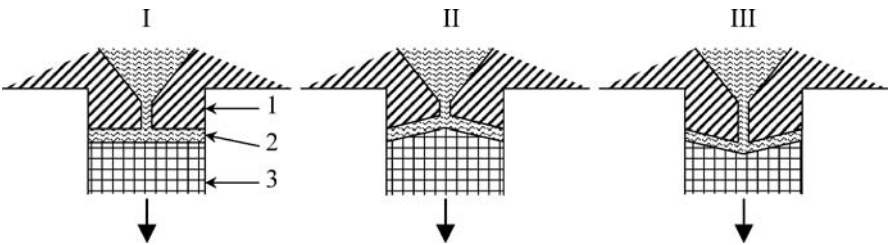


**Fig. 6.5.** Sketches of different shapes of crucible dies: I, flat; II, concave; III, convex (1, crucible die; 2, meniscus; 3, growing crystal)

### 6.3.3 Influence of Growth Atmosphere

Crystals containing Ga were grown from stoichiometric melt using an oxidizing atmosphere containing 2 vol% of oxygen. Considering the short growth time, usually 1–2 h, we have also tried to grow GGG from stoichiometric melt in a neutral atmosphere. In this case, whitish polycrystalline samples were obtained. Their XRD patterns showed the presence of a mixture of the main garnet phase with low intensity reflections of an unidentified secondary phase.

The use of an oxidizing atmosphere is harmful to Ir crucibles, particularly to crucibles with shaped dies. Crystal shaping strongly depends on the edge sharpness of the die, because it is easy to control the growth process using minimal overheating of the melt when the meniscus is fixed on the sharp edge of the die. An example of the ideal case, with a sharp edge, is shown in Fig. 6.6, I. This sharp edge becomes rounded after a few growth runs in an oxidizing atmosphere, see Fig. 6.6, II. With increasing of the edge bluntness control of the growth and especially shape of the growing crystal becomes difficult, see Fig. 6.6, III. Some overheating of the melt is required to maintain the desired shape of the growing crystal, see Fig. 6.6, IV. However, it is known that overheating of the melt during garnet crystal growth makes crystallization of the secondary perovskite phase together with main garnet phase possible, and this should therefore be avoided [37]. On the other hand,

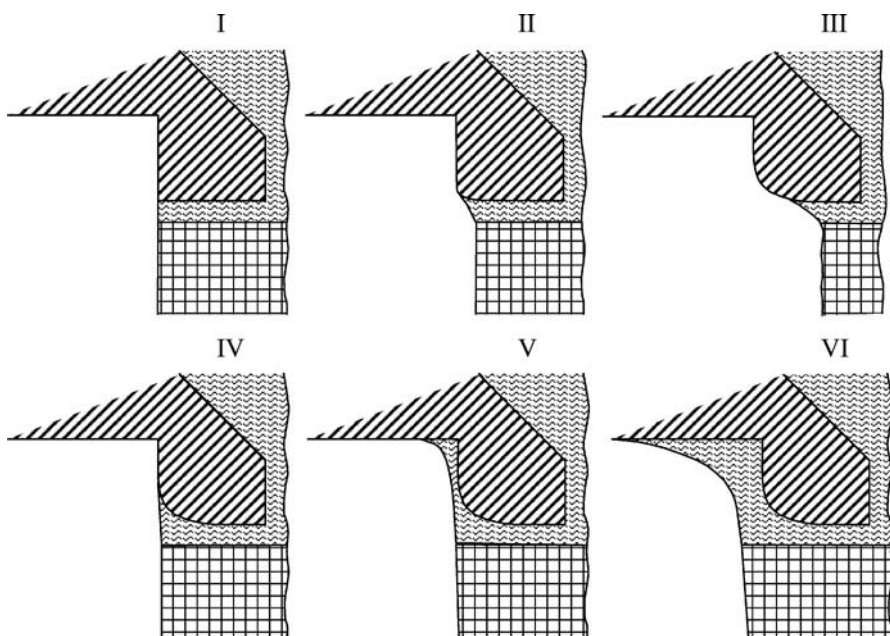


**Fig. 6.6.** Influence of die edge sharpness on crystal growth: **I**, sharp; **II**, slightly oxidized (blunt); **III**, heavily oxidized; **IV**, growth with moderate overheating; **V**, melt overflow; **VI**, complete loss of control over shape

overheating of a wettable melt (which is the case for rare-earth gallium garnets and an Ir crucible) can easily result in the overflow or the overspreading of the melt beyond the edge of the die (see Fig. 6.6, V) and complete loss of control over the growth process (see Fig. 6.6, VI).

### 6.3.4 Compositional Uniformity of $\mu$ -PD Crystals

The similarity of the  $\mu$ -PD and EFG methods allows us to use the impurity/dopant distribution model developed for EFG. It was assumed that steady-state EFG proceeds with an effective segregation coefficient ( $k_{\text{eff}}$ ) of unity or close to unity [38]. This hypothesis was confirmed experimentally [39]. Nevertheless, it can only be achieved if a fast growth speed,  $\geq 1$  mm/min, is used as well as a long capillary channel connecting the bulk melt and the crystal growth interface.

In practice,  $k_{\text{eff}}$  is observed to differ from unity, and some variations in the dopant concentration in the axial and radial directions are seen. This nonuniformity is shown in Fig. 6.7. This may be attributed to the fact that the dopant distribution in the meniscus above the growth interface does not reach a completely steady state, or it may indicate that thermal convection in the meniscus cannot be ignored. Indeed, if a crucible with a die is used the meniscus volume increases in the form of thin film under the die, and so the thermocapillary Marangoni convection increases sharply. This is clearly

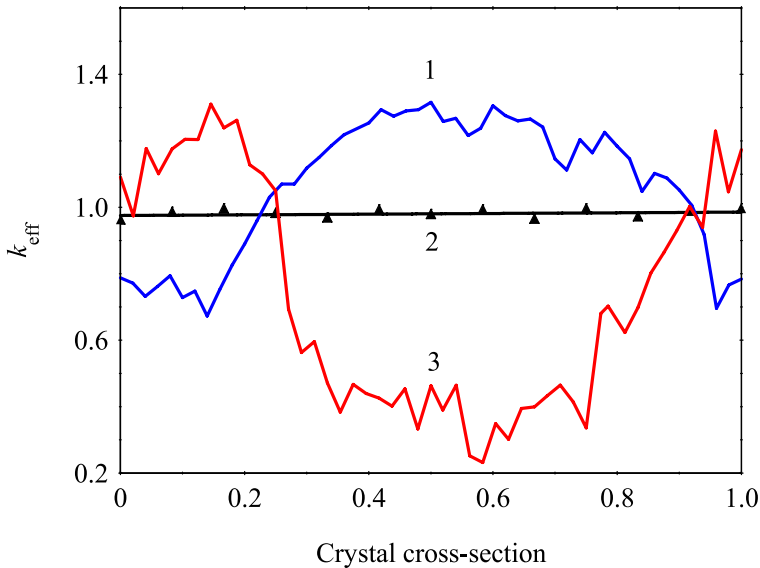


**Fig. 6.7.** Effective segregation coefficient over the radial (1) and axial (2) cross-sections of shaped Yb-doped  $\text{Gd}_3\text{Ga}_5\text{O}_{12}$  (5 mol%) crystal; radial cross-section (3) of shaped Pr-doped  $\text{Y}_2\text{SiO}_5$  (0.25 mol%) crystal

seen in the case of Pr-doped  $\text{Y}_2\text{SiO}_5$ , where heavier Pr ions are pushed to the edge of the crystal by convection flows. It should be noted that this particular sample was grown with a relatively slow pulling rate of 0.05 mm/min, and the effective segregation coefficient is below unity in the central part of the crystal while it is greater than unity at the crystal edge [40]. In the case of Yb-doped GGG, where the Gd and Yb ions are very similar, the fast pulling rate of 0.3 mm/min and (therefore) the fast crystallization rate exert the greatest influence over the convection, and so the highest dopant concentration occurs in the central part of the crystal in front of the capillary channel.

However, the axial dopant distribution is quite uniform, with an effective segregation coefficient of close to unity, see Fig. 6.7. It should be mentioned that the crucible charge was consumed in full during the growth experiments described above and the uniformity of the dopant distribution suggests a complete absence of melt backflow through the capillary channel. If one compares Czochralski-grown crystals with those grown by the  $\mu$ -PD method, the latter have higher compositional homogeneity.

### 6.3.5 Quality of $\mu$ -PD Crystals

Crystal quality is an important parameter for all crystal growth techniques, and one that heavily influences the particular applications of the crystals grown. When comparing the  $\mu$ -PD and Czochralski methods, one should bear in mind that the former is a unique screening tool for materials since it allows

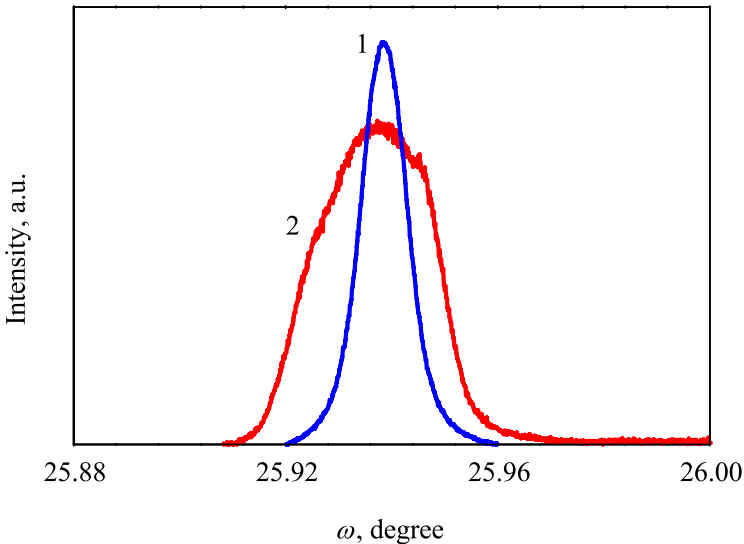


**Fig. 6.8.** XRCs for (444) reflection in Yb-doped (5 mol%)  $\text{Gd}_3\text{Ga}_5\text{O}_{12}$  crystals grown at different pulling rates: 1, 0.05 mm/min (FWHM = 37 arcsec); 2, 0.3 mm/min (FWHM = 104 arcsec)

promising material compositions to be rapidly grown for subsequent characterization. It is distinguished by fast growth speed and high axial temperature gradients of  $10^2$  to  $10^4$  °C/cm, which can have a negative influence on crystal quality. High-temperature gradients result in thermal stress, which fortunately does not lead to fracture in ductile isotropic garnets, but it does degrade optical quality due to stress-induced birefringence. Results from X-ray rocking curve (XRC) analyses of Yb-doped GGG (5 mol%) samples grown at different pulling rates are shown in Fig. 6.8. The diffraction peak (444) for the sample grown at a pulling rate of 0.05 mm/min is relatively sharp, with a full width at half maximum (FWHM) of only about 37 arcsec, while the peak for the sample grown at a pulling rate of 0.3 mm/min is wider – 104 arcsec. This example demonstrates that giving up one of the most important benefits obtained from the use of the  $\mu$ -PD method as a materials screening technique, namely its high growth rate, can improve crystal quality to the level of Czochralski-grown optical crystals.

## 6.4 Summary

This chapter has shown how some of the problems that are encountered during the growth of mixed garnets via the Czochralski method can be successfully overcome by using the  $\mu$ -PD growth method instead. These issues are circumvented by employing standard  $\mu$ -PD growth conditions developed for fast materials screening. Moreover, crystals of optical quality can be grown via  $\mu$ -PD by adjusting the growth parameters used.

## References

1. G. Menzer, Z. Kristallogr., **63**, 157 (1926)
2. S. Geller, Z. Kristallogr., **125**, 1 (1967)
3. H.S. Yoder, M.L. Keith, Am. Miner., **36**, 519 (1951)
4. S. Geller, M.A. Gilleo, Acta Cryst., **10**, 239 (1957)
5. J.E. Geusic, H.M. Marcos, L.G. Van Uitert, Appl. Phys. Lett., **4**, 182 (1964)
6. R.C. Linares, Solid State Commun., **2**, 229 (1964)
7. A.H. Bobeck, E.G. Spencer, L.G. Van Uitert, S.C. Abrahams, R.L. Barnes, W.H. Grodkiewicz, R.C. Sherwood, P.H. Schmidt, D.H. Smith, E.M. Walters, Appl. Phys. Lett., **17**, 131 (1970)
8. C.D. Brandle, A.J. Valentino, J. Cryst. Growth, **12**, 3 (1972)
9. C.D. Brandle, D.C. Miller, J.W. Nielsen, J. Cryst. Growth, **12**, 195 (1972)
10. C.D. Brandle, R.L. Barnes, J. Cryst. Growth, **26**, 169 (1974)
11. D. Mateika, R. Laurien, Ch. Rusche, J. Cryst. Growth, **56**, 677 (1982)
12. D. Mateika, E. Volkel, J. Haisma, J. Cryst. Growth, **102**, 994 (1990)
13. S.J. Schneider, R.S. Roth, J.L. Waring, J. Res. Nat. Bur. Standards, **65A**, 345 (1961)
14. E.D. Kolb, R.A. Laudise, J. Cryst. Growth, **29**, 29 (1975)

15. M. Nikl, J. Pejchal, E. Mihokova, J.A. Mares, H. Ogino, A. Yoshikawa, T. Fukuda, A. Vedda, C. D'Ambrosio, *Appl. Phys. Lett.*, **88**, 141916 (2006)
16. W. Piekarczyk, A. Pajaczkowska, *J. Cryst. Growth*, **46**, 483 (1979)
17. H. Kimura, A. Miyazaki, *J. Cryst. Growth*, **250**, 251 (2003)
18. K. Chow, G.A. Keig, A.M. Hamley, *J. Cryst. Growth*, **23**, 58 (1974)
19. Y. Kuwano, *J. Cryst. Growth*, **57**, 353 (1982)
20. L. van Pieterse, M. Heeroma, E. de Heer, A. Meijerink, *J. Lumin.*, **91**, 177 (2000)
21. N. Guerassimova, N. Garnier, C. Dujardin, A.G. Petrosyan, C. Pedrini, *Chem. Phys. Lett.*, **339**, 197 (2001)
22. L.D. DeLoach, S.A. Payne, L.L. Chase, L.K. Smith, W.L. Kway, W.F. Krupke, *IEEE J. Quantum Elect.*, **29**, 1179 (1993)
23. D.M. Baney, G. Rankin, K.W. Chang, *Appl. Phys. Lett.*, **69**, 1662 (1996)
24. A. Yoshikawa, T. Akagi, M. Nikl, N. Solovieva, K. Lebbou, C. Dujardin, C. Pedrini, T. Fukuda, *Nucl. Instrum. Methods A*, **486**, 79 (2002)
25. A. Yoshikawa, M. Nikl, H. Ogino, J.-H. Lee, T. Fukuda, *J. Cryst. Growth*, **250**, 94 (2003)
26. H. Ogino, A. Yoshikawa, J.-H. Lee, M. Nikl, N. Solovieva, T. Fukuda, *J. Cryst. Growth*, **253**, 314 (2003)
27. A. Yoshikawa, H. Ogino, J.-H. Lee, M. Nikl, N. Solovieva, N. Garnier, C. Dujardin, K. Lebbou, C. Pedrini, T. Fukuda, *Opt. Mater.*, **24**, 275 (2003)
28. A. Yoshikawa, H. Ogino, J.B. Shim, V.V. Kochurikin, M. Nikl, N. Solovieva, S. Ono, N. Sarakura, M. Kikuchi, T. Fukuda, *Opt. Mater.*, **26**, 529 (2004)
29. M. Nikl, A. Yoshikawa, T. Fukuda, *Opt. Mater.*, **26**, 545 (2004)
30. A. Novoselov, A. Yoshikawa, H. Ogino, M. Nikl, J. Pejchal, T. Fukuda, *Opt. Mater.*, **26**, 539 (2004)
31. A. Novoselov, A. Yoshikawa, M. Nikl, N. Solovieva, J.-H. Lee, T. Fukuda, *Radiat. Meas.*, **38**, 481 (2004)
32. Y. Guyot, H. Canibano, C. Goutaudier, A. Novoselov, A. Yoshikawa, T. Fukuda, G. Boulon, *Opt. Mater.*, **27**, 1658 (2005)
33. Y. Guyot, H. Canibano, C. Goutaudier, A. Novoselov, A. Yoshikawa, T. Fukuda, G. Boulon, *Opt. Mater.*, **28**, 1 (2006)
34. A. Novoselov, Y. Kagamitani, T. Kasamoto, Y. Guyot, H. Ohta, H. Shibata, A. Yoshikawa, G. Boulon, T. Fukuda, *Mater. Res. Bull.*, **42**, 27 (2007)
35. D.I. Levinson, P.I. Antonov, *J. Cryst. Growth*, **50**, 320 (1980)
36. V.I. Chani, A. Yoshikawa, Y. Kuwano, K. Hasegawa, T. Fukuda, *J. Cryst. Growth*, **204**, 155 (1999)
37. I.A. Bondar, L.P. Mezentseva, *Prog. Cryst. Growth Charact.*, **16**, 81 (1988)
38. J.C. Swarts, T. Surek, B. Chalmers, *J. Electron. Mater.*, **4**, 255 (1975)
39. S. Matsumura, T. Fukuda, *J. Cryst. Growth*, **34**, 350 (1976)
40. A. Novoselov, H. Ogino, A. Yoshikawa, M. Nikl, J. Pejchal, A. Beitlerova, T. Fukuda, *Opt. Mater.*, in press

# 7 Isothermal Flux Evaporation Diameter Control

Valery I. Chani and Kheirreddine Lebbou

**Abstract.** Diameter self-control is introduced, as observed experimentally during  $\text{Bi}_4\text{Ge}_3\text{O}_{12}$  fiber crystal growth. In accordance with the phase diagram of the  $\text{Bi}_2\text{O}_3$ – $\text{GeO}_2$  system, diameter control was managed by compensating for solidification with the evaporation of volatile  $\text{Bi}_2\text{O}_3$  self-flux, which was added to the crucible in excess. The outer diameter of the capillary channel was either 310 or 650  $\mu\text{m}$ . Crystals up to 400 mm in length and with diameters ranging from 50 to 300  $\mu\text{m}$  were produced at pulling-down rates of 0.04–1.00 mm/min. The melt composition and the pulling-down rate were the only two parameters that determined the fiber diameter: it was generally independent of variations in the power supplied to the crucible. The diameter of the crystal was therefore determined by the rate of  $\text{Bi}_2\text{O}_3$  evaporation. As a result, uniformly ( $\pm 10\%$ ) shaped fibers were produced without the need for process automation.

## 7.1 Introduction

As discussed in Chap. 4, the application of weight sensors to control the diameters of crystals grown using the  $\mu$ -PD method (as practiced in Czochralski (CZ) growth systems) has not yet been achieved. Some studies where the weight of the crystal is monitored have been reported [1, 2], but such measurements have not been used to control the crystal diameter during  $\mu$ -PD growth yet.

On the other hand, uniformly shaped fibers can be produced using existing equipment. This can be achieved by manipulating the physical and chemical properties of the materials involved in the growth process appropriately. In particular, the evaporation of volatile constituents of the target crystal can be used to control the shape of the fiber. Prototype procedures for conventional flux growth where saturation of the melt is supported by the continuous evaporation of the flux are well known [3, 4]. This process is sometimes called the isothermal flux evaporation [5–9] technique. The evaporation rate can be controlled by manipulating the dimensions of the aperture of the lid and/or enforced air flow produced by the vent [4], the surface area of the melt/atmosphere interface (Fig. 4.1), and the temperature.

This section demonstrates how two originally independent processes of mass transfer (solidification of the fiber and evaporation of a volatile ingredient) can compensate each other. As a result, the stationary growth of uni-

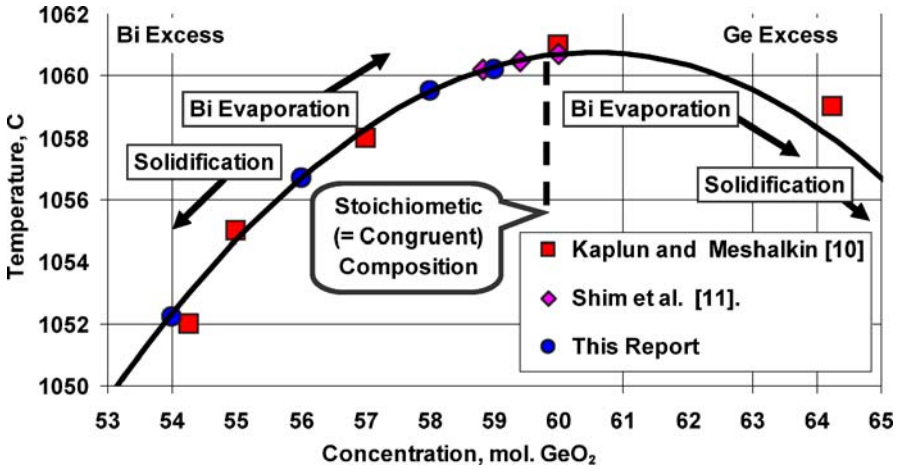


Fig. 7.1. Phase diagram of  $\text{Bi}_2\text{O}_3\text{-GeO}_2$  system [10] and melt compositions tested by BGO growth [11,14] (Table 7.1)

formly shaped (constant diameter) fiber crystals can be achieved.  $\text{Bi}_4\text{Ge}_3\text{O}_{12}$  (BGO) crystal is one such material that combines both congruent melting (Fig. 7.1) [10] and a relatively high rate of evaporation of one of its constituents, namely  $\text{Bi}_2\text{O}_3$  [11]. BGO crystals have great potential as scintillating material, and high-quality BGO bulk crystals are grown by industrial CZ technique, especially when some special modifications are applied to the method [12,13].

## 7.2 Crucibles

Conventional resistive micro-pulling-down ( $\mu$ -PD) equipment similar to that described elsewhere (see [15–19]) was applied to produce the fibers. Pt crucibles similar to those shown in Fig. 7.2 were made, containing capillaries with outer diameters of about 310 or 650  $\mu\text{m}$ . The shape and dimensions of an actual capillary can be seen in Fig. 7.3. The boat-like container section of the crucible was produced with a constant horizontal cross-section to keep the area of the melt/air interface constant independent of the melt level. This kept the rate of evaporation of  $\text{Bi}_2\text{O}_3$  constant during the entire growth run.

Crucibles similar to that shown in Fig. 7.2 and used in resistively heated  $\mu$ -PD systems are not available commercially. Most of them are made manually. Therefore the dimensions and proportions of the crucibles vary significantly even when they are all produced by the same individual. However, the shape reproducibility of the crucibles is very important because it ultimately determines the vaporization rate of the volatile constituent during growth.

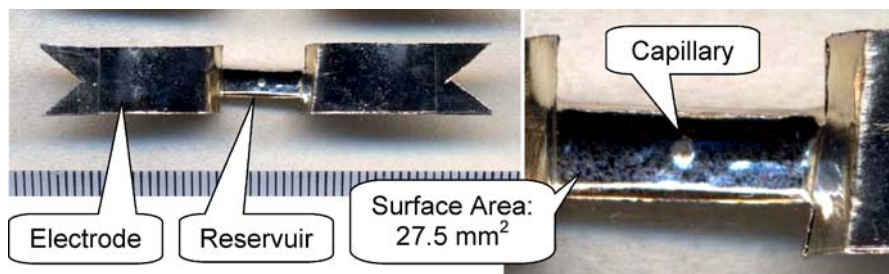


**Fig. 7.2.** Scanograph image (*left*, scale in mm) of the crucible as produced using flat office scanner and its magnified part (*right*) used for measurement of the melt surface area with “Image Tool” [20] software

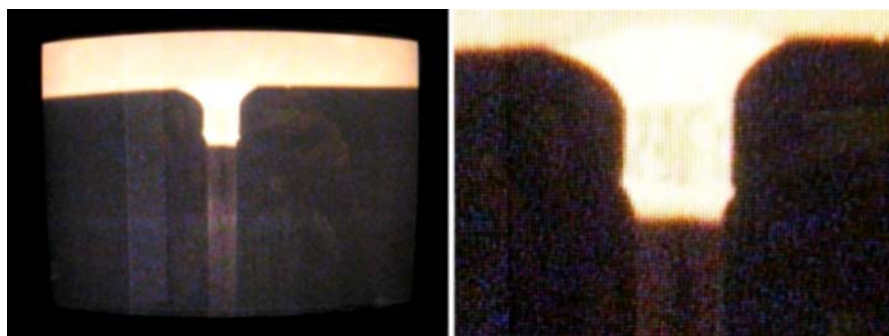


**Fig. 7.3.** View of the growth zone seen from the screen of the monitor coupled to CCD video camera at different magnifications. The capillary diameter is 650  $\mu\text{m}$

The melt/air surface area for the crucible shown in Fig. 7.2 was measured to be 27.5 mm<sup>2</sup> with an accuracy of better than 1%. These data were required to compare the shapes of the crucibles and to estimate the rate of evaporation.

Multiple use of a crucible was attempted in order to maintain reproducible conditions of evaporation and growth. Fortunately, repeated (5–10 times) use of a crucible was possible after removing the remaining melt with a hot mixture of HNO<sub>3</sub>O + H<sub>2</sub>O (1:2 volume ratio) at a temperature of 60–70 °C for several hours, and then finally the crucible was boiled in distilled water.

The main reason for using miniature ( $\varnothing$  310  $\mu\text{m}$ ) capillaries was to establish stable meniscus shape (Fig. 7.3) when thin fiber crystals are grown. However, an additional advantage of this miniaturization was the decrease in the surface area of the melt/air interface positioned in the vicinity of the capillary (Figs. 4.1 and 7.3). This minimized evaporation from the surface situated between the crystal and the capillary, allowing this evaporation to be ignored.

### 7.3 Starting Materials for $\text{Bi}_4\text{Ge}_3\text{O}_{12}$ (BGO) Growth

Both BGO single crystals produced by the CZ technique and corresponding mixtures (see Table 7.1) produced from  $\text{Bi}_2\text{O}_3$  and  $\text{GeO}_2$  oxides (of purity 99.999% and 99.998%, respectively) were used as starting materials for BGO growth. In contrast to the single-crystalline raw material, all of the mixtures contained an excess of volatile  $\text{Bi}_2\text{O}_3$ . The starting mixtures listed in Table 7.1 also correspond to the points shown on the left slope of the phase diagram in Fig. 7.1.

A largely typical growth process was used [15–19]. However, several steps were somewhat different from the conventional routine. Firstly, the stages of melting, homogenization, and seeding of the melt were shortened as much as possible to avoid uncontrollable evaporation of the volatile oxide. In addition, the melt was cooled to complete solidification immediately after the separation of the crystal from the meniscus during the final stage of growth when repeated seeding (see [14]) was not practiced. Both of these alterations were aimed at minimizing the evaporation of the constituents at the stages where the melt loss (in the BGO stoichiometric ratio) associated with actual growth did not occur. This made it possible to maintain the melt composition at a very constant level. Therefore, the raw materials were never melted during the preliminary heating of the hot zone of the system (the surrounding outer heater and the afterheater [15–18]).

The heating of the crucible and the subsequent melting of the raw starting materials were normally initiated just before seeding. The seed was first brought up to the tip of the crucible (Fig. 7.4, 1) until contact with the capillary and/or still solid melt inside it (Fig. 7.4, 2). Then the crucible was heated for 2–5 minutes in order to melt the raw materials (Fig. 7.4, 3). The top part of the seed was then remelted by lifting it upward (Fig. 7.4, 4). The purpose of this step was to “push” the just-melted and therefore poorly reacted and homogenized oxides inside the capillary into the bulk of the overheated melt and replace them with freshly melted single-crystalline BGO seed. The volume of the melted part of the seed was normally about twice that of the melt inside the capillary, as estimated by considering the diameters of the capillary and the seed. It was noted from a practical point of view that the

**Table 7.1.** Compositions of starting materials and capillary diameters used for BGO fiber crystal growth (CR = crystal)

Melt	$\text{Bi}_2\text{O}_3$ , mol%	$\text{GeO}_2$ , mol%	Starting material	Capillary diameter, $\mu\text{m}$
CR	40	60	Dispersed CZ crystal	310, 650
1	46	54	Mixture of powders	310, 650
2	44	56	Mixture of powders	310, 650
3	42	58	Mixture of powders	650
4	41	59	Mixture of powders	310

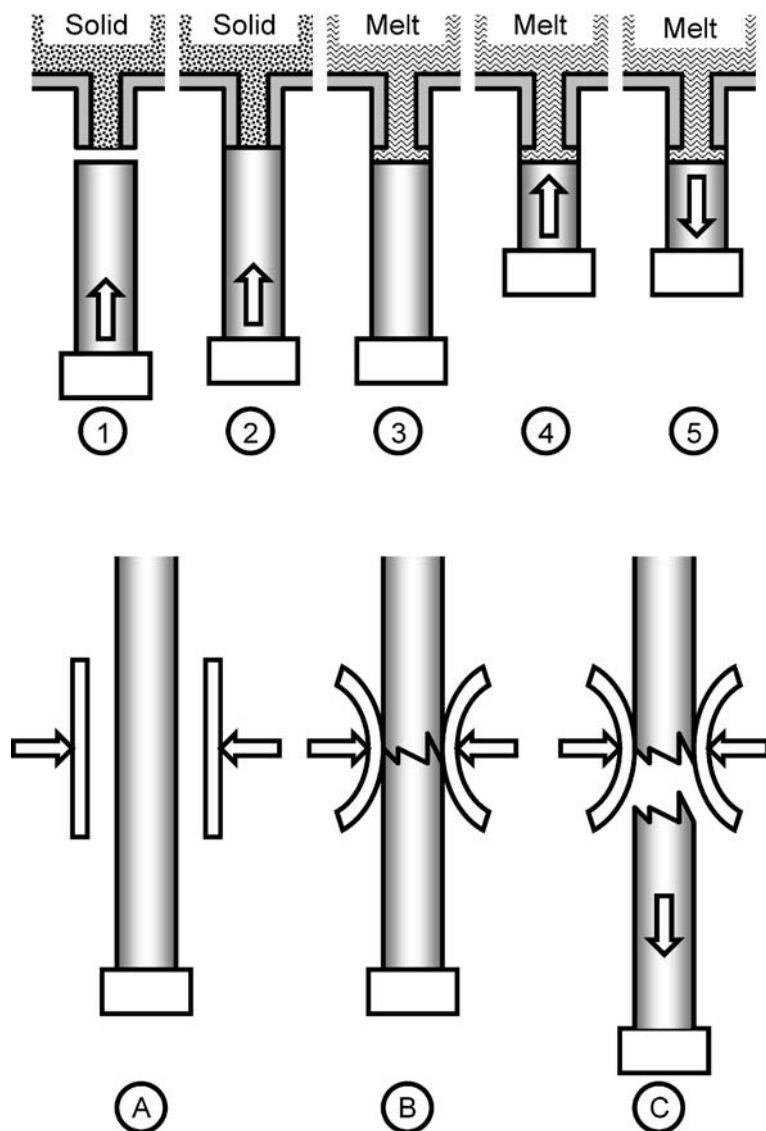


**Fig. 7.4.** Schematic of seeding (five stages 1–5, above) and controlled separation (fracture) of the as grown fiber from the seed (three stages A–C, below)

crystallization progressed much more smoothly when the just-melted single-crystalline seed was used as the starting material during the initial growth stage. Growth was then started by continuously increasing the pulling-down rate and adjusting the crucible temperature (Fig. 7.4, 5). The initial procedure was usually performed for 15–30 min to avoid any significant change in the melt composition.

The total time of these growth processes ranged from 5 to 70 hours, depending on the pulling-down rate applied (See Table 7.2 for reference). As a rule, no growth parameters were modified throughout the entire process. The dimensions of the growth zone, including the meniscus height and the fiber diameter, were measured directly from the screen of the monitor (Fig. 7.3) during the entire pulling process. The scale corresponding to maximal magnification of the image was preliminary determined using a length standard. The maximum fiber length was 400 mm; this parameter was limited by the length of the pulling mechanism and the length of the seed. Self-separation of the as-grown crystals from the melt occurred in processes where the height of the meniscus was unstable (Table 7.2).

The procedure used to remove the fiber after growth is not usually discussed when fibers with conventional diameters (0.5–1.0 mm) or bulk crystals (see Fig. 4.15) are produced with the  $\mu$ -PD technique. However, a new problem [14] was encountered when the process described above was used, especially when the fiber diameter ranged from 50 to 200  $\mu\text{m}$  (Table 7.2). The high flexibilities of the crystals resulting from their small diameters resulted in their uncontrollable fracture, due to the action of bending forces originating from vibrations and gravity. To localize this crack formation, simple accessories were designed that permitted the preliminary separation of the as grown fiber from the seed or the seed-attached part of the crystal. Schematics showing how these accessories were applied are also illustrated in Fig. 7.4A–C.

**Table 7.2.** Growth conditions and dimensions of BGO fibers

Fiber	Capillary, $\mu\text{m}$ ( $\pm 10 \mu\text{m}$ )	Pulling, mm/min	Meniscus/height, $\mu\text{m}$ ( $\pm 10 \mu\text{m}$ )	Diameter, $\mu\text{m}$ ( $\pm 10 \mu\text{m}$ )	Length, mm
1-1*	310	0.06	80	240, stable	214
1-2	310	0.20	80	135, stable	271
1-4	310	0.60	80	95, stable	267
1-5	310	0.28	80	130, stable	273
1-8	310	0.20	80	105, stable	270
1-7	650	0.70	125–265	205–595	145, separated
2-1	650	0.24	–	250–360	28, separated
2-2	650	0.07	125–170	480–510	215, separated
2-3	650	0.20	140–170	350–405	89, separated
2-4	310	0.20	125	125, stable	266
2-5	310	0.24	105	80–105	263
4-2	310	0.04	120	95–280	175
4-3	310	0.04	90	290, stable	150

\* The first number represents the melt composition according to Table 7.1

## 7.4 BGO Growth from Stoichiometric Melt

The growth of BGO fiber crystals from stoichiometric melt [11] using an uncovered crucible in air is a fundamentally unstable process. Evaporation of  $\text{Bi}_2\text{O}_3$  occurs and is easily detected through visual observations of the surfaces of the parts forming the  $\mu$ -PD system. It is difficult to avoid or considerably decrease the evaporation by attempting to modify the set-up or the temperature parameters (gradients) that act in the vicinity of the crucible and the solid/liquid interface. As a result, only a short section (a few centimeters in length) of each crystal is of acceptable optical quality.

The growth of BGO fibers from a melt formed from a stoichiometric mixture of  $\text{Bi}_2\text{O}_3$  and  $\text{GeO}_2$  oxides resulted in the continuous evaporation of  $\text{Bi}_2\text{O}_3$  along with the corresponding enrichment of the melt with  $\text{GeO}_2$  oxide, which played the role of the flux. The process therefore corresponded to the flux growth of a congruently melting compound (the right slope of the phase diagram shown in Fig. 7.1) because of the partial evaporation of  $\text{Bi}_2\text{O}_3$  [11]. As the melt composition was self-modified, a continuous change in the solidification temperature (Fig. 7.1) was observed with a corresponding displacement of the solid/liquid interface in the downward direction (see Fig. 4.4). The position of the crucible and the power applied were fixed. Therefore, the resulting increase in the meniscus height (together with the effects of surface tension) modified the shape of the meniscus, especially the region that contacted the melt/crystal interface, ultimately decreasing the fiber diameter.

It is generally necessary to continuously adjust the temperature of the crucible to keep the diameter constant. Period measurements of the fiber diameter are possible via images similar to those shown in Fig. 7.3. Such measurements allow the operator to modify (decrease) the melt temperature just enough to keep the diameter constant. However, this still means that the diameter is controlled manually. Examples of such temperature corrections can be seen in Fig. 7.5. While the rate of temperature decrease can be estimated from the phase diagram (the right slope of the diagram in Fig. 7.1), the melt composition, the melt/air surface area (Fig. 7.2), the temperature of the melt surface, etc., there are too many parameters to be able to perform an accurate control of the whole system.

It is important to note that the process of enrichment of the melt with  $\text{GeO}_2$  oxide during BGO growth is irreversible. Once the melt becomes Bi-poor, it is not possible to establish constant melt properties (the solidification temperature and the subsequent shape of the meniscus). Two events, the BGO growth (I) and the evaporation of  $\text{Bi}_2\text{O}_3$  (II), modify the system in the same way: they further enrich the melt with  $\text{GeO}_2$ . These modifications are illustrated by the two parallel arrows pointing in the same direction on the right slope of the phase diagram (Fig. 7.1). Thus, for all  $\text{GeO}_2$ -rich systems, evaporation of the bismuth oxide only increases the dissolution of the melt and the transformation from a melt to a flux system.

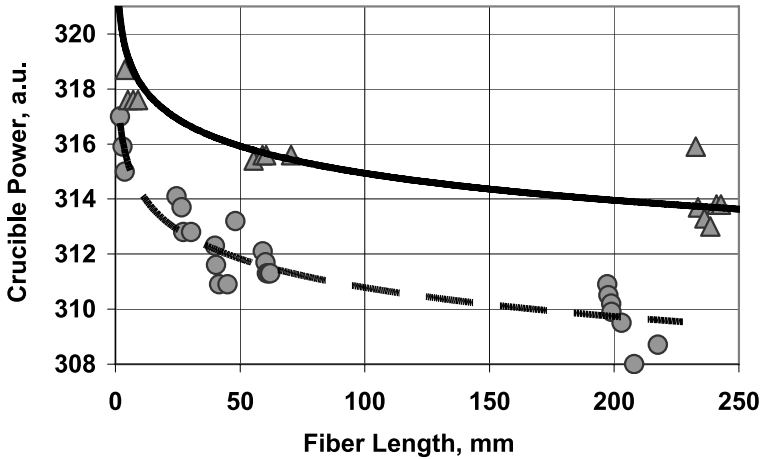


Fig. 7.5. Typical temperature adjustment necessary to maintain stable diameter of BGO fiber crystal grown from stoichiometric BGO melt

## 7.5 BGO Flux Growth from $\text{Bi}_2\text{O}_3$ -Enriched Melts

The evolution of the melt produced with an excess of  $\text{Bi}_2\text{O}_3$  (Table 7.1) can be expected to differ significantly from that described in the previous section. Once the system (the melt) has been described by the points positioned on the left side of the diagram (Fig. 7.1), the melt composition can be stabilized by two processes acting in opposite directions. Melt removal due to the crystal growth (solidification at the stoichiometric ratio of BGO) will result in the enrichment of the liquid phase with  $\text{Bi}_2\text{O}_3$ . On the other hand, evaporation of the  $\text{Bi}_2\text{O}_3$  will enrich the melt with  $\text{GeO}_2$ . The directions of these melt transformations (which follow from two independent mass transfer phenomena) are opposite, as illustrated by the two arrows positioned on the left slope of the phase diagram (Fig. 7.1). Thus, there may be conditions that allow these two processes to compensate each other, making the melt composition and the meniscus shape stable.

The evaporation of any particular material ( $\text{Bi}_2\text{O}_3$  in our case) is a function of many parameters, but it is typically constant for any particular melt composition when the area of the melt/air interface and temperature of the interface are constant. These conditions can easily be established when the crucible is produced with a constant cross-section (see Sect. 7.2) and the power supplied to the crucible is fixed. It is also not a problem to produce a melt of any composition where, in the optimal case, the melt transformations resulting from both processes (solidification and evaporation) will compensate each other.

The dimensions of some fibers produced via the controlled evaporation of  $\text{Bi}_2\text{O}_3$  are listed in Table 7.2. The crystals produced from crucibles containing capillaries  $310\ \mu\text{m}$  in diameter were very uniform in shape, according to

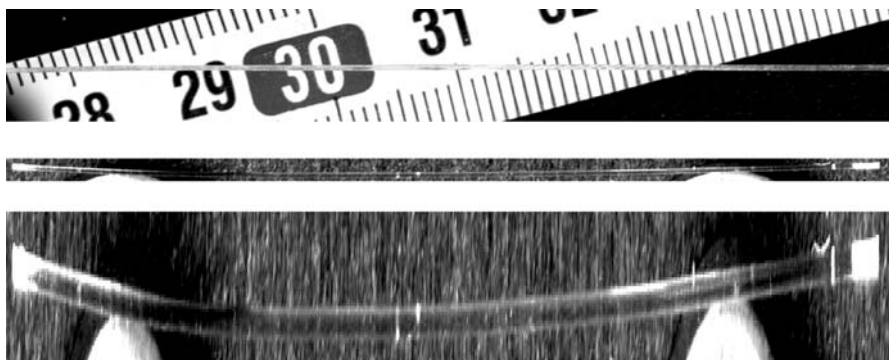


**Fig. 7.6.** View of BGO fibers: photograph of  $\varnothing 300\ \mu\text{m}$  fiber (*top*), scanograph image of the 1–1 fiber of  $\varnothing 240\ \mu\text{m}$  (Table 7.2) as produced using office flat scanner (*middle*), and same digital image expanded in vertical direction to demonstrate diameter uniformity (*below*)

measurements taken directly from the screen of the monitor (Fig. 7.3) with an accuracy of about  $\pm 10\ \mu\text{m}$ . These data were compared with measurements taken from photo- and scanograph images (Fig. 7.6) taken with a flat-bed office scanner to a similar accuracy. Both sets of data correlated well within the measurement error. It was also observed that the deviations of the diameters of the fibers produced from melts intentionally enriched with  $\text{Bi}_2\text{O}_3$  were within the accuracy of the measurement. This never happened when stoichiometric raw materials were used (see Sect. 7.4).

## 7.6 Evaporation-Induced Diameter Control

In the case of conventional  $\mu$ -PD fiber crystal growth from a congruently melting composition, the diameter of the crystal is controlled by simply adjusting the power supplied to the crucible. Decreasing the power (i.e., the melt temperature) results in a decrease in the height of the molten zone (Table 7.2) which causes the solid/liquid interface to move closer to the bottom of the crucible capillary (Figs. 1.2 and 7.3). This ultimately increases the diameter at a constant pulling-down rate. This strategy is very similar to that used in the Czochralski process.

However, in the process managed through the evaporation of one of the constituents ( $\text{Bi}_2\text{O}_3$ ), the diameter is controlled exclusively by the rate of solidification, which is predetermined by the rate of evaporation (Fig. 7.1). This is one of the disadvantages of evaporation-induced diameter control, because it is practically impossible to adjust the  $\mu$ -PD system to grow fibers with different diameters when the pulling rate is fixed.

In the case of BGO crystal growth, the evaporation is intense (experimental observation), and it is supposedly constant due to the constant tem-

perature used and the dimensions of the melt/air interface. Thus, the rate of solidification (the mass growth rate,  $S$ , mg/min) is also constant (experimental observation, Fig. 7.7):

$$S = \frac{\Delta m}{\Delta t} = \frac{\pi d^2 \Delta L}{4 \Delta t} \rho = \frac{\pi d^2 f}{4} \rho = \text{const.}, \tag{7.1}$$

where  $m$  is the BGO crystal weight,  $d$  is the crystal diameter, and  $\Delta L$  is the length of the solid produced at time  $\Delta t$ .  $\rho$  is the density of BGO ( $7.13 \text{ g/cm}^3$  [22]). The parameters  $d$  and  $f$  are available from Table 7.2. This equation implies that the change in the melt composition ( $\Delta m$ ) due to BGO growth can be found experimentally.

Figure 7.7 demonstrates the correlation between the pulling rate  $f$  and the the diameter  $d$  resulting from (7.1). The solidification rate is independent of the pulling rate when the melt temperature is constant (i.e., there is a linear dependence). Thus, the fiber diameter only depends on the pulling-down rate. Moreover, the solidification rate depends upon the area of the melt/air interface (Fig. 7.2) and the temperature: both affect the evaporation rate [14].

The principles explained qualitatively with the aid of the arrows in Fig. 7.1 can be represented quantitatively as follows. Consider an initially  $\text{Bi}_2\text{O}_3$ -rich melt ( $\text{BGO}:\text{Bi}_2\text{O}_3 = m:n$ , wt ratio). Evaporation ( $\Delta n$ ) without growth changes the melt composition per time  $\Delta t$  in the following way:

$$\text{BGO}:\text{Bi}_2\text{O}_3 = m : (n - \Delta n). \tag{7.2}$$

When both evaporation and growth occur, the melt changes as follows:

$$\text{BGO}:\text{Bi}_2\text{O}_3 = (m - \Delta m) : (n - \Delta n). \tag{7.3}$$

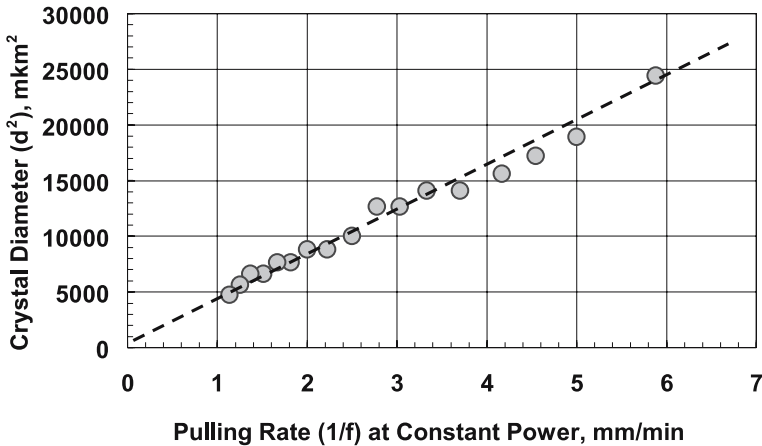


**Fig. 7.7.** BGO fiber crystal diameter,  $d(d^2)$  vs. pulling-down rate  $f(1/f)$ .  $S = \text{const.}$  for whole range of pulling-down rates (linear dependence) according to (7.1) for the melt No. 1 (Table 7.1)

Stationary conditions mean that the melt composition is constant over the entire process, which gives us the final mass balance equation:

$$m : n = (m - \Delta m) : (n - \Delta n). \quad (7.4)$$

$m$  and  $n$  can be calculated from Table 7.1, and  $\Delta m$  can be found experimentally from (7.1). Thus,

$$\Delta n = n \left[ 1 - \frac{(m - \Delta m)}{m} \right]. \quad (7.5)$$

$S$  was determined as 0.024 mg/min ( $\Delta m = 0.024$  mg per  $\Delta t = 1$  min) experimentally [14] using (7.1) and Fig. 7.7 for melt no. 1 ( $\text{Bi}_2\text{O}_3:\text{GeO}_2 = 46:54$ , mol% according Table 7.1). The melt level was 2.0 mm according to the geometry of the crucible. Hence, the melt volume was  $55 \text{ mm}^3$  and the total mass of the melt was 392 mg ( $m = 325$  mg, and  $n = 67$  mg). The evaporation rate, calculated from Eqs. (7.1)–(7.5), was  $\Delta n = 0.0049$  mg/min or 7.1 mg/day, which appears adequate.

Direct measurement of the evaporation rate is difficult because of the deposition and partial remelting of vaporized  $\text{Bi}_2\text{O}_3$  on the crucible electrodes (Figs. 1.2, 7.2, and 7.3). Therefore, it is not easy to determine the  $\text{Bi}_2\text{O}_3$  loss directly by weighing the crucibles before and after growth.

It was also not possible to perform evaporation-supported diameter control for 650- $\mu\text{m}$  diameter capillaries [14]. The process was unstable; self-separation of the fibers from the meniscus frequently occurs (Table 7.2). Replacing the 310- $\mu\text{m}$  diameter capillary with a 650- $\mu\text{m}$  capillary increased the dimensions of the meniscus considerably. Therefore, the meniscus was unstable when the capillary/crystal diameter ratio was extremely high. Increasing the fiber diameter was also problematic, because it was difficult to increase the dimensions of the crucible reservoir and therefore the evaporation rate: the space available inside the outer heater of the apparatus was limited. Therefore, it was not possible to replace the crucible with one that had a cross-section that was four times as large (Fig. 7.2).

There are no fundamental restrictions on the growth of relatively thick fibers (over 300  $\mu\text{m}$  in thickness) when the process is self-controlled by evaporation. Thus, a relatively low evaporation rate results in a low solidification rate according to Eqs. (7.1) and (7.4). This corresponds to a small fiber diameter (50–200  $\mu\text{m}$ ). The intensity of  $\text{Bi}_2\text{O}_3$  evaporation was suited to fiber growth using a 310- $\mu\text{m}$  diameter capillary, but it was not sufficient to be able to use a 650- $\mu\text{m}$  diameter capillary [14]. Considering the melt composition range given in Table 7.1 and Fig. 7.1, decreasing the pulling-down rate is the only approach that can be employed to grow large-diameter fibers using a 650- $\mu\text{m}$  capillary.

## 7.7 Summary

An evaporation-induced diameter control scheme applicable to fiber crystal growth using a  $\mu$ -PD system was introduced. Conditions resulting in the self-equilibration of two independent mass transfer processes (evaporation of a volatile constituent and the solidification of the target crystal) were analyzed. As a result, the growth of uniformly ( $\pm 10\%$ ) shaped  $\text{Bi}_4\text{Ge}_3\text{O}_{12}$  fiber crystals 50–300  $\mu\text{m}$  in diameter was demonstrated. Approximate rules associated with this process are listed below:

- (1) The rate of stationary solidification (the amount of material solidified per unit of time, g/min) depends on the melt composition and the rate of evaporation of the volatile constituent
- (2) The rate of solidification is generally independent of the melt temperature (when the dependence of the evaporation on the temperature is negligible)
- (3) The melt temperature affects the position of the crystal/melt phase interface, but not the crystal diameter
- (4) The fiber diameter can be set by adjusting the pulling-down rate appropriately.

## References

1. K. Lebbou, D. Perrodin, V.I. Chani, O. Aloui, A. Brenier, J.M. Fourmigue, O. Tillement, J. Didierjean, F. Balembois, P. Gorges, *J. Am. Ceram. Soc.*, **89**(1), 75 (2006)
2. B. Hautefeuille, K. Lebbou, C. Dujardin, J.M. Fourmigue, L. Grosvalet, O. Tillement, C. Pédrini, *J. Cryst. Growth*, **289**, 172 (2006).
3. Y. Sumiyoshi, M. Ushino, *J. Am. Ceram. Soc.*, **73**(10), 3015 (1990)
4. K. Watanabe, *Cryst. Res. Technol.*, **34**(1), 47 (1999)
5. E.A. Goodilin, E.A. Pomerantseva, V.V. Krivetsky, D.M. Itkis, J. Hester, Yu.D. Tretyakov, *J. Mater. Chem.*, **15**, 1614 (2005)
6. C.M. Jones II, J., *Am. Ceram. Soc.*, **54**(7), 347 (1971)
7. W.H. Grodkiewicz, D.J. Nitti, *J. Am. Ceram. Soc.*, **49**(10), 576 (1966)
8. M. Kajivara, *J. Mater. Sci.*, **23**, 3600 (1988)
9. S. Armaki, R. Roy, *J. Mater. Sci.*, **3**, 643 (1968)
10. A.B. Kaplun, A.B. Meshalkin, *J. Cryst. Growth*, **167**, 171 (1996)
11. J.B. Shim, J.H. Lee, A. Yoshikawa, M. Nikl, D.H. Yoon, T. Fukuda, *J. Cryst. Growth*, **243**, 157 (2002)
12. Yu.A. Borovlev, N.V. Ivannikova, V.N. Shlegel, Ya.V. Vasiliev, V.A. Gusev, *J. Cryst. Growth*, **229**, 305 (2001)
13. M.G. Vasiliev, O.N. Budenkova, V.S. Yuferev, V.V. Kalaev, V.N. Shlegel, N.V. Ivannikova, Ya.V. Vasiliev, V.M. Mamedov, *J. Cryst. Growth*, **275**, 745 (2005)
14. V.I. Chani, K. Lebbou, B. Hautefeuille, O. Tillement, J.-M. Fourmigue, *Cryst. Res. Technol.*, **41**(10), 972 (2006)
15. T. Fukuda, P. Rudolph, S. Uda, (eds.), *Fiber Crystal Growth from the Melt* (Springer, Berlin, 2004)

16. D.H. Yoon, *Opto-Electron. Rev.*, **12**(2), 199 (2004)
17. D.H. Yoon, T. Fukuda, *J. Cryst. Growth*, **144**, 201 (1994)
18. Y.M. Yu, V.I. Chani, K. Shimamura, T. Fukuda, *J. Cryst. Growth*, **171**, 463 (1997)
19. V.I. Chani, K. Shimamura, T. Fukuda, *Cryst. Res. Technol.*, **34**, 519 (1999)
20. UTHSCSA, *Image Tool* (University of Texas Health Science Center, San Antonio, TX)
21. V.I. Chani, A. Yoshikawa, Y. Kuwano, K. Inaba, K. Omote, T. Fukuda, *Mater. Res. Bull.*, **35**(10), 1615 (2000)
22. R. Nutt, *Mol. Imag. Biol.*, **4**, 11 (2002)

# 8 Eutectic Fibers with Self-Organized Structures

Dorota A. Pawlak

**Abstract.** The growth of self-organized structures by the micro-pulling-down method is described. This type of growth is based on the directional solidification of eutectics. Potential applications of these structures in modern photonics, in fields such as photonic crystals and metamaterials, are discussed.

## 8.1 Introduction

In recent years, two different types of materials have been undergoing development in the area of photonics: photonic bandgap materials [1–4] (photonic crystals) and metamaterials [5–12]. In photonic crystals, the wavelength of the light is comparable to the periodicity of the structure, resulting in a photonic bandgap effect. In metamaterials, on the other hand, the wavelength is much bigger than the structure of the matter involved, so only effective properties (such as the effective permittivity and permeability) are important; diffraction does not take place in metamaterials. There are many sophisticated methods for obtaining these two types of materials, and one of these is *self-organization*.

## 8.2 Eutectics and Their Microstructures

One very promising approach to the growth of self-organized micro- and nanostructures is based on the directional solidification of eutectics. A eutectic is characterized by the formation of two unmixable crystals from a completely mixable melt. Metal–metal eutectics have been studied for many years, due to their excellent mechanical properties. Recently oxide–oxide eutectics have also been studied, due to their excellent flexural strength and creep resistance at high temperatures [13–17]. Oxide–oxide eutectics have also recently been studied as potential optical materials [18,19] and have been identified as materials that could act as photonic crystals [20,21], though this is yet to be proven. Directionally solidified eutectics (DSE) could be used to manipulate light in different ways.

The eutectic reaction is the same for all binary eutectics. It represents the coupled growth of two phases from a binary liquid [22]. During cooperative

growth, the alpha phase rejects atoms of B and the beta phase rejects atoms of A [23]. As Hecht et al. [22] state: “Coupled growth leads to a periodic concentration profile in the liquid close to the interface that decays in the direction perpendicular to the interface much faster than in the single phases solidification”. Eutectics can form different micro- and nanostructures depending on different factors, such as the entropy of melting of both phases. Such phases have been classified by Hunt and Jackson as: (i) nonfaceted–nonfaceted, when both phases have low entropies of melting, yielding a regular structure; (ii) nonfaceted–faceted, where one phase has a low and the other a high entropy of melting, resulting in irregular or complex microstructures; and (iii) faceted–faceted, where both phases have high entropies of melting, which produces independent crystals [24]. Eutectic microstructures can exhibit many geometrical forms. They can be regular lamellar, regular rodlike, irregular, complex regular, quasi-regular, broken lamellar, spiral, and globular.

### 8.3 Self-Organized Structures Grown by the $\mu$ -PD Method

There are many methods for growing eutectics, such as laser-heated pedestal growth (LHPG), the edge-defined film-fed growth (EFG) technique, the Bridgman method, and the micro-pulling down ( $\mu$ -PD) method. The  $\mu$ -PD method [25] was developed for the growth of single-crystal fibers, but it is also perfectly suited to the directional solidification of eutectics [14, 15]. In this section, the application of the  $\mu$ -PD method to the growth of self-organized microstructures is overviewed.

A fully aligned eutectic structure can only be obtained when the crystal/melt interface is flat. The other conditions required are: a steep temperature gradient, a slow growth rate, and the absence of convection [23, 26]. All of these conditions can be realized in the  $\mu$ -PD system. The only issue is the Marangoni convection that occurs at the meniscus under the nozzle (capillary) when the meniscus is high. However, the Marangoni convection in the meniscus depends strongly on the meniscus height; it does not exist for a low meniscus [27].

One of the most interesting geometries observed in eutectics is rodlike structure. Taking into account only minimum interface principles, the rodlike pattern is expected to appear when the volume fraction of one of the phases is  $\leq 1/\pi$  [23, 28]. The self-organized rodlike microstructure of the  $\text{Tb}_3\text{Sc}_2\text{Al}_3\text{O}_{12}$ – $\text{TbScO}_3$ , (garnet–perovskite) eutectic grown by the  $\mu$ -PD method is illustrated in Fig. 8.1 [29].

The microrods of  $\text{TbScO}_3$  tend to pack hexagonally in the matrix of  $\text{Tb}_3\text{Sc}_2\text{Al}_3\text{O}_{12}$ . Terbium–scandium perovskite has a higher density ( $6.752 \text{ g/cm}^3$ ) [30] than the garnet phase ( $6.014 \text{ g/cm}^3$ ) [31]. Considering the respective densities, the perovskite phase should have a higher refractive index than the garnet phase. In the transmission images, the perovskite

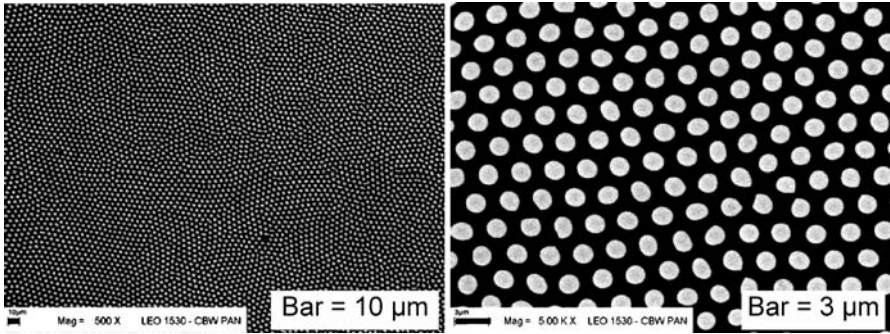


**Fig. 8.1.** The self-organized rodlike microstructure as seen on cross-section of  $\text{Tb}_3\text{Sc}_2\text{Al}_3\text{O}_{12}\text{-TbScO}_3$  eutectic (*left*: magnification  $\times 500$ , *right*: magnification  $\times 5000$ ). Reprinted with permission from [29]. Copyright (2006) American Chemical Society

phase appears as bright spots. This can be explained as being due to the light-guiding effects of rods of higher refractive index material [20]. The difference between the refractive indices of these materials is needed not only for the light-guiding effect but also for the photonic bandgap effect. The terbium–scandium–aluminum garnet has additional value, since it exhibits a high Faraday effect, and can therefore be used in the optical isolator of a blue light laser [31–34].

Investigating the orientations of both the microrods and the matrix by X-ray diffraction, one finds that the garnet matrix grows in just one crystallographic direction of the regular system,  $\langle 111 \rangle$ , while the pattern-forming phase, the perovskite phase, does not grow in any particular direction if the whole eutectic rod is considered [29]. This may be due to inhomogeneous growth conditions during the formation of the eutectic grains. Nevertheless, when the adjacent microrods were investigated by the electron backscattering diffraction (EBSD), it was found that they grow in the same crystallographic direction [35].

It is also possible to dope both phases with active elements in order to obtain emission (this is actually necessary for some potential metamaterial applications) [36]. In particular, doping with praseodymium has been already tested [29,35]. It was found that the praseodymium cations were distributed in both phases (garnet and perovskite). The concentration of the dopant tended to be higher in the perovskite phase, as expected. This is due to the different structures of both phases. The dodecahedral sites of the garnet and the larger icosahedral sites of the perovskite are the two positions most preferable to the lanthanide ions. Hence, large lanthanide ions like praseodymium will most likely replace ions in larger, 12-coordinated cation sites in perovskite. This approach permits the partially selective doping of eutectics.

The size of the eutectic microstructure can be controlled by the pulling rate to a reasonable degree. Higher pulling rates yield smaller structures.

This size control is important for potential applications of such materials. Eutectic microstructures of  $\text{Tb}_3\text{Sc}_2\text{Al}_3\text{O}_{12}$ - $\text{TbScO}_3$  grown at five different pulling rates have been studied. The mean diameter of the microrod changes as follows: 3.3(0.05), 2.2(0.04), 1.8(0.07), 1.2(0.07), 0.7(0.08)  $\mu\text{m}$ , respectively, for pulling rates of 0.15, 0.3, 0.4, 1.0 and 4.0 mm/min [29]. The change in the microstructure with pulling rate is shown in Fig. 8.2.

For most eutectics the following relation is valid:

$$\lambda\nu^2 = \text{const.}, \quad (8.1)$$

where  $\nu$  is the growth rate, and  $\lambda$  is the lamellar spacing [23, 24].

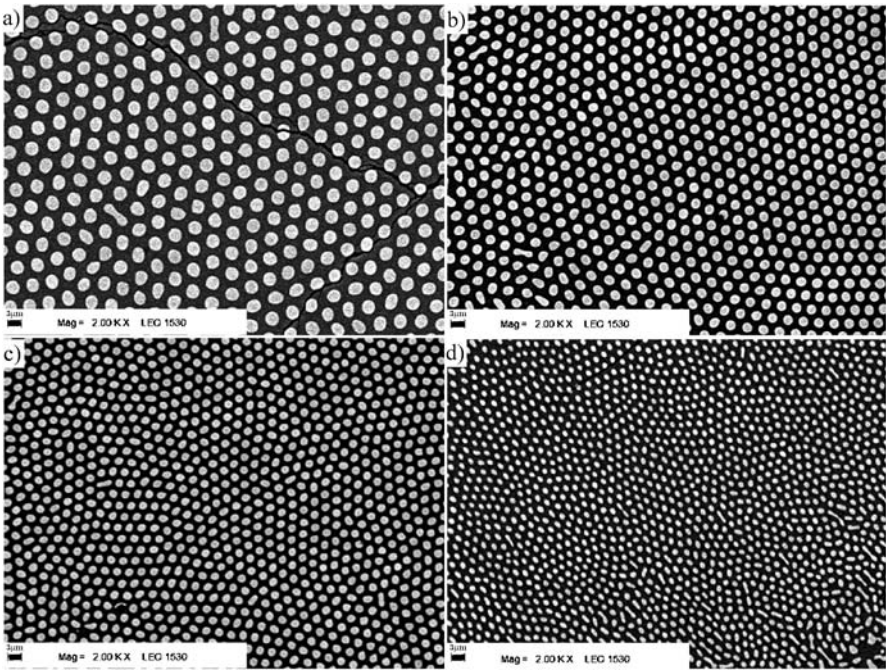
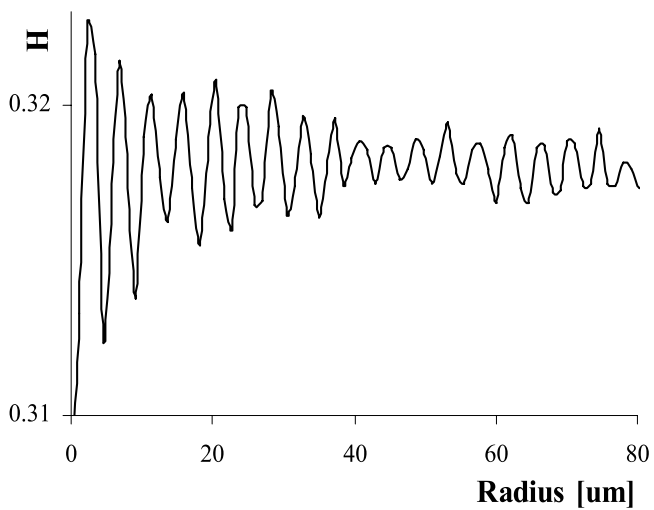
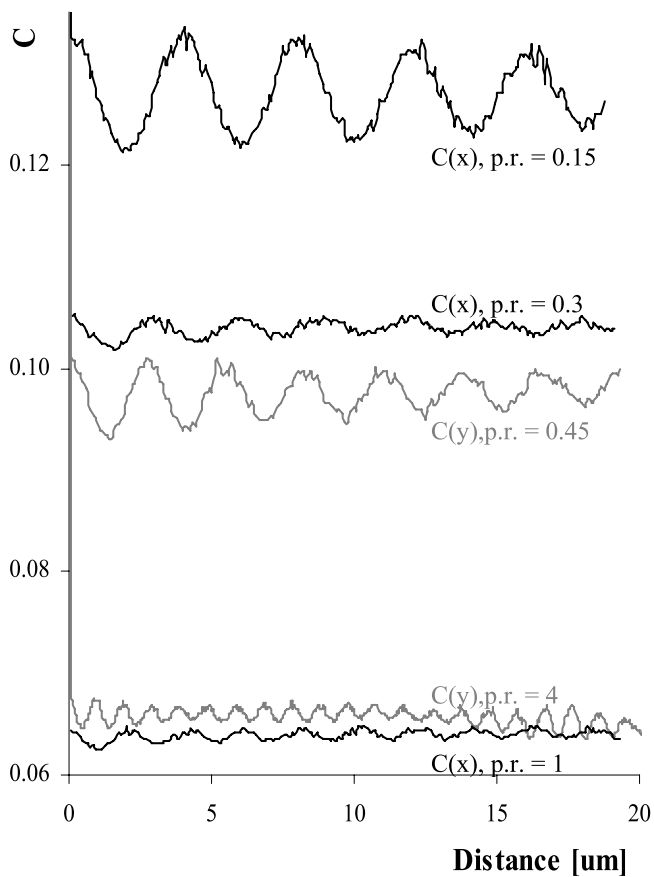


**Fig. 8.2.** Dimensions of the microstructure of  $\text{Tb}_3\text{Sc}_2\text{Al}_3\text{O}_{12}$ - $\text{TbScO}_3$  binary eutectic produced at different pulling rates: **a** 0.15 mm/min, **b** 0.3 mm/min, **c** 0.45 mm/min, **d** 1 mm/min. Reprinted with permission from [29]. Copyright (2006) American Chemical Society. One bar corresponds to 3  $\mu\text{m}$

**Fig. 8.3.** The covariance function along horizontal,  $C(x)$ , and vertical,  $C(y)$ , directions for the eutectics grown with pulling rates of 0.15, 0.3, 0.45, 1.0 and 4.0 mm/min (*top*) and **b**) an example of radial distribution function for a sample grown with 0.15 mm/min pulling rate (*bottom*). Reprinted with permission from [29]. Copyright (2006) American Chemical Society



This is why different microstructure sizes can be obtained for different eutectics with the same pulling rate. The smallest average microrod diameter in a rodlike eutectic microstructure obtained by the micro-pulling-down method so far is 390 nm, for a  $\text{PrAlO}_3\text{-PrAl}_{11}\text{O}_{18}$  eutectic grown with a pulling rate of 5 mm/min (Pawlak et al., *PrAlO<sub>3</sub>-PrAl<sub>11</sub>O<sub>18</sub> eutectic - its microstructure and spectroscopic properties*, submitted to Cryst. Growth Des.). This eutectic has a density of  $3.1 \times 10^6$  microrods/mm<sup>2</sup>.

In the case of the  $\text{Tb}_3\text{Sc}_2\text{Al}_3\text{O}_{12}\text{-TbScO}_3$  eutectic, the local ordering of the microstructure is rather high, as shown by a linear covariance analysis [29]. Linear covariance analysis describes the probability of finding an object at some distance from a similar object. In Fig. 8.3a, the results from linear covariance analyses of eutectics grown with pulling-down rates of 0.15, 0.3, 0.45, 1.0 and 4.0 mm/min are shown. The results cover a range of 20  $\mu\text{m}$ . Some of them are presented along the horizontal direction,  $C(x)$ , and some are shown in the vertical direction,  $C(y)$ . The systematically repeating peaks in this function indicate that the structure shows strong periodicity at scales of  $\geq 20 \mu\text{m}$  [29]. The other measure of how the microrods are distributed is the radial distribution function (RDF) [37]. This is the probability  $H(r)$  of finding the particles at a specified radius,  $r$ . The RDF for one of the samples of a  $\text{Tb}_3\text{Sc}_2\text{Al}_3\text{O}_{12}\text{-TbScO}_3$  eutectic grown at a pulling rate of 0.15 mm/min is presented in Fig. 8.3b. The periodicity of this function over a range of 80  $\mu\text{m}$  indicates that the eutectic microstructure is periodic over the same distance.

Another example of a eutectic grown by the  $\mu$ -PD method for which rodlike microstructure has been observed is  $\text{PrAlO}_3\text{-PrAl}_{11}\text{O}_{18}$ . The microrods consisted of the  $\text{PrAlO}_3$  phase, and they were embedded in the  $\text{PrAl}_{11}\text{O}_{18}$  phase. The interesting feature of this eutectic is that, while the compound  $\text{PrAlO}_3$  has a few phase transitions, it seems that  $\text{PrAlO}_3$  loses its phase transitions when it is packed pseudo-hexagonally in the form of microrods inside the  $\text{PrAl}_{11}\text{O}_{18}$  phase matrix (Andrzejewski et al., to be published). In this eutectic, increasing the pulling rate improves the quality of the microstructure. In the case of the highest pulling rate applied (5 mm/min), the rods have a circular shape. However, the cross-sections of those produced at lower pulling rates are slightly triangular (Pawlak et al., *PrAlO<sub>3</sub>-PrAl<sub>11</sub>O<sub>18</sub> eutectic - its microstructure and spectroscopic properties*, submitted to Cryst Growth Des). Figure 8.4 shows longitudinal sections of these eutectics. Only short pieces of the microrods are seen in the SEM images. This is probably because the specimens were not cut exactly parallel to the growth axis.

Other microstructure geometries associated with eutectics grown by  $\mu$ -PD have been observed, for example, in the  $\text{PrAlO}_3\text{-Pr}_2\text{O}_3$  eutectic. This eutectic grows in a complex regular microstructure (Pawlak et al., *The PrAlO<sub>3</sub>-Pr<sub>2</sub>O<sub>3</sub> eutectic, its instability, microstructure and luminescent properties*, accepted to Chem Mater). This means that eutectic grains are produced where one of the phases forms a skeletal structure. The eutectic forms inside the skeletal

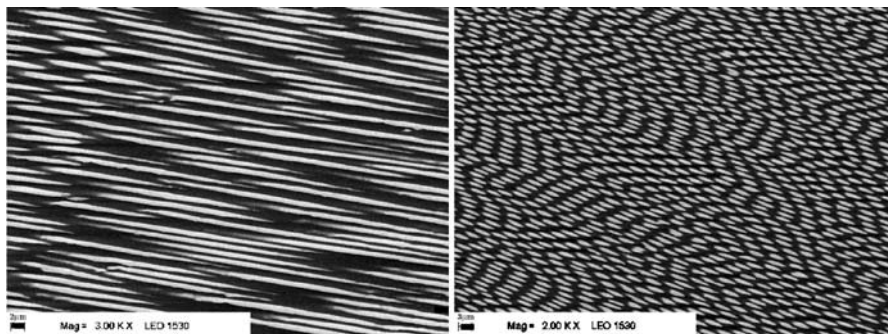


**Fig. 8.4.** The longitudinal cross-section of the microrods formed in  $\text{PrAlO}_3$ - $\text{PrAl}_{11}\text{O}_{18}$  eutectic [37]. Bars are  $2\ \mu\text{m}$  (left) and  $3\ \mu\text{m}$  (right)

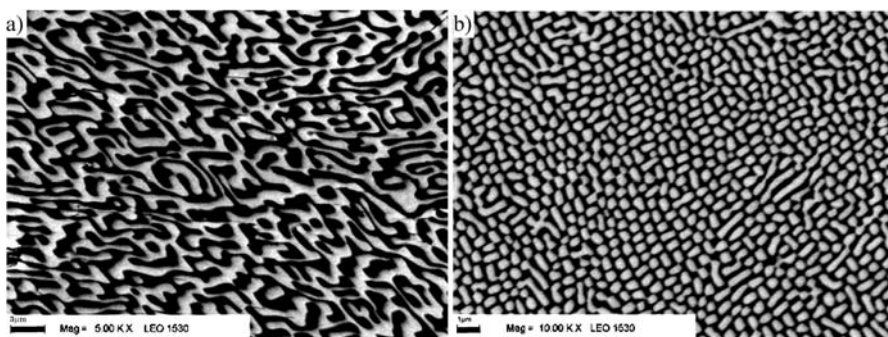


**Fig. 8.5.** The cross-section of two types of microstructures observed in  $\text{PrAlO}_3$ - $\text{Pr}_2\text{O}_3$  eutectic: percolated-like structure (left) and brick-like structure (right) [40]. Bars are  $3\ \mu\text{m}$  (left) and  $1\ \mu\text{m}$  (right)

structure. In the case of the  $\text{PrAlO}_3$ - $\text{Pr}_2\text{O}_3$  eutectic, two main types of microstructures were observed in the skeletal structure of  $\text{PrAlO}_3$  (the black color in the images). A kind of percolated structure is shown in Fig 8.5, left, and a brick-like structure is illustrated in Fig. 8.5, right (Pawlak et al., *The  $\text{PrAlO}_3$ - $\text{Pr}_2\text{O}_3$  eutectic, its instability, microstructure and luminescent properties*, accepted to Chem Mater).

## 8.4 Hybrid Structures

For some applications, such as metamaterials, hybrid materials (such as dielectric-metal structures) might be necessary. Data are scarce on such mixed eutectics in the literature. One way to obtain such a hybrid material is to etch one of the two phases of the binary eutectic away and fill the empty space with, for example, a metal. This approach has been already presented for the  $\text{Tb}_3\text{Sc}_2\text{Al}_3\text{O}_{12}$ - $\text{TbScO}_3$  eutectic. A metallodielectric sur-

face is obtained. In fact, two types of surfaces were observed experimentally: a surface of  $\text{TbScO}_3$  rods packed pseudo-hexagonally in air, as shown in Fig. 8.6a, or a surface of pseudo-hexagonally arranged holes in the matrix of  $\text{Tb}_3\text{Sc}_2\text{Al}_3\text{O}_{12}$ , as shown in Fig. 8.6b [20, 29]. The first type of surface was obtained while etching the off-eutectic structure formed in the outer part of the  $\text{Tb}_3\text{Sc}_2\text{Al}_3\text{O}_{12}$  rod with orthophosphoric acid. In this case the garnet phase was etched more rapidly. The second type of surface was obtained while etching the  $\text{Tb}_3\text{Sc}_2\text{Al}_3\text{O}_{12}$ - $\text{TbScO}_3$  eutectic rod. In this case the hole structure was obtained due to the more rapid etching of the perovskite phase. Metallodielectric surfaces were created after metal deposition onto these structures. The surface obtained by covering the structure from Fig. 8.6a with metal is presented in Fig. 8.6c. After removing the metal “bumps” formed on the dielectric rods, a structure of dielectric rods embedded in metal can be achieved [29]. The structure obtained when the structure from Fig. 8.6b is covered with metal is shown in Fig. 8.6d. After removing

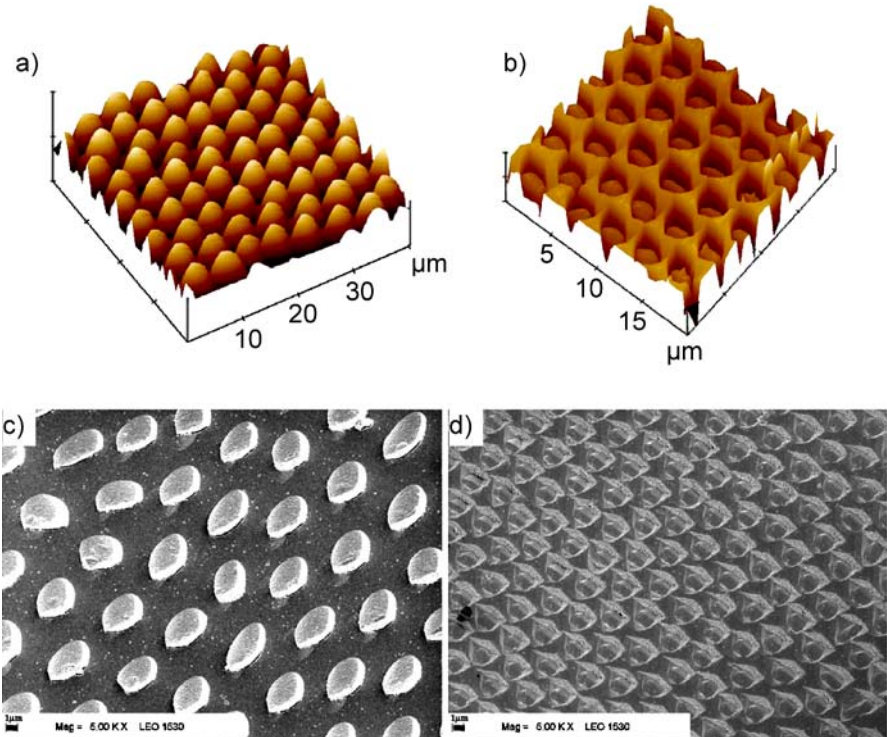


**Fig. 8.6.** **a** AFM image of the array of  $\text{TbScO}_3$  microrods embedded in air, **b** AFM image of the array of holes embedded in  $\text{Tb}_3\text{Sc}_2\text{Al}_3\text{O}_{12}$ , **c** structure obtained by depositing metal on the structure shown in AFM image (a), and **d** structure obtained by depositing metal on the structure shown in AFM image (b) [29]. Bars are 3  $\mu\text{m}$  (c) and 1  $\mu\text{m}$  (d)

the metal on the garnet matrix, a structure consisting of pseudo-periodically packed metal particles in a dielectric matrix can be achieved [29]. These types of structures may find application as plasmonic materials. The properties of similar metallodielectric structures have been already studied theoretically [38, 39].

## 8.5 Potential Applications

Directionally solidified eutectics can be described as being composite materials with complex and homogeneous microstructures that enable their properties to be controlled [40]. Eutectics are special materials that are both monolithic and multiphasic [40]. They show great potential for various optical, electronic and magnetic applications [41]. Eutectics have two types of properties: additive and product [42]. Electrical conductivity and elastic stiffness are examples of additive properties. They depend on the spatial distributions and volume fractions of the phases. Hardness and optical interference are examples of product properties. Product properties result from interactions between the phases. They depend on structural factors such as phase size or periodicity [40]. Product properties can exist in the eutectic as a whole, but not in the particular phases comprising the eutectic [40]. These product properties could be used to define metamaterials, since “metamaterials are engineered composites that exhibit superior properties that are not found in nature and not observed in the constituent materials”.

There might be a number of potential applications for the electromagnetic properties of directionally solidified eutectics. Eutectics may be exploited as optical materials; for example, a bunch of microfibers in a bulk phase could be used in various photonic devices. One future application could be that a laser beam could be generated in a bunch of microfibers and/or they could be used to transmit this light. There is also the possibility that they could be used to rotate polarized light when the material is placed in an external magnetic field (Faraday effect). Other applications considered depend on the particular properties of the individual phases.

Two potential applications of the product properties of eutectics are envisaged at the moment. The first is the application of eutectics as photonic crystals. The most interesting eutectic microstructures from the point of view of their use as photonic crystals would be microstructures with regular shapes: lamellar for one-dimensional photonic crystals or rodlike for two-dimensional ones. The photonic band gap effect would result from the periodicity of the structure of the eutectic and the difference between the refractive indices of its phases. In this case, an advantage of using eutectics is that the individual properties of the phases which comprise the eutectic, like nonlinear effects and lasing properties (when doped with active element), can be used as well as its product properties. The Faraday effect (observed for example in  $\text{Tb}_3\text{Sc}_2\text{Al}_3\text{O}_{12}$ ) should be enhanced in photonic crystal structures

(magnetophotonic crystals) [43, 44]. Eutectics could therefore provide extra, advantageous, properties in addition to the photonic band gap effect.

Another potential application of eutectics based on their product properties could be as metamaterials, as described above. Other forms of eutectic microstructure beyond lamellar and rodlike may also be useful for metamaterials applications. For example, percolated structures could be used to obtain huge dielectric constants [45], and spiral eutectics might be considered for chiral metamaterials [46, 47]. The globular microstructure could find application in potentially invisible materials [36] or in plasmon tunable materials, if the structures were metallodielectric [48].

Research in this area should be targeted at elucidating the relationship between microstructures and properties of eutectic composites, designing self-organized materials with different functional properties, and controlling growth processes in order to obtain desired microstructures.

## References

1. S. John, *Phys. Rev. Lett.*, **58**, 2486 (1987)
2. E. Yablonowitch, *Phys. Rev. Lett.*, **58**, 2059 (1987)
3. J.D. Joannopoulos, P.R. Villeneuve, S. Fan, *Nature*, **386**, 143 (1997)
4. A. Von Blaaderen, *Science*, **282**, 887 (1998)
5. J.B. Pendry, *Phys. Rev. Lett.*, **85**, 3966 (2000)
6. R. Shelby, D.R. Smith, S. Schultz, *Science*, **292**, 77 (2001)
7. S. Linden, C. Enkrich, M. Wegener, J. Zhou, T. Koschny, C.M. Soukoulis, *Science*, **306**, 1351 (2004)
8. T.J. Yen, W.J. Padilla, N. Fang, D.C. Vier, D.R. Smith, J.B. Pendry, D.N. Basov, X. Zhang, *Science*, **303**, 1494 (2004)
9. J.B. Pendry, *Science*, **306**, 1353 (2004)
10. N. Fang, H. Lee, Ch. Sun, X. Zhang, *Science*, **308**, 534 (2005)
11. D.R. Smith, J.B. Pendry, M.C.K. Wiltshire, *Science*, **305**, 788 (2004)
12. M.C.K. Wiltshire, J.B. Pendry, I.R. Young, D.J. Larkman, D.J. Gilderdale, J.V. Hajnal, *Science*, **291**, 849 (2001)
13. Y. Waku, N. Nakagawa, T. Wakamoto, H. Ohtsubo, K. Shimizu, Y. Kohtoku, *Nature*, **389**, 49 (1997)
14. J.H. Lee, A. Yoshikawa, S.D. Durbin, D.H. Yoon, T. Fukuda, Y. Waku, *J. Cryst. Growth*, **222**, 791 (2001)
15. J.H. Lee, A. Yoshikawa, H. Kaiden, K. Lebbou, T. Fukuda, D.H. Yoon, Y. Waku, *J. Cryst. Growth*, **231**, 179 (2001)
16. N. Nakagawa, H. Ohtsubo, A. Mitani, K. Shimizu, Y. Waku, *J. Eur. Ceramic Soc.*, **25**, 1251 (2005)
17. P. Rudolf, T. Fukuda, *Cryst. Res. Technol.*, **34**, 3 (1999)
18. R.I. Merino, *Phys. Rev. B*, **56**, 10907 (1997)
19. V.M. Orera, *Appl. Phys. Lett.*, **71**, 2746 (1997)
20. D.A. Pawlak, G. Lerondel, I. Dmytruk, Y. Kagamitani, S. Durbin, T. Fukuda, *J. Appl. Phys.*, **91**, 9731 (2002)
21. R.I. Merino, J.I. Pena, A. Larrea, G.F. de la Fuente, V.M. Orera, *Recent Res. Dev. Mater. Sci.*, **4**, 1 (2003)

22. U. Hecht, L. Granasy, T. Pusztai, B. Bottger, M. Apel, V. Witusiewicz, L. Ratke, J. De Wilde, L. Froyen, D. Camel, B. Drevet, G. Faivre, S.G. Fries, B. Legendre, S. Rex, *Mater. Sci. Eng.*, **R46**, 1 (2004)
23. R.L. Ashbrook, *J. Am. Ceram. Soc.*, **60**, 428 (1977)
24. J.D. Hunt, K.A. Jackson, *Trans. AIME*, **236**, 843 (1966)
25. D.H. Yoon, I. Yonenaga, N. Ohnishi, T. Fukuda, *J. Cryst. Growth*, **142**, 339 (1994)
26. F.R. Mollard, M.C. Flemings, *Trans. AIME*, **10**, 1534 (1967)
27. B. M. Epelbaum, in *Fiber Crystal Growth from the Melt*, ed. by T. Fukuda, P. Rudolph, S. Uda (Springer, Berlin, 2004), pp 107
28. L.M. Hogan, R.W. Kraft, F.D. Lemkey, in *Advances in Materials Research*, vol. 5, ed. by H. Helman (Wiley-Interscience, New York, 1971), pp. 83–216
29. D.A. Pawlak, K. Kolodziejak, S. Turczynski, J. Kisielewski, K. Rozniatowski, R. Diduszko, *Chem. Mater.*, **18**, 2450 (2006)
30. International Centre for Diffraction Data, *ICDD Grant-in-Aid: JCPDS 27-0599* (P. McCarthy, Penn State Univ., PA, 1974)
31. D.A. Pawlak, Y. Kagamitani, A. Yoshikawa, K. Wozniak, H. Sato, H. Machida, T. Fukuda, *J. Cryst. Growth*, **226**, 341 (2001)
32. Y. Kagamitani, D.A. Pawlak, H. Sato, A. Yoshikawa, H. Machida, T. Fukuda, *Jpn. J. Appl. Phys.*, **41**(1), 6020 (2002)
33. A. Yoshikawa, Y. Kagamitani, D.A. Pawlak, H. Sato, H. Machida, T. Fukuda, *Mater. Res. Bull.*, **37**, 1 (2002)
34. Y. Kagamitani, D.A. Pawlak, H. Sato, A. Yoshikawa, H. Machida, T. Fukuda, *J. Mater. Res.*, **19**, 579 (2004)
35. K. Kolodziejak, S. Turczynski, R. Diduszko, L. Klimek, D.A. Pawlak, *Opto-electron. Rev.*, **14**, 203 (2006)
36. F.J. Garcia de Abajo, G. Gomez-Santos, L.A. Blanco, A.G. Borisov, S.V. Shabanov, *Phys. Rev. Lett.*, **95**, 067403 (2005)
37. K.H. Hanisch, D. Stoyan, *J. Microsc.* **122**, 131 (1981)
38. J.B. Pendry, L. Martin-Moreno, F.J. Garcia-Vidal, *Science* **305**, 847 (2004)
39. F.J. Garcia-Vidal, L. Martin-Moreno, J.B. Pendry, *J. Optics A*, **7**, S97 (2005)
40. J. Llorca, V.M. Orera, *Prog. Mater. Sci.*, **51**, 711 (2006)
41. F.S. Galasso, *J. Metals*, **17**, 1, 1967
42. A. Kelly, *An introduction to composite materials*, in *Concise Encyclopedia of Composite Materials* (Pergamon, New York, 1994)
43. I.L. Lyubchanskii, N.N. Dadoenkova, M.I. Lyubchanskii, E.A. Shapovalov, Th. Rasing, *J. Phys. D*, **36**, R277 (2003)
44. C. Koerdt, G.L.J.A. Rikken, E.P. Petrov, *Appl. Phys. Lett.*, **82**, 1538 (2003)
45. C. Pecharroman, F. Esteban-Betegon, J.F. Bartolome, S. Lopez-Esteban, J.S. Moya, *Adv. Mater.*, **13**, 1541 (2001)
46. J. B. Pendry, *Science*, **306**, 1353 (2004)
47. V.A. Fedotov, P.L. Mladyonov, S.L. Prosvirnin, A.V. Rogacheva, Y. Chen, N.I. Zheludev, *Phys. Rev. Lett.*, **97**, 167401 (2006)
48. S. Riikonen, I. Romero, F.J. Garcia de Abajo, *Phys. Rev. B*, **71**, 235104 (2005)

Part III

**Growth and Characterization  
of Oxide  $\mu$ -PD Crystals I:  
Scintillation and Laser Materials**

# 9 Scintillating Bulk Oxide Crystals

Akira Yoshikawa and Martin Nikl

**Abstract.** The application of the micro-pulling-down ( $\mu$ -PD) method to the growth of scintillating bulk (over 1 mm in diameter or cross-section) crystals, as well as to investigations of their optical and luminescent properties, is reviewed. One of the aims of this chapter is to demonstrate how  $\mu$ -PD facilitates rapid material screening and the development of new crystalline materials. This technique allows relatively large crystalline specimens to be fabricated within a short period of time. Such crystals can be grown large enough to allow to characterize any of their properties, including their photo- and radioluminescence, their decay kinetics and their light yields. The growth and subsequent characterization of the scintillation properties of Yb-doped  $\text{Y}_3\text{Al}_5\text{O}_{12}$ ,  $\text{Lu}_3\text{Al}_5\text{O}_{12}$ ,  $\text{YAlO}_3$ ,  $(\text{Lu},\text{Y})\text{AlO}_3$ , Bi-doped  $\text{Y}_3\text{Ga}_5\text{O}_{12}$ ,  $\text{Gd}_3\text{Ga}_5\text{O}_{12}$ ,  $\text{Lu}_3\text{Ga}_5\text{O}_{12}$ , Pr-doped  $\text{Y}_3\text{Al}_5\text{O}_{12}$ ,  $\text{Lu}_3\text{Al}_5\text{O}_{12}$ ,  $\text{YAlO}_3$ ,  $\text{Y}_2\text{SiO}_5$ ,  $\text{Lu}_2\text{SiO}_5$  have been reported recently. The ability to control the crystal shape is an additional advantage of the  $\mu$ -PD method. It is therefore possible to produce shaped and/or device-sized crystals from the melt using a single-step process. Recent improvements in the  $\mu$ -PD method have made it possible to grow crystals using  $\mu$ -PD that are comparable in terms of quality with those grown by Czochralski (Cz), Bridgman, or other classical growth technologies.

## 9.1 Introduction

The study of emission centers in various crystal hosts, including Yb-doped  $\text{Y}_3\text{Al}_5\text{O}_{12}$  (YAG),  $\text{Lu}_3\text{Al}_5\text{O}_{12}$  (LuAG),  $\text{YAlO}_3$  (YAP),  $(\text{Lu},\text{Y})\text{AlO}_3$  (LuYAP), Bi-doped  $\text{Y}_3\text{Ga}_5\text{O}_{12}$  (YGG),  $\text{Gd}_3\text{Ga}_5\text{O}_{12}$  (GGG),  $\text{Lu}_3\text{Ga}_5\text{O}_{12}$  (LuGG), Pr-doped YAG, LuAG, YAP,  $\text{Y}_2\text{SiO}_5$  (YSO), and  $\text{Lu}_2\text{SiO}_5$  (LSO), is an active area of fundamental research that attracts the attention of industry. It is often necessary to understand the factors that drive the optical processes that occur in crystals with different concentrations of dopants in order to be able to estimate the figure-of-merit of a particular material when used in a device. Interactions between dopant ions and lattice phonons, dopant aggregation, concentration quenching, and energy transfer processes are typical examples of phenomena that determine the directions of research efforts. Furthermore, the spatial distribution of the dopant ions in the crystals is another important factor that affects the spectral and temporal properties of the emission [1,2]. A series of crystals with different dopant concentrations but similar (and preferably high) crystalline perfection are needed for such studies.

The micro-pulling-down ( $\mu$ -PD) method permits the growth of single crystals using a negligible amount of raw material compared to conventional bulk

crystal growth techniques. Less than 1 g of starting powder is typically required to perform the process. Furthermore, only 5–12 hours of growth are needed because of the extremely high growth speed (0.05–1 mm/min) enabled by  $\mu$ -PD systems. Both of these advantages make the  $\mu$ -PD method a unique tool for the preparation and screening of single-crystalline materials [3].

The  $\mu$ -PD method is a melt growth technique and can be categorized under shaped crystal growth methods [4]. In the case of  $\mu$ -PD, the crucible plays two important roles. It not only contains the melt, but it also has a shaper (or die) in the bottom, which makes the system suitable for shaped crystal growth. The prototype of the modern version of the  $\mu$ -PD system was proposed by Ohnishi of the Electrotechnical Laboratory in Tsukuba, Japan, and it was first established at Fukuda Laboratory in the Institute for Materials Research, Tohoku University, Japan [5–8], over a decade ago. In this chapter, the development of novel scintillator crystals using the  $\mu$ -PD method is reviewed.

## 9.2 Charge Transfer Luminescence of $\text{Yb}^{3+}$

Due to the fact that the charge transfer (CT) luminescence transition includes both ligand and central metal ions, it is expected that  $\text{Yb}^{3+}$  CT emission characteristics are strongly dependent on the type of ligand ion present and the local symmetry of the central metal and ligand ions. Moreover, the particular distortion (relaxation) of the excited state of the center, which depends on the symmetry of the phonon modes and other particular features of the host, is an additional factor that influences the luminescence characteristics.  $\text{Yb}^{3+}$  CT luminescence is always identified by the need for an energy separation of about  $10,000 \text{ cm}^{-1}$  between the two emission subbands, which is provided by the distance between the  ${}^2\text{F}_{7/2}$  and  ${}^2\text{F}_{5/2}$  levels of  $\text{Yb}^{3+}$ . The CT process is illustrated in Fig. 9.1.

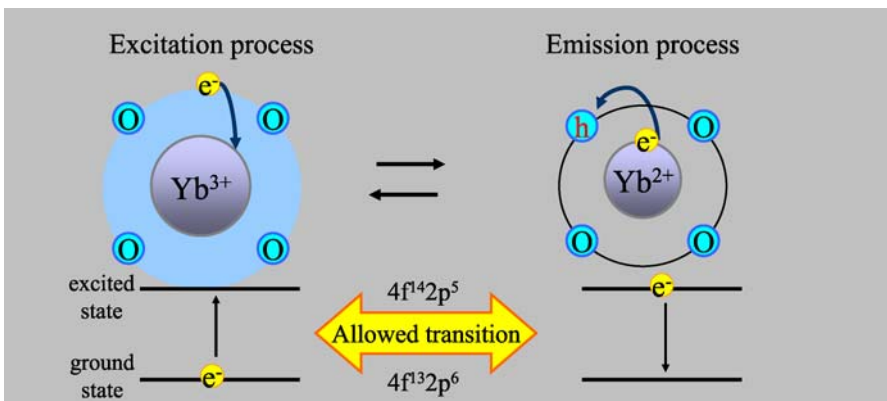


Fig. 9.1. Schematic diagram of  $\text{Yb}^{3+}$  charge transfer state

### 9.3 Growth of Yb-Doped Garnets

A number of Yb-doped crystals with garnet structure that demonstrate scintillating properties have been produced by  $\mu$ -PD technology [9–14]. If we consider the crystal chemistry of the garnets and dimensional factors, the  $\text{Yb}^{3+}$  cations fit well into dodecahedral sites in the garnet structure [15]. Therefore, these cations can be incorporated into the garnet lattice without much effort, as shown by attempts to substitute rare-earth host cations for other functional dopants, such as  $\text{Nd}^{3+}$  or  $\text{Pr}^{3+}$ .

Bulk crystals of  $\text{Yb:Y}_3\text{Ga}_5\text{O}_{12}$  and  $\text{Yb:Lu}_3\text{Al}_5\text{O}_{12}$  with diameters of about 3 mm were produced from an iridium crucible that was manufactured to contain a die of appropriate shape [10]. Inductive heating at a frequency of 15 or 20 kHz ([13] and [10, 14], respectively) was applied to control the temperature of the melt and the behavior of the meniscus. Sometimes the temperature was measured using an optical pyrometer [13]. The starting materials were prepared from corresponding oxides of 99.99% purity. Pre-sintered (at 1400 °C for 24 h) single garnet phase polycrystalline solids were also used as raw materials, according to [13]. An atmosphere of Ar + 1%  $\text{O}_2$  gas flow [10] was used for the growth of  $\text{Yb:Y}_3\text{Ga}_5\text{O}_{12}$ . Pure Ar gas was used in the case of  $\text{Yb:Lu}_3\text{Al}_5\text{O}_{12}$  growth. Admixing of Ar gas with oxygen was required to suppress the decomposition of gallium oxide (see Chap. 6 for details). In some cases its concentration was increased to 2% [13, 14]. [111]-oriented crystalline rods of the corresponding undoped garnets were used as seeds. Typical growth rates applied were 0.05–0.50 mm/min, and the crystals produced were about 3 mm in diameter, replicating the shape of the die. The crystals were up to several centimeters long (Figs. 9.2 and 9.3).

The melt did not wet the Ir crucible during  $\text{Yb:Lu}_3\text{Al}_5\text{O}_{12}$  growth [11]. This is considered to be notable disadvantage of the system from the point of view of shaped bulk crystal growth. To improve the behavior of the system, the melt was slightly overheated. As a result, the melt viscosity was decreased, which aided the spread of the fluid over the bottom surface of the die. The crystals were typically free of cracks and second-phase inclusions and suitable for preliminary optical characterizations.

Sometimes pale blue coloration of the crystals was observed, because the growth was performed in an inert atmosphere [12]. It was suggested that existence of color centers and the reduction of  $\text{Yb}^{3+}$  to  $\text{Yb}^{2+}$  was the main reason for the coloration. After annealing the as-grown materials in air at 1400 °C for 20 h, the crystals became colorless. The as-grown crystals were cut into plate-shaped specimens and polished for preliminary optical characterization. The dimensions of the specimens were approximately  $1 \times 3 \times 8$  mm (Fig. 9.4). Examples of the  $\text{Yb:LuAG}$  radioluminescence spectra obtained are shown in Fig. 9.5.

The chemical composition and the spatial distributions of the constituents were studied across the crystal volume via electron probe microanalysis

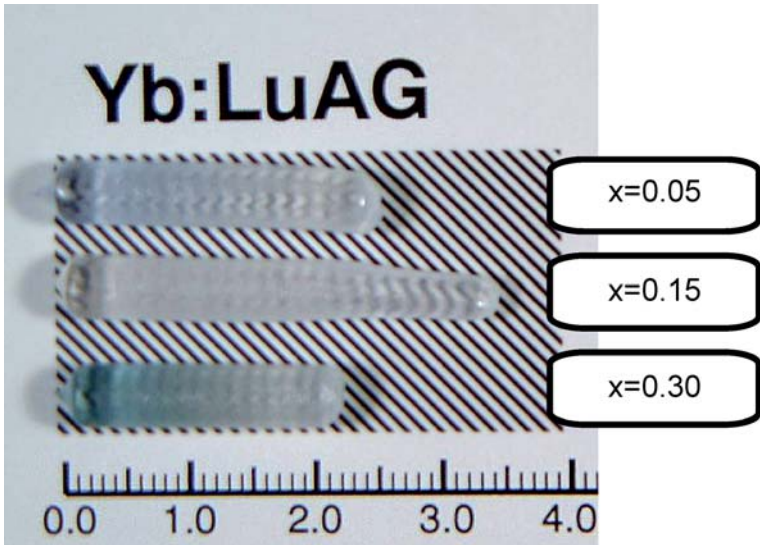


Fig. 9.2. View of  $(\text{Lu}_{1-x}\text{Yb}_x)_3\text{Al}_5\text{O}_{12}$   $\mu$ -PD crystals (Scale is in mm)

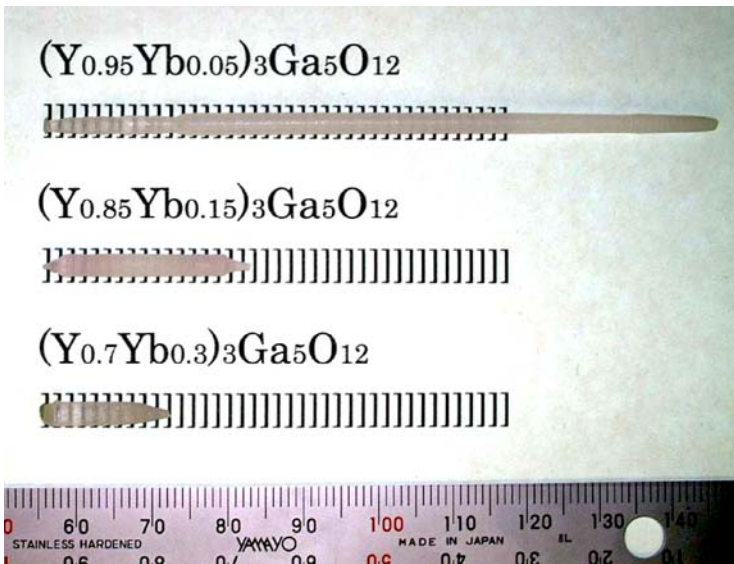


Fig. 9.3. Yb doped  $\text{Y}_3\text{Ga}_5\text{O}_{12}$   $\mu$ -PD crystals (Scales are in mm)

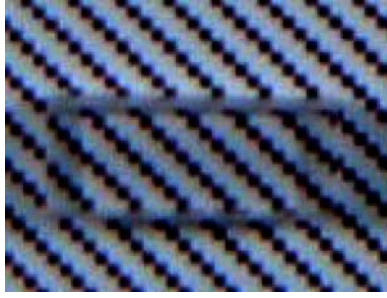


Fig. 9.4. View of polished plate specimen produced from  $\mu$ -PD rod shaped crystal

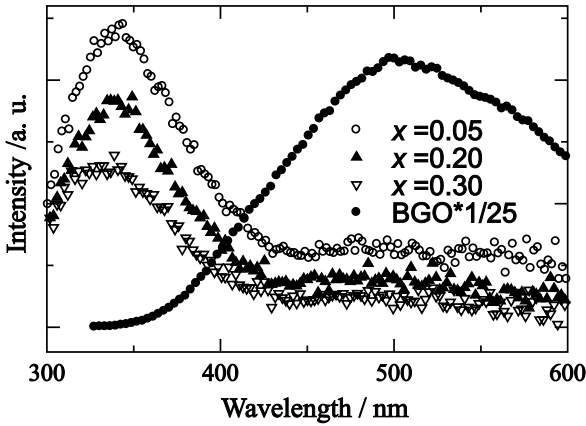


Fig. 9.5. Radioluminescence spectra of  $(\text{Lu}_{1-x}\text{Yb}_x)_3\text{Al}_5\text{O}_{12}$  at RT ( $x = 0.05, 0.20, 0.30$ ) compared in an absolute way with the standard BGO sample. Excitation by X-ray, 35 keV, 16 mA

(EPMA) in order to characterize the chemical homogeneities of the materials (Fig. 9.6). This made it possible to identify the advantages and disadvantages of any particular growth process and to predict the steps that could improve the behavior of the system, aiding the development of the procedure. The formation of continuous solid solutions in the  $(\text{Lu}_{1-x}\text{Yb}_x)_3\text{Al}_5\text{O}_{12}$  and  $(\text{Y}_{1-x}\text{Yb}_x)_3\text{Ga}_5\text{O}_{12}$  systems was confirmed based on the results from X-ray diffraction (XRD) analysis. The dependences of the lattice parameters on the crystal composition were linear [12, 13], and corresponded well to Vegard's law (see Chap. 6 for details).

The growth of more complicated (triple) solid solution crystals of  $(\text{Gd}_{0.95-x}\text{Yb}_{0.05}\text{Lu}_x)_3\text{Ga}_5\text{O}_{12}$  ( $0.0 \leq x \leq 0.9$ ) and  $\text{Gd}_{0.15}\text{Yb}_{0.15}\text{Lu}_{2.70}(\text{Al}_x\text{Ga}_{1-x})\text{O}_{12}$  ( $0.0 \leq x \leq 1.0$ ) was also demonstrated in [14]. The growth conditions used were similar to those described above.

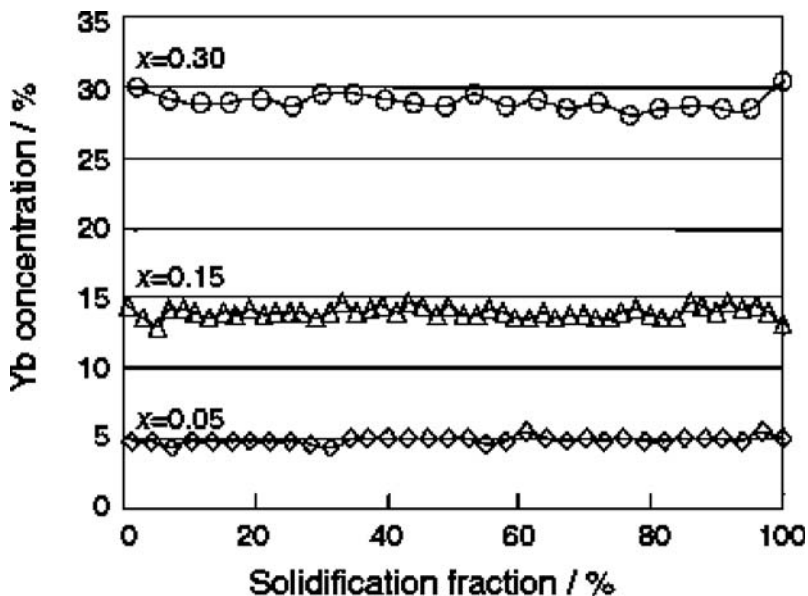


Fig. 9.6. Distribution of Yb along growth axis in solid solution crystals produced from  $(\text{Lu}_{1-x}\text{Yb}_x)_3\text{Al}_5\text{O}_{12}$  melts according to EPMA measurements [11]

## 9.4 Growth of Yb-Doped Perovskites and Other Oxides

Starting materials were typically prepared from stoichiometric mixtures of powders of corresponding oxides of  $4N$ – $5N$  purity. Polycrystalline specimens of nominal composition  $(\text{Y}_{1-x}\text{Yb}_x)\text{AlO}_3$  were produced at the preliminary stage by solid state reactions performed at temperatures just below the estimated melting points of the corresponding compounds in order to examine the phase formation near the solidus line. Thereafter, phase identification was performed at room temperature in air using powder XRD analysis. The apparatus used was a Rigaku RINT-Ultima diffractometer operating with a  $\text{CuK}\alpha$  X-ray source (40 kV, 40 mA).

It was found that the ranges of Yb substitution observed in the above solid solutions depended on the type of the host lattice. For the garnet structure, unlimited solubility in the solid state was observed in the case of  $(\text{Lu}_{1-x}\text{Yb}_x)_3\text{Al}_5\text{O}_{12}$  (see Chap. 6). However, in the case of  $(\text{Y}_{1-x}\text{Yb}_x)\text{AlO}_3$ , the solubility of  $\text{Yb}^{3+}$  in the perovskite structure was limited within the range of  $x = 0.0$ – $0.45$ . Increasing the  $\text{Yb}^{3+}$  substitution resulted in second-phase formation, which is definitely not acceptable when single-crystal growth is performed from the melt.

Crystals of Yb:YAIO<sub>3</sub>, Yb:YAP were grown by the  $\mu$ -PD method using an iridium crucible with a die. The crucible was heated inductively at a frequency of 20 kHz. The pulling rate was 0.05–0.3 mm/min. The seed materials used

were [100] YAP. A selection of Yb-doped perovskite-type crystals grown by the  $\mu$ -PD method are illustrated in Fig. 9.7.

Excitation and emission spectra of Yb:YAP are shown in Fig. 9.8. The charge transfer luminescence of  $\text{Yb}^{3+}$  exhibits a double-peak spectrum with maxima at 345–350 nm and 515–520 nm; the separation of the peaks in energy fits the required energy difference of about  $10,000\text{ cm}^{-1}$  defined by the distance between the  ${}^2\text{F}_{5/2}$  and  ${}^2\text{F}_{7/2}$  levels of  $\text{Yb}^{3+}$ . The excitation spectrum ( $\lambda_{\text{em}} = 350\text{ nm}$ ) peaks round 240 nm, which is consistent with the absorption spectrum. The slight asymmetry of the 345 nm emission peak on the low-energy side and the distinct excitation peak at approximately 280 nm may be related to trace amounts of  $\text{Yb}^{2+}$  ions, taking into account the reported characteristics of the  $\text{Yb}^{2+}$  center in oxide-based compounds. The temperature dependence of the integrated emission spectra (inset of Fig. 9.8) shows enhanced quenching of the CT emission at RT [16].

Results for the  $\mu$ -PD growth of  $\text{Ca}_8(\text{La}_{1-x}\text{Yb}_x)_2(\text{PO}_4)_6\text{O}_2$  fiber-type crystals are illustrated in Fig. 9.9. The growth of Yb:YVO<sub>4</sub> crystals by  $\mu$ -PD was also attempted. However, the process was difficult to control because of extremely high wetting between the melt and Ir [6]. As a result, the melt climbed up the crucible outer wall and stabilization of the meniscus shape was impossible.

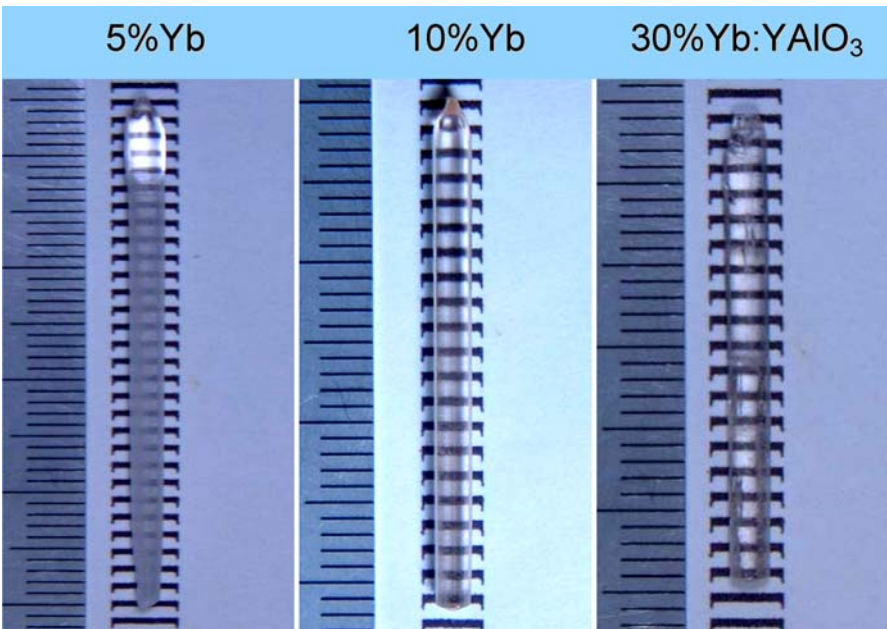


Fig. 9.7. View of Yb-doped  $\text{YAlO}_3$   $\mu$ -PD crystals (Scales are in mm)

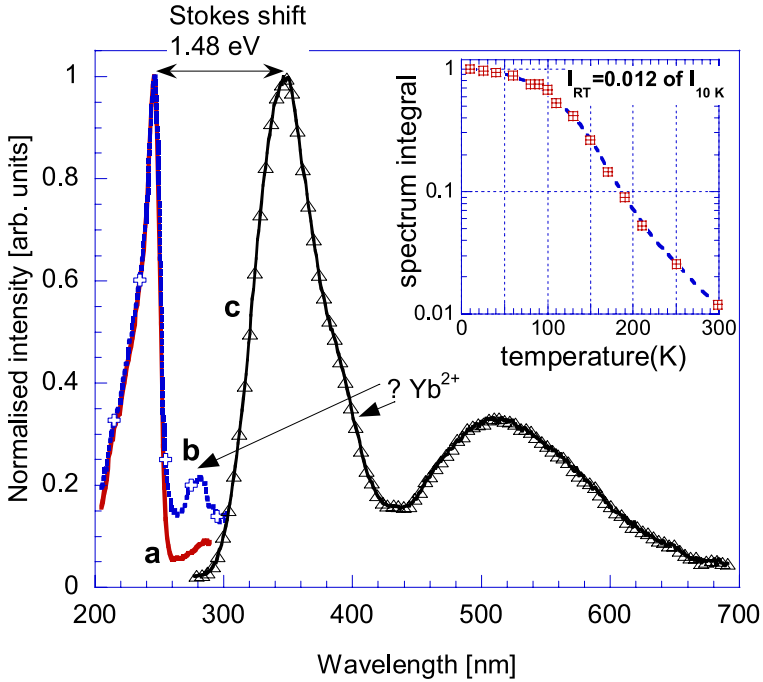


Fig. 9.8. Excitation (a,b) and emission (c) spectra of Yb1%:YAP sample at 9 K. a  $\lambda_{em} = 350$  nm, b  $\lambda_{em} = 400$  nm and c  $\lambda_{em} = 230$  nm. In the inset temperature dependence of integrated emission spectra is given under excitation at 230 nm

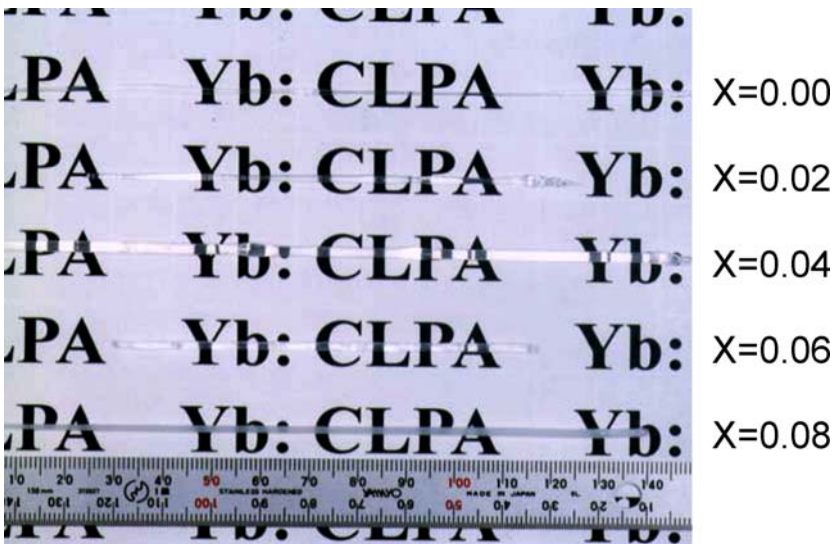
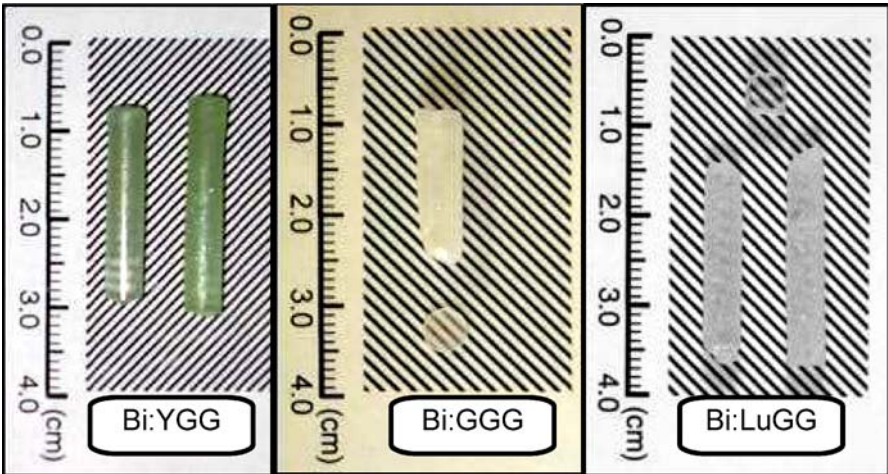


Fig. 9.9. View of  $\text{Ca}_8(\text{La}_{1-x}\text{Yb}_x)_2(\text{PO}_4)_6\text{O}_2$   $\mu$ -PD fiber crystals

## 9.5 Growth of Bi-Doped Garnets

The  $\mu$ -PD growth of Bi-doped crystals was also examined in order to study the performance of the  $\text{Bi}^{3+}$  cation as a luminescent center. The ultimate aim of these experiments was to develop a high-density scintillator host such as  $\text{Lu}_3\text{Ga}_5\text{O}_{12}$ . In the case of Ce-doped gallium garnets (YGG, GGG, LuGG), the luminescence is most probably quenched due to the photoionization of the  $\text{Ce}^{3+}$  excited state. However, luminescence from the Bi  $6p-6s$  transition can be observed in such hosts.

Starting materials were prepared from a stoichiometric mixture of 4N-purity  $\text{Y}_2\text{O}_3$ ,  $\text{Gd}_2\text{O}_3$ ,  $\text{Lu}_2\text{O}_3$ , and  $\text{Ga}_2\text{O}_3$  and 3N-purity  $\text{Bi}_2\text{O}_3$  powders. Bi-doped  $\text{Y}_3\text{Ga}_5\text{O}_{12}$  (Bi:YGG),  $\text{Gd}_3\text{Ga}_5\text{O}_{12}$  (Bi:GGG), and  $\text{Lu}_3\text{Ga}_5\text{O}_{12}$  (Bi:LuGG) single crystals were grown using an iridium crucible with a die (Fig. 9.10). The crucible was heated inductively at a frequency of 30 kHz. The growth rate was 0.05–0.3 mm/min. A [111]  $\text{Y}_3\text{Al}_5\text{O}_{12}$  crystal was used as a seed for the initial experiments and  $\mu$ -PD crystals of identical composition were used in following growths. The growth atmosphere was a mixture of Ar +  $\text{O}_2$  (2 vol%) to suppress the dissociation and evaporation of the gallium ox-



**Fig. 9.10.** View of Bi-doped gallium garnet crystals grown by the  $\mu$ -PD method: YGG:Bi (0.06%), GGG:Bi (0.1%), and LuGG:Bi (0.04%) (from left to right)

**Table 9.1.** Composition ratios (atomic) of constituents occupying the dodecahedral sites of garnet crystals produced from the melt by the  $\mu$ -PD process

$(\text{Bi,Gd})_3\text{Ga}_5\text{O}_{12}$	[Bi]/[Gd] in the melt	0.005	0.010	0.050
	[Bi]/[Gd] in the crystal	0.00102	0.00126	0.00141
$(\text{Bi,Lu})_3\text{Ga}_5\text{O}_{12}$	[Bi]/[Lu] in the melt	0.050	0.100	0.150
	[Bi]/[Lu] in the crystal	0.00039	0.00083	0.00100

ides. Phase identification and composition analysis were performed by XRD and EPMA, respectively.

High evaporation of  $\text{Bi}_2\text{O}_3$  was observed in all growth experiments. Moreover, it is well known from flux growth in practice that the segregation coefficient of  $\text{Bi}^{3+}$  in any garnet structure is low. Therefore, the Bi content in the Bi-doped  $\text{Gd}_3\text{Ga}_5\text{O}_{12}$  [17] and  $\text{Lu}_3\text{Ga}_5\text{O}_{12}$  [18] crystals was also very low. Experimental data reflecting the incorporation of  $\text{Bi}^{3+}$  cations into the garnet structure are summarized in Table 9.1. It is important to note that these data cannot be used to simply calculate the segregation coefficients of  $\text{Bi}^{3+}$  because the melt composition was not constant due to the high evaporation. However, the values given in Table 9.1 are probably the only experimental results related

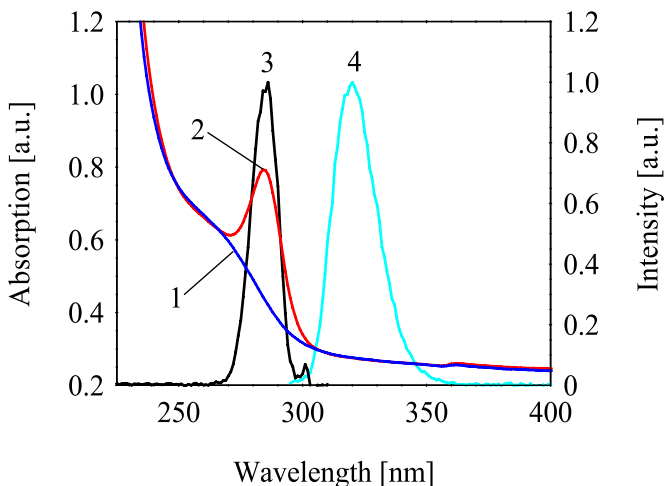


**Fig. 9.11.** Absorption (1,2), excitation (3), and emission (4) spectra of undoped (1) and Bi-doped (2–4)  $\text{Lu}_3\text{Ga}_5\text{O}_{12}$  (Bi = 0.083 mol%) at R.T. (1,2) and 8 K (3,4);  $\lambda_{\text{em}} = 320 \text{ nm}$  (3),  $\lambda_{\text{ex}} = 285 \text{ nm}$  (4)

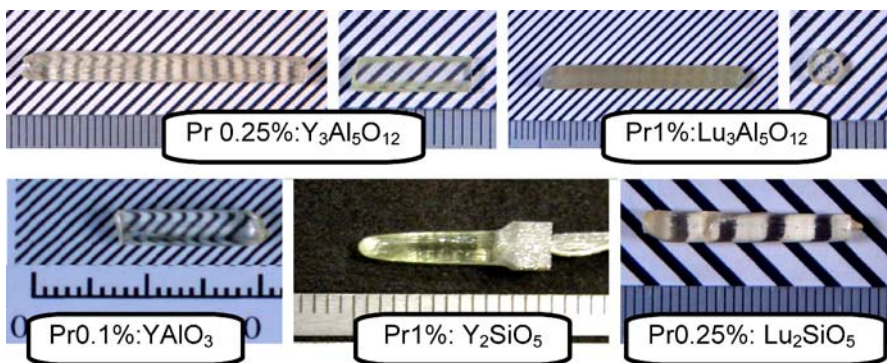


**Fig. 9.12.** Pr-doped YAG, LuAG, YAP, YSO and LSO single crystals grown by the  $\mu$ -PD method

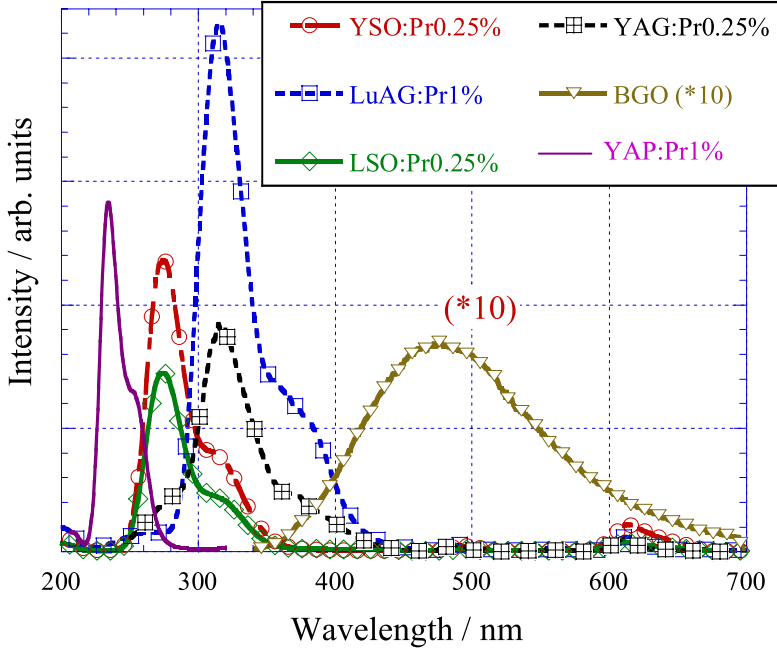


**Fig. 9.13.** Radioluminescence spectra of Pr-doped LuAG, YAG, YAP, YSO, LSO grown by the  $\mu$ -PD method (exc. X-ray, RT)

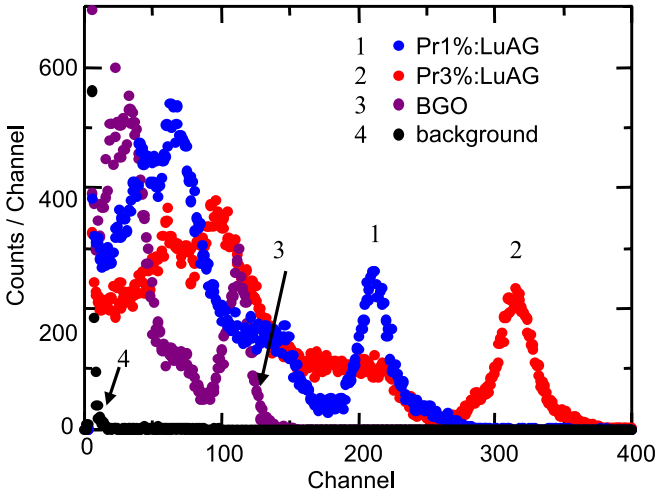


**Fig. 9.14.** Photoelectron yield measurement of Pr:LuAG under  $\gamma$ -ray of  $^{137}\text{Cs}$  radioisotope (spectrally uncorrected). Curve number marks the photopeak at curves 1–3

to the melt growth of Bi-doped garnets performed at the temperature range of 1500–2000 °C currently available. Thus, these results can only be used to get preliminary estimates for the segregation coefficients. Examples of the absorption, excitation and emission spectra of Bi:LuAG are given in Fig. 9.11.

## 9.6 Pr-Doped Crystals

Pr-doped oxide crystals are also recognized as being promising scintillating materials. Fast and intense emission is expected from the  $5d-4f$  transition of the  $\text{Pr}^{3+}$  ion when the host lattice has a medium-strong crystal field, which shifts the lowest  $5d$  state below the  $^1\text{S}_0$  level of  $\text{Pr}^{3+}$  and

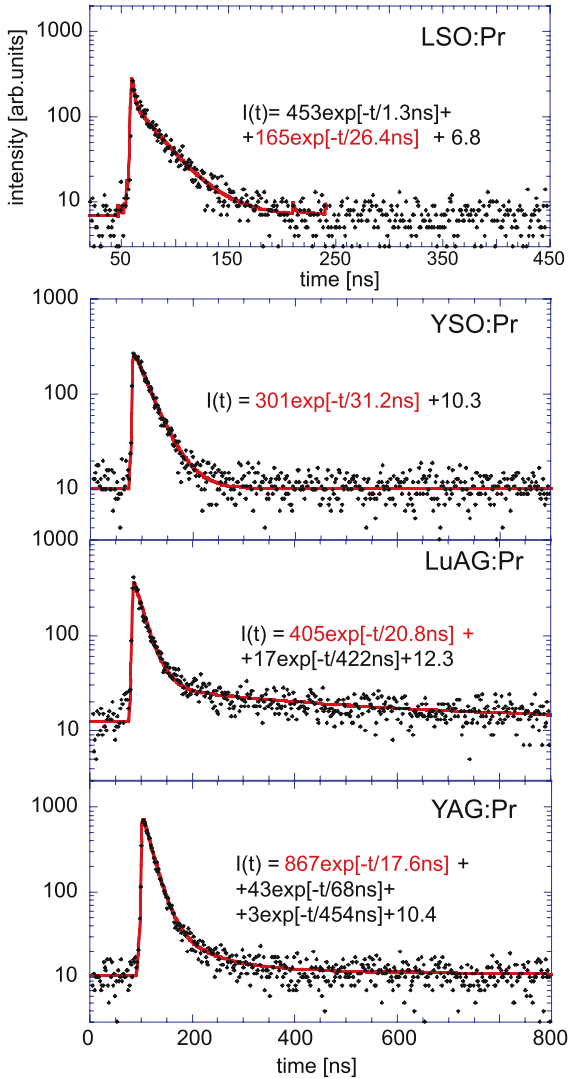


**Fig. 9.15.** Spectrally unresolved scintillation decays excited by 511 keV photons from  $^{22}\text{Na}$  radioisotope. *Solid line* is the convolution between instrumental response and function  $I(t)$  in the figure

makes the  $5d-4f$  radiative transition possible. Therefore, Pr-doped  $\text{Y}_3\text{Al}_5\text{O}_{12}$ ,  $\text{Lu}_3\text{Al}_5\text{O}_{12}$ ,  $\text{YAlO}_3$ ,  $\text{Y}_2\text{SiO}_5$ , and  $\text{Lu}_2\text{SiO}_5$  were also prepared by the  $\mu$ -PD method (Fig. 9.12). Their radio-luminescence spectra are shown in Fig. 9.13. It was found that Pr:LuAG is the most efficient scintillator among the above crystals. Photoelectron yield measurements of Pr:LuAG under  $\gamma$ -ray excitation are shown in Fig. 9.14.

Scintillation decays are summarized in Fig. 9.15. In YAG and LuAG hosts, the dominant scintillation decay times of about 16 ns and 20 ns, respectively, are very similar to those obtained from photoluminescence. These times are about 2.5 and six times shorter than the scintillation decay times for Ce-doped LuAG or YAG, respectively. In the case of LuAG:Pr, there is a noticeable slow decay component, of the order of several hundreds of ns, which is completely analogous to that observed in LuAG:Ce [19]. In the case of LSO:Pr, the dominant decay time of about 26 ns is several times longer than that obtained from photoluminescence decay ( $\sim 6$  ns), and this can be explained by  $\text{Pr}^{3+}$  center ionization [20], i.e., the onset of delayed recombination processes on a nanosecond timescale.

## 9.7 Device Size Shaped Crystal Growth

Since the bottom of the crucible can be used as a die, it is possible to produce crystals of various shapes using the  $\mu$ -PD method. The geometrical configuration (shape) of the die is one of the most important parameters for precise shape control. The shape of the crucible die is generally designed taking



Fig. 9.16. LuAG single crystal with square rod shape grown by the  $\mu$ -PD method

into account the wetting angle between the crucible material and the melt under specific growth atmosphere conditions. Recent improvements in the  $\mu$ -PD process permit the fabrication of device size shaped crystals: square and cylindrical rods, tubes, and plates. As an example, a LuAG crystal grown in the form of a rectangular (square) rod is shown in Fig. 9.16. It is worth noting that  $\text{Yb}^{3+}:\text{LuAG}$  yields the best performance among garnets for Yb lasing [16], and  $\text{Pr}^{3+}:\text{LuAG}$  provides the best performance among Pr-doped scintillators [21].

## References

1. G. Boulon, *Opt. Mater.*, **22**, 85 (2003)
2. C.W.E. van Eijk, *Nucl. Instrum. Meth. A*, **509**, 17 (2003)
3. A. Yoshikawa, M. Nikl, G. Boulon, T. Fukuda, *Opt. Mater.*, in press
4. A.V. Stepanov, *Zh. Techn. Fiz.*, **29**, 382 (1959)
5. D.H. Yoon, I. Yonenaga, T. Fukuda, N. Ohnishi, *J. Cryst. Growth*, **142**, 339 (1994)
6. T. Fukuda, P. Rudolph, S. Uda, (eds.), *Fiber Crystal Growth from the Melt*, (Springer, Berlin, 2004)
7. A. Yoshikawa, B.M. Epelbaum, T. Fukuda, K. Suzuki, Y. Waku, *Jpn. J. Appl. Phys.*, **38**, L55 (1999)
8. A. Yoshikawa, T. Satonaga, K. Kamada, H. Sato, M. Nikl, N. Solovieva, T. Fukuda, *J. Cryst. Growth*, **270**, 427 (2004)
9. H. Ogino, A. Yoshikawa, J.H. Lee, M. Nikl, N. Solovieva, T. Fukuda, *Opt. Mater.*, **26**, 535 (2004)
10. A. Yoshikawa, T. Akagi, M. Nikl, N. Solovieva, K. Lebbou, C. Pedrini, T. Fukuda, *Nucl. Instrum. Meth. A*, **486**, 79 (2002)
11. A. Yoshikawa, H. Ogino, J.L. Lee, M. Nikl, N. Solovieva, N. Garnier, C. Du-jardin, K. Lebbou, C. Pedrini, T. Fukuda, *Opt. Mater.*, **24**, 275 (2003)
12. H. Ogino, A. Yoshikawa, J.H. Lee, M. Nikl, N. Solovieva, T. Fukuda, *J. Cryst. Growth*, **253**, 314 (2003)
13. A. Yoshikawa, M. Nikl, H. Ogino, J.H. Lee, T. Fukuda, *J. Cryst. Growth*, **250**, 94 (2003)
14. A. Novoselov, A. Yoshikawa, H. Ogino, M. Nikl, J. Pejchal, T. Fukuda, *Opt. Mater.*, **26**, 541 (2004)
15. V.I. Chani, Y M. Yu, K. Shimamura, T. Fukuda, *Mater. Sci. Eng. R*, **20**(6), 281 (1997)
16. J.B. Shim, A. Yoshikawa, M. Nikl, N. Solovieva, J. Pejchal, D.H. Yoon, T. Fukuda, *J. Cryst. Growth*, **256**, 298 (2003)
17. A. Novoselov, A. Yoshikawa, M. Nikl, N. Solovieva, T. Fukuda, *Nucl. Instrum. Meth. A*, **537**, 247 (2005)
18. A. Novoselov, A. Yoshikawa, M. Nikl, J. Pejchal, T. Fukuda, *J. Cryst. Growth*, **292**, 236 (2006)
19. M. Nikl, *Phys. Stat. Sol. A*, **202**, 201 (2005)
20. M. Nikl, H. Ogino, A. Yoshikawa, E. Mihokova, J. Pejchal, A. Beitlerova, A. Novoselov, T. Fukuda, *Chem. Phys. Lett.*, **410**, 218 (2005)

21. M. Nikl, J. Pejchal, A. Yoshikawa, T. Fukuda, A. Krasnikov, A. Vedda, K. Nejezchleb, in *Proceedings of the Eighth International Conference on Inorganic Scintillators and their Use in Scientific and Industrial Applications (SCINT2005)*, 19–23 September, 2005, Alushta, Ukraine, ed. by B. Grinyev and A. Gektin, pp. 89–94

# 10 Scintillating Crystals: $\text{Ce}^{3+}:\text{YAlO}_3$ and $\text{Yb}^{3+}:\text{Lu}_3\text{Al}_5\text{O}_{12}$

Mohamed Alshourbagy, Alessandra Toncelli, and Mauro Tonelli

**Abstract.** The growth and scintillation performance of single-crystal fibers of both  $\text{Ce}^{3+}:\text{YAlO}_3$  and  $\text{Yb}^{3+}:\text{Lu}_3\text{Al}_5\text{O}_{12}$  are described. The results demonstrate the ability of the micro-pulling-down technique to grow scintillator crystals in shapes suitable for device applications.

## 10.1 Introduction

At present, various scintillators such as  $\text{Ti}:\text{NaI}$ ,  $\text{Ti}:\text{CsI}$ , etc., are used in a number of applications in research, medicine and industry. Some new materials, for example  $\text{CeF}_3$ ,  $\text{Ce}:\text{Y}_3\text{Al}_5\text{O}_{12}$  (YAG), and others, are also being studied [1]. Dense and fast radiation scintillators are required by various fields, including high-energy physics, astrophysics, and medicine. Several studies [2, 3] have shown that  $\text{Ce}^{3+}$ -doped  $\text{YAlO}_3$  (Ce:YAP) is a good candidate material for  $\gamma$ -ray detectors. Ce:YAP is an attractive scintillator that exhibits fast scintillation, a high light yield, and excellent mechanical and chemical properties. It is mechanically hard, chemically stable, insoluble in inorganic acids, and resistant to alkali. Its mechanical properties allow the deposition of very thin layers of reflectors onto its surfaces. Compared with other scintillators, Ce:YAP has a relatively high density and a short decay time.

On the other hand, materials based on aluminum garnet are promising for rare-earth ( $\text{Re}^{3+}$ )-based scintillators; for example,  $\text{Yb}^{3+}$ -doped  $\text{Lu}_3\text{Al}_5\text{O}_{12}$  (Yb:LuAG) has attracted much interest for fast scintillator applications and in high-energy physics (for the detection of neutrinos).

Ce:YAP and Yb:LuAG single crystals are usually grown by the Czochralski (CZ) method and then processed (oriented, cut into a suitable shape, and polished) to fit device requirements. The growth of shaped crystals (fibers) by the micro-pulling-down method ( $\mu$ -PD) is a cost-efficient option because  $\mu$ -PD-grown crystals have almost device-ready shapes (which simplifies crystal processing). Moreover,  $\mu$ -PD is relatively cheap in terms of the apparatus required and the running costs involved. The method also permits the growth of crystals in shapes that are not easily obtained with conventional methods. In this chapter, the  $\mu$ -PD growth of  $\text{Ce}^{3+}$ -doped  $\text{YAlO}_3$  fibers of high quality and transparency is introduced. In particular, a large amount of cerium (up to 0.7 mol%) can be incorporated into the lattice without constitutional supercooling effects and/or second-phase precipitations using  $\mu$ -PD. This is

possible due to the relatively high growth rates and the high temperature gradient near the vicinity of the solid/liquid interface during growth. The growth of up to 50% Yb-doped LuAG fibers has also been demonstrated.

Device-size crystals can be grown using  $\mu$ -PD without any degradation in quality or cracking and with low thermal strain compared to other methods. Moreover, precise control of the temperature and the crystal shape is easy in a  $\mu$ -PD system.

## 10.2 Growth of $\text{Ce}^{3+}:\text{YAlO}_3$

Ce:YAP single crystals are typically grown by the CZ method in molybdenum or iridium crucibles in a reducing atmosphere. The  $\text{Ce}^{3+}$  activator cation has a radius of 1.18 Å and an electron configuration of  $4f^1$ . The size of the  $\text{Ce}^{3+}$  and its chemical similarity to  $\text{Y}^{3+}$  suggest that it would preferentially replace  $\text{Y}^{3+}$  (1.06 Å) sites in the perovskite structure rather than the  $\text{Al}^{3+}$  (0.51 Å) sites. However, the radius of  $\text{Ce}^{3+}$  is still 12% larger than that of  $\text{Y}^{3+}$ . Therefore it is difficult to incorporate large amounts of cerium into the lattice in CZ growth without constitutional supercooling and second-phase precipitations, since the maximum concentration of  $\text{Ce}^{3+}$  in the crystal is limited by its low segregation coefficient and the growth conditions. Another problem related to the growth of crystals by the CZ method (with subsequent cutting of the crystal into pixel elements) is crack and twin formation. Easy twinning arises in the Ce:YAP crystal due to the similarity between the  $a$  (5.3265 Å) and  $b$  (5.1777 Å) lattice parameters [4]. However, the thermal expansion coefficients of YAP along the three crystallographic axes ( $4.2 \times 10^{-6}$ ,  $5.1 \times 10^{-6}$  and  $11.7 \times 10^{-6} \text{ K}^{-1}$  for  $a$ ,  $b$ , and  $c$ , respectively) differ greatly [5], which causes thermal stresses during crystal cooling. It is also responsible for twin and crack nucleation in Ce:YAP crystals.

The starting mixture of powders was loaded into an iridium crucible placed on a zirconia pedestal in a vertical high-purity and high-density alumina ceramic tube. The crucible was inductively heated using an RF coil coupled to an RF generator. Dense alumina and zirconia tubes were placed around the crucible for thermal insulation. Moreover, a vertical quartz tube was also used to improve thermal isolation (Fig. 10.1).

A  $\langle 001 \rangle$ -oriented Ce:YAP square rod about 2 mm on a side, cut from CZ-grown crystal, was used as the seed. The crystals were grown at various pulling rates from 0.02 to 0.10 mm/min. Undoped and  $\text{Ce}^{3+}$ -doped YAP single-crystal fibers with lengths of up to 150 mm and diameters of 0.5 mm to 2.5 mm were produced by the  $\mu$ -PD method. Short (10–15 mm) Ce:YAP crystals with large diameters (2.0–2.5 mm), intended for scintillation applications, were also grown. The scintillation performances of these  $\mu$ -PD crystals were compared with YAP pixels of a similar size cut and polished from commercial CZ crystal and used in  $\gamma$ -ray detectors for medical applications. In order to achieve this goal, the crucible nozzle was adapted to incorporate

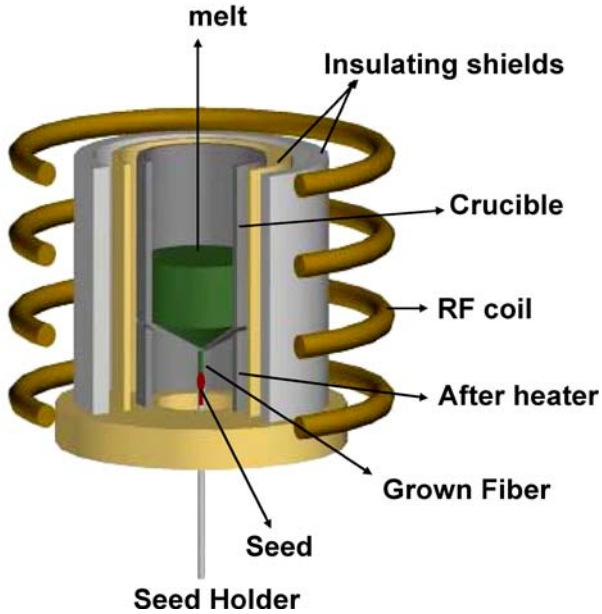


**Fig. 10.1.** Schematic diagram of hotzone part of  $\mu$ -PD growth apparatus

a die with an inner diameter of 2 mm. Thus, crystals about 2.5 mm in diameter were grown. As expected, better quality crystals were produced at low pulling-down rates. The best ones were grown at 0.05 mm/min. The crystals were typically transparent, crack-free, and single-phase (no garnet phase was apparent). Visible inclusions were not observed (Fig. 10.2).

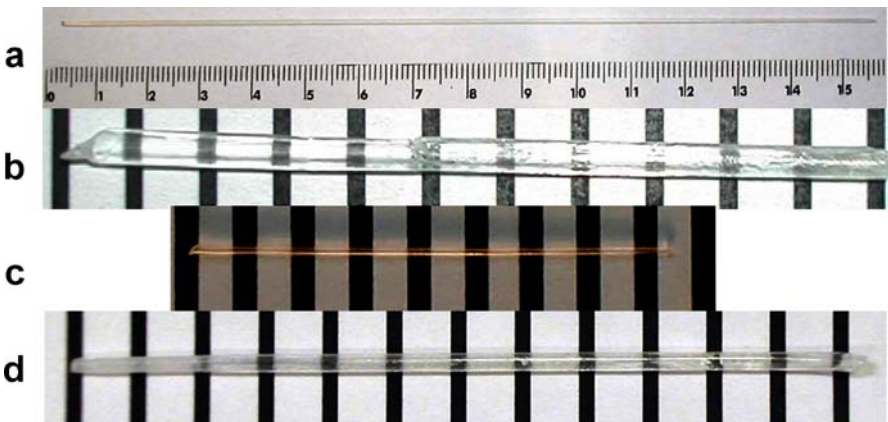


**Fig. 10.2.**  $\mu$ -PD YAP crystals: **a** 150 mm long of un-doped YAP, **b** 55 mm long of 0.2% Ce:YAP, **c** 40 mm long of 0.5% Ce:YAP, and **d** 60 mm long of 0.7% Ce:YAP

### 10.3 $\text{Ce}^{3+}:\text{YAlO}_3$ : Spectroscopy, Absorption, and Fluorescence

Figure 10.3 illustrates the results from absorption measurements of 0.2% Ce:YAP and 0.5% Ce:YAP fibers. Since  $4f \rightarrow 5d$  transitions are not parity-forbidden, they have very high absorption (and emission) cross-sections. This leads to a very high absorption coefficient in the UV absorption region, even for low-doped samples.

This fact, together with the small transversal dimensions of the crystals, makes measurements relatively difficult unless the sample is very thin. For this reason, very thin optically polished slices of fibers were prepared for absorption measurements: 0.3 mm thick for 0.2% Ce:YAP, and 0.25 mm thick for 0.5% Ce:YAP. In spite of the very low thickness (0.21 mm) of the most heavily doped samples, saturation of the absorption was unavoidable. Optical absorption bands from  $\text{Ce}^{3+}$  in 0.2% Ce:YAP and 0.5% Ce:YAP were observed due to electric dipole transitions from the  ${}^2F_{5/2}$  ground state to the first  $5d^1$  excited state. The spectra show four peaks at 303 nm, 291 nm, 275 nm, and 238 nm. These values are identical to those reported in [6]. Based on spectroscopic data, Weber [7] established the energy level diagram of the  $4f$  and  $5d$  configurations of  $\text{Ce}^{3+}$  in YAP at 300 K.

The four peaks seen in Fig. 10.3 originate from  $\text{Ce}^{3+}$  doping. An additional weak peak at about 220 nm exists in the energy level diagram for  $\text{Ce}^{3+}$ -doped YAP, but this is not very easy to spot in the absorption spectra of 0.2% Ce:YAP and 0.5% Ce:YAP. However, it is clearly visible in the

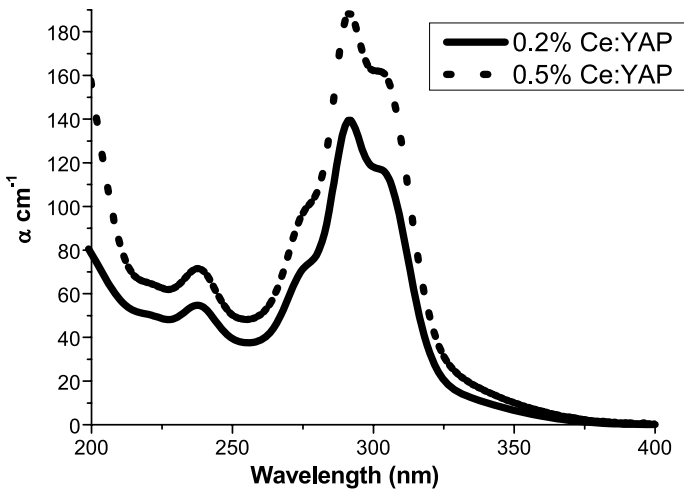


**Fig. 10.3.** Ce:YAP absorption spectrum in UV region for 0.2% Ce:YAP and 0.5% Ce:YAP

0.7% Ce:YAP spectrum. These five bands are all assigned to the  $5d$  levels of  $\text{Ce}^{3+}$ .

Figure 10.4 shows the polarized emission cross-section spectra, evaluated by means of the so-called  $\beta$ - $\tau$  method [8], from the  $\text{Ce}^{3+}$  in a 0.5% Ce:YAP fiber crystal, together with the spectra from the Ce:YAP pixel for comparison. These spectra arise from the transitions from the lowest crystal field components of the  $5d^1$  excited state to the  ${}^2F_{5/2}$  and  ${}^2F_{7/2}$  ground states, and present two largely overlapping broad bands with main peaks of  $6.61 \times 10^{-18} \text{ cm}^2$  located at 377 nm for the  $\sigma$  polarization and  $2.55 \times 10^{-18} \text{ cm}^2$  at 383 nm for the  $\pi$  polarization. The emission spectra from the pixel were very similar to those from the fibers. The slight dissimilarities observed in the peak positions and in the line shapes are probably related to different reabsorption processes inside the two samples. Indeed, it is possible that some photons in the short-wavelength part of the emission spectrum are reabsorbed before escaping the crystal due to the very high line strength of the transition. Since this probability depends on the doping concentration and the geometry of the sample, different specimens may exhibit small differences in their spectra.

The decay time was also measured for three  $\mu$ -PD crystals and a Ce:YAP crystal (pixel) grown by the CZ method for comparison. Experimental lifetime values were fitted to a unique exponential profile and the decay time was found to be 22 ns [9], in excellent agreement with published data [10].

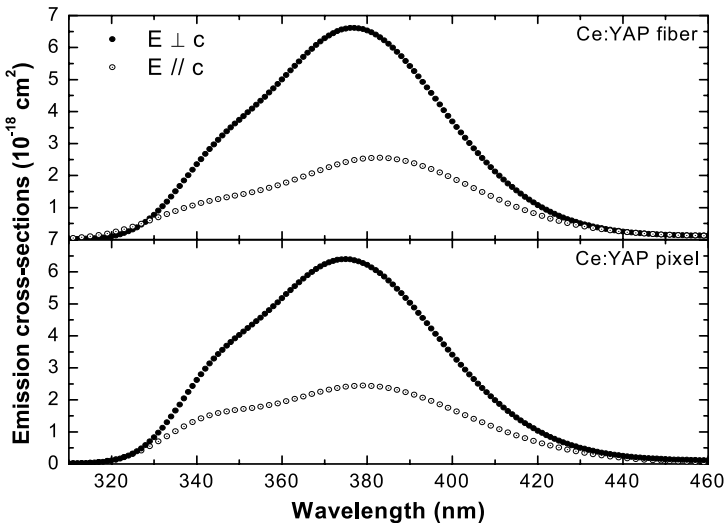


**Fig. 10.4.** Polarized room temperature emission cross-sections of the 0.5% Ce:YAP fiber crystal obtained from the emission spectra of  $5d \rightarrow 4f$  (*above*) and that of Ce:YAP pixel (*below*)

## 10.4 Scintillation Performance of $\text{Ce}^{3+}:\text{YAlO}_3$

The scintillation light yields were measured under gamma-ray excitation ( $^{22}\text{Na}$ ). The measurement set-up was a simple gamma-ray spectroscopy system with a photomultiplier tube (PMT) and multichannel analyzer. The photoelectron yield was defined as the number of photoelectrons ( $N_{\text{pe}}$ ) created at the photocathode of the PMT. The relationship between this number and the original number of photons per MeV ( $\Psi$ ) is

$$N_{\text{pe}} = \psi \cdot \varepsilon_{\text{QE}} E \cdot E_{\gamma} \cdot \eta, \quad (10.1)$$

where  $E_{\gamma}$  is the gamma-ray energy in MeV,  $\eta$  is the light collection efficiency, and  $\varepsilon_{\text{QE}}$  is the average quantum efficiency. The photoelectron yield of the YAP fibers was estimated in two ways: (i) via comparison with a calibrated scintillator (a BGO crystal was chosen as the reference crystal); (ii) using the single photoelectron electron peak of the photomultiplier tube (PMT), known as the Bertolaccini method [11]. More details on these calibration methods can be found in [9] and Table 10.1.

The spectra in Fig. 10.5 show the energy lost from gamma rays in a commercially produced  $2 \times 2 \times 10 \text{ mm}^3$  Ce:YAP crystal (CZ) and in 0.2% Ce:YAP and 0.5% Ce:YAP  $\mu$ -PD fiber crystals [9]. All measurements were repeated several times under the same conditions. Table 10.1 summarizes the results, including the relative light outputs and the energy resolution at 511 keV (when measurements were possible). The two fibers had nearly same light output (Table 10.1 and Fig. 10.5). This is seen from the position of the Compton edge. However, the 0.5% doped crystal had a much better energy resolution than the 0.2% one because it had a clear photopeak. The 0.2% Ce-doped fiber had no visible photopeak, which is unusual because the resolution normally depends on the photon statistics, which are nearly the same for both the 0.5% doped and the 0.2% doped crystals. Thus, the degradation of the energy resolution originated from another source. This may be the result nonuniform doping with cerium, very high absorption, nonuniform light collection from the surface, and/or crystal imperfections. The  $\mu$ -PD crystal yielded about 40% of the light output of the Ce:YAP pixel (CZ).

**Table 10.1.** Results from measurements of different scintillators (RLO = relative light output)

Scintillator	Compton edge (chn)	Photopeak (chn)	FWHM (chn)	RLO %	$N_{\text{pe}}$ (scint. Cal.)	$N_{\text{pe}}$ (PMT. Cal.)
Ce:YAP Pixel	1875±18	3022±13	10.8±0.2	100	1314±228	883±16
0.5% Ce:YAP	712±34	1191±62	15.9±1.4	39	518±149	328±18
0.2% Ce:YAP	743±15	–	–	41	549±99	347±18
BGO	880±10	1391±59	14.8±0.7	46	605±109	383±18

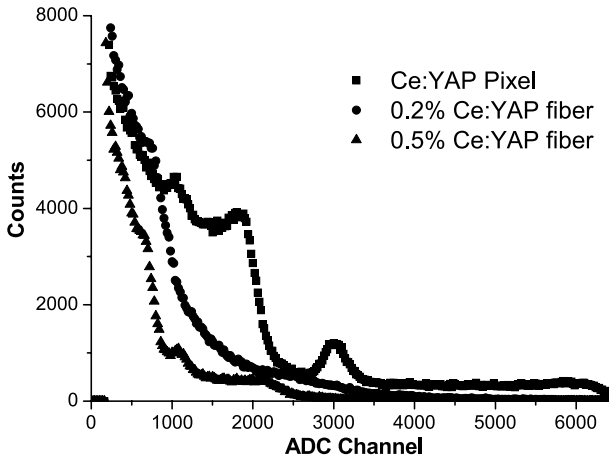


**Fig. 10.5.** Spectrum of 0.2% Ce:YAP and 0.5% Ce:YAP  $\mu$ -PD fiber crystals together with that of  $2 \times 2 \times 10 \text{ mm}^3$  Ce:YAP pixel produced from commercial CZ crystal

## 10.5 Growth and Spectroscopy of $\text{Yb}^{3+}:\text{Lu}_3\text{Al}_5\text{O}_{12}$

Fast Yb-doped scintillators are currently needed for low-background physics and for detecting neutrinos [12].  $\text{Yb}^{3+}$ -doped yttrium–aluminum garnets (YAG) and perovskites have primarily been developed for use as IR laser media. These crystals are transparent and have high heat conductivities and good mechanical properties. Along with IR emission,  $\text{Yb}^{3+}$  ions embedded into various hosts show charge transfer (CT) luminescence, which is interesting by itself. This CT luminescence has two bands in the UV (CT state  ${}^2\text{F}_{7/2}$ ) and the visible (CT state  ${}^2\text{F}_{5/2}$ ). A general feature of the CT luminescence of  $\text{Yb}^{3+}$  is its strong thermal quenching. Scintillation is fast, from a few to tens of ns depending on the temperature, the nature of the irradiation, and the content of Yb in the crystal [12].

The aim of this section is to discuss the crystal growth conditions and scintillation features of heavily Yb-doped LuAG. Since the segregation coefficient of Yb in garnet is close to unity, it is possible to incorporate large amounts of Yb into the lattice using the  $\mu$ -PD method without constitutional supercooling and second-phase precipitations. Up to 50% Yb-doped LuAG crystals have been grown by  $\mu$ -PD.

The crucible design was that of a cylinder with conical bottom and a capillary nozzle 2 mm in inner diameter with a tip 0.5 mm in diameter, enabling the growth of rod-shaped crystals 2.5 mm in diameter. The growth of high-quality crystals required controlled melting of the initial part of the original seed prior to the start of pulling, in order to eliminate some of the surface defects from the seed crystal that could propagate during the growth. The controlled seed melting was performed by immersing the seed into the cru-

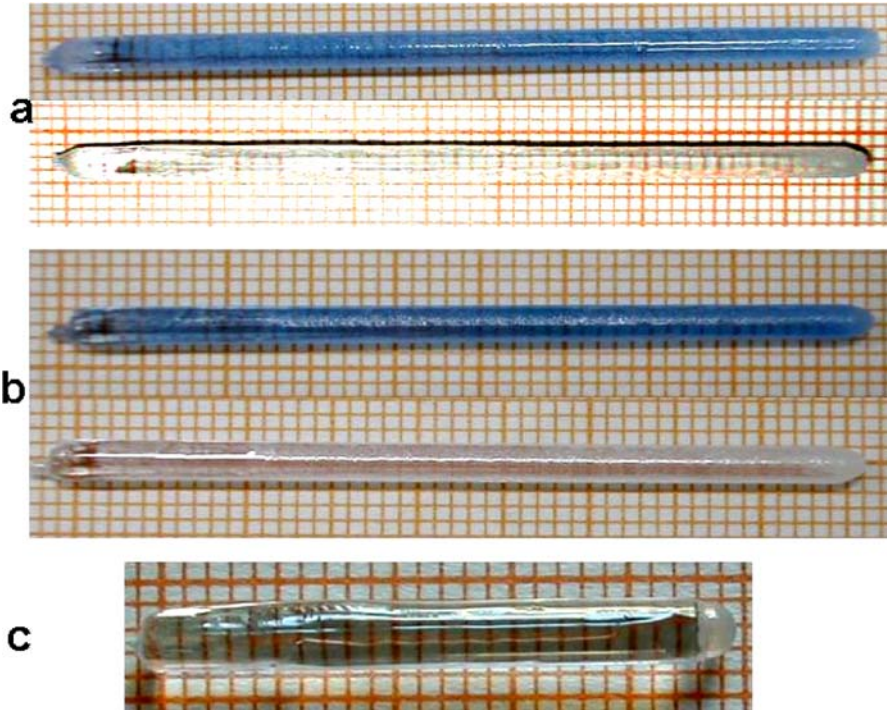


**Fig. 10.6.** Yb:LuAG  $\mu$ -PD crystals: **a** 10% Yb:LuAG before (*above*) and after (*below*) annealing, **b** 15% Yb:LuAG before (*above*) and after (*below*) annealing, and **c** 50% Yb doped LuAG

cible nozzle. Usually about 1 mm of the seed length was remelted just before the start of growth. The results from this growth are shown in Fig. 10.6. Transparent and crack-free crystals were obtained for these Yb<sup>3+</sup> concentrations. No visible inclusions were observed. As-grown crystals were pale blue in color. This may suggest the existence of color centers or even Yb<sup>2+</sup>, as indicated in the absorption spectra, because the crystals were grown in inert atmosphere and Yb<sup>3+</sup> can easily be reduced to Yb<sup>2+</sup>. After annealing in air at 1400 °C for 24 h, the color vanished.

## 10.6 Absorption and Fluorescence of Yb<sup>3+</sup>:Lu<sub>3</sub>Al<sub>5</sub>O<sub>12</sub>

The absorption spectra of as-grown 5% Yb:LuAG before and after annealing were measured in the wavelength range 200–3000 nm (Fig. 10.7). The figure shows that two absorption bands are positioned near 368.4 and 593.4 nm. These bands disappear after annealing at 1400 °C in air for 24 h (Fig. 10.7). Moreover, the 368.4 nm absorption band is attributed to the  $4f \rightarrow 5d$  transition of Yb<sup>2+</sup> in the LuAG host. Annealing of the LuAG crystals at different

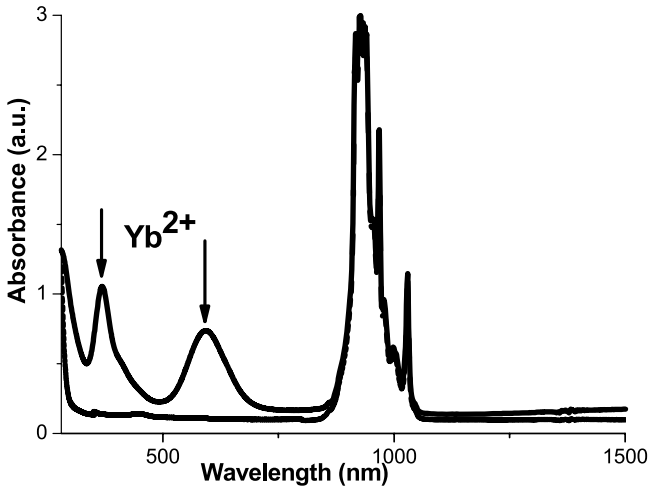
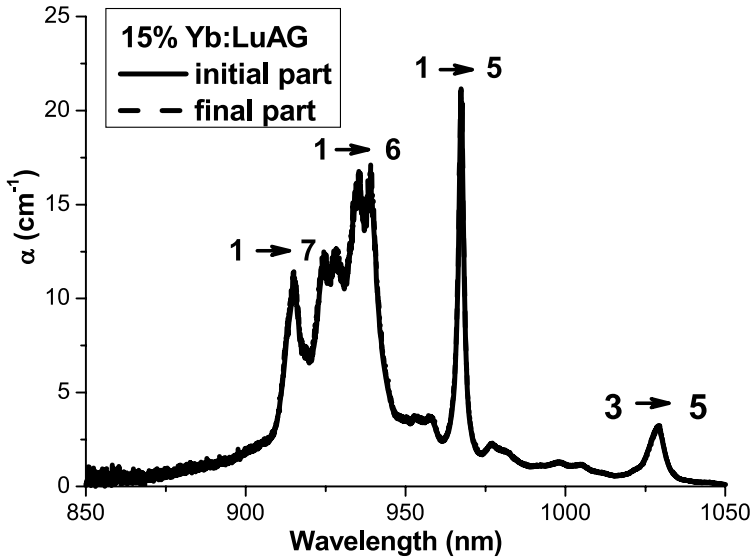


Fig. 10.7. Absorption spectra of 5% Yb:LuAG before and after annealing

thermal conditions verified that these two absorption bands weakened or disappeared simultaneously. Thus, the F center from  $Yb^{2+}$  is responsible for the absorption at 593.4 nm.

One of the advantages of  $\mu$ -PD is the high homogeneity in dopant distribution obtained along the growth axis. The distribution of  $Yb^{3+}$  cations was tested through absorption measurements. Comparison of the optical properties of  $\mu$ -PD crystals with those reported in the literature for bulk crystals produced with other methods was therefore possible. Measurements made in the 200–3000 nm wavelength region confirmed the absence of impurities to within the sensitivity of the spectrophotometer. The  $\mu$ -PD crystals had similar characteristics to those observed in bulk crystals grown by alternative techniques. The spectra taken from the initial and final portions of the same  $\mu$ -PD crystal overlapped perfectly, which confirmed the homogeneity of the  $Yb^{3+}$  distribution in the axial direction (Fig. 10.8). In particular, the peak values for the  ${}^2F_{7/2} \rightarrow {}^2F_{5/2}$  transition were  $\alpha = 21.06 \text{ cm}^{-1}$  at 967.3 nm in the initial part of the fiber and  $\alpha = 21.16 \text{ cm}^{-1}$  at 967.4 nm in the final part. Thus, the absorption coefficients were practically equal, as expected:  $\alpha_{\text{initial}} \approx \alpha_{\text{final}}$ . A comparison of the absorption coefficients associated with  $Yb^{3+}$  is also presented in Table 10.2.

Although the Yb ion has a simple electronic structure, with only one excited state ( ${}^2F_{5/2}$ ) above the ground state ( ${}^2F_{7/2}$ ), the absorption spectra are rather complicated because they consist of many different lines.  $Yb^{3+}$  ions replace  $Lu^{3+}$  in dodecahedral crystallographic sites (c-sites) of garnet structure with  $D_2$  local symmetry. The crystal field splits each manifold into  $(2J+1)/2$  Stark sublevels, where  $J$  is the total angular momentum of the  $4f^{13}$



**Fig. 10.8.** Adsorption spectra of 15% Yb:LuAG measured for initial and final parts of  $\mu$ -PD crystal. The arrows indicate the adsorption transitions between Stark levels corresponding to Fig. 10.9

**Table 10.2.** Absorption coefficients of transitions corresponding to Fig. 10.9

Bands $\text{cm}^{-1}/\text{Yb}^{3+}$ dopant	1 $\rightarrow$ 7	1 $\rightarrow$ 6	1 $\rightarrow$ 5	3 $\rightarrow$ 5
2.0% Yb:LuAG	1.43	2.04	2.62	0.47
5.0% Yb:LuAG	3.50	5.15	6.73	1.08
10% Yb:LuAG	6.67	10.12	13.37	1.97
15% Yb:LuAG	11.41	17.09	21.16	3.24
50% Yb:LuAG	33.1	51.20	33.05	5.60

electrons of the  $\text{Yb}^{3+}$ ; in this way, the  ${}^2\text{F}_{7/2}$  ground manifold splits into four sublevels, while  ${}^2\text{F}_{5/2}$  splits into three sublevels.

Therefore, a maximum of twelve lines are expected at the room temperature absorption and emission spectra. As for the  $\mu$ -PD crystals (Fig. 10.7), eleven absorption lines were observed in  $\text{Yb}^{3+}$ -doped LuAG. The main absorption peaks are labeled with arrows indicating the absorption transitions between Stark levels shown in Fig. 10.9.

Figure 10.10 shows the emission spectrum of a 15% Yb:LuAG  $\mu$ -PD crystal. Similar to absorption, the emission spectrum had a series of spectral lines corresponding to transitions between the various Stark sublevels shown in Fig. 10.9. This spectrum mainly differs from the absorption spectrum in

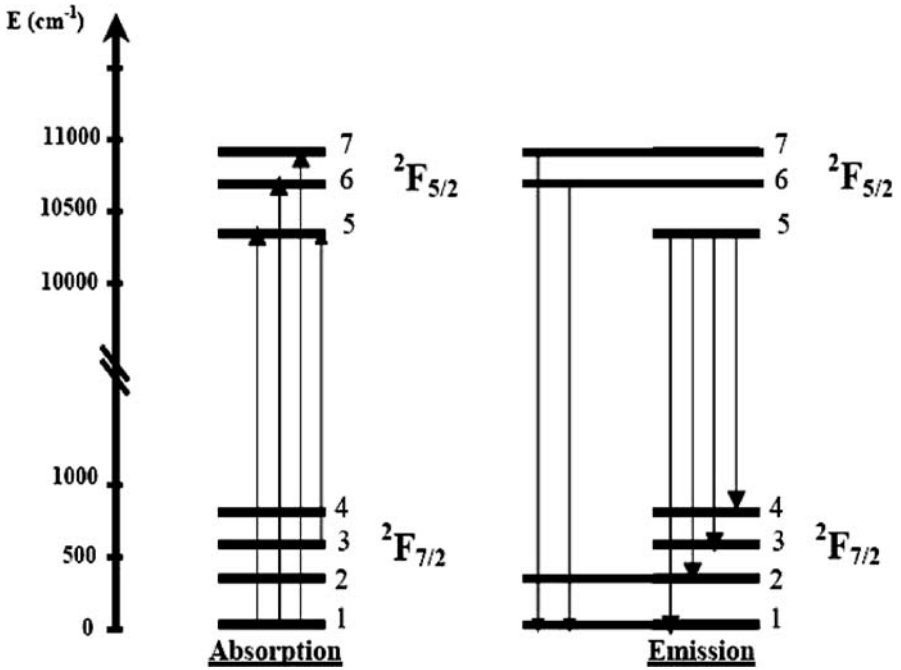


Fig. 10.9. Schematic energy levels diagram of  $\text{Yb}^{3+}$  for absorption, ( $^2\text{F}_{7/2} \rightarrow ^2\text{F}_{5/2}$  transition), and emission, ( $^2\text{F}_{5/2} \rightarrow ^2\text{F}_{7/2}$  transition)

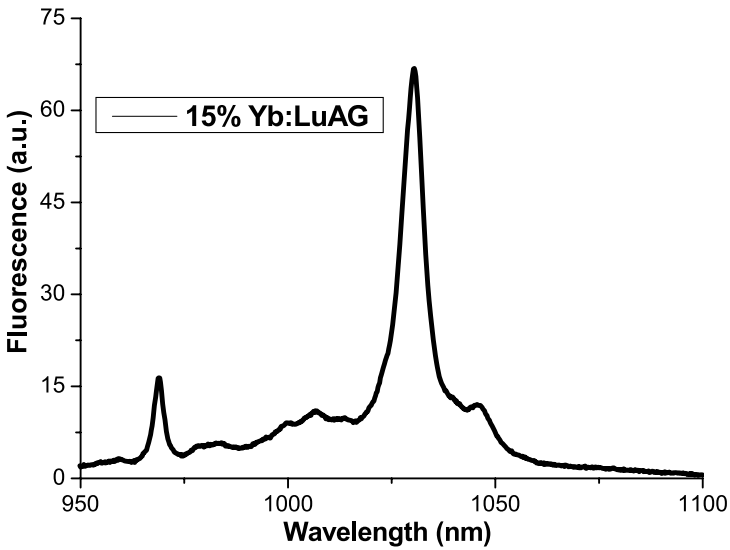


Fig. 10.10. Fluorescence spectrum of the  $^2\text{F}_{5/2} \rightarrow ^2\text{F}_{7/2}$  transition in 15%  $\text{Yb}:\text{LuAG}$

terms of the line intensities, largely due to the different Boltzmann populations of the starting levels.

## 10.7 Summary

The growth of Ce-doped YAP single-crystal fibers of different lengths and diameters by the  $\mu$ -PD method was introduced. The absorption and emission spectra of  $\mu$ -PD crystals are in good agreement with those reported in the literature. The light yields from these crystals are around 40% of those measured for commercial YAP pixels, and are similar to that of a  $\text{Bi}_4\text{Ge}_3\text{O}_{12}$  (BGO) crystal. At least two  $\mu$ -PD crystals had very similar light yields, differing by only 5% despite their significantly different doping levels (0.2% Ce:YAP and 0.5% Ce:YAP). Surprisingly, despite their similar light yields, the 0.2% cerium-doped crystal did not display a visible photopeak, while the 0.5% doped one did. These results are very promising if one takes into account the fact that the  $\mu$ -PD growth parameters are not completely optimized.

Heavily Yb (50%)-doped LuAG crystals were grown without constitutional supercooling and second-phase precipitations. The crystals were transparent, crack-free and no visible inclusions were observed. The distribution of  $\text{Yb}^{3+}$  along the growth axis was found to be homogeneous by absorption measurements.

The  $\mu$ -PD technique is capable of producing single-crystalline materials with uniform distributions of active dopants and with an optical quality comparable to or better than that of bulk crystals produced by conventional melt growth techniques. These features, in combination with their relatively low production and mechanical processing costs, demonstrate the potential of  $\mu$ -PD systems for commercialization. Shaped (fiber, rod, etc.) crystal growth, which leads to a relatively simple cutting procedure, and relatively low apparatus and running costs are additional advantages of this method that make it attractive in both research and industry.

## References

1. S. Andersen et al., Nucl. Instrum. Meth., **332**, 373 (1993)
2. J.A. Mares, M. Nikl, K. Blazek, Phys. Stat. Sol., **127**, K605 (1991)
3. J.A. Mares, M. Nikl, C. Pedrini, B. Moine, K. Blazek, Mater. Chem. Phys., **32**, 342 (1992)
4. G. Neuroth, F. Wallrafen, J. Cryst. Growth, **435**, 198–199 (1999)
5. G.J. Zhao, X.H. Zeng, S.M. Zhou, J. Xu, Y.L. Tian, W.X. Huang, Phys. Stat. Sol. A, **199**(2), 186–191 (2003)
6. S. Kammoun, M. Kamoun, Phys. Stat. Sol. B, **229**(3), 1321–1327 (2002)
7. M.J. Weber, J. Appl. Phys., **44**, 3205 (1973)

8. B. Aull, H. Jenssen, IEEE J. Quantum Electron., **18**, 925 (1982)
9. M. Alshourbagy, A. Toncelli, M. Tonelli, D. Herbert, A. Del Guerra, in 4<sup>th</sup> *International Symposium on Laser, Scintillation and Nonlinear Optical Materials*, Prague, Czech Republic, 27–30 June 2006, THU-O19
10. M. Nikl, Phys. Stat. Sol. A, **178**, 595 (2002)
11. M. Bertolaccini, S. Cova, C. Bussolatti, *A Technique for Absolute Measurement of the Effective Photoelectron per keV Yield in Scintillation Counters*, Proc. Nucl. Electr. Symp. (Versailles, France, 1968)
12. S. Belogurova, G. Bressi, G. Carugno, Yu. Grishkin; Nucl. Instrum. Meth. A, **516**, 58–67 (2004)

# 11 YAG:Nd<sup>3+</sup>: $\mu$ -PD and Czochralski Growth and Properties

Kherreddine Lebbou and Didier Perrodin

**Abstract.** Y<sub>3</sub>Al<sub>5</sub>O<sub>12</sub> (YAG) fiber-shaped single crystals about 1 m long and 0.3–1.0 mm in diameter, intended for laser applications, are discussed. Crystals with these dimensions are difficult to produce by simply cutting bulk crystals grown by the Czochralski technique or other related melt growth processes. The shape of the fibers permits the development of new optical components based on YAG crystals that have optical and thermal efficiencies that approach those of silica glass fibers. This chapter compares the physicochemical properties of YAG bulk and fiber crystals. The potential development of lasers based on single-crystalline fibers is discussed.

## 11.1 Introduction

YAG crystal has a garnet cubic structure of type {A<sub>3</sub><sup>III</sup>}[B<sub>2</sub><sup>III</sup>](C<sub>3</sub><sup>III</sup>)O<sub>12</sub>, space group  $Ia\bar{3}d$ . It forms in a Y<sub>2</sub>O<sub>3</sub>–Al<sub>2</sub>O<sub>3</sub> binary system. This structure provides a great scope for substitution at all of its cationic sites: dodecahedral {A}, octahedral [B], and tetrahedral (C). In the case of Y<sub>3</sub>Al<sub>5</sub>O<sub>12</sub>, the yttrium is located at the dodecahedral (largest) sites and the aluminum occupies the octahedral and tetrahedral sites. Because of size effects, rare earth (Re<sup>3+</sup>) dopants can partially replace the Y<sup>3+</sup> situated at the dodecahedral sites. The cubic YAG structure ( $a = 12.01$ ) is stable from room to melting temperatures, and YAG melts congruently at 1980 °C [1]. Table 11.1 summarizes the properties of YAG. Numerous YAG production methods were tested until the industrial production of YAG was achieved. An examination of the YAG crystal growth methods reported in the literature clearly indicates that growth from the melt is the best way to obtain high-optical-quality YAG, and the Czochralski (CZ) technique is currently the industrial method most commonly used to grow YAG bulk crystal from the melt.

YAG crystals have been grown by various growth technologies, such as CZ, Bridgman, edge-defined film-fed growth (EFG), LHPG, and the micro-pulling-down method ( $\mu$ -PD). This material is the most common oxide laser host. It was discovered in 1964 by Geusic and Van Uitert. The laser market has developed considerably since the introduction of the first ruby laser in 1960. Lasers are now advanced optical tools, used for an extraordinarily wide range of applications, which include medical, industrial, and military appli-

**Table 11.1.** Properties of YAG

Structure (space group)	Cubic ( $Ia\bar{3}d$ )
Density ( $\text{g}/\text{cm}^{-3}$ )	4.553
Phonon energy ( $\text{cm}^{-1}$ )	700
Cross-section (Nd)	$4.2 \times 10^{-19} \text{ cm}^{-2}$
Hardness (Mohs)	8.5
Thermal conductivity at 300 K ( $\text{W}/\text{mK}$ )	13
Thermal dilatation coefficient ( $10^{-6} \text{ m}/\text{K}$ )	7.5
Transmission window ( $\mu\text{m}$ )	0.24–6
Melting temperature	1980
Type of melting	Congruent
Refraction index	1.823
Starting material powder price (4N), 100 g	$\approx 450 \text{ US\$}$
Crystal price (1 kg)	$\approx 15000 \text{ US\$}$
Laser crystal orientation	$\langle 111 \rangle$
Fiber price (900 mm)	1100 US\$
Crystal dopant concentration ( $\text{Nd}^{3+}$ ), optical grade	0.1–1.2 at%
Transparency	visible

cations.  $\text{Y}^{3+}$  is optically inactive and can be substituted by active cations of  $\text{Nd}^{3+}$ ,  $\text{Ho}^{3+}$ ,  $\text{Er}^{3+}$ ,  $\text{Tm}^{3+}$ , and  $\text{Yb}^{3+}$ . For scintillation applications, YAG crystals are doped with  $\text{Ce}^{3+}$ , yielding yellow crystals. Yttrium–aluminum garnet crystals doped with Ce, Tb, and Eu are fast scintillators with excellent mechanical properties and chemical resistance. YAG scintillation detectors are preferred for electron microscopy, electron and X-ray imaging.

Thousands of meters of YAG boules are grown each year, and much effort has been expended in improving crystal quality. In particular, modeling efforts, such as those of Derby et al. [2], have a strong potential for technological and economic impact. There are a great number of articles and patents that describe successful improvements in YAG crystal growth technology. The application of the CZ technique leads to single crystals with bulk geometries (cylinders), which then require considerable and delicate machining and finishing to get useful single crystals (which are usually thin slices or fibers). Moreover, this process requires that the procedure is halted each time the melt in the crucible is used up. The CZ method also needs a considerable volume of melt (on the order of several liters). This constitutes a major shortcoming, because the crucibles are fabricated from rare metals such as iridium and are therefore expensive. These crucibles also have limited lifetimes (only a few crystallization cycles) because of chemical and thermal corrosion, which again increases the cost of the crystals considerably. This is why a great deal of effort has been recently made to develop processes and equipment that would allow the continuous preparation of preshaped crystals. In particular, methods of preparing fiber-shaped crystals through the use of a crucible

with a special shape (a fixed-drop configuration) were established. This approach meant that little or no machining of the as-produced single crystals was required.

Shaped crystal growth, and especially pulling-down technology, is immature. This process has been applied to grow silicon in the form of thin sheets [3]. This technique saves materials, lowering the cost of continuously producing semiconductor ribbons [4]. Three processes have been used to grow single-crystalline sheets and other shaped crystals. They are known as: (i) the Stepanov technique; (ii) the inverted Stepanov technique; and (iii) EFG. One of the main differences between these three processes is the magnitude of the contact angle ( $\phi$ ) between the molten silicon and the die material. For EFG,  $\phi$  should be much smaller than  $90^\circ$  (wetting). On the other hand,  $\phi$  should be larger than  $90^\circ$  in the Stepanov technique (nonwetting), while it can be more or less than  $90^\circ$  in the inverted Stepanov technique. Initially, pulling-down was used to manufacture semiconductor compounds, in a process where continuous crystalline tape was produced from the melt [5]. At around the same time, Jean Ricard et al. developed a process for continuous pulling-down crystal growth and film deposition [6, 7]. The process [7] was applied to Si, NaCl, Al<sub>2</sub>O<sub>3</sub>, ruby, and sapphire growth.

Single-crystal fibers are promising materials for high-optical-energy density lasers, including high-gain YAG:Nd. Much effort has focused on sapphire and YAG:Nd fibers [8–11] because these crystals are relatively easy to grow in a fiber shape and they can provide a basic understanding of the growth process and optical properties of single-crystal fibers. The micro-pulling-down ( $\mu$ -PD) technique is now routinely used to grow high-quality fibers used in 1.064- $\mu\text{m}$  and 1.32- $\mu\text{m}$  guided Nd-YAG fiber lasers [12]. This method allows the production of single-crystal fibers such as YAG with the following basic characteristics:

- the fiber is unusually long (up to 1 m)
- the diameter of the fiber is small
- high crystal quality is achieved
- highly doped crystals can be grown compared to those grown using CZ.

These properties make fiber crystals very attractive for a wide range of applications in lasers and optics. These fiber crystals should lead to the development of new optical components with high optical and thermal performances due to their high optical quality, which is similar to that of silica fibers. However, one of the main problems associated with pulling-down growth is the the ability of the process (and corresponding equipment) to produce considerably thin fibers. So far, the stationary pulling-down growth of single-crystalline fibers as thin as silica glass fiber (10  $\mu\text{m}$ ) has not been reported. The smallest diameter of a single-crystal fiber produced from the melt of the same composition is limited to few hundred microns because the melt behaves in fundamentally different ways when it is solidified into glass and crystalline solid. However, the demand for such thin fibers is very high.

YAG:Nd<sup>3+</sup> is ordinarily grown with dopant concentrations of 0.18–1.2%. It is possible to produce a relative variation in dopant concentration of less than 1% in  $\mu$ -PD fibers about 40 cm long. This is generally impossible when growth is performed by the CZ technique. The high chemical homogeneity of the fibers and the uniformity in their optical parameters have resulted in their use in lasers. When used for amplifier applications, single crystal fibers can handle more power and they reduce amplification noise compared to glass fibers. YAG single-crystal fibers can also be clad similar to glass fibers to profit from light guiding. This cladding morphology is comparable to that of glass optical fibers and will be crucial to the development of YAG single-mode crystal fibers [13].

## 11.2 Bulk and Fiber YAG Crystals Grown by Czochralski and $\mu$ -PD

The growth of bulk [14–16] and fiber [17] YAG single crystals and the characteristics of the resulting crystals have been widely studied. When intended for laser applications, the YAG crystals are doped with Nd<sup>3+</sup> in order to give them desirable properties. The doping level must be controlled precisely and be uniform throughout the crystal boule or the fibers at both macroscopic and microscopic scales. The growth of YAG crystals with high Nd<sup>3+</sup> concentrations is important, for example, in the case of Q-switch applications. Moreover, a high dopant concentration reduces excessive absorption without inducing heat effects such as thermal lensing [18].

Unfortunately, it is difficult to grow YAG:Nd with Nd<sup>3+</sup> concentrations of greater than 1.3% because of the difference in size between Nd<sup>3+</sup> and Y<sup>3+</sup>. The large ionic diameter of Nd<sup>3+</sup> makes it difficult to incorporate it into the Y<sup>3+</sup> site of the crystal lattice. The ionic radius of Y<sup>3+</sup> is 1.01 Å and that of Nd<sup>3+</sup> is 1.12 Å, giving a difference of about 10%. Therefore, it is difficult to grow highly doped YAG:Nd from the melt. In this case, the distribution coefficient  $k$  is much smaller than 1. The incorporation of large amounts of Nd<sup>3+</sup> causes stresses within the structure and increases the number of defects in it (such as inclusions, dislocation arrays, and striations) if the growth conditions are not carefully optimized. In general, the YAG crystals grown by the CZ technique are faceted via the facet segregation effect. The lattice parameter of the faceted regions has been shown to be slightly greater than that of the unfaceted ones [19]. The lattice strains associated with such facets can be observed through an optical microscope.

In CZ growth, the shape of the growth interface must be carefully controlled. This is achieved by optimizing the thermal gradient. This should be sufficient to prevent both faceting at the interface and constitutional supercooling at the boundary layer near the interface. On the other hand, very large thermal gradients must be avoided, since this can lead to large thermal stresses that increase the dislocation density and grain boundary forma-

tion. The stabilization of the thermal gradient is also an important factor in YAG:Nd bulk crystal growth. The growth rate remains constant with stable gradients and low temperature fluctuations, and fluctuations in Nd<sup>3+</sup> concentration are minimized. It is often easier to control the shape of the interface using  $\mu$ -PD than using a CZ system. In  $\mu$ -PD the interface is generally flat when YAG:Nd crystals are grown (Fig. 11.1). In both techniques, a flat solid/liquid interface is established by optimizing the hot zone configuration. This is a critical factor that allows the production of high-quality  $\mu$ -PD fibers with shapes close to that of an ideal cylinder. The shape of the interface is an additional growth parameter that represents the relationship between the axial and the radial temperature gradient in the vicinity of the interface, and finally the ability of the growth system to prevent faceting of the fibers [20].

According to our results, for a melt that corresponds well to congruent YAG, stationary growth conditions are observed when the meniscus length is  $H = 50 \mu\text{m}$ . A study of propagation loss in YAG:Nd fibers indicated that the dominant loss mechanism is surface scattering due to variations in fiber diameter that occur during growth as a result of thermal and mechanical instabilities. Bulk scattering caused by residual crystal defects near the fiber core can be made negligible through proper control of the fiber growth rate [21].

In the case of YAG bulk crystals grown by the CZ technique, the difficulties are related to mechanical and thermal instabilities. Mechanical instabilities follow from irregular rotation and translation and the size of the

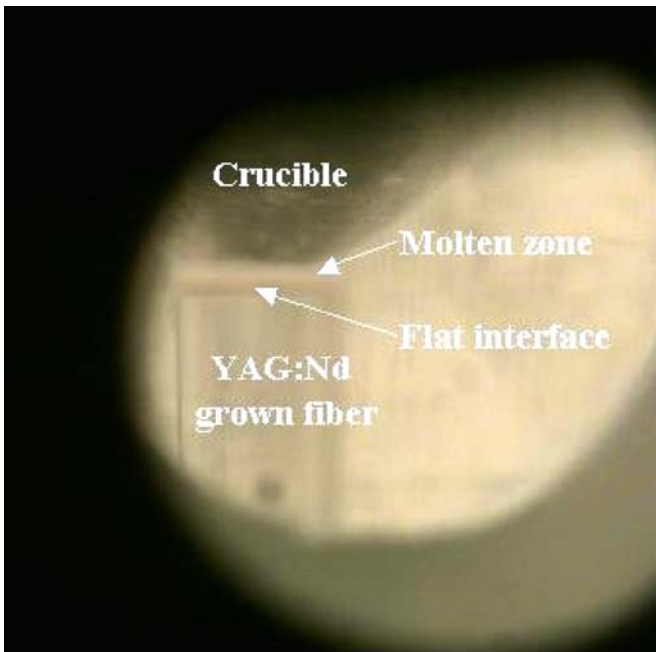


**Fig. 11.1.** Flat crystallization interface in YAG:Nd fiber crystal growth by  $\mu$ -PD

crystal. Temperature fluctuations are caused by poor environmental control of variables such as room temperature and process water. In a CZ system, the thermal gradient depends on the hot zone design. Low chemical homogeneity and the presence of a number of defects are the main disadvantages of bulk YAG:Nd crystals grown by the CZ method. The formation of interfacial facets near the core region of the crystal results in impurities and dopant inhomogeneities, mechanical stress, and stress-induced birefringence, which all affect the optical quality of the crystal. It is possible to avoid these bulk defects by cutting the rods around the core region. This is, in fact, the standard method of manufacturing laser rods from a CZ-grown boule. Obviously this method cannot be applied to single-crystal fibers [22]. YAG:Nd fibers grown by  $\mu$ -PD using an appropriate pulling rate and capillary die ( $\varnothing \leq 1$  mm) are free of core and scattering issues. They can therefore be utilized as grown. Figure 11.2 shows a  $\mu$ -PD-grown YAG:Nd fiber and a rod cut from a CZ boule.

In CZ crystal growth, the process is controlled by crystal or crucible weighing and an automatic diameter control system, which are needed to maintain the equilibrium during growth. However, the relation between the rate of change of the crystal weight and the radius is not a simple one because the load cell measures not only the static weight of the crystal but also the surface tension forces. There are a number of software programs that allow diameter control, although they sometimes cost about 30% of the price of the machine. In contrast, the process used to grow monodimensional fiber crystals by  $\mu$ -PD appears to be simpler than that used to grow bulk crystals by the CZ method (especially in the case of YAG). However, the simplicity of the

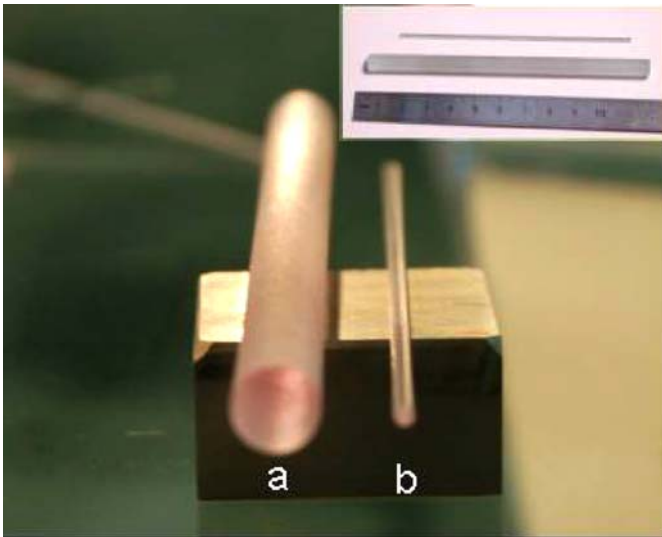


**Fig. 11.2.** YAG:Nd single crystal rod cut from the boule grown by Czochralski technique (a) and the fiber grown by  $\mu$ -PD (b)

operation depends on the size of the crucible, amount of melt in the crucible, the configuration of the thermal insulation around the crucible, and the sizes of the seeds and the fibers.

A few grams of starting material are needed to grow one meter of fiber crystal. However, over one kilogram of raw materials is normally required to fill about 70% of the crucible volume when growing bulk YAG with a CZ system. Crucible charging is also a time-consuming process when bulk crystals are considered. In the case of fibers, crucible loading is realized in one step. It is often difficult to apply continuous charging to the CZ process because of fluctuations resulting from the charging. One other advantage of  $\mu$ -PD is that it is relatively simple to clean the crucible after growth. This is performed, in particular, by adding Al<sub>2</sub>O<sub>3</sub> oxide in order to form eutectic YAG–Al<sub>2</sub>O<sub>3</sub>. In this case, it is easy to remove the melt from the crucible using high pulling rates (10 mm/min) [23, 24].

### 11.3 YAG Fiber and Bulk Crystal Characterization

Whatever the growth technology and the starting composition used, YAG:Nd crystals are normally transparent, even for a high Nd<sup>3+</sup> concentration (1.4%). The first fast characterization of the resulting crystal is based on nondestructive analysis. One of the procedures performed to gauge the potential applications of the fibers is an examination of the variation in fiber diameter. This is generally not necessary for CZ bulk crystals, because the boule is cut into pieces as per the design of the device that it is used in. CZ boules have to be polished for optical characterization. The shape of a fiber is much closer to the shape of the final product (a cylindrical laser rod), which makes their optical characterization easier. Figure 11.3 illustrates some YAG fibers grown by  $\mu$ -PD [25].

YAG fibers are normally oriented along the  $\langle 111 \rangle$  direction; they are typically transparent and homogeneous in diameter. The cross-section of the fiber is nearly circular with weak faceting, depending on the pulling rate and the power supplied to the crucible. The presence of facets is particularly related to segregation because the segregation coefficient of Nd is  $< 1$ . The standard method of post-growth machining practiced for CZ-grown crystals is generally not applicable to fibers. It is evident that even slight faceting decreases crystal quality and affects optical properties [22]. The neodymium distribution along the growth axis is uniform. In spite of weak faceting, significant variations in the concentration of the dopant in fibers up to 60 cm long are generally not detected. Significant variations in Nd<sup>3+</sup> concentration are however observed for lengths of  $> 60$  cm (Fig. 11.4).

YAG crystals grown by the CZ method show some scattering in the center of the crystal volume, which is observed by means of polarized optical microscopy. This scattering is known as a threefold strain, and it is observed near the center of bulk crystals grown on  $\langle 111 \rangle$ -oriented seeds. To study this phe-

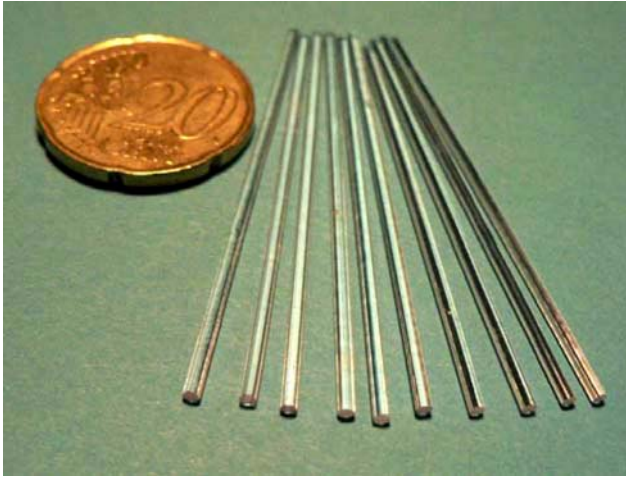


**Fig. 11.3.** High quality fiber crystals grown by  $\mu$ -PD under stationary growth conditions (FiberCryst Company)

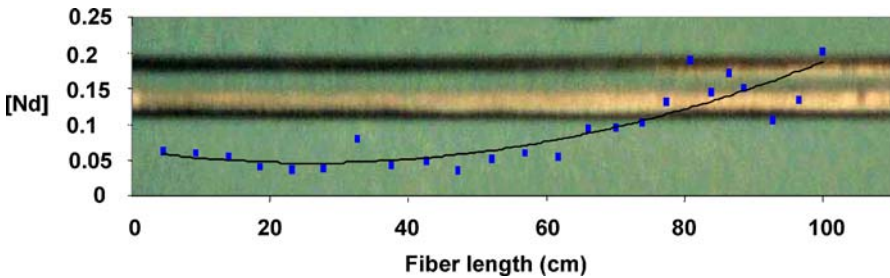


**Fig. 11.4.**  $\text{Nd}^{3+}$  distribution along YAG (111) fiber. The Nd concentration is practically stable up to 60 cm length

nomenon, the optical properties of YAG fibers were characterized as a function of pulling rate using relatively short specimens cut from long fibers and optically polished at both extremities. The specimens were inspected for the scattering visualization. Figure 11.5 shows the optically polished surface of a fiber grown along the  $\langle 111 \rangle$  direction from a melt doped with 0.1%  $\text{Nd}^{3+}$ . The fiber contains three fringes (black color), indicating good planarity, and hexagonal facets were not detected.

Fibers with diameters of about 1 mm or less were typically free of scattering. In contrast, the large-diameter crystals produced using the same pulling-down conditions exhibited scattering in the axial center of the crystal. When the pulling rate was changed quickly, regular striation along the direction of growth was detected, similar to that observed in the bulk crystals produced by CZ method. These striations can be related to variations in composition arising from modifications made to the growth parameters.

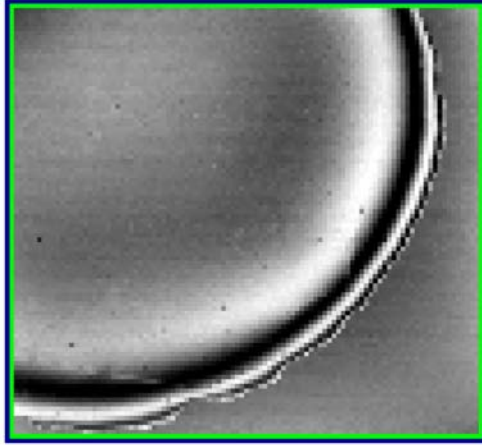


**Fig. 11.5.** Polished cross-section of YAG:Nd<sup>3+</sup> fiber grown along  $\langle 111 \rangle$  direction. The fiber diameter is 900  $\mu\text{m}$

The emission spectrum of the single-crystal fiber was obtained under excitation from a pulsed dye laser at 750 nm. The results are shown in Fig. 11.6. The observed spectrum was in good agreement with that of a specimen cut from CZ-grown bulk crystal and measured under the same conditions. At room temperature, the optically excited luminescence of the YAG:Nd<sup>3+</sup> crystal occurs at four main infrared wavelengths that correspond to transitions from the  $^4F_{3/2}$  state to Stark components of manifolds of the ground  $^4I_j$  term.

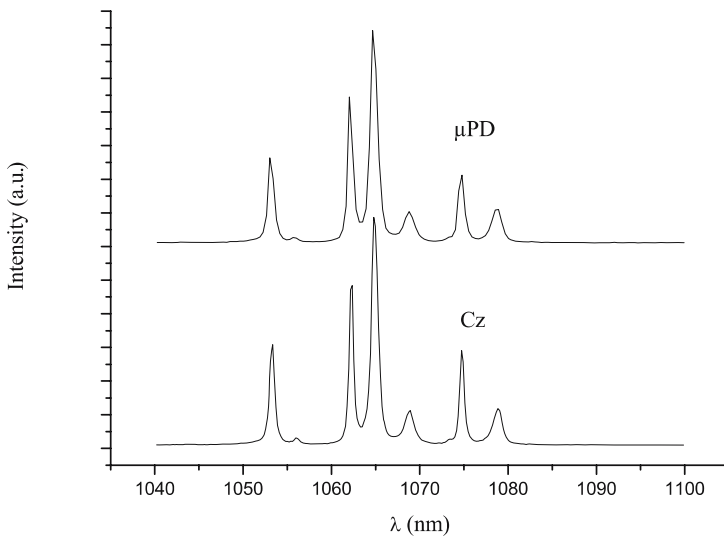


**Fig. 11.6.** Emission spectrum of Nd:YAG fiber and bulk crystals

The  ${}^4F_{3/2} \rightarrow {}^4I_{11/2}$  transition used for four-level laser emission at 1064 nm has been confirmed. Lifetimes for both the crystal fibers and the CZ bulk crystals were also examined; the values were 240  $\mu\text{s}$ , in good agreement with those reported in the literature (Fig. 11.7) [26].

In order to estimate the quality of the YAG fibers, optical characterization was performed, wherein a focused beam from a helium–neon laser was sent through the fiber in the axial direction. The output beam intensity was recorded with a digital camera connected to the computer. The best fiber gave a near-Gaussian profile (Fig. 11.8) under transmitted light, which confirmed that the fibers were defect-free and of high optical grade [27].

The light transmission and light-guiding properties of single-crystal fibers polished at both extremities as well as a rod cut from bulk crystal grown via CZ and mechanically machined to be close to the fiber size were measured at different wavelengths. It was found that the transmission of the fiber was close to 100% at 632.8 nm, and that it was higher than the transmission of the rod cut from bulk crystal and optically polished. The performance of the  $\mu\text{-PD}$ -grown fibers was confirmed by the light-guiding measurements; the fibers performed better than the rods cut from CZ crystals. Table 11.2 summarizes the light transmission and light-guiding measurements obtained at different wavelengths.

Laser emission was measured inside a two-mirror cavity. The output mirror had a transmission of 47% at 1064 nm and a curvature radius of 100 mm. The laser emission at 1064 nm was performed with a low threshold (around 10 W of pump power). The laser efficiencies of the rod prepared from the bulk crystal grown by the CZ technique and the fibers obtained by  $\mu\text{-PD}$

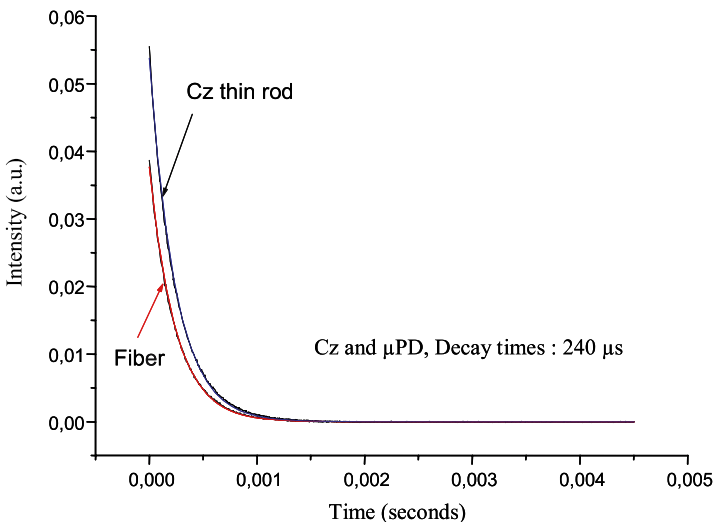
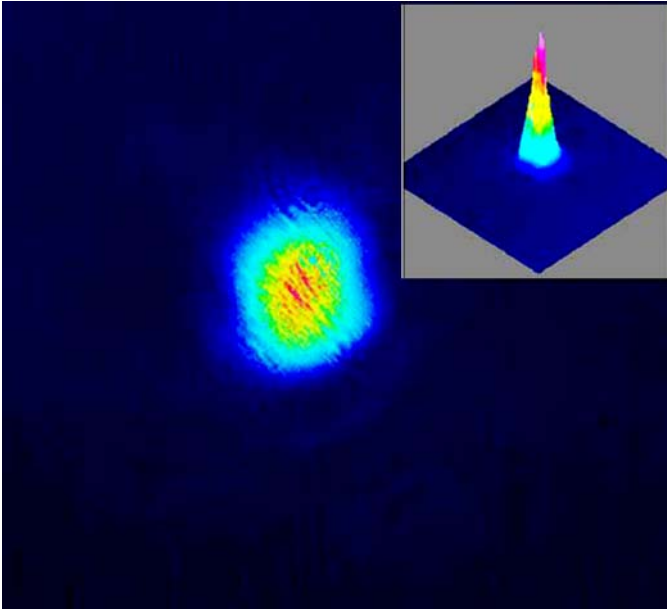


Fig. 11.7. Lifetime measurement for YAG:Nd fiber and bulk crystals



**Fig. 11.8.** Intensity profile of the transmitted light of a helium-neon laser beam sent through the YAG fiber

**Table 11.2.** Comparison of light transmission and light-guiding properties of  $\mu$ -PD-grown fiber crystals and a thin rod produced from a CZ boule crystal

YAG:Nd <sup>3+</sup> Crystal	Transmission (%)		Guiding (%)		
	632.8 nm	594 nm	808 nm	632.8 nm	594 nm
Cz thin rod ( $50 \times 1 \text{ mm}^2$ )	90.4	10	7.2	79.5	5.4
$\mu$ -PD fiber crystal ( $50 \times 1 \text{ mm}^2$ )	98.6	37.3	9	92.7	30.1

are shown in Fig. 11.9. Thus, 10.2 W of laser emission was achieved with the fibers, with an  $M^2$  quality factor of 5 for an absorbed pump power of 54 W. This leads to a slope efficiency of 22%. No thermal management problems were detected: no fracture, no coating damage, and the laser power was very stable.

The laser efficiency of the CZ rod crystal was about 56%, which is typical of YAG laser crystals. This study was performed by the ELSA team of the Optical Institute's Charles Fabry Laboratory [27]. This represents a dramatic improvement in terms of laser power for the single-crystal fiber produced in shape-ready form by  $\mu$ -PD technology. These results reflect a considerable improvement in the fiber crystal quality. Figure 11.10 illustrates the evolution of the laser power of YAG fibers as a function of time. It is clear that the

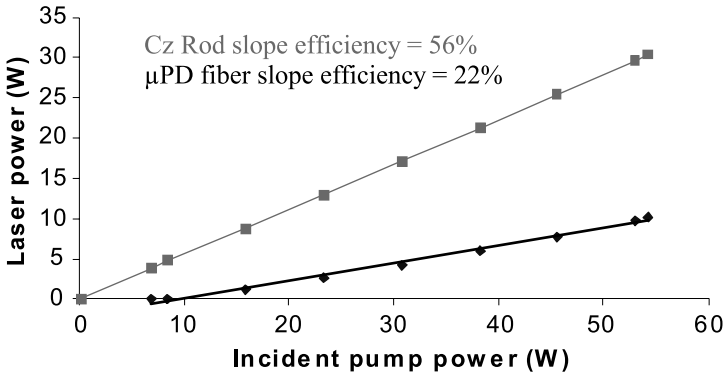


Fig. 11.9. Laser efficiency in continuous wave at 1064 nm of Nd:YAG single crystal fiber and bulk crystal

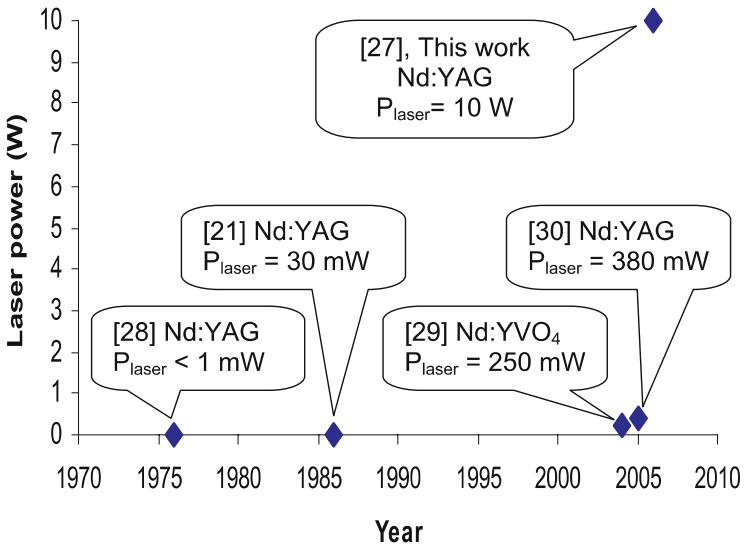


Fig. 11.10. Fiber laser powers milestones

YAG fiber crystals grown by  $\mu$ -PD could be used as substitutes for bulk YAG crystals grown by the CZ method. It is also obvious that the industrialization and commercialization of YAG crystals grown by  $\mu$ -PD requires the joint consideration of problems related to crystal growth technology, optics, lasers, and component design.

*Acknowledgement.* The authors are grateful to the staff of Fibercryst for their cooperation and for providing the facilities for crystal growth. They thank J. Didierjean, F. Balembois, P. Georges from ELSA (IOTA Laboratory) for their collaboration and great efforts in laser generation and improving fiber optics. We thank Professor V. Chani for a critical review of this chapter. We are indebted to the Lyon region, the CNRS and the French Ministry of Defense for their financial support.

## References

1. R.R. Monchamps, J. Cryst. Growth, **11**, 310 (1971)
2. J.J. Derby, R.A. Brown, J. Cryst. Growth, **83**, 137 (1987)
3. S. Berkman, M.T. Duffy, H.E. Temple, US Patent, 4,356, 152 (26 Oct. 1982)
4. S. Berkman, M.T. Duffy, Kyong Min Kim, G.W. Cullen, US Patent, 4,099,924 (11 July 1978)
5. J.J.L.E. Brissot, US Patent, 4,125,425 (14 Nov. 1978)
6. J. Ricard, C. Excoffon, US Patent, 4,233,338 (11 Nov. 1980)
7. J. Ricard, US Patent, 4,565,600 (21 Jan. 1986)
8. C.A. Burrus, Electron Lett., **12**(22), 600 (1976)
9. J. Stone, C.A. Burrus, Fibers Integr. Opt., **2**(1), 19 (1979)
10. M. Digonnet, C. Gaeta, H.J. Shaw, J. Lightwave Technol., **LT4**, 454 (1986)
11. V.I. Chani, A. Yoshikawa, Y. Kuwano, K. Hasegawa, T. Fukuda, J. Cryst. Growth, **204**, 155 (1999)
12. K. Lebbou, D. Perrodin, B. Hautefeuille, C. Dujardin, A. Brenier, J.M. Fourmigue, O. Tillement, C. Pédrini, in *4<sup>th</sup> International Symposium on Laser, Scintillator and Nonlinear Optical Materials*, June 26–30, 2006, Prague, Czech Republic
13. M.J.F. Digonnet, C.J. Gaeta, D.O. Meara, H.J. Shaw, J. Lightwave Technol., **LT5**, 642 (1987)
14. D.T.J. Hurle, (ed.), *Handbook of Crystal Growth* (North-Holland, Amsterdam, 1994)
15. B.R. Pamplin, *Crystal Growth*, 2nd edn. (Pergamon, Oxford, 1980)
16. D.T.J. Hurle, *Crystal Pulling From the Melt* (Springer, Berlin, 1993)
17. T. Fukuda, P. Rudolph, S. Uda, *Fiber Crystal Growth From the Melt*, Adv. Mater. Res. (Springer, Berlin, 2004)
18. E. Kanchanavaleerat, D. Cochet-Muchy, M. Kokta, J. Stone-Sundberg, P. Sarkies, J. Sarkies, J. Sarkies, Opt. Mater., **26**, 337 (2004)
19. B. Cockayne, J.M. Roslington, A.W. Vere, J. Mater. Sci., **8**, 382 (1973)
20. K. Lebbou, D. Perrodin, V.I. Chani, O. Tillement, O.A. Lebbou, J.M. Fourmigue, J. Didierjean, F. Balembois, P. Goerges, J. Am. Ceram. Soc., **89**(1), 77 (2006)
21. M. Digonnet, C. Gaeta, H.J. Shaw, J. Lightwave Technol., **LT4**(4), 454 (1986)
22. R.S. Fiegelson, J. Cryst. Growth, **79**, 669 (1986)
23. A. Yoshikawa, B.M. Epelbaum, T. Fukuda, K. Suzuki, Y. Waku, Jpn. J. Appl. Phys., **28**, L55 (1999)
24. A. Laidoune, H. Lahrach, Y. Kagamitani, K. Lebbou, F. Carrillo, C. Goutaudier, O. Tillement, J. Phys. IV, **113**, 129 (2004)
25. Fibercryst, *Website*, Accessed February 21, 2007, <http://www.fibercryst.com/>

26. K. Lebbou, A. Brenier, O. Tillement, J. Didierjean, F. Balembois, P. Georges, D. Perrodin, J.M. Fourmigue, *Opt. Mater.*, accepted
27. J. Didierjean, M. Castaing, F. Balembois, P. Georges, D. Perrodin, J.M. Fourmigué, K. Lebbou, A. Brenier, O. Tillement, *Opt. Lett.*, accepted
28. J. Stone, *App. Phys. Lett.*, **29**, 37 (1976)
29. A.S.S. de Camargo, *Opt. Lett.*, **29**, 59 (2004)
30. V.B. Tsvetkov, *Advanced Solid-State Photonics*, Technical Digest (The Optical Society of America, Washington, DC, 2005)

# 12 High-Melting Rare-Earth Sesquioxides: $\text{Y}_2\text{O}_3$ , $\text{Lu}_2\text{O}_3$ , and $\text{Sc}_2\text{O}_3$

Akira Yoshikawa and Andrey Novoselov

**Abstract.** In this chapter the application of the  $\mu$ -PD method to the crystal growth of refractory rare-earth sesquioxides with melting temperatures of over 2400 °C is demonstrated and discussed.

## 12.1 Introduction

Three main elements are necessary to obtain a laser: the laser host, the active ion, and the optical pump source. These elements are interactive and must be selected carefully and self-consistently to achieve a given system performance [1]. With the recent advances in and ready availability of InGaAs high-power laser diodes emitting between 900 and 990 nm,  $\text{Yb}^{3+}$  activator ions have gained renewed attention (they first gained prominence in the mid-1970s due to their use in flashlamp-pumped Yb-doped  $\text{Y}_3\text{Al}_5\text{O}_{12}$  or “YAG”) [2]. The  $\text{Yb}^{3+}$  ion possesses many advantages that arise due to its simple electronic structure, which involves only two states, the  ${}^2\text{F}_{5/2}$  excited state and the  ${}^2\text{F}_{7/2}$  ground state associated with spin-orbit coupling. Since there is only one  ${}^2\text{F}_{5/2}$  excited state, there is no excited state absorption, no cross-relaxation process and no more up-conversion or any internal mechanism which might otherwise impede population inversion and so reduce the effective laser cross-section in crystals without any other impurities. The main advantage of  $\text{Yb}^{3+}$  is its broad absorption band (about ten times broader than that of  $\text{Nd}^{3+}$ ), which is ideally suited for diode pumping. The low thermal load observed in  $\text{Yb}^{3+}$ -doped crystals (11% relative to 30–40% in  $\text{Nd}^{3+}$ -doped) is another feature that is important for high power applications [3, 4].

The laser performance of Yb-doped YAG strongly depends on temperature [5]. Therefore, new single-crystal hosts that possess the mechanical and optical advantages of YAG but surpass its thermal properties are needed. Rare-earth sesquioxides such as  $\text{Y}_2\text{O}_3$ ,  $\text{Lu}_2\text{O}_3$  and  $\text{Sc}_2\text{O}_3$  meet these requirements. They possess high values of thermal conductivity (13.6 for  $\text{Y}_2\text{O}_3$ , 12.5 for  $\text{Lu}_2\text{O}_3$ , and 16.5  $\text{W/m} \cdot \text{K}$  for  $\text{Sc}_2\text{O}_3$ ), greater than that of undoped YAG (11  $\text{W/m} \cdot \text{K}$ ) [6]. If the crystals are doped with 3 at% ytterbium ions, the thermal conductivity drops considerably: in case of yttria to 7.7, scandia to 6.6  $\text{W/m} \cdot \text{K}$ , while in lutecia the thermal conductivity decreases only slightly

to 11.0, and in YAG it drops to  $6.8 \text{ W/m} \cdot \text{K}$ . Their optical properties are characterized by a wide transparency, e.g., from  $0.23$  to  $8 \mu\text{m}$  (in the case of  $\text{Y}_2\text{O}_3$ ), which is higher than that of YAG (only  $0.24$ – $6 \mu\text{m}$ ). In addition, the effective phonon energies of  $\text{Y}_2\text{O}_3$ ,  $\text{Lu}_2\text{O}_3$  and  $\text{Sc}_2\text{O}_3$  are low compared to those of other oxides. Low phonon energy means low nonradiative transition rates between metastable electronic levels of luminescent ions incorporated into the lattices and therefore higher radiative probabilities and higher quantum efficiencies of their optical transitions.

The crystal structure of  $\text{Y}_2\text{O}_3$ ,  $\text{Lu}_2\text{O}_3$ ,  $\text{Sc}_2\text{O}_3$  and  $\text{Yb}_2\text{O}_3$  is another attractive feature. In general, isotropic crystals are preferable for optical applications. Furthermore, such crystals are easy to grow because of their thermal isotropy. At room temperature,  $\text{Y}_2\text{O}_3$ ,  $\text{Lu}_2\text{O}_3$ ,  $\text{Sc}_2\text{O}_3$ , and  $\text{Yb}_2\text{O}_3$  have bixbyite-type structures (C-modification), which is body-centered cubic, space group  $\text{Ia}\bar{3}$ , and contains 32 metal cations and 48 oxygen anions per unit cell or 16 formula units [7]. The rare-earth cations are situated at the centers of deformed cubes, in which six out of the eight corners are occupied by oxygen ions (Fig. 12.1). The unit cell contains 24 sites of  $\text{C}_2$  symmetry and 8 sites of  $\text{C}_{3i}$  symmetry. The lattice parameters are  $9.846$  ( $\text{Sc}_2\text{O}_3$ ),  $10.391$  ( $\text{Lu}_2\text{O}_3$ ),  $10.432$  ( $\text{Yb}_2\text{O}_3$ ), and  $10.602 \text{ \AA}$  ( $\text{Y}_2\text{O}_3$ ) [8]. The cubic structure is stable up to the melting point except in the case of  $\text{Y}_2\text{O}_3$ , which undergoes a phase transition to a high-temperature hexagonal structure close to the melting point [9].

Summarizing, we could say that there is only one problem (albeit an important one) with these very attractive laser hosts: bulk single-crystal growth of refractory rare-earth sesquioxides is not yet well established.

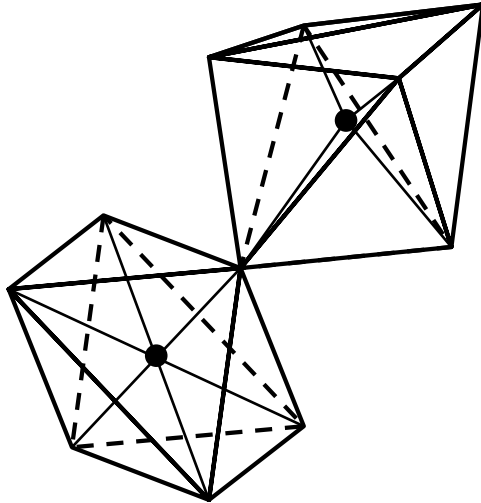


**Fig. 12.1.** Coordination about an oxygen ion in the bixbyite structure

## 12.2 Current Status of Crystal Growth Techniques for Refractory Rare-Earth Sesquioxides

The high melting points (over  $2400^\circ\text{C}$ ) of rare-earth sesquioxides impose severe limitations on the crystal growth techniques that can be applied to them. The high-temperature melt is very reactive, and so to avoid contamination with crucible material, crucible-free growth techniques such as the flame fusion or Verneuil method [10], a floating zone (FZ) technique called laser-heated pedestal growth (LHPG) [11, 12], or skull-melting (also known as the cold container method) [13] are used. In the Verneuil method, a powdered target material is melted by dropping it through a flame onto the seed or ceramic pedestal. Because it is difficult to control the completeness of the melting and cooling rates are high, the optical properties of the grown crystals are moderate, but still good enough for stimulated emission [14]. LHPG is a variety of FZ in which the heat of a laser beam melts a target material with a melting temperature of up to  $3000^\circ\text{C}$ . The method is suitable for growing fiber crystals for active, passive and nonlinear optical devices with diameters of up to 1 mm [12, 15]. However, this advantage becomes a disadvantage when larger crystals are required. Skull-melting uses a water-cooled crucible-like structure with a radiofrequency (RF)-heated melt that is held inside a thin solid skull-like shell of the same composition, thus preventing the contact of the melt with the crucible. The batch of crystal produced in this way can be quite big, up to tens of kilograms, but because the crystallization starts at many points simultaneously, it consists of smaller accidentally oriented crystals with high thermal stress [16].

Crystal growth from the crucible is generally more controllable and thus the quality of the crystals grown is higher. The most widely used growth method is the Czochralski technique [17]. The crystals obtained are expected to have low thermal stress and to be of high optical quality. However, the high melting points of rare-earth sesquioxides require that the crucible and surrounding thermal insulation are able to withstand these extreme conditions. The crucible must remain stable at a temperature well above the melting point of the growing material and should be resistant to chemical reactions with the melt. Thus, crucible materials usually employed, such as Pt or Ir, cannot be used. Fornasiero and coworkers [18] tested tungsten, molybdenum, and rhenium, and found that only rhenium (melting point  $3180^\circ\text{C}$ ) satisfies these requirements and could therefore be used for the Czochralski growth of rare-earth sesquioxides. However, at temperatures above  $2000^\circ\text{C}$ , Re reacts with the  $\text{ZrO}_2$  and  $\text{HfO}_2$  ceramics commonly used for thermal insulation. To avoid this, three Re rods were welded to the crucible as holders, so that the crucible was completely surrounded by gas, inert He, Ar, or a reducing mixture with 10–15 vol% of  $\text{H}_2$  without contacting the insulation. The crystals were grown in thin disks up to 10 mm in diameter and 3–6 mm thick. The failure to grow larger crystals was explained by the high emissivity of the melt combined with the opacity and low thermal conductivity of the grow-

ing crystal at high temperature. As a consequence, strong local overheating of the growth interface made process control impossible. As-produced Yb-doped  $\text{Sc}_2\text{O}_3$  crystals were used in laser experiments that demonstrated that the crystal quality required considerable improvement.

The Bridgman technique was also applied to grow Yb-doped  $\text{Y}_2\text{O}_3$ ,  $\text{Lu}_2\text{O}_3$ , and  $\text{Sc}_2\text{O}_3$  [19]. The Re crucible with the melt was lowered into the temperature gradient field and the crystallization was started from the bottom up. A seed crystal can be placed at the crucible bottom and the crystals grown are expected to be free of thermal stress except for a small volume near the crucible walls. The experimental set-up used was similar to that used for the Czochralski growth described above. The crystals were up to  $1\text{ cm}^3$  in volume and were tested in a diode-pumped laser set-up, but their optical quality was not high enough. The most successful growths were carried out by the heat exchanger method (HEM) [6] derived from the Bridgman technique. In this method, the crucible is set in an isothermal environment instead of being lowered through a temperature gradient field [20]. The solidification is performed by the controlled flow of the cooling gas through a heat exchanger at the center of the bottom of the crucible, where the seed is placed, and the crystallization starts from the cooled seed. However, the best  $\text{Sc}_2\text{O}_3$  crystals were grown without seed. These consisted of large crystallites, the biggest of which was  $4\text{--}5\text{ cm}^3$ , and others near the crucible walls were small and polycrystalline. The cooling gas applied was not sufficient to crystallize all of the melt, and the top part of the solidified melt contained gas bubbles.

Shaped growth of  $\text{Sc}_2\text{O}_3$  crystals by the EFG method was also reported [21]. A general schematic of the EFG technique can be found in Chap. 1. The crucible and the shaper were made of tungsten and growth was performed in Ar. Scandia ceramics was used for seeding and a piece of ceramics was placed on the top of the shaper to control the melting of the crucible charge. Rods with dimensions of  $\varnothing 3 \times 500\text{ mm}$  and  $\varnothing 10 \times 50\text{ mm}$  were produced. The rods were originally black with a silvery shade, but became colorless and transparent after annealing at  $2000\text{ }^\circ\text{C}$  in vacuum.

For the sake of scientific discussion, we should mention recent work on Yb-doped  $\text{Y}_2\text{O}_3$  transparent ceramics prepared by a vacuum sintering, which is currently the only method that allows the production of large laser media of sufficient quality based on rare-earth sesquioxides [22]. Other methods, such as flux [23] and electrochemical approaches [24], have produced crystals of rather limited size and crystal quality.

### 12.3 Application of the $\mu$ -PD Method

Since a diode-pumped solid-state laser needs an active element in the shape of a thin disk, which is easily prepared by cutting a  $\mu$ -PD-grown single-crystal rod,  $\mu$ -PD seems to be a very promising method for producing such elements using refractory rare-earth sesquioxides.

### 12.3.1 Set-Up, Crucible, Atmosphere, and “Crystal Growth Adventures” in the Very Beginning

Our interest in rare-earth sesquioxides arose in the late 1990s after a discussion between K. Petermann from the Institute of Laser Physics in Hamburg and B. Epelbaum, at that time a member of our team, during the 12<sup>th</sup> International Conference on Crystal Growth, held in Jerusalem, Israel, 1998. During the following year, K. Petermann visited Tohoku University to give a lecture on 31 August describing their advances in growth experiments, and A. Yoshikawa paid a reciprocal visit to Hamburg in October 1999. Shortly after, with the kind assistance of B. Epelbaum, a design for the Re  $\mu$ -PD crucible was developed. This crucible had an outer diameter of 16 mm, a conical section 9 mm in length and of angle  $45^\circ$ , a capillary channel of  $\varnothing 0.4$  mm, and a full crucible length of 45 mm. It should be noted that the cost of Re crucible was very high, and so over half a year passed before we obtained two crucibles.

The dimensions of the hot zone in  $\mu$ -PD are quite small compared with conventional Czochralski or Bridgman ones. This allowed us to quickly try out several thermal set-up combinations. This simplicity and ease of use is another advantage of the  $\mu$ -PD method. Three identical thermal zone set-ups making use of alumina, magnesia and zirconia ceramics were constructed, and experiments were finally started with the participation of J.H. Lee. YAG (melting temperature  $1970^\circ\text{C}$ ) was chosen as the target material, and standard alumina thermal insulation and an Ar protective atmosphere were used in the first experiment. When the temperature approached around  $1800^\circ\text{C}$ , black-colored fumes, most probably originated from the oxidation of Re, were observed and the growth had to be terminated. Although rhenium is sufficiently resistant to oxide melt, it has a very high sensitivity to any oxidizing agents present in the growth atmosphere, as well as to surrounding ceramics. To decrease the undesirable crucible oxidation, we added 1 and then 2 vol% of  $H_2$  to the growth atmosphere, and finally a mixture of high-purity Ar (99.999%) and 3–4 vol% of  $H_2$  was chosen. This proportion of  $H_2$  is lower than that used in work [18], 10–15 vol%, but it was found to be high enough to prevent the crucible from severe oxidization and yet still comply with security standards related to working with hydrogen gas.

After successfully growing YAG fiber crystals, sapphire, with its higher melting temperature of  $2050^\circ\text{C}$ , became the next target material on the path to growing rare-earth sesquioxides. Crucible cleaning is an important stage in any growth experiment, and boiling in an  $H_3PO_4+H_2SO_4$  mixture is routinely applied to clean a  $\mu$ -PD crucible made of iridium. However, the use of the same procedure to clean up the rhenium crucible containing the remains of the YAG melt was a big mistake; after 30 min of boiling we found that the crucible – not the YAG melt – was partially dissolved. This problem made us change our plans and move directly to  $Y_2O_3$  growth experiments.  $Y_2O_3$  can be dissolved in boiling hydrochloric acid and it is still safe for a rhenium

crucible. The remains of the partially dissolved crucible were used to prepare a cap for the remaining one. Without the cap we were not able to melt the  $Y_2O_3$  powder, even after increasing the radiofrequency generator power up to the maximum level. Covering the crucible with the cap provided extra thermal insulation, and so the use of the cap and radiofrequency heating resulted in the presence of (long-awaited) traces of melt at the crucible die. However, just before the W–Re wire used for seeding was lifted up to touch the melt, the picture from the CCD camera used to monitor the growth process was lost and some suspicious metallic sounds were noticed from the inside of the growth chamber. The experiment was stopped and after disassembling the growth chamber we found the hot zone to be destroyed. The alumina ceramic did not survive the high temperatures of  $> 2000\text{ }^\circ\text{C}$ ; the alumina stage, where the rhenium afterheater and the crucible were placed, was partially melted, causing the system to tilt and fall. Therefore, the alumina was replaced with magnesia ceramic since this more resistive to thermal stress (more so than zirconia ceramic in fact). Nevertheless, in the hydrogen-containing atmosphere at high temperatures, decomposition of MgO probably occurred and so decomposition products were deposited on the surface of the quartz tube surrounding the hot zone of the  $\mu$ -PD system, thus making visual control of the growth experiment impossible. Consequently, a combination of a zirconia ceramic thermal insulation set-up and an Ar+H<sub>2</sub> (3 vol%) growth atmosphere were used in subsequent experiments.

### 12.3.2 $\mu$ -PD Crystal Growth Results

$Y_2O_3$  was the first target material tested for the  $\mu$ -PD growth of rare-earth sesquioxides because it combines good laser host properties with a relatively low price of high-purity raw material powder (4N): an important feature considering the high probability of growth failure in initial experiments. The relative ease of rhenium crucible cleaning via boiling in HCl was an extra advantage. The availability of the seed crystal was another important factor for the first crystal growth experiments. Fiber crystals grown using seed crystals cut from Czochralski boules are the most common seeds used for  $\mu$ -PD experiments, but no seed crystal was available for the refractory rare-earth sesquioxides. Attempts to grow fiber crystals using W–Re wire for seeding were not successful. Therefore, a piece of high-purity yttria ceramic tube was used as a seed in order to grow the first yttria crystals, shown in Fig. 12.2. These crystals, still attached to the ceramic, were then used for seeding in the subsequent experiments.

Thus,  $(Yb_xY_{1-x})_2O_3$  ( $x = 0, 0.005, 0.01, 0.05, 0.08, 0.15, 0.20, 0.30$  and  $0.50$ ) shaped crystals were produced [25–27]. The rhenium crucible used in this and subsequent shaped growth experiments was 30 mm in outer diameter and 45 mm in length, with a shaped die of  $\varnothing 5 \times 2$  mm. The crystals of best quality were obtained at a pulling rate of 0.1 mm/min. As-grown crystals were 4.2 mm in diameter and 10–20 mm in length (Fig. 12.3). There was some in-

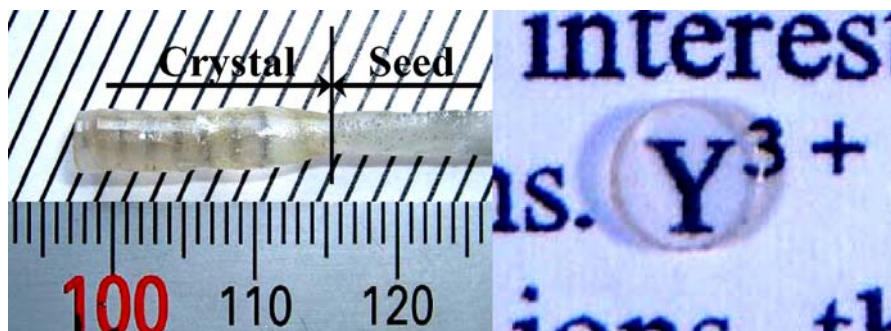


Fig. 12.2. The  $\mu$ -PD grown  $\text{Y}_2\text{O}_3$  crystal and its cross-section

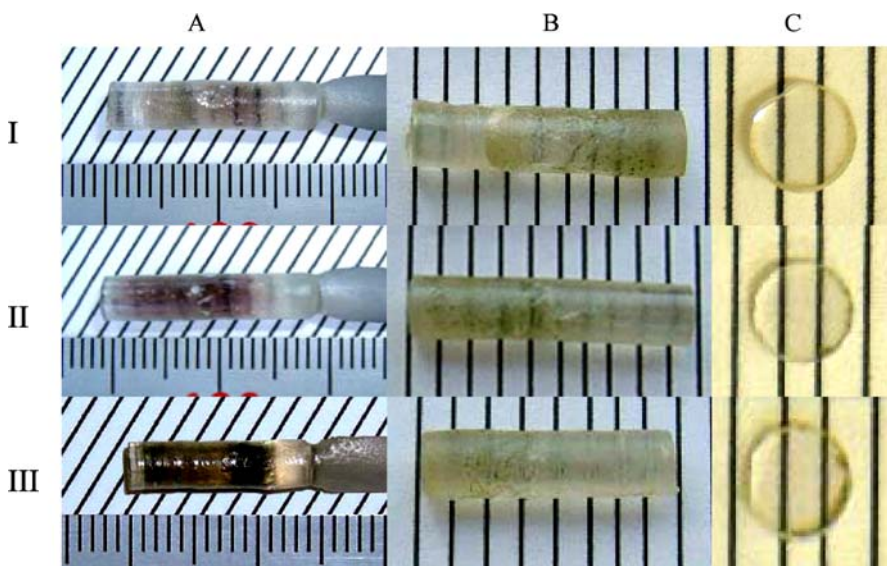


Fig. 12.3. Examples of Yb-doped  $\text{Y}_2\text{O}_3$  crystals: *I* – 5.0, *II* – 8.0 and *III* – 15.0 mol%; **A** – as-grown, **B** – annealed in air at  $1450^\circ\text{C}$  during 30 h, **C** – cut and polished

stability in crystal diameter but their surface was rather smooth.  $\text{Y}_2\text{O}_3$  melt wets rhenium well, making melt overflow more likely and therefore growth control troublesome. Yb-doped  $\text{Y}_2\text{O}_3$  has a gray-blue color, and its intensity depends on the Yb content. The blue coloration of Yb:YAG crystals grown in a neutral Ar or  $\text{N}_2$  atmosphere, which should actually be considered to be reducing at high temperatures, was associated with  $\text{Yb}^{3+} \rightarrow \text{Yb}^{2+}$  reduction [28]. In the case of Yb: $\text{Y}_2\text{O}_3$ , the atmosphere was definitely reducing, and so the appearance of  $\text{Yb}^{2+}$  ions was possible, and oxygen vacancies may have occurred too. The coloration was removed by annealing in air at  $1450^\circ\text{C}$

for 30 h. The crystals then became transparent without any visible defects; see Fig. 12.3.

Samples of the crystal compositions grown were examined using the XRD technique and comprised a single bixbyite phase, with no impurity phase observed. An example of the compositional dependence of the lattice constant of  $(Yb_xY_{1-x})_2O_3$  samples is given in Fig. 12.4. It has a linear character in the compositional interval studied and follows Vegard's law. Thus it was concluded that a continuous series of solid solutions was formed.

When crystal growth experiments with  $Lu_2O_3$  were initiated, it became clear that the rare-earth sesquioxide melting temperatures reported in the literature are quite approximate. Indeed, there is wide variation between different authors, e.g., the following melting points have been reported for  $Y_2O_3$ : 2410 [29], 2430 [18], 2440 [9] and 2450 °C [30]; for  $Lu_2O_3$ : 2427 [31], 2450 [6] and 2510 °C [9]; and for  $Sc_2O_3$ : 2405 [21], 2430 [18,23] and 2470 °C [9]. From our experiments, we came to the conclusion that only the data provided in [9] correlated with our observations. Because the melting temperature of  $Lu_2O_3$  is higher than that of  $Y_2O_3$ , and the wetting of the  $Lu_2O_3$  melt to the rhenium crucible is stronger, the potential for overflow increases. This greatly influenced the yields from the crystal growth experiments but we

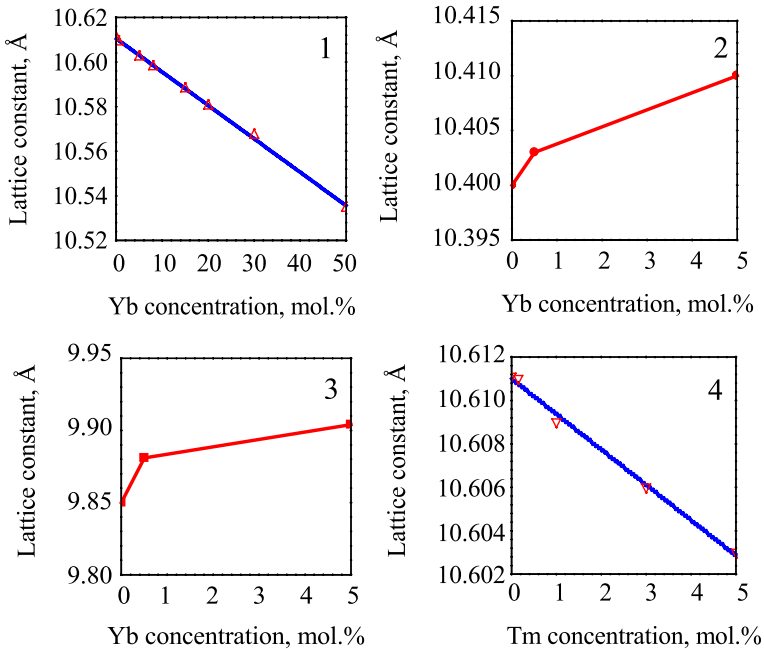


**Fig. 12.4.** Compositional dependence of the lattice constant of the  $\mu$ -PD grown crystals: Yb-doped  $Y_2O_3$  (1),  $Lu_2O_3$  (2) and  $Sc_2O_3$  (3), and Tm-doped  $Y_2O_3$  (4)

succeeded in growing a number of  $(\text{Yb}_x\text{Lu}_{1-x})_2\text{O}_3$  ( $x = 0, 0.005$ , and  $0.05$ ) single crystals using a ceramic seed [32]. As-grown crystals were 4.2 mm in diameter and 8–10 mm in length. The crystal surface was not as smooth as in the case of  $\text{Y}_2\text{O}_3$ , and some faceting was noted, but they were less colored. Annealing in air at  $1450^\circ\text{C}$  for 30 h was performed, and after cutting and polishing we did not observe any visible defects in these transparent samples. Phase homogeneity was investigated by XRD and no impurity phase was detected. The concentration dependence of the lattice parameter is shown in Fig. 12.4. Because of the limited number of experimental points, we could not definitively conclude that a continuous series of solid solutions were formed, but the results do suggest this.

Growth experiments with  $\text{Sc}_2\text{O}_3$  were even more complicated. Besides a high but not well-defined melting temperature and the now familiar problem with the high wettability of the melt, no scandia ceramic was available for seeding. Thus we had to seed using W–Re wire since it was the only material stable at these extreme conditions, and a few  $(\text{Yb}_x\text{Sc}_{1-x})_2\text{O}_3$  ( $x = 0, 0.005$ , and  $0.05$ ) single crystals were successfully grown in this way [33]. Pulling rates varied from 0.02 to 0.1 mm/min. The as-grown crystals were colored various tints of red, from pink to brownish, with no dependency on the dopant level observed; see Fig. 12.5. The crystals were 4.3 mm in diameter and around 10 mm in length, with strongly faceted surfaces. After annealing in air at  $1400^\circ\text{C}$  for 24 h, the crystals became colorless and transparent, but some defective skin (similar to that noted during the  $\mu$ -PD crystal growth of  $\text{Tb}_3\text{Sc}_2\text{Al}_3\text{O}_{12}$  garnet [34]) was observed. XRD analysis showed that the crystals grown were single-phase, and the concentration dependence of the lattice parameter is also given in Fig. 12.4. Similar to Yb-doped  $\text{Lu}_2\text{O}_3$ , we

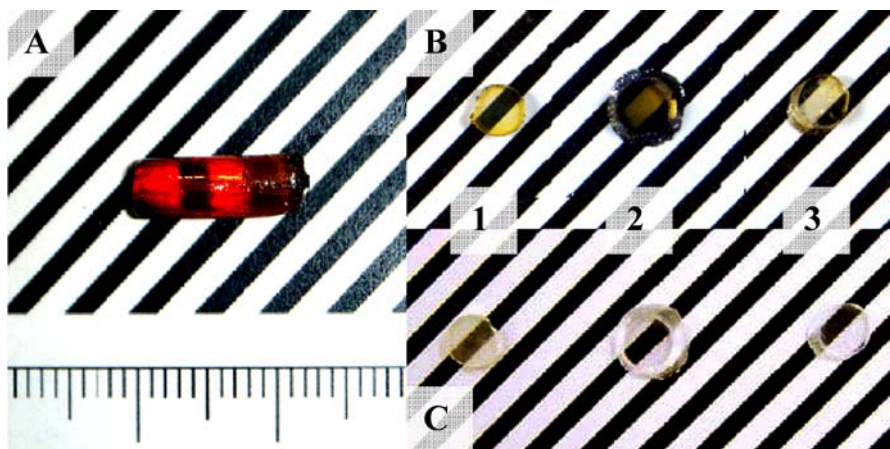


**Fig. 12.5.** The  $\mu$ -PD grown  $\text{Sc}_2\text{O}_3$  crystals: **A** – as-grown; **B** – cross-sections, 1 – 0.0, 2 – 0.05 and 3 – 5.0 mol%; **C** – cross sections of the crystals after annealing in air at  $1400^\circ\text{C}$  during 30 h

could not unambiguously conclude that a continuous series of solid solutions were formed.

Rare-earth sesquioxides were the crystals of interest in this work because they were considered to be promising laser hosts for doping with  $\text{Yb}^{3+}$ . However, they can be used as hosts for another active rare-earth ion as well.  $\text{Tm}^{3+}$  was proposed as a dopant for laser-diode-pumped solid-state lasers [35]. This can utilize commercially available laser diode pumping near 800 nm and operate in the eye-safe spectral range around 1.5–2  $\mu\text{m}$ , which is of interest for laser surgery and environmental sensing. To investigate the optical properties of Tm and to examine the suitability of rare-earth sesquioxides as a host for this activator, single crystals of  $(\text{Tm}_x\text{Y}_{1-x})_2\text{O}_3$  ( $x = 0.0015, 0.01, 0.03$  and  $0.05$ ) were also grown [36]. The crystals obtained were 4.2 mm in diameter and 13–20 mm in length, transparent, and free of visible defects. As the Tm content was increased some greenish coloration appeared, but after annealing at 1450 °C for 30 h the crystals became colorless. XRD patterns contained only reflections from the bixbyite single phase, with no impurity phase detected. The concentration dependence of the lattice parameter shown in Fig. 12.4 has linear character, following Vegard's law.

### 12.3.3 Crystal Quality

Crystal quality has a critical impact on laser performance. There are potentially a variety of types of defects that may occur: low crystallinity, color centers, impurities such as  $\text{Yb}^{2+}$  ions or inclusions of the crucible material, and stress-induced birefringence. Color centers found in rare-earth sesquioxide crystals grown in highly reducing atmosphere as well as  $\text{Yb}^{2+}$  cations can be removed completely by annealing at elevated temperatures in air. The application of a protective atmosphere during crystal growth allows crucible oxidation to be minimized and thus avoids the formation of rhenium precipitates in the crystals. A low pulling rate and carefully established thermal conditions help to decrease thermal stress.

The crystallinity of the  $\mu$ -PD crystals was examined by X-ray rocking curve (XRC) analysis for the (222) diffraction peak. Figure 12.6 shows XRCs for two  $\text{Y}_2\text{O}_3$  samples. The diffraction peak (222) is sharp with full widths at half maximum (FWHMs) of about 68 (undoped  $\text{Y}_2\text{O}_3$ ) and 72 arcsec ( $\text{Yb}:\text{Y}_2\text{O}_3$ , 5 mol%). FWHMs of about 80 and 100 arcsec were measured for undoped  $\text{Lu}_2\text{O}_3$  and  $\text{Sc}_2\text{O}_3$   $\mu$ -PD crystals, respectively. The main reason for the poorer crystallinity of the  $\text{Sc}_2\text{O}_3$  samples is believed to be the use of W–Re wire for seeding. Utilization of the best crystal grown for seeding in subsequent experiments would be helpful. These results are quite good taking into account that we are at the very earliest stage of applying the  $\mu$ -PD method to the growth of refractory rare-earth sesquioxides, and further improvement is expected.

The homogeneity of the dopant distribution was investigated by electron probe microanalysis. Results are given in Fig. 12.7 and demonstrate that the

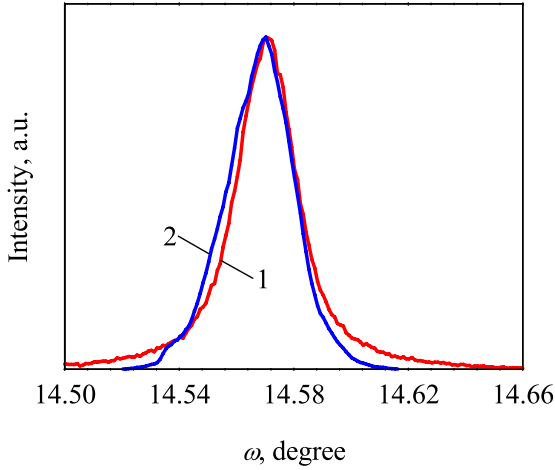


**Fig. 12.6.** X-ray rocking curves for the (222) reflection of  $\text{Y}_2\text{O}_3$  crystal samples: 1 – undoped and 2 –  $\text{Yb}:\text{Y}_2\text{O}_3$  (5 mol%)

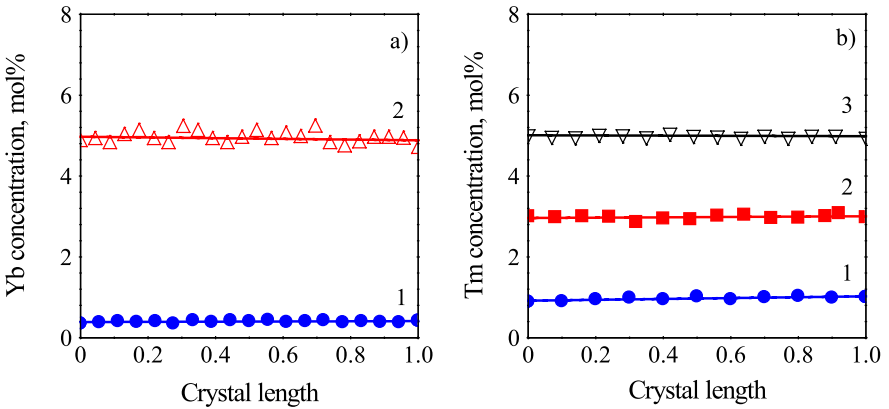


**Fig. 12.7.** Axial dopant distribution profile: **a** –  $\text{Yb}$ -doped  $\text{Lu}_2\text{O}_3$ , 1 – 0.5 and 2 – 5.0 mol%; **b** –  $\text{Tm}$ -doped  $\text{Y}_2\text{O}_3$ , 1 – 1.0, 2 – 3.0 and 3 – 5.0 mol%

$\mu$ -PD-grown crystals are of high axial compositional homogeneity. Natural convection was restricted in the crucible capillary micronozzle and the effective segregation coefficient of each constituent became unity along the growth axis, leading to a homogeneous composition throughout the crystal. However, in the case of  $\text{Yb}$ -doped  $\text{Sc}_2\text{O}_3$ , because of the large weight difference between the light scandium ion and the heavier ytterbium ion, thermocapillary Marangoni convection may play a role when a slow crystal pulling rate is applied, thus leading to some dopant nonuniformity across the radial crystal cross-section.

### 12.3.4 Thermal Conductivity

Thermal conductivity is another important characteristic of a laser crystal. High thermal conductivity becomes of particular importance when pumping by a high-power laser diode is considered. Because of its lower brightness compared to conventional lasers, optimizing pump-to-cavity mode matching requires a thin laser crystal but also one with a high dopant concentration to ensure reasonable absorption. However, published data on the thermal conductivities of rare-earth sesquioxides are contradictory. For example, the thermal conductivity of  $\text{Y}_2\text{O}_3$  has been measured as high as  $27 \text{ W/m} \cdot \text{K}$  [37], while a much lower value of  $13.6 \text{ W/m} \cdot \text{K}$  has also been reported [6]. To clarify this ambiguity, we obtained more refined data on the thermal conductivities of pure and Yb-doped  $\text{Y}_2\text{O}_3$ ,  $\text{Lu}_2\text{O}_3$ ,  $\text{Sc}_2\text{O}_3$  and Tm-doped  $\text{Y}_2\text{O}_3$  [27,32,36]. These data were calculated using updated values for thermal diffusivity, heat capacity, and density. Thermal diffusivity was measured by a laser flash method with a Nd glass laser (1060 nm) and an InSb infrared detector under vacuum. Heat capacity was determined with differential scanning calorimetry in the temperature range from room temperature to 823 K in a high-purity (99.999%) argon atmosphere. Density was obtained by the Archimedes method. The compositional dependency of thermal conductivity, see Fig. 12.8, showed an expected drop as the dopant concentration was increased. In the case of Yb: $\text{Lu}_2\text{O}_3$  (5 mol%), the thermal conductivity decreases slightly from 14.32 to 12.42  $\text{W/m} \cdot \text{K}$ . A more pronounced drop from 15.94 to 8.34  $\text{W/m} \cdot \text{K}$  was observed for Yb: $\text{Y}_2\text{O}_3$  (5 mol%), and from 15.94 to 7.46  $\text{W/m} \cdot \text{K}$  for Tm: $\text{Y}_2\text{O}_3$  (5 mol%). The most severe decrease was found for Yb: $\text{Sc}_2\text{O}_3$  (5 mol%), from 14.6 to 4.12  $\text{W/m} \cdot \text{K}$ . When the Yb ion replaces Lu (both of which have very similar atomic weights), the phonons are not scattered as much as in the case of Yb-doped  $\text{Sc}_2\text{O}_3$ , where difference between the heavy Yb and the light Sc ions is significant.

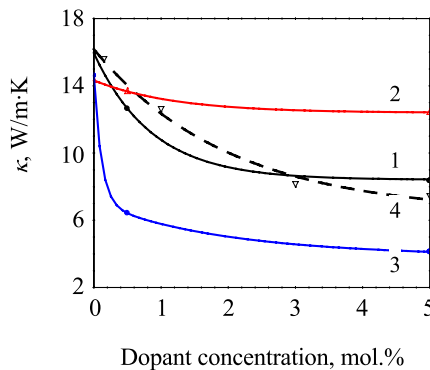


**Fig. 12.8.** Concentration dependence of thermal conductivity of Yb-doped (1–3) and Tm-doped (4) samples: 1, 4 –  $\text{Y}_2\text{O}_3$ , 2 –  $\text{Lu}_2\text{O}_3$  and 3 –  $\text{Sc}_2\text{O}_3$

### 12.3.5 Selected Optical Properties

The absorption, emission and Raman spectra recorded for Yb-doped Y<sub>2</sub>O<sub>3</sub> samples appeared to be very similar to those obtained on LHPG fibers [38], and so their Yb<sup>3+</sup> Stark level assignments were used [32]. The energy diagram of Yb<sup>3+</sup> was calculated from the experimental absorption and emission data. The results are provided in Table 12.1, where the data for Yb-doped Lu<sub>2</sub>O<sub>3</sub> and Sc<sub>2</sub>O<sub>3</sub> are listed too. The Raman shifts acquired at room temperature exhibited their highest energy transition at 377 cm<sup>-1</sup>. The absorption spectrum of the Yb:Y<sub>2</sub>O<sub>3</sub> (5 mol%) crystal sample (Fig. 12.9) consisted of three lines assigned to transitions from the lowest level of the ground state to the three components of the excited state: the zero-line centered at 975 nm and the 1–7 and 1–6 lines at around 905 and 950 nm, respectively. The emission spectrum exhibits high-intensity and broad lines at 1029 nm that most probably contain the transition of the first excited multiplet to both the second and third Stark levels of the fundamental because of the low energy splitting of these two levels. The low efficiency of the 0-line emission at 979 nm is favorable to a quasi-four-level scheme for laser application. The decay time of the <sup>2</sup>F<sub>5/2</sub> excited state was measured on the 1030 nm emission line after irradiating with a 904-nm excitation wavelength and it was approximated to 1.25 ms via single exponential fitting. Corresponding decay times of Yb-doped Lu<sub>2</sub>O<sub>3</sub> and Sc<sub>2</sub>O<sub>3</sub> are also provided in Table 12.1.

In Tm:Y<sub>2</sub>O<sub>3</sub>, laser excitation in the Tm<sup>3+</sup>(4f<sup>12</sup>) <sup>3</sup>H<sub>4</sub> multiplet at room temperature results in a broadband emission at around 2 μm, suitable for an eye-safe solid-state laser [36]. This emission originates mainly from <sup>3</sup>F<sub>4</sub> → 4f<sup>12</sup> lower level transitions. The <sup>3</sup>F<sub>4</sub> fluorescence decay time increased significantly from 0.60 to 3.08 ms as the Tm<sup>3+</sup> content was increased from 0.15 to 5 mol%, respectively.

**Table 12.1.** Results of attempts to interpret the Yb<sup>3+</sup> energy level schemes and measured <sup>2</sup>F<sub>5/2</sub> decay times in μ-PD-grown rare-earth sesquioxides. All samples were 5 mol% Yb-doped

Parameters		Host crystal		
Energy, cm <sup>-1</sup>		Y <sub>2</sub> O <sub>3</sub>	Lu <sub>2</sub> O <sub>3</sub>	Sc <sub>2</sub> O <sub>3</sub>
<sup>2</sup> F <sub>5/2</sub>	7	11080.3	11071.7	11186.9
	6	10554.1	10528.5	10626.9
	5	10282.8	10243.8	10257.5
<sup>2</sup> F <sub>7/2</sub>	4	918.7	980.7	985
	3	493.4	561.8	653.9
	2	339.9	414.5	458
	1		0	
τ, ms		1.25	1.29	0.59

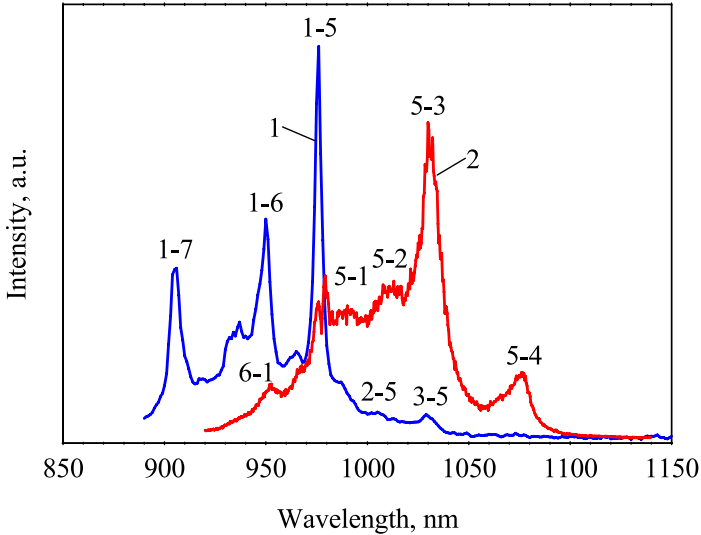


**Fig. 12.9.** Absorption (1) and emission (2) spectra of Yb-doped (5 mol%)  $\text{Y}_2\text{O}_3$   $\mu$ -PD crystal

## 12.4 Conclusions

We have described the results of  $\mu$ -PD single-crystal growth experiments using rare-earth sesquioxides with high melting temperatures of around 2400–2500 °C. Some supplementary data on the crystallinity, compositional homogeneity, thermal conductivity and optical properties of the single crystals obtained have been provided and discussed. Since the laser crystals used inside laser cavities do not need large rods (only small ones, on the scale of the cylindrical rods demonstrated), the  $\mu$ -PD method can be considered to be a competitor to the conventional Czochralski or Bridgman laser crystal growth methods and the laser ceramic production technique.

## References

1. W. Koecher, *Solid-state laser engineering*, 5th edn. (Springer, Berlin, 1999)
2. G.A. Bogomolova, D.N. Vylegzhanin, A.A. Kaminskii, *J. Exp. Theor. Phys.*, **42**, 440 (1976)
3. L.D. DeLoach, S.A. Payne, L.L. Chase, L.K. Smith, W.L. Kway, W.F. Krupke, *IEEE J. Quantum Elect.*, **29**, 1179 (1993)
4. D.M. Baney, G. Rankin, K.W. Chang, *Appl. Phys. Lett.*, **69**, 1662 (1996)
5. D.S. Sumida T.Y. Fan, in *Advanced Solid State Lasers*, ed. by T.Y. Fan, B.H.T. Chai, *Opt. Soc. Am. Proc.*, vol. 20 (Optical Society of America, Washington, DC, 1994), p. 100

6. V. Peters, A. Bolz, K. Petermann, G. Huber, *J. Cryst. Growth*, **237-239**, 879 (2002)
7. L. Pauling, M.D. Shappel, *Z. Kristallogr.*, **75**, 128 (1930)
8. F. Hanic, M. Hartmanova, G.G. Knab, A.A. Urusovskaya, K.S. Bagdasarov, *Acta Cryst. B*, **40**, 76 (1984)
9. A.V. Shevthenko, L.M. Lopato, *Thermochim. Acta*, **93**, 537 (1985)
10. R.A. Lefever, G.W. Clark, *Rev. Sci. Instrum.*, **33**, 769 (1962)
11. D.B. Gasson, B. Cockayne, *J. Mater. Sci.*, **5**, 100 (1970)
12. J. Stone, C.A. Burrus, *J. Appl. Phys.*, **49**, 2281 (1978)
13. V.V. Osiko, *J. Cryst. Growth*, **65**, 235 (1983)
14. N.C. Chang, *J. Appl. Phys.*, **34**, 3500 (1963)
15. M.M. Fejer, J.L. Nightingale, G.A. Magel, R.L. Byer, *Rev. Sci. Instrum.*, **55**, 1791 (1984)
16. H.J. Scheel, T. Fukuda, (ed.), *Crystal Growth Technology* (Wiley, Chichester, 2003)
17. J. Czochralski, *Z. Phys. Chem.*, **92**, 219 (1918)
18. L. Fornasiero, E. Mix, V. Peters, K. Petermann, G. Huber, *Cryst. Res. Technol.*, **34**, 255 (1999)
19. K. Petermann, L. Fornasiero, E. Mix, V. Peters, *Opt. Mater.*, **19**, 67 (2002)
20. F. Schmid, D. Viechnicki, *J. Am. Ceram. Soc.*, **53**, 528 (1970)
21. A.P. Belousenko, L.M. Zatulovskii, D.Ya. Kravetskii, N.S. Kostenko, B.L. Muravich, S.V. Tsvinskii, V.M. Lebedev, in *Proceedings of the 9<sup>th</sup> National Conference on the Production of the Shaped Crystals and Products by the Stepanov Method and their Applications in the Nation Economy* (Ioffe Physico-Technical Institute, Leningrad, 1982), p. 276 (in Russian)
22. J. Kong, J. Lu, K. Takaichi, T. Uematsu, K. Ueda, D.Y. Tang, D.Y. Shen, H. Yagi, T. Yanagitani, A.A. Kaminskii, *Appl. Phys. Lett.*, **82**, 2556 (2003)
23. C. Chen, B. M. Wanklyn, P. Ramasamy, *J. Cryst. Growth*, **104**, 672 (1990)
24. N. Imanaka, Y.W. Kim, T. Masui, G. Adachi, *Cryst. Growth Des.*, **3**, 289 (2003)
25. A. Novoselov, J.H. Mun, A. Yoshikawa, G. Boulon, T. Fukuda, in *Proceedings of Materials Research Society Fall 2004 Meeting: Solid-State Chemistry of Inorganic Materials V*, ed. by J. Li, N.E. Brese, M.G. Kanatzidis, M. Jansen, vol. 848 (Mater. Res. Soc., Warrendale, PA, 2005), p. 281
26. J.H. Mun, A. Novoselov, A. Yoshikawa, G. Boulon, T. Fukuda, *Mater. Res. Bull.*, **40**, 1235 (2005)
27. J.H. Mun, A. Jouini, A. Novoselov, A. Yoshikawa, T. Kasamoto, H. Ohta, H. Shibata, M. Isshiki, Y. Waseda, G. Boulon, T. Fukuda, *Jpn. J. Appl. Phys.*, **45**, 5885 (2006)
28. Z. Frukacz, D.A. Pawlak, in *Encyclopedia of Materials: Science and Technology*, ed. K.H.J. Buschow, R.W. Cahn, M.C. Flemings, B. Ilschner, E.J. Kramer, S. Mahajan, P. Veyssiere (Elsevier Science, Amsterdam, 2001), p. 3455
29. L.M. Lopato, A.V. Shevchenko, A.E. Kushchevskii, S.G. Tresvyatskii, *Inorg. Mater.*, **10**, 1276 (1974)
30. B.M. Tissue, Lizhu Lu, Li Ma, Weiyi Jia, M.L. Norton, W.M. Yen, *J. Cryst. Growth*, **109**, 323 (1990)
31. G. Adachi, N. Imanaka, *Chem. Rev.*, **98**, 1479 (1998)
32. J.H. Mun, PhD Thesis (Tohoku University, Sendai, 2006)
33. R. Simura, A. Jouini, J.H. Mun, A. Brenier, A. Yoshikawa, G. Boulon, T. Fukuda, *Opt. Mater.*, in press

34. D.A. Pawlak, G. Lerondel, I. Dmytruk, Y. Kagamitani, S. Durbin, P. Royer, T. Fukuda, *J. Appl. Phys.*, **91**, 9731 (2002)
35. E.C. Honea, R.J. Beach, S.B. Sutton, J.A. Speth, S.C. Mitchell, J.A. Skidmore, M.A. Emanuel, S.A. Payne, *IEEE J. Quantum Electron.*, **33**, 1592 (1997)
36. J.H. Mun, A. Jouini, A. Novoselov, Y. Guyot, A. Yoshikawa, H. Ohta, H. Shibata, Y. Waseda, G. Boulon, T. Fukuda, *Opt. Mater.*, in press
37. P.H. Klein, W.J. Croft, *J. Appl. Phys.*, **38**, 1603 (1967)
38. L. Laversenne, Y. Guyot, C. Goutaudier, M.Th. Cohen-Adad, G. Boulon, *Opt. Mater.*, **16**, 475 (2001)

# 13 MgAl<sub>2</sub>O<sub>4</sub> Spinel Laser Crystals: Pure and Ti-, Mn-, or Ni-Doped

Anis Jouini

**Abstract.** The shaped bulk single-crystal growth of pure and transition metal ions (Ti, Mn and Ni)-doped MgAl<sub>2</sub>O<sub>4</sub> spinel (melting point is 2135 °C) is introduced. The crystals were grown by the  $\mu$ -PD method in reducing Ar or N<sub>2</sub> atmosphere. The optimization of crystal growth parameters for shaped spinel compounds is described and the potential of these compounds as new efficient solid-state lasers with promising optical properties is outlined.

## 13.1 MgAl<sub>2</sub>O<sub>4</sub> Properties and Applications

Magnesium aluminate spinel (MgAl<sub>2</sub>O<sub>4</sub>) is a complex oxide with a high melting point (2135 °C). It has good thermal and mechanical properties, high hardness, a low neutron absorption cross-section, and low electrical loss. These special properties make MgAl<sub>2</sub>O<sub>4</sub> a potential candidate for a variety of technological applications, such as a substrate for microelectronics or an inert matrix for actinide fuels (reducing the environmental impact of radioactive waste).

MgAl<sub>2</sub>O<sub>4</sub> can easily be activated by transition metal (TM) ions like Ti, Cr, Mn, Fe, Co and Ni for applications in a number of optical devices: (1) Ti-doped MgAl<sub>2</sub>O<sub>4</sub> could provide an alternative (tunable) spectral range with longer a emission lifetime than Ti-doped  $\alpha$ -Al<sub>2</sub>O<sub>3</sub>, and a different optical absorption region suitable for pumping by sources other than flash lamps [1–5]; (2) Cr<sup>3+</sup>-doped MgAl<sub>2</sub>O<sub>4</sub> is an obvious candidate for producing tunable solid-state lasers (replacing conventional dye lasers) [6, 7] and for fiber-optic thermometer applications (replacing ruby crystals) [8]; (3) Mn<sup>2+</sup>- and Fe<sup>3+</sup>-doped MgAl<sub>2</sub>O<sub>4</sub> have been extensively studied due to their potential use in short-wavelength solid-state lasers [9–13]; (4) passive Q-switching of a diode pumping at 1.35  $\mu$ m Nd:KGd(WO<sub>4</sub>)<sub>2</sub> and other Nd laser crystals has been demonstrated using Co<sup>2+</sup>-doped stoichiometric and nonstoichiometric MgO  $\times$  nAl<sub>2</sub>O<sub>3</sub> ( $1 \leq n \leq 3$ ) saturable absorbers [14–17]; (5) a spectroscopy study of Ni<sup>2+</sup>-doped MgAl<sub>2</sub>O<sub>4</sub> was performed in order to assess its laser potential in the near-infrared region [18, 19].

Recently, the successful growth of high-quality (100)-oriented undoped and Ti-, Mn-, and Ni-doped spinel by the  $\mu$ -PD method was reported [4, 5, 13]. Strong blue emission was observed in the case of Ti-doped MgAl<sub>2</sub>O<sub>4</sub>, green

emission from the Mn-doped  $\text{MgAl}_2\text{O}_4$ , and infrared emission from the Ni-doped  $\text{MgAl}_2\text{O}_4$ . The emission intensity and the decay time were studied as a function of the transition metal ion doping concentration.

## 13.2 Crystal Structure of $\text{MgAl}_2\text{O}_4$

Magnesium aluminate spinel crystal is very specific with respect to its crystalline cubic structure: (space group  $Fd\bar{3}m(O_h^7)$  and lattice parameter  $a = 0.80887(2)$  nm) [20]. A unit cell of a spinel consists of eight face-centered cubic units and therefore 32 oxygen ions. In this type of close packing, 8 from 64 tetrahedral ( $T_d$ ) and 16 from 32 octahedral ( $O_h$ ) sites in the unit cell are occupied by  $\text{Mg}^{2+}$  and  $\text{Al}^{3+}$  cations, respectively. The structural peculiarity of  $\text{MgAl}_2\text{O}_4$  crystals is the existence of cationic disorder, i.e., in the distribution of both  $\text{Mg}^{2+}$  and  $\text{Al}^{3+}$  between the tetrahedral ( $T_d$ ) and octahedral ( $O_h$ ) positions. The structural chemical formula of the spinel can be written as  $(\text{Mg}_{1-i}\text{Al}_i)^{Td}[\text{Mg}_i\text{Al}_{2-i}]^{Oh}\text{O}_4$ , where  $i$  represents the degree of inversion. The round brackets indicate those ions occupying tetrahedral sites with full  $T_d$  symmetry, and square brackets indicate ions occupying octahedral sites with  $D_{3d}$  symmetry. The measured degree of inversion of natural spinel crystals is low, but artificially grown crystals have up to 30% of their cations disordered. Therefore, the inversion leads to the formation of charged defects  $[\text{Mg}_{\text{Octa}}^{2+}]^-$  and  $(\text{Al}_{\text{Tetra}}^{3+})^+$ , so-called anti-site defects, which may influence the crystal quality and optical properties.

## 13.3 Crucibles and Growth Details

The main difficulty involved in growing high-melting oxides such as spinel from the melt is the common use of iridium as the crucible material because it is chemically resistant to molten oxides. Its melting point (2410 °C) is only slightly higher than that of  $\text{MgAl}_2\text{O}_4$  (2135 °C). Because of the poor thermal conductivity of most oxide melts, the crucible wall must stay at a considerably higher temperature than 2135 °C in order to keep the material molten in the crucible. As a consequence, the iridium is approaching its own melting point and so any inhomogeneity in the crucible leads to localized overheating and catastrophic failure of the crucible. Therefore, in the case of  $\text{MgAl}_2\text{O}_4$ , an Ir–Re(2%) alloy was used [4]. The alloy combines the properties of the Ir crucibles used for the growth of  $\text{Y}_3\text{Al}_5\text{O}_{12}$  (m.p.  $\sim 2000$  °C) and the Re ones used for sesquioxide growth (m.p.  $\sim 2450$  °C).

Pure, Ti, Mn, and Ni-doped  $\text{MgAl}_2\text{O}_4$  crystals were successfully grown by the  $\mu$ -PD method. Starting materials were prepared from stoichiometric mixtures of  $\text{Al}_2\text{O}_3$  (5N), MgO (4N),  $\text{TiO}_2$  (4N), MnO (4N), and NiO (4N) powders produced by High Purity Chemicals Co. (Japan). Nominal molar percentages of transition metals were chosen ( $0.01 \leq x_{\text{Ti}} \leq 2$  mol%),

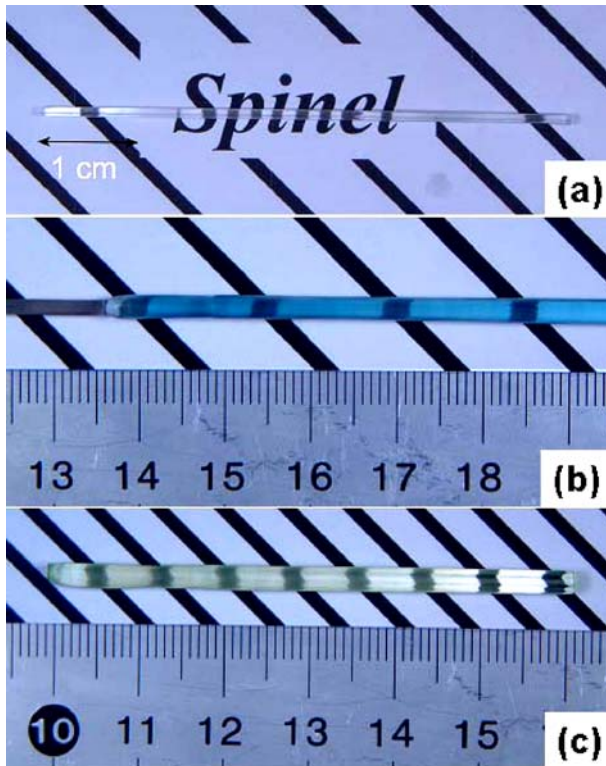


**Fig. 13.1.** As grown: **a**  $\varnothing$  1 mm rod-shaped undoped MgAl<sub>2</sub>O<sub>4</sub>, **b**  $\varnothing$  3 mm rod-shaped 0.2 mol% Ti-doped MgAl<sub>2</sub>O<sub>4</sub>, and **c** 2 mol% Mn-doped MgAl<sub>2</sub>O<sub>4</sub> spinel single crystals

$0.1 \leq x_{\text{Mn}} \leq 10 \text{ mol\%}$ , and  $0.1 \leq x_{\text{Ni}} \leq 10 \text{ mol\%}$ , where  $x$  = doping concentration). After modifying the bottom part of the crucible (the die), 1- and 3-mm rod-shaped and 5-mm square-shaped single crystals a few cm (up to 10 cm) in length were grown (Figs. 13.1 and 13.2). The lengths of the crystals were restricted only by the amount of raw material. Transparent colorless MgAl<sub>2</sub>O<sub>4</sub> crystals change to green (Mn) or blue (Ti and Ni) colored ones when doped. This coloration increases as the doping concentration increases, and disappears or changes when the crystals are annealed under air, which leads to the oxidation of TM doping cations.

### 13.4 X-Ray Characterization

X-ray powder diffraction (XRD) analysis was carried out in air at room temperature using a Rigaku RINT-Ultima diffractometer with a CuK $\alpha$  X-ray source (40 kV, 40 mA) in order to identify the phase compositions of the crys-

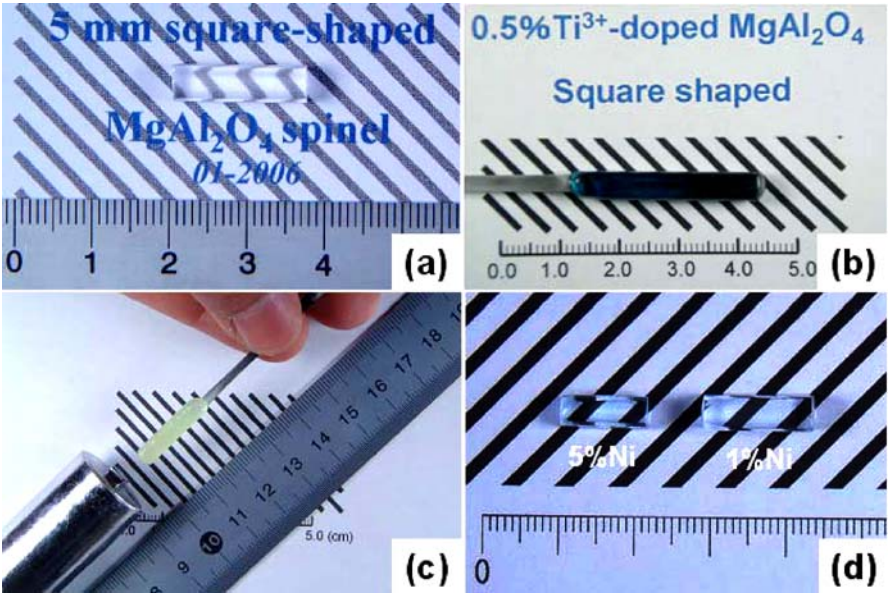


Fig. 13.2. As grown 5 mm square-shaped: a undoped, b 0.5 mol% Ti-doped, c 5 mol% Mn-doped and d polished Ni-doped MgAl<sub>2</sub>O<sub>4</sub> spinel single crystals

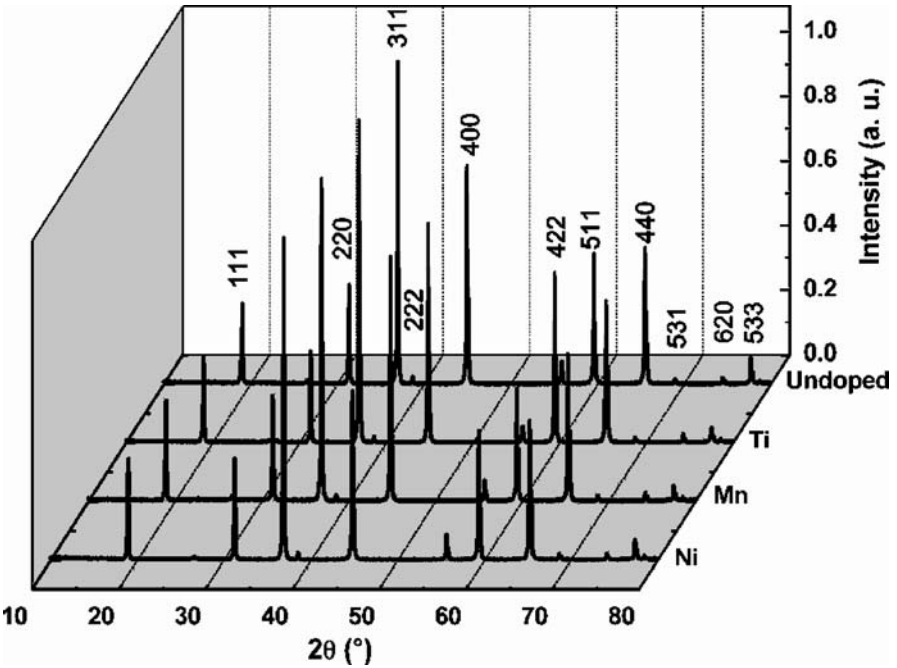


Fig. 13.3. XRD profile of undoped and 1 mol% transition metal ions-doped MgAl<sub>2</sub>O<sub>4</sub> spinel single crystals

**Table 13.1.** Structural parameters of transition metal ions [23]

Ion	Mg <sup>2+</sup>	Ni <sup>2+</sup>	Mn <sup>2+</sup>	Ti <sup>3+</sup>	Ti <sup>4+</sup>	Mn <sup>3+</sup>	Al <sup>3+</sup>
Number of 3 <i>d</i> electrons	0	6	3	1	0	2	0
Ionic radius in octahedral coordination (Å)	0.720	0.690	0.67	0.67	0.605	0.58	0.535
Ionic radius in tetrahedral coordination (Å)	0.57	0.55	0.66	–	0.42	–	0.39

tals. The diffraction pattern was scanned over the  $2\theta$  range from  $3^\circ$  to  $80^\circ$  in steps of  $0.02^\circ$ . The evolution of the powder XRD as a function of transition metal doping is shown in Fig. 13.3. No impurity phases were detected. Therefore it was concluded that complete solid solutions were formed. Dopants with ionic radii different from those of Mg<sup>2+</sup> and Al<sup>3+</sup> (Table 13.1) create centers of distortion in the spinel lattice. Therefore the peaks are shifted to the left (Fig. 13.3). This corresponds to an increase in the lattice constant that remains constant for a doping concentration of less than 1 mol%. The quality of the crystals grown was characterized by X-ray rocking curve measurements.  $\omega$  scans were carried out for the reflection from the (400) plane corresponding to the  $\langle 100 \rangle$  direction. The full width at half-maximum (FWHM) was measured to be  $0.0198^\circ$ . According to the results of the measurements, the spinel single crystals studied, which were grown by the  $\mu$ -PD method, show high crystallinity compared with other MgAl<sub>2</sub>O<sub>4</sub> crystals grown by the floating-zone method [2, 12] or the Verneuil technique, which is known to produce nonstoichiometric and strained crystals [21].

### 13.5 Segregation and Axial Distribution of Components

Results from the quantitative analysis of TM (Ti and Mn) cation distribution along the growth  $a$ -axis, performed for 1 mol% TM-doped MgAl<sub>2</sub>O<sub>4</sub> crystals using the electron probe microanalysis (EPMA), are shown in Fig. 13.4. The doping was homogeneous along the growth axis, and the effective segregation coefficient was close to unity in all cases [13]. This is due to structural similarities between the TM active ions that substitute Mg<sup>2+</sup> and Al<sup>3+</sup> in the spinel crystals and the low volatilization of oxide raw materials. The Ti and Mn oxides apparently reacted when heated up, and did not evaporate from the melt at low doping concentrations ( $x_{\text{TM}} \geq 1$ ). However, in the case of Ni-doped crystals, some evaporation during the growth was detected, and the effective segregation coefficient for Ni was around 0.7 [22]. The migration of the Ti doping ions to the outer part of the crystal during growth is clearly shown in Fig. 13.5. This inhomogeneous distribution along the cross-section was only observed in the case of Ti doping.

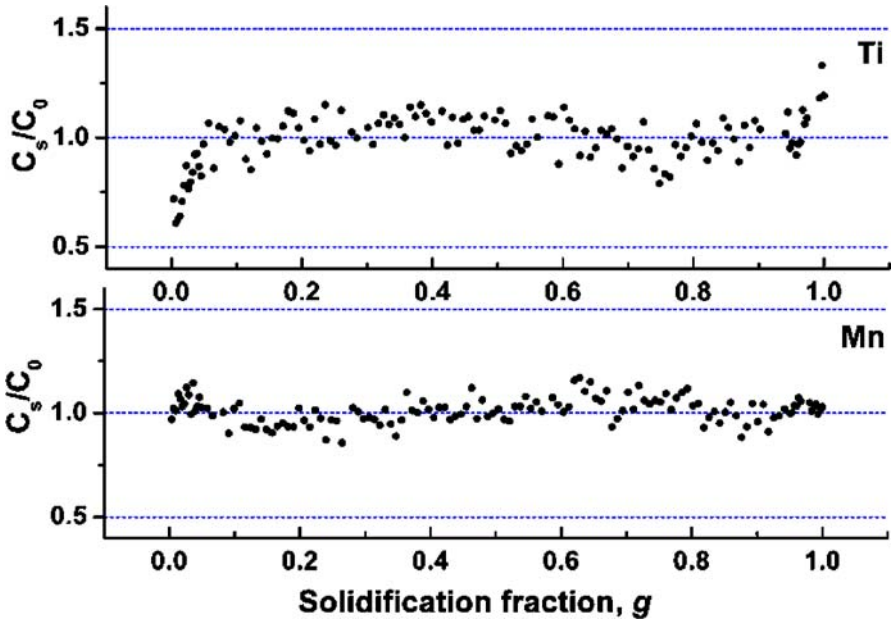


Fig. 13.4. EPMA profile of 1 mol% transition metal ions-doped  $MgAl_2O_4$  spinel single crystals

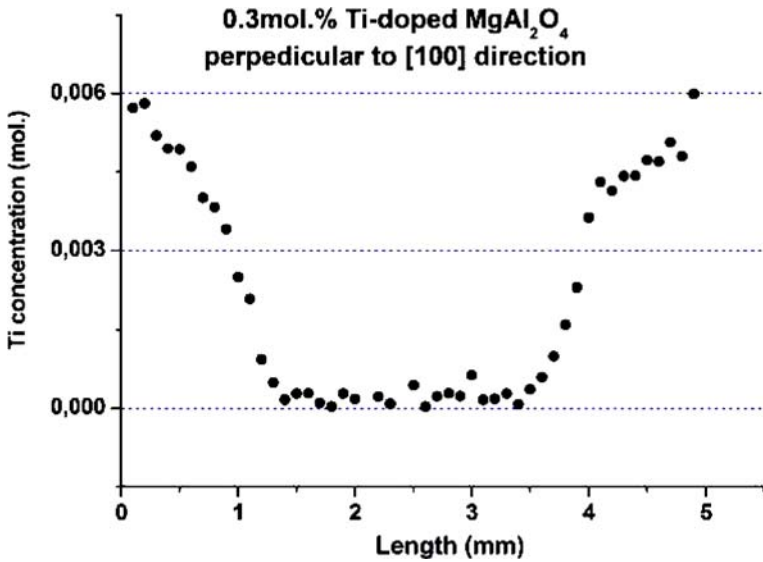


Fig. 13.5. Cross-section EPMA profile of 0.3 mol% Ti-doped  $MgAl_2O_4$  spinel single crystals

### 13.6 Thermal Properties

Two important laser parameters, the thermal expansion and the thermal conductivity, were measured. The thermal expansion coefficient was calculated by thermomechanical analysis to be  $8.48 \times 10^{-6} \text{ }^\circ\text{C}^{-1}$  at  $1200 \text{ }^\circ\text{C}$  for undoped MgAl<sub>2</sub>O<sub>4</sub> [13]. This is comparable to those of other commercial laser materials like Nd:YAG or Yb:YAG. Furthermore, the room-temperature thermal diffusivity was measured by the laser flash method. One surface of the specimen was irradiated by a Nd<sup>3+</sup>-glass laser. The temperature response at the other surface of the specimen was measured using an InSb infrared detector. The thermal diffusivity was calculated using the following equation:

$$\alpha = \frac{1.37 \cdot L^2}{\pi^2 \cdot t_{1/2}}, \quad (13.1)$$

where  $\alpha$ ,  $L$ , and  $t_{1/2}$  are the thermal diffusivity, the sample thickness, and the time to reach half of the maximum temperature rise, respectively. In the case of undoped MgAl<sub>2</sub>O<sub>4</sub>, the thermal diffusivity was  $7.19 \text{ m}^2 \text{ s}^{-1}$  at  $298 \text{ K}$ .

The heat capacity, an important factor which influences the damage threshold of the laser crystals, was measured by a differential scanning calorimeter (DSC) using  $\alpha\text{-Al}_2\text{O}_3$  as a standard sample between  $523 \text{ K}$  and  $823 \text{ K}$  via the following equation:

$$C_{P,S} = C_{P,R} \times \frac{S_S \cdot W_R}{S_R \cdot W_S}, \quad (13.2)$$

where  $C_{P,S}$ ,  $W_S$ ,  $S_S$  and  $C_{P,R}$ ,  $W_R$ ,  $S_R$  are the heat capacity, the weight and the real area of the DSC curve of the sample (S) and the reference (R), respectively. The average weight of the well-polished studied crystals was about  $50 \text{ mg}$ . The heat capacity increases linearly with temperature and decreases as the TM doping concentration increases. The thermal conductivity  $\kappa$  was calculated from the thermal diffusivity  $\alpha$ , the heat capacity  $C_P$ , and the density  $\rho = 3.45 \text{ g cm}^{-3}$  for undoped MgAl<sub>2</sub>O<sub>4</sub> using the following expression:

$$\kappa = \alpha \times C_P \times \rho. \quad (13.3)$$

**Table 13.2.** The thermal properties of Ti-doped MgAl<sub>2</sub>O<sub>4</sub> as a function of Ti content

	Mg(Al <sub>1-x</sub> Ti <sub>x</sub> ) <sub>2</sub> O <sub>4</sub>							
Ti content, x (mol)	0	0.001	0.003	0.004	0.005	0.006	0.008	0.01
Specific heat capacity (J g <sup>-1</sup> K <sup>-1</sup> )	0.911	0.767	0.703	0.800	0.796	0.823	0.564	0.552
Thermal diffusivity (10 <sup>-6</sup> m <sup>2</sup> s <sup>-1</sup> )	7.19	6.59	6.03	6.28	6.32	5.35	4.95	5.74
Ionic conductivity (W m <sup>-1</sup> K <sup>-1</sup> )	22.61	17.45	14.63	13.33	12.55	11.20	9.633	10.93

The thermal conductivity decreased exponentially as the contents of Ti and Mn increased. The results for Ti-doped  $\text{MgAl}_2\text{O}_4$  are summarized in Table 13.2. The thermal conductivity of undoped  $\text{MgAl}_2\text{O}_4$  ( $22.61 \text{ Wm}^{-1} \text{ K}^{-1}$ ) can be approximately considered to be an average between the results for MgO and  $\alpha\text{-Al}_2\text{O}_3$ , as reported by Slack in [24].

### 13.7 Spectroscopy of Ti, Mn, and Ni-Doped $\text{MgAl}_2\text{O}_4$

Optical absorption measurements were performed from the ultraviolet to the infrared regions using a dual beam spectrophotometer. The microluminescence spectra were investigated under the fourth and third  $\text{Nd}^{3+}$ :YAG harmonic (266 nm and 355 nm) pulsed laser excitations (Spectra Physics Quanta-Ray, GCR130), which deliver pulses of 10 ns duration and a spectral width of  $0.1 \text{ cm}^{-1}$ . The laser signal was reflected by two mirrors so that it passed through an optical microscope, exciting about  $50 \mu\text{m}$  of the horizontal surfaces of the studied samples. Time-resolved emission spectra were measured with the following features: i) a delay time after the excitation pulse of 1 ns to 1  $\mu\text{s}$  and a gate width of 0.5  $\mu\text{s}$  to 5 ms; ii) a spectral detection range of 200 nm to 800 nm. The luminescence observed was analyzed using a f-125 monochromator with a grating of 400 and 1200 grooves/mm, and detected by an Instaspec V detector combined with a gated intensified charge-coupled device (CCD) camera (calibrated using standard Hg lamp rays). Excitation of the  $\text{Ni}^{2+}$  fluorescence was performed with i) a frequency-doubled  $\text{Nd}^{3+}$ :YAG laser (10 ns, 10 Hz) pumping a Quantel two-amplifier-stage dye laser containing a mixture of DCM and LDS698 in order to generate a beam in the 640–650 nm range, and ii) an optical parametric oscillator (OPO) pumped by a Nd:YAG laser. The energy of the beam was maintained at around 1 mJ/pulse throughout the measurements. The specific infrared fluorescence was selected using a Jobin Yvon HR250 monochromator fitted with a 600 grooves/mm grating blazed at  $1 \mu\text{m}$ . The signal was detected by an intermediate North Coast germanium cell, cooled by liquid nitrogen, and sent into a Stanford SRS 250 boxcar averager. The decay kinetics were recorded with a Lecroy LT 342 digital oscilloscope. Samples 1–3 mm in thickness were polished for all of the measurements.

#### 13.7.1 Ti-Doped $\text{MgAl}_2\text{O}_4$

Ti-Doped  $\alpha\text{-Al}_2\text{O}_3$  sapphire is the most successful tunable solid-state laser in the near-IR, with a broad emission band centered at 750 nm which corresponds to the  ${}^2E_g \rightarrow {}^2T_{2g}$  transition inside the  $3d^1$  configuration of the  $\text{Ti}^{3+}$  ion located in the  $\text{Al}^{3+}$  site of octahedral symmetry. This system provides a wide tuning range extending from 660 to 1100 nm, with a high cross-section ( $6 \times 10^{-19} \text{ cm}^2$ ) but a low radiative decay time (3.85  $\mu\text{s}$ ). For a long time, efforts have been made to dope other oxide hosts with  $\text{Ti}^{3+}$  ions in order to provide

alternative tunable spectral ranges with longer lifetimes, especially in the visible region. Blue emission of strong intensity was observed from Ti-doped MgAl<sub>2</sub>O<sub>4</sub> crystals upon fourth-harmonic Nd:YAG pulsed laser excitation at 266 nm. As an example, the time-resolved emission spectra of a 0.3 mol% Ti-doped MgAl<sub>2</sub>O<sub>4</sub> sample is shown in Fig. 13.6.

Room-temperature (RT) optical absorption spectra of Mg(Al<sub>1-x</sub>Ti<sub>x</sub>)<sub>2</sub>O<sub>4</sub> (with  $x = 0, 0.1$  and  $0.5$ ) as a function of Ti concentration are also shown in Fig. 13.6. No absorption was detected for undoped MgAl<sub>2</sub>O<sub>4</sub>, and when doped with titanium, three broad bands of absorption were observed. In the ultraviolet region, a strong absorption edge arising at 300 nm and peaking at 217 nm was observed, and a red-shift of the absorption edge was evident once the MgAl<sub>2</sub>O<sub>4</sub> was Ti-doped. This edge (at 4.15 eV) is located far from the band-gap energy of the undoped crystal (at 9 eV). This is most probably due to parity-allowed charge transfer between Ti<sup>4+</sup> and Ti<sup>3+</sup> ions sited in crystal. Similar behavior was observed in sapphire, and it was reported that the Ti<sup>4+</sup> in sapphire is responsible for the 190 nm absorption band [25–27]. However, the visible absorption band with a maximum at 485 nm is assigned to the possible crystal field transition (<sup>2</sup>T<sub>2g</sub> → <sup>2</sup>E<sub>g</sub>) of octahedrally coordinated Ti<sup>3+</sup>. While, the broad band at 780 nm appears to be due to the charge transfer transition between coupled iron–titanium ion pairs (Ti<sup>4+</sup> + Fe<sup>2+</sup> → Ti<sup>3+</sup> + Fe<sup>3+</sup>). To confirm the origin of this parasitic absorption, which is obviously a disadvantage to laser operation for emissions higher than 500 nm, two 5-mm square-shaped crystals were grown under similar conditions. Both had the same Ti concentration (0.3 mol%), but one of them was co-doped with 0.05 mol% of Fe (4N Fe<sub>2</sub>O<sub>3</sub> raw material). The increase in the absorption around 780 nm in the co-doped Ti/Fe sample clearly demonstrated the effect of the iron contamination. Both the bluish color and the two broad bands at 485 and 780 nm observed in the case of Ti-doped MgAl<sub>2</sub>O<sub>4</sub> disappeared completely when the crystals were annealed in air at 1400 °C. This may be due

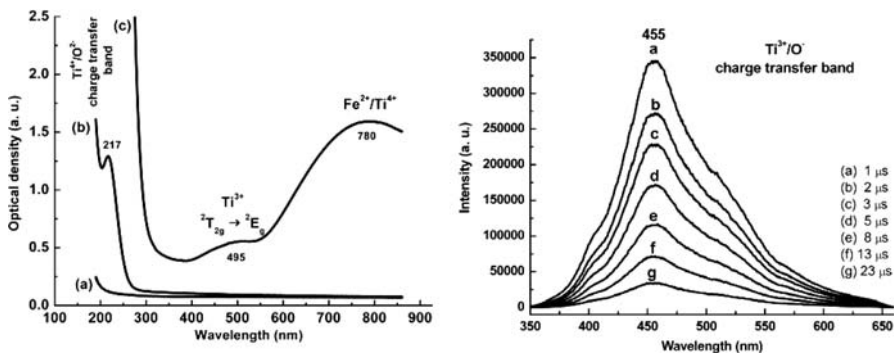


**Fig. 13.6.** Room temperature absorption spectra of as-grown Mg(Al<sub>1-x</sub>Ti<sub>x</sub>)<sub>2</sub>O<sub>4</sub> ( $x = 0$  (a),  $x = 0.1\%$  (b) and  $x = 0.5\%$ ) (left) and time-resolved blue emission from Mg(Al<sub>0.997</sub>Ti<sub>0.003</sub>)<sub>2</sub>O<sub>4</sub> spinel upon excitation at  $\lambda_{\text{exc}} = 266$  nm (right)

to the oxidation of titanium and iron ions. The broadband emission observed around 455 nm (FWHM = 90.5 nm) with two shoulders at 400 nm and 500 nm is shifted with respect to the 490 nm emission band of samples grown under oxidizing atmosphere [3]. The exponential decay time of this emission band was measured from time-resolved spectra to be 5.7  $\mu$ s, which is close to the decay time of 6.6  $\mu$ s of the 490 nm emission band in [3]. This means that the same type of center is responsible for this blue emission in the two types of crystals. Low-temperature measurements are needed to clarify this point. This overlap between the absorption and emission spectra (Fig. 13.6) does not prevent laser action in the crystals, and excited state absorption (ESA) measurements are needed in this region.

The first blue laser oscillations were obtained upon pumping at 266 nm using a Nd:YAG pulsed laser. An improvement in the crystal quality is needed as well as more anti-reflection coating in order to decrease the laser pumping power required to obtain the laser emission and to increase the efficiency.

### 13.7.2 Mn-Doped MgAl<sub>2</sub>O<sub>4</sub>

RT optical absorption and emission spectra from 5% Mn-doped MgAl<sub>2</sub>O<sub>4</sub> in the 300–600 nm range, including identified absorption peaks, and the corresponding Orgel diagram are shown in Fig. 13.7. The ground state is the sextet A<sub>1</sub> level, whereas all of the excited d-levels are doublet or quartet states. Consequently, all transitions involving the ground state are parity- and spin-forbidden, and the Mn<sup>2+</sup> optical absorption intensity is quite low. This problem can be resolved by increasing the doping Mn concentration. Strong green emission was observed from Mn<sup>2+</sup>-doped MgAl<sub>2</sub>O<sub>4</sub> upon third-harmonic Nd:YAG pulsed laser excitation at 355 nm (Fig. 13.7). This non-structural emission band (FWHM = 32 nm) is attributed to transitions

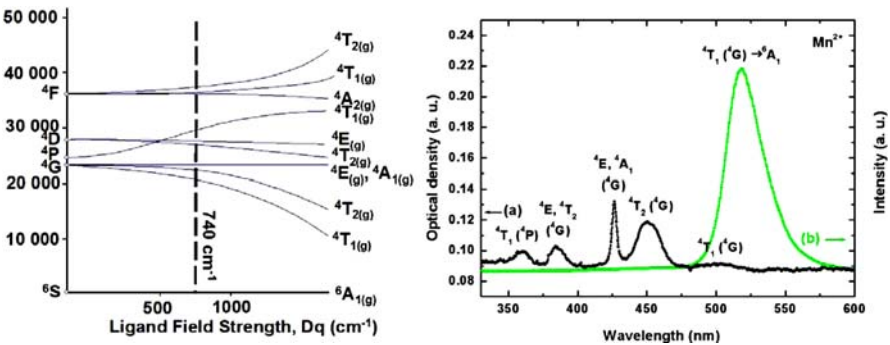
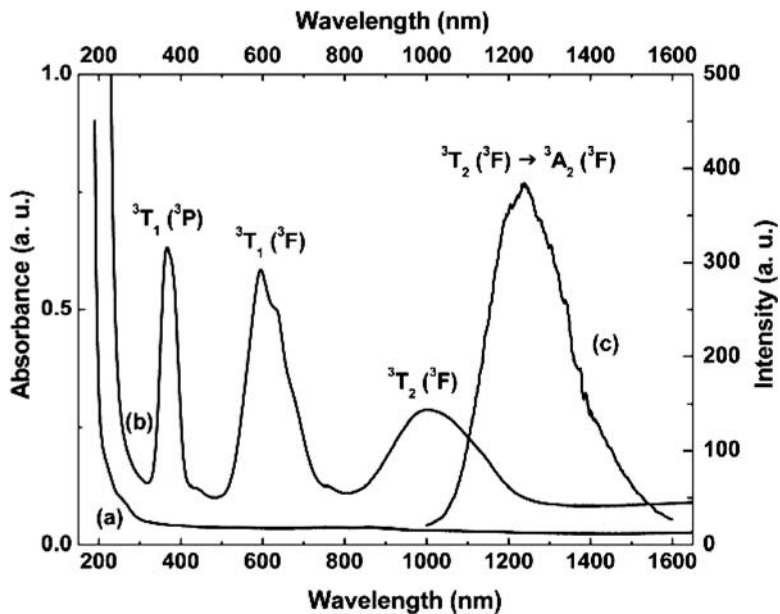


Fig. 13.7. Orgel diagram of Mn-doped MgAl<sub>2</sub>O<sub>4</sub> (left) and RT absorption (a) and strong green emission (b) from (Mg<sub>0.95</sub>Mn<sub>0.05</sub>)Al<sub>2</sub>O<sub>4</sub> spinel upon excitation at  $\lambda_{exc} = 355$  nm (right)

from the lowest excited state  ${}^4T_1$  to the ground state  ${}^6A_1$  of  $Mn^{2+}$  ( $3d^5$ ) ions at tetrahedral sites with quite low crystal field strength. Due to the spin selection rule, the exponential decay time measured at RT was rather long; around 6.11 ms. Their broad green emission with long decay time makes  $Mn^{2+}$ -doped  $MgAl_2O_4$  single crystals promising laser materials if the ESA in the visible range could be compensated by high-doping with manganese [9–13].

### 13.7.3 Ni-Doped MgAl<sub>2</sub>O<sub>4</sub>

Divalent  $Ni^{2+}$  ( $3d^8$ )-doped  $Y_3Al_5O_{12}$  and  $Gd_3Sc_2Ga_3O_{12}$  have been proposed as new solid-state tunable lasers [28]. However, due to strong excited state absorption that overlaps with the fluorescence band, no laser oscillation has been performed at RT [29]. Only a few reports have been dedicated to the growth and optical spectroscopy of octahedrally coordinated Ni-doped  $MgAl_2O_4$  [18, 19, 22]. Notably, the ground state absorption (GSA) of Ni-doped  $MgAl_2O_4$  reveals the presence of three strong broadband ranges at 367 nm, 595 nm and 1004 nm. They are definitely attributed to spin-allowed transitions from the  ${}^3A_2({}^3F)$  ground state to the excited orbital triplets  ${}^3T_1({}^3P)$ ,  ${}^3T_1({}^3F)$ , and  ${}^3T_2({}^3F)$ , respectively. The strong absorption around 1  $\mu m$  is highly suited to InGaAs laser diode emission in the 900–980 nm region, and



**Fig. 13.8.** RT absorption spectra of as-grown undoped  $MgAl_2O_4$  (a) and 10 mol% Ni-doped one (b) and RT infrared emission from 10 mol% Ni-doped  $MgAl_2O_4$  (c) upon excitation at  $\lambda_{exc} = 646$  nm

was developed in the 1990s to pump Er-doped fiber amplifiers for commercial use in the telecommunication industry.

The absorption spectra of both undoped and nominally 10 mol% Ni-doped  $\text{MgAl}_2\text{O}_4$  displayed in Fig. 13.8 show typical absorption from octahedrally coordinated  $\text{Ni}^{2+}$  in  $\text{MgAl}_2\text{O}_4$ . Strong infrared emissions attributed to the  ${}^3\text{T}_2({}^3\text{F}) \rightarrow {}^3\text{A}_2({}^3\text{F})$  transition were recorded upon red excitation at 646 nm (Fig. 13.8). The same result was obtained upon excitation at 980 nm. The broadness of this band (FWHM = 180 nm) makes Ni-doped spinel materials promising candidates for infrared laser oscillation around 1.3  $\mu\text{m}$ . In addition, the room temperature (RT)  ${}^3\text{T}_2({}^3\text{F})$  decay time upon Nd:YAG laser excitation at 646 nm was measured to be quite long ( $\tau = 0.85$  ms) when compared to other transition metals. One should note that the ESA spectra measured by Kuleshov et al., who stated that the  ${}^3\text{T}_2({}^3\text{F}) \rightarrow {}^3\text{A}_2({}^3\text{F})$  emission at 1180 nm overlaps the  ${}^3\text{T}_2({}^3\text{F}) \rightarrow {}^3\text{T}_1({}^3\text{F})$  transition, could be the only factor that prevents lasing in these crystals [19].

## 13.8 Conclusions

Shaped transition metal-doped  $\text{MgAl}_2\text{O}_4$  spinel single crystals with high melting temperatures were successfully grown from the melt using the  $\mu$ -PD technique. The optical quality of these crystals is generally close to that of crystals grown by the Czochralski method. In addition to the good thermal properties of  $\text{MgAl}_2\text{O}_4$ , promising spectroscopic properties based on  $3d \leftrightarrow 3d$  transitions and covering a wide spectral range between 350 and 1600 nm were obtained. The first blue laser oscillation was obtained from Ti-doped  $\text{MgAl}_2\text{O}_4$ . Considering their high probability of ESA and their nonradiative lifetimes, Mn- and Ni-doped  $\text{MgAl}_2\text{O}_4$  possess good potential as new solid-state laser materials in the visible and infrared regions, respectively.

## References

1. L.E. Bausa, I. Vergara, J. Garcia-Solé, W. Strek, P.J. Deren, J. Appl. Phys. **68**, 736 (1990)
2. E. Hanamura, Y. Kawabe, H. Takashima, T. Sato, A. Tomita, J. Nonlinear Opt. Phys., **12**, 467 (2003)
3. T. Sato, M. Shirai, K. Tanake, Y. Kawabe, E. Hanamura, J. Lumin., **114**, 155 (2005)
4. A. Jouini, H. Sato, A. Yoshikawa, T. Fukuda, K. Kato, E. Hanamura, J. Cryst. Growth, **287**, 313 (2006)
5. A. Jouini, H. Sato, A. Yoshikawa, T. Fukuda, G. Boulon, G. Panczer, K. Kato, E. Hanamura, J. Mater. Res., **21**, 2337 (2006)
6. W. Strek, P. Deren, B. Jezowska-Trzebiatowska, J. Lumin., **40–41**, 421 (1988)
7. P. J. Deren, M. Malinowski, W. Strek, J. Lumin., **68**, 91 (1996)

8. H. Aizawa, N. Ohishi, S. Ogawa, E. Watanabe, T. Katsumata, S. Komuro, T. Morikawa, E. Toba, *Rev. Sci. Instrum.*, **73**, 3089 (2002)
9. R. Clausen and K. Petermann, *IEEE J. Quantum Electron.* **24**(6), 1114 (1988)
10. R. Clausen, K. Petermann, *J. Lumin.*, **40–41**, 185 (1988)
11. K. Petermann, R. Clausen, E. Heumann, M. Ledig, *Opt. Commun.*, **70**(6) 483 (1989)
12. A. Tomita, T. Sato, K. Tanaka, Y. Kawabe, M. Shirai, K. Tanaka, E. Hanamura, *J. Lumin.*, **109**, 19 (2003)
13. A. Jouini, A. Yoshikawa, T. Fukuda, G. Boulon, *J. Cryst. Growth*, 293, **517** (2006)
14. K.V. Yumashev, I.A. Denisov, N.N. Posnov, N.V. Kuleshov, R. Moncorge, *J. Alloy. Comp.*, **341**, 366 (2002)
15. M. Kokta, D. Peressini, J. Cooke, K. Goodnight, US Patent, 6,839,362 (4 Jan 2005)
16. N.V. Kuleshov, V.P. Mikhailov, V.G. Scherbitsky, P.V. Prokoshin, K.V. Yumashev, *J. Lumin.*, **55**, 265 (1993)
17. J.L. Stone-Sundberg, M.R. Kokta, N.S. Prasad, R.K. Shori, in *Solid State Lasers XIV: Technology and Devices*, ed. by H.J. Hoffman and R.K. Shori, Proc. SPIE, vol. 5707 (SPIE, Bellingham, WA, 2005), p. 128
18. C. Wyon, J. J. Aubert and F. Auzel, *J. Cryst. Growth*, **79**(1–3), 710 (1986)
19. N.V. Kuleshov, V.G. Shcherbitsky, V.P. Mikhailov, S. Kück, J. Koetke, K. Petermann, G. Huber, *J. Lumin.*, **71**, 265 (1997)
20. H. Sawada, *Mater. Res. Bull.*, **30**, 341 (1995)
21. F.H. Lou, D.W.G. Ballentyne, *J. Phys. C*, **1**(2), 608 (1968)
22. A. Jouini, A. Yoshikawa, Y. Guyot, A. Brenier, T. Fukuda, G. Boulon, *Opt. Mater.*, in press
23. R. D. Shannon, *Acta Cryst. A*, **32**, 751 (1976)
24. G.A. Slack, *Phys. Rev.*, **126**(2), 427 (1962)
25. P.F. Moulton, *J. Opt. Soc. Am. B*, **3**, 125 (1986)
26. G. Nath, G. Walda, *Z. Naturforsch. A*, **23**, 524 (1968)
27. T.S. Bessonova, M.P. Stanislavskii, V.A. Khaimov-Malkov, *Opt. Spectrosc. (USSR)*, **41**, 87 (1976)
28. E.P. Dubrovina, V.A. Sandulenko, M.I. Demchuk, N.V. Kuleshov, V.P. Mikhailov, *Chem. Phys. Lett.*, **170**(5–6), 473 (1990)
29. S. Kück, *Appl. Phys. B*, **72**, 515 (2001)

Part IV

**Growth and Characterization  
of Oxide  $\mu$ -PD Crystals II:  
Assorted Materials**

# 14 $\text{K}_3\text{Li}_2\text{Nb}_5\text{O}_{15}$ Fiber and Plate Crystals

Minoru Imaeda and Katsuhiro Imai

**Abstract.** The growth and homogeneity of second harmonic generation (SHG) in  $\text{K}_3\text{Li}_2\text{Nb}_5\text{O}_{15}$  (KLN)-type fiber and plate single crystals grown by the micro-pulling-down method are reviewed. The uniformities of fiber crystals up to 300 mm long and plates up to  $1 \times 15 \times 100$  mm in size were examined via lattice constant and SHG wavelength measurements. Fluctuations in composition along the growth axis were negligible. However, variations in the phase-matching wavelength along the radial direction were easily detected. The phase-matching wavelength decreases when the lithium content in the starting melt and the pulling-down rate are increased. Results from X-ray rocking-curve analysis of these crystals are reviewed, as are some optical measurements, such as those of the acceptance temperature and wavelength and the wavelength conversion ratio.

## 14.1 Introduction

Potassium lithium niobate  $\text{K}_3\text{Li}_{2-x}\text{Nb}_{5+x}\text{O}_{15+2x}$  (KLN) crystals are promising materials for the development of blue laser sources based on second harmonic generation (SHG). KLN has a large nonlinearity ( $d_{31} = -14.0$  pm/V), a low optical loss, and wide noncritical phase-matching range (790–920 nm depending on the Li/Nb ratio) at room temperature.

KLN was first reported in 1967 by Bonner and Uitert [1–3] as one of a series of ferroelectric mixed alkali metal niobates with a tetragonal tungsten bronze structure (space group:  $P4bm$ , point group:  $4mm$ ). These crystals have excellent electrooptic and nonlinear optical properties. KLN is transparent between 350 and 5000 nm, has a ferroelectric Curie temperature of 420 °C, and exhibits a linear electrooptic effect with a half-wave retardation of about 930 V. The dielectric constant along the  $c$ -axis is about 100 at room temperature, and the  $d_{33}$  and  $d_{31}$  coefficients of SHG are about the same as those of  $\text{LiNbO}_3$  (LN). Moreover, KLN has a very high optical damage threshold [4] compared to LN crystals. Indeed, this is considerable disadvantage of LN when used in high-power laser applications.

Related  $\text{K}_3\text{Li}_2(\text{Nb}_{1-A}\text{Ta}_A)_5\text{O}_{15}$  (KLTN) crystals formed through the partial replacement of Nb with Ta can be grown by the Kyropoulos technique. The growth conditions, crystal structure, lattice constants, and dielectric Curie temperature of KLTN were reported in [5–7]. Crystals of reasonable optical quality were obtained by pulling the crystals along the  $a$  axis. Crystals grown along the  $c$  axis were not large enough. These KLTN crystals

have orthorhombic structure at room temperature for  $A > 0.55$ . The phase diagram shown in Fig. 14.1 illustrates the wide field of formation of solid solutions with KLN structure. The dependencies of the lattice constant and the dielectric Curie temperature on the Nb content were reported in [8].

There is much interest in developing compact blue light sources for high-density optical storage and laser projection display systems. Therefore, KLN crystals have been investigated [9–11] as a material which can potentially substitute the  $\text{KNbO}_3$  (KN) crystals used for the frequency doubling of near-infrared GaAlAs diode laser radiation at room temperature. The disadvantages of KN are its instability to, say, mechanical shocks and/or the fact that it overheats at temperatures above  $40^\circ\text{C}$ . Both of these phenomena result in the formation of multidomain structure.

Improvements in the crystal growth procedure have permitted the preparation of KLN crystals with higher lithium contents than in previously reported materials [1]. Increasing the mole fraction of lithium improves the birefringence, leading to noncritical phase-matching at a shorter wavelength range of the optical spectrum (Fig. 14.2). Using this approach, the wavelength of noncritical SHG at room temperature can be positioned in the range 790–920 nm.

Bulk KLN crystals of sufficient size and with a high chemical homogeneity are required for practical applications. However, such crystals have not been obtained using the Kyropoulos or Czochralski techniques because KLN forms a wide range of solid solutions. The segregation coefficients of the constituents are not equal to unity. Therefore, the crystals are not uniform in terms of

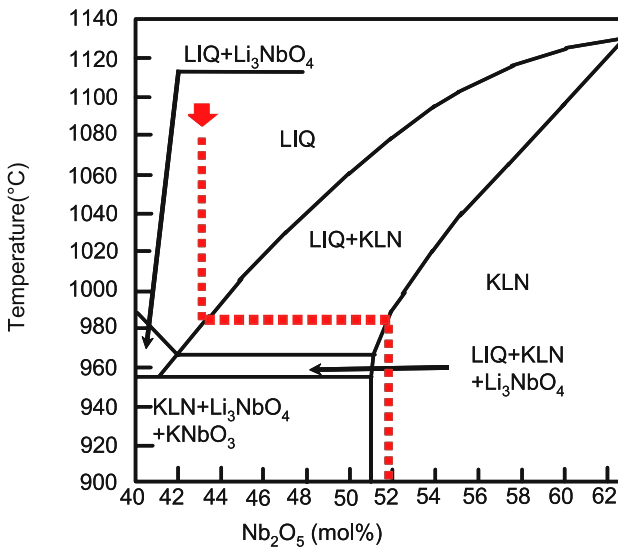


**Fig. 14.1.** The 30 mol%  $\text{K}_2\text{O}$  section of the phase diagram of the  $\text{K}_2\text{O}-\text{Li}_2\text{O}-\text{Nb}_2\text{O}_5$  system

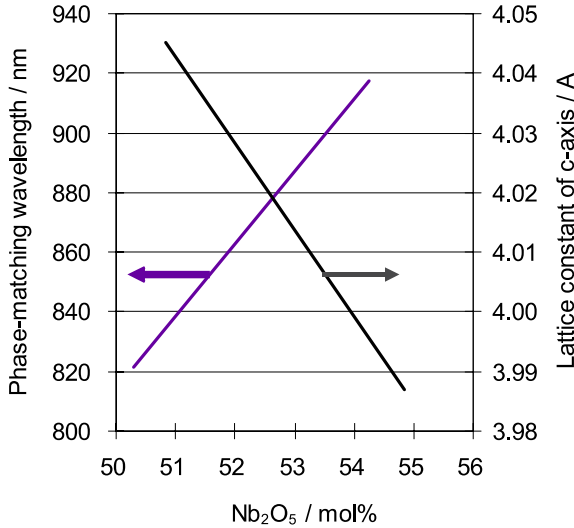


**Fig. 14.2.** Dependence of phase-matching wavelength of SHG and lattice constant of  $c$ -axis on  $\text{Nb}_2\text{O}_5$  content in the melt

their compositions and lattice parameters. As a result, crack formation is normally observed. Similar problems were reported in [12] for other crystals with the tungsten-bronze structure ( $\text{Ba}_2\text{NaNb}_5\text{O}_{15}$ ).

The micro-pulling-down ( $\mu$ -PD) method [13, 14] is an alternative crystal growth procedure that results in the formation of homogeneous [15–17] KLN crystals free of cracks and compositional fluctuations. It should be noted that the  $\mu$ -PD system is appropriate for single-crystal growth of incongruently melting materials.

The following section summarizes the results obtained from the  $\mu$ -PD growth of KLN fiber and plate crystals intended for microchip SHG laser applications [18–22]. The crystallinity, optical properties and homogeneity of the KLN crystals produced by the  $\mu$ -PD technique are discussed. Thereafter, the strategy used to control the phase-matching wavelength (by modifying the melt composition and the pulling-down rate) is reviewed. X-ray rocking curve measurements and optical characterization of transmission and SHG properties are also presented.

## 14.2 Crystal Growth and Characterization Details

Starting powders of  $\text{K}_2\text{CO}_3$  (3N),  $\text{Li}_2\text{CO}_3$  (4N) and  $\text{Nb}_2\text{O}_5$  (4N) were mixed together in the ratio  $\text{K}:\text{Li}:\text{Nb} = 30:y:z$  ( $18 < y < 23$  and  $47 < z < 52$ , noting that  $y+z = 70$ , Fig. 14.1) and sintered in an electric furnace at  $900^\circ\text{C}$  for four hours. The sintered material was then loaded into a Pt crucible (Fig. 14.3),

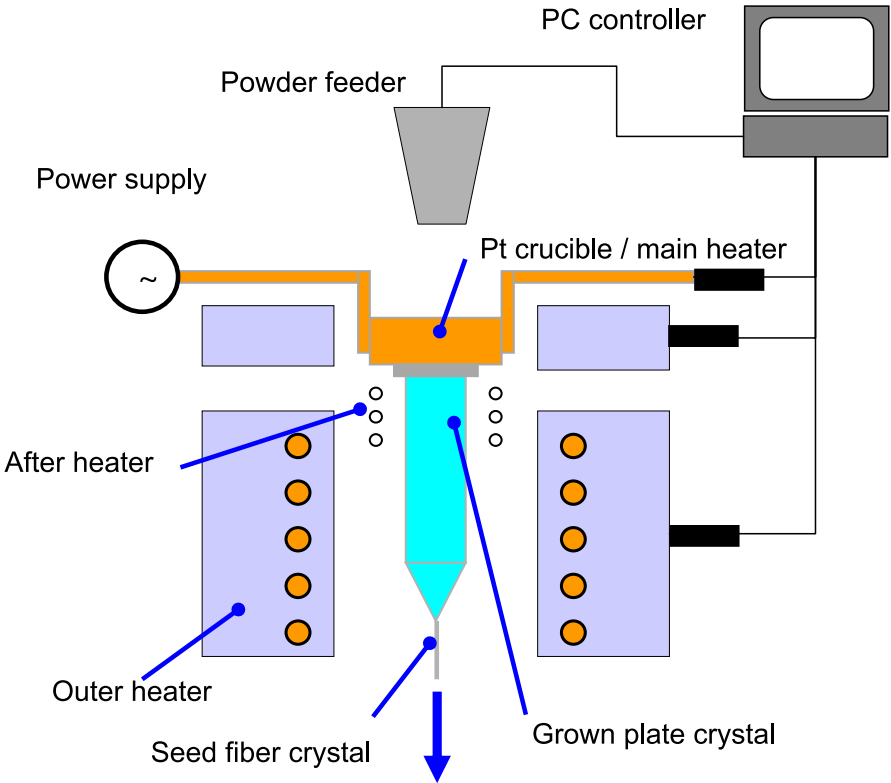


**Fig. 14.3.** Schematic diagram of  $\mu$ -PD apparatus used for plate crystal growth

heated to  $1050^\circ\text{C}$  to melt it, and left for 20 minutes to allow the melt to homogenize. The seed crystals had  $\langle 110 \rangle$  orientations. The fiber crystals were produced by pulling down the melt through the capillary nozzle in the crucible bottom in an air atmosphere. The crystal diameter was kept constant by controlling the temperature of the crucible and the afterheaters during growth. More details on the  $\mu$ -PD method used are available from [15]. Single-crystal plates of width 15 mm were pulled down from the original (large) Pt crucible designed for plate crystal growth. The seed crystals used for the plate growth were also of  $\langle 110 \rangle$  orientation. Moreover, an automatic powder feeding system was used to control the KLN composition.

Crystal morphology was inspected with an optical microscope. The crystallinity was examined via X-ray rocking curve measurements obtained with a Philips MRD diffractometer and a high angular resolution monochromator [23] using four Ge (440) reflections. The incident beam of Cu-K $\alpha$  was collimated to be  $1 \times 1 \text{ mm}^2$ .

The transmission was measured along the  $\langle 110 \rangle$  direction using a Hitachi U-340 spectrometer in the wavelength range 340–1000 nm. SHG properties

were inspected at room temperature in the range 780–940 nm using a CW-Ti:Al<sub>2</sub>O<sub>3</sub> laser (model 3900 from Spectra-Physics).

### 14.3 Shape and Crystallinity of KLN Fibers and Plates

The KLN fiber crystals were colorless and had rectangular cross-sections with well-developed (110) and (001) facet planes. Three hundred millimeter long fibers 0.6–1.0 mm in diameter (or cross-section) were grown with a maximal solidification fraction of  $g = 0.9$ . Moreover, KLN plates that were about 150 mm long, 15 mm wide and 1 mm thick with the largest face oriented [001] were also produced (Fig. 14.4). The plate crystals were grown with a continuous charging system, and the amount of melt in the crucible was held constant during the entire process. This allowed the composition of the plate crystal to remain fixed and independent of the solidification fraction. Both shoulder parts were grown by controlling the temperature of the crucible.

No macroscopic defects such as cracks, inclusions, and bubbles were observed in the crystals. The surfaces of the crystals were flat and smooth. Thus, the diameters of the fibers and the thicknesses and widths of the plates were nearly constant in the steady-state growth region. Various pulling-down rates were tested for the fibers, and the highest rate resulting in crack-free single crystals was 2 mm/min. Increasing the pulling-down rate above this value often led to the formation of cracks and bubbles during growth, and control of the crystal diameter became difficult.

X-ray rocking curves of the crystals grown were examined using (550) reflection at a Bragg angle of 25.7 deg for Cu-K $\alpha$  radiation. The FWHM value from the rocking curves obtained for the fiber crystals produced at a pulling-down rate of 0.2 mm/min was 17 seconds. It became larger for higher pulling-down rates (for example, 28 seconds for a rate of 1.3 mm/min), indicating that the crystallinity decreased as the growth rate decreased. X-ray rocking curves of  $c$  plane, (002) reflection at a Bragg angle of 23° exhibited larger FWHM values than those of the  $a$  plane.



Fig. 14.4.  $\mu$ -PD KLN plate crystal (120 × 15 × 1 mm); scale in mm

*c* plane reflection was studied for the plate crystals grown at a pulling-down rate of 0.1 mm/min. Growth of the plate crystals at a pulling-down rate of over 0.17 mm/min was difficult to control. Therefore, the optimal rate was considered to be 0.10 mm/min. The FWHM values of the rocking curves were measured and a typical result was about 30 seconds.

### 14.4 Homogeneity of KLN Plates and Fiber

The variation in the lattice constant along the growth axis was measured by X-ray diffraction, and the results are shown in Fig. 14.5 as a function of the fed powder. The part of the plate crystal examined (100–130 mm in length) corresponded to the steady-state growth stage. It was found that the lattice constant along the *c* axis was smaller than expected from the phase diagram because the melt was Li-poor. The Li content in KLN can be established to an accuracy of better than  $\Delta x = 0.01$ , at least for the composition range discussed here ( $x = 0.1-0.3$ ). It is evident that the homogeneity of the plate crystals produced with continuous charging was exceptionally high.

The homogeneity of the component distribution perpendicular to the growth axis was examined by optical measurements. The phase-matching wavelength for SHG in the (110) cross-section was precisely measured for a polished KLN chip cut from a fiber crystal grown at a pulling-down rate of

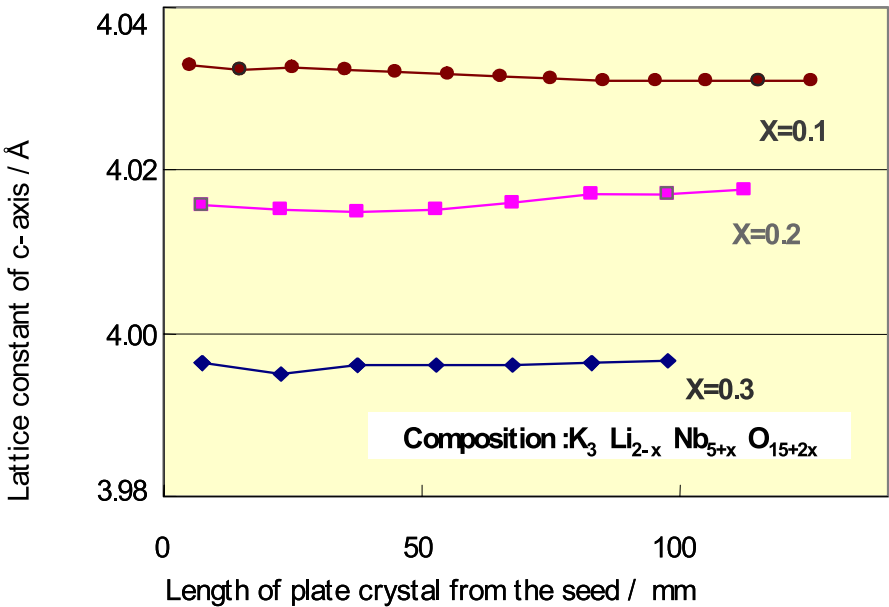


Fig. 14.5. Distribution of lattice constant along growth axis for the  $\mu$ -PD KLN plate crystal (about  $120 \times 15 \times 1$  mm in dimensions)

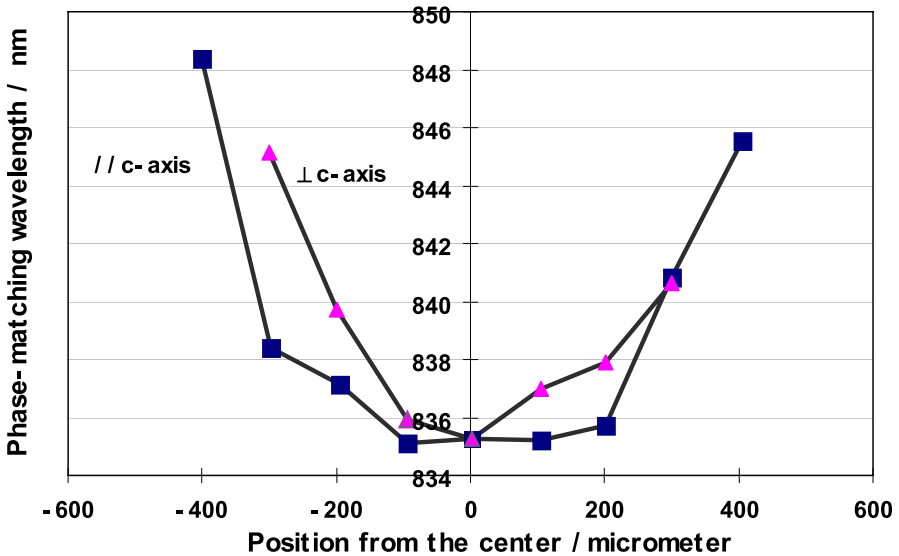


Fig. 14.6. Distribution of phase-matching wavelength in the (110) plane of  $\mu$ -PD fiber crystal

0.2 mm/min. The crystal was mounted on an optical stage and mapping analysis was performed by moving the stage in 0.1 mm intervals. The results from analyzing along the centerline are plotted in Fig. 14.6. The phase-matching wavelength varied parabolically, with the minimum corresponding to the center of the crystal. The maximum difference between the phase-matching wavelength,  $\Delta\lambda$ , at the center and at the edge was 16 nm. Several crystals grown at different pulling-down rates were inspected, and it was found that  $\Delta\lambda$  increased with increasing pulling-down rate.

## 14.5 Properties of the SHG Element

As-grown KLN fiber and plate crystals were highly transparent in the visible region of the spectrum. This transparency decreased rapidly at around 390 nm and dropped to zero at 354 nm. The absorption edge of the  $\mu$ -PD crystals was at a shorter wavelength than in crystals produced by the TSSG process [24]. The absorption coefficient was about  $0.9 \text{ cm}^{-1}$  at  $\lambda = 400 \text{ nm}$ , which is better than that of TSSG-grown KLN,  $2.1 \text{ cm}^{-1}$ . The transmission in the  $\lambda > 600 \text{ nm}$  region was almost constant and no unusual absorption peaks were detected up to 1000 nm.

The single-pass SHG conversion efficiency of the KLN crystal plates was measured. A crystal chip with an axial length of 4 mm was cut from a plate and both (110) planes were mechanically polished before measurements were performed. A pumping beam from a  $\text{Ti}:\text{Al}_2\text{O}_3$  laser was focused with an

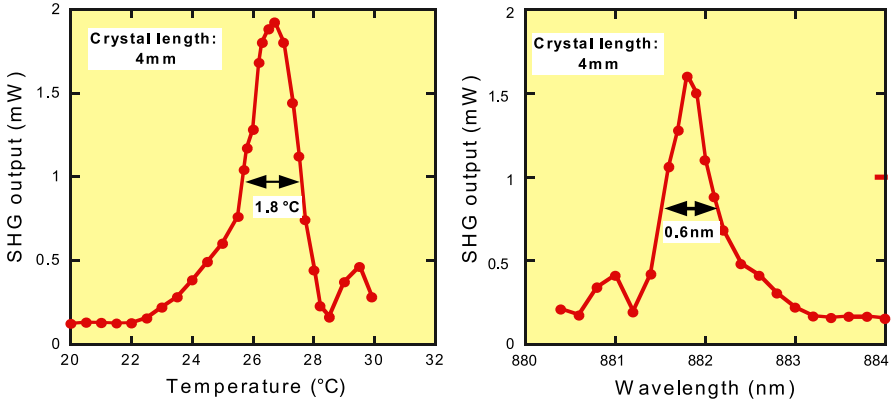


Fig. 14.7. Acceptance temperature and wavelength for the  $\mu$ -PD plate crystal

$f = 50$  mm lens, which had a 30- $\mu$ m beam waist, and directed onto the crystal. The phase-matching wavelength was 900 nm at room temperature, and 2 mW of SHG output was observed with 1.1 W of pumping. The conversion efficiency was estimated to be about 2%/W, which is over 50% of the theoretical value.

The acceptance temperature and wavelength of the plate crystals were also studied (Fig. 14.7). These parameters were measured using a 4-mm-long chip and found to be 0.72  $^{\circ}$ C-cm and 0.24 nm-cm, respectively. These values are smaller than the reported values, because the homogeneity of the  $\mu$ -PD crystals is better than that of TSSG-grown KLN [23]. These characteristics are very important to the design of the SHG devices using KLN chips as wavelength doublers.

## 14.6 Effect of Pulling-Down Rate on Li/Nb Content in KLN

Figure 14.8 shows the variation in phase-matching wavelength as a function of pulling-down rate. Different symbols correspond to different crystals grown from different starting melts. The potassium content was fixed at 30 according to the ratio of K:Li:Nb (= 30: $y$ : $z$ ) and the Li/Nb ratio ( $y$ : $z$ ) varied from 18:52 to 23:47. The phase-matching wavelength became shorter as the pulling-down rate increased. For example, the crystals grown from a starting-melt of  $y$ : $z = 20$ :50 had phase-matching wavelengths of 889, 875, 854, and 840 nm at pulling-down rates of 0.67, 1.00, 1.33, and 1.67 mm/min, respectively.

On the other hand, the phase-matching wavelength increased as the  $y$ : $z$  ratio of the starting melt decreased. The crystals grown from starting melts of  $y$ : $z = 22$ :48, 21:49, and 20:50 exhibited phase-matching wavelengths of 815, 852, and 875 nm, respectively, when a pulling-down rate of 1 mm/min was applied. As a result, SHG phase-matching was achieved between 800 and 920 nm

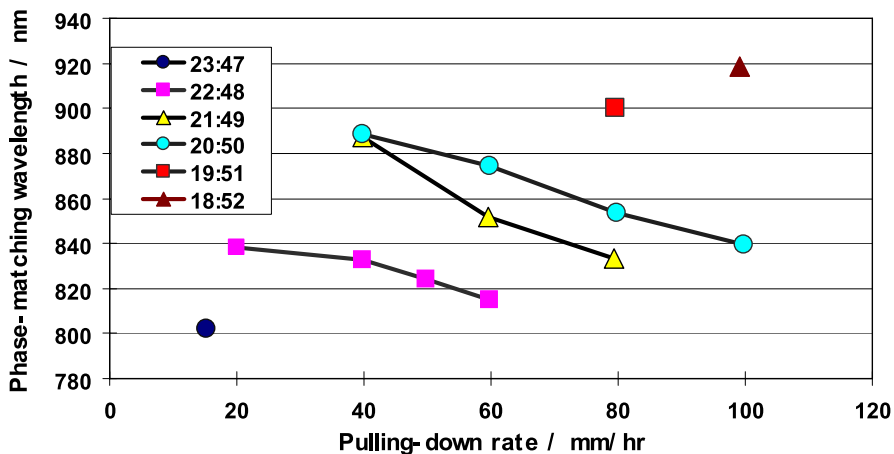


Fig. 14.8. Relationship between phase-matching wavelength, pulling-down rate and Li:Nb ratio (shown in the legend) in the starting melt

by controlling the starting melt composition and the pulling-down rate. This would permit second-harmonic blue laser generation at wavelengths ranging from 400 to 460 nm to be achieved using the KLN crystals discussed here.

## 14.7 Summary

KLN shaped crystals (fibers and plates) grown by the  $\mu$ -PD process have high crystallinity, X-ray rocking curve FWHMs of less than  $20^\circ$ , and good chemical homogeneities along the growth axis (the variation in Li content is less than  $\Delta x = 0.01$ ). However, a variation in the phase-matching wavelength is easily detectable in the radial direction. The SHG efficiency of the crystals reviewed in this chapter was 2%/W for a 4-mm chip, which is over 50% of the maximum theoretical value. The acceptance temperature and wavelength were found to be  $0.72^\circ\text{C cm}$  and  $0.24\text{ nm cm}$ , respectively. The starting-melt composition and the pulling-down rate can be used to control the phase-matching wavelength, which ranges from 800 to 920 nm for  $\mu$ -PD KLN crystals. As a result, second-harmonic blue laser generation is possible at wavelengths ranging from 400 to 460 nm using these crystals.

## References

1. W.A. Bonner, W.H. Grodkiewicz, L.G.V. Uitert, J. Cryst. Growth, **1**, 318 (1967)
2. L.G.V. Uitert, S. Singh, H.J. Levinstein, J.E. Geusic, W.A. Bonner, Appl. Phys. Lett., **11**, 161 (1967)

3. L.G.V. Uitert, S. Singh, H.J. Levinstein, J.E. Geusic, W.A. Bonner, *Mater. Res. Bull.*, **3**, 47 (1968)
4. R. Clarke, F.W. Ainger, J.C. Burfoot, *J. Phys. Colloq.*, **C2**(22), 143 (1973)
5. T. Fukuda, *Jpn. J. Appl. Phys.*, **8**, 122 (1969)
6. T. Fukuda, H. Hirano, S. Koike, *J. Cryst. Growth*, **6**, 293 (1970)
7. T. Fukuda, *Jpn. J. Appl. Phys.*, **9**, 599 (1970)
8. B.A. Scott, E.A. Giess, B.L. Olson, G. Burns, A.W. Smith, D.F. O'Kane, *Mater. Res. Bull.*, **5**, 47 (1970)
9. M. Ouwerkerk, *Adv. Mater.*, **3**, 399 (1991)
10. J.J.E. Reid, *Appl. Phys. Lett.*, **62**, 19 (1993)
11. J.J.E. Reid, M. Ouwerkerk, L.J.A.M. Beckers, *Philips J. Res.*, **46**, 199 (1992)
12. B.A. Scott, E.A. Giess, D.F. O'Kane, *Mater. Res. Bull.*, **4**, 111 (1969)
13. D.H. Yoon, I. Yonenaga, T. Fukuda, N. Ohnishi, *J. Cryst. Growth*, **142**, 339 (1994)
14. D.H. Yoon, T. Fukuda, *J. Cryst. Growth*, **144**, 201 (1994)
15. D.H. Yoon, P. Rudolph, T. Fukuda, *J. Cryst. Growth*, **144**, 207 (1994)
16. D.H. Yoon, M. Hashimoto, T. Fukuda, *Jpn. J. Appl. Phys.*, **33**, 3510 (1994)
17. Y. Mori, T. Sasaki, T. Obana, M. Yoshimura, N. Ohnishi, T. Fukuda, *Tech. Dig. Compact Blue-Green Lasers*, **1**, 52 (1994)
18. K. Imai, M. Imaeda, S. Uda, T. Taniuchi, T. Fukuda, *J. Cryst. Growth*, **177**, 79 (1997)
19. K. Imai, T. Taniuchi, T. Fukuda, M. Imaeda, *Tech. Dig. Conf. Laser Electro-Optics*, **15**, CMC3 (1996)
20. K. Imai, M. Imaeda, T. Taniuchi, T. Fukuda, *Tech. Dig. Conf. Laser Electro-Optics*, **89**, WK3 (1997)
21. M. Imaeda, K. Imai, T. Fukuda, *Proc. Int. Symp. Laser Nonlinear Optical Materials*, **188**, T8.3 (1997)
22. A. Onoe, T. Yoshino, K. Imai, M. Imaeda, K. Chikuma, *Jpn. J. Appl. Phys.*, **41**, 5697 (2002)
23. W.J. Bartels, *J. Vac. Sci. Technol. B*, **1**, 338 (1983)
24. Y. Furukawa, S. Makio, T. Miyai, M. Sato, H. Kitayama, Y. Urata, T. Taniuchi, T. Fukuda, *Appl. Phys. Lett.*, **68**, 744 (1996)

# 15 Piezoelectric Langasite-Type Crystals

Tsuguo Fukuda, Hiroshi Machida

**Abstract.** Details of the growth of langasite-type crystals by the micro-pulling-down method are described. The application of the method for advanced materials research and the optimization of crystal growth conditions are also outlined.

## 15.1 Introduction

Gallate crystals such as  $\text{La}_3\text{Ga}_5\text{SiO}_{14}$  (LGS; langasite) and  $\text{La}_3\text{Me}_{0.5}\text{Ga}_{5.5}\text{O}_{14}$  (LMG;  $\text{Me} = \text{Nb}^{5+}, \text{Ta}^{5+}$ ) with  $\text{Ca}_3\text{Ga}_2\text{Ge}_4\text{O}_{14}$  (CGG)-type structure [1] have been reported to be promising materials for piezoelectric applications in mobile communications devices [2–5] due to their high frequency stability and high electromechanical coupling factors. These crystals have actually been used in both bulk- (BAW) and surface-acoustic wave (SAW) devices [3, 6–9].

The structure of CGG is trigonal with point group 32 and can be described as a framework constructed from corner-sharing tetrahedrons with Ga and Ge atoms in two sites (2*d* and 3*f*) and octahedrons with Ga atoms in the 1*a* site (Fig. 15.1). There are four types of cation sites in a langasite-type structure of chemical formula  $\text{A}_3\text{BC}_3\text{D}_2\text{O}_{14}$ . A and B represent decahedral sites (twisted Thomson cubes) coordinated by eight oxygen atoms and octahedral site coordinated by six oxygen atoms, respectively. Both C and D represent tetrahedral sites coordinated by four oxygen atoms. However, the

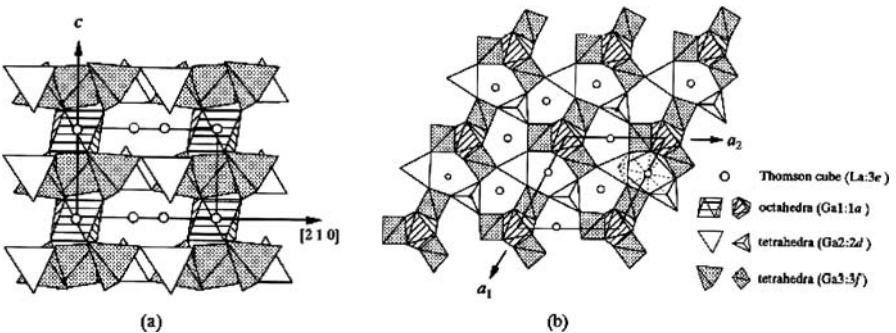


**Fig. 15.1.** Projection of the  $\text{A}_3\text{BC}_3\text{D}_2\text{O}_{14}$  structure **a** along the [010] direction and **b** normal to the [001] direction [10]

D site is a little smaller than the C site. The cation occupation at each site is illustrated in Fig. 15.2.

To aid further development, many new compounds with the CGG structure have been studied by the micro-pulling-down ( $\mu$ -PD), Czochralski (CZ) [11–18], Bridgman [19] and liquid phase epitaxy [20] methods. The  $\mu$ -PD method is especially a convenient and fast method to use to find out whether single crystals can be grown from the melt or not: it is often used to analyze the behavior of a compound and for pre-growth melt testing.

Three groups of langasite-type crystals are discussed in this chapter. First of all, LGS,  $\text{Sr}_3\text{Nb}_{1-x}\text{Ga}_{3+(5/3)x}\text{Si}_2\text{O}_{14}$  (SNGS) and  $\text{Ca}_3\text{Nb}_{1-x}\text{Ga}_{3+(5/3)x}\text{Si}_2\text{O}_{14}$  (CNGS) crystal growth via  $\mu$ -PD was examined in order to investigate the influence of the contents of Nb and Ga on the properties of these crystals, and to elucidate their morphologies [21]. The crystals grown were examined for defect formation and their piezoelectric properties were studied. These results were compared with those obtained for LGS. Second, crystals of alkali-earth cation (Sr, Ba)-substituted LGS and LMG ( $\text{La}_3\text{Me}_{0.5}\text{Ga}_{5.5}\text{O}_{14}$ ,  $\text{M} = \text{Nb}^{5+}, \text{Ta}^{5+}$ ) were also grown to search for novel materials that are superior to the pure compounds [22]. Third,  $\text{La}_3\text{M}^{4+}\text{Ga}_5\text{O}_{14}$  ( $\text{LM}^{4+}\text{G}$ ;  $\text{M} = \text{Ti}, \text{Zr}, \text{Hf}$ ) crystals were grown in order to investigate the crystal chemistry of their langasite structure. Thus, the distributions of tetravalent cations (Ti, Zr, Hf) were clarified [10].

The  $\mu$ -PD method has recently been adopted as an actual material production process for langasite-type crystals, largely because the  $\mu$ -PD configuration permits continuous melt feeding.

The wettability between the melt and the crucible material is extremely important in  $\mu$ -PD and determines most of the growth parameters. To measure the contact angle, langasite melt drops were formed on flat metal plates made from potential crucible materials and heated by RF power [23]. The

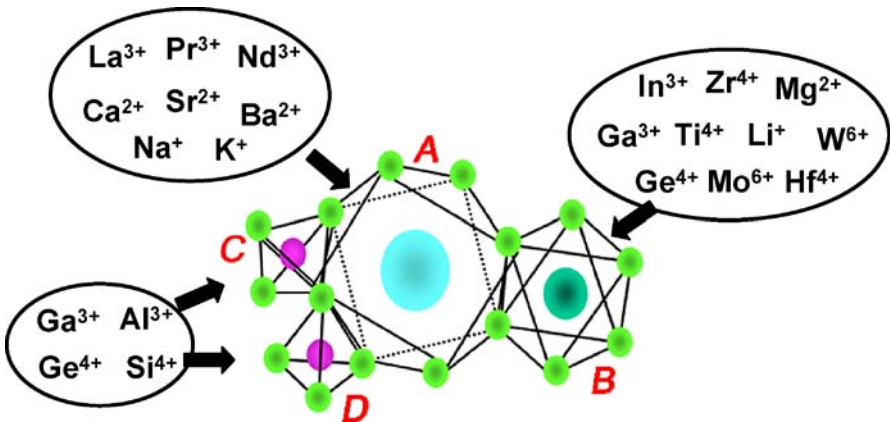


Fig. 15.2. Schematic diagram of the  $\text{A}_3\text{BC}_3\text{D}_2\text{O}_{14}$  structure and the cations occupying each site

geometry of the drops was observed using a CCD camera. Pt–Au alloys were found to have large contact angles with LGS melt [23]. In this chapter, the process of selecting an appropriate crucible material for  $\mu$ -PD growth is introduced in some detail. As a result of these preliminary tests, and following the fabrication of a Pt–Au crucible, langasite plate crystals ( $1 \times 15 \times 70$  mm) of acceptable quality were grown. Thus, the successful production of langasite crystals by  $\mu$ -PD instead of the CZ method was demonstrated.

## 15.2 $\text{Sr}_3\text{Nb}_{1-x}\text{Ga}_{3+(5/3)x}\text{Si}_2\text{O}_{14}$ and $\text{Ca}_3\text{Nb}_{1-x}\text{Ga}_{3+(5/3)x}\text{Si}_2\text{O}_{14}$

The properties of  $\text{Sr}_3\text{Nb}_{1-x}\text{Ga}_{3+(5/3)x}\text{Si}_2\text{O}_{14}$  (SNGS) and  $\text{Ca}_3\text{Nb}_{1-x}\text{Ga}_{3+(5/3)x}\text{Si}_2\text{O}_{14}$  (CNGS) depend on their Nb and Ga contents, i.e., the value of  $x$  [21]. Therefore, fiber-shaped crystals of these compounds with various compositions were produced by  $\mu$ -PD from a capillary 2.0 mm in length and 0.8 mm in diameter. The crucible was made from Pt–Rh (10%) alloy because the melting points of these compounds are relatively low (1320–1400 °C), and the capillary channel was positioned at the center of the crucible bottom. The crucible was heated resistively by passing a current through it. The shape of the crucible is described in detail in [24]. Growth was performed under normal atmosphere, and the pulling-down rate was 0.02–0.30 mm/min. The temperature distribution around the capillary was controlled by a Pt–Rh afterheater.

The quality of the  $\text{Sr}_3\text{Nb}_{1-x}\text{Ga}_{3+(5/3)x}\text{Si}_2\text{O}_{14}$  ( $x = 0, 0.05, 0.1, 0.25$ ) crystals was examined visually and by XRD powder phase analysis. For  $x = 0.25$ , the crystals were opaque and had small inclusions of a secondary phase. All of the other crystals comprised a single langasite phase. In the case of  $\text{Ca}_3\text{Nb}_{1-x}\text{Ga}_{3+(5/3)x}\text{Si}_2\text{O}_{14}$  ( $x = 0, 0.05, 0.1$ ), only the composition with  $x = 0$  permitted the growth of single crystals without any impurities. The other fibers (those with  $x = 0.05, 0.1$ ) were opaque and had foreign phase inclusions. The surfaces of the as-grown SNGS and CNGS crystals were not smooth. Moreover, a number of cracks and other defects were also observed, as seen in Fig. 15.3.

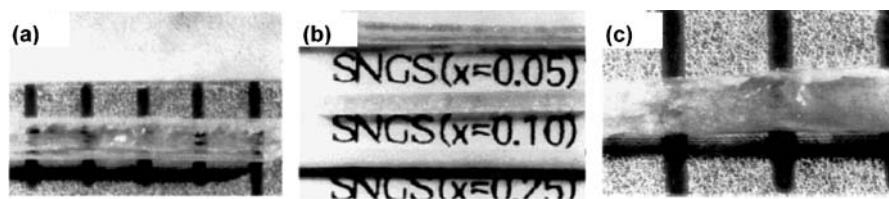


**Fig. 15.3.** The  $\mu$ -PD crystals of SNGS and CNGS: **a** SNGS with  $x = 0$ , **b** SNGS with  $x = 0.05$  (top), 0.10 (middle), and 0.25 (bottom), and **c** CNGS with  $x = 0$  [21]

In terms of piezoelectric properties, SNGS and CNGS were reported to be noticeably superior to LGS. The piezoelectric coefficient ( $d_{12}$ ) of SNGS crystal exhibits a much stronger temperature dependence than that of CNGS crystal [21].

### 15.3 Sr-/Ba-Substituted $\text{La}_3\text{Ga}_5\text{SiO}_{14}$ and $\text{La}_3\text{Me}_{0.5}\text{Ga}_{5.5}\text{O}_{14}$ (Me = Nb, Ta)

It has been reported that increasing the lattice parameter leads to an increase in the piezoelectric modulus  $|d_{11}|$  of langasite-type crystals (Fig. 15.4) [22]. This tendency is particularly noticeable in RGS ( $\text{Re}_3\text{Ga}_5\text{SiO}_{14}$ ; Re = Nb, Pr, La) crystals. One simple way to obtain materials with large lattice parameters is to replace  $\text{La}^{3+}$  with larger cations. However,  $\text{La}^{3+}$  is the largest of all of the trivalent rare-earth cations. An alternative is to replace the  $\text{La}^{3+}$  with larger alkali-earth (AE) cations (Sr, Ba), in which case charge compensation is also required in the langasite lattice. Therefore, the  $\mu$ -PD growth of Sr-/Ba-substituted LGS,  $\text{La}_3\text{Nb}_{0.5}\text{Ga}_{5.5}\text{O}_{14}$  (LNG) and  $\text{La}_3\text{Ta}_{0.5}\text{Ga}_{5.5}\text{O}_{14}$  (LTG) was attempted in the hope of fabricating materials with the properties superior to those of the pure compounds. These substitutions result in crystals of chemical formulae  $\text{La}_{3-x}\text{AE}_x\text{Ga}_{4-x}\text{Si}_{1+x}\text{O}_{14}$  and  $\text{La}_{3-x}\text{AE}_x\text{M}_{0.5+x/2}\text{Ga}_{5.5-x/2}\text{O}_{14}$  (AE = Sr, Ba,  $x = 0.25$ – $1.0$ , M = Nb, Ta). The structures of these materials were also examined by XRD analysis.

Single-phase powders used as starting materials were melted in a Pt/Rh crucible with a capillary nozzle (0.8–1.0 mm in diameter) set at the crucible bottom. The crystals were grown at a pulling-down rate of 0.2 mm/min in air with a meniscus height of about 200  $\mu\text{m}$ . The purities of the crystals grown by  $\mu$ -PD together with those obtained by solid-state reaction are described in Table 15.1. The solubility limit of  $\text{Sr}^{2+}$  in these crystals was observed to be

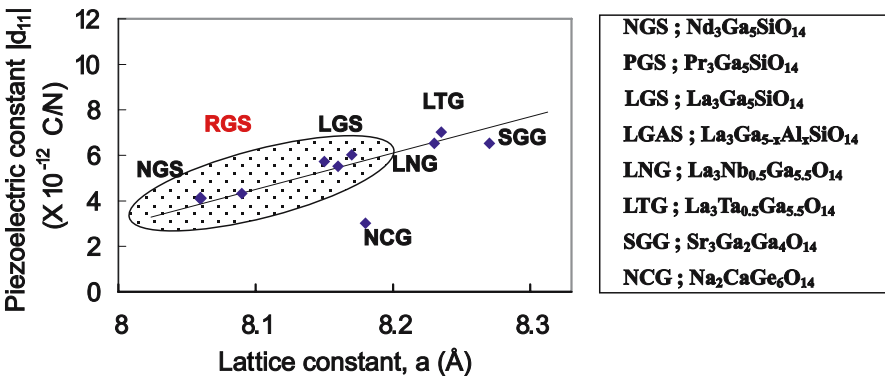


Fig. 15.4. Piezoelectric modulus  $|d_{11}|$  versus the lattice parameter,  $a$  in  $\text{Ca}_3\text{Ga}_2\text{Ge}_4\text{O}_{14}$ -type crystals

**Table 15.1.** Synthesis of langasite-type materials by solid-state reaction and  $\mu$ -PD growth. “O” indicates single-phase products with  $\text{Ca}_3\text{Ga}_2\text{Ge}_4\text{O}_{14}$  structure, and “X” indicates mixtures with an impurity phase. Bars (“–”) indicate that the experiments were not carried out

AE	Sr	Sr	Sr	Sr	Ba	Ba	Ba	Sintering method
$x$	0.25	0.50	0.75	1.00	0.25	0.50	1.00	Solid-state reaction
LGS	O	O	O	X	O	X	X	Solid-state reaction
LNG	O	X	–	–	X	–	–	Solid-state reaction
LTG	O	O	O	X	O	X	–	Solid-state reaction
LGS	X	X	–	–	X	–	–	Micro-pulling-down
LNG	X	–	–	–	X	–	–	Micro-pulling-down
LTG	O	X	X	–	X	–	–	Micro-pulling-down

greater than that of  $\text{Ba}^{2+}$ . Only Sr-substituted LTG (Sr:LTG) with  $x = 0.25$  was grown as a single crystal without any impurities. Moreover, it was found that the lattice parameters in the Sr:LTG compounds varied as a function of Sr content,  $x$ . The structure of Sr:LTG was a little different from that of pure LTG [22]. It was suggested that the coexistence of  $\text{La}^{3+}$  and  $\text{Sr}^{2+}$  at the A sites of LGS reduces the piezoelectric modulus  $|d_{11}|$ . It seems likely that appropriate substitution of the cations situated at other (B, C, and D) sites in LGS, LNG and LTG would improve the piezoelectric properties of these crystals.

## 15.4 $\text{La}_3\text{M}^{4+}\text{Ga}_5\text{O}_{14}$ (M = Ti, Zr, Hf) Growth and Structure

In  $\text{La}_3\text{Ga}_5\text{SiO}_{14}$  and  $\text{La}_3\text{Ga}_5\text{GeO}_{14}$ , it is known that both the Si and Ge atoms only occupy the tetrahedral  $2d$  sites. In  $\text{La}_3\text{Me}_{0.5}\text{Ga}_{5.5}\text{O}_{14}$  (LMG, Me =  $\text{Nb}^{5+}$ ,  $\text{Ta}^{5+}$ ),  $\text{Me}^{5+}$  and  $\text{Ga}^{3+}$  were known to coexist at the octahedral  $1a$  site. However, the distribution of tetravalent cations (Ti, Zr, Hf) in the structure of  $\text{La}_3\text{M}^{4+}\text{Ga}_5\text{O}_{14}$  ( $\text{LM}^{4+}\text{G}$ ; M = Ti, Zr, Hf) was not clear. Therefore, the growth of these crystals by  $\mu$ -PD was attempted with a view to subsequent phase identification by XRD [10].

The results of this  $\mu$ -PD growth suggested that  $\text{La}_3\text{M}^{4+}\text{Ga}_5\text{O}_{14}$  crystals cannot be grown from stoichiometric melts. Nevertheless, the  $\text{La}_3\text{TiGa}_5\text{O}_{14}$  crystal was transparent (and yellow in color) except for very small opaque parts at the start of growth (Fig. 15.5). According to XRD analysis, the transparent and opaque parts were formed by langasite and  $\text{LaGaO}_3$  phases, respectively. It was therefore assumed that  $\text{La}_3\text{TiGa}_5\text{O}_{14}$  crystals can only be grown by solution growth techniques such as the flux method, considering that  $\text{La}_3\text{TiGa}_5\text{O}_{14}$  melts incongruently.

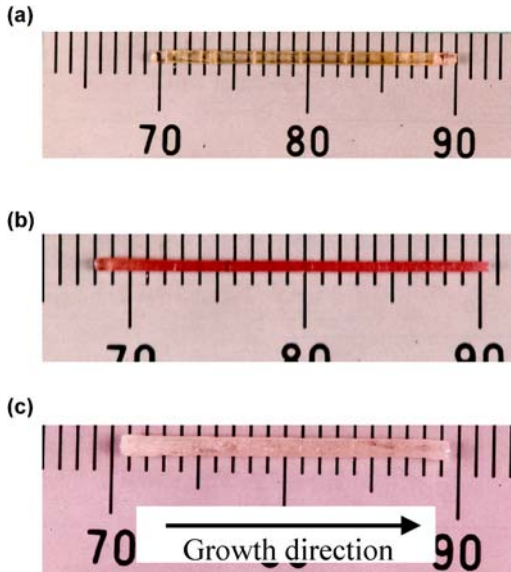


**Fig. 15.5.** **a**  $\text{La}_3\text{TiGa}_5\text{O}_{14}$ , **b**  $\text{La}_3\text{ZrGa}_5\text{O}_{14}$  and **c**  $\text{La}_3\text{HfGa}_5\text{O}_{14}$  crystals grown by the  $\mu$ -PD method [22]

Structural analysis indicated that the  $\text{Ti}^{4+}$  cations occupy both octahedral and tetrahedral  $3f$  sites. Moreover, the smaller tetrahedral  $2d$  sites are most probably only occupied by  $\text{Ga}^{3+}$  cations. Therefore, the proposed structural formula of  $\text{La}_3\text{TiGa}_5\text{O}_{14}$  is  $(\text{La}_3)^{3e}(\text{Ti}_{0.72}\text{Ga}_{0.28})^{1a}(\text{Ti}_{0.33}\text{Ga}_{2.67})^{3f}(\text{Ga}_2)^{2d}\text{O}_{14}$ , with the Wyckoff-site notation superscripted [10].

## 15.5 $\text{La}_3\text{Ga}_5\text{SiO}_{14}$ Plate Crystal Growth

The  $\mu$ -PD technique had only been used for materials analysis of langasite-type crystals; no reports concerning the development of the corresponding crystal growth procedure and its crystal properties were found. Moreover, technical improvements in  $\mu$ -PD had not been examined from the point of view of high-quality crystal growth. These crystals are normally grown by the CZ method, although  $\text{La}_3\text{Ga}_5\text{SiO}_{14}$  melts incongruently [23]. The  $\mu$ -PD system is superior to CZ for incongruent crystal growth because it is much easier to modify the  $\mu$ -PD configuration to include a continuous feeding system. Thus, the  $\mu$ -PD apparatus can be adapted for the industrial production of langasite crystals.

In general, discussions of  $\mu$ -PD growth stability focus on the shape of the meniscus positioned between the capillary nozzle and the crystal, because the shape is controlled by the growth parameters. However, the growth stability obtained using the  $\mu$ -PD method also depends on the wettability between

the melt and the crucible material. Therefore, the development of langasite crystal growth by  $\mu$ -PD was examined based on the wetting properties of the melt. It was observed experimentally that the langasite melt wets most of the crucible materials typically used for the growth of oxide crystals well. This is one of the reasons why the growth of large bulk crystals or plates has not yet been established.

The experimental results for the wetting properties of LGS melt drops in contact with various crucible materials are shown in Fig. 15.6 [25]. The crucible materials tested were: Ir, Ir-Rh, Pt, Pt-Rh, Pt-Au, Mo, Ta, Re, and W. Powders corresponding to the desired crystal/melt composition were melted onto each metal plate using the RF heating. The contact angle was measured using images obtained from a CCD camera after rapid cooling of the melt drops. It was found that the melt wets almost all materials with a contact angle of about  $10^\circ$  or less. Pt-Au alloy was the only exception, yielding a contact angle of about  $75^\circ$  that is high enough to permit a stable meniscus shape. This was confirmed by performing LGS plate crystal growth from a Pt-Au crucible [25].

The starting materials used for plate crystal growth were single-phase powders that were placed and then melted in a Pt-Au (5%) crucible with a die  $1\text{ mm} \times 15\text{ mm}$  in cross-section positioned at the bottom. The crystals were grown at a pulling-down rate of  $0.5\text{--}1.0\text{ mm/min}$  in a  $\text{N}_2 + 10\% \text{ O}_2$  atmosphere [25]. Figure 15.7 shows a langasite plate crystal  $1\text{ mm}$  in thickness and  $70\text{ mm}$  in length. The crystal was transparent and exhibited no cracks throughout the whole plate.

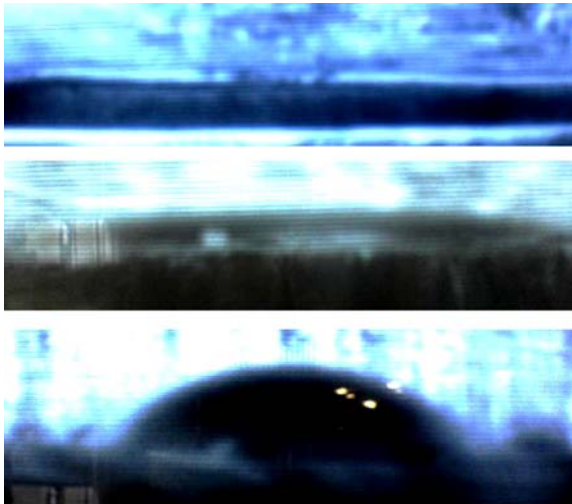


**Fig. 15.6.** View of the LGS melt drop on the metal plate. The contact angles between the melt and the metal plates are  $0^\circ$  for Pt (*above*),  $8^\circ$  for Ir (*middle*), and  $75^\circ$  for Pt-Au alloy (*below*)

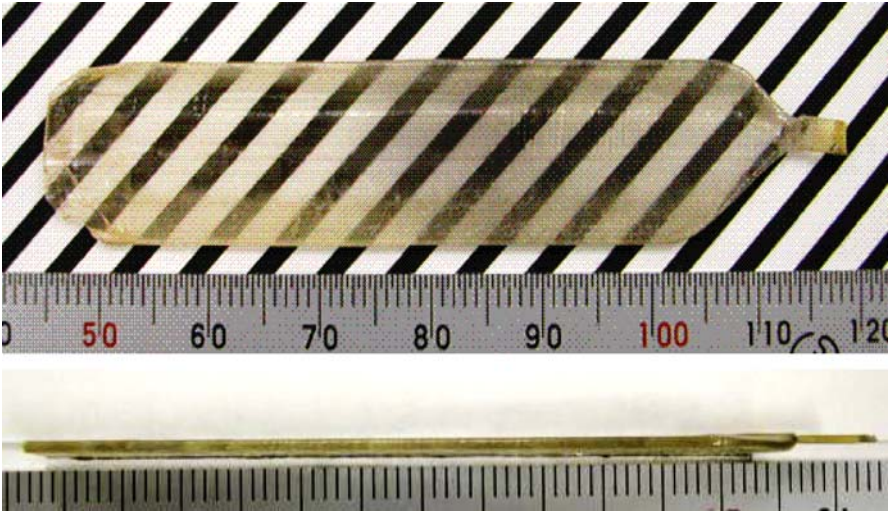


**Fig. 15.7.** LGS plate crystal with dimensions of  $1 \times 15 \times 70$  mm (scale in mm): face view (*above*) and side view (*below*)

For the crucibles made from the other materials listed above, the melt was observed to spread across the surface of the die and the crucible bottom. Areas outside of the shape-forming die were therefore coated with melt. It is evident that stable growth conditions cannot be established when the solid/liquid interface is not controlled by the edges of the die. This situation is similar to classic EFG crystal growth when pulling is performed in the upward direction. The crystals produced in these uncontrolled conditions had many defects, such as cracks, voids, and inclusions, even when the pulling-down rate was reduced to about 0.05 mm/min. However, when the melt did not wet the crucible, rod-shaped LGS and SGG crystals with cross-sections of  $5 \times 5$  mm were also successfully grown (Fig. 15.8). Both types of crystal were transparent and single-phase (Sasaki et al., to be published). These experiments confirmed the ability of the  $\mu$ -PD system to produce bulk langasite crystals similar to those grown through the CZ method.

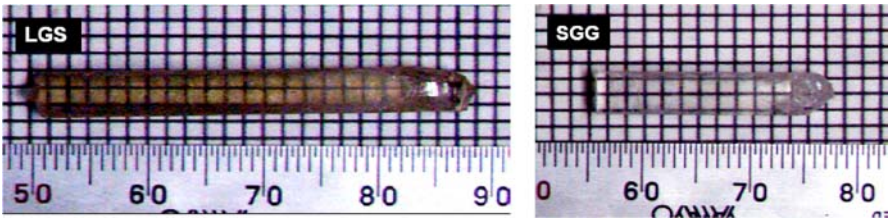


**Fig. 15.8.** Rod shaped crystals of langasite family produced by  $\mu$ -PD technique with cross-section of  $5 \times 5$  mm:  $\text{La}_3\text{Ga}_5\text{SiO}_{14}$  (*left*) and  $\text{Sr}_3\text{Ga}_2\text{Ge}_4\text{O}_{14}$  (*right*)

## References

1. E.L. Belokoneva, M.A. Simonov, A.V. Butashin, B.V. Mill, N.V. Belov, *Sov. Phys. Dokl.*, **26**, 931 (1980)
2. Yu.V. Pisarefsky, P.A. Senyushencov, P.A. Popov, B.V. Mill, *Proc. IEEE Int. Freq. Cont. Symp.*, **653** (1995)
3. H. Takeda, K. Shimamura, T. Kohno, T. Fukuda, *J. Cryst. Growth*, **169**, 503 (1996)
4. Yu.V. Pisarevsky, P.A. Senyushenkov, B.V. Mill, N.A. Moiseeva, *Proc. IEEE Inter. Freq. Cont. Symp.*, 742 (1998)
5. H. Kawanaka, H. Takesa, K. Shimamura, T. Fukuda, *J. Cryst. Growth*, **183**, 274 (1998)
6. I.H. Jung, J.M. Ko, K.B. Shim, T. Fukuda, K.H. Auh, *J. Cryst. Growth*, **220**, 275 (2000)
7. I.H. Jung, K.H. Auh, *Mater. Lett.*, **41**, 241 (1999)
8. J. Bohm, E. Chilla, C. Flannery, H.J. Frohlich, T. Hauke, R.B. Heimann, M. Hengst, U. Staube, *J. Cryst. Growth*, **293**, 216 (2000)
9. S. Uda, A. Bungo, C. Jian, *Jpn. J. Appl. Phys.*, **5516**, 38 (1999)
10. H. Takeda, T. Kato, V.I. Chani, K. Shimamura, T. Fukuda, *J. Alloys Compd.*, **290**, 244 (1999)
11. M. Kumatoriya, H. Sato, J. Nakanishi, T. Fujii, M. Kadota, Y. Sakabe, *J. Cryst. Growth*, **229**, 289 (2001)
12. S. Uda, O. Buzanov, *J. Cryst. Growth*, **211**, 318 (2000)
13. H. Takeda, K. Shimamura, V.I. Chani, T. Fukuda, *J. Cryst. Growth*, **197**, 204 (1999)
14. J. Bohm, E. Chilla, C. Flannery, H.J. Frohlich, T. Hauke, R.B. Heimann, M. Hengst, U. Straube, *J. Cryst. Growth*, **216**, 293 (2000)
15. J. Sato, H. Takeda, H. Morikoshi, K. Shimamura, P. Rudolph, T. Fukuda, *J. Cryst. Growth*, **191**, 746 (1998)
16. R. E. Leshchuk, A. E. Nosenko, *Inorg. Mater.*, **36**(12), 1268 (2000)
17. I.H. Jung, A. Yoshikawa, T. Fukuda, K.H. Auh, *J. Alloys Compd.*, **339**, 149 (2002)
18. H. Takeda, K. Shimamura, V.I. Chani, T. Kato, T. Fukuda, *Cryst. Res. Technol.*, **34**, 1141 (1999)
19. S. Uda, H. Inaba, J. Harada, K. Hoshikawa, *J. Cryst. Growth*, **271**, 229 (2004)
20. V.I. Chani, H. Takeda, T. Fukuda, *Mater. Sci. Eng. B*, **60**, 212 (1999)
21. I.H. Jung, Y.H. Kang, K.B. Shim, A. Yoshikawa, T. Fukuda, K.H. Auh, *Jpn. J. Appl. Phys.*, **40**, 5706 (2001)
22. H. Takeda, T. Kato, V.I. Chani, H. Morikoshi, K. Shimamura, T. Fukuda, *J. Alloys Compd.*, **290**, 79 (1999)
23. S.Q. Wang, S. Uda, *J. Cryst. Growth*, **250**, 463 (2003)
24. D.H. Yoon, I. Yonenaga, N. Onishi, T. Fukuda, *J. Cryst. Growth*, **142**, 423 (1994)
25. A. Sasaki, T. Fujiwara, H. Machida, Japan Patent, 2005-275771 (22 Sept. 2005)

# 16 Shaped Sapphire: Rods, Tubes, and Plates

Hiroki Sato

**Abstract.** In this chapter, the ability of the micro-pulling-down ( $\mu$ -PD) method to grow “device size” and “device shaped” crystals is reviewed. Process details, characterization results, and general advantages of using the  $\mu$ -PD method in this field are discussed based on experiences of sapphire growth.

## 16.1 Introduction

Sapphire ( $\text{Al}_2\text{O}_3$ ) crystal is an important material used in high technology, particularly in optical and electrooptical applications. When used as an optical material, sapphire has a broad transmission band encompassing the ultraviolet, visible, and infrared spectral regions. Sapphire also possesses very good mechanical and physical properties, such as tensile strength, abrasion resistance, thermal conductivity and mechanical stability, which result in outstanding thermal shock resistance [1]. In the 1960s, large crystals of sapphire were required for transparent armor applications because of its high hardness and toughness. Therefore, several crystal growth processes were adapted to produce large sapphire crystals [2–7].

The device size required from the industry is getting smaller and smaller. Therefore, the importance of shaped crystal growth is getting greater and greater. Shaped crystal growth technologies have many advantages over bulk crystal growth methods. The cost of crystals produced directly with dimensions suitable for device applications is generally lower because of the resulting simplification of the crystal machining stage. A sizeable number of papers on the use of the micro-pulling-down ( $\mu$ -PD) growth as (i) a fiber crystal growth technique and (ii) a quick sample preparation method have been published over the past ten years. However, these two applications do not represent the entire potential of  $\mu$ -PD. In this chapter, the  $\mu$ -PD growth of shaped sapphire crystals with various cross-sections is discussed.

## 16.2 General Growth Details

The crystals were grown by the  $\mu$ -PD method from iridium crucibles. Figure 16.1 shows a schematic illustration of the  $\mu$ -PD set-up.  $\text{Al}_2\text{O}_3$  (5N) powder was used as the raw material; this was loaded into a crucible about

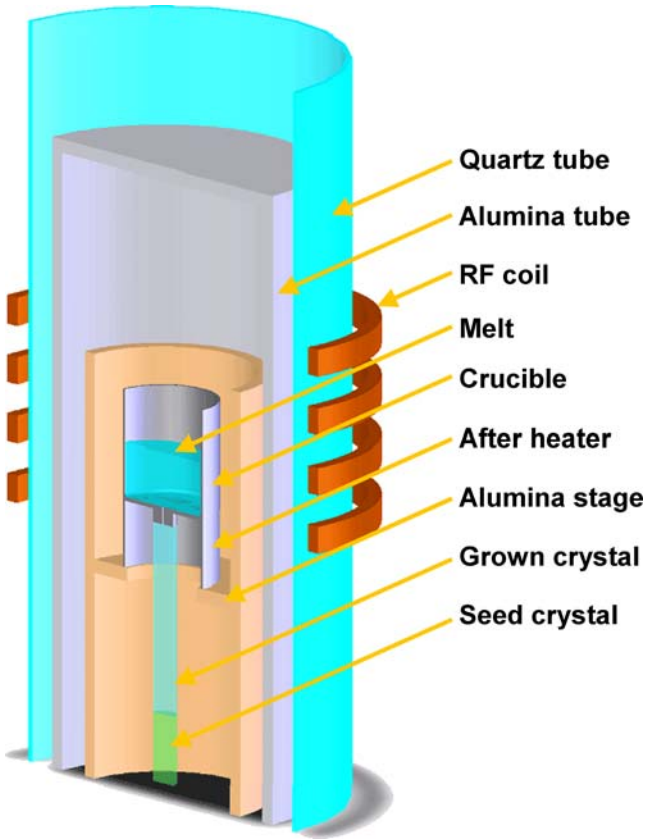


**Fig. 16.1.** Schematic illustration of the  $\mu$ -PD setup

45 mm high by 22 mm in diameter. The crucible was placed on an alumina pedestal in a vertical quartz tube and was heated using an RF generator. The calibrated orifice in the crucible bottom was about 0.4 mm in diameter. The crucible temperature was controlled using the RF coil, which was about 55 mm long with four windings. The crucible was charged to about 5–10 vol% with respect to the melt. High-density and high-purity (99.7%) alumina ceramic surrounded the crucible for thermal insulation. The crystals were grown in argon atmosphere (gas flow 1.01/min) to avoid oxidation of the crucible. Visual observations of the meniscus region, the solid–liquid interface, and the growing crystals were made with a CCD camera and monitor.

A  $\langle 0001 \rangle$ -oriented single crystal of sapphire grown by the edge-defined film-fed growth (EFG) method was used as a seed crystal. This seed was attached to a holder equipped with an  $x$ – $y$  manipulator for final alignment to the crucible die.

### 16.3 Sapphire Rod

A specially designed crucible was used to grow rod-shaped sapphire crystals. Figure 16.2 shows an image of the crucible used to grow the rod-shaped crystal. The die used had a rectangular (square) cross-section 5 mm on a side. The melt flowed through an opening in the center of the die about 0.4 mm in diameter. Initially, the seed was placed into contact with the melt situated on the outer side of the die. Thereafter, the cross-section of the crystal was increased by increasing the RF power.

Small windows in the afterheater and the insulation around the hot zone are generally necessary in order to be able to observe the melt meniscus and the growing crystal with a CCD camera. However, cracks often formed at the side of the crystal situated near the windows. To understand the reason for these cracks, the temperature distribution near the die was measured. Figure 16.3a shows the results from these measurements. Notable asymmetry in the spatial distribution in temperature was detected, which was the result of the asymmetrical configuration of the hot zone due to the presence of the windows.

To improve the temperature profile, four windows arranged in tandem were cut in both the afterheater and the heat shield. The spatial temperature distribution for this modified set up is shown in Fig. 16.3b. Upon comparing the temperature profiles obtained for both the one-window and the multi-window arrangements, the positive effect of this modification is evident. The modification should reduce the stress inside the growing crystal.

Figure 16.4 (left) shows the shaped sapphire crystals with square cross-sections of 5 mm grown using this technique. Crack- and inclusion-free shaped crystals were successfully grown using the multiwindow set-up. The  $\varnothing$  5 mm Cr-doped sapphire rod crystals illustrated in Fig. 16.4 (right) were also grown using a similar procedure.

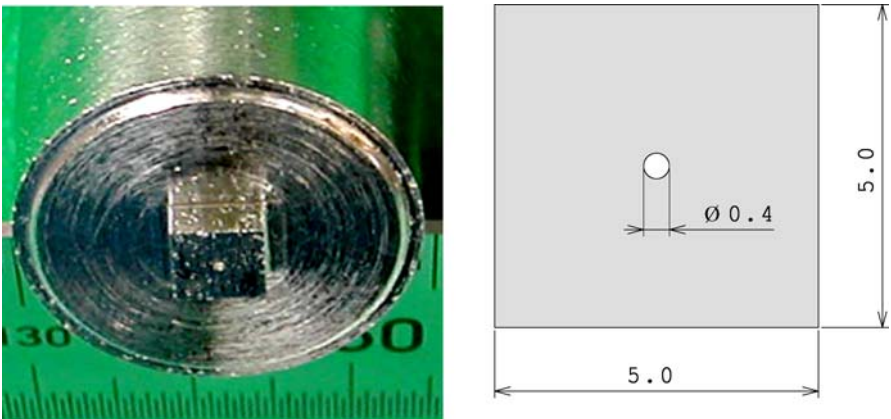


**Fig. 16.2.** View of the bottom of the crucible for the growth of shaped sapphire in 5 mm square. *Right figure* indicates the dimensions of the die

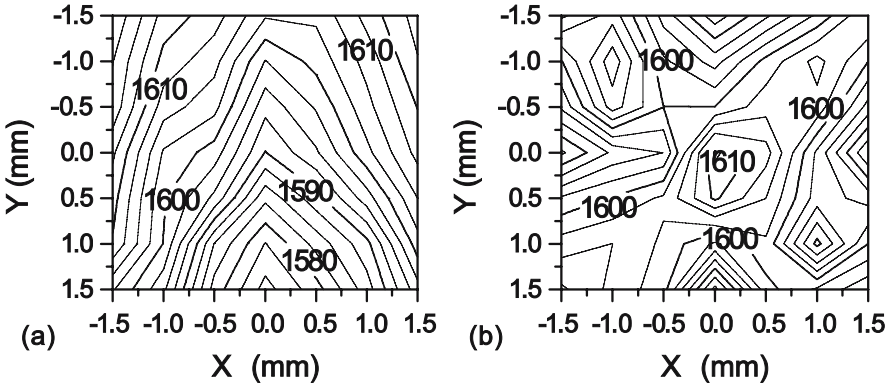


Fig. 16.3. Temperature distribution near the die

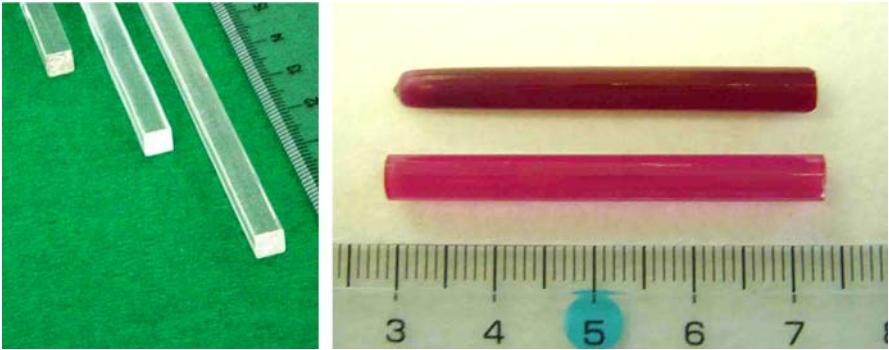
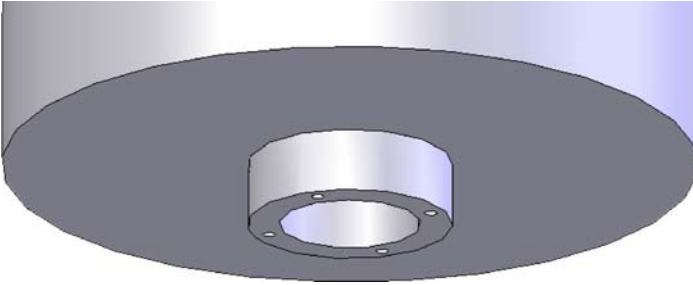


Fig. 16.4. Shaped sapphire crystals: 5 mm square (left) and  $\varnothing$  5 mm Cr-doped (right) rods

### 16.4 Sapphire Tube

Tube-shaped sapphire crystals are considered for applications in special windows, high-pressure reactors, engines, and chemical vapor deposition (CVD) systems. Therefore, the growth of tube-shaped sapphire crystal was also performed to establish a process suitable for the production of tube-shaped materials. Figure 16.5 schematically illustrates the design of the bottom of the crucible used to grow tubular crystals. A ring-shaped die was installed at the bottom to support the formation of a ring-like melt column. The outer and inner diameters of the die were 6 and 4 mm, respectively. The height of the die was 2 mm. Four holes were cut in the die to improve the melt supply, especially during the stage of shoulder growth.

Figure 16.6 shows tubular crystals of sapphire grown using this crucible. When the growth temperature was relatively low, the crystal shape was unstable, as shown in Fig. 16.6 (left). The effect of the growth speed on the crystal quality was also examined. The growth speed was changed from 0.5 mm/min



**Fig. 16.5.** Schematic illustration of the die for the growth of tube crystal

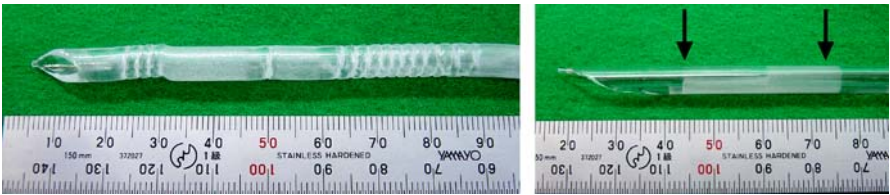


**Fig. 16.6.** Tube sapphire crystals grown under low temperature (*left*) and that grown at higher temperature with change the pulling speed (*right*)

to 2.0 mm/min during the growth process. Figure 16.6 (right) illustrates the result of this action. The left side of the crystal shows initial crystal growth. In this figure, the growth speed was 0.5 mm/min up to the left arrow. Thereafter, the speed was increased to 2.0 mm/min. The figure shows that the grown tube crystal became opaque after the increase in speed was imposed. Starting from the right arrow in Fig. 16.6 (right), the pulling speed was decreased back to 0.5 mm/min. Thus, the starting growth conditions were restored, and the crystal grown was again transparent. The opacity of the middle part of the crystal was due to the formation of gas bubbles of molten  $\text{Al}_2\text{O}_3$  inside the crystal [8].

By modifying the growth conditions, such as the pulling speed and the power (the temperature of the meniscus), inclusion-free smooth tubular crystals of sapphire were grown (Fig. 16.7). The point at which growth was initi-

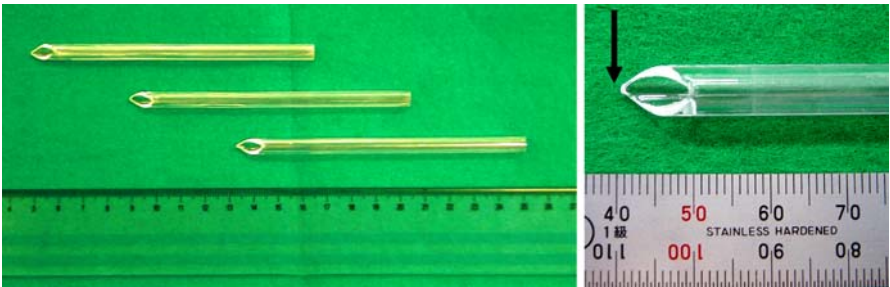


**Fig. 16.7.** Tube shaped sapphire grown under optimized growth conditions

ated is illustrated in Fig. 16.7 (right) by the arrow. The pulling was started after the first contact between the seed and the meniscus. Thereafter, the dimensions of the tube fragment increased continuously until both sides of the partially developed tube finally joined up with each other and the desired shape was formed.

## 16.5 Sapphire Plate

Sapphire plate crystals are also desired by industry for use as inexpensive substrates for gallium/aluminum nitride epitaxy, optical windows, etc. EFG systems with molybdenum crucibles and a resistive carbon heaters are generally used to grow plate sapphire crystals.

A first attempt to produce sapphire plates by  $\mu$ -PD was also made using a Mo crucible. After vacuuming the inner volume of the quartz tube surrounding the hot zone with a rotary pump, high-purity argon was introduced into the growth zone to establish an atmosphere that was not oxidizing. Then the plate crystal was grown (Fig. 16.8). The surface of the resulting crystal was coated with a black substance due to molybdenum oxidation. The formation of these particles was unavoidable in  $\mu$ -PD, even when some hydrogen was admixed with the argon to form a reducing atmosphere. In the case of EFG growth, the growth chamber is vacuumed using both rotary and diffusion pumps to achieve high vacuum. Moreover, the heater used in EFG is made from graphite. Thus, a small amount of CO gas is formed at elevated temperatures [8]. The reducing nature of the CO suppresses the oxidation of the molybdenum. However, in the case of  $\mu$ -PD, there are many sources of oxygen situated close to the meniscus (the oxide ceramics of the thermal insulators and the supports). Therefore, the ideal reducing atmosphere could not be realized. This is why, even when hydrogen gas was supplied, molybdenum oxidation could not be avoided.



**Fig. 16.8.** Sapphire plate crystal grown by the  $\mu$ -PD method using molybdenum crucible

Based on the above results, the application of an iridium crucible was considered to be more appropriate for the growth of transparent plate crystals. The shape of the outlet channel in the crucible die was also examined. In the  $\mu$ -PD method, one or several pinholes are typically cut in the die to allow melt to flow from the crucible. However, the effect of using a crucible with a slit-type capillary channel on the growth of the plate sapphire crystals was also tested here. Figure 16.9 (left and center) illustrates both types of crucible. Figure 16.9 (right) shows a side view of the slit-type crucible. The dies were also slightly curved at the end to simplify plate width enlargement during the early stages of crystal growth.

Figure 16.10 shows crystals grown using both crucibles. In the case of the pinhole-type crucible, the shoulder part was grown by increasing the power after contact with the seed. However, the crystal width occasionally decreased a little, and sometimes it was difficult to keep the width constant. On the other hand, in the case of the slit-type crucible, the shoulder part did not grow at all, as was expected. However the width of the crystal was easy to keep constant, as shown in Fig. 16.10 (bottom).

The plate sapphire crystals grown in this way were cut and polished and then transmission measurements were performed. Figure 16.11 shows optical spectra obtained for as-grown sapphire plate crystals produced by  $\mu$ -PD, EFG, and commercially available wafer cut from CZ crystal. Some absorption bands were observed in the EFG-grown sapphire. This is due to the formation of oxygen vacancies in the crystal. The use of a graphite heater and graphite components in the growth chamber of a typical EFG system results in the formation of CO gas and therefore a reducing atmosphere [9]. The optical absorption of as-grown sapphire at 206, 225 and 255 nm corresponds to F- and F<sup>+</sup>-centers [10–12]. These vacancies were created by the reducing atmosphere. Therefore, these sapphire crystals with absorption bands need to be annealed after growth. On the other hand, the  $\mu$ -PD crystals had no absorption bands, and transmission was similar to that measured for commercially available wafers (CZ).



**Fig. 16.9.** Bottom view of the crucibles for the growth of the plate sapphire crystals with pin-hole (*left*) and slit-hole (*center*). *Right Fig.* is side view

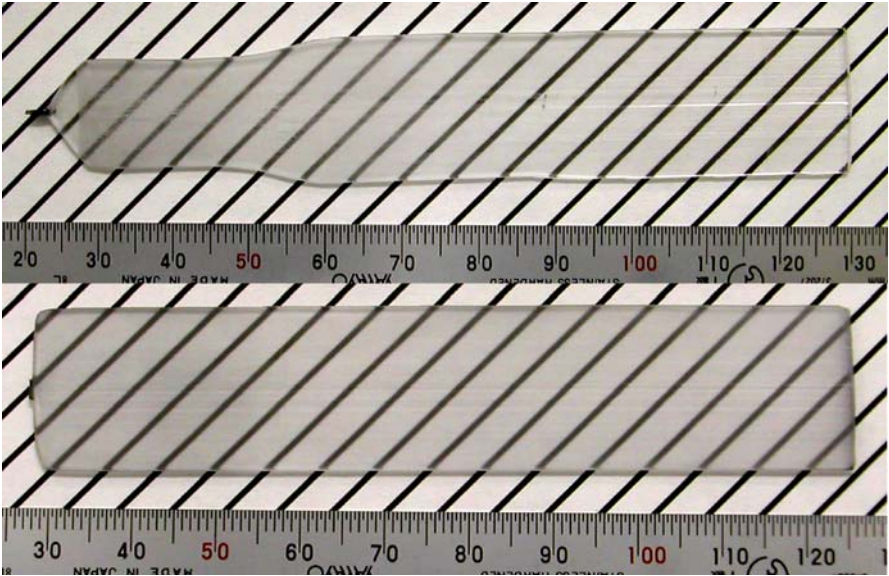


Fig. 16.10. Typical sapphire plate crystals grown by the  $\mu$ -PD method using the crucibles with pin-hole (*above*) and slit-hole (*below*)

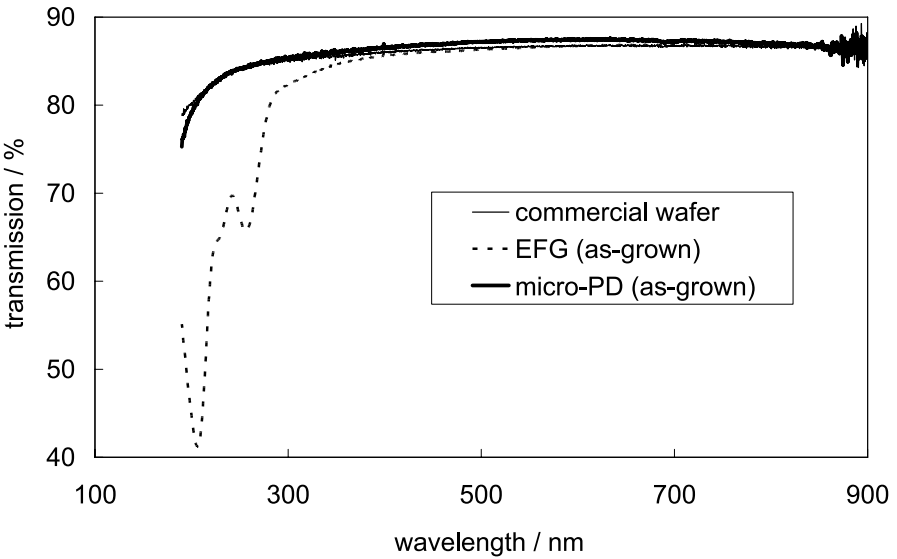
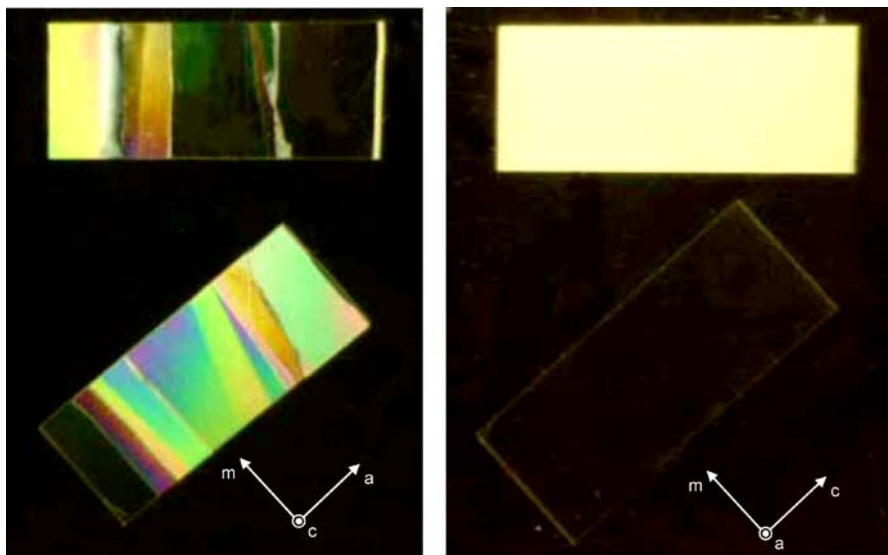
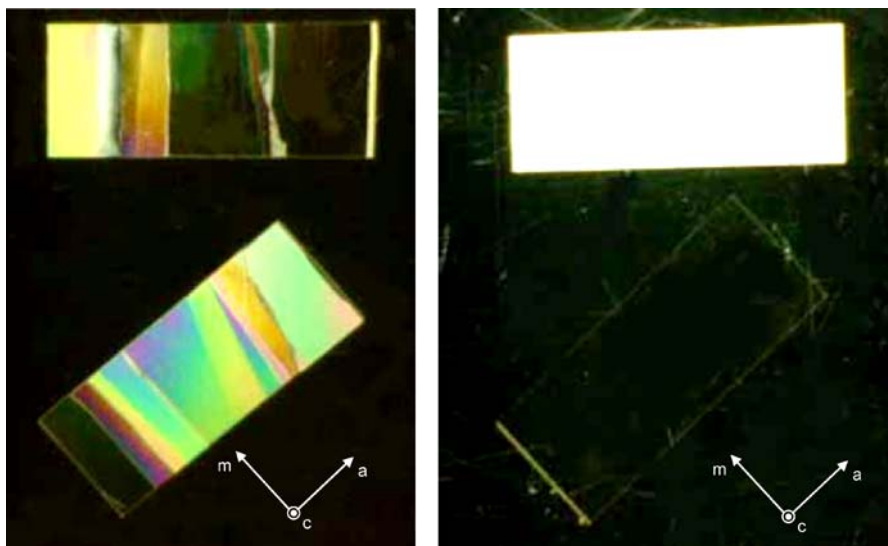


Fig. 16.11. Transmission spectra for sapphire plate crystal grown by  $\mu$ -PD and other growth techniques. Commercial wafers refers to CZ crystal



**Fig. 16.12.**  $\mu$ -PD grown sapphire plate crystals observed using crossed Nicols:  $c$ -plane (*left*) and  $a$ -plane (*right*)



**Fig. 16.13.**  $\mu$ -PD sapphire plate crystals observed using crossed Nicols: grown under conventional conditions (*left*) and modified ones (*right*)

The polished sapphire wafers were examined using crossed nicols (see Fig. 16.12). Very few subgrain boundaries were detected in the *a*-plane sapphire wafers. However, *c*-plane wafers had a number of these boundaries, as can be seen in Fig. 16.12 (left).

However, subgrain-free *c*-plane sapphire plate was obtained by modifying the hot zone of the  $\mu$ -PD set-up to achieve a lower temperature gradient and precise control of the crystal orientation to within  $0.5^\circ$ . This modification also significantly decreased the thermal stresses in the plate (Fig. 16.13).

Etching characterization was also performed on these samples in order to visualize microdefects. The etching was carried out with potassium hydroxide (KOH), which was loaded into a nickel crucible and heated to  $390^\circ\text{C}$ . Polished sapphire wafers were treated in melted KOH solution for 15 minutes. Figure 16.14 shows the results of the etching. For comparison purposes, the results obtained for commercially available sapphire wafer are also shown in Fig. 16.14. It is evident from the figure that the etch pit density (EPD) decreased when the thermal stresses in the plate were decreased.

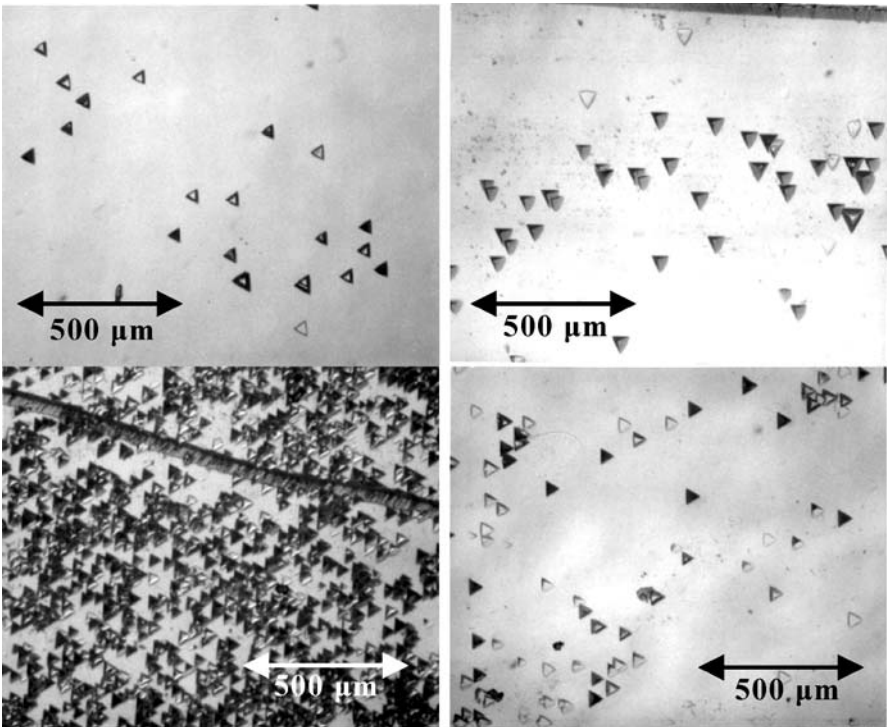


**Fig. 16.14.** Etching result for commercial *c*-plane wafer and  $\text{EPD} \approx 1.5 \times 10^4$  (above-left), *a*-plane wafer grown by  $\mu$ -PD and  $\text{EPD} \approx 2.8 \times 10^4$  (above-right), *c*-plane wafer grown by  $\mu$ -PD at normal conditions and  $\text{EPD} \approx 9.8 \times 10^5$  (below-left), and *c*-plane wafer grown by  $\mu$ -PD at modified conditions and  $\text{EPD} \approx 3.4 \times 10^4$  (below-right)

## 16.6 Summary

The growth of shaped sapphire crystals by the  $\mu$ -PD method was examined. Various modifications of the growth conditions, such as the growth speed, the temperature gradient, the thermal set-up, etc., were tested in order to improve the growth of shaped sapphire crystals. Rods with square and round cross-sections, plates, and tubes were successfully grown. Partial characterization of plate crystals of sapphire grown by the  $\mu$ -PD method demonstrated that, when optimized growth conditions are used, the resulting  $\mu$ -PD crystal quality is similar to that obtained by other methods such as EFG. Thus, it is clear that the  $\mu$ -PD system is suited to not only quick sample preparation, but also to the mass-production of shaped crystals.

## References

1. F. Schmid, C.P. Khattak, SPIE, **1112**, 25 (1989)
2. F. Schmid, C.P. Khattak, D.M. Felt, Am. Ceram. Soc. Bull., **73**(2), 39 (1994)
3. C.P. Khattak, F. Schmid, J. Cryst. Growth, **225**, 572 (2001)
4. C.P. Khattak, F. Schmid, SPIE, **1780**, 41 (1992)
5. J.W. Locher, H.E. Bates, W.C. Severn, B.G. Pazol, A.C. DeFranzo, SPIE, **1780**, 49 (1992)
6. V.A. Borodin, V.V. Sidorov, S.N. Rossolenko, J. Cryst. Growth, **104**, 69 (1990)
7. V.A. Borodin, V.V. Sidorov, S.N. Rossolenko, J. Cryst. Growth, **198–199**, 201 (1999)
8. O. Bunoïu, F. Defoort, J.L. Santailier, T. Duffar, I. Nicoara, J. Cryst. Growth, **275**, e1707 (2005)
9. Ye.V. Kryvonosov, Funct. Mater., **1**, 105 (1994)
10. B.D. Lee, J.H. Ir, Phys. Rev. B, **15**(8), 4065 (1977)
11. B.D. Evans, B. Stapelbrock, Phys. Rev. B, **18**, 7089 (1978)
12. S.Y. La, R.H. Bartram, R.T. Cox, J. Phys. Chem. Solids, **34**, 1079 (1973)
13. D.Y. Smith, D.L. Dexter, Prog. Optics, **10**, 165 (1972)

# 17 Doped LiNbO<sub>3</sub> Crystals

Dae-Ho Yoon

**Abstract.** Lithium niobates (LiNbO<sub>3</sub>) doped with rare-earth ions have received much attention in optical communications research since they provide a broad range of laser sources emitting (and pumping) at wavelengths of 1.34  $\mu\text{m}$  and (Er<sup>3+</sup>) and 1.54  $\mu\text{m}$  (Nd<sup>3+</sup>). In this chapter, the micro-pulling-down growth of LN fiber crystals doped with various active ions and the effect of doping on their photoluminescent properties are discussed.

## 17.1 Introduction

Lithium niobate, LiNbO<sub>3</sub> (LN), is a material that combines excellent electrooptic, acoustooptic and nonlinear properties with the potential for rare-earth or transition metal doping. The material can be used in bulk form or as a low-loss optical waveguide [1]. In particular, erbium Er<sub>2</sub>O<sub>3</sub> (Er)-doped LN has been proposed to be a very useful material for optical storage, optoelectronics, and waveguide devices [2]. Such crystals can emit second-harmonic radiation through quasi-phase matching [3] and green light through up-conversion at room temperature [4] simultaneously, combining the nonlinear optical properties of LN with the spectral properties of Er. High-quality Er:LN single crystals without subgrain boundaries are generally required for such applications.

Also, because of their high electrooptical and nonlinear coefficients, LN single crystals doped with Nd<sup>3+</sup> can be used in continuous-wave (CW), self Q-switched or self frequency-doubled compact diode-pumped minilasers emitting in the infrared or green regions [5,6], and they are suitable for integrated optics. However, it is difficult to achieve both high optical quality and high Nd<sup>3+</sup> concentration in LN crystals intended for application in lasers and amplifiers. Moreover, the congruent composition of LN is different from stoichiometric LiNbO<sub>3</sub>. Therefore, it is also difficult to produce defect-free LN from the melt that is different from congruently melting LN [7].

Recently, some materials have attracted a great deal of attention as candidates for use in a new generation of high-speed, efficient, multifunctional optical devices. Among these materials, small-diameter long-length fiber-like crystals are under consideration for a number of electrooptical applications [8–10] because of their extended interaction lengths and high optical intensities.

Fiber crystals are suitable for nonlinear optical and electrooptical applications [8, 9, 11, 12] such as second-harmonic generation (SHG), micro laser sources, and optical memory arrangements. They can also be expected to be highly efficient due to their high surface–volume ratios, their long interaction lengths, and their high crystal quality [13, 14]. In microcrystals, the shape is especially important, because the crystal cross-section approaches the diameter of the stimulating laser mode. Therefore, the correlation between crystal surface morphology and crystal growth parameters, like the starting composition of the melt and the temperature field, are of considerable interest when attempting to optimize the SHG properties of such crystals. In the sections below, rare-earth-doped LN fiber crystals grown from congruent or stoichiometric melts by the micro-pulling-down ( $\mu$ -PD) method are overviewed. The characteristics of the  $\mu$ -PD method (a high pulling rate and low thermal strain compared to other growth methods) and the possibility of growing crystal from off-congruent melt [15] are also discussed.

## 17.2 LiNbO<sub>3</sub> Crystal Growth

The two main problems associated with growing LN single crystals from a congruent melt are direct current (DC) drift and optical damage. The latter is influenced by the photorefractive effect [16], which is composition-sensitive. Although it is known that the crystals of almost stoichiometric composition are obtained from Li<sub>2</sub>O-rich liquid, homogeneous LN single crystals are difficult to grow from melts with more than 48.6 mol% Li<sub>2</sub>O using the conventional Czochralski (CZ) method because of segregation [17]. Thus, different parts of CZ LN crystals of near-stoichiometric composition are destroyed at different external conditions. Also, multidomain structure, growth ridges, and structural defects negatively affect the quality of as-grown CZ crystals [18, 19]. To overcome these problems with CZ growth, LN crystals were grown by a laser-heated pedestal growth (LHPG) method by Luh et al. [20], and the resulting crystals were single-domain.

In order to establish an alternative way to obtain LN crystals free from the above-listed shortcomings, the  $\mu$ -PD method [21] was examined, since it provides good control over shape and segregation. Using the  $\mu$ -PD method, LN single crystals 60–800  $\mu$ m in diameter were grown along the  $x$ -axis,  $y$ -axis, and the  $z$ -axis. Figure 17.1 illustrates typical LN crystals grown along the  $x$ -axis. The  $x$ -oriented LN crystals had lengths of up to 10 cm and highly constant diameters. The aspect ratio (crystal length to crystal diameter) was about 200. The fibers were homogeneous and colorless throughout. The diameter was invariable independent of the growth direction. The crystals grown from different melts (the congruent composition with 48.6 mol% Li<sub>2</sub>O, the stoichiometric melt with 50 mol% Li<sub>2</sub>O, and another composition with 58 mol% Li<sub>2</sub>O) were crack-free until the  $g$  value (solidification ratio of the melt) was about 1.

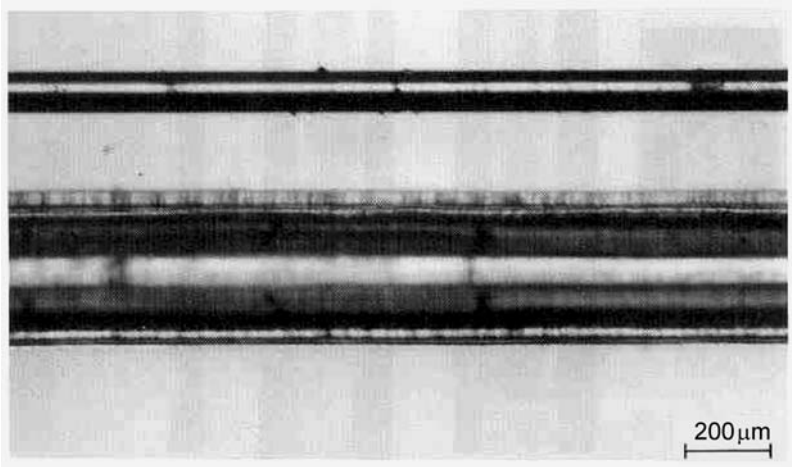


**Fig. 17.1.** LN fiber crystals grown along  $x$ -axis from 48.6 mol% Li<sub>2</sub>O melt with diameters of 60 (*above*) and 300  $\mu\text{m}$  (*below*) [22]

LN fiber crystals with diameters of 500  $\mu\text{m}$  are illustrated in Fig. 17.2. The morphology of the fiber crystal depends on the growth direction; it is very sensitive to orientation. Growth ridges with widths of about 50  $\mu\text{m}$ , elongated along the growth axis, were typically observed on the crystal surface. They reflect the twofold symmetry of the  $x$ - or  $y$ -orientations or the threefold symmetry of the  $z$ -orientation, respectively, and are positioned similarly to those in CZ crystals [19].

The cross-section of an  $x$ -oriented crystal with characteristic twofold symmetry is shown in Fig. 17.3a. Figure 17.3b and c show the morphologies of growth ridges of two crystals grown at the same growth rate (60 mm/h) but under different temperature gradients. It can be seen that the ridge width increases when the temperature gradient is decreased from 200 to 300  $^{\circ}\text{C}/\text{mm}$ .

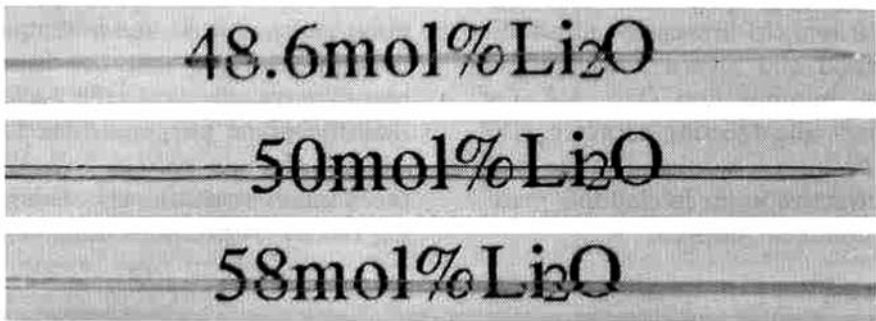


**Fig. 17.2.**  $x$ -oriented LN fiber crystals with diameters of 500  $\mu\text{m}$ , grown from the melts with 48.6, 50.0 and 58.0 mol% Li<sub>2</sub>O [23]

The ridge width to crystal diameter ratio is clearly larger in single microcrystals. The as-grown crystals were generally single-domain when the diameter was small.

Dislocations in the LN fiber crystals were studied by X-ray topography. Figure 17.4a–c are topographic images obtained under different diffraction

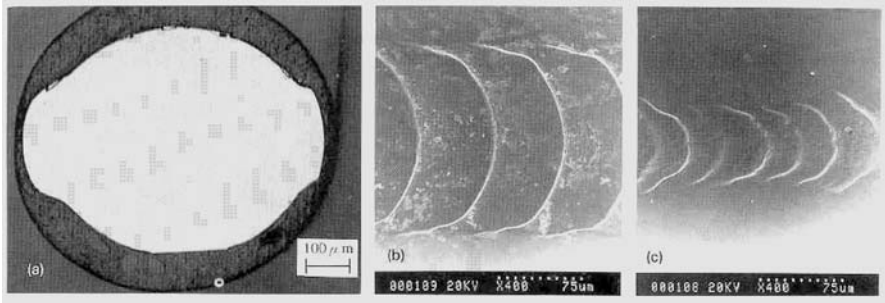


**Fig. 17.3.** Morphology of *x*-oriented LN fiber crystal grown at a pulling rate of 60 mm/min: **a** typical cross-section at a temperature gradient of 200 °C/mm; **b** growth ridges observed on the crystal grown under temperature gradient of 200 °C/mm and those **c** under a temperature gradient of 300 °C/mm [23]



**Fig. 17.4.** X-ray topographs of LN single crystal of **a** perpendicular and **b–d** parallel planes along the *x*-axis taken from different diffraction plane as attached: **a**, **b** and **c**  $\mu$ -PD crystal; **d** CZ crystal (Marker represents 500  $\mu$ m) [21]

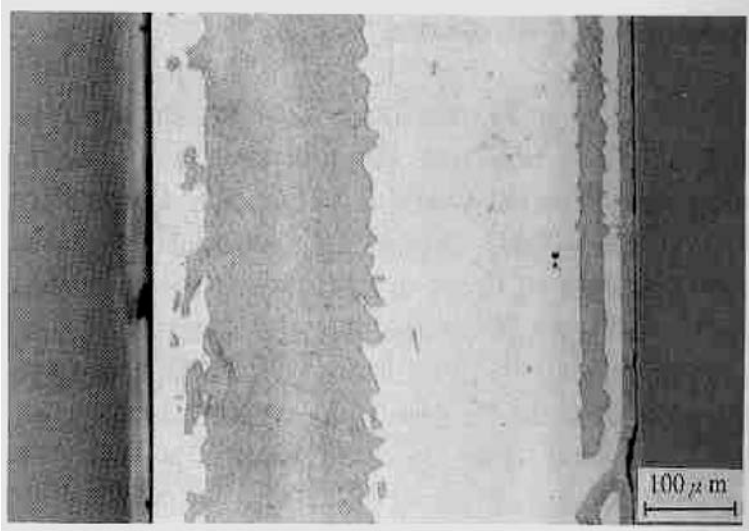


**Fig. 17.5.** Etched surface seen on  $y$ -face of an  $a$ -axis grown LN crystal [21]

conditions. For comparison, Fig. 17.4d depicts a LN wafer cut from CZ crystal; many dislocations and subgrain boundaries can be seen. In contrast, dislocations and subgrain boundaries were not detected in the  $\mu$ -PD crystal. Etch pits reveal points of intersection between dislocations and the surface. Figure 17.5 is a view of the etched surface as seen on the  $y$ -face of an LN  $\mu$ -PD crystal grown along the  $a$  axis. Dislocation etch pits were not detected, correlating with the results from X-ray topography. It is well known that dislocations are directly due to thermal stresses. The ideal stress-free state is rarely realized in conventional crystals because of the presence of a nonlinear temperature gradient [24]. A correlation between thermal stress and crystal diameter has been proposed [25]. Therefore, it was empirically demonstrated that the  $\mu$ -PD crystals were dislocation-free.

### 17.3 Er-Doped LiNbO<sub>3</sub>

Er-doped LN fibers were used to investigate the physical mechanisms of two-photon and excited-state absorption under near-infrared (NIR) diode laser excitation [26–28]. Room-temperature green up-conversion lasers were also obtained by pumping Er-doped LN with infrared (IR) lasers [29–31]. LN doping is an important task because it enables the properties of the active Er<sup>3+</sup> ions to be combined the excellent nonlinear, electrooptical and acoustooptical properties of LN [32]. Moreover, Er:LN has been proposed as being a very useful material for optical storage, optoelectronics, and waveguide devices [33].

Therefore, Er:LN single-crystal fibers with congruent and stoichiometric compositions were also grown by the  $\mu$ -PD method. The crystals were transparent, but the color of the crystals grown changed from colorless to pink depending on the  $\text{Er}^{3+}$  content in the crystal. The  $\text{Er}^{3+}$  cations were distributed homogeneously along the growth axis [34] because natural convection is limited in the capillary micronozzle.

Figure 17.6 shows the up-conversion intensity measured in the congruent Er:LN fiber crystals. Er:LN demonstrates strong up-conversion emission in the green wavelength region of 540 ~ 560 nm. The dominant peaks in up-conversion intensity observed around 550 nm result from  $^4\text{S}_{3/2} \rightarrow ^4\text{I}_{15/2}$  transitions, while the small peaks around 530 nm are from  $^2\text{H}_{11/2} \rightarrow ^4\text{I}_{15/2}$  transitions [35]. The measured up-conversion intensity for the 3 mol% Er-doped crystals was about 3.5 times greater than that of 1 mol% Er:LN for the same pump intensity. Thus, the intensity of up-conversion increased almost linearly with the  $\text{Er}^{3+}$  content. Similarly, the stoichiometric LN exhibited the strongest peak intensity at around 550 nm. The measured up-conversion intensity of a 1 mol% Er-doped stoichiometric LN fiber was about twice that of a 3 mol% Er-doped congruent LN fiber (Fig. 17.7). This means that stoichiometric LN is preferable over congruent LN.

Transmission spectra taken at room temperature are shown in Fig. 17.8. Several energy bands from the LN fiber crystals can be seen. The observed

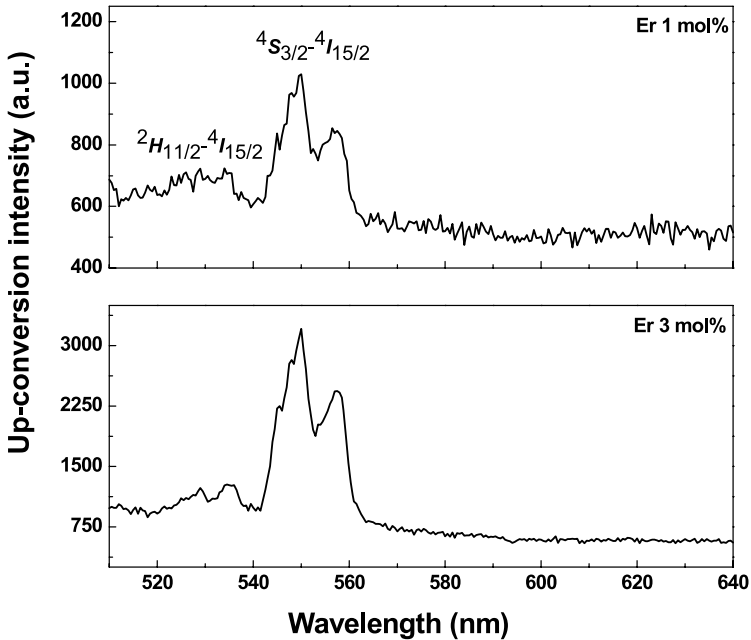


**Fig. 17.6.** The up-conversion intensity of congruent Er:LN fiber crystals: **a** 1 mol%-Er:LN and **b** 3 mol% Er:LN [36]

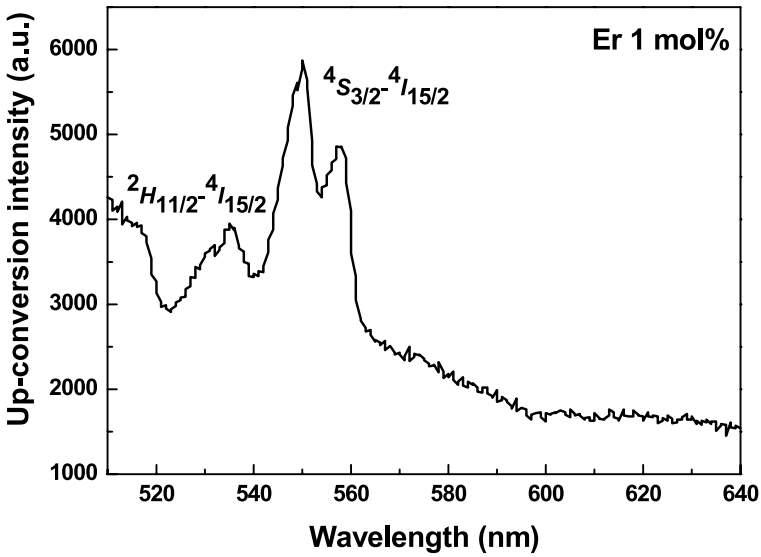


Fig. 17.7. Up-conversion intensity of stoichiometric LN crystal doped with 1 mol% Er [36]

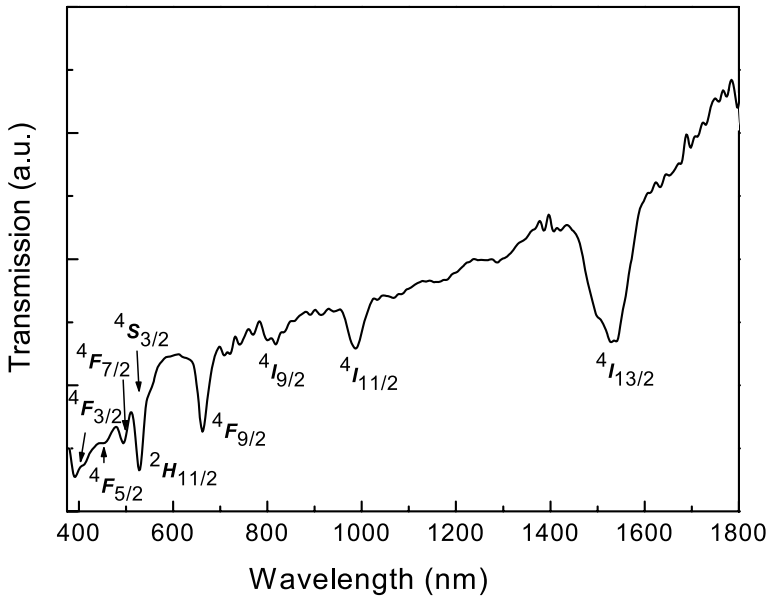
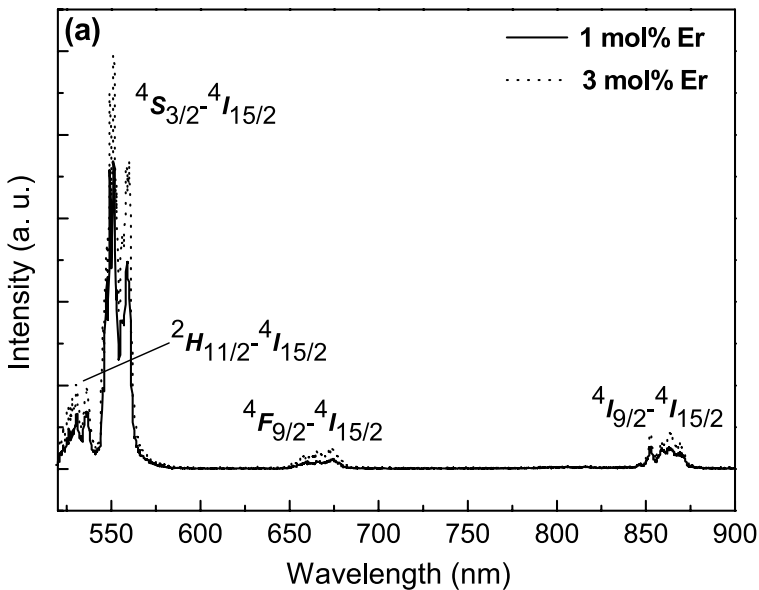


Fig. 17.8. The transmission spectra of Er:LN fiber

energy bands result from the  $f_{11}$  electronic configuration of the  $\text{Er}^{3+}$  cations and transitions from the ground state  $^4I_{15/2}$  to excited states with the  $^4f_{11}$  configuration. The double spectrometer technique was also used in order to study the photoluminescence (PL) at room temperature. The 514 nm line of an Ar ion laser was used as the excitation source. Figure 17.9 illustrates PL spectra of 1 and 3 mol% Er-doped stoichiometric LN fibers obtained with an input power of 50 mW. Emission peaks were detected at 520–540, 545–560, 650–675, and 850–875 nm. The peaks correspond to energy transitions from the  $^2H_{11/2}$ ,  $^4S_{3/2}$ ,  $^4F_{9/2}$ , and  $^4I_{9/2}$  levels to the ground state of  $^4I_{15/2}$  ( $^4S_{3/4} \rightarrow ^4I_{15/2}$ ,  $^4F_{9/2} \rightarrow ^4I_{15/2}$ ,  $^4I_{9/2} \rightarrow ^4I_{15/2}$ , and  $^4I_{13/2} \rightarrow ^4I_{15/2}$ ).

Figure 17.10 shows how the intensities of the strongest PL peaks change with the Er content and the input power. At 50 mW of input power, the intensities of the strongest peaks of the 3 mol% Er-doped stoichiometric LN fiber crystals were about 1.5 times greater than those of the 1 mol% Er-doped ones. Moreover, several of the strongest intensities of the 3 mol% Er:LN  $\mu$ -PD crystals were greater than those of the 1 mol% doped ones at input powers of 100 mW and 150 mW. Namely, the intensity of the 3 mol% Er-doped LN crystal was greater than that of the 1 mol% Er-doped one at the same wavelength. The intensity increased as the Ar ion laser power increased. The peak with the highest intensity was detected in the green, at 520–560 nm. This peak at around 550 nm was due to the  $^4S_{3/2} \rightarrow ^4I_{15/2}$  transition, and the small peak at around 530 nm was due to the  $^2H_{11/2} \rightarrow ^4I_{15/2}$  transition.



**Fig. 17.9.** PL spectra of Er-doped stoichiometric LN crystal at room temperature and input power of 50 mW, using the 514 nm line of an Ar-ion laser [37]

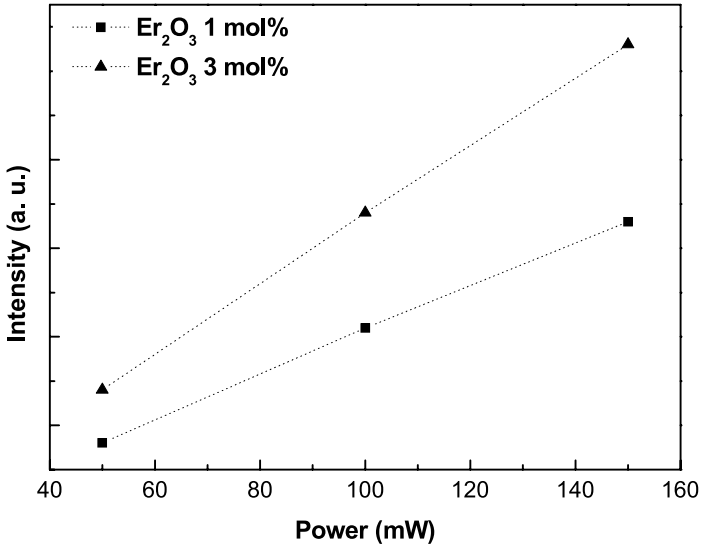


Fig. 17.10. The intensities of the strongest photoluminescence peaks vs. input power as measured for the  $\mu$ -PD LN crystals grown with different content of Er [34]

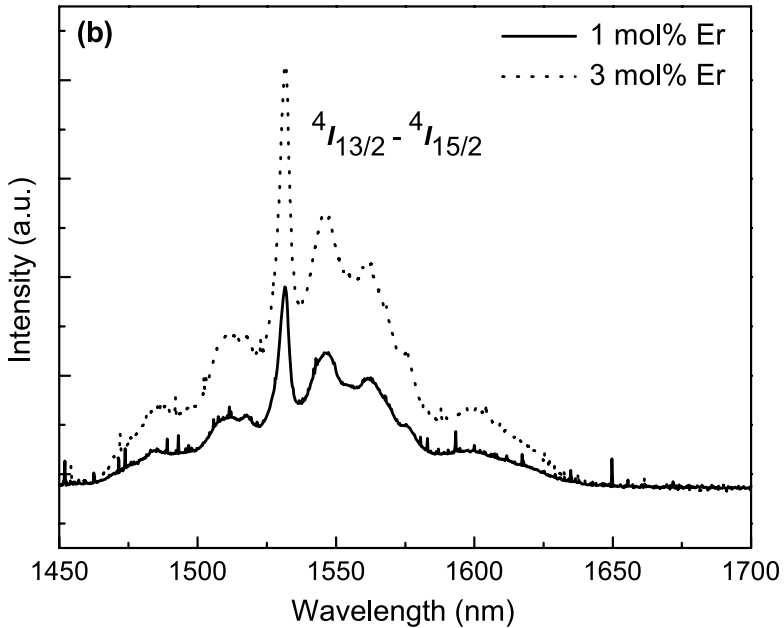


Fig. 17.11. PL spectra of 1 and 3 mol% Er-doped stoichiometric LN  $\mu$ -PD crystals

In the congruent LN crystals grown with the same dopant contents, the peak with the highest intensity was positioned at 540–565 nm (a region about 25 nm wide), but the peaks at 520–540 nm were small [37]. The stoichiometric LN crystals exhibit more stable emission around 550 nm than the congruent LN crystals because the emission peak is narrow (about 15 nm). Therefore, fewer transitions to the energy levels surrounding  ${}^4F_{9/2}$  occur in the stoichiometric crystals and so the efficiency of the  ${}^4F_{9/2} \rightarrow {}^4I_{15/2}$  transition at around 550 nm is higher. These stoichiometric Er:LN  $\mu$ -PD crystals are expected to find a wide range of applications in this wavelength range because their intensity at  $\sim 550$  nm (green) is strong compared with other ranges.

Figure 17.11 shows PL spectra in the range 1500–1570 nm, including peaks corresponding to energy transitions from the  ${}^4I_{13/2}$  level to the  ${}^4I_{15/2}$  ground state. The peaks with the strongest intensities were detected in the IR wavelength range 1525–1575 nm. These peaks at around 1530 nm result from  ${}^4I_{13/2} \rightarrow {}^4I_{15/2}$  transitions. The intensities of these peaks increase with increasing Er content.

## 17.4 Nd-Doped LiNbO<sub>3</sub>

A Nd<sup>3+</sup>-based compact diode-pumped self-frequency-doubled laser that emits green radiation is another possible application of LN, and one that should be suitable for use in optical data storage, undersea imaging, medical diagnosis, excitation sources (to replace ion gas lasers in scientific work), and the pumping of parametric oscillators and amplifiers [38]. Therefore, near-stoichiometric LN fiber crystals doped with Nd were also grown by the  $\mu$ -PD method. The crystals were transparent and their colors ranged from colorless to blue, depending on the Nd<sup>3+</sup> content. Their surfaces were very smooth, and their diameters were almost constant. The fibers were crack-free and did not contain visible defects. Segregation was insignificant because of the negligible natural convection in the capillary [39, 40]. As a result, the Nd<sup>3+</sup> was homogeneously distributed along the growth axis [41]. The optical properties of these Nd:LN  $\mu$ -PD crystals were measured using a laser system. The laser source provided unpolarized light. This incident light was directed along the direction of growth. The transmission spectrum of a Nd:LN fiber is shown in Fig. 17.12.

Figure 17.13 shows fluorescence spectra from 1 and 3 mol% Nd-doped near-stoichiometric LN  $\mu$ -PD crystals obtained in the wavelength range 800 ~ 900 nm. The measurements were taken via a double spectrometer technique at room temperature using an Ar ion laser as the excitation source. The peak fluorescence intensity of the 3 mol% Nd-doped stoichiometric LN was about three times greater than that of the 1 mol% Nd-doped one over the same wavelength range. The strongest fluorescence intensity was detected at 880 nm (corresponding to the  ${}^4F_{3/2} \rightarrow {}^4I_{9/2}$  transition).

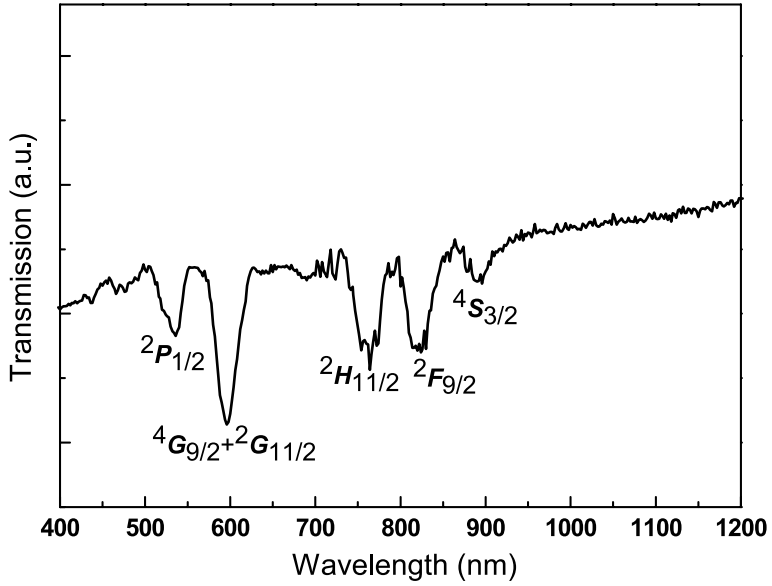


Fig. 17.12. Transmission spectra of Nd:LN  $\mu$ -PD crystal

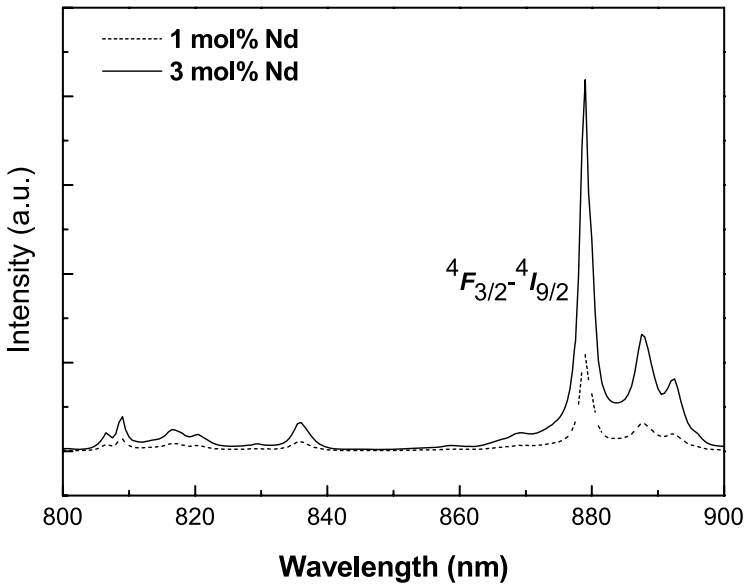
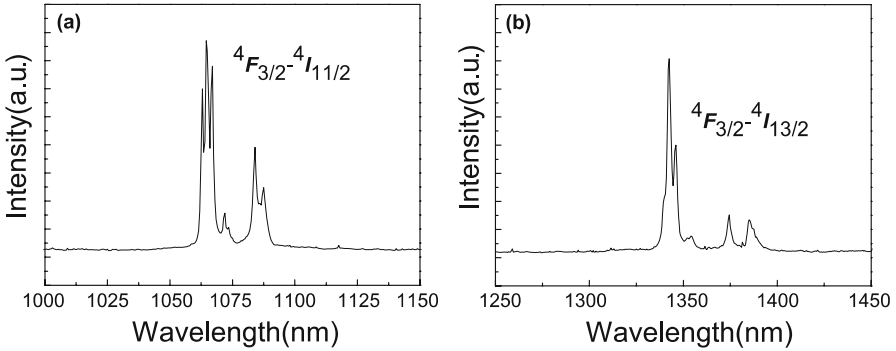


Fig. 17.13. Fluorescence spectra of Nd:LN  $\mu$ -PD crystal



**Fig. 17.14.** PL spectra of 3 mol% Nd-doped stoichiometric LN fiber crystals at 1000–1150 nm wavelength (a) and 1250–1450 nm wavelength (b)

Figure 17.14 show fluorescence spectra from 3 mol% Nd-doped near-stoichiometric LN fiber crystal obtained over two wavelength ranges, 1000–1150 and 1250–1450 nm. Because the energy levels are linked to the crystal-field splitting of each spin-orbit [42], triplet and doublet peaks can be seen in Fig. 17.14a and b. The strongest peaks in the fluorescence spectra were found at 1060 and 1340 nm, which correspond to the  ${}^4F_{3/2} \rightarrow {}^4I_{11/2}$  and  ${}^4F_{3/2} \rightarrow {}^4I_{13/2}$  transitions, respectively. When an 800-nm photon interacts with a  $\text{Nd}^{3+}$  ion, it has a high probability of being absorbed and exciting a ground state  ${}^4I_{9/2}$  ion to the  ${}^4F_{5/2}$  level. The ion then quickly relaxes to the  ${}^4F_{3/2}$  level, dumping its energy into the medium in the form of vibrations (phonons). This level is metastable and the ion will eventually emit a photon of light at  $\sim 880$  nm, returning it to the ground state. This spontaneous emission of light is called fluorescence.  $\text{Nd}^{3+}$  ions also show  ${}^4F_{3/2} \rightarrow {}^4I_{11/2}$  transitions that result in emission at  $\sim 1060$  nm and  ${}^4F_{3/2} \rightarrow {}^4I_{13/2}$  transitions yielding 1340-nm emission, respectively.

## 17.5 Summary

Lithium niobate is exceptionally popular optical material because of its large nonlinear optical coefficient and numerous favorable physical properties. As a result,  $\text{LiNbO}_3$  crystal growth technology is particularly well developed compared to that for other oxide materials. The development of an additional crystal growth method ( $\mu$ -PD) should make it possible to obtain LN with novel properties. The  $\mu$ -PD growth of rare-earth-doped LN fiber crystals was performed in order to investigate how a high temperature gradient at the solid–liquid interface and an elongated crystal shape affects the crystal properties.

The spectroscopic properties of LN fiber crystals produced by  $\mu$ -PD were also studied. Changes in the energy levels of LN fiber single crystals were

confirmed upon doping with rare-earth elements (Er and Nd). The strongest spectral peaks from the Er:LN fibers were found at 550 and 1530 nm, while the strongest peaks in the photoluminescence spectra from the Nd:LN fibers were detected at 880, 1060 and 1340 nm. Thus, the crystals discussed above are expected to be applied in various fields (UV-visible lasers, telecommunication systems, displays, etc.).

## References

1. B. Herreos, G. Lifante, *Appl. Phys. Lett.*, **72**, 531 (1998)
2. M. Tsuda, K. Inoue, S. Inoue, A. Makishima, *J. Appl. Phys.*, **85**, 29 (1999)
3. V. Bermudez, J. Capmany, J. Garcia Sole, E. Diehgueuz, *Appl. Phys. Lett.*, **73**, 593, (1998)
4. J. Zheng, Y. Lu, G. Luo, J. Ma, Y. Lu, *Appl. Phys. Lett.*, **72**, 1808 (1998)
5. J. Capmany, D. Jaque, J.A. Sanz García, J. García Solé, *Opt. Commun.*, **161**, 253 (1999)
6. T.Y. Fan, A. Cordova-Plaza, M.J.F. Digonnet, R.L. Byer, H.J. Shaw, *J. Opt. Soc. Am. B*, **3**(1), 140 (1986)
7. J.M. Ko, H. Cho, S.H. Kim, J.K. Choi, K.H. Auh, *J. Kor. Ass. Cryst. Growth*, **5**, 318 (1995)
8. S. Sudo, I. Yokohama, A. Cordova-Plaza, M.M. Fejer, R.L. Byer, *Appl. Phys. Lett.*, **56**, 1931 (1990)
9. L. Hesselink, S. Redfield, *Opt. Lett.*, **56**, 877 (1988)
10. H. Yoshinaga, K. Kitayama, *Appl. Phys. Lett.*, **56**, 1728 (1990)
11. J. Stone, C.A. Burrus, A.G. Dentai, *Appl. Phys. Lett.*, **29**, 37 (1976)
12. D.H. Jundt, M.M. Fejer, R.L. Byer, *Appl. Phys. Lett.*, **55**, 2170 (1989)
13. D.H. Yoon, M. Hashimoto, T. Fukuda, *Jap. J. Appl. Phys.*, **33**, 3510 (1994)
14. C.A. Burrus, J. Stone, *J. Appl. Phys.*, **49**, 3118 (1978)
15. K. Imai, M. Imaeda, S. Uda, T. Taniuchi, T. Fukuda, *J. Cryst. Growth*, **177**, 79 (1997)
16. K. Kawasaki, Y. Okano, S. Kan, M. Sakamoto, K. Hoshikawa, T. Fukuda, *J. Cryst. Growth*, **119**, 317 (1992)
17. H.M. O'Bryan, P.K. Gallagher, C.D. Brandle, *J. Am. Ceram. Soc.*, **68**, **493** (1985)
18. K. Nassau, H.J. Livingstein, G.M. Loiacono, *J. Phys. Chem. Solids*, **27**, 983 (1966)
19. N. Niizeki, T. Yamada, H. Toyoda, *Jap. J. Appl. Phys.*, **6**, 318 (1967)
20. Y.S. Luh, R.S. Feigelson, M.M. Fejer, R.L. Byer, *J. Cryst. Growth*, **78**, 135 (1986)
21. D.H. Yoon, I. Yonenaga, T. Fukuda, N. Ohnishi, *J. Cryst. Growth*, **142**, 339 (1994)
22. D.H. Yoon, I. Yonenaga, T. Fukuda, *Cryst. Res. Technol.*, **29**, 1119 (1994)
23. D.H. Yoon, T. Fukuda, *J. Cryst. Growth*, **144**, 201 (1994)
24. B.K. Vainshtein, V.M. Fridkin, V.L. Indenbom, *Modern Crystallography, Vol. 2, Structure of Crystals*, Springer Series in Solid-State Sciences, Vol. 21 (Springer, Berlin, 1982)
25. S.V. Tsvinsky, *Fiz. Metallov Metalloved.*, **25**, 1013 (1968)

26. S. Arahira, K. Watanabe, K. Shinozaki, Y. Ogawa, *Opt. Lett.*, **17**, 1679 (1992)
27. J. Thogersen, N. Bjerre, J. Mark, *Opt. Lett.*, **13**, 197 (1993)
28. R.L. Laming, S.B. Poole, E. J. Tarbox, *Opt. Lett.*, **13**, 1084 (1988)
29. J.F. Massicott, M.C. Brierley, R. Wyatt, S.T. Davey, D. Szebesta, *Electron Lett.*, **29**, 2119 (1993)
30. J. Y. Allain, M. Monerie, H. Poignant, *Electron Lett.*, **28**, 111 (1992)
31. T.J. Whitley, C.A. Millar, R. Wyatt, M.C. Brierly, D. Szebesta, *Electron Lett.*, **27**, 1785 (1991)
32. M. Fleuster, Ch. Buchal, E. Snoeks, A. Ploman, *J. Appl. Phys.*, **75**, 173 (1994)
33. M. Tsuda, K. Inoue, S. Inoue, A. Makishima, *J. Appl. Phys.*, **85**, 29 (1999)
34. J.W. Shur, W.S. Yang, S.J. Suh, J.H. Lee, T. Fukuda, D.H. Yoon, *J. Cryst. Growth*, **229**, 223 (2001)
35. J. Amin, B. Dussardier, T. Schweizer, M. Hempstead, *J. Lumin.* **69**, 17 (1996)
36. J.W. Shur, W.S. Yang, S.J. Suh, J.H. Lee, T. Fukuda, D.H. Yoon, *Cryst. Res. Technol.*, **37**, 353 (2002)
37. W.S. Yang, S.J. Suh, J.H. Lee, T. Fukuda, D.H. Yoon, *J. Kor. Cryst. Growth*, **9**, 377 (1999)
38. J. Capmany, D. Jaque, J.A. Sanz García, J. García Solé, *Opt. Commun.*, **161**, 253 (1999)
39. S. Uda, K. Shimamura and T. Fukuda, *J. Crystal Growth* **155**, 229 (1995)
40. S. Uda, J. Kon, J. Ichikawa, K. Inaba, K. Shimamura, T. Fukuda, *J. Cryst. Growth*, **179**, 567 (1997)
41. J.W. Shur, T.I. Shin, S.M. Lee, S.W. Baek, D.H. Yoon, *Mater. Sci. Eng. B*, **105**, 16 (2003)
42. J. Schamps, F. Delattre, J.P. Flament, I. Noriet, *Opt. Mater.* **19**, 47 (2002)

# 18 Growth of Olivine and Wüstite Crystals

Steffen Ganschow and Detlef Klimm

**Abstract.** The growth of wüstite and olivine crystals by the micro-pulling-down technique is described. In both cases, growth requires precise control of the partial pressure of oxygen in the ambient atmosphere, which is achieved through the use of a dilute CO–CO<sub>2</sub> mixture. Unusual features of these growth processes are also discussed in some detail.

## 18.1 Introduction

Magnesium-rich olivine, (Mg,Fe)<sub>2</sub>SiO<sub>4</sub>, is the major component of peridotite, the dominant type of rock present in the Earth's upper mantle. Successive pressure-dependent phase transitions of olivine give rise to the most prominent seismic discontinuities at 410 km and 660 km that mark the mantle's transition zone [1]. The flow of heat and matter in this transition zone governs the evolution of the Earth's surface, including spectacular features like volcanism.

Wüstite, Fe<sub>x</sub>O, is an end-member of magnesiowüstite, one of the principal phases in the lower mantle, and also one of the products of olivine decomposition in the transition zone. Ringwood [2] proposed a model for the Earth's core where wüstite was the major light component. Wüstite is probably the only mineral that occurs in both the core and the mantle. Studies of phase transformations, redox equilibria, etc., of wüstite are hence significant since they aid our understanding of the formation of the core and its interaction with the mantle.

Synthetic minerals are of great interest for modern geophysical research. In contrast to natural specimens, the properties of laboratory-grown single crystals, like the basic composition, the type of impurities present, and their concentrations, can be adjusted. Samples with specific properties tailored "on-demand" permit the relationships between structural and physical characteristics of the minerals to be studied. Crystal growth can therefore contribute to a better understanding of the processes that occur inside our home planet.

From the point of view of crystal growth, both olivine and wüstite are linked by one fundamental question: how it is possible that iron appears only in the bivalent state in these minerals? Like every transition metal,

iron can easily change its valence upon changes in temperature  $T$ , oxygen partial pressure  $p_{\text{O}_2}$ , and the chemical environment. It is known to occur in trivalent (hematite,  $\text{Fe}_2\text{O}_3$ ; magnetite,  $\text{Fe}_3\text{O}_4$ ), bivalent (magnetite, wüstite), and metallic (various modifications of Fe) states. Of course, an  $x$ - $T$  phase diagram can be drawn to illustrate the relationships between the phases of the Fe-O system [3]. However, the partial pressure of oxygen that is required to stabilize a particular condensed phase of Fe-O cannot be obtained from this type of phase diagram.

Phase diagrams plotted in the  $T - RT \ln p_{\text{O}_2}$  plane are an alternative way to show the regions in which different condensed phases are stable [4]. In such diagrams, the predominant regions of condensed phases are separated by straight lines, provided that the neighboring phases do not mix and that the vapor pressures of these phases can be neglected. The phase boundaries are marked by lines on the Ellingham diagram ( $\Delta G^0 = \Delta H^0 - T\Delta S^0 = -RT \ln p_{\text{O}_2}$ ), representing the formation of oxides.

For practical purposes, it is often more informative to use  $\log_{10} p_{\text{O}_2}$  instead of  $RT \log_{10} p_{\text{O}_2}$  as the ordinate. This change in ordinate results in the main regions being separated by curved lines, but in this case the partial pressure of oxygen can be read directly from the ordinate. Figure 18.1 shows such a diagram for the Fe-O system.  $p_{\text{O}_2} = \text{const}$  corresponds to a horizontal line in this diagram, and it is obvious that all such lines only cross the  $\text{Fe}_x\text{O}$  phase field for a limited range of  $T$ . Furthermore, melt growth processes occur within temperature ranges that usually span hundreds of Kelvins. In such cases, the

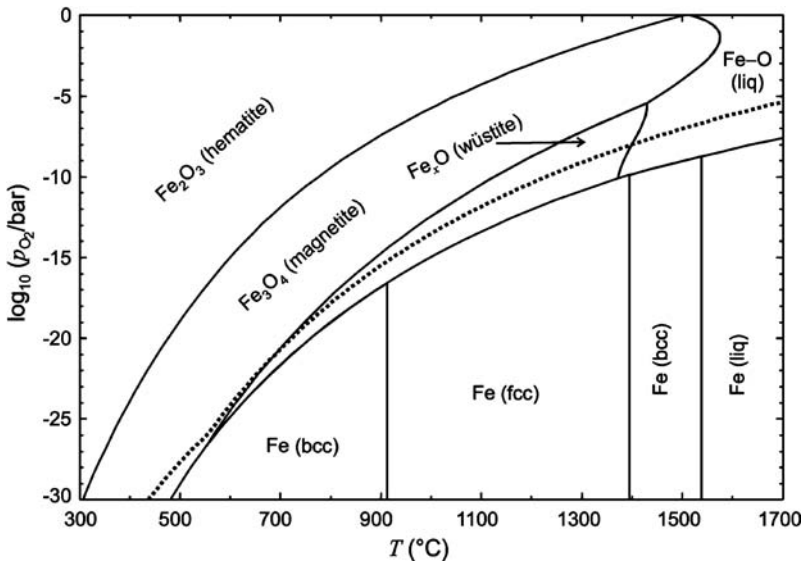


**Fig. 18.1.** Phase diagram Fe-O in the coordinates. The *dotted line* represents for the gas mixture 85% Ar + 10%  $\text{CO}_2$  + 5% CO (total pressure of 1 bar) used for the  $\text{Fe}_x\text{O}$  crystal growth

required variation in the partial pressure of oxygen with temperature can be obtained by using mixtures of gases that contain at least one oxygen-supplying component. In practice, mixtures of CO and CO<sub>2</sub> that make use of the temperature-dependent equilibrium



have proved to be suited to this purpose. Knowing the equilibrium constant  $K = p_{\text{CO}} p_{\text{O}_2}^{1/2} p_{\text{CO}_2}^{-1}$ , one can easily calculate the oxygen partial pressure obtained for any temperature and any CO–CO<sub>2</sub> mixture. The dotted line in Fig. 18.1 shows that the  $p_{\text{O}_2}$  from a mixture of 10% CO<sub>2</sub> and 5% CO in argon fits the region Fe<sub>x</sub>O where dominates well over an extended temperature range. Such an atmosphere should therefore be well-suited for use during processes where crystals containing ferrous ions are grown [5].

## 18.2 Wüstite: Fe<sub>x</sub>O

### 18.2.1 Phase Diagram of the Fe–O System

The Fe–O system was first studied thoroughly by Darken and Gurry in the 1940s [6, 7]. These authors determined the equilibrium relations between the partial pressure of oxygen, the temperature, and the compositions of various iron oxides, and then constructed the  $x$ – $T$  phase diagram for the system (Fig. 18.2). Over the years, this phase diagram has been refined and extended by several groups, experimentally as well as computationally [3, 8–12], but the principal relations are still valid.

Although the region in which wüstite exists is rather broad,  $x \approx 0.83$ – $0.96$ , this does not include stoichiometric wüstite, “FeO”. Moreover, at room temperature, wüstite is thermodynamically unstable: it decomposes in a eutectoid reaction to form magnetite Fe<sub>3</sub>O<sub>4</sub> and metallic iron Fe at 560 °C. However, it has been demonstrated experimentally that it is possible to suppress this decomposition and freeze-in the high-temperature state by rapidly cooling the melt-grown crystals [13, 14]. Therefore, it was assumed that the micro-pulling-down ( $\mu$ -PD) technique would be suitable for the growth of wüstite crystals, since the high temperature gradients used permit fast cooling.

### 18.2.2 Wüstite $\mu$ -PD Growth

The starting material used for the  $\mu$ -PD growth of Fe<sub>x</sub>O crystals was iron(II) oxalate dihydrate, FeC<sub>2</sub>O<sub>4</sub>·2H<sub>2</sub>O (Alfa Aesar, Puratronic, 99.999%). The material was melted in an inductively heated, conical platinum crucible with an inner diameter of 13 mm and total height of 35 mm. The orifice at the tip of the cone had an inner diameter of about 0.8 mm. The crucible was covered with a platinum lid and placed on an alumina pedestal. Porous alumina

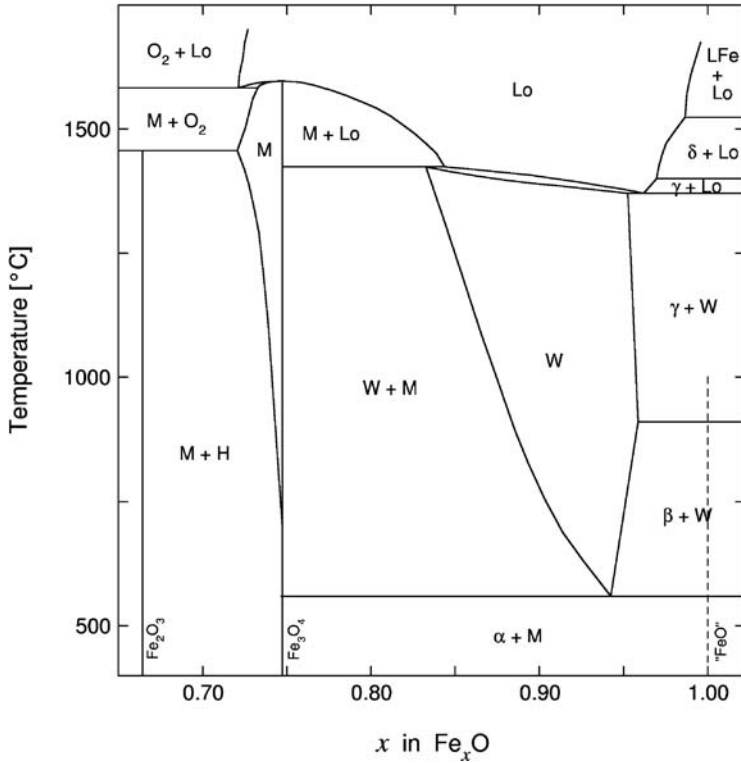


**Fig. 18.2.** Phase diagram of the Fe–O system (after [1]). W = wüstite, M = magnetite, H = hematite, Lo = liquid oxide, LFe = liquid Fe,  $\alpha$  =  $\alpha$ -Fe,  $\beta$  =  $\beta$ -Fe,  $\gamma$  =  $\gamma$ -Fe,  $\delta$  =  $\delta$ -Fe

tubes were used for thermal insulation. The experiments were carried out in a water-cooled vacuum chamber exhausted to  $< 10^{-2}$  mbar and refilled to normal pressure with a gas mixture of 5 vol% CO + 10 vol% CO<sub>2</sub> + 85 vol% Ar (see the previous section). The first crystals were grown on Y<sub>3</sub>Al<sub>5</sub>O<sub>12</sub> or Al<sub>2</sub>O<sub>3</sub> seeds because FeO seeds were not available. As soon as sufficient solidified material was produced, randomly oriented FeO chips were used as seeds. The crystals were pulled at rates of between 0.5 and 50 mm/min.

FeO melt wets platinum almost perfectly, similar to a number of other oxide melts. At lower pulling rates ( $v \leq 1$  mm/min), the diameter of the growing crystal was easily maintained at around 2 mm by changing the power supplied to the heater. The diameter of the growing crystal increased at higher pulling rates, similar to [15]. At very high pulling rates ( $v \geq 10$  mm/min), the diameter self-adjusted to some value that was probably determined by limited mass flow through the capillary; for the given crucible geometry and a crystal diameter of 5 mm, the flow velocity in the capillary was about 40 times greater than the pulling rate, i.e., up to 800 mm/min! This is more than

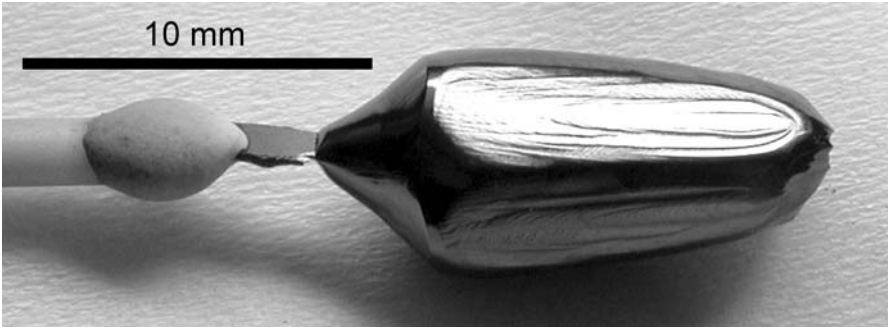


**Fig. 18.3.** Wüstite  $\mu$ -PD crystal grown at a pulling rate of 20 mm/min

twice as much as the maximum value reported previously [15]. At this stage, changes to the power supplied to the heater have hardly any effect because of the great thermal inertia of the set-up and the vast amount of latent heat released over time. Crystals grown at low pulling rates had a rod-like shape, whereas those grown at high pulling rates were rather thick and not much longer than 1 cm (Fig. 18.3).

### 18.2.3 Structure Analysis

The crystals grown were examined by an X-ray diffraction technique. Typical powder patterns are shown in Fig. 18.4. The crystals grown at a low pulling rate (and consequently low cooling rate) contained magnetite, whereas the crystals grown at a high pulling rate were single-phase wüstite.

The room-temperature lattice constant of a single crystal, determined by X-ray diffraction, was 4.312 Å. Using an empirical relation between the lattice parameter and the stoichiometry, the composition of crystals grown was estimated to be  $\text{Fe}_{0.956}\text{O}$  [14]. This composition corresponds to the limit of solubility on the iron-rich side of the phase formation field of the phase diagram, which confirms the proper selection of the growth atmosphere.

## 18.3 Olivine: $\text{Mg}_2\text{SiO}_4$ – $\text{Fe}_2\text{SiO}_4$

### 18.3.1 Phase Diagram of the $\text{Mg}_2\text{SiO}_4$ – $\text{Fe}_2\text{SiO}_4$ System

Olivine is a continuous series of solid solutions of forsterite,  $\text{Mg}_2\text{SiO}_4$ , and fayalite,  $\text{Fe}_2\text{SiO}_4$  [16]. So far, single crystals of olivine with various  $[\text{Fe}]/[\text{Mg}]$  ratios have been obtained by the floating-zone method [17, 18]. The large difference between the melting points of both end members ( $T_{\text{Fe}_2\text{SiO}_4}^m = 1205^\circ\text{C}$  and  $T_{\text{Mg}_2\text{SiO}_4}^m = 1890^\circ\text{C}$ ) causes a big difference between the positions of the

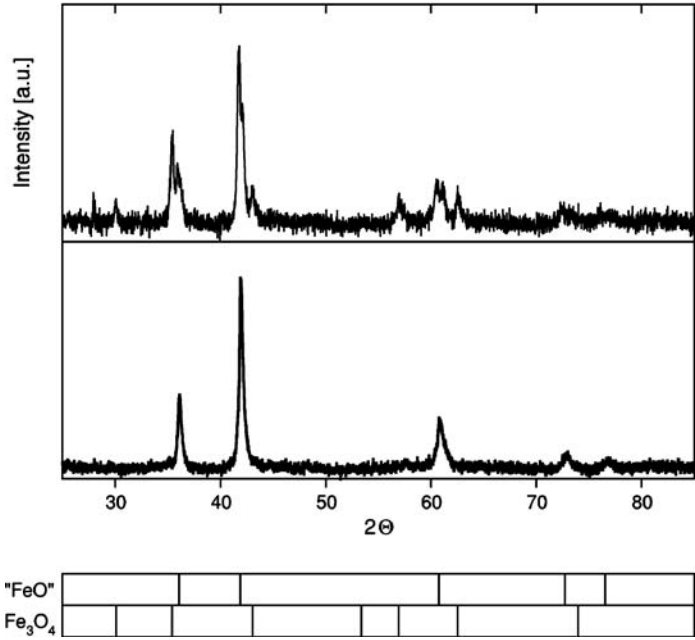


Fig. 18.4. X-ray patterns for the crystals grown at low pulling rate of 0.5 mm/min, (above) and high pulling rate of 50 mm/min (below)

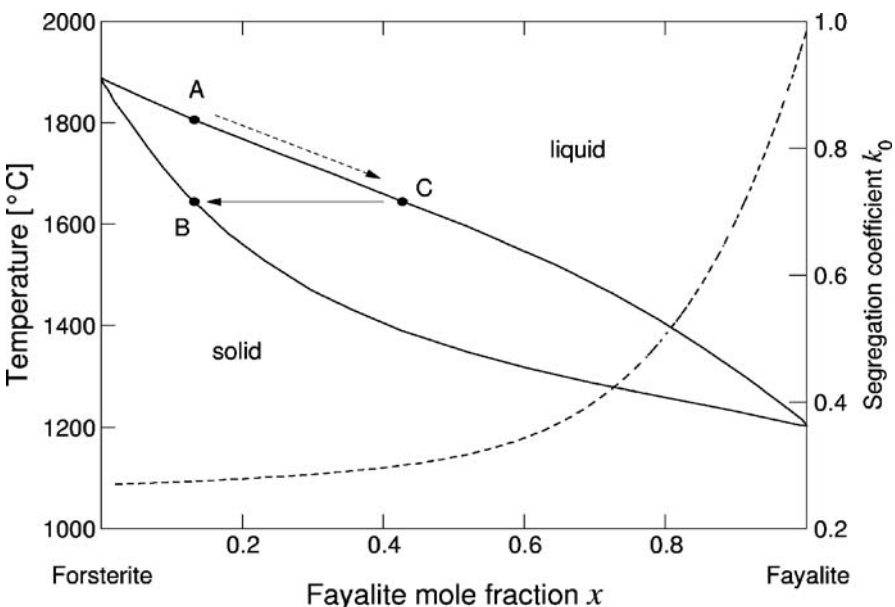
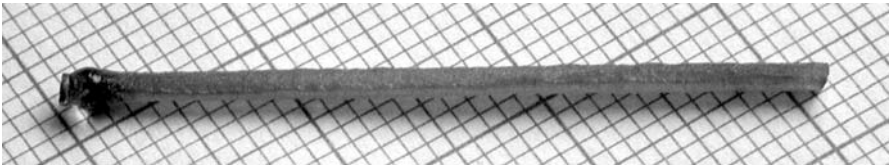


Fig. 18.5. The forsterite-fayalite system. The phase diagram was computed using the FactSage software package [19]. The dashed line represents the segregation coefficient of fayalite

solidus and liquidus curves and strong segregation: the equilibrium segregation coefficient  $k_0$  of fayalite in magnesium-rich olivine is only about 0.3 (Fig. 18.5). However, for a typical  $\mu$ -PD arrangement with a capillary length (i.e., diffusion boundary layer thickness) of about 1 mm and a diffusion coefficient  $D$  not significantly exceeding  $10^{-5}$  cm<sup>2</sup>/s, an effective segregation coefficient  $k_{\text{eff}} \approx 1$  should be expected at moderate pulling rates ( $< 1$  mm/min).

### 18.3.2 Olivine $\mu$ -PD Growth

Olivine crystals were grown using the same apparatus described in Sect. 18.2.2. Due to the high melting point of Mg-rich olivine, iridium was used as the crucible material. In the first heating cycle, small fragments of Czochralski-grown forsterite single crystals free from obvious impurities were melted in the crucible under a nitrogen atmosphere. After this step, enough fayalite was added to the crucible in the form of a stoichiometric mixture of SiO<sub>2</sub> and FeC<sub>2</sub>O<sub>4</sub> × 2H<sub>2</sub>O powders to get an initial melt composition that could be described as  $(1-x)\text{Mg}_2\text{SiO}_4 + x\text{Fe}_2\text{SiO}_4$ . The second melting cycle and crystal pulling was carried out either under nitrogen (99.999% purity), or under the same CO–CO<sub>2</sub> mixture described in Sect. 18.2.2. The crystals were grown on [100] forsterite seeds at a constant pulling rate of 0.5 mm/min.



**Fig. 18.6.** Olivine  $\mu$ -PD crystal (scale in mm)

### 18.3.3 Growth Results

The crystals grown had diameters slightly larger than the orifice and were up to 100 mm long. Depending on the actual amount of fayalite added, their colors varied from pale to intensely brown. Longitudinal cuts were prepared so that the chemical compositions of the crystals could be inspected by energy-dispersive X-ray analysis. As expected, the fayalite concentration along the crystal's axis was found to be nearly constant (Fig. 18.7). Obvious deviations were detected only at the part of the crystal grown at the very beginning, when the crystal diameter and pulling-down rate were not yet steady. It should be noted here that the crystals showed distinct radial segregation, with a fayalite-poor core and a thin rim typically 100  $\mu$ m in thickness that was strongly enriched in fayalite [20]. This phenomenon is the subject of ongoing detailed study [21].

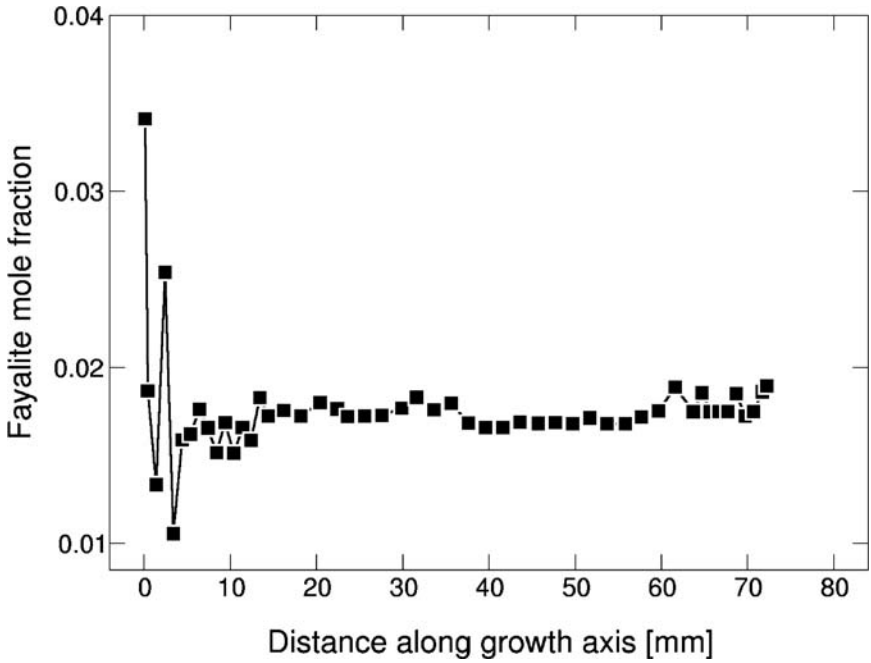


**Fig. 18.7.** Distribution of fayalite along the growth axis. The fayalite mole fraction in the melt,  $x_0$ , was 0.045

The procedure described was highly reproducible for melts with low fayalite concentrations (molar fraction  $x \leq 0.15$ ). The growth process became unsteady at higher fayalite concentrations. A look at the phase diagram in Fig. 18.5 explains this behavior. Let's assume an initial melt with  $x_0 \approx 0.13$  (point "A"). Due to crystallization, the composition of the melt at the interface,  $x_{if}$ , changes along  $A \rightarrow C$  down the liquidus line. If the pulling speed is high enough ( $v \gg D \cdot \delta \approx 0.1$  mm/min), then  $x_{if}$  quickly reaches  $k_0 \cdot x_0$  (point "C"). The composition of the melt inside the crucible remains practically unchanged over this period. From here on, the crystal grows with composition "B", equal to initial melt "A", i.e., the effective segregation coefficient takes a value of 1 until most of the melt is solidified. During this stage, the temperature inside the crucible must be higher than the liquidus temperature of the initial melt,  $T^\ell(x_0)$ . The temperature in front of the growth interface is below the liquidus temperature  $T^\ell(x_{if} = k_0 \cdot x_0)$ . Therefore, the temperature of the bulk melt in the crucible and that of the growth interface are different (see Fig. 18.8), according to the following expression:

$$\Delta T = T_{\text{bulk}} - T_{\text{if}} > T^\ell(x_0) - T^\ell(x_{\text{if}}) = \Delta T^\ell . \tag{18.2}$$

In the forsterite–fayalite system,  $\Delta T^\ell$  reaches values of more than 250 K. The crucible used in the experiments had a wall thickness of about 1 mm,

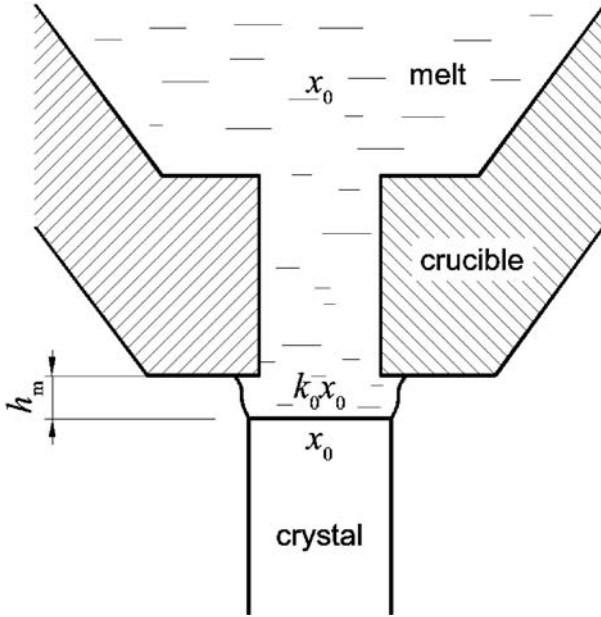


Fig. 18.8. Detail of the  $\mu$ -PD growth

and it seems reasonable to assume that the temperature gradient inside the capillary is rather small. Therefore, the largest temperature drop occurred in the meniscus liquid zone just below the crucible. As  $\Delta T^\ell$  increases the height of the meniscus  $h_m$  increases too, in order to satisfy the above inequality (18.2). For a supposed axial temperature gradient of 1000 K/cm, which is typical of a  $\mu$ -PD system,  $h_m$  should increase to  $> 2.5$  mm. The maximum stable meniscus height is given by [22]:

$$h_{\max} = r \cos \varphi_0 \left[ a \cosh \left( \frac{r_{\text{sh}}}{r \cos \varphi_0} \right) - a \cosh \left( \frac{1}{\cos \varphi_0} \right) \right], \quad (18.3)$$

where  $r$  is the fiber radius,  $r_{\text{sh}}$  is the radius of the shaper (i.e., the die), and  $\varphi_0$  is the contact angle between the crystal and the melt. In the growths introduced above,  $h_{\max}$  was considerably less than 1 mm! There are two ways to overcome this problem: (i) simply increase the axial temperature gradient, or (ii) use a crucible with a long tube-like capillary. Such a capillary would allow a larger temperature difference  $\Delta T$  to be obtained, so inequality (18.2) would easily be fulfilled, even at meniscus heights smaller than  $h_{\max}$ .

### 18.4 Summary

The experiments described above demonstrated that the micro-pulling-down technique can be successfully applied to the growth of the geophysically im-

portant crystalline materials wüstite and olivine. It can be used to produce small samples for laboratory experiments at comparably low costs. However, further improvements of the growth technique are required to obtain high-quality samples for direct application.

## References

1. G. Helffrich, B. Wood, *Nature*, **412**, 501 (2001)
2. A. Ringwood, *Geochim. J.*, **11**, 111 (1977)
3. B. Sundmann, *J. Phase Equilib.*, **12**, 127 (1991)
4. A. Pelton, in *Phase Transformation in Materials*, ed. by P. Haasen (VCH, Weinheim, 1991), p. 5
5. D. Klimm, S. Ganschow, *J. Cryst. Growth*, **275**, e849 (2005)
6. L. Darken, R. Gurry, *J. Am. Chem. Soc.*, **45**, 1398 (1945)
7. L. Darken, R. Gurry, *J. Am. Chem. Soc.*, **68**, 798 (1946)
8. C. Carel, *Mem. Sci. Rev. Metall.*, **64**, 737 (1967)
9. E. Takayama, N. Kimizuka, *J. Electrochem. Soc.*, **127**, 970 (1980)
10. E. Jacobsson, *Scand. J. Metall.*, **14**, 252 (1985)
11. Y. Fei, S. Saxena, *Phys. Chem. Miner.*, **13**, 311 (1986)
12. A. Ringwood, W. Hibberson, *Phys., Chem. Miner.*, **17**, 313 (1990)
13. J. Burmeister, *Mat. Res. Bull.*, **1**, 117 (1966)
14. J. Berthon, A. Revcolevschi, H. Morikawa, B. Touzelin, *J. Cryst. Growth*, **47**, 736 (1979)
15. V.I. Chani, A. Yoshikawa, H. Machida, T. Satoh, T. Fukuda, *J. Cryst. Growth*, **210**, 663 (2000)
16. E. Levin, C. Robbins, H. McMurdie, (eds.), *Phase Diagrams for Ceramists* (The American Ceramic Society, Columbus, OH, 1964), Fig. 687
17. S. Hosoya, H. Takei, *J. Cryst. Growth*, **57**, 343 (1982)
18. T. Tsai, S. Markgraf, M. Higuchi, R. Dieckmann, *J. Cryst. Growth*, **169**, 764 (1996)
19. GTT Technologies, *FactSage Website*, Accessed February 25, 2007, <http://www.factsage.com>
20. S. Ganschow, D. Klimm, *Cryst. Res. Technol.*, **40**, 359 (2005)
21. D. Maier, R. Bertram, D. Rhede, D. Klimm, R. Fornari, *Opt. Mater.*, in press
22. P. Rudolph, T. Fukuda, *Cryst. Res. Technol.*, **34**, 3 (1999)

Part V

**Growth and Characterization  
of Non-Oxide  $\mu$ -PD Crystals**

# 19 Silicon Fiber Crystals

Mohamed Alshourbagy, Alessandra Toncelli, and Mauro Tonelli

**Abstract.** The progress and problems (including growth instability) associated with growing silicon fiber crystals by the  $\mu$ -PD technique are overviewed. The growth system was improved by adapting the design of the hot zone; this resulted in a smooth temperature gradient inside and under the hot zone. The temperature was stabilized down to  $\Delta T \approx 0.2^\circ\text{C}$  using this approach. Etching and thermal treatment was used to minimize impurity levels.

## 19.1 Introduction

The thermal and mechanical properties of silicon (Si) are extremely favorable from the point of view of reducing thermal noise in the suspended optics of interferometric gravitational wave detectors [1–3]. The main optical system of such a detector makes use of massive mirrors ( $> 20$  kg in mass in VIRGO) that need very strong and safe suspension fibers. If the mirrors are suspended on four fibers, the fiber diameter should be about 0.4–0.5 mm. In addition, the length of each fiber should be about 30–40 cm to minimize the resonant frequency of the pendulum. However, Si fibers are not commercially available in these dimensions. Moreover, over 95% of the solar cells produced worldwide are made from silicon due to its low cost and high efficiency [4, 5].

The micro-pulling-down ( $\mu$ -PD) method allows Si crystals to be grown in specific shapes, such as fibers, rods, or ribbons. Si crystals are typically grown by the floating zone (FZ) and Czochralski (CZ) techniques. While the FZ technique is based on the inductive heating of a polycrystalline silicon rod by an RF coil, the CZ method uses polycrystalline Si fragments, which are melted in a silica crucible positioned in a resistive graphite heater.  $\mu$ -PD is different from both of these systems.

Many parameters affect the  $\mu$ -PD growth of Si. For example, the low viscosity of the Si melt causes the shape of the meniscus (its height) to be unstable, resulting in variations in the fiber diameter. Unlike CZ growth, there is almost direct contact between the crystal and the crucible in  $\mu$ -PD, which can stress the crystal and/or contaminate it. Si is a highly reactive material and is therefore very sensitive to these factors. According to [6, 7], the stable growth of Si crystals via  $\mu$ -PD requires a large meniscus diameter and a meniscus height of less than 0.20–0.25 mm if the pulling rate does

not exceed 1.5 mm/min. The high temperature gradient used in the  $\mu$ -PD system, together with the high thermal conductivity of Si, can result in uncontrollable growth interface behavior, which in some cases can cause partial freezing of the melt during growth, or even the complete termination of the process. For these reasons, the  $\mu$ -PD growth of Si is often more complicated than Si growth using traditional methods. Beside this, Si is highly reactive chemically. Therefore, it is also difficult to find a crucible material that does not react with the Si and so does not contaminate the crystal. Some of these problems and solutions to them are discussed in detail in the sections below.

### 19.2 $\mu$ -PD System and Temperature Profile

A schematic diagram of the  $\mu$ -PD system used to grow Si is shown in Fig. 19.1. An amorphous carbon crucible was placed on a short afterheater (AH); both were heated by a RF generator with a maximum power of 20 kW operated at a frequency of 77 kHz. The inductor was about 80 mm long and 70 mm in diameter with eight windings. The crucible and the afterheater were placed on a ZrO<sub>2</sub> ceramic base held by a vertical ceramic tube. High-density and high-purity 99.7% Al<sub>2</sub>O<sub>3</sub> and ZrO<sub>2</sub> ceramics were placed around the crucible for

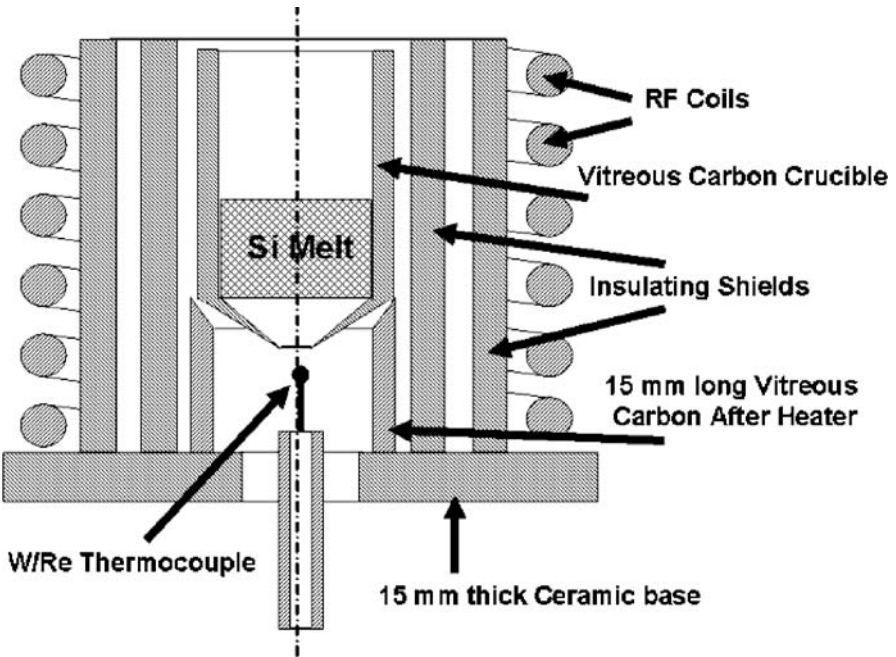


Fig. 19.1. Hot zone in  $\mu$ -PD system

thermal insulation. The whole construction was placed in a vacuum chamber connected to a primary pump and a turbo molecular pump. The pressure limit of the system was  $10^{-7}$  mbar, and the growth process was typically carried out in static 5N-purity Ar atmosphere.

A smooth temperature gradient must be established under the hot zone (Fig. 19.1) before  $\mu$ -PD growth of high-quality Si can be achieved. Therefore, various RF coil positions, afterheater dimensions, and insulating shields were tested in order to optimize the temperature gradient. From the very beginning, the unstable behavior of the melt interface during several growth runs was associated with temperature gradients that were probably extremely steep for Si fiber growth. Note that the same assembly was suitable for other insulating materials. This is why the temperature gradient was examined—to investigate the thermal environment around the crystal during the growth process, and to work out how to make it smoother. To do this, the seed crystal was replaced with a W/Re thermocouple that was pulled under the empty crucible in a similar manner to the crystal pulling performed during growth. The thermocouple had a positive lead made of tungsten (W) and a negative lead made of tungsten–26% rhenium (W–26% Re), and provided a measurement range of 0–2320 °C. The experiment was repeated with different set-up conditions by varying the design of the hot zone in order to identify the most suitable set-up for Si growth.

First, a vitreous carbon crucible and a 15-mm-long afterheater made from the same material were tested (Fig. 19.1, Table 19.1). The temperature distribution measured is shown in Fig. 19.2, curve 1. A temperature gradient of 55 °C/mm was measured, which was exceedingly steep. A high power supply was needed to heat the crucible. It is worth noting that more power was needed to obtain the same temperature conditions when the crucible was used for the second time than during initial heating. This was probably due to a chemical reaction between the Si melt and the crucible, which limited its lifetime. The temperature distributions of other set-ups within the hot zone were then tested (Table 19.1).

The second set-up contained a vitreous carbon crucible together with a 30-mm-long graphite afterheater, in order to check the effect of different

**Table 19.1.** Descriptions of the hot zone and afterheater (AH) designs tested with the vitreous carbon (VC) crucible

Set-up	Crucible material	AH material	AH height, mm	ZrO <sub>2</sub> base thickness, mm
1	VC	VC	15	15
2	VC	Graphite	30	15
3	VC inside graphite	Graphite	30	5
4	VC inside graphite	Graphite + graphite tube under the AH	30 + 30 of graphite tube	5

AH materials on the temperature gradient profile (Table 19.1 and curve 2 of Fig. 19.2).

In the third set-up (Table 19.1 and curve 3 of Fig. 19.2), the vitreous carbon crucible was inserted inside a graphite crucible with a 30-mm-long graphite AH, and the  $ZrO_2$  ceramic base was thinner than before. It is clear from curves 2 and 3 of Fig. 19.2 that the temperature gradient was smooth until a short distance ( $\approx 15$  mm) from the bottom of the crucible. An abrupt change in the temperature gradient ( $\approx 55^\circ\text{C}/\text{mm}$ ) occurred between  $\approx 15$  and  $\approx 25$  mm. This region was still inside the graphite afterheater, but outside the RF coil. This was probably the reason for the steeper temperature gradient. The almost identical curves (2 and 3 of Fig. 19.2) mean that a long graphite afterheater with a VC crucible or a VC crucible inside a graphite one is effective at producing a smooth temperature distribution up to  $\approx 15$  mm from the bottom of the crucible.

The final configuration tested (Fig. 19.2, curve 4) was found to be the most effective. In this set-up, the vitreous carbon crucible was placed inside a graphite holder mounted on a long (30-mm) graphite AH with a thin  $ZrO_2$  ceramic base (5 mm thick). The RF coil was displaced down the ceramic base. Moreover, a small graphite tube (30 mm in length and 13 mm in diameter) was positioned under the afterheater. As a result, a temperature gradient of about  $15^\circ\text{C}/\text{mm}$  was established for an extended distance in and under the hot zone instead of the gradient of  $55^\circ\text{C}/\text{mm}$  observed in previous designs. These conditions were applied in subsequent growth runs, resulting in a considerable improvement in the stability of Si growth.

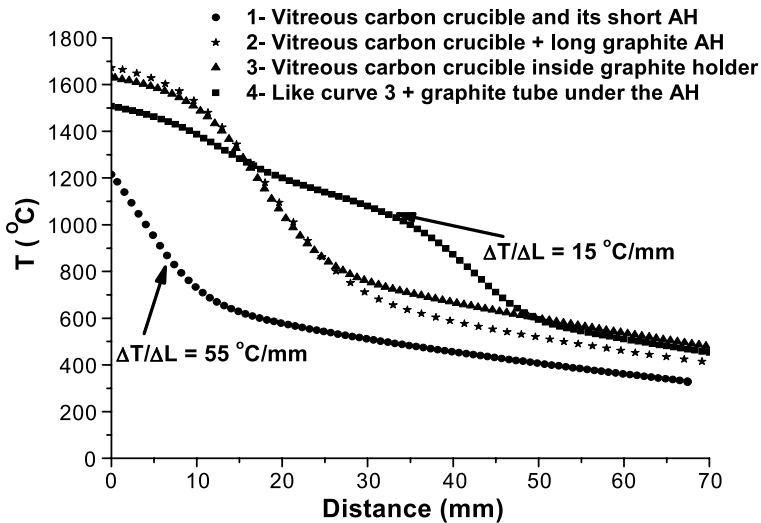


**Fig. 19.2.** Temperature profile in  $\mu$ -PD hot zone corresponding to different designs. The distance was measured from the bottom of the crucible. AH = after heater

### 19.3 Temperature Stability

The temperature instability of the hot zone is another problem. Temperature control is generally achieved by monitoring the RF power delivered from the RF generator if there is no temperature sensor (thermocouple) in the system. During Si growth, the power was controlled by an external voltage (0–10 V) regulated by the computer. Under these conditions, the stability of the power supplied by the RF generator was  $\approx 5\%$ , as described by the generator manufacturer, assuming that the input voltage of 380 V is perfectly stable. This stability is sufficient for most insulating materials, but unfortunately not for Si. To test how much the temperature fluctuates, a thermocouple was placed between the crucible and the first insulating shield. It was observed that the temperature sometimes fluctuated by more than  $3^\circ\text{C}$  at constant voltage. This was one of the reasons for the unstable growth observed when constant power was supposedly supplied to the crucible.

In order to improve the temperature stability, direct temperature control was attempted. The growth control software (LabView) was modified to allow the temperature to be read from the thermocouple placed near (outside) the crucible, and so that it could stabilize the temperature by controlling the voltage supplied from the computer. The stabilization provided by the PID loop reduced the magnitude of the temperature fluctuations such that  $\Delta T \approx 0.2^\circ\text{C}$ .

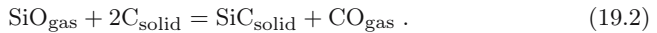
### 19.4 Crucibles

Si melt has a low viscosity, a high surface tension, and it is extremely reactive with most other materials. Therefore, very few crucible materials are suitable for Si growth. Crucibles made from high-density ( $> 1.75\text{ g/cm}^3$ ) graphite are commonly used for Si growth [8]. In this case, the Si melt is always saturated with carbon, leading to the formation of foreign SiC particles in the presence of CO and SiO gases. This affects the meniscus temperature and hence the growth stability and the diameter of the crystal. In the worst case, SiC particles block the capillary channel and terminate melt transport through it. Moreover, the Si melt reacts with the graphite of the crucible and diffuses into it due to the porosity of the graphite. This damages the crucible (cracks form).

Several reasons for the appearance of CO in the growth atmosphere were suggested in [9–11]. It could originate from the polycrystalline Si starting material, dissolved parts of the carbon crucible, and residual gases from the heated graphite. Si melt is always saturated with carbon in a graphite crucible. Therefore, CO probably acts to transport carbon:



This reaction occurs near the melt surface. SiO reacts with hot graphite according to the following reaction:



Thereafter, the CO molecules produced undergo reaction (19.1) and so these two reactions occur for an indefinite period. Another disadvantage of graphite crucibles is their short lifetime due to the formation of cracks after a few growth processes. Vitreous carbon is a good alternative crucible material for the growth of Si for the following reasons. In contrast to graphite, it is nonporous on the macro scale. Si melt reacts only with the first layers of a vitreous carbon crucible wall. The reaction then stops because Si cannot continue to diffuse inside the carbon bulk. There are also numerous voids between the graphite layers, which are 1–3 nm in size. Because of this structural disorder, vitreous carbon is very different from low-density graphite; vitreous carbon has poor electrical and thermal conductivities.

## 19.5 Growth Details and Results

Si pieces of 5N purity were used as starting material. They were placed into the vitreous carbon crucible, which was then set inside the graphite holder heated with the RF coil. Two types of vitreous carbon crucible were used. One was a conventional  $\mu$ -PD crucible with a micronozzle about 0.3 or 0.5 mm in diameter at the bottom. This was used to produce thin fibers (from 0.4 to 0.7 mm in diameter). The other type of crucible had a nozzle with an inner diameter of about 1 mm and a total bottom diameter of 2 or 3 mm, and was used to grow rod-shaped Si.

As a first step, a  $\langle 100 \rangle$ -oriented rod cut from a Si wafer was used as a seed. The growth of high-quality fibers requires the controlled melting of the top part of the seed prior to the start of the pulling process. This was performed by pushing the seed into the crucible nozzle. About 1 mm of the seed crystal was usually melted just before the start of growth. Sometimes this was not possible, probably because of the presence of impurities on the seed surface or oxide particles formed in previous growth processes.

Two operations were performed to minimize the effects of these impurities. First, chemical etching of the seed was performed to remove its surface layer. A mixture of HF and HNO<sub>3</sub> diluted with water or acetic acid was used to achieve isotropic etching. A relatively low etching velocity can be achieved using a 75% HNO<sub>3</sub> + 20% HF + 5% water solution (for about two minutes). The second operation included heat treatment of the  $\mu$ -PD chamber at a temperature of about 950 °C during the evacuation process. At this stage, any gases or impurities adsorbed by various materials were removed from the chamber or minimized. Premelting of about 1 mm of the seed was also performed just after the first contact between the seed and the meniscus.

The crystals were grown at pulling rates of 0.1–2.0 mm/min, and they were 0.4–3.0 mm in diameter (depending on the shape and dimensions of the crucible) and 40–310 mm in length. Self-separation of the fiber from the melt meniscus was not observed. However, the growth processes were not perfectly stable and some sudden changes in the meniscus shape and/or diameter did occur, probably due to fluctuations in the RF power supply or interactions between the Si melt and the crucible. Partial freezing of the melt to the crucible bottom was also sometimes observed. Such events occurred more frequently when small afterheaters were used instead of long ones. Nevertheless, most of the fibers had good shape quality. Figure 19.3 illustrates three stages of growth, as recorded by a CCD camera: (a) pre-seeding, with the seed positioned below the crucible; (b) seeding and initiation of growth; (c) stationary growth. The meniscus melt was clear (Fig. 19.3c), so it was relatively simple to control the growth process by varying the pulling rate and the RF power.

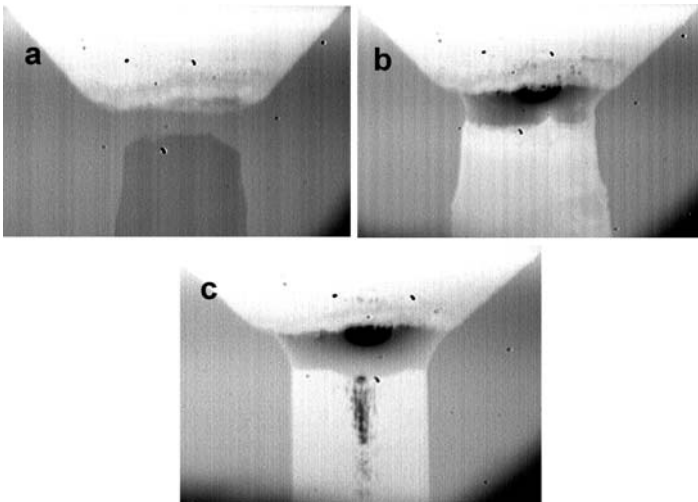


Fig. 19.3. Three main stages of Si fiber  $\mu$ -PD growth

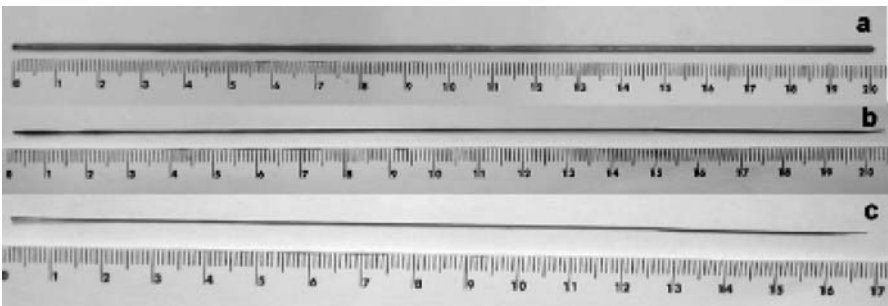
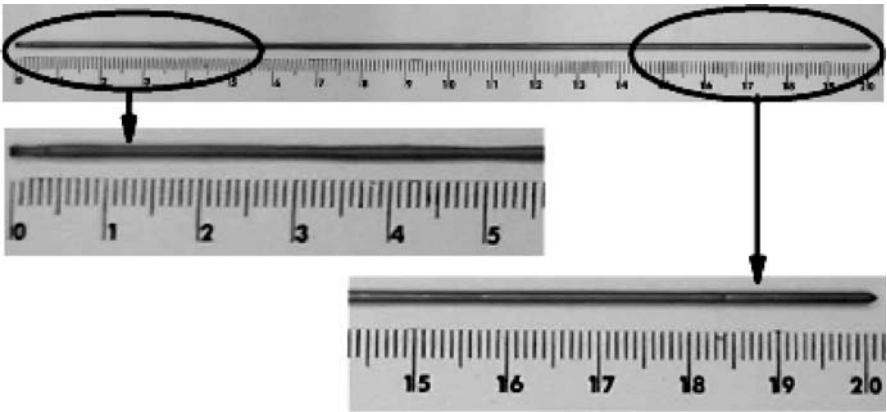


Fig. 19.4. Si fiber crystals with dimensions of  $\varnothing 2.5 \times 200$  (a),  $\varnothing 1.2 \times 210$  (b), and  $\varnothing 0.7 \times 165$  (c)



**Fig. 19.5.** Si fiber crystal: *left arrow* indicates starting part with some irregularity in diameter, and *right arrow* indicates end part with better fiber shape

Some typical Si crystal fibers with different diameters and lengths grown using this technique are shown in Fig. 19.4. It was difficult to control the diameters of the thin fibers because of the temperature fluctuations. Therefore, some of the fibers varied in diameter; the diameter fluctuated by about 0.5 mm when the average diameter was  $\sim 1$  mm.

The application of precise temperature control via the thermocouple and the growth of relatively thick crystals improved shape regularity. The crystal shown in Fig. 19.5 has an average diameter of about 2.5 mm and its diameter fluctuates by  $\sim 0.3$  mm. Tens of Si crystals were grown with lengths of up to 310 mm. However, most of these were not perfectly cylindrical.

## 19.6 Structural Analysis and Characterization

X-ray diffraction analysis (the Laue method) was used to identify the orientations of the Si fiber crystals. All of the regions of the crystals with high shape quality were single-crystalline. However, the orientations of the crystals changed along the fiber length at the points (about every 10 to 20 mm) where the diameter fluctuated. Thus, the fibers were not single-crystalline over the whole crystal length, but comprised several single-crystalline portions. The incorporation of carbon particles into the Si lattice with the subsequent twisting and formation of the reoriented crystallite is considered to be a possible reason for these transformations.

The purity of the Si fiber crystals was verified by powder X-ray diffraction. The patterns shown in Fig. 19.6A were obtained by fitting the measurements to the profile calculated from the known cubic structure of Si [12]. The fits were obtained by refining the unit cell axis length, which converged at  $a = 5.4299$ . All peaks in the pattern were clear and were easily indexed.

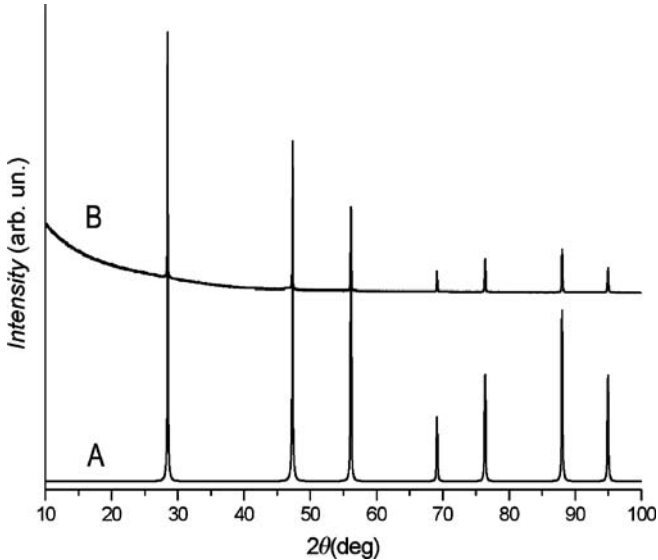


**Fig. 19.6.** Measured (B) and calculated (A) XRD patterns for Si. The pattern B has been obtained from powdered fiber using Cu-K $\alpha$  radiation

Single-phase cubic-type structure was formed in as-grown Si fiber crystals, and no impurity phases were observed. It should be pointed out that 100% of the melt was usually solidified into the fiber and that no shift in the melt composition resulting from second-phase formation was detected during growth. Moreover, according to their absorption spectra, the absorption edge of the Si fibers occurred close to 1048 nm. This is in good agreement with results reported elsewhere, and it corresponds well to that observed for pure silicon produced without impurities.

## 19.7 Conclusions

This chapter discussed the growth stability and characterization of Si fiber crystals grown by the  $\mu$ -PD technique. A smooth temperature gradient in and under the hot zone can be obtained for an extended distance by improving the design of the insulation. Temperature fluctuations can be reduced to as low as  $\Delta T \approx 0.2^\circ\text{C}$  (as compared with  $\Delta T \approx 3^\circ\text{C}$ ). Chemical etching and thermal treatment are effective tools for minimizing impurity levels.

*Acknowledgement.* The authors wish to thank Tsuguo Fukuda and Akira Yoshikawa for helpful discussions and their support when developing the  $\mu$ -PD apparatus. This work was supported by INFN in the Virgo R&D program, by the European Commission in the FP6 framework (project ILIAS, research activity JR3-STREGA), and by the Italian Ministry of University and Research (MIUR-PRIN-2002).

## References

1. M. Alshourbagy, P. Amico, et al., *Class. Quantum Grav.*, **23**, S277 (2006)
2. F. Acernese, P. Amico, M. Alshourbagy, et al. (VIRGO collaboration), *Class. Quantum Grav.*, **22**, S869–S880 (2005)
3. M. Alshourbagy, P. Amico, et al., *Rev. Sci. Instrum.*, **77**, 044502 (2006)
4. R. Bisconti, H. Ossenbrink, *Sol. Energy Mater. Sol. Cells*, **48**, 1 (1997)
5. T. Minemoto, M. Murozono, et al., *Sol. Energy Mater. Sol. Cells*, **90**, 3009 (2006)
6. K. Shimamura, S. Uda, T. Yamada, S. Sakaguchi, T. Fukuda, *Jpn. J. Appl. Phys.*, **35**, L793 (1996)
7. T. Fukuda, P. Rudolph, S. Uda, (eds.), *Fiber Crystal Growth from the Melt* (Springer, Berlin, 2004)
8. M.N. Leipold, T.P. O'Donnell, M.A. Hagan, *J. Cryst. Growth*, **50**, 366 (1980)
9. F. Schmidt, C.P. Khattak, T.G. Digges, L. Kaufman, *J. Electrochem. Soc.*, **126**, 938 (1979)
10. R.W. Series, K.G. Barraclough, *J. Cryst. Growth*, **63**, 219 (1983)
11. T. Inada, T. Fujii, T. Kihuta, T. Fukuda, *Appl. Phys. Lett.*, **50**, 143 (1987)
12. M.E. Straumanis, E.Z. Aka, *J. Appl. Phys.*, **23**, 330 (1952)

# 20 LiF, LiYF<sub>4</sub>, and Nd- and Er-Doped LiYF<sub>4</sub> Fluoride Fibers

Ana Maria do Espirito Santo and Sonia Licia Baldochi

**Abstract.** The growth of constant-diameter single-crystal fibers of fluoride is reviewed. The reproducible solidification of LiF and LiYF<sub>4</sub> single-crystal fibers by the micro-pulling-down technique was achieved through precise system control. The effects of the purity of the raw materials, the growth atmosphere, composition, doping, and other growth parameters on the fiber quality are discussed.

## 20.1 Introduction

Techniques for growing single crystals have been developed over the course of many decades in order to meet the needs for fundamental research and applications in many different areas. Indeed, fluoride crystals have been used in research and in technologies such as dosimeters and X-ray monochromators, but mainly in optical devices, such as optical windows and laser hosts [1]. Recent research into fluoride single-crystal fiber growth has opened up new potential applications of this class of materials. For instance, the light-guiding properties of these fibers can be combined with the conversion properties of single crystals to produce efficient active laser media. As a result, the development of compact diode-pumped solid-state systems can be expected.

The two most common methods of single-crystal fiber growth from the melt are laser-heated pedestal growth (LHPG) [2] and micro-pulling-down ( $\mu$ -PD) [3]. Due to the absence of a crucible and the use of a CO<sub>2</sub> laser to perform the melting, the LHPG method is especially useful for high melting point materials that absorb well at 10.6  $\mu$ m. However, stable growth over a long pulling period, ensuring constant-diameter fibers, can be achieved more easily using the  $\mu$ -PD system. Both methods have been used for the growth of fluoride fiber crystals, but the  $\mu$ -PD has been found to be more appropriate for this class of materials; firstly due to the typically low melting points of fluorides, and secondly because the reactive environment usually employed for fluoride growth is not appropriate for the optical components of LHPG systems. In particular, Shaw and Chang [4] reported some problems related to (i) the purity of feeding rod, and (ii) controlling the atmosphere during the LHPG growth of LiYF<sub>4</sub> (YLF). However, more promising results were reported for the  $\mu$ -PD growth of fluoride fibers [5]. Some experimental

aspects of the  $\mu$ -PD growth of LiF, YLF, and Nd- and Er-doped YLF fibers are discussed below.

Single crystals of alkali halides, like LiF, have played a major role in solid-state research. Because of their highly ionic bonding, their high structural symmetry and their wide band gaps, they quickly became model systems for basic experimental and theoretical investigations in insulators. Similarly, LiF was found to be a suitable material for studying basic technical problems associated with  $\mu$ -PD fluoride growth [6]. Therefore, the process developed for LiF growth was also found to be appropriate for the growth of other fluoride fiber crystals [5].

YLF crystal is a well known laser host. Its crystalline matrix can be doped with several rare earth ions. This makes it possible to take full advantage of the emission process and energy transfer mechanisms that might occur among the ions, resulting in various efficient solid-state laser systems [7].

## 20.2 Apparatus and Starting Materials

The growth of fluoride single-crystal fibers presents an interesting challenge since their preparation requires specific procedures, suitable equipment, and involves following standard safety protocols, due to the use of toxic and/or corrosive materials. Although these procedures are also used in the growth of bulk crystals, some of them may require more critical control in the case of fiber growth. For example, YLF is moisture- and oxygen-sensitive, and so a dry working environment (or a reactive one) is needed during the growth process. The use of a dry inert gas or a reactive atmosphere during YLF fiber-pulling can affect the balance of interfacial tension at the solid-liquid interface considerably, affecting the wetting properties of the interfacial system significantly. This is not observed during YLF bulk crystal growth.

As illustration, Fig. 20.1 shows a schematic of the main parameters that need to be considered for the growth of fluoride fibers by the  $\mu$ -PD method based on a resistive heating system. Region I represents the main heater or crucible. It is important to consider here the effects of the interaction of the molten fluoride with the atmosphere and with spurious impurities in the reagents as well as the melting behavior of the fluoride. Region II represents the capillary nozzle, the afterheater and the growth interface; important characteristics to focus on here are growth parameters such as the pulling rate and the thermal gradient. These parameters need to be controlled during any process of crystal growth from the melt, where the heat flow defines the thermal geometry and the meniscus shape. Finally, region III corresponds to the required characteristics of the resulting fluoride fibers, such as the structural quality, optical quality, and dopant distribution that must be achieved for practical applications.

Molten fluorides can be very corrosive and so only a few types of crucible can be used to hold them. The usual choice is platinum (Pt) or graphite. Both

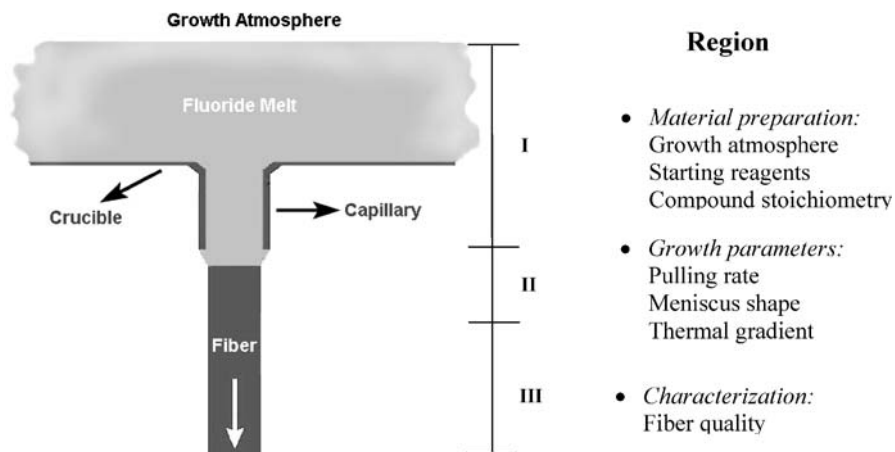


**Fig. 20.1.** Schematic diagram of the main parameters to be considered for the growth of complex fluorides by the  $\mu$ -PD method

can be used in inductive heating systems and they are usually manufactured with a fixed shape (in terms of their size and the geometry of the orifice at the bottom of the crucible). The crucibles used in  $\mu$ -PD with resistive heating are usually made in laboratories from a Pt foil and constructed in a shape that is easily adapted to any particular purpose.

Fluorides are very sensitive to oxygen and moisture contamination. Even traces of water present in the growth chamber react with the melt, producing hydroxide ions in the crystals [1, 8]. These impurities reduce the optical quality of the crystal, leading, for instance, to significant losses in optical performance. Therefore, an inert or reactive atmosphere is always required to keep the melt oxygen- and moisture-free.

Nowadays, most commercial  $\mu$ -PD equipment is designed to operate under controlled atmosphere by using a growth chamber to be just operated under a flow of inert gas or by using a vacuum-tight chamber that allows the growth under flow and low positive pressures ( $\sim 5$ – $10$  psi). The second option is ideal for fluoride fiber growth. A gas flow may be helpful during the pulling process, but experimental results show that a vacuum prior to the melting is also important since it minimizes the amount of contamination from the growth environment. In particular, the amount of contamination from moisture was estimated by applying infrared spectroscopy to transparent and colorless LiF crystal fibers grown (i) under an inert gas flow, and (ii) after the thermal treatment of the growth chamber under vacuum and, then, back-filled with ultrapure and dry inert gas [6]. LiF fibers with low concentration of hydroxyl groups were successfully obtained in the second case, yielding improved optical transparency in the near-infrared region of the spectrum.

For more complex fluorides, such as YLF, the use of a reactive atmosphere during the melting and fiber pulling is required in addition to the previous thermal treatment of growth chamber under vacuum. The application of a reactive gas (HF or  $\text{CF}_4$ ) during  $\mu$ -PD requires the use of a growth chamber (and internal components) constructed from materials resistant to the corrosive nature of these gases. The most appropriate materials for this task are platinum and graphite for the crucibles and the afterheaters; and Monel (Ni-Cu alloy with some additives), copper, and stainless steel (at low temperatures) for the growth chamber and their components [9]. The growth chambers of commercial inductive  $\mu$ -PD systems are usually made of stainless steel, which is relatively resistant to HF corrosion at low temperatures. A steel chamber is enough since the chamber wall is kept at low temperatures by employing a cooling water system or by using highly efficient thermal isolation of the hot region around the crucible, especially considering its lower cost when compared to that of a chamber made of Monel.

Quartz growth chambers are also commonly used in commercial  $\mu$ -PD systems. However, they cannot be used with highly corrosive gases like HF because of the potential reaction of silica with fluorides. Nevertheless, it is possible to use them in atmospheres that are not very corrosive. Figure 20.2



**Fig. 20.2.** View of adapted commercial  $\mu$ -PD system during LiF fiber pulling with Pt crucible in detail [6, 29]

shows a typical resistive  $\mu$ -PD system used to grow LiF and YLF fibers in a flow of a mixture of inert gas (75%) and CF<sub>4</sub> (25%). Since the hot region is relatively small compared to the size of the silica chamber, and the fraction of reactive gas is reduced, the corrosion of the quartz chamber does not affect the growth process. Nevertheless, after several experiments, the quartz chamber becomes milky.

The successful growth of fluorides is also strongly dependent on the use of high-purity chemicals. A wide variety of relatively pure fluoride compounds are currently commercially available. Most ternary or even more complex fluorides such as YLF or LiSrAlF<sub>6</sub> are usually obtained by co-melting the basic components just before crystal growth. This process, namely synthesis, also serves as a preliminary chemical treatment of the compound, and is usually done under reactive atmosphere. Since the use of strongly corrosive atmospheres, like HF, directly in the growth chamber is always cumbersome, a good option is to treat (or synthesize) the initial reagents in a separate equipment especially designed for the use of HF [1, 9]. The solid material produced is later transferred to the fiber growth apparatus.

A second option is to melt the compounds directly in the growth chamber under a low-corrosive atmosphere, such as a mixture of CF<sub>4</sub> and an inert gas. Although CF<sub>4</sub> is usually considered to be a secondary reactive agent that should be used in addition to HF, it gave acceptable results when used as the primary reactive agent during YLF growth. The advantage of using CF<sub>4</sub> is that it produces a “double purification effect” by removing traces of water and generating a small amount of HF [1, 10]. Problems with corrosion of the growth system are minimized when only traces of HF are present during growth.

Pieces of fluoride crystals that were grown beforehand under an inert or reactive atmosphere are another appropriate starting material for fiber growth. LiF crystals purified and grown by zone melting in HF were successfully used for the fluoride fiber growth under Ar flow. Pure and homogeneous fibers of YLF, BaF<sub>2</sub>, and BaLiF<sub>3</sub> were also produced from pieces of crystal under a CF<sub>4</sub> and/or Ar flow.

According to the phase diagram of the LiF–YF<sub>3</sub> system [11], the YLF melts incongruently. The YLF phase can be only obtained from a liquid slightly enriched with LiF. The congruent/incongruent melting behavior of YLF has been extensively discussed in the literature [11–13]. It was found that the starting composition of the melt can be close to the stoichiometric one if contamination from moisture is removed. It was possible to grow YLF crystals by the Czochralski technique from the melt with an initial molar composition of 50.5% LiF: 49.5% YF<sub>3</sub> [14]. However, a starting composition of 52% LiF:48% YF<sub>3</sub> [15] is typically used because of the minor “incongruency” effect resulting from residual moisture.

Different compositions were tested for the growth of pure YLF fibers. The best results were observed for an initial mixture of LiF:YF<sub>3</sub> = 51.2 mol%: 48.8 mol%, corresponding to an excess of LiF of 5 mol% in the YLF melt.

Fibers with relatively short peritectic portions (10 mm) and long stoichiometric single-phase YLF regions (60 mm) were obtained [5] (see also Sect. 20.4).

### 20.3 Growth Parameters For LiF and YLF Growth

As pointed out by Uda [16], in order to grow constant-diameter fibers, invariant growth conditions need to be established during the pulling process. In practice this is achieved by employing constant pulling-down rate and heater output power, a symmetric crucible configuration, and a uniform capillary nozzle.

No particular problems related to composition deviation, wetting, and defects originating from segregation or faceting have been noted during LiF fiber growth. Thus, stable growth is easily achieved. Figure 20.3 shows a transparent and colorless LiF crystal fiber with a uniform diameter that was grown by the  $\mu$ -PD technique with resistive heating. Fibers with lengths of up to 100 mm were pulled from capillaries with inner diameters of 0.5–1 mm and lengths of 2–3 mm. The pulling rates were 0.6–1.5 mm/min, depending on the capillary diameter. Uniform fibers were stably grown over the entire range of pulling rates when the fiber diameter  $d$  was in the range  $0.5 \leq d \leq d_c$ , where  $d_c$  is the capillary diameter [17]. Also, the relationship between the heater power and the pulling rate was carefully controlled.

The temperature gradient close to the die is set by adjusting the currents applied to the crucible and the afterheater, but it also depends on material properties. The temperature distribution during LiF fiber growth was estimated to be 1200 °C/cm. The axial temperature gradient in the solid near the growth interface was measured during the steady-state growth of a fiber with a diameter of 0.8 mm. The value of the gradient was less than those observed for oxides and eutectics with high melting points (from 3000 °C/cm to 13000 °C/cm [18, 19]). This was expected considering the low melting point of LiF (m.p. = 848 °C; most oxides have m.p. > 1000 °C), which resulted in a smoother temperature distribution in this region.

It is more difficult to achieve stable growth conditions for YLF fiber growth. In addition to the incongruent melting of YLF and its high sensitivity to moisture and oxygen contaminations, phenomena related to wetting and segregation complicate the seeding and growth stabilization.

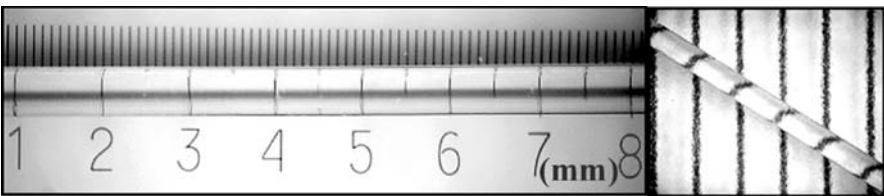


**Fig. 20.3.** As-grown LiF fiber with diameter of 600  $\mu\text{m}$  [6, 29]

A migration of the melt to the crucible wall and a change in the appearance of the melt from transparent to opaque were detected when YLF was grown in only a prepurified Ar atmosphere. The first phenomenon was observed from the beginning of the melting process. The melt moved down through the capillary and then coated the outer walls of both the capillary and the crucible. This made seeding and meniscus adjustment difficult, and both conditions are essential for stable fiber growth. In order to reduce this wetting effect, the balance between the interfacial tensions must be considered. There are two possibilities: change the atmosphere or change the crucible material. Since Pt is the best material for fluoride growth, the only real option was to investigate the influence of the gas composition on the wetting. Fiber growths performed under argon, nitrogen and a mixed gas flow of argon plus carbon tetrafluoride (CF<sub>4</sub>) were compared. The use of the last atmosphere resulted in a reduction in the wetting, and this was sufficient for meniscus anchoring and seeding. Furthermore, the CF<sub>4</sub> gas is an efficient fluorinating agent that removes moisture and reduces oxyfluoride formation. The melt maintained under this atmosphere was colorless and transparent throughout growth.

Homogeneous, transparent and constant-diameter single-crystalline fibers of undoped YLF were obtained with diameters of 0.6–0.8 mm and lengths of up to 60 mm (Fig. 20.4). The fibers were grown at a constant rate of 0.75 mm/min from a capillary with an inner diameter of 0.8 mm and a length of about 2.0 mm. The initial seeding was performed by contacting a platinum wire 1 mm in diameter with the drop in the capillary tip. Thereafter, a *c*-oriented piece of the fiber grown was used as seed.

The methodology developed for the growth of undoped YLF fibers was also suitable for rare-earth-doped YLF (10 mol% and 40 mol% for Er, and 1.7 mol% for Nd). The “melting incongruence” of lithium lanthanide (Ln) tetrafluorides (LiLnF<sub>4</sub>) decreases with as the atomic number of the Ln increases. In the case of Er-doped YLF, the incongruence decreases as the amount of dopant increases (Y can be completely substituted by Er, resulting in LiErF<sub>4</sub>). In contrast, doping the YLF host with Nd increases the incongruence. Therefore, only a limited concentration of Nd in YLF is allowed. The Nd segregation coefficient, *k*, in YLF bulk crystal is usually less than unity, i.e., the host tends to reject Nd incorporation and the distribution of

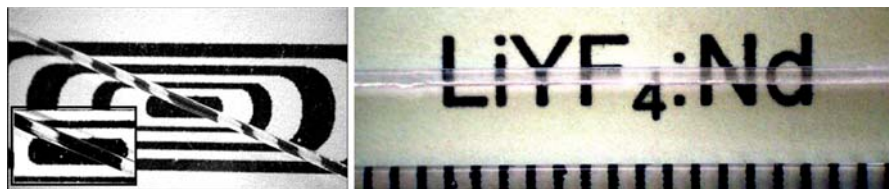


**Fig. 20.4.** YLF fiber grown from a melt with 5 mol% of LiF excess, with constant rate of 0.75 mm/min, under mixed flow of Ar plus CF<sub>4</sub> (*left*), and Nd-doped YLF fiber growth under similar conditions (*right*) [5, 6, 29]

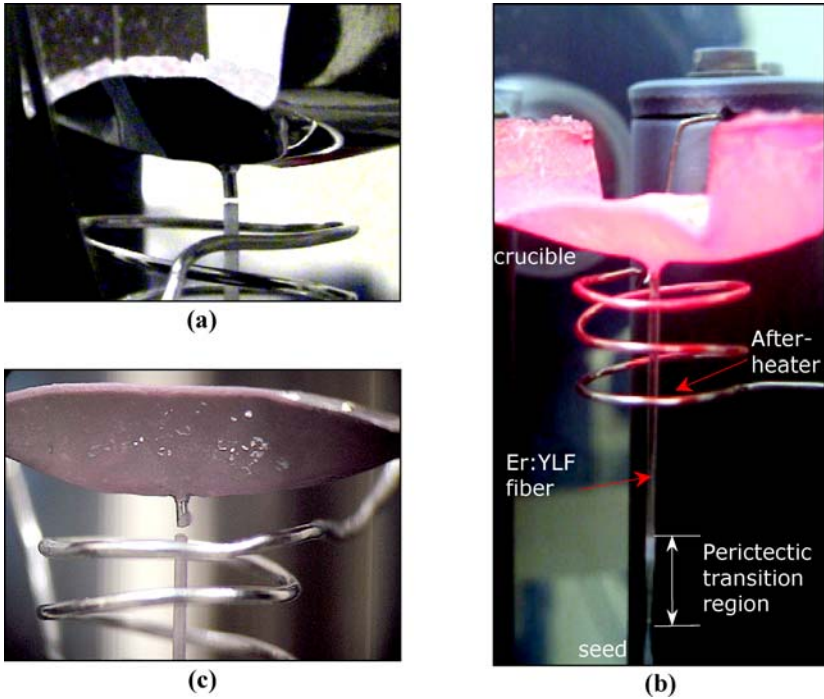


**Fig. 20.5.** Crucible wetting during Er:YLF (40 mol% Er) fiber growth: **a** before melting, **b** steady-state fiber growth, **c** end of the pulling process

Nd is inhomogeneous throughout the crystal. However, homogeneously distributed Nd-doped YLF single-crystalline fibers were obtained by the  $\mu$ -PD method [20]. The stoichiometric phase is long, bright, transparent, and largely free of cracks (Fig. 20.4).

The effect of wetting is more apparent when doped YLF fibers are grown by  $\mu$ -PD. The doping modifies the properties of the melt, including the balance between the interfacial tensions between the solid, liquid and gas phases. Nevertheless, it is also possible to control the seeding and meniscus in this case and establish stable growth, as shown in Fig. 20.5b. First an opaque part corresponding to the peritectic transition region (see also Sect. 20.4) is observed, and then the stoichiometric Er-doped YLF transparent phase follows. The walls of the capillary tip remain free from the liquid film and the growth is fed only by the melt passing through the capillary. Figure 20.5c shows the crucible at the end of the pulling process; the image shows that some solidified melt migrated on the crucible wall due to the wetting effect.

## 20.4 Characterization

Studies of the properties of fiber crystals by traditional materials characterization techniques, such as optical spectroscopy or X-ray powder diffraction (XRD), is often complicated due to the small fiber size and/or the small amount of sample available for measurements. Because of these limitations, nondestructive methods are more attractive for single-crystal fiber characterization.

The Raman spectrum for a perfect crystal should contain delta function bands at the optical mode frequencies of the fundamental transitions in the reciprocal lattice. The base width of the first-order band results from several factors, such as the instrumental set-up, anharmonic interactions among phonons, phonons coupling with other excitations, and lattice long-range disorder, structural defects [21]. A comparative structural analysis can be performed using Raman spectra of several crystals with the same chemical compositions and crystallographic orientations. This can be done by evaluating the relative widths of the main Raman peaks at low frequencies, since the instrumental set-up was the same for each crystal (in other words, the contribution of the instrumental set-up to the base width is the same for each crystal). The thinner the band, the higher the structural quality of the crystal.

Depolarized micro-Raman spectroscopy, performed in the range 200–500 cm<sup>-1</sup>, was used to compare the optical and structural properties of undoped YLF  $\mu$ -PD fibers with those of YLF bulk crystal grown by the Czochralski technique [20]. The fiber and bulk crystals yielded similar Raman spectra, so their structural and optical qualities were comparable.

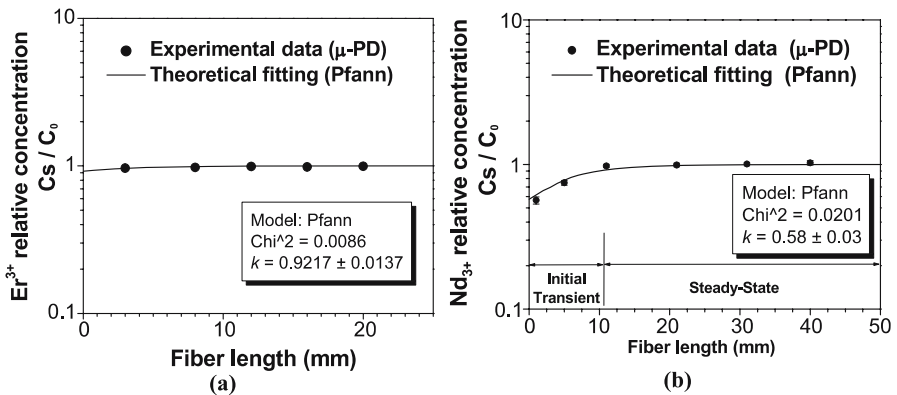


**Fig. 20.6.** Concentration and distribution fitting curves of RE ions along YLF fibers with nominal concentration of **a** 40 mol% of Er<sup>3+</sup> and **b** 1.7 mol% of Nd<sup>3+</sup> [29]

X-ray fluorescence is another nondestructive analytical method that can be used to quantitatively measure dopant distributions and segregation coefficients ( $k$ ). Figures 20.6a and b show the curve fits obtained for the relative dopant distributions. The nominal concentration of  $\text{Er}^{3+}$  was 40 mol% ( $k = 0.92 \pm 0.01$ ), and the nominal concentration of  $\text{Nd}^{3+}$  was 1.7 mol% ( $k = 0.58 \pm 0.03$ ) in the Er- and Nd-doped YLF fibers, respectively. The distribution coefficient  $k$  was estimated via the classical Pfann relationship by fitting the experimental results to (20.1) [22]:

$$\frac{C_s}{C_0} = \left[ 1 - (1 - k) \exp\left(-k\frac{x}{l}\right) \right]. \quad (20.1)$$

Here  $C_s$  is the  $\text{RE}^{3+}$  (trivalent rare-earth) concentration at a distance  $x$  from the beginning of the solidified YLF phase along the fiber;  $C_0$  is the nominal  $\text{RE}^{3+}$  concentration, and  $l$  is the length of the liquid zone (approximately 2.5 mm). The liquid zone covers the meniscus height and the capillary channel length [23]. As expected for erbium doping, a homogeneous distribution was observed along the YLF phase, since the  $\text{Er}^{3+}$  cation has a segregation coefficient  $k$  that is close to unity in YLF host. It is also known that  $\text{Y}^{3+}$  can be completely replaced with  $\text{Er}^{3+}$  in YLF.

In contrast to  $\text{Er}^{3+}$ , the  $\text{Nd}^{3+}$  segregation coefficient in YLF bulk crystal is considerably less than unity. The  $\text{Nd}^{3+}$  distribution in the fiber with nominal concentration of 1.7 mol%  $\text{Nd}^{3+}$  shows a transient at the beginning of the YLF phase (known as the “initial transient”, I.T.). After  $\sim 10$  mm of the YLF stoichiometric phase has grown, the  $\text{Nd}^{3+}$  concentration reaches its maximum level, which is very close to the nominal concentration. After the initial transient (Fig. 20.6b), the Nd content remains uniform along the fiber (known as the steady-state, S.S., region).

Axially homogeneous fibers can be grown provided that the meniscus geometry is controlled precisely, since this influences the segregation during  $\mu$ -PD fiber-pulling considerably. Here, the initial transient can again be described by the Pfann relationship. However, the segregation coefficient of  $\text{Nd}^{3+}$  in  $\mu$ -PD is greater than that found in YLF bulk crystals grown by the Czochralski technique, where  $k$  is about 0.33. This result is similar to others observed elsewhere [24–26]. This phenomenon is, in fact commonly observed when the  $\mu$ -PD method is used, due to the behavior of the capil-

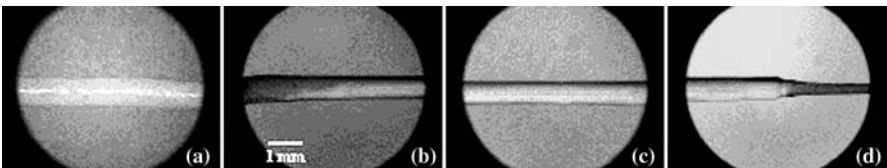


**Fig. 20.7.** Optical micrographs of different regions along YLF fiber grown from a melt with 10 mol% of LiF excess [5, 29]

lary and meniscus regions, the melt flows, and the solute-stirring solid-liquid interface [27, 28].

As-grown fibers can be also characterized by optical microscopy. Figure 20.7 shows a series of micrographs from different regions of a YLF fiber grown from a melt with a 10 mol% excess of LiF. The evolution for the formation of the YLF phase was noted and subsequent XRD analysis allowed the identification of the different phases along the fiber. Initially, an opaque region was crystallized (Fig. 20.7a), followed by a semi-transparent region attributed to the peritectic reaction denoting the initial crystallization of the transparent YLF phase (Fig. 20.7b). A stoichiometric YLF phase that is homogeneous and regular in diameter can be seen in Figure 20.7c. At the end of the pulling process, the fiber again became opaque (Fig. 20.7d). In this region, the solidified fiber corresponds to the eutectic mixture.

Considering the application of single-crystal fibers in optical devices, as compact all-solid-state lasers pumped by diode laser, it is important to study their optical properties in order to assess the final quality of the grown fibers. Optical spectroscopy, a nondestructive technique, can be used to compare the optical parameters of an Nd-doped YLF fiber with a Nd-doped YLF bulk crystal. The absorption and emission spectra of both were measured under same conditions. Similar were obtained in both cases [20].

Scanning electron microscopy (SEM) and XRD are also very useful for fiber characterization, especially for the analysis of incongruent melting materials such as YLF. However, both of these are destructive methods. Figure 20.8 illustrates the microstructures formed during YLF fiber growth from a melt containing a 20 mol% excess of LiF performed at a high pulling rate (1.5 mm/min). At the start of growth, eutectic microstructures composed of LiF (dark regions) and YLF (light gray regions) were incorporated into the major YLF phase. At the end of the fiber a third phase, YF<sub>3</sub> (the white regions), was also identified. This suggests that the pure YLF phase cannot be isolated as a single crystal phase when the above conditions are used, i.e., a high pulling rate and 20 mol% of LiF in the initial melt.

## 20.5 Summary

Highly transparent and homogeneous LiF as well as undoped and rare-earth-doped YLF fibers can be successfully grown by the  $\mu$ -PD method, provided that the growth atmosphere and stoichiometry are precisely controlled. Different nondestructive analytical methods used for fiber characterization have also been discussed, since the results obtained from them can be used to further improve the  $\mu$ -PD technology.

*Acknowledgement.* The authors are grateful to FAPESP and CNPq for their financial support (FAPESP 00/00234-1, 01/7337-3 and CNPq 420177/2005-1). Fig-

ures 20.2, 20.3, 20.4, 20.6b and 20.7 were reprinted from [5,6,20] with permission from Elsevier.

## References

1. S.L. Baldochi, S.P. Morato, *Fluoride bulk crystals growth*, in *Encyclopedia of Materials: Science and Technology*, ed. by K.H.J. Buschow, R.W. Cahn, M.C. Flemings, B. Ilchner, E.J. Kramer, S. Mahajan (Elsevier Science Amsterdam, 2001), pp. 3200–3205

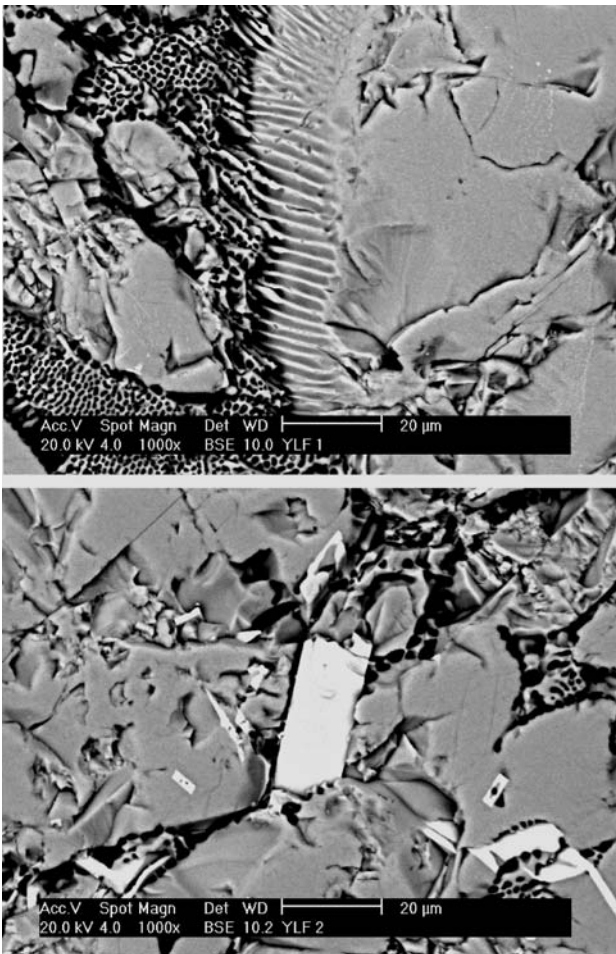


**Fig. 20.8.** Optical micrographs of different regions along YLF fiber grown from a melt with 20 mol% of LiF excess [5]

2. R.S. Feigelson, *Growth of fiber crystals*, in *Crystal Growth of Electronic Materials*, ed. by E. Caldis (Elsevier Science, Amsterdam, 1985), p. 127
3. T. Fukuda, P. Rudolph, S. Uda, (eds.), *Fiber Crystal Growth from the Melt*, Adv. Mater. Res. (Springer, Berlin, 2004)
4. L.B. Shaw, R.S.F. Chang, J. Cryst. Growth, **112**, 731 (1991)
5. A.M.E. Santo, I.M. Ranieri, G.E.S. Brito, B.M. Epelbaum, S.P. Morato, N.D. Vieira Jr., S.L. Baldochi, J. Cryst. Growth, **275**, 528 (2005)
6. A.M.E. Santo, B.M. Epelbaum, S.P. Morato, N.D. Vieira Jr., S.L. Baldochi, J. Cryst. Growth, **270**, 121 (2004)
7. N.D. Vieira Jr., I.M. Ranieri, L.V.G. Tarelho, N.U. Wetter, S.L. Baldochi, L. Gomes, P.S.F. de Matos, W. de Rossi, G.E.C. Nogueira, L.C. Courrol, E.A. Barbosa, E.P. Maldonado, S.P. Morato, J. Alloys Compd., **344**, 231 (2002)
8. B.P. Sobolev, Crystallogr. Rep., **47**(1), S63 (2002)
9. J. Grannec, L. Lozano, *Preparative methods, in Inorganic Solid Fluorides*, ed. by P. Hagenmuller (Academic, New York, 1985)
10. R.C. Pastor, K. Arita, Mater. Res. Bull., **11**, 1037 (1976)
11. R.E. Thoma, C.F. Weaver, H.A. Friedman, H. Insley, L.A. Harris, H.A. Yakel, J. Phys. Chem., **65**, 1096 (1961)
12. H. Safi, I.R. Harris, B. Cockayne, J.G. Plant, J. Mater. Sci., **16**, 3203 (1981)
13. R. Uhrin, R.F. Belt, J. Cryst. Growth, **38**, 38 (1977)
14. I.M. Ranieri, S.P. Morato, L.C. Courrol, H.M. Shihomatsu, A.H.A. Bressiani, N.M.P. Moraes, J. Cryst. Growth, **209**, 906 (2000)
15. A. Bensalah, K. Shimamura, V. Sudesh, H. Sato, K. Ito, T. Fukuda, J. Cryst. Growth, **223**, 539 (2001)
16. S. Uda, *Fundamentals of growth dynamics of the micro-pulling-down method, in Fiber Crystal Growth from the Melt*, Adv. Mater. Res., ed. by T. Fukuda, P. Rudolph, S. Uda (Springer, Berlin, 2004), pp. 47–50
17. P. Rudolph, A. Yoshikawa, T. Fukuda, Jpn. J. Appl. Phys., **39**, 5966 (2000)
18. S. Uda, W.A. Tiller, J. Cryst. Growth, **121**, 93 (1992)
19. D.H. Yoon, T. Fukuda, J. Cryst. Growth, **144**, 201 (1994)
20. A.M.E. Santo, A.F.H. Librantz, L. Gomes, P.S. Pizani, I.M. Ranieri, N.D. Vieira Jr., S.L. Baldochi, J. Cryst. Growth, **292**, 149 (2006)
21. P.W. Atkins, *Spectroscopy 1: Rotational and Vibrational Spectra*, in *Physical Chemistry*, 5th edn. (Oxford University Press, Oxford, 1994), pp. 539–586
22. W.G. Pfann, Am. Inst. Mining Met. Eng., **194**, 747 (1952)
23. B.M. Epelbaum, *Practice of micro-pulling-down growth, in Fiber Crystal Growth from the Melt*, Adv. Mater. Res., ed. by T. Fukuda, P. Rudolph, S. Uda (Springer, Berlin, 2004), pp. 103–108
24. V.I. Chani, A. Yoshikawa, Y. Kuwano, K. Hasegawa, T. Fukuda, J. Cryst. Growth, **204**(1–2), 155 (1999)
25. V.I. Chani, A. Yoshikawa, Y. Kuwano, K. Inaba, K. Omote, T. Fukuda, Mater. Res. Bull., **35**(10), 1615 (2000)
26. B. Hautefeuille, K. Lebbou, C. Dujardin, J.M. Fourmigue, L. Grosvalet, O. Tillement, C. Pédrini, J. Cryst. Growth, **289**, 172 (2006)
27. N. Schäfer, T. Yamada, K. Shimamura, H.J. Koh, T. Fukuda, J. Cryst. Growth, **166**, 675 (1996)
28. H.J. Koh, N. Schäfer, K. Shimamura, T. Fukuda, J. Cryst. Growth. **167**, 38 (1996)
29. Figures 8.2 (2),(3),(4),(6B) and (7) reprinted from references [5, 6, 20] with permission from Elsevier

# 21 Binary Fluorides: (Gd,Y)F<sub>3</sub> and K(Y,Lu)<sub>3</sub>F<sub>10</sub>

Akira Yoshikawa and Tomohiko Satonaga

**Abstract.** The growth of rare-earth fluoride solid-solution crystals by the micro-pulling-down method is reviewed, focusing on the trifluorides Gd<sub>1-x</sub>Y<sub>x</sub>F<sub>3</sub> and Gd<sub>1-x</sub>Yb<sub>x</sub>F<sub>3</sub> ( $x = 0.12$ – $0.42$ ) in particular. Details on the growth of Pr-doped KY<sub>3</sub>F<sub>10</sub> single crystals 0.5–3.0 mm in diameter and 35–45 mm in length are also presented. When single-phase solidification was achieved, the crystals had no any visible inclusions or cracks. The KY<sub>3</sub>F<sub>10</sub> crystals were transparent and slightly green in color. The luminescence spectra and decay kinetics measured at 80–300 K of a number of YF<sub>3</sub>–GdF<sub>3</sub> mixed crystal hosts co-doped with Ce<sup>3+</sup> and Me<sup>2+</sup> (Me = Mg, Ca, Sr, Ba) cations are also discussed.

## 21.1 Introduction

The growth of rare-earth trifluoride crystals by the micro-pulling-down method ( $\mu$ -PD) [1,2] was achieved using  $\mu$ -PD equipment adapted for fluoride systems [3–5]. These crystals are considered to be suitable host materials for laser or scintillator applications due to their high transparency over a wide wavelength region from the ultraviolet (UV) to the infrared (IR). Therefore, one of the aims when studying binary fluorides was to develop novel host crystals suitable for optical applications. Ce:AE:(Gd,Y)F<sub>3</sub> (AE = alkaline earth) crystals are examples of such materials.

Rare-earth trifluoride crystals have low refractive indices, which limit the nonlinear effects obtained under high-power laser source pumping, as well as low phonon energies. Visible continuous-wave (CW) solid-state lasers are of great interest for applications in high-density data storage and laser displays. However, it is difficult to produce such lasers using rare-earth-doped crystals due to the lack of suitable pump sources. The up-conversion of infrared pump photons with energy transfer from Pr<sup>3+</sup> to Yb<sup>3+</sup> in (Pr<sup>3+</sup>,Yb<sup>3+</sup>)-co-doped LiYF<sub>4</sub> [6] (i.e., the doping of Gd<sub>1-x</sub>Yb<sub>x</sub>F<sub>3</sub> with Pr<sup>3+</sup>) has been examined as a possible approach to overcoming this problem.

The crystal structures and phase transition temperatures of trifluorides change systematically with rare-earth (RE) atomic number (and therefore ionic radius [7]), as illustrated in Fig. 21.1. However, two groups of trifluoride compounds – Sm, Eu, Gd (with large ionic radii) and Er, Y, Tm, Yb, Lu (with small ionic radii) – have subsolidus phase transitions below the solidus line on the phase diagram. This prevents the growth of single-crystalline

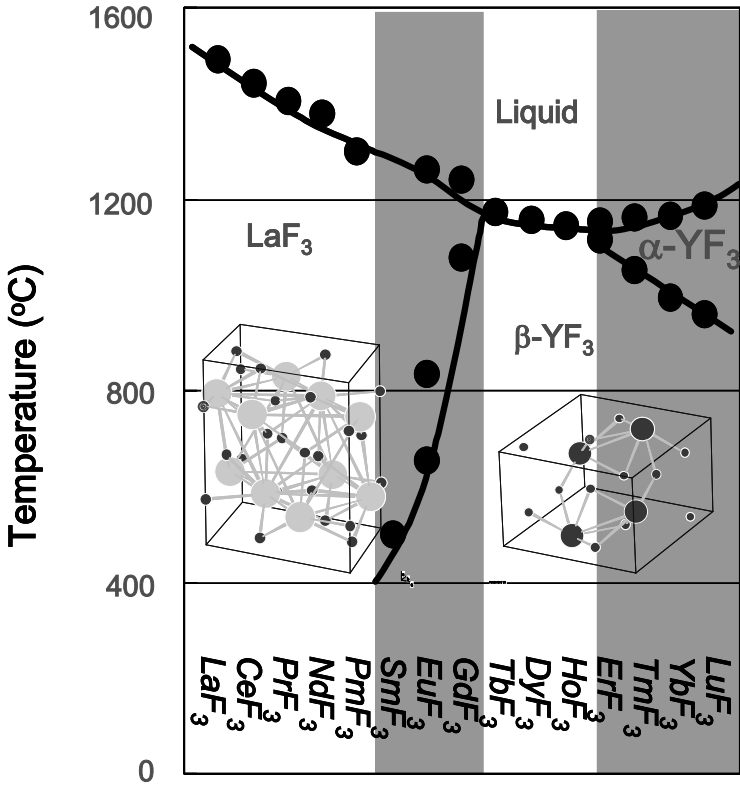


Fig. 21.1. Phase formation of rare-earth trifluorides according to [7]

substances of high optical quality. Due to this disadvantage, single crystals of SmF<sub>3</sub>, EuF<sub>3</sub>, GdF<sub>3</sub>, ErF<sub>3</sub>, TmF<sub>3</sub>, YbF<sub>3</sub>, and LuF<sub>3</sub> cannot be obtained from stoichiometric melts.

Using REAlO<sub>3</sub> perovskites as an analogy, the phase transition temperature depends on the type of RE in REAlO<sub>3</sub>, or the compositional ratio of RE to RE<sup>1</sup> (the solid solution ratio) in (RE,RE<sup>1</sup>)AlO<sub>3</sub>. If the phase transition temperature becomes higher than the melting temperature, the solid solution does not have any phase transitions between room temperature and the melting temperature. Such single crystals can be grown from the melt.

On the other hand, the structural stability can be considered based on the effect of the solid solution ratio. According to the semi-empirical model described in [8–10], the behavior of any oxide structure is characterized by the set of equilibrium cation sizes that can be determined for any crystallographic sublattice. The change of phase transition temperature mentioned above can be discussed in relation to this concept. To be exact, the structural stability increases if the solid solution ratio corresponds to the optimal ratio. In this case, more energy is required before the phase transition can occur. As

a result, the phase transition temperature increases. When the solid solution ratio is optimized, the stable phase does not have phase transition.

Following this idea, the growth of solid solution crystals containing a couple of cations with large (Sm, Eu, and Gd) and small (Er, Tm, Yb, and Lu) ionic radii was assumed to be possible due to the presence of a compositional range (field in the phase diagram) that is free from any subsolidus phase transitions. This is why the growth of disordered mixed crystals of Gd<sub>1-x</sub>Y<sub>x</sub>F<sub>3</sub> ( $x = 0.4-0.6$ ) containing optically inactive Y<sup>3+</sup> cations was examined [3, 4]. The approach was also extended to the design of novel rare-earth trifluorides that are free from any phase transitions. In particular, Gd<sub>1-x</sub>Yb<sub>x</sub>F<sub>3</sub> crystals were grown for the purpose of IR pumping up-conversion. These were obtained by simply replacing the Y<sup>3+</sup> cations in the Gd<sub>1-x</sub>Y<sub>x</sub>F<sub>3</sub> structure with Yb<sup>3+</sup>.

Recently, interest in the formation and behavior of Pr<sup>3+</sup> luminescence centers in materials with intermediate or high crystal field strength has also increased. Such materials can provide  $5d-4f$  radiative transitions with fast decay times that are shifted to high energy compared with Ce<sup>3+</sup> cations in the same crystal host. Considering the experimental data available for Ce-doped fluorides, the KY<sub>3</sub>F<sub>10</sub> host exhibits the lowest-energy Ce<sup>3+</sup> emission at about 350 nm [11]. This fact motivated the study of Pr-doped fluorides. Attempts were also made to examine the ability of the  $\mu$ -PD system to produce rod-shaped KY<sub>3</sub>F<sub>10</sub> crystals. The crystals were sufficiently large to be able to perform basic luminescent characterization and fast materials screening. The crystal growth of isomorphous derivatives of KY<sub>3</sub>F<sub>10</sub> produced by replacing Y<sup>3+</sup> with other RE cations (Lu) was also tested in order to check the possibility of increasing the density of the host crystal. KY<sub>3</sub>F<sub>10</sub> is a cubic crystal (space group Fm3m) with a lattice constant of  $a = 1.1543$  nm, and it melts congruently at a temperature of about 1000 °C.

## 21.2 (Gd,Y)F<sub>3</sub> Growth Details

Details on the  $\mu$ -PD growth of fluoride were reported in [5]. Starting materials were prepared from a stoichiometric mixture of 99.99% pure GdF<sub>3</sub>, YF<sub>3</sub>, CeF<sub>3</sub>, SrF<sub>2</sub>, BaF<sub>2</sub>, SrF<sub>2</sub>, or CaF<sub>2</sub> (in the case of doping with Ce, Sr, Ba, or Ca) powders. They were carefully mixed and placed into the carbon crucible. The crucible was surrounded by an external carbon heater that was inductively heated using a radiofrequency (RF) generator. The melting was performed at a temperature of about 1200 °C under a mixture of high-purity Ar and CF<sub>4</sub> gases. The process was carried out in a growth chamber (see Fig. 21.2 and Chap. 3 for references).

First of all, the chamber was evacuated to 10<sup>-3</sup> torr. Thereafter the crucible was heated to 500 °C in order to remove possible sources of contamination of the growth environment with oxygen (from moisture in the raw materials and the chamber surface). The system was then maintained at this



**Fig. 21.2.** View of  $\mu$ -PD apparatus with growth chamber designed for growth systems with aggressive  $\text{CF}_4$  environment

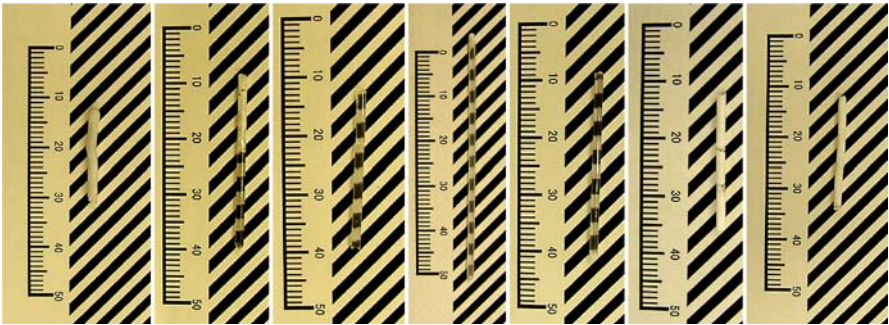


**Fig. 21.3.** View of the fibers produced from  $(\text{Gd}_{1-x}\text{Y}_x)\text{F}_3$  melts with  $x = 0.0, 0.2, 0.4, 0.5, 0.6, 0.8, 1.0$  (from left to right) The  $(\text{Gd}_{1-x}\text{Y}_x)\text{F}_3$  fibers with  $x = 0.2, 0.4, 0.5, 0.6$  had acceptable optical quality

temperature for about 1 h. During this baking procedure, the chamber was evacuated to  $10^{-4}$  torr. After the baking, the vacuum system was switched off and high-purity  $\text{CF}_4$  (99.999%) was let into the chamber.

W–Re alloy wire was used as a seed material to initiate solidification at the preliminary stage. Subsequent experiments were carried out using a  $(\text{Gd},\text{Y})\text{F}_3$  single-crystal seed. The range of pulling-down rates applied was 0.05–0.50 mm/min. A number of  $(\text{Gd}_{1-x}\text{Y}_x)\text{F}_3$  melts with  $x = 0.0, 0.2, 0.4, 0.5, 0.6, 0.8, 1.0$  were tested using the  $\mu$ -PD system in order to examine the

applicability of the strategy for optimizing the crystal composition described above. The fibers produced from these melts are illustrated in Fig. 21.3.

### 21.3 (Gd,Y)F<sub>3</sub> Characterization

Preliminary evaluation of the crystal quality was achieved through visual and microscopic observation (Fig. 21.3). Detailed analysis was based on the results of XRD characterization (Fig. 21.4), which demonstrated that (Gd<sub>1-x</sub>Y<sub>x</sub>)F<sub>3</sub> mixtures form continuous solid solutions from  $x = 0.0$  to 1.0 with  $\beta$ -YF<sub>3</sub> structure. Therefore, it was concluded that opaque solids formed for  $x = 0.0, 0.8,$  and 1.0 due to a phase transition between the  $\alpha$ -YF<sub>3</sub> and  $\beta$ -YF<sub>3</sub> phases.

Figure 21.5 illustrates the variations in the concentration of Y observed along the growth axes of (Gd<sub>1-x</sub>Y<sub>x</sub>)F<sub>3</sub> solid solutions. In the case of  $x \leq 0.4$ , the Y concentration increases when the solidification fraction increases. However, when  $x \geq 0.5$ , the Y concentration decreases as the solidification fraction increases. Similar behavior was observed in [9, 10] for the growth of garnet solid solutions.

The trend shown in Fig. 21.5 is in good agreement with the corresponding solid-solution phase diagram. However, this is not a typical  $\mu$ -PD growth system. In the general case of  $\mu$ -PD growth, the segregation coefficients are close to unity. However, the melt does not wet the crucible in nonwetting (Gd<sub>1-x</sub>Y<sub>x</sub>)F<sub>3</sub>/graphite system. Therefore, growth is performed using a cru-

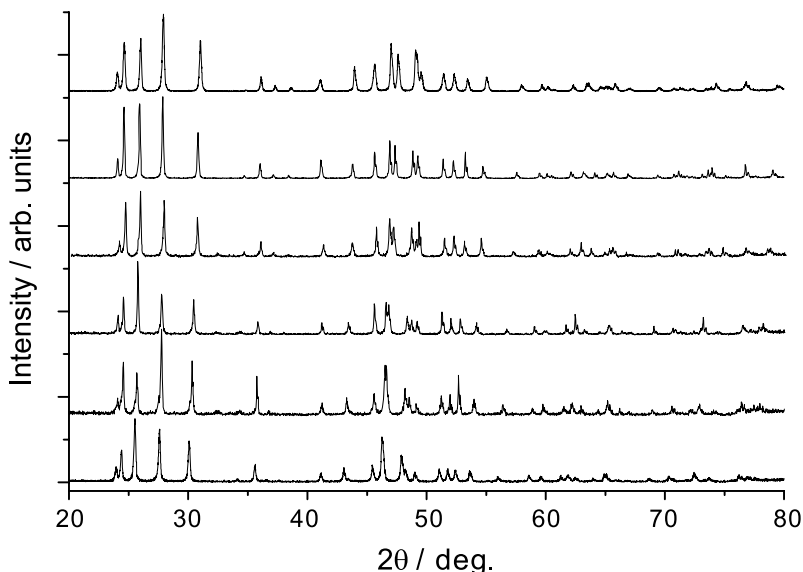


Fig. 21.4. Powder X-ray diffraction patterns of (Gd<sub>1-x</sub>Y<sub>x</sub>)F<sub>3</sub>

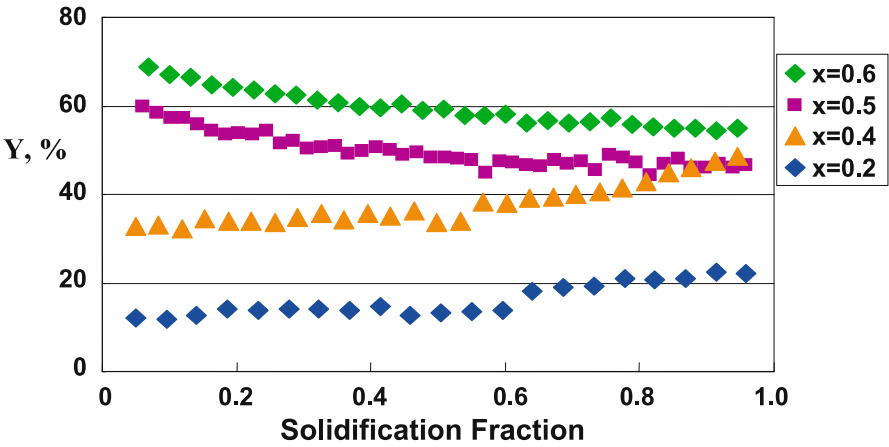


Fig. 21.5. Variation of Y concentration in  $(Gd_{1-x}Y_x)F_3$  solid solutions

cible with an opening of maximum diameter and minimum length. As a result, unidirectional melt feeding conditions are not established in the system.

The growth results described above demonstrated that structural design considerations are acceptable for  $(Gd_{1-x}Y_x)F_3$  host crystals. The ability of the crystal host to accept suitable luminescent centers through its doping was then examined. Luminescence from perturbed  $Ce^{3+}$  sites is possible when  $REF_3$  crystals are co-doped with alkaline-earth cations. Therefore, the growth of  $(Gd_{1-x}Y_x)F_3$  co-doped with Ce and Ba, Sr, or Ca was also performed. The growth results are illustrated in Fig. 21.6. Radioluminescence and photolu-

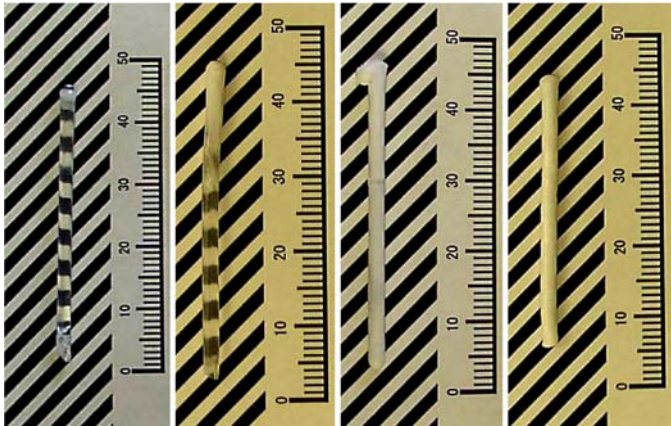
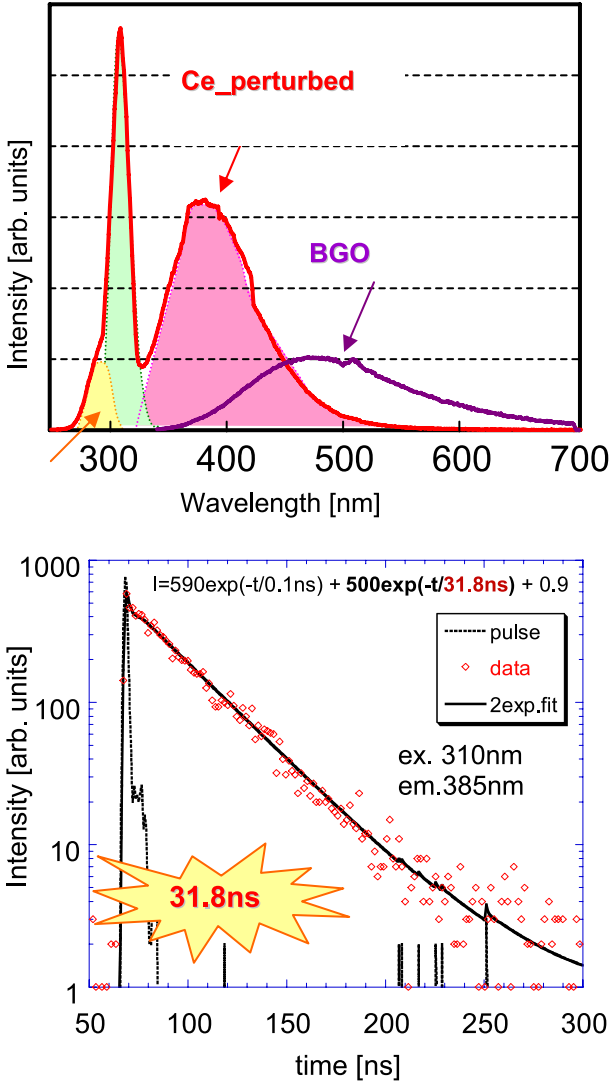


Fig. 21.6. Results of solidification of binary fluoride  $Ce:Sr:(Gd,Y)F_3$  melts by  $\mu$ -PD technique. The melt compositions were Ce 1%, Sr 0.1%,  $(Gd_{0.55}Y_{0.43})F_3$ , Ce 3%, Sr 3%,  $(Gd_{0.47}Y_{0.47})F_3$ , Ce 3%, Sr 0.2%,  $(Gd_{0.628}Y_{0.34})F_3$ , and Ce 3%, Sr 3%,  $(Gd_{0.70}Y_{0.24})F_3$  (from left to right)



**Fig. 21.7.** Radio luminescence emission excited by X-ray (*top*) and photo luminescence decay time (*bottom*) of Ce 1%, Sr 0.1% doped (Gd<sub>0.55</sub>Y<sub>0.43</sub>)F<sub>3</sub>  $\mu$ -PD fiber crystal

miniscence decay time data are presented in Fig. 21.7. Luminescence from perturbed Ce<sup>3+</sup> sites was observed in this system.

The doping of (Gd,Y)F<sub>3</sub> crystals with Ba is not very efficient because of the considerable difference between the cation radii of Ba<sup>2+</sup> and the rare-earth host cations. Doping with Ca is, however, much simpler due to the similar sizes of the corresponding host and guest cations. As a result, the

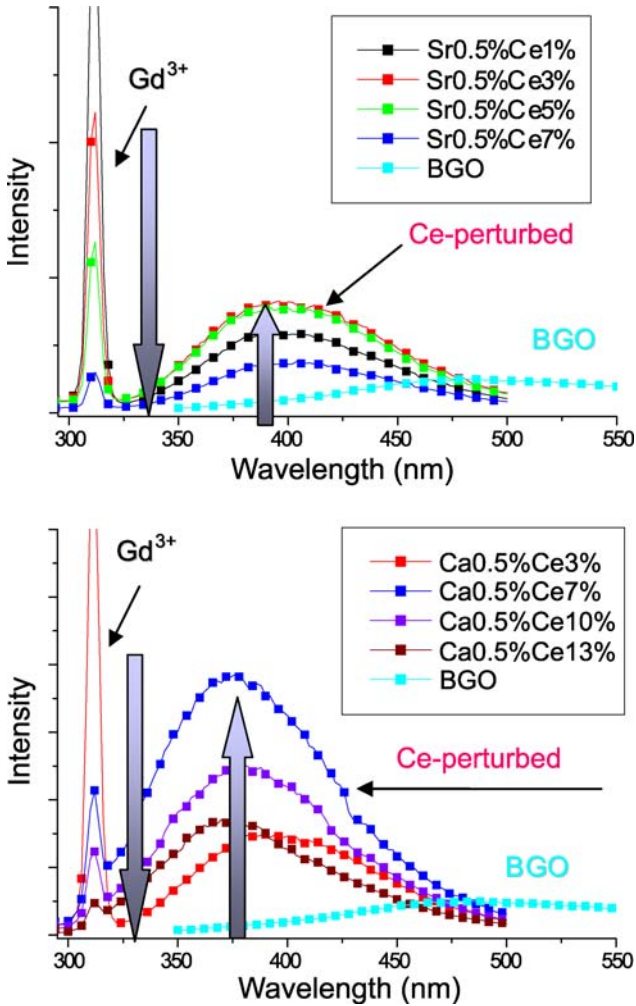


**Fig. 21.8.** Photoluminescence spectra (exc = 270 nm) of Sr, Ce: (Gd,Y)F<sub>3</sub> (*top*) and Ca, Ce: (Gd,Y)F<sub>3</sub> (*bottom*) crystals

highest luminescent intensity from perturbed Ce<sup>3+</sup> sites was observed in the Ce:Ca:(Gd,Y)F<sub>3</sub> crystals (Fig. 21.8). Doping with Ca<sup>2+</sup> yields the most efficient luminescent centers. However, this effect may arise due to simply the concentration of perturbed Ce<sup>3+</sup> sites.

### 21.4 (Gd,Yb)F<sub>3</sub> Growth Details

$\mu$ -PD growth was performed from a number of Gd<sub>1-x</sub>Yb<sub>x</sub>F<sub>3</sub> melts ( $x = 0.05, 0.1, 0.2, 0.3, 0.5$ ). The intended crystal diameter was about 2.0 mm

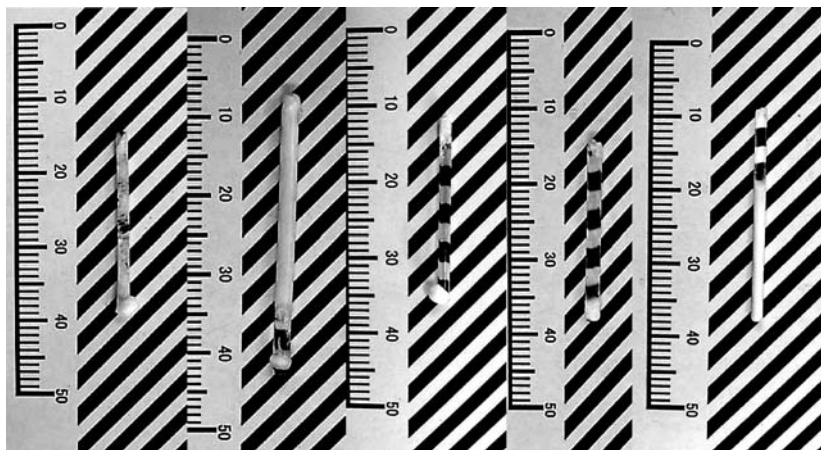


**Fig. 21.9.** View of  $\mu$ -PD crystals produced from  $\text{Gd}_{1-x}\text{Yb}_x\text{F}_3$  melts ( $x = 0.05, 0.1, 0.2, 0.3, 0.5$ , from left to right, scales in mm)

(Fig. 21.9). As expected, the average RE cationic radii gradually changed with the  $x$  value due to the formation of single-phase solid solutions. The  $\text{Gd}_{1-x}\text{Yb}_x\text{F}_3$  ( $x = 0.2$  and  $0.3$ ) fibers were colorless and transparent with thin opaque regions at both edges.  $\text{Gd}_{1-x}\text{Yb}_x\text{F}_3$  ( $x = 0.1$ ) crystals were colorless and transparent in their end regions.  $\text{Gd}_{1-x}\text{Yb}_x\text{F}_3$  ( $x = 0.5$ ) crystals were colorless and transparent in their initial growth regions.  $\text{Gd}_{1-x}\text{Yb}_x\text{F}_3$  ( $x = 0.05$ ) crystals were opaque.

## 21.5 (Gd,Yb)F<sub>3</sub> Characterization

The chemical compositions of the crystals grown were examined using two JEOL analyzers (a JXA-8600L and a JXA-8621MX). The axial distributions of  $\text{Yb}^{3+}$  cations in undoped  $\text{Gd}_{1-x}\text{Yb}_x\text{F}_3$  crystals were measured using an electron probe microanalyzer (EPMA). The results are shown in Fig. 21.10. Significant  $\text{Yb}^{3+}$  concentration gradients were observed in the transparent regions of the crystals ( $x = 0.12$ – $0.42$ ). An increase in  $\text{Yb}^{3+}$  content with increasing solidification fraction was detected in all of the crystals. The reason for the scatter in  $\text{Yb}^{3+}$  concentration in the opaque parts of the fibers was surface roughness caused by polycrystallization resulting from subsolidus phase transitions. The effective segregation coefficient ( $k_{\text{eff}}$ ) of  $\text{Yb}^{3+}$  in  $\text{Gd}_{1-x}\text{Yb}_x\text{F}_3$  was 0.575.

The compositions of undoped  $\text{Gd}_{1-x}\text{Yb}_x\text{F}_3$  solid-solution crystals changed continuously according to the solidus line. The opaque parts of the crystals corresponded well to solidified material that had passed through subsolidus phase transitions. Moreover, the melting temperatures of the  $\text{Gd}_{1-x}\text{Yb}_x\text{F}_3$  solid solutions decreased with increasing  $\text{Yb}^{3+}$  content because the effective

segregation coefficient ( $k_{\text{eff}}$ ) of  $\text{Yb}^{3+}$  was less than unity. Thus it was confirmed that the temperatures of the solidus and subsolidus phase transitions and the structures of the  $\text{GdF}_3$  and  $\text{YbF}_3$  end members are adequately described by Fig. 21.1. Therefore, it was proposed that the phase diagram for the  $\text{GdF}_3$ – $\text{YbF}_3$  system should be similar to that shown in Fig. 21.11.

Characterizations of crystalline phases and lattice parameter determinations were performed by X-ray powder diffraction (XRD) using a Rigaku

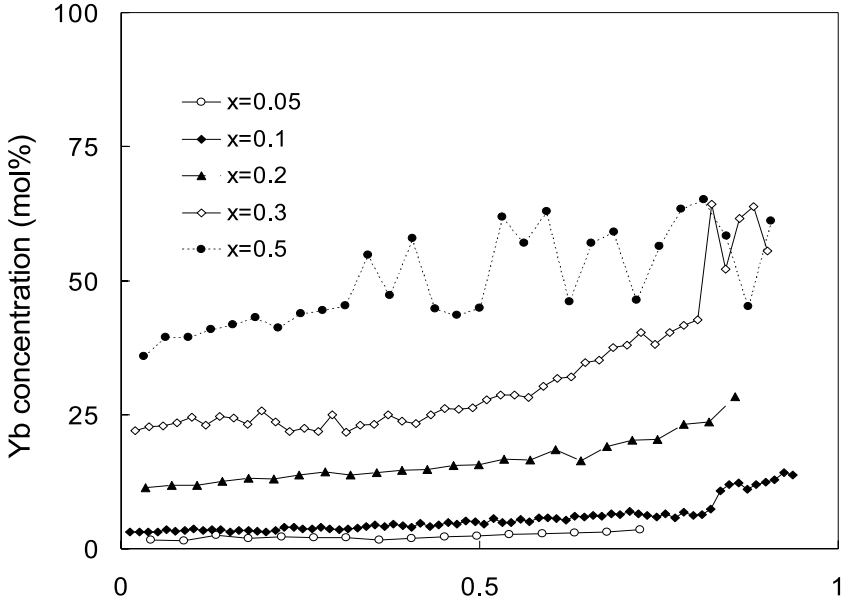


Fig. 21.10. Axial distribution of  $\text{Yb}^{3+}$  in  $\mu$ -PD crystals produced from  $\text{Gd}_{1-x}\text{Yb}_x\text{F}_3$  melts ( $x = 0.05, 0.1, 0.2, 0.3, 0.5$ ). See Fig. 21.9 for reference

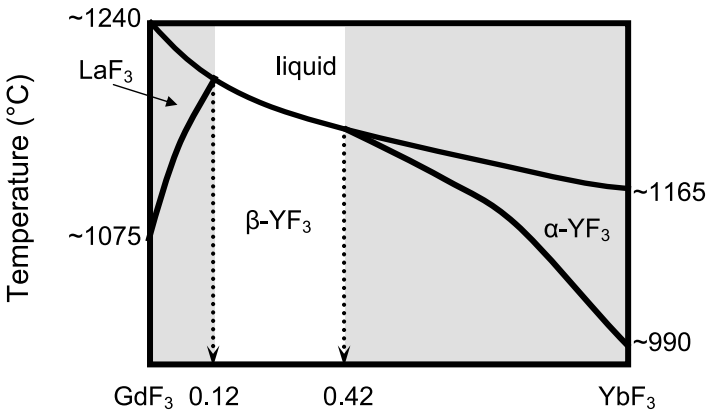
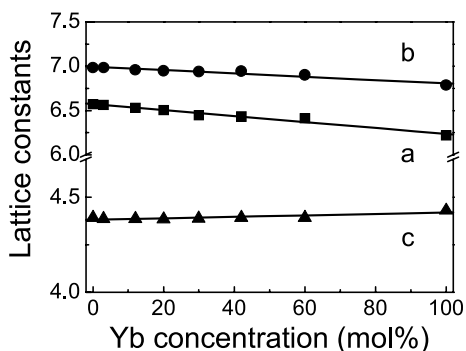


Fig. 21.11. Phase stability of  $(\text{Gd},\text{Yb})\text{F}_3$

**Table 21.1.** Properties of rare-earth trifluorides (*a*, *b*, and *c* are lattice parameters)

	Density (g/cm <sup>3</sup> )	Ionic radii (Å)	<i>a</i> (Å)	<i>b</i> (Å)	<i>c</i> (Å)
$\beta$ -GdF <sub>3</sub>	7.06(b)	1.11	6.568	6.982	4.392
TbF <sub>3</sub>	7.23(b)	1.09	6.508	6.949	4.387
DyF <sub>3</sub>	7.47	1.07	6.458	6.907	4.380
HoF <sub>3</sub>	7.64	1.05	6.404	6.875	4.378
$\beta$ -YbF <sub>3</sub>	8.17(b)	1.00	6.217	6.786	4.431
$\beta$ -LuF <sub>3</sub>	8.29(b)	0.99	6.150	6.762	4.468

**Fig. 21.12.** Variations of lattice parameters in Gd<sub>1-x</sub>Yb<sub>x</sub>F<sub>3</sub> solid solution crystals

RINT 2000 apparatus (air, room temperature, and  $2\theta = 20\text{--}55^\circ$ ). The X-ray source was CuK $\alpha$ , (40 kV, 40 mA). According to the XRD measurements, the Gd<sub>1-x</sub>Yb<sub>x</sub>F<sub>3</sub> crystals were single-phase materials formed between GdF<sub>3</sub> and YbF<sub>3</sub> end members. The calculated lattice parameters decrease for the *a* and *b* axes and increase for the *c* axis with increasing Yb<sup>3+</sup> concentration (Fig. 21.12), which is in good agreement with the concept of the average ionic radii. The calculated average ionic radii were comparable to those of TbF<sub>3</sub>, DyF<sub>3</sub>, and HoF<sub>3</sub>, which do not exhibit any phase transitions in the solid state. The cationic radii of the RE that form these compounds are intermediate between trifluorides with larger and smaller ionic radii (Table 21.1 and Fig. 21.1).

## 21.6 Pr-Doped (Gd,Yb)F<sub>3</sub> Growth

Crystals of GdF<sub>3</sub>–YbF<sub>3</sub> grown with the partial replacement of RE cations with Pr<sup>3+</sup> were pale green in color. An example of such a crystal is shown in Fig. 21.13. Neither visible inclusions nor cracks were observed in the crystals. They were transparent upon visual observation. The variation in Pr<sup>3+</sup> con-

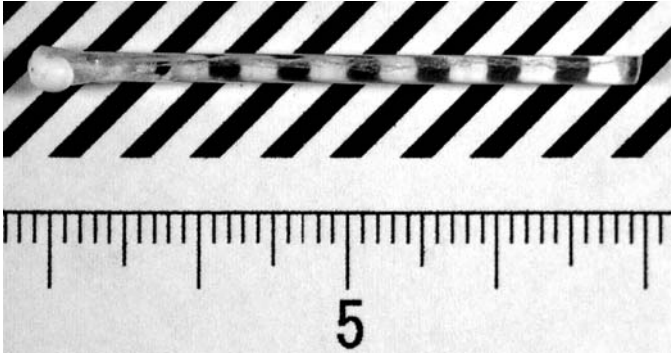


**Fig. 21.13.** View of 1%  $\text{Pr}^{3+}$ -doped  $\text{Gd}_{0.74}\text{Yb}_{0.25}\text{F}_3$   $\mu$ -PD crystal (Scale in mm)

centration along the growth axis of a 1%  $\text{Pr}^{3+}$ -doped  $\text{Gd}_{0.74}\text{Yb}_{0.25}\text{F}_3$  single crystal was not significant, and the  $\text{Pr}^{3+}$  concentration was  $\sim 1\%$  along the whole length of the material (Fig. 21.14).

Crystals of mixed  $\text{GdF}_3$ - $\text{YbF}_3$  binary fluorides further doped by  $\text{CeF}_3$  and  $\text{MeF}_2$  ( $\text{Me} = \text{Mg}, \text{Ca}, \text{Sr}, \text{Ba}$ ) were also grown by the  $\mu$ -PD method under a protective atmosphere. The starting materials were prepared from a stoichiometric mixture of 99.99% pure  $\text{CeF}_3$ ,  $\text{YF}_3$ ,  $\text{GdF}_3$ , and  $\text{MeF}_2$  ( $\text{Me} = \text{Mg}, \text{Ca}, \text{Sr}, \text{Ba}$ ) powders. The growth procedure was performed using carbon crucibles surrounded by refractory carbon heated inductively with a RF generator in a high-purity  $\text{Ar} + \text{CF}_4$  atmosphere. The crucible was heated to a melting temperature of about  $1250^\circ\text{C}$ . A  $\text{Gd}_{0.5}\text{Y}_{0.5}\text{F}_3$  single crystal was used as the seed to trigger growth. A typical growth rate was  $\sim 0.16$  mm/min. Luminescence of the  $\text{Pr}^{3+}$ -doped  $\text{Gd}_{0.75}\text{Yb}_{0.25}\text{F}_3$   $\mu$ -PD crystals was observed after infrared ytterbium excitation at room temperature, as shown in Fig. 21.15.

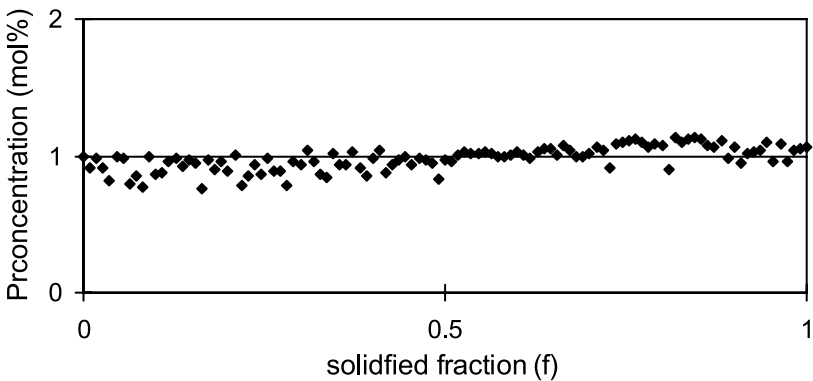
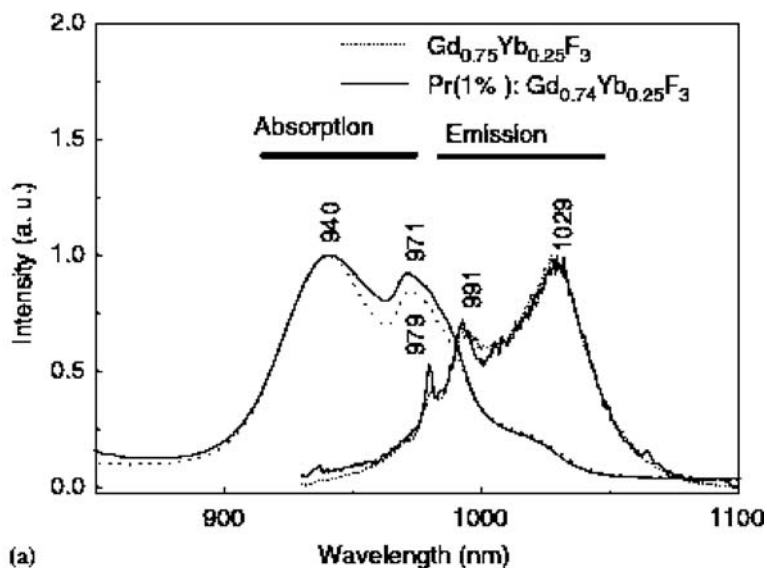
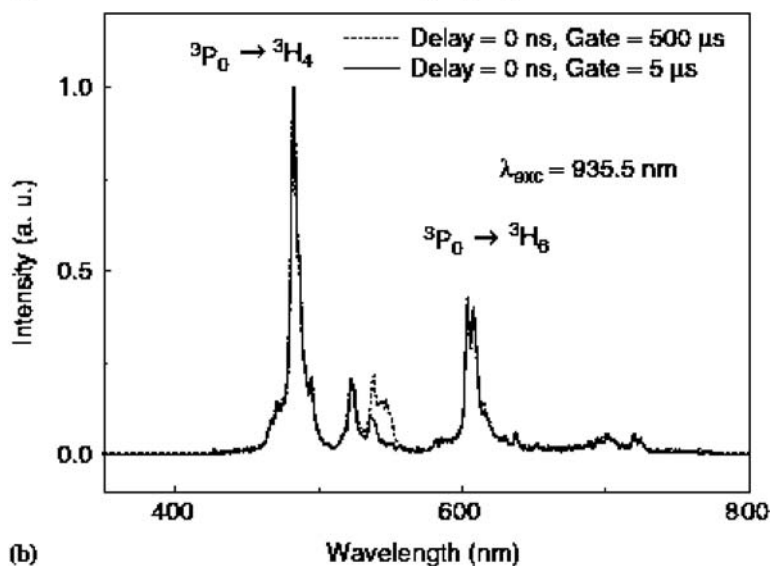


**Fig. 21.14.** Axial distribution of  $\text{Pr}^{3+}$  in  $\mu$ -PD crystal produced from 1%  $\text{Pr}^{3+}$ -doped  $\text{Gd}_{0.74}\text{Yb}_{0.25}\text{F}_3$  melt



(a)



(b)

**Fig. 21.15.** Absorption and infrared emission spectra of undoped and Pr<sup>3+</sup>-doped Gd<sub>0.75</sub>Yb<sub>0.25</sub>F<sub>3</sub> under IR excitation, of which spectra are from Yb<sup>3+</sup> (*above*) and room-temperature visible emission of Pr<sup>3+</sup>-doped Gd<sub>0.75</sub>Yb<sub>0.25</sub>F<sub>3</sub> under infrared ytterbium excitation (*below*)

Other rare-earth trifluoride rod-like crystals, namely (Pr,Ce)F<sub>3</sub>, with typical dimensions of  $\varnothing 2 \times 40$  mm were also produced using the  $\mu$ -PD technique and the above procedure. The crystals were normally transparent and free of cracks. Second-phase inclusions were not detected.

## 21.7 KY<sub>3</sub>F<sub>10</sub> Growth Details

KY<sub>3</sub>F<sub>10</sub>-type crystals were grown from starting (stoichiometric) mixtures produced from 4N powders of KF, YF<sub>3</sub>, and PrF<sub>3</sub>. Nominally, Y<sup>3+</sup> cations were replaced with Pr<sup>3+</sup> according to the formula K(Y<sub>1-x</sub>Pr<sub>x</sub>)<sub>3</sub>F<sub>10</sub>. Crystal growth was carried out using carbon crucibles under an Ar + CF<sub>4</sub> atmosphere. Platinum wire was initially used instead of a crystal seed, but subsequent growths were carried out using a KY<sub>3</sub>F<sub>10</sub> seed crystal obtained in the previous run. The growth rate was 0.05–0.50 mm/min. The process (i.e., the crystal diameter) was controlled by visually monitoring the image of the growth interface (see Fig. 21.16). Images of the crystals and results from their XRD characterization are illustrated in Figs. 21.17 and 21.18, respectively.

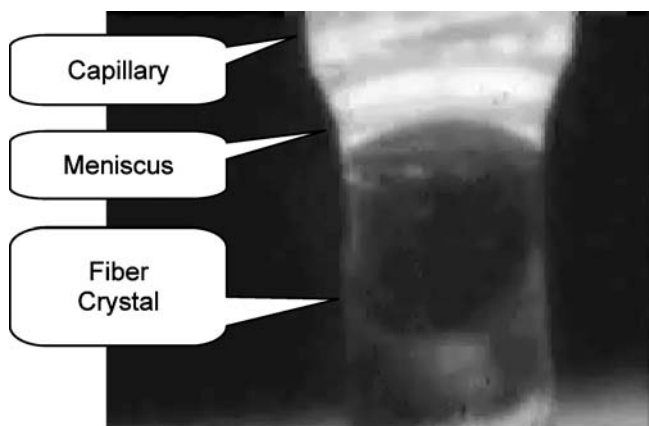


**Fig. 21.16.** Typical view of meniscus zone observed during  $\mu$ -PD growth of KY<sub>3</sub>F<sub>10</sub> along  $\langle 111 \rangle$  axis. Pulling-down rate was 0.1–1 mm/min

## 21.8 KY<sub>3</sub>F<sub>10</sub> Characterization

The segregation coefficient of Pr<sup>3+</sup> in the KY<sub>3</sub>F<sub>10</sub> host crystals was considerably less than unity. This is illustrated in Fig. 21.20. This phenomenon is commonly observed in practical doped crystal growth when the sizes of the host and guest cations are very different (Pr<sup>3+</sup> is considerably larger than Y<sup>3+</sup>). Therefore, the chemical homogeneity of Pr<sup>3+</sup>-doped KY<sub>3</sub>F<sub>10</sub> crystals produced without feeding was low.

A broad absorption peak centered at about 208 nm can be seen in Fig. 21.21; the low-energy side of this peak extends to 225 nm. The small absorption peak at  $\sim 295$  nm can be related to Ce<sup>3+</sup> centers present as accidental impurities, because it matches the excitation spectrum of Ce<sup>3+</sup> emission, which peaks at around 350 nm in the KYF host. The Ce may have been an impurity in the raw PrF<sub>3</sub> material. However, while its presence was ob-

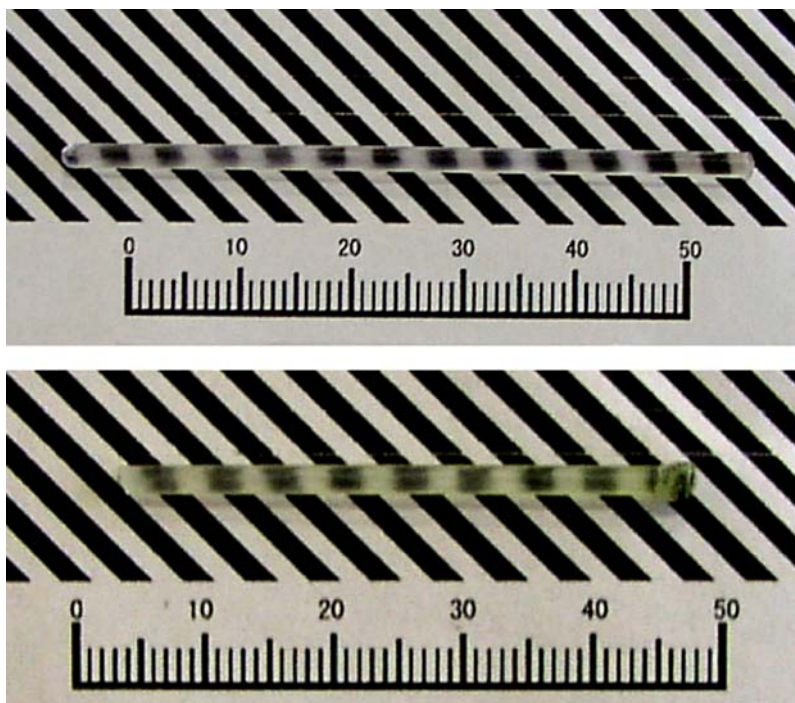


Fig. 21.17.  $K(Y_{0.99}Pr_{0.01})_3F_{10}$  (above) and  $K(Y_{0.97}Pr_{0.03})_3F_{10}$  (below)  $\mu$ -PD crystals (Scales in mm)

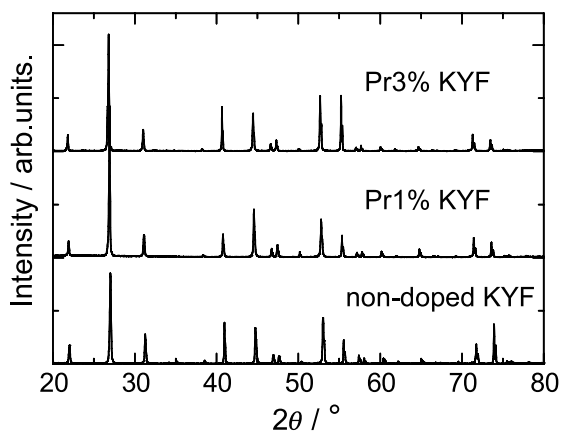
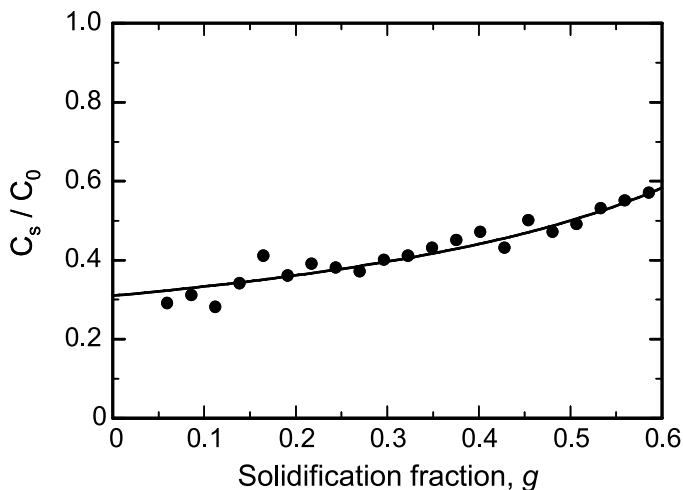


Fig. 21.18. Variation of XRD data with level of Pr-doping of  $KY_3F_{10}$   $\mu$ -PD crystals



**Fig. 21.20.** Distribution of  $\text{Pr}^{3+}$  along growth axis of  $\text{KY}_3\text{F}_{10}$   $\mu$ -PD crystals

served in the absorption spectrum, it could not be detected by composition analysis using EPMA. Therefore, the quantity of Ce was estimated to be less than a few ppm.

A band related to Ce occurs in the emission spectrum shown in Fig. 21.21 too. Taking into account the separation in energy between the positions of the  $\text{Ce}^{3+}$  and  $\text{Pr}^{3+}$  ground states ( $11\,000\text{--}13\,000\text{ cm}^{-1}$ ), and the conclusion that the  $5d$  states of both ions are located at about the same energy [12], the 208 nm absorption peak in Fig. 21.21 can be ascribed to the lowest  $4f\text{--}5d$  transition of  $\text{Pr}^{3+}$ , even if the separation in energy in this case is about  $14\,000\text{ cm}^{-1}$ , i.e., somewhat above the upper limit mentioned before. The broad emission spectrum with peaks at around 241 nm and 258 nm is well matched to the  $5d\text{--}4f$  emission of  $\text{Pr}^{3+}$ . The difference in energy between the subpeaks closely matches the difference between the two lowest  ${}^3\text{H}_4$  and  ${}^3\text{H}_5$   $4f$  levels of  $\text{Pr}^{3+}$ , and the precise final states within the  ${}^3\text{H}_x$  multiplet can thus be assigned as shown in Fig. 21.21. The related excitation spectrum (taken at  $\text{em.} = 260\text{ nm}$ ) occurs within the low-energy region of the absorption spectrum described above, and the position of its peak actually matches the energetic separation criterion mentioned above more closely. The disagreement between the absorption and excitation spectra in Fig. 21.21 cannot be explained satisfactorily at present. Pr has two valence states:  $\text{Pr}^{3+}$  and  $\text{Pr}^{4+}$ . In this study, traces of  $\text{Pr}^{4+}$  were not detected. Thus, an additional study of the  $\text{Pr}^{3+}/\text{Pr}^{4+}$  ratio is required to understand the conversion efficiency of  $\text{Pr}^{3+}$   $5d\text{--}4f$  luminescence. Figure 21.22 shows the fast luminescence decay of the  $5d\text{--}4f$  emission of  $\text{Pr}^{3+}$  center in  $\text{KY}_3\text{F}_{10}$  host, which lends support to the idea that the luminescence comes from  $5d\text{--}4f$  transitions. A single exponential curve fit (shown by the solid line in Fig. 21.21) yields a decay time of about 24 ns, which is close to the value expected for this kind of radiative transition.

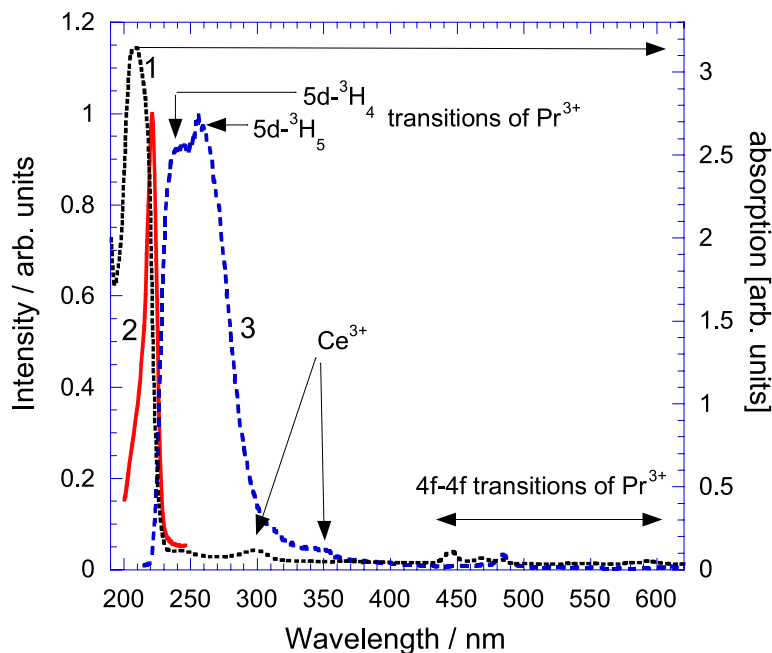


**Fig. 21.21.** Absorption (1), excitation (em. = 210 nm) (2), and emission (ex. = 210 nm) (3) spectra of Pr 1%: KY<sub>3</sub>F<sub>10</sub> at room temperature

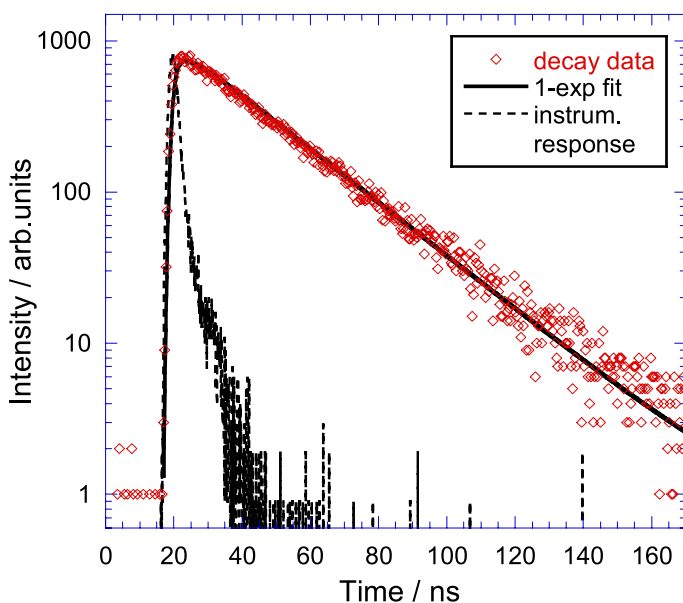


**Fig. 21.22.** Normalized decay curve of the 240 nm emission (exc = 218 nm) Pr 1%: KY<sub>3</sub>F<sub>10</sub>. Solid line is the convolution of the instrumental response to the excitation pulse (also in the figure) with the single exponential function with the decay time of 24 ns

## 21.9 K(Y,Lu)<sub>3</sub>F<sub>10</sub> Solid Solutions

K(Y,Lu)<sub>3</sub>F<sub>10</sub> solid-solution crystals with different levels of substitution of Y<sup>3+</sup> with Lu<sup>3+</sup> were also grown, in a procedure similar to that described in previous sections. The growth conditions of both undoped and 1% Pr-doped K(Y,Lu)<sub>3</sub>F<sub>10</sub> crystals were examined. The crystals had reasonable optical quality, as shown in Fig. 21.23.

The crystals produced from K(Y,Lu)<sub>3</sub>F<sub>10</sub> melts where 0–40% of the Y in the crystals was replaced with Lu were single-phase materials according to Fig. 21.24. The structure of these  $\mu$ -PD crystals was similar to that of the undoped KY<sub>3</sub>F<sub>10</sub> reported previously, and second-phase inclusions were not detected.

The segregation coefficient of Pr<sup>3+</sup> in K(Y,Lu)<sub>3</sub>F<sub>10</sub> was considerably less than unity, similar to that of the KY<sub>3</sub>F<sub>10</sub> end member (see previous section). However, the segregations of both host RE cations (Y<sup>3+</sup>

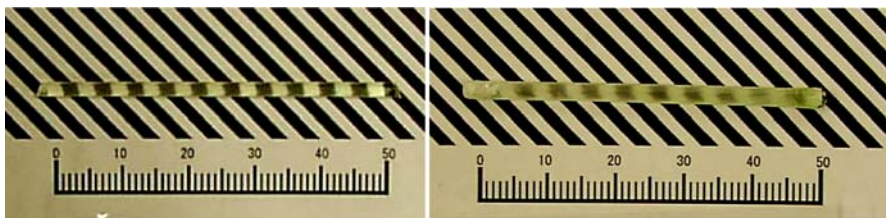


Fig. 21.23. K(Y<sub>0.79</sub>Lu<sub>0.20</sub>Pr<sub>0.01</sub>)<sub>3</sub>F<sub>10</sub> (left) and K(Y<sub>0.59</sub>Lu<sub>0.40</sub>Pr<sub>0.01</sub>)<sub>3</sub>F<sub>10</sub> (right)  $\mu$ -PD crystals (Scales are in mm)

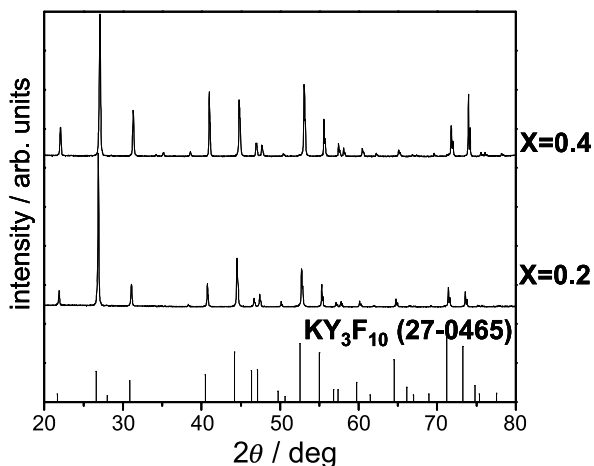
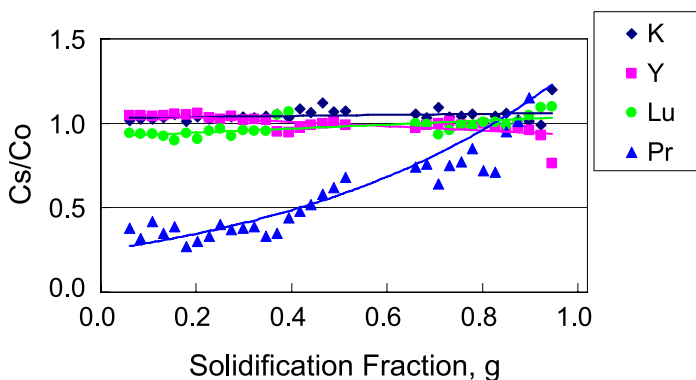
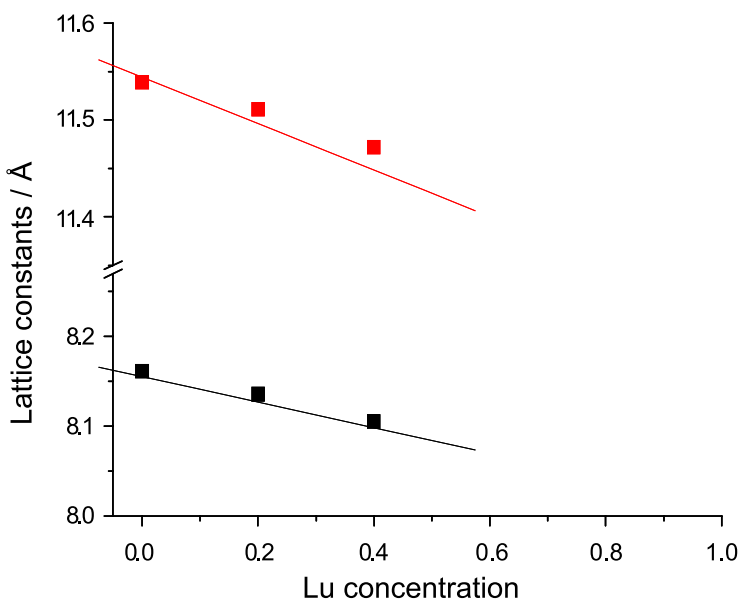


Fig. 21.24. X-ray diffraction data for 1% Pr-doped  $\mu$ -PD crystals: K(Y<sub>0.79</sub>Lu<sub>0.20</sub>Pr<sub>0.01</sub>)<sub>3</sub>F<sub>10</sub> (top), K(Y<sub>0.59</sub>Lu<sub>0.20</sub>Pr<sub>0.01</sub>)<sub>3</sub>F<sub>10</sub> (middle), and reference data for KY<sub>3</sub>F<sub>10</sub> end member

and Lu<sup>3+</sup>) between the liquid and solid phases were very similar, as illustrated in Fig. 21.25. The cation K<sup>+</sup> was distributed uniformly along the growth axis because the melt did not contain any particles that could be considered to be appropriate competitors (both chemically and dimensionally) to K<sup>+</sup> at its specific crystallographic sites in the structure of KY<sub>3</sub>F<sub>10</sub>.



**Fig. 21.25.** Axial cation distribution in  $\mu$ -PD fiber crystal produced from  $K(Y_{0.59}Lu_{0.40}Pr_{0.01})_3F_{10}$  melt



**Fig. 21.26.** Evolution of lattice constant of  $Pr1\%:K(Y_{1-x}Lu_x)_3F_{10}$  as a function of Lu concentration

It is evident that substitution of relatively large  $Y^{3+}$  cations with smaller  $Lu^{3+}$  cations resulted in the continuous decrease in lattice constants expected from applying Vegard's law. This tendency was observed experimentally, as seen in Fig. 21.26.

## 21.10 Summary

The growth, appearance, and spectroscopic properties of fluoride-based solid-solution crystals were examined and discussed in this chapter. While the ability of  $\mu$ -PD to enable exceptionally fast and cost-effective examinations of melt compositions prior to the growth of bulk oxide crystals was demonstrated many years ago, the results presented here illustrate that this express growth, together with the strategy of rapidly testing basic crystal parameters (phase and chemical composition, lattice parameters, segregation, homogeneity, etc.), is also applicable to non-oxide materials.

Needless to say, these miniature crystals can also be used for rapid preliminary examinations of the physical properties (including spectroscopic ones) of such crystals. These results allow an informed final decision to be made about whether the material has the potential to be used in actual devices. Corresponding characterizations of the crystals reported here were also performed, and for those readers who are interested in learning more about these tests, a number of references [5, 12–15] are recommended.

## References

1. T. Fukuda, P. Rudolph, S. Uda, (eds.), *Fiber Crystal Growth from the Melt* (Springer, Berlin, 2004)
2. V.I. Chani, A. Yoshikawa, Y. Kuwano, K. Inaba, K. Omote, T. Fukuda, *Mater. Res. Bull.*, **35**(10), 1615 (2000)
3. A. Yoshikawa, K. Kamada, T. Satonaga, K. Aoki, M. Nikl, T. Fukuda, *65th Autumn Meeting of the Japanese Society of Applied Physics (JSAP)*, Sendai, Japan (2004)
4. A. Yoshikawa, K. Kamada, K. Aoki, T. Satonaga, T. Fukuda, *Proc. 49th Symp. on Synthetic Crystals*, Tsukuba, Japan (2004)
5. A. Yoshikawa, T. Satonaga, K. Kamada, H. Sato, M. Nikl, N. Solovieva, T. Fukuda, *J. Cryst. Growth*, **270**, 427 (2004)
6. T. Sandrock, E. Heumann, G. Huber, B.T. Chai, in *OSA Proc. on Advanced Solid State Lasers*, vol. 1, ed. by S.A. Payne, C. Pollack (Opt. Soc. Am., Washington, DC, 1996), p. 550
7. P.P. Fedorov, B.P. Sobolev, *Crystallogr. Rep.*, **40**(2), 284 (1995)
8. V.I. Chani, Y.M. Yu, K. Shimamura, T. Fukuda, *Mater. Sci. Eng. R.*, **20**(6), 281 (1997)
9. V.I. Chani, A. Yoshikawa, H. Machida, T. Fukuda, *Mater. Sci. Eng. B.*, **75**(1), 53 (2000)

10. V.I. Chani, A. Yoshikawa, H. Machida, T. Fukuda, *J. Cryst. Growth*, **212**(3–4), 469 (2000)
11. R.Yu. Abdulsabirov, M.A. Dubinski, B.N.Kazakov, N.I. Silkin, Sh.I. Jagulin, *Kristallografia*, **32**, 951 (1987)
12. K.J. Kim, A. Jouini, A. Yoshikawa, R. Simura, G. Boulon, T. Fukuda, *J. Cryst. Growth*, in press
13. R. Simura, A. Jouini, K. Kamada, A. Yoshikawa, K. Aoki, Y. Guyot, G. Boulon, T. Fukuda, *J. Cryst. Growth*, **295**, 102 (2006)
14. R. Simura, A. Jouini, K. Kamada, A. Yoshikawa, K. Aoki, Y. Guyot, G. Boulon, T. Fukuda, *J. Cryst. Growth*, **291**, 309 (2006)
15. A. Yoshikawa, K. Kamada, M. Nikl, K. Aoki, H. Sato, J. Pejchal, T. Fukuda, *J. Cryst. Growth*, **285**, 445 (2005)

# 22 Shaped Fluorides

Tomohiko Satonaga

**Abstract.** The growth of shaped fluoride crystals ( $\text{PrF}_3$ ,  $\text{CaF}_2$ ,  $\text{BaF}_2$ , etc.) by the micro-pulling-down method is reviewed. Plates of size  $1 \times 10$  mm and rods with (cylindrical and rectangular/square) cross-sections of up to 4 mm were grown. The wetting properties of a number of fluorides with respect to the most common crucible materials (platinum, iridium, and carbon) as well as their temperature dependences are presented. The wetting measurements obtained were used to optimize the behavior of various melt–crucible combinations in actual growth processes.

## 22.1 Introduction

Recently, the Czochralski (CZ) growth of various single-crystalline fluoride materials has been the subject of intense study [1–3]. The growth of these crystals became possible after the development of precise atmosphere control systems and procedures, which were needed to avoid contamination of the crystals with oxygen from the starting materials, the gaseous environment, and parts of the growth system. On the other hand, a number of novel oxide single crystals have also been produced by melt growth via the micro-pulling-down ( $\mu$ -PD) method. The applicability of this technique to rapid material growth and examination and to shaped crystal growth was also tested [4]. It was assumed that both of these factors could be combined in order to obtain a general expansion in fluoride crystal growth technology and its transfer from laboratory conditions to industrial processes. As a result, the application of  $\mu$ -PD technology to the growth of shaped fluoride-type crystals was proposed [5–7]. The practical realization of this idea is overviewed in this chapter.

Fluoride single crystals have wide band gaps and demonstrate superior transmission over a wide range of wavelengths, from the VUV to the infrared. These materials are under systematic investigation because of their potential applications in various fields, including optical lithography in the short wavelength region, in solid-state UV lasers, in eye-safe lasers for environmental sensing, in scintillation detectors, and in medical applications.

The growth of shaped fluoride crystals (both cylindrical and rectangular rods as well as plates) is introduced below. The main goal of shaped crystal growth is to develop time- and cost-saving shape-ready technology.  $\text{PrF}_3$  crystal is considered here to be the main target and model material. Ce-doped  $\text{PrF}_3$  and other rare-earth fluoride crystals are known to be partic-

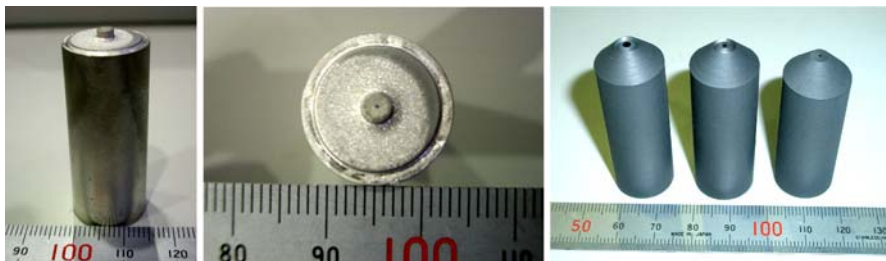
ularly promising materials for scintillating applications because they possess a number of attractive properties, such as fast luminescence due to  $Ce^{3+} 4f-5d$  transitions [7]. The growth of other fluorides ( $CaF_2$ ,  $BaF_2$ , etc.) is also discussed.

## 22.2 Growth Atmosphere and Crucibles

The crystal growth was performed in a sealed vacuum chamber using crucibles similar to those shown in Fig. 22.1. More details on the apparatus used are available in other sections that describe fluoride crystal growth. The basic growth routine used was very similar to that practiced for the  $\mu$ -PD growth of oxide crystals. However, the environment control procedure was more complicated and time-consuming. Vacuum treatment was performed prior to growth. The growth chamber was first evacuated to  $10^{-5}$  Torr by rotary and diffusion pumps. At this stage, traces of water and oxygen from the growth chamber and starting materials were effectively removed. Thereafter, high-purity Ar gas (99.9999%) was progressively introduced into the growth chamber. As a next step, the power supplied to the crucible was increased and then the starting materials were melted. The chamber was modified so that there was a  $CaF_2$  window in the system that could be used to observe of the meniscus region, the solid/liquid interface, and the crystal visually using a charge-coupled device (CCD) camera and monitor.

Carbon, platinum and iridium were used as crucible materials. The configurations of some of the crucibles are illustrated in Fig. 22.1. A general comparison of these crucible materials is provided in Table 22.1. Considering the growth system applied in the processes described here, the crucibles were surrounded by refractory carbon that was inductively heated using a radiofrequency (RF) generator. Details of a prototype of this apparatus are available in Chap. 3.

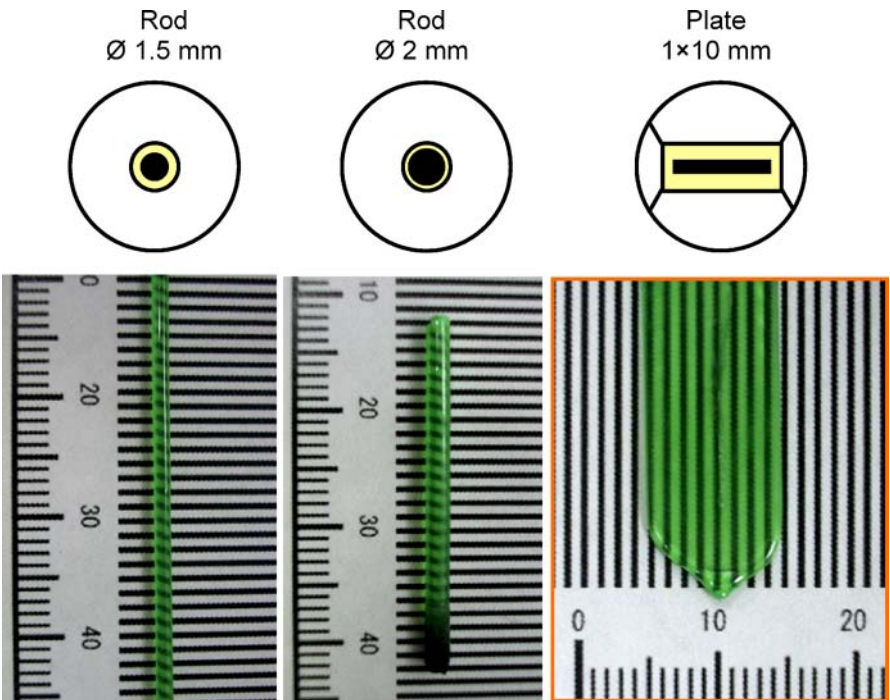
Different modifications of the crucibles were examined in terms of the shape of the die. Some examples of die configurations are illustrated in Fig. 22.2, together with the crystals produced from such crucibles. It is gener-



**Fig. 22.1.** Side and bottom views of platinum (*left* and *middle*) and carbon (*right*) crucibles used in  $\mu$ -PD growth of fluoride crystals

**Table 22.1.** Comparison of carbon (C), platinum (Pt), and iridium (Ir) when used as crucible materials for the  $\mu$ -PD growth of fluoride crystals

	Application temperature	Wetting	Crystal $\varnothing$ , mm	Advantages	Disadvantages
C	Suitable for any fluorides	Very low	< 2	Cheap (i) and relatively simple fabrication (ii)	Carbon inclusions on the surface and end parts of the crystals (i) and small crystal diameter (ii)
Pt	< 1450 °C	Low, but acceptable	No limit	Simple control of crystal shape (i) and low contamination from crucible (ii)	Expensive and time-consuming production (i) and time-consuming crucible cleaning (ii)
Ir	Suitable for any fluorides	Same	Same	Same	Same

**Fig. 22.2.** Examples of the shapes of the dies made on the bottom of carbon crucibles used for  $\mu$ -PD growth of  $\text{PrF}_3$  crystals (*above*) and view of the crystals produced from corresponding crucibles (*below*)

ally assumed that the shape (cross-section) of the crystal replicates the shape of the (edges of the) die when appropriate growth parameters are applied. However, it is not possible to replicate the die shape identically because of number of factors that affect the behavior of the meniscus. The wettability of the melt is one of these. Therefore, the wetting properties of various melts with respect to various crucible materials are considered in detail in the following section.

## 22.3 Wetting and $\text{PrF}_3$ Growth

The starting material was commercially available high-purity ( $> 99.99\%$ )  $\text{PrF}_3$  powder. Identical mixtures were used for both wetting angle measurements and actual crystal growth. The wetting angle measurements were performed using images of the melt drop sitting on a horizontal plate made from the material used for crucible fabrication. Images produced at the melting point of  $\text{PrF}_3$  ( $\pm 10^\circ\text{C}$ ) can be seen in Fig. 22.3.

The behavior of the melt and its wetting performance can be improved by changing the temperature of the system. In some cases, this improves the ability of the liquid substance to spread along the die surface, which can improve the behavior of the meniscus and the growth system as a whole,

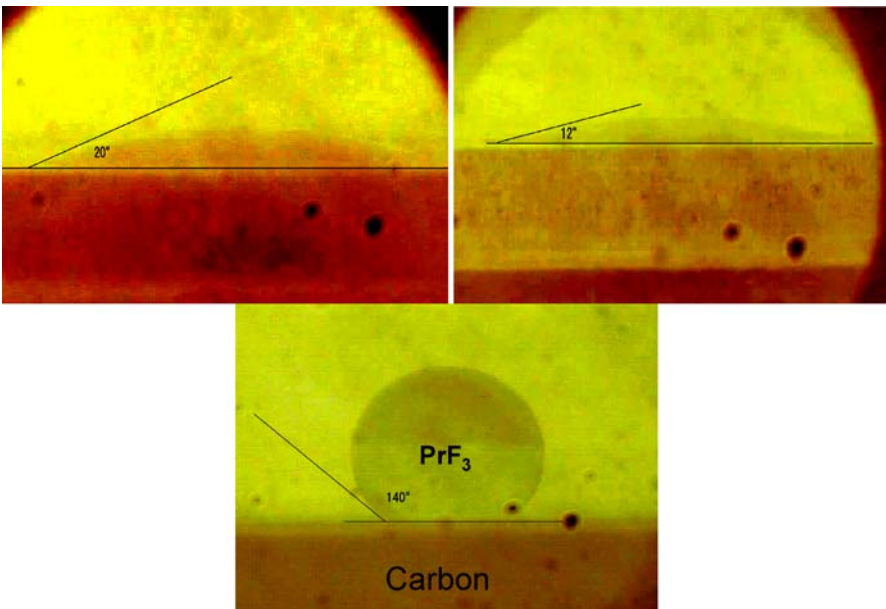


**Fig. 22.3.** Appearance of  $\text{PrF}_3$  drop sited on platinum (*left*), iridium (*right*), and carbon (*bottom*) plates. The measured wetting angles are  $20^\circ$ ,  $12^\circ$ , and  $140^\circ$ , respectively

making it possible to bring the crystal shape close to the shape of the die. Therefore, temperature dependence of the wetting angle was also studied for  $\text{PrF}_3$  melt on various crucible materials by simply varying the temperature of the system and recording the images obtained by a CCD cam-

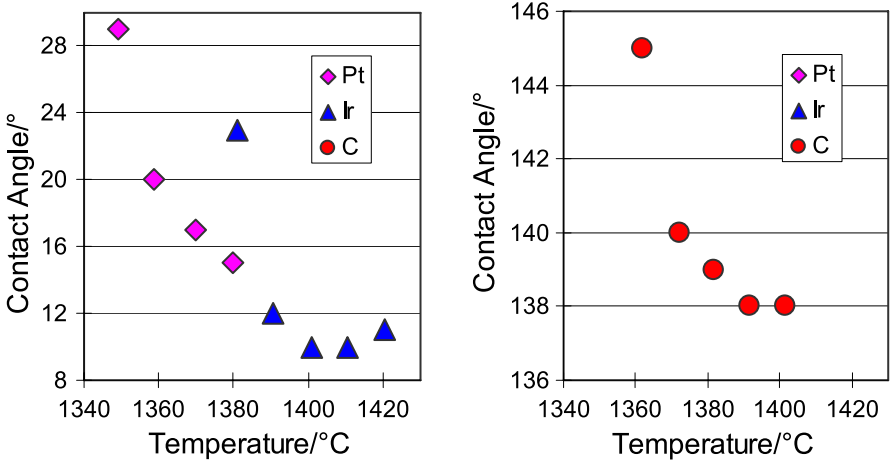
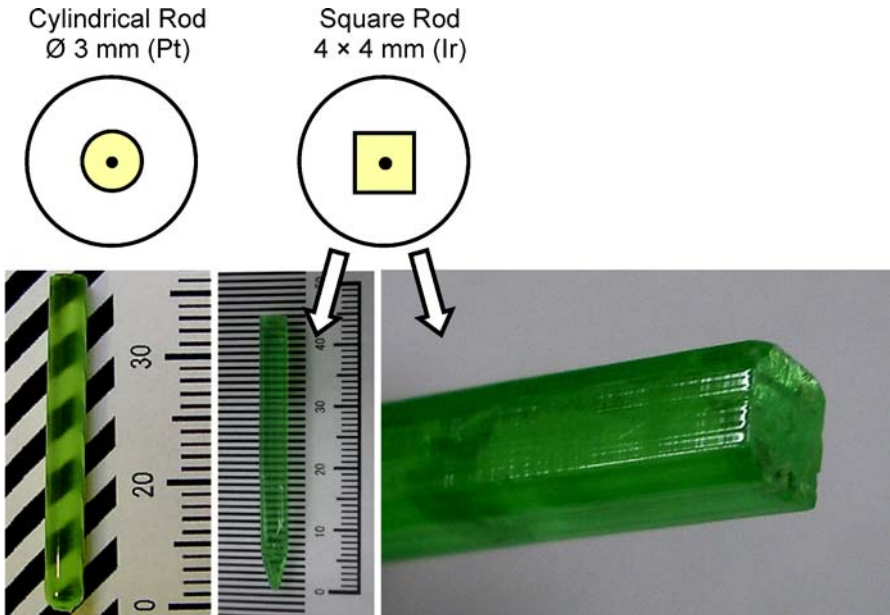


**Fig. 22.4.** Contact angle vs. temperature measured for  $\text{PrF}_3$  melt sited on metallic (Pt or Ir) plate (*left*) and on carbon one (*right*)



era. The results for the wetting properties of  $\text{PrF}_3$  are summarized in Fig. 22.4.

When carbon crucibles were used, relatively large (bulk) rod crystals of  $\text{PrF}_3$  could not be grown because of the low wettability of the melt. The maximal dimensions of the crystals produced were limited by the dimensions (inner diameter) of the opening (capillary channel) made in the die part of the crucible. Similar results were observed for the  $\mu$ -PD growth of oxide crystals, based on a comparison of the behavior of wettable and nonwettable melts performed in [8]. On the other hand, increasing the dimensions of the opening made in the die was also not an option due to the increased possibility of the melt flowing out of the crucible due to gravity. Thus, the application of metallic (Pt or Ir) crucibles, which are wetted by  $\text{PrF}_3$  melt according to Fig. 22.4 (left), was the only approach that could be used to increase the crystal diameter. The crucible bottom designs used for the crystal growth from the Pt and Ir crucibles are illustrated in Fig. 22.5.

Thus, wetting is an important parameter in the  $\mu$ -PD process. It determines the level of interaction between the melt (liquid phase) and the crucible die (solid phase).

## 22.4 $\text{CaF}_2$ and $\text{BaF}_2$ Crystals

Similar tests of the wetting properties between the melt and carbon (the crucible material) were also performed before attempting to grow other fluorides ( $\text{CaF}_2$ ,  $\text{BaF}_2$ , etc.) The results from these wettability tests of fluoride substances sitting on carbon are presented in Fig. 22.6. The poor wetting observed for  $\text{CaF}_2$  was similar to that of  $\text{PrF}_3$  (see Fig. 22.4 for comparison).

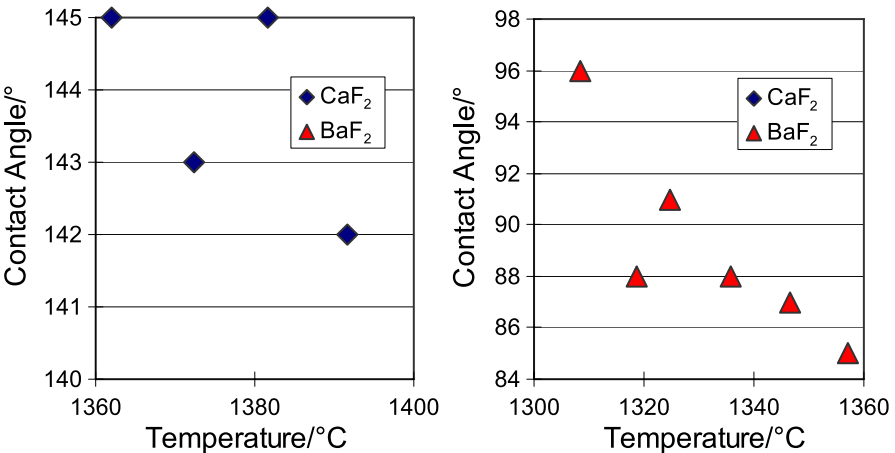


**Fig. 22.6.** Contact angle vs. temperature measured for  $\text{CaF}_2$  (left) and  $\text{BaF}_2$  (right) melts on carbon plate

However, the wetting angles measured for  $\text{BaF}_2$  on carbon were considerably less, demonstrating that  $\text{BaF}_2$  melt was more inclined to spread along the die surface.

### 22.4.1 Other Fluorides

Some of the fluoride crystals produced in fiber (less than 1 mm in diameter) and bulk (over 1 mm in diameter) form are illustrated in Fig. 22.7 (the crucible materials used are also indicated).  $\text{CaF}_2$  and  $\text{BaF}_2$  crystals were grown from carbon crucibles at pulling-down rates of 0.05–0.50 mm/min in an Ar atmosphere (after vacuuming at about  $10^{-3}$  Pa). The crystal diameters were 1.0–2.0 mm.  $\text{BaF}_2$  3.0 mm in diameter was produced at a pulling rate of 0.05–0.30 mm/min from a Pt crucible.

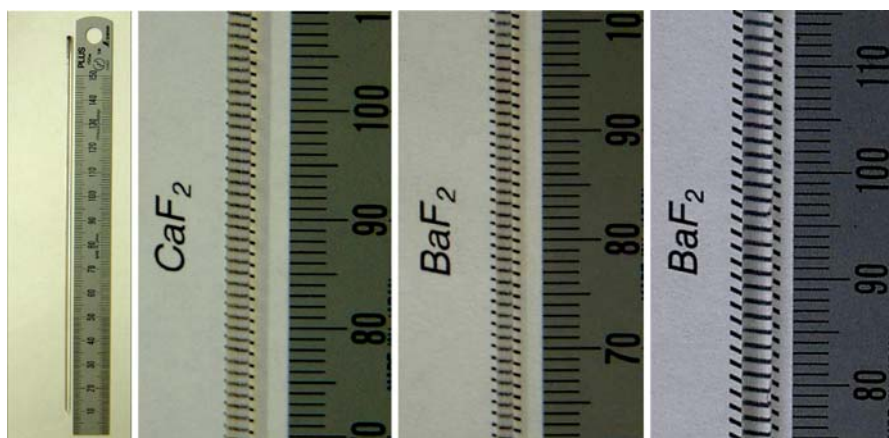


**Fig. 22.7.** View of  $\text{CaF}_2$  and  $\text{BaF}_2$  crystals produced with various diameters from different crucibles: (from left to right)  $\text{CaF}_2$  of  $\varnothing$  1 mm (C),  $\text{CaF}_2$  of  $\varnothing$  2 mm (C),  $\text{BaF}_2$  of  $\varnothing$  1 mm (C),  $\text{BaF}_2$  of  $\varnothing$  3 mm (Pt). Scales are in mm

## 22.5 Doped Crystals

A number of rod-type bulk crystals co-doped with functionally active cations were also grown by  $\mu$ -PD. This was performed in order to investigate the segregation phenomenon in the corresponding fluoride systems. These data are particularly useful for the future development of novel fluorides with specified dopant concentrations and/or distributions within the crystal structure. The growth procedure was similar to that described above. Images of some of these crystals are given in Fig. 22.8.

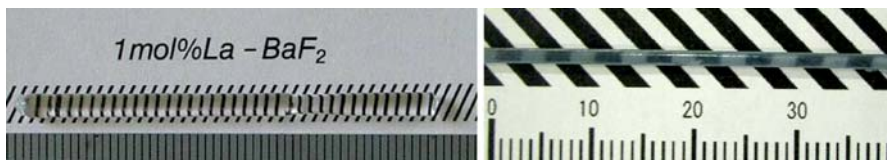


**Fig. 22.8.** View of 1 mol%-doped  $\text{CaF}_2$  of  $\varnothing$  3.0 mm (C crucible) and 3 mol% Ce-doped  $\text{NdF}_3$  (Pt crucible)  $\mu$ -PD crystals

## 22.6 Summary

The growth of shaped (bulk) fluoride crystals by  $\mu$ -PD was reviewed. The results from crystal characterizations [5–7] demonstrate that these materials possess acceptable functional properties. Therefore, we can conclude that the  $\mu$ -PD technology is certainly appropriate for the laboratory growth of a number of fluoride bulk/shaped crystals, and most probably applicable to their industrial commercialization.

## References

1. K. Shimamura, S.L. Baldochi, I.M. Ranieri, H. Sato, T. Fujita, V.L. Mazzocchi, C.B.R. Parente, C.O. Paiva-Santos, C.V. Santilli, N. Sarukura, T. Fukuda, *J. Cryst. Growth*, **223**(3), 383 (2001)
2. H. Sato, H. Machida, M. Nikl, A. Yoshikawa, T. Fukuda, *J. Cryst. Growth*, **250**(1–2), 221 (2003)
3. H. Sato, A. Bensalah, H. Machida, M. Nikl, T. Fukuda, *J. Cryst. Growth*, **253**(1–4), 83 (2003)
4. T. Fukuda, P. Rudolph, S. Uda, (eds.), *Fiber Crystal Growth from the Melt*, (Springer, Berlin, 2004)
5. A. Yoshikawa, K. Kamada, T. Satonaga, K. Aoki, M. Nikl, T. Fukuda, *65th Autumn Meeting of the Japanese Society of Applied Physics (JSAP)*, Sendai, Japan (2004)
6. A. Yoshikawa, K. Kamada, K. Aoki, T. Satonaga, T. Fukuda, *Proceedings of the 49th Symposium on Synthetic Crystals*, Tsukuba, Japan (2004)
7. A. Yoshikawa, T. Satonaga, K. Kamada, H. Sato, M. Nikl, N. Solovieva, T. Fukuda, *J. Cryst. Growth*, **270**, 427 (2004)
8. V.I. Chani, A. Yoshikawa, H. Machida, T. Satoh, T. Fukuda, *J. Cryst. Growth*, **210**(4), 663 (2000)

# 23 Metal Alloy Fibers

Akira Yosikawa and Yuji Sutou

**Abstract.** The purpose of this short chapter is to discuss the ability of the micro-pulling-down system to grow metallic alloy fibers. Preliminary examinations of the material properties of fibers grown in this way and their applicability to industrialization are particularly useful. Some examples of the solidification of such alloys are given here.

The solidification of metallic alloy fibers using the micro-pulling-down ( $\mu$ -PD) system is another application of the method discussed in this book. Interest in growing such fibers has arisen, for example, from the need to develop a novel device called a stent. Stents are predominantly utilized to permanently widen narrow arteries by inserting them inside the human body. This type of treatment improves blood flow, aiding the delivery of oxygen to organs. The two most important properties of stents are therefore expandability and flexibility. The fabrication of these devices is typically achieved by weaving thin wires or by cutting tubes with a laser.

Polycrystalline Ni–Ti shape memory alloys (SMA) are widely used to assemble the stents. Ni–Ti has excellent flexibility and shape maintenance, due to its superelasticity/pseudoelasticity (PE), compared with other conventional medical materials such as stainless steel (AISI316L). It has recently become necessary to improve the flexibility of these stent materials still further, due to the fact that stent is now also being applied to peripheral vessels and carotid arteries near the skin.

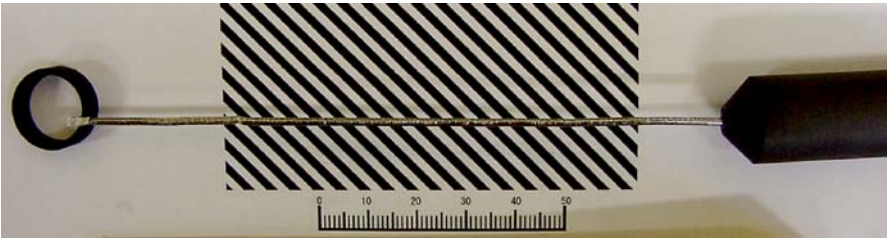
It is known that single-crystalline SMAs exhibit high ductility and a large PE recoverable strain [1]. For example, a recoverable strain of over 18% can be obtained in Cu-based SMAs crystals of a specific orientation [2, 3], while polycrystalline Ni–Ti SMAs possess a recoverable strain of only about 8%. Therefore, the production of single-crystalline thin fibers and tubes with PE properties is an important task that should permit the development of the next generation of stents possessing improved performance.

Ni<sub>54</sub>Ga<sub>27</sub>Fe<sub>19</sub> alloy [4–6] fibers have been produced using  $\mu$ -PD apparatus with inductive RF heating. A recoverable strain of over 13% was observed in these materials oriented along the  $\langle 100 \rangle$ , direction according to [7]. This crystals were grown from a graphite crucible 15 mm in diameter and 150 mm in length. The crucible was heated to the melting temperature of the mixture placed into the crucible reservoir. The process temperature was about

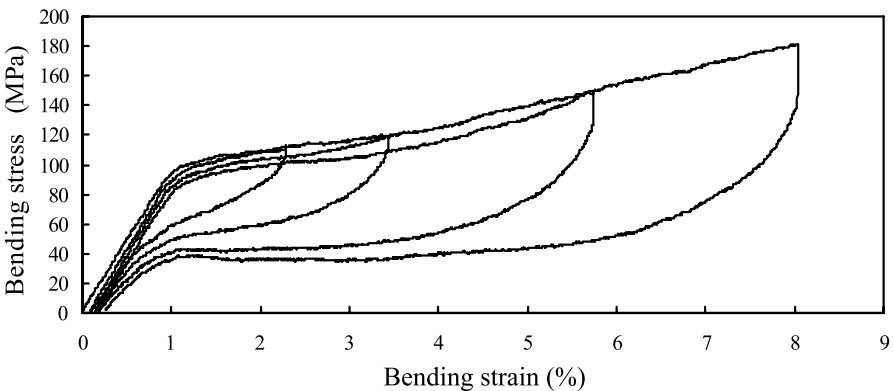
1200 °C. The procedure was performed in an Ar atmosphere to avoid oxidation of both the crucible and the melted material. The pulling-down rate used was 10 mm/h. An image of the fiber together with the crucible is given in Fig. 23.1.

Figure 23.2 shows stress–strain curves measured at room temperature using a bending cyclic test for a  $\text{Ni}_{54}\text{Ga}_{27}\text{Fe}_{19}$  fiber crystal with a diameter of 1.5 mm and length of about 100 mm. This material demonstrated excellent superelasticity (over 8%). Moreover, according to preliminary reports, similar fibers can also be used as magnetically controlled actuator materials, since Ni–Ga–Fe alloys also have ferromagnetic properties [4–6]. These SMA fiber crystals produced using  $\mu$ -PD are therefore considered to be promising materials for both medical and engineering applications.

The  $\mu$ -PD solidification of  $\text{Cu}_{72}\text{Al}_{17}\text{Mn}_{11}$  alloy was chosen as an alternative procedure for fabricating Cu-based SMA single crystals. This alloy system is made from cheaper constituents than standard Ni–Ti alloy, which makes it more cost-effective to use. It also demonstrates a large recoverable strain [8,9]. The solidification was performed from an  $\text{Al}_2\text{O}_3$  ceramic crucible, which is illustrated in Fig. 23.3 together with the as-grown fiber.



**Fig. 23.1.** View of Ni–Ga–Fe alloy fiber produced from carbon crucible (*right*) with conically shaped bottom (Scale in mm)



**Fig. 23.2.** Stress–strain curves of  $\text{Ni}_{54}\text{Ga}_{27}\text{Fe}_{19}$  fiber crystal as measured at room temperature



**Fig. 23.3.** View of  $\text{Cu}_{72}\text{Al}_{17}\text{Mn}_{11}$  alloy fiber produced from  $\text{Al}_2\text{O}_3$  ceramic crucible (left) with spherically shaped bottom (Scale in mm)

Both of the growth processes introduced above were relatively stable in terms of the diameter of the resulting fiber. Moreover, no problems related to melt overflow resulting from inappropriate wetting properties, degradation of the melt performance, etc., were detected.

*Acknowledgement.* Authors would like to thank Prof. Katsunari Oikawa, Prof. Kiyoshi Yamauchi, Prof. Ryosuke Kainuma and Prof. Kiyohito Ishida for their fruitful suggestions and valuable discussion throughout study of the materials discussed in this chapter.

## References

1. T. Saburi, S. Nenno, *Proc. Int. Conf. on Solid-Solid Phase Transformations*, ed. by H.I. Aaronson, D.E. Laughlin, R.E. Sekerka, C.M. Wayman (AIME, New York, 1982), pp. 1455–79
2. K. Otsuka, H. Sakamoto, K. Shimizu, *Acta Metall.*, **27**, 585 (1979)
3. T. Saburi, Y. Inada, S. Nenno, N. Hori, *J. Phys. C*, **4**, 633 (1982)
4. K. Oikawa, T. Ota, T. Ohmori, Y. Tanaka, H. Morito, A. Fujita, R. Kainuma, K. Fukamichi, K. Ishida, *Appl. Phys. Lett.*, **81**, 5201 (2002)
5. K. Oikawa, T. Ota, Y. Sutou, T. Ohmori, R. Kainuma, K. Ishida, *Mater. Trans.*, **43**, 2360 (2002)
6. H. Morito, A. Fujita, K. Fukamichi, T. Ota, R. Kainuma, K. Ishida, K. Oikawa, *Mater. Trans.*, **44**(4), 661 (2003)
7. Y. Sutou, N. Kamiya, T. Omori, R. Kainuma, K. Ishida, K. Oikawa, *Appl. Phys. Lett.*, **84**, 1275 (2004)
8. R. Kainuma, S. Takahashi, K. Ishida, *Metall. Mater. Trans. A*, **27**, 2187 (1996)
9. Y. Sutou, T. Omori, R. Kainuma, N. Ono, K. Ishida, *Metall. Mater. Trans. A*, **33**, 2817 (2002)

## Afterword

When preparing their manuscripts, all of the authors tried their best to make their chapters flow together to form a continuous story about micro-pulling-down crystal growth in terms of its developmental history, its achievements, and perspectives on it. Their efforts to create a volume as close as possible to a one-author monograph are appreciated greatly. It was their wish to make the text and the style uniform and convenient for every reader.

Sometimes the authors' point of view and conclusions were different from those of the editors. Where such conflicts occurred, the authors' opinions took priority because all of the authors are experts in their particular fields. Therefore, all of the contributions that appear in this book represent, to some degree, the personal opinions of the authors, but not those of the editors.

Much effort has been expended to ensure that the discussions and conclusions that appear in this volume are free from logical errors and/or omissions. However, we understand that in some cases the readers will not accept the authors' point of view, due to their own experience and scientific background. The authors and editors are open to criticism and subsequent discussions on the topics of their contributions. It is well known that differences of opinion often ultimately drive us toward a better understanding of the physical or chemical process in question. An improved understanding of novel technology, including the one that is the subject of this book, is also expected when disagreements between different points of view regarding this technology are resolved.

Many researchers, representing various countries, contributed to the development of the technological innovations and specific materials discussed in this book. These people, ranging from students and technicians to professors and leaders of research projects, often educated the authors through direct collaboration and/or discussions about problems directly or indirectly related to the topics reviewed here. Therefore, the authors wish to thank G. Boulon, E. Casse, S.D. Durbin, J.-M. Fourmigue, C. Fujuwara, K. Hasegawa, A. El Hassouni, B. Hautefeuille, K. Inaba, K. Inoue, Y. Kagamitani, H. Kaiden, K. Kamada, K.J. Kim, A.V. Klassen, V.V. Kochurikhin, J.M. Ko, L.L. Kuandykov, Y. Kuwano, C.W. Lan, J.H. Lee, M. Man-

sori, B.V. Mill, J.H. Mun, H. Ogino, C. Pédrini, I.M. Ranieri, P. Rudolph, A. Sasaki, N. Schäfer, J.B. Shim, K. Shimamura, Y. Shoji, R. Simura, T. Shishido, H. Takeda, S. Uda, Y.M. Yu, M. Zhuravleva, and many others for sharing their experiences, their technical assistance, and their collaborations.

January 2007

*T. Fukuda*

*V.I. Chani*

# Index

- absorption 105, 162, 167, 168, 187,  
199, 225, 255, 285, 297, 314
  - cross-sections 162
  - optical 210
  - spectra 166
- activator 160
- afterheater 27, 288
  - multi-window 40, 63, 241
  - window 39
- anisotropy 79
- annealing 166
- antisite defect 103
- aspect ratio 3, 10, 86, 252
- atmosphere 267
  - Ar and CF<sub>4</sub> gases 303
  
- blue laser sources 219
- Bridgman 98, 130, 190, 230
  - vertical 98
- bubble 7, 15, 85, 190, 223, 243
  
- capillary action 20
  - measurement 20
- capillary channel 76, 191
  - laminar flow 97
  - pinholes 245
  - SiC 281
  - slit-type 245
- cation distribution 207
  - along the growth axis 207
  - axial 319
  - inhomogeneous 207
  - K(Y<sub>0.59</sub>Lu<sub>0.40</sub>Pr<sub>0.01</sub>)<sub>3</sub>F<sub>10</sub> 319
  - Pr<sup>3+</sup> along growth axis of KY<sub>3</sub>F<sub>10</sub> 316
- Ce<sup>3+</sup> 160
- Ce:YAP 159, 163
- charge transfer luminescence 149
  
- color centers 145, 166
- composition 269
- contact angle 41, 230, 327
  - measurement 326
  - vs. temperature 327
- continuous feeding 10
- crucible 12, 29, 33, 278, 281, 288
  - Al<sub>2</sub>O<sub>3</sub> 332
  - amorphous carbon 278
  - carbon 303
  - cross-section 122
  - graphite 5, 280, 282, 331
  - Ir-Re(2%) 204
  - iridium 12, 174
  - material 33
  - Mo 39
  - multicapillary 78
  - multidie 65
  - Pt 221
  - shape 36
  - vitreous carbon 279, 282
- crucible cleaning 191, 325
  - boiling in HCl 192
  - H<sub>3</sub>PO<sub>4</sub>+H<sub>2</sub>SO<sub>4</sub> mixture 191
  - HNO<sub>3</sub>O + H<sub>2</sub>O 117
- crucible material 230, 324
  - carbon 324
  - graphite 288
  - Ir, Ir-Rh, Pt, Pt-Rh, Pt-Au, Mo, Ta, Re, and W 235
  - iridium 103, 239, 324
  - molybdenum 244
  - platinum 288, 324
  - Pt-Au alloys 231
  - Pt-Rh (10%) alloy 231
  - rhodium 189
- crystal 3
  - (β<sub>II</sub>)-Li<sub>3</sub>VO<sub>4</sub> 6

- (Gd,Y)F<sub>3</sub> 304  
 (Tm<sub>x</sub>Y<sub>1-x</sub>)<sub>2</sub>O<sub>3</sub> 196  
 (Yb<sub>x</sub>Sc<sub>1-x</sub>)<sub>2</sub>O<sub>3</sub> 195  
 (Yb<sub>x</sub>Y<sub>1-x</sub>)<sub>2</sub>O<sub>3</sub> 192  
 Al<sub>2</sub>O<sub>3</sub> 239  
 BaF<sub>2</sub> 328  
 Bi<sub>12</sub>SiO<sub>20</sub> 12, 13  
 Bi<sub>4</sub>Ge<sub>3</sub>O<sub>12</sub> 9  
 CaF<sub>2</sub> 328  
 CaWO<sub>4</sub> 5, 9  
 Ce:AE:(Gd,Y)F<sub>3</sub> 301  
 Cr-doped sapphire 241  
   garnet 101  
 Gd<sub>3</sub>Ga<sub>5</sub>O<sub>12</sub> 101  
 Gd<sub>3</sub>Sc<sub>2</sub>Al<sub>3</sub>O<sub>12</sub> 13  
 K<sub>3</sub>Li<sub>2</sub>Nb<sub>5</sub>O<sub>15</sub> 5, 219  
 K(Y,Lu)<sub>3</sub>F<sub>10</sub> 318  
 KNbO<sub>3</sub> 9  
 KY<sub>3</sub>F<sub>10</sub> 314  
 La<sub>3</sub>Ga<sub>5</sub>SiO<sub>14</sub> 229  
 La<sub>3</sub>M<sup>4+</sup>Ga<sub>5</sub>O<sub>14</sub> 230  
 La<sub>3</sub>Me<sub>0.5</sub>Ga<sub>5.5</sub>O<sub>14</sub> 229  
 Li<sub>2</sub>B<sub>4</sub>O<sub>7</sub> 12  
 Li<sub>3</sub>VO<sub>4</sub> 15  
 LiF 287  
 LiNbO<sub>3</sub> 5, 11, 12, 251  
 LiTb<sub>0.9</sub>Eu<sub>0.1</sub>P<sub>4</sub>O<sub>12</sub> 93  
 Lu<sub>2</sub>O<sub>3</sub> 188  
 NdF<sub>3</sub> 330  
   piezoelectric 229  
 PrF<sub>3</sub> 323  
   price 174  
 Re<sub>3</sub>Ga<sub>5</sub>SiO<sub>14</sub>; Re = Nb, Pr, La 232  
   sapphire 239  
 Sc<sub>2</sub>O<sub>3</sub> 188  
 Si<sub>1-x</sub>Ge<sub>x</sub> 5  
 Tb<sub>3</sub>Ga<sub>5</sub>O<sub>12</sub> 17  
 TiO<sub>2</sub> 11  
 Y<sub>2</sub>O<sub>3</sub> 188  
 Y<sub>3</sub>Al<sub>5</sub>O<sub>12</sub> 101, 173  
 Y<sub>3</sub>Fe<sub>2</sub>(FeO<sub>4</sub>)<sub>3</sub> 101  
 Y<sub>3</sub>Ga<sub>5</sub>O<sub>12</sub> 101  
 Yb<sub>2</sub>O<sub>3</sub> 188  
 YVO<sub>4</sub> 11  
 crystal field 167, 213, 303  
 crystal rotation 10  
 Cu<sub>72</sub>Al<sub>17</sub>Mn<sub>11</sub> 332  
 Czochralski 101, 111, 123, 173, 189,  
   230, 295  
   decay kinetic 143  
   decay time 159, 163, 199, 307, 316  
   diameter control 113, 123  
     evaporation-induced 123  
   diameter ratio 125  
     capillary/crystal 125  
   die 19, 20, 37, 78, 105, 326  
     concave 108  
     convex 108  
     porous 78  
     ring-shaped 242  
     shape 107  
   dopant distribution 110, 167, 197, 296  
     along the growth axis 256  
     axial 111  
     Nd 294  
     neodymium 179  
   drops 187  
   Earth's upper mantle 265  
   Edge-Defined Film-Fed Growth (EFG)  
     3, 18, 110, 130, 175, 190, 236, 244  
     inverted 21  
   effective segregation coefficient 111,  
     197, 207, 271, 309  
     Yb<sup>3+</sup> in Gd<sub>1-x</sub>Yb<sub>x</sub>F<sub>3</sub> 309  
   Electron Back-Scattering Diffraction  
     (EBSD) 131  
   Ellingham diagram 266  
   emission 163, 168, 181, 199, 256, 288,  
     297, 307, 316  
     blue 203, 211  
     broadband 212  
     cross-section 163  
     green 204  
     infrared 204  
   energy levels diagram 169  
   EPMA 208, 309, 316  
   equilibrium segregation coefficient  
     271  
   Equipment 45  
   equipment  
     manufacturer 49  
   Etch Pit Density (EPD) 248  
   eutectic 127  
     directional solidification 129

- etching 136
- hybrid structures 135
- oxide-oxide 129
- periodicity of the structure 137
- PrAlO<sub>3</sub>-Pr<sub>2</sub>O<sub>3</sub> 134
- PrAlO<sub>3</sub>-PrAl<sub>11</sub>O<sub>18</sub> 134
- rodlike structure 130
- selective doping 131
- structure 129
- Tb<sub>3</sub>Sc<sub>2</sub>Al<sub>3</sub>O<sub>12</sub>-TbScO<sub>3</sub> 130
- eutectic composites 37
- evaporation 13, 70, 113
  - Bi<sub>2</sub>O<sub>3</sub> 115, 121
  - flux 113
  - isothermal 113
  - rate 125
- faceting 82, 104, 105, 176, 195
- fayalite 269
- feeding 8, 11, 12
  - automatic 222
  - continuous 8, 61, 223, 230, 234
  - powder 11
  - rods 11
  - unidirectional 306
- fiber crystal 16, 22, 36, 55, 93, 96, 106, 115, 163, 175, 189, 222, 252
  - Bi<sub>4</sub>Ge<sub>3</sub>O<sub>12</sub> 84
  - fluoride 287
  - KNbO<sub>3</sub> 83
  - metallic alloy 331
- floating zone 5, 10
  - crucible-less 6
- flow velocity 268
- fluoride 287, 301
  - binary 301
  - Ce-doped 303
  - Pr-doped 303
  - shaped 323
  - trifluoride 301
- flux 14, 79, 93
  - Bi<sub>2</sub>O<sub>3</sub> 115
  - LiPO<sub>4</sub> 93
  - LiVO<sub>3</sub> 15
  - self-flux 115
- flux growth 9, 74
- forsterite 269
- freezing 283
- FZ 76
- gamma-ray spectroscopy 164
- garnet 131
  - dodecahedral sites 131
- gravity 9
- growth
  - from stoichiometric melt 72
  - growth atmosphere 34, 70, 103, 191 (75%) and CF<sub>4</sub> (25%) 291
  - Ar+H<sub>2</sub> (3 vol%) 192
  - argon 240
  - die edge sharpness 109
  - formation of CO gas 245
  - N<sub>2</sub> + 10% O<sub>2</sub> 235
  - neutral-to-oxidizing 103
  - reducing 196
- growth chamber 57, 244, 303
  - atmosphere control 323
  - CaF<sub>2</sub> window 324
  - copper 290
  - Ni-Cu alloy 290
  - size 291
  - stainless steel 290
  - traces of water 289
  - vacuum treatment 324
- growth interface 6, 104, 190, 288
  - boundary layer near 176
  - conical 104
  - visualization 57
- growth step 82
- Heat Exchanger Method (HEM) 190
- heater 6, 10, 13
  - carbon 303
  - external 303
  - graphite 244
  - iridium 10, 11, 14
  - molybdenum 14
  - outer 52, 118
  - platinum 15
  - resistive 13
  - strip 6, 10, 11, 15
- heating 5, 6, 8, 27
  - external 5, 6, 30, 32
  - inductive 30, 32, 54, 331
  - internal 5, 6, 8, 28, 30
  - resistive 28, 30, 51, 116, 244, 288
  - RF 5, 12, 30, 32, 240
- high-melting oxides 204
- homogeneity 224

- impurities 288
- inclusion 103, 176
  - eutectic mixtures 106
- industrialization 59
- ionic radii 207, 301, 311
  - average 311
- isothermal flux evaporation 115
- langasite 229
  - cation sites 229
- laser 173, 210, 251, 287, 301, 323
  - blue 212
  - emission 182
  - infrared 214
  - projection display 220
  - tunable solid-state 210
- laser host 187
- Laser-Heated Pedestal Growth (LHPG)
  - 3, 16, 130, 189, 252, 287
- lattice constant 107, 269
  - compositional dependence 194
  - variation 224
- light yield 143, 170
- light-guiding 183
- $\text{Lu}_3\text{Al}_5\text{O}_{12}$  165
- luminescence 105, 144, 165, 181, 312
  - Bi-doped crystals 151
  - $\text{Pr}^{3+}$  303
- magnetite 267
- Marangoni convection 22, 93, 110, 130
- melt 69, 109
  - backflow through the capillary 111
  - composition 69
  - eutectic 97
  - mixing 93
  - overflow 110
  - overheating 109
  - Si 281
  - stoichiometric 302
- melt flow 76
- meniscus 96, 108, 117, 277, 288
  - length 177
- meniscus height 273
- metamaterials 137
- $\text{MgAl}_2\text{O}_4$  203
  - Ti-doped 211
- micro-pulling-down 3, 17, 23
- microrod 130
  - $\text{TbScO}_3$  130
- minerals
  - synthetic 265
- multicrystal growth 63
- $\text{Ni}_{54}\text{Ga}_{27}\text{Fe}_{19}$  331
  - stress-strain curves 332
  - superelasticity 332
- Ni-Ti 331
- olivine 264
- orientation 22, 42, 284
  - off-angle 43
- outer heater 28
- oxidation 205
  - doping cations 205
- partial pressure 266
  - of oxygen 266
- perovskite 130, 302
  - icosahedral sites 131
- phase 302
  - formation 302
- phase diagram 220, 310
  - $\text{LiF-YF}_3$  291
- phase transition 134, 301
  - subsolidus 301
  - temperature 301
- phase-matching 224
- photoluminescence 258
- photonic crystals 129
- polycrystalline materials 11
  - $\text{Bi}_{2.1}\text{Y}_{0.1}\text{Sr}_{1.9}\text{CaCu}_{2-x}\text{Li}_x\text{O}_8$  11
  - superconducting 11
- powder pattern 269
- pulling-down rate 226, 283
- radioluminescence 143, 147, 153
- rare-earth sesquioxide 187
- rotation 11
- sapphire
  - Ti-Doped 210
- scanograph 123
- scattering 179
- scintillation 159, 174
  - detector 323
  - light yield 164
- scintillation decay 155

- scintillator 105, 144, 155
  - Pr-doped 156
  - Pr-doped oxide crystals 154
- Second Harmonic Generation (SHG) 219
- seed 82, 106, 282
  - W–Re alloy 304
  - W–Re wire 192
  - yttria ceramic 192
- segregation 19, 22, 71, 98, 165, 179, 207, 220, 252, 271, 292
  - coefficient 305
  - effect of growth rate 72
  - Yb in garnet 165
- segregation coefficient 270, 293
  - of  $\text{Pr}^{3+}$  in  $\text{K}(\text{Y}, \text{Lu})_3\text{F}_{10}$  318
  - of  $\text{Pr}^{3+}$  in the  $\text{KY}_3\text{F}_{10}$  314
- self-organized structures 129
- Shape Memory Alloys (SMA) 331
- shaped crystal 8, 11, 175
  - cylindrical 14
  - fluoride 323
  - growth steps 83
  - plate 14, 36, 37, 221, 222, 231, 244
  - rod 36, 190, 205, 236, 241, 313, 329
  - round 106
  - square 106, 205
  - tube 14, 36, 242
- shaper 13, 14, 18
  - porous 19
- SHG output 226
- silicon 277
  - impurities 282
- skull-melting 189
- solid solution 5, 75, 104, 195, 269, 301, 305, 318
  - continuous 305
  - $\text{Gd}_{1-x}\text{Yb}_x\text{F}_3$  309
  - ratio 302
- spectroscopy 210
- spinel 202, 206
  - structure 204
- Stark level 168
- stent 331
- Stepanov 3, 18, 24, 107, 175
- structural stability 302
- temperature
  - instability 281
  - temperature distribution 39, 54, 56, 241, 292
    - asymmetrical 39, 241
  - temperature gradient 84, 94, 112, 130, 160, 177, 253, 273, 278, 285, 292
  - thermal conductivity 174, 198, 209, 210, 239, 278
  - thermal expansion 209
  - thermocouple 281
  - transition metal 203
  - transmission 182, 222, 239, 256, 323
    - sapphire 246
  - transparency 188, 289
- TSSG 225
- Vegard's law 107, 147, 194, 320
- Verneuil 101, 189
- vibrations 10, 59
- VIRGO 277
- wüstite 264
- wetting 6, 19, 21, 40, 175, 235, 292, 325
  - influence of the gas composition 293
    - LGS 231
    - $\text{Lu}_2\text{O}_3$  melt 194
    - rhenum 193
    - $\text{Y}_2\text{O}_3$  193
- X-ray diffraction (XRD) 131, 206, 231, 284, 295, 305, 310, 315
- X-ray Rocking Curve (XRC) 112, 197, 207, 223